THERMO-TECTONIC EVOLUTION AND SOURCE ROCK MATURATION IN THE GIPPSLAND BASIN (OFFSHORE VICTORIA) AND IN THE CENTRAL EROMANGA BASIN (COOPER REGION), AUSTRALIA

Von der Fakultät für Georessourcen und Materialtechnik

der Rheinisch-Westfälischen Technischen Hochschule Aachen

zur Erlangung des akademischen Grades eines

Doktors der Naturwissenschaften

genehmigte Dissertation

vorgelegt von

Joschka Röth, M.Sc.

Berichter: Univ.-Prof. Dr.rer.nat. Ralf Littke

Univ.-Prof. Dr.rer.nat. Magdalena Scheck-Wenderoth

Tag der mündlichen Prüfung: 22.12.2020

Diese Dissertation ist auf den Internetseiten der Universitätsbibliothek online verfügbar.

Für Liesl, Hans und Anton.



We are all visitors

To this time, this place.

We are just passing through.

Our purpose here is to observe,

To learn, to grow, to love … and then

…

We return home.

Australian Aboriginal proverb

ABSTRACT

Increasing global demand for primary energy calls for new exploration activities, requires steady reassessment of existing energy resources, and is continuously driving technological innovation. Especially in Australia, the world's largest coal exporter, incentives are growing to produce cleaner, more efficient and sustainable energy.

The Australian continent features a multitude of partly overlapping and stacked sedimentary basins, which are hosting large amounts of various energy resources. The methodology of numerical basin and petroleum system modeling has established as an important tool to understand the multiple geological factors, which are interacting in sedimentary systems and which decide about the timing of generation, quality and quantity of generated energy resources, e.g. oil and gas. A brief introduction of this methodology is given in the first chapter together with an overview of Australia's energy resources. The second chapter provides an overview about the tectonic evolution of Australia. The main part of the thesis contains three individual studies about two important Australian petroleum provinces: the Gippsland Basin and the Cooper/Eromanga Basin couplet.

In chapter 3, numerical basin modeling was performed to investigate the thermo-tectonic evolution of the offshore Gippsland Basin and the consequences for source rock maturation and petroleum generation. An extensive 3D dataset of the Gippsland Basin was modified and analyzed. Methods also included the seismic interpretation of sedimentary horizons and the basement topography, mapping of major faults and magmatic features and the application of numerical crustal layer models. The thermal history was reconstructed by using a two-step inversion workflow, which derives crustal stretching from tectonic subsidence and then converts stretching maps into basal heat flow maps. The new data was then integrated into the existing digital 3D basin model and scenario modeling was performed based on a purpose-built calibration matrix. Results show that substantial stretching caused increased heat flow throughout the basin center in the Middle Cretaceous. Maturation of Late Cretaceous source rocks and associated petroleum generation occurred during Paleocene and Neogene because of thermal subsidence rather than transient basal heat flow.

Chapter 4 deals with the analysis of the source rock potential of the Middle Jurassic Birkhead Formation and the Early Cretaceous Murta Formation based on 55 core samples taken from eight petroleum wells in the Eromanga Basin. Applied methods include Rock-

Eval pyrolysis, organic petrography and organic geochemical analysis to evaluate the paleo-depositional environment, petroleum generation potential, and thermal maturity of these two Mesozoic source rock formations. Results show that the Birkhead Formation has a generally higher source potential than the Murta Formation, but features a lower conversion. Biomarker analysis indicates terrestrial/lacustrine paleo-depositional environment for both formations. During petrographic analysis, numerous remains of higher land plants (vitrinite, cutinite) were found in either formation, while typical fresh-water green algae was detected only in the Murta Formation. Both source rock formations are thermally immature to early mature and are expected to have locally contributed to hydrocarbon migration and charge of the Eromanga petroleum system.

In Chapter 5, the existing 3D basin model of the Cooper/Eromanga basin couplet was modified and analyzed. Comprehensive literature research, new input from recent studies (including obtained source rock data from chapter 4) and remarkably detailed vitrinite reflectance profiles helped to improve the model input. Calibrated local heat flow trends from 1D petroleum system models were projected to regional heat flow maps and then used as input for the 3D model. The output of the 3D model includes detailed source rock maturation maps, kerogen transformation maps and the subsurface temperature distribution throughout the entire basin history. Analysis of layer thickness maps and depocentre migration provided additional insights into the complex tectonic evolution. It turned out that the early geological history of the Cooper Basin was mainly characterized by the formation of a pull-apart basin, which transformed into a piggyback basin before it was blanketed by the deposits of the Eromanga Basin. Intermittently, the study area was strongly affected by a continental hot spot and a previously overlooked intracontinental shear zone. Extraordinary sedimentation rates during the Middle Cretaceous were accompanied by a strong regional hydrothermal event, which obviously overprinted all previous thermal signals and caused rapid source rock maturation and intense hydrocarbon generation.

ZUSAMMENFASSUNG

Weltweit wachsender Bedarf an Primärenergie erfordert neue Explorationsaktivitäten, verlangt eine ständige Neubewertung der vorhandenen Energieressourcen und treibt die technologische Innovation kontinuierlich voran. Insbesondere in Australien, dem weltweit größten Kohle-Exporteur, wachsen die Anreize, sauberere, effizientere und nachhaltigere Energie zu produzieren.

Der australische Kontinent weist eine Vielzahl sich teilweise überlappender und übereinander gestapelter Sedimentbecken auf, die große Mengen verschiedener Energieressourcen beherbergen. Die Methodik der numerischen Sedimentbecken-Modellierung hat sich als wichtiges Instrument zum Verständnis der zahlreichen geologischen Faktoren etabliert, die in den Sedimentsystemen zusammenwirken und über den Zeitpunkt der Bildung, die Qualität und die Quantität der generierten Energieressourcen, z.B. Erdöl und Erdgas, entscheiden. Zusammen mit einem Überblick über die Energieressourcen Australiens, wird im ersten Kapitel eine kurze Einführung in die Methodik gegeben. Das zweite Kapitel fasst die tektonische Entwicklung Australiens zusammen. Der Hauptteil der Arbeit enthält drei Einzelstudien über zwei wichtige australische Erdölprovinzen: das Gippsland Becken und das Cooper/Eromanga Becken.

In Kapitel 3 wurde eine numerische Sedimentbeckenmodellierung durchgeführt, um die thermo-tektonische Entwicklung des seewärtigen Gippsland Beckens und die Folgen für die Reifung der Muttergesteine und die Erdölproduktion zu untersuchen. Ein umfangreicher 3D-Datensatz des Gippsland Beckens wurde modifiziert und analysiert. Zu den Methoden gehörten auch die seismische Interpretation von Sedimenthorizonten und die Modifizierung der Topographie des Grundgebirges, die Kartierung von Hauptverwerfungen und magmatischen Merkmalen sowie die Anwendung von numerischen Krustenschichtmodellen. Die thermische Entwicklung wurde mit Hilfe eines zweistufigen Verfahrens rekonstruiert, das die Krustendehnung aus tektonischer Absenkung ableitet und dann aus der Dehnung den basalen Wärmefluss errechnet. Die neuen Daten wurden dann in das bestehende digitale 3D-Beckenmodell integriert, und auf der Grundlage einer speziellen Kalibrierungsmatrix wurden verschiedene Szenarien berechnet. Die Ergebnisse zeigen, dass erhebliche Dehnung in der Mittelkreide zu einem erhöhten Wärmestrom im Beckenzentrum führte. Die Hauptreifung der spätkretazischen Muttergesteine und die damit verbundene Erdölbildung traten während des Paläozäns und im Neogen allerdings eher als Folge von thermischer Absenkung auf.

Kapitel 4 befasst sich mit der Analyse der Birkhead-Formation aus dem mittleren Jura und der Murta-Formation aus der frühen Kreidezeit anhand von 55 Kernproben, die aus acht Erdölbohrungen im Eromangabecken entnommen wurden. Zu den angewandten Methoden gehören Rock-Eval-Pyrolyse, organische Petrographie und organisch-geochemische Analyse zur Bewertung der Paläo-Ablagerungsbedingungen, des Erdölbildungspotenzials und der thermischen Reife dieser beiden mesozoischen Erdöl-Muttergesteine. Die Ergebnisse zeigen, dass die Birkhead-Formation im Allgemeinen ein höheres Erdölbildungspotenzial als die Murta-Formation besitzt, jedoch eine geringere Umwandlung aufweist. Die Biomarker-Analyse zeigt für beide Formationen ein terrestrisch/lakustrisches Paläo-Ablagerungmilieu an. Bei der petrographischen Analyse wurden in beiden Formationen zahlreiche Überreste von höheren Landpflanzen (Vitrinit, Cutinit) gefunden, während typische Süßwasser-Grünalgen nur in der Murta-Formation auftreten. Beide Formationen sind thermisch unreif bis frühreif und sie haben offenbar lokal zu Migration und Reservoirbildung im Eromanga-Erdölsystem beigetragen haben.

In Kapitel 5 wurde das bestehende 3D-Beckenmodell des Cooper/Eromanga-Beckenpaares modifiziert und analysiert. Umfassende Literaturrecherche, neuer Input (einschließlich der in Kapitel 4 erhaltenen Daten) und bemerkenswert detaillierte Vitrinitreflexionsprofile trugen zur Verbesserung des Modells bei. Kalibrierte lokale Wärmeflusstrends aus 1D-Erdölsystem-Modellen wurden auf regionale Wärmefluss-karten projiziert und dann als Input für das 3D-Modell verwendet. Zu den Ergbenissen der 3D-Modellierung gehören detaillierte Reifekarten der Muttergesteine, Karten zur Kerogen-Transformation und zur Temperaturverteilung über die gesamte Geschichte des Beckens. Die Analyse von Schichtmächtigkeiten und Migration von Depozentren lieferte zusätzliche Einblicke in die komplexe tektonische Entwicklung. Es zeigt sich, dass die frühe geologische Geschichte des Cooperbeckens hauptsächlich durch die Bildung eines pull-apart Beckens gekennzeichnet war, das sich in ein piggyback Becken verwandelte, bevor es von Sedimenten des Eromangabeckens überlagert wurde. Zeitweise wurde das Untersuchungsgebiet stark durch einen kontinentalen Hot Spot und eine bisher übersehene Scherzone beeinflusst. Außergewöhnliche Sedimentationsraten während der mittleren Kreide wurden von einem starken regionalen hydrothermalen Ereignis begleitet, das offensichtlich alle früheren thermischen Signale überlagerte und eine rasche Reifung der Muttergesteine und eine intensive Kohlenwasserstoffbildung verursachte.

ACKNOWLEDGEMENTS

First, I would like to acknowledge Prof. Dr. Dietrich H. Welte, who motivated me to start this project and who realized a travel grant (funded by VAG e.V., Vereinigung Aachener Geowissenschaftler) to cover the field trip to Australia for core inspection and sampling.

I would like to thank my supervisor, Univ.-Prof. Dr. Ralf Littke, who gave me this unique opportunity to fine-tune my geological expertise. From start to finish, he gave regular support during data evaluation and sample collection, he provided invaluable feedback on preliminary results and draft manuscripts and he always increased the pressure at the right time in the right quantity to help me achieving important milestones.

I would also like to acknowledge Geoscience Australia (GA) for providing the datasets used in this thesis and for the original PetroMod model of the Gippsland Basin, which was built in conjunction with Schlumberger. In this context, I am also particularly thankful for the great support and hospitality of Dr. Lisa Hall and Dr. Chris Boreham.

Additionally, I like to thank Schlumberger GmbH Aachen for providing the academic software licenses and for the individual support by Dr. Thomas Hantschel, Dr. Björn Wygrala, Dr. Adeline Parent, Dr. Daniel Palmowski, Dr. Thomas Fuchs, Cassandra Warren, Nour Koronful, Sami Sheyh Husein, Carlos Andres Sanchez Torres, Carlos Hidalgo Calderon, Anett Engbrodt, Eva Krejci and Dr. Wolf Rottke.

I am very thankful for the inspiration I received from Univ.-Prof. Dr. Klaus Reicherter, Prof. Dr. Janos Urai, Prof. Dr. Christoph Hilgers, Dr. Stefan Back, Prof. Dr. Magdalena Scheck-Wenderoth, Dr. Anna Uffmann, Dr. Victoria Sachse and Dr. Ralph Bähr.

Further, I am thankful for the logistic and scientific support of my colleagues at the institute of Geology and Geochemistry of Petroleum and Coal (RWTH Aachen University): Alireza Baniasad, Felix Froidl, Anna Kutovaya, Qian Zhang, Garri Gaus, Linda Burnaz, Louisa Helm, Donka Macherey, Kerstin Windeck and Dr. Laura Zieger.

I would also like to thank Assoc. Prof. David McKirdy, Dr. Bernd Michaelsen, Dr. Scott Bryan, Dr. Ian Duddy, Dr. Oliver Gaede, Mark Kelly, Chris Hansen, Bernadette Parkes, Alison Troup, David Groom, Tony Hill, Jo Davies, John Ostlender, Catharina Lesche, Denise Knebel, Carolin Mießen, Yury Karpov, Ivan Kurchatov and Aleksandra Glazyrina.

I gratefully acknowledge that my big family and many close friends continuously supported me with all they could give.

Finally, I thank my wife for the incredible amounts of love and motivation!

CONTENTS

1 INTRODUCTION 1

1.1 PRIMARY ENERGY DEMAND AND THE GEOLOGICAL SUBSURFACE 1

1.2 AUSTRALIA'S ENERGY RESOURCES OVERVIEW 3

1.3 PETROLEUM SYSTEMS AND THE GLOBAL CARBON CYCLE 8

1.4 NUMERICAL BASIN AND PETROLEUM SYSTEM MODELING 11

1.5 OBJECTIVES AND ORGANIZATION OF THE THESIS 13

2 TECTONIC EVOLUTION OF AUSTRALIA 19

2.1 OVERVIEW 19

2.2 PROTEROZOIC AUSTRALIA 20

2.3 PALEOZOIC AUSTRALIA 28

2.4 MESOZOIC AUSTRALIA 35

2.5 CAINOZOIC AUSTRALIA 39

2.6 PRESENT-DAY AUSTRALIA 40

3 LITHOSPHERIC EVOLUTION, THERMO-TECTONIC HISTORY AND SOURCE ROCK MATURATION IN THE GIPPSLAND BASIN, VICTORIA, SOUTHEASTERN AUSTRALIA 47

ABSTRACT 48

3.1 INTRODUCTION 49

3.1.1 Geological background and structural evolution 50

3.1.2 Sedimentary evolution and stratigraphy 55

3.1.3 Magmatism and volcanism 57

3.1.4 Present-day heat flow 57

3.2 METHODS, DATA AND MODELLING 57

3.2.1 Seismic interpretation of faults, surfaces and magmatic features 62

3.2.2 Fault modeling 66

3.2.3 Thermal modelling 67

3.2.4 Scenarios for the crustal layer model 71

3.2.5 Well data calibration and thermal conductivity 72

3.3 RESULTS AND INTERPRETATION 72

3.3.1 Crustal layer modelling results ... *72*
3.3.2 Burial history and temperature evolution ... *78*
3.3.3 Basal heat flow evolution and lithospheric layer dynamics ... *82*
3.3.4 Present-day surface heat flow ... *83*
3.3.5 Source rock thermal maturity and kerogen transformation ... *84*
3.3.6 Thermal evolution of source rocks and critical moment ... *87*
3.4 DISCUSSION AND UNCERTAINTIES OF THE MODEL ... 89
3.4.1 Basin architecture, stratigraphy and facies distribution ... *91*
3.4.2 Paleo-elevation and amount of erosion ... *91*
3.4.3 Mapping of faults ... *91*
3.4.4 Magmatism and volcanism ... *92*
3.4.5 Crustal geometry and composition ... *93*
3.4.6 Crustal extensional model ... *94*
3.4.7 Timing and magnitude of extension ... *94*
3.4.8 Paleo-heat flow and paleo-temperature ... *95*
3.4.9 Source rock thermal maturity and kerogen transformation ... *96*
3.5 CONCLUSIONS ... 97
3.6 COPYRIGHT / DATA AVAILABILITY STATEMENT ... 99
4 THE BIRKHEAD AND MURTA FORMATIONS – ORGANIC GEOCHEMISTRY AND ORGANIC PETROGRAPHY OF MESOZOIC FLUVIO-LACUSTRINE SOURCE ROCKS IN THE EROMANGA BASIN, CENTRAL AUSTRALIA ... 101
ABSTRACT ... 102
4.1 INTRODUCTION AND OBJECTIVES ... 103
4.2 GEOLOGICAL SETTING AND PETROLEUM SYSTEM ... 107
4.2.1 The Birkhead Formation ... *108*
4.2.2 The Murta Formation ... *110*
4.2.3 Petroleum systems ... *111*
4.3 MATERIALS AND ANALYTICAL METHODS ... 112
4.3.1 Organic petrography ... *115*
4.3.2 Bulk organic geochemistry ... *117*
4.3.3 Molecular organic geochemistry ... *118*
4.4 RESULTS ... 120
4.4.1 Organic richness and carbonate content (TOC, TIC, TC, $CaCO_3$) ... *125*
4.4.2 Sulphur content (TS) ... *125*

4.4.3 Rock-Eval pyrolysis *125*
4.4.4 Thermal maturity (Vitrinite reflectance VR_r; Rock-Eval T_{max};) *126*
4.4.5 Organic petrography *126*
4.4.6 Normal alkanes and acyclic isoprenoids *130*
4.4.7 Alicyclic isoprenoids *130*
4.4.8 Aromatic compounds *131*
4.5 DISCUSSION 134
4.5.1 Biological precursors and paleo-depositional environment *134*
4.5.2 Thermal maturity *140*
4.5.3 Petroleum generation potential *142*
4.6 CONCLUSIONS 147
5 DOWN UNDER AND UNDER COVER: FREQUENT HYDROTHERMAL ACTIVITY AND STRIKE-SLIP TECTONICS IN THE COOPER BASIN AND CENTRAL EROMANGA BASIN CONFIRMED BY SUBSIDENCE HISTORY ANALYSIS AND BASIN MODELLING 149
ABSTRACT 150
5.1 INTRODUCTION 151
5.2 GEOLOGICAL BACKGROUND 154
5.2.1 Cooper Basin *156*
5.2.2 Eromanga Basin *157*
5.2.3 Lake Eyre Basin *158*
5.2.4 Petroleum systems *158*
5.3 MATERIALS AND METHODS 162
5.3.1 Stratigraphic input *163*
5.3.2 Boundary conditions *168*
5.3.3 Petroleum system settings and source rock assignment *169*
5.3.4 Heat flow and thermal modelling *169*
5.4 RESULTS 170
5.4.1 Calibration of bottom hole temperature and thermal maturity *170*
5.4.2 Tectonic subsidence and sedimentation rate *176*
5.4.3 Evolution of basal heat flow and temperature *176*
5.4.4 Evolution of source rock thermal maturity and transformation ratio *177*
5.4.5 Layer thickness and depocentre migration *180*
5.4.6 Basal heat flow maps *186*
5.4.7 Maximum temperature maps *188*

5.4.8 Thermal maturity maps *190*
5.5 DISCUSSION AND REMAINING UNCERTAINTIES 192
5.5.1 Permo-Triassic tectonics *192*
5.5.2 Neotectonics and topography *195*
5.5.3 Jurassic and Cretaceous tectonics *199*
5.5.4 Uncertainties of thermal history *202*
5.5.5 Palaeozoic thermal evolution *203*
5.5.6 Mesozoic thermal evolution *204*
5.5.7 Cainozoic to present-day thermal evolution *205*
5.5.8 Implications on hydrocarbon generation and exploration outlook *208*
5.6 CONCLUSIONS 209
6 CONCLUDING REMARKS AND OUTLOOK 211
6.1 SUMMARY OF GENERATED DATA AND ITS RELEVANCE 211
6.2 CONCLUSIONS FROM NUMERICAL MODELLING AND STRUCTURAL ANALYSIS 213
6.3 INFLUENCE OF TECTONICS ON HEAT FLOW 216
6.4 EFFECTS ON SOURCE ROCK MATURATION 221
6.5 LATERAL MOVEMENTS OF THE CRUST AND LIMITS OF MODELLING 222
6.6 RELEVANCE OF OBTAINED KNOWLEDGE AND OUTLOOK 223
7 REFERENCES 225
8 APPENDICES 260
APPENDIX 1 (CHAPTER 3) 261
APPENDIX 2 (CHAPTER 4) 263
APPENDIX 3 (CHAPTER 5) 305
CURRICULUM VITAE 353

LIST OF TABLES

TABLE 1.1: AUSTRALIAN NON-RENEWABLE ENERGY RESOURCES (AERA, 2020A). A. INCLUDES ECONOMIC DEMONSTRATED RESOURCES AND SUBECONOMIC DEMONSTRATED RESOURCES; B. INCLUDES RESERVES; C. INCLUDES RESERVES AND CONTINGENT RESOURCES; D. RECOVERABLE COAL RESOURCES; E. RECOVERABLE RESOURCES AT <US$130/KG; F. A CONVERSION INTO ENERGY CONTENT EQUIVALENT FOR THORIUM WAS NOT AVAILABLE AT THE TIME OF PUBLICATION; G. EXCLUDES THORIUM RESOURCES. KT = THOUSAND TONNES; LPG = LIQUEFIED PETROLEUM GAS; PJ = PETAJOULE. 4

TABLE 1.2: RENEWABLE ELECTRICITY GENERATION CAPACITY IN AUSTRALIA (AERA, 2020A). A. LARGE-SCALE ELECTRICITY GENERATION CAPACITY. B. LARGE-SCALE ELECTRICITY GENERATION CAPACITY (SMALL-SCALE ROOFTOP SOLAR INSTALLATION GENERATION CAPACITY). C. INCLUDES BIO GENERATION CAPACITY FROM BAGASSE, LANDFILL GAS AND SEWAGE, FOREST RESIDUES AND OTHER SOURCES. MW = MEGAWATT. 6

TABLE 3.1: LAYER SPLITTING AND SPLIT RATIOS AS APPLIED IN THE AGE ASSIGNMENT. . 60

TABLE 3.2: CALIBRATION MATRIX FOR THE RESULT ANALYSIS OF THE INVERSION TO LITHOSPHERIC LAYER THICKNESS (STEP 1) AND INVERSION TO HEAT FLOW (STEP 2). CALCULATED OUTPUT, WHICH FITS THE CALIBRATION WINDOW IN BOLD AND ITALIC. THICKNESS OF THE ENTIRE LITHOSPHERE INCLUDES THE SEDIMENTARY COLUMN IN THE CENTRAL DEEP (~7 KM AT AFTER STRETCHING (103 MA); ~13 KM AT PRESENT DAY). VALUE RANGES FOR CALIBRATION ARE TAKEN FROM LITERATURE OR DERIVED FROM LITERATURE VALUES: 1) AITKEN ET AL., 2013; 2) KENNETT & SALMON, 2012; 3) ALLEN & ALLEN, 2013; 4) GREEN ET AL., 1995; 5) HOLGATE & GERNER, 2010. 73

TABLE 3.3: LIST OF MOST RELEVANT UNCERTAINTIES, THEIR CHARACTERISTICS AND IMPACT ON THE MODEL AND ITS RESULTS. SOME SUGGESTIONS FOR IMPROVEMENT IN FUTURE STUDIES ARE GIVEN. 90

TABLE 4.1: OVERVIEW OF THE COMPLETE SAMPLE SET USED IN THIS STUDY. ROCK-EVAL PYROLYSIS AND PETROGRAPHIC DETERMINATION OF THERMAL MATURITY WAS PERFORMED ON ALL SAMPLES (RESULTS SUMMARIZED IN TABLE 4.2). ASTERISKS INDICATE SAMPLES, WHICH UNDERWENT MOLECULAR ORGANIC GEOCHEMICAL

ANALYSIS DUE TO HIGH TOC (AT LEAST TWO SAMPLES PER WELL, SEE TABLE 4.4). MD = MEASURED DEPTH. TD = TOTAL DEPTH. 113

TABLE 4.2: OVERVIEW OF ROCK-EVAL PYROLYSIS RESULTS (S1, S2, OIL SATURATION INDEX OSI, PRODUCTION INDEX PI, AND HYDROGEN INDEX HI) SORTED AFTER FORMATION AND INCLUDING ELEMENTAL COMPOSITION (TOC, TIC, AND TS) AND VITRINITE REFLECTANCE (VRR MEAN, WITH STANDARD DEVIATION S). SAMPLES WITH ASTERISK UNDERWENT MOLECULAR ORGANIC GEOCHEMICAL ANALYSIS (SEE TABLE 4.4). 116

TABLE 4.3: LIST OF IDENTIFIED BIOMARKER PEAKS USED IN THIS STUDY (MOST RELEVANT PEAKS ARE SHOWN IN FIGURE 4.5; SEE TABLE 4.4 FOR RESULTING MOLECULAR RATIOS). 119

TABLE 4.4: RESULTS OF MOLECULAR ORGANIC GEOCHEMISTRY SORTED AFTER FORMATION AND DISTINGUISHED BETWEEN GC-FID AND GC-MS (SEE TABLE 4.3 FOR ABBREVIATIONS). SOURCE-RELATED BIOMARKER RATIOS ARE IN ITALIC, ALL REMAINING PARAMETERS ARE MATURITY-RELATED. A) PETERS ET AL., 2005A; B) CONNAN & CASSOU, 1980; C) PETERS ET AL., 1999; D) PETERS ET AL., 2005B; E) SCALAN & SMITH, 1970; F) TEN HAVEN & RULLKÖTTER, 1988; G) FAN ET AL., 1987; H) SEIFERT & MOLDOWAN, 1980; I) MOLDOWAN ET AL., 1985; J) SEIFERT ET AL., 1981; SEIFERT & MOLDOWAN, 1986; K) HUGHES ET AL., 1995; L) MASLEN ET AL., 2011; M) RADKE ET AL., 1982. 122

TABLE 4.5: SUMMARY OF THE MAIN SOURCE ROCK CHARACTERISTICS OF THE MURTA AND BIRKHEAD FORMATIONS. 147

TABLE 5.1: OVERVIEW OF ASSIGNED LAYERS AND THEIR AGES USED AS INPUT FOR THE NUMERICAL MODELS (MODIFIED AFTER HALL ET AL., 2019). 164

TABLE 5.2: OVERVIEW OF MAIN LITHOLOGIES, CORRESPONDING THERMAL CONDUCTIVITY VALUES (FROM BEARDSMORE, 2004) AND ASSIGNMENT OF PETROLEUM SYSTEM ELEMENTS. 167

TABLE 5.3: OVERVIEW OF SOURCE ROCK PROPERTIES AND ASSIGNMENT OF KINETIC MODELS. VALUES FROM HALL ET AL. (2016A) AND REFERENCES THEREIN. [1)]TOC AND HI VALUES OF BIRKHEAD AND MURTA FORMATIONS COMPLEMENTED BY THE RESULTS OF CHAPTER 4). 169

TABLE 5.4: OVERVIEW OF ASSIGNED BASAL HEAT FLOW TRENDS FOR THE EIGHT SELECTED CALIBRATION WELLS. REGIONAL MIDDLE CRETACEOUS PEAK (99.5 MA) IN BOLD LETTERS. 171

LIST OF FIGURES

FIGURE 1.1: GLOBAL ANNUAL PRIMARY ENERGY CONSUMPTION BY SECTOR FROM 1993 TO 2018 (BP, 2019). 2

FIGURE 1.2: GLOBAL ENERGY-RELATED CO_2 EMISSIONS FROM 1900 TO 2020 (IEA, 2020B). 3

FIGURE 1.3: DISTRIBUTION OF AUSTRALIA'S MAJOR (CONTAINING MORE THAN 1,500 PJ) NON-RENEWABLE ENERGY RESOURCES (AERA, 2020A). 5

FIGURE 1.4: DISTRIBUTION OF AUSTRALIA'S RENEWABLE ENERGY RESOURCES, EXCLUDING BIO AND HYDRO RESOURCES (AERA, 2020A). 7

FIGURE 1.5: PREDICTED TEMPERATURE AT 5 KM DEPTH, SHOWING HSA EXPLORATION WELLS, HOT SPRING LOCATIONS AND AREAS WITH >3 KM DEPTH AND/OR 200 °C AT 5 KM DEPTH (AERA, 2020B). HSA = HOT SEDIMENTARY AQUIFER. 8

FIGURE 1.6: SCHEME OF A SIMPLE (CONVENTIONAL) PETROLEUM SYSTEM (MODIFIED AFTER DEMBICKI, 2017). 9

FIGURE 1.7: SCHEMATIC OVERALL PERTURBATION OF THE GLOBAL CARBON CYCLE CAUSED BY ANTHROPOGENIC ACTIVITIES (FRIEDLINGSTEIN ET AL., 2019 AND REFERENCES THEREIN). VALUES AVERAGED GLOBALLY FOR THE DECADE 2009–2018. 11

FIGURE 2.1: SCHEMATIC OVERVIEW OF MAIN TECTONIC ELEMENTS OF THE PRESENT-DAY AUSTRALIAN CONTINENT (AFTER MYERS ET AL., 1996; TEASDALE ET AL., 2001, 2003; CAWOOD & KORSCH, 2008; HUSTON ET AL., 2012). CC = CURNAMONA CRATON, GC = GAWLER CRATON, MC = MAWSON CRATON, NAE = NORTH AUSTRALIAN ELEMENT, SAE = SOUTH AUSTRALIAN ELEMENT, TAS = TASMANIA, TE = TASMAN ELEMENT, WAE = WEST AUSTRALIAN ELEMENT. NOTE: THE MAWSON CRATON (TODAY ANTARCTICA) IS DISPLAYED CLOSER TO AUSTRALIA COMPARED TO REALITY. 20

FIGURE 2.2: CHRONOLOGIC OVERVIEW OF TERRANES AND CONTINENTAL TECTONIC UNITS, WHICH PARTICIPATED IN THE ASSEMBLY OF AUSTRALIA IN GEOLOGIC HISTORY AND REPEATEDLY FORMED SUPERCRATONS AND SUPERCONTINENTS (AFTER HUSTON ET AL., 2012; MODIFIED AFTER LI, 2002). WAE = WEST AUSTRALIAN ELEMENT, NAE =

North Australian Element, SAE = South Australian Element, PA = Proto-Australia. 21

Figure 2.3: Simplified paleotectonic layout of main tectonic elements during the period of Nuna assembly / Proto-Australia I (after Myers et al., 1996; Teasdale et al., 2001, 2003; Cawood & Korsch, 2008; Huston et al., 2012). CC = Curnamona Craton, GC = Gawler Craton, KC = Kimberley Craton, MC = Mawson Craton, NAE = North Australian Element, PC = Pilbara Craton, SAE = South Australian Element, TAS = Tasmania, WAE = West Australian Element, YC = Yilgarn Craton. 22

Figure 2.4: Simplified paleotectonic layout of main tectonic elements during the period of Nuna supercontinent (after Myers et al., 1996; Teasdale et al., 2001, 2003; Cawood & Korsch, 2008; Huston et al., 2012). CC = Curnamona Craton, GC = Gawler Craton, MC = Mawson Craton, NAE = North Australian Element, SAE = South Australian Element, TAS = Tasmania, WAE = West Australian Element..... 22

Figure 2.5: Simplified paleotectonic layout of main tectonic elements during the period of Nuna break-up (after Myers et al., 1996; Teasdale et al., 2001, 2003; Cawood & Korsch, 2008; Huston et al., 2012). CC = Curnamona Craton, GC = Gawler Craton, MC = Mawson Craton, NAE = North Australian Element, SAE = South Australian Element, TAS = Tasmania, WAE = West Australian Element..... 23

Figure 2.6: Simplified paleotectonic layout of main tectonic elements during the period of Proto-Australia II (after Myers et al., 1996; Teasdale et al., 2001, 2003; Cawood & Korsch, 2008; Huston et al., 2012). CC = Curnamona Craton, GC = Gawler Craton, MC = Mawson Craton, NAE = North Australian Element, SAE = South Australian Element, TAS = Tasmania, WAE = West Australian Element..... 24

Figure 2.7: Simplified paleotectonic layout of main tectonic elements during the phase of Rodinia assembly (after Myers et al., 1996; Teasdale et al., 2001, 2003; Li & Powell, 2001; Li, 2002; Giles et al., 2004; Cawood & Korsch, 2008; Huston et al., 2012). AFO = Albany-Fraser Orogen, CC = Curnamona Craton, GC = Gawler Craton, MC = Mawson Craton, MO = Musgravian Orogen, NAE = North Australian Element, RO = Rudall Orogen, SAE =

South Australian Element, SCB = South China Block, SO = Sibao Orogen, TAS = Tasmania (position speculative), THZ = Torrens Hinge Zone, WAE = West Australian Element. 24

Figure 2.8: Simplified paleotectonic layout of main tectonic elements during the late Rodinia period (after Shaw et al., 1991; Myers et al., 1996; Li & Powell, 2001; Teasdale et al., 2001, 2003; Betts et al., 2002; Li, 2002; Cawood & Korsch, 2008; Huston et al., 2012). AG = Adelaidian Geosyncline, CC = Curnamona Craton, CSB = Centralian Superbasin, GC = Gawler Craton, MC = Mawson Craton, NAE = North Australian Element, SAE = South Australian Element, SCB = South China Block, TAS = Tasmania, TL = Tasman Line (after Teasdale, 2001), THZ = Torrens Hinge Zone, WAE = West Australian Element. 27

Figure 2.9: Simplified paleotectonic layout of main tectonic elements during the break-up of Rodinia (after Shaw et al., 1991; Preiss, 1993; Powell et al., 1994; Myers et al., 1996; Li & Powell, 2001; Teasdale et al., 2001, 2003; Betts et al., 2002; Li, 2002; Cawood & Korsch, 2008; Huston et al., 2012). 1 = Amadeus Basin, 2 = Ngalia Basin, 3 = Georgina Basin, AG = Adelaidian Geosyncline, CC = Curnamona Craton, GC = Gawler Craton, MC = Mawson Craton, NAE = North Australian Element, OB = Officer Basin, PO = Paterson Orogen, SAE = South Australian Element, SCB = South China Block, TAS = Tasmania, TL = Tasman Line (after Teasdale, 2001), THZ = Torrens Hinge Zone, WAE = West Australian Element. 27

Figure 2.10: Overview of Neoproterozoic and Early-Middle Paleozoic tectonic events in western, central and eastern Australia (from Huston et al., 2012). 28

Figure 2.11: Simplified paleotectonic situation during the Petermann Orogeny (after Teasdale et al. 2001) and the Late Neoproterozoic Trans-Australian Fold Belt (TAFB, after Wopfner, 1997, also called Paterson-THZ Shear Zone after Teasdale et al., 2001). CC = Curnamona Craton, MC = Mawson Craton, NAE = North Australian Element, SAE = South Australian Element, TAS = Tasmania, THZ = Torrens Hinge Zone, TL = Tasman Line (after Teasdale et al., 2001), WAE = West Australian Element. 29

FIGURE 2.12: SIMPLIFIED PALEOTECTONIC SITUATION DURING THE CAMBRIAN RIFTING (AFTER TEASDALE ET AL. 2001). CC = CURNAMONA CRATON, MC = MAWSON CRATON, NAE = NORTH AUSTRALIAN ELEMENT, SAE = SOUTH AUSTRALIAN ELEMENT, TAFB = TRANS-AUSTRALIAN FOLD BELT (AFTER WOPFNER, 1997), TAS = TASMANIA, THZ = TORRENS HINGE ZONE, TL = TASMAN LINE (AFTER TEASDALE ET AL., 2001), WAE = WEST AUSTRALIAN ELEMENT. 29

FIGURE 2.13: SIMPLIFIED PALEOTECTONIC SITUATION DURING THE DELAMERIAN OROGENY (AFTER TEASDALE ET AL. 2001). CC = CURNAMONA CRATON, MC = MAWSON CRATON, NAE = NORTH AUSTRALIAN ELEMENT, SAE = SOUTH AUSTRALIAN ELEMENT, TAFB = TRANS-AUSTRALIAN FOLD BELT (AFTER WOPFNER, 1997), TAS = TASMANIA, THZ = TORRENS HINGE ZONE, TL = TASMAN LINE (AFTER TEASDALE ET AL., 2001), WAE = WEST AUSTRALIAN ELEMENT. 30

FIGURE 2.14: SIMPLIFIED PALEOTECTONIC SITUATION DURING THE ORDOVICIAN EXTENSION (AFTER TEASDALE ET AL. 2001). AB = AMADEUS BASIN, CC = CURNAMONA CRATON, EWB = EASTERN WARBURTON BASIN, MC = MAWSON CRATON, NAE = NORTH AUSTRALIAN ELEMENT, SAE = SOUTH AUSTRALIAN ELEMENT, TAS = TASMANIA, THZ = TORRENS HINGE ZONE, TL = TASMAN LINE (AFTER TEASDALE ET AL., 2001), WAE = WEST AUSTRALIAN ELEMENT, WWB = WESTERN WARBURTON BASIN. 31

FIGURE 2.15: SIMPLIFIED PALEOTECTONIC SITUATION DURING THE ALICE SPRINGS OROGENY (AFTER TEASDALE ET AL. 2001 AND KLOOTWIJK, 2013). AB = AMADEUS BASIN, CC = CURNAMONA CRATON, EWB = EASTERN WARBURTON BASIN, MC = MAWSON CRATON, NAE = NORTH AUSTRALIAN ELEMENT, SAE = SOUTH AUSTRALIAN ELEMENT, SAFZ = SOUTHERN AUSTRALIAN FAULT ZONE (AFTER TEASDALE ET AL., 2003), TAS = TASMANIA, THZ = TORRENS HINGE ZONE, TL = TASMAN LINE (AFTER TEASDALE ET AL., 2001), WAE = WEST AUSTRALIAN ELEMENT, WWB = WESTERN WARBURTON BASIN. OLEPOLOKO FAULT AFTER WONG ET AL. (2018). 31

FIGURE 2.16: THE TASMANIDES IN EASTERN AUSTRALIA (AFTER ROSENBAUM, 2018). UNDERLYING MAGNETIC INTENSITY MAP FROM GEOSCIENCE AUSTRALIA (MILLIGAN & FRANKLIN, 2004). SEE ORIGINAL PUBLICATION FOR ADDITIONAL ABBREVIATIONS. DARK YELLOW ELLIPSE SHOWS APPROXIMATE LOCATION OF THE PENNSYLVANIAN-TRIASSIC COOPER BASIN. 33

FIGURE 2.17: THE LAYOUT OF GONDWANA DURING THE LATE PALEOZOIC (FROM FERGUSSON & HENDERSON, 2015). CRATONS IN AUSTRALIA AND ANTARCTICA ARE FROM MYERS ET AL. (1996) AND BOGER (2011) RESPECTIVELY. AFMB = ALBANY–FRASER–MUSGRAVE BELT, DO = DELAMERIAN OROGEN, NAC = NORTH AUSTRALIAN CRATON, RP = RÍO DE LA PLATA CRATON, SAC = SOUTH AUSTRALIAN CRATON, SF = SÃO FRANCISCO CRATON, TC = TANZANIA CRATON, AND WAC = WEST AUSTRALIAN CRATON. 34

FIGURE 2.18: MIDDLE JURASSIC PALEO-TECTONIC RECONSTRUCTION JUST BEFORE PANGEA BREAKUP (175 MA, MODIFIED AFTER LI & POWELL, 2001). ANDEAN-TYPE MAGMATIC ARC ALONG THE PALEO-PACIFIC OCEAN WITH BROAD FORELAND BASINS OVER CENTRAL EASTERN AUSTRALIA. EB = EROMANGA BASIN, LHR = LORD HOWE RISE, NEO = NEW ENGLAND OROGEN, NZ = NEW ZEALAND, SAFZ = SOUTHERN AUSTRALIAN FRACTURE ZONE, SB = SURAT BASIN, TAS = TASMANIA, TL = TASMAN LINE. 36

FIGURE 2.19: THE KEY TECTONIC BASIN PHASES, WHICH INFLUENCED THE EVOLUTION OF THE SOUTHERN MARGIN OF AUSTRALIA DURING THE MESOZOIC (INCLUDING THE GIPPSLAND BASIN, SEE RED CIRCLE; COMPILED AND MODIFIED AFTER TEASDALE ET AL, 2003). GREEN AND RED ARROWS INDICATE THE MAIN TECTONIC STRESS DIRECTION DURING EXTENSIONAL AND COMPRESSIONAL BASIN PHASES, RESPECTIVELY. A) LATE-JURASSIC TO EARLY CRETACEOUS NW-SE EXTENSION (ONSET SOUTHERN OCEAN OPENING, 155 – 120 MA); B) EARLY-MID CRETACEOUS NE-SW EXTENSION (120 – 100 MA); C) MID-CRETACEOUS NW-SE COMPRESSION (100 – 90 MA); D) LATE CRETACEOUS NNE-SSW EXTENSION (TASMAN SEA SPREADING, 93 – 80 MA);. ANT = ANTARCTICA; SAFZ = SOUTHERN AUSTRALIAN FAULT ZONE; TS = TASMAN SEA. ALL MAPS SHOW TOP TOWARDS NORTH. PLEASE NOTE DIFFERENT MAP SCALES. 37

FIGURE 2.20: RECONSTRUCTION OF THE PALEOGEOGRAPHIC SITUATION DURING THE OROGENIC COLLAPSE AND BREAKUP OF THE EASTERN MARGIN OF GONDWANA (ALBIAN/CENOMANIAN BOUNDARY (100 MA), MODIFIED AFTER BRYAN ET AL. 1997, VEEVERS ET AL. 2000, NORVICK ET AL. 2001, MORTIMER 2008, KUSKY ET AL. 2014, SCHWARTZ ET AL. 2016, MÜLLER ET AL. 2016). AUSTRALIA, TASMANIA (TAS), ANTARCTICA AND ZEALANDIA ARE STILL COMBINED WHILE THE PHOENIX AND PACIFIC PLATES ARE SUBDUCTED. BB = BASS BASIN, CB = COOPER BASIN (LIGHT BROWN POLYGON), EAN = EAST ANTARCTICA, EB = EROMANGA BASIN, GB = GIPPSLAND BASIN (RED CIRCLE), LFB = LACHLAN FOLD BELT, NC = NEW

Caledonia, NEO = New England Orogen, NPR = North Phoenix Ridge, OT = Otway Basin, SAFZ = Southern Australian Fracture Zone, SB = Surat Basin, SPR = South Phoenix Ridge, TL = Tasman Line, TR = Tasman Ridge, TSC = Tasman Spreading Centre, WAN = West Antarctica, WVP = Whitsunday Volcanic Province. Black rectangle shows extent of Figure 6.1.....38

Figure 2.21: Middle Eocene paleo-tectonic reconstruction (45 Ma, modified after Li & Powell, 2001). GB = Gippsland Basin, LEB = Lake Eyre Basin, LHR = Lord Howe Rise, MB = Murray Basin, NEO = New England Orogen, NZ = New Zealand, SAFZ = Southern Australian Fracture Zone, TAS = Tasmania, TL = Tasman Line.....39

Figure 2.22: Topography and bathymetry map of present-day Australia with rheological provinces (grey outlines, from Müller et al., 2012) and with Kati-tanda (Lake Eyre) and Kunama Namadgi (Mount Kosciuszko) marking the lowest and highest points of continental Australia, respectively.....41

Figure 2.23: Stress trajectories based on the Australian stress map (Hillis & Reynolds, 2000). 41

Figure 2.24: Present-day seismicity of Australia indicating the main seismic zones (modified after Hillis et al., 2008). Red ellipse shows aligned seismicity probably related to the Central Eromanga Shear Zone (CESZ), a newly interpreted tectonic feature (see Chapter 5). 42

Figure 2.25: Depth to the base of the Lithosphere below Australia (Kennett & Salmon, 2012). Grid resolution: 0.5 x 0.5 degree. CB = Cooper Basin, EB = Eromanga Basin, GB = Gippsland Basin. 43

Figure 2.26: Depth to the Moho below Australia (mean Moho elevation, modified after Aitken et al., 2013). CB = Cooper Basin, CC = Curnamona Craton, EB = Eromanga Basin, GC = Gawler Craton, GB = Gippsland Basin, LO = Lachlan Orogen, NEO = New England Orogen. Refer to original publication for further abbreviations. 43

Figure 2.27: Gravity anomaly map of Australia (from Bacchin et al., 2008, Bouguer onshore, free-air offshore). a) Overview of the entire Australian

CONTINENT AND SURROUNDINGS. B) ZOOM INTO THE AREA AROUND THE COOPER BASIN. C) ZOOM INTO AREA AROUND THE GIPPSLAND BASIN. 45

FIGURE 2.28: MAGNETIC ANOMALY MAP OF AUSTRALIA (FROM MILLIGAN ET AL., 2010). A) OVERVIEW OF THE ENTIRE AUSTRALIAN CONTINENT AND SURROUNDINGS. B) ZOOM INTO THE AREA AROUND THE COOPER BASIN. C) ZOOM INTO AREA AROUND THE GIPPSLAND BASIN. 45

FIGURE 3.1: GEOGRAPHIC AND STRUCTURAL OVERVIEW OF THE STUDY AREA. A) OVERVIEW MAP OF AUSTRALIA, SURROUNDED BY THE INDIAN OCEAN, THE SOUTHERN OCEAN, THE TASMAN SEA AND THE CORAL SEA. THE SMALL BLACK RECTANGLE INDICATES THE EXTENT OF FIGURE 3.1B. B) STRUCTURAL ELEMENTS OF THE GIPPSLAND BASIN (MODIFIED AFTER GOLDIE DIVKO ET AL. 2010, BASEMENT TOPOGRAPHY WITHIN THE AOI (GREY ISOLINES) AFTER POWER ET AL. 2001). THE BLACK LINES INDICATE THE ORIENTATION OF 2D SECTIONS (FIGURE 3.4 & FIGURE 3.13). 50

FIGURE 3.2 (PREVIOUS PAGE): STRATIGRAPHY, PETROLEUM SYSTEM ELEMENTS AND TECTONIC EVOLUTION OF THE GIPPSLAND BASIN (COMPILED AND MODIFIED AFTER NORVICK ET AL. 2001, BERNECKER & PARTRIDGE 2001, WOOLLANDS & WONG 2001, AND TEASDALE ET AL. 2003). THE SUBDIVISION OF MAJOR STRATIGRAPHIC UNITS AND GROUPS IS DISPLAYED WITH REPRESENTATIVE LITHOLOGY AND RELEVANT STRATIGRAPHIC FEATURES. IMPORTANT HYDROCARBON OCCURRENCES ARE INDICATED AS CIRCLES. THE TIMING OF PETROLEUM SYSTEM ELEMENTS IS SHOWN IN DIRECT RELATION TO TECTONIC PROCESSES AND THE THERMAL EVOLUTION. LARGE ARROWS INDICATE THE MAIN TECTONIC STRESS DIRECTION DURING EXTENSIONAL (E) AND COMPRESSIONAL (C) BASIN PHASES, RESPECTIVELY (ACCORDING TO TABLE 3.1). THE ILLUSTRATED HEAT FLOW TREND WITH ASSOCIATED SYN-RIFT AND POST-RIFT PHASES IS DERIVED FROM THERMAL MODELLING PERFORMED IN THIS STUDY. THE RED TREND LINE IS REPRESENTATIVE FOR THE BASIN CENTER, WHILE THE GREY TREND LINE CORRESPONDS WITH THE NORTHERN AND SOUTHERN TERRACES. STARS INDICATE INCREASED VOLCANIC ACTIVITY (CAMPANIAN AND CARRAJUNG VOLCANICS). 55

FIGURE 3.3: OVERVIEW OF THE MODEL GEOMETRY AND THE APPLIED WORKFLOW FOR FAULT INTERPRETATION. A) GEOMETRY OF THE 3D BASIN MODEL OF THE GIPPSLAND BASIN (VERTICAL EXAGGERATION FACTOR = 5.00). UPPER CRETACEOUS AND CENOZOIC POST-RIFT SUCCESSIONS REST UNCONFORMABLE ON THICK LOWER CRETACEOUS SYN-RIFT DEPOSITS. SEE TABLE 3.1 FOR DETAILED ASSIGNMENT AND

splitting of layers. Black polygons represent outlines of oil and gas fields. b) Manual grid-parallel picking of faults along 2D sections (scroll increment: 500 m). c) Quality control of fault interpretations with attribute volumes (e.g. amplitude contrast). d) Overview of all fault segments (edited and merged) selected for the fault framework in the structural model (~150 segments). Seismic inline 4719 is displayed in Figure 3.4 in more detail. 59

Figure 3.4: Example from seismic interpretation. a) Seismic inline 4719 from 3DGEO (2011, see Figure 3.1 for orientation). b) Seismic interpretation along inline 4719. Red rectangle indicates extent of Figure 3.4c & Figure 3.4d. 63

Figure 3.5: Mapped magmatic intrusions a) and subaerial flows b) along the edge of the Northern Terrace with selected well locations where volcanic material was intersected. The extracted 'geobodies' which represent the magmatic intrusions are aligned along large faults. Green extensional arrows (E3) indicate the paleo-stress direction. Corresponding transtensional fault activity (indicated by black kinematic arrows) probably triggered magmatism and volcanism along the Rosedale Fault System during the Campanian. The diameter of the mapped intrusive bodies ranges between 1 and 5 km. All mapped magmatic intrusions emplaced within the Emperor subgroup (Emp). The interpreted contemporaneous subaerial volcanic flows correspond to the Golden Beach (GB, Campanian Volcanics) and the Halibut (HB, Carrajung Volcanics) subgroups. AOI = Area of Interest; black rectangle: extent of Figure 3.5a & Figure 3.5b within the AOI; RFS = Rosedale Fault System; LWFS = Lake Wellington Fault System. 66

Figure 3.6: Cartoon of the three principal phases of the simplified McKenzie crustal model and involved relevant physical parameters (after McKenzie 1978 and Hantschel & Kauerauf 2009). a) The pre-rift phase (I) is characterized by low tectonic activity. It is followed by the syn-rift (II), during which deformation of the crust and upwelling of the asthenosphere occurs. A depression forms at the surface, which fills with water and sediments. Throughout the post-rift phase (III) cooling of the lithosphere results in thermal subsidence, facilitating accommodation

space for additional sediment input. b) While the top of the lithosphere remains fixed, the TB isotherm (TB = temperature at the base of the lithosphere; TB = ¾ TM = 1,333 °C. TM = pyrolite melting temperature) ascends and the heat flow (Q) increases. A short interphase of post-rift inversion with uplift and erosion is possible before the isotherm drops again during the post-rift phase (III). The individual stretching factors (β) are describing the thickness variations (h) of the crust and the mantle over time. c) The layers of the lithosphere react differently to tectonic forces and temperature changes due to varying density (ρ) and thermal conductivity (λ). The heat flow (Q) from the asthenosphere to the surface is controlled by the distance of the thermal boundaries (TS = surface temperature; TB = temperature at the base of the lithosphere) to each other. The heat transfer and the temperature distribution in the sedimentary basin itself are controlled by the basal heat flow, the water depth (hw) and the TSWI = sediment water interface temperature (SWIT). 69

Figure 3.7: Fitting the theoretical subsidence to tectonic subsidence based on 1D-extractions. a) Overview of calibration boreholes used in this study located in the Central Deep of the Gippsland Basin (Archer-1 not shown, contours are depth-to-basement after Power et al., 2001). b) A representative extraction performed along the well path of Veilfin-1. Based on its gradient the total subsidence curve (sediment-filled basin) can be separated into two phases: syn-rift and post-rift. After removing the sediment load, the fit of the theoretical subsidence and the tectonic subsidence (basin filled with water) can then be achieved by fitting the stretching parameters (correct timing of rifting and selection of suitable pre-rift thickness; a good fit is characterized by small subsidence differences (theoretical subsidence − tectonic subsidence ≈ 0). c) Resulting thickness of the crust after stretching varies between 8 km in the Central Deep and 25 km below the rift shoulders (pre-rift thickness set to 25 km). d) The rift axis is underlain by a stretched mantle with minimum thickness values less than 20 km. Below the rift shoulders (e.g. Southern Platform) the upper mantle keeps its original thickness (pre-rift

value set to 40 km). Please note that three different thickness scales are used in a), c) and d)..... 70

Figure 3.8: Tectonic subsidence fit, resulting stretching maps after lithospheric layer thickness inversion and calculated heat flow trends extracted at Cobia-1. Inversion results for (a) Scenario A, (b) Scenario B, (c) Scenario C, and (d) Scenario D. Note that stretching maps have different scales. 76

Figure 3.9: Comparison of the modelled temperature evolution of scenario C with selected well data. (a) Map of estimated maximum temperature at the top of the Strzelecki Group with depth isolines and well locations. Thermal maxima of about 185 °C are located within the deep troughs. (b) Plots of modelled temperature (blue) and vitrinite reflectance (black) of scenario C at selected well locations compared with well data (cross). Expected trends (drawn as orange dashed lines) at the northern and southern terraces are discussed in the text..... 80

Figure 3.10: Burial history plots with a) maximum temperature overlay extracted at Cobia-1 (see Figure 3.7 for borehole location) based on scenario C). The highest geothermal gradient was established after the basin inversion between about 93 Ma and 80 Ma. All formations except the Lower Strzelecki Group reached their individual maximum temperature at present day. b) Transformation ratio (TR) over time extracted at Cobia-1 based on scenario C. The Kipper Shale and the Golden Beach source rocks initiate significant kerogen transformation during the Paleocene (TR > 10 %). The critical moment (TR > 50 %) for the Kipper Shale occurred already in the early Eocene, while the Golden Beach subgroup surpassed its critical moment in the Miocene. The Lower Halibut source rocks just started to generate substantial amounts of petroleum in the Mio-/Pliocene..... 81

Figure 3.11: The evolution of the calculated heat flow for the offshore Gippsland Basin based on the crustal layer model of scenario C. a) Basal heat flow shortly after onset of rifting and initial subsidence (140 Ma, Lower Strzelecki formation). b) Basal heat flow after rapid subsidence at rifting maximum (103 Ma, Upper Strzelecki formation). c) Basal heat flow

shortly after the uplift and erosion, which occurred at the transition between syn-rift and post-rift (93 Ma, Lower Emperor formation). d) Basal heat flow after substantial cooling during the early post-rift (50 Ma, Upper Halibut formation). e) The present-day basal heat flow. f) Surface heat flow at present day (0 Ma). Shown values were picked at the lower left corner of the labels. Crosshairs indicate borehole locations of Veilfin-1, Cobia-1 and Volador-ST1 (from West to East, compare Figure 3.14). 83

Figure 3.12: Thermal maturity variations at the tops of the assigned source rock sublayers based on scenario C (at present day; vitrinite reflectance, Easy%Ro after Sweeney & Burnham 1990). a) At the bottom of the Emperor subgroup (Kipper Shale, deposited before 90.3 Ma). b) At the top of the Emperor subgroup (Kipper Shale, deposited before 90.0 Ma). c) In the middle of Golden Beach *T. apoxyeximus zone* (deposited before 83.50 Ma). d) In the middle of Golden Beach *T. lillii zone* (deposited before 78.0 Ma). e) In the middle of lower Halibut *lower F. longus zone* (deposited before 67.0 Ma). f) In the middle of lower Halibut *upper F. longus zone* (deposited before 66.0 Ma). The shown source rock intervals represent sublayers already and were again subdivided for more detailed analysis; numbers in brackets indicate the number of the displayed sublayer (from 1 = bottom to 4 = top). Shown values were picked at the lower left corner of the labels. Crosshairs indicate borehole locations of Veilfin-1, Cobia-1 and Volador-ST1 (from West to East, compare Figure 3.14). 85

Figure 3.13: The spatial variation of the magnitude of kerogen transformation (TR = transformation ratio) at the tops of the assigned source rock sublayers based on scenario C (at present day). a) At the bottom of the Emperor subgroup (Kipper Shale, deposited before 90.3 Ma). b) At the top of the Emperor subgroup (Kipper Shale, deposited before 90.0 Ma). c) In the middle of Golden Beach T. apoxyeximus zone (deposited before 83.50 Ma). d) In the middle of Golden Beach T. lillii zone (deposited before 78.0 Ma). e) In the middle of lower Halibut *lower F. longus zone* (deposited before 67.0 Ma). f) In the middle of lower Halibut *upper F. longus zone* (deposited before 66.0 Ma). The shown source rock intervals represent sublayers already and were again subdivided for more detailed analysis; numbers in

brackets indicate the number of the respective sublayer (from 1 = bottom to 4 = top). Shown values were picked at the lower left corner of the labels. Crosshairs indicate borehole locations of Veilfin-1, Cobia-1 and Volador-ST1 (from West to East, compare Figure 3.14). 86

Figure 3.14: Present-day maturity of the sedimentary fill of the Gippsland Basin from west to east based on scenario C (see Figure 3.1 for orientation of the section; vitrinite reflectance, Easy%Ro after Sweeney & Burnham 1990). In the west (shelf areas), higher maturity levels are generally encountered at shallower depths compared to the east (deep water). Note that none of the wells reaches down to the lowermost formations of the Latrobe Group (i.e. Emperor). The stippled line at borehole Volador-ST1 indicates that the well path is a few km away from the shown section. .. 87

Figure 3.15: Evolution of temperature a), thermal maturity b) and transformation ratio c) at three selected calibration boreholes based on scenario C at three selected boreholes in the basin center (see Figure 3.7 & Figure 3.14 for borehole locations). Thresholds for thermal maturation and kerogen transformation are given as horizontal lines. 88

Figure 3.16: Comparison of all modelled accumulations with the known reservoirs (black polygons) with open faults from 145 Ma to 45 Ma and closed faults from 45 Ma until 0 Ma. Most of the large known accumulations are filled and the match is generally sufficient. Some "new" oil accumulations are modelled in the South, East and Northeast. Fields of the Northern Terrace (Baleen, Moby, Kipper and Sole) are not charged. Model resolution / grid cell size: 500 m * 500 m. DFS = Darriman Fault System. FFS = Foster Fault System. RFS = Rosedale Fault System. 93

Figure 4.1: Overview of the study area and sample locations. A) The location of the study area at the border between South Australia and Queensland. The Jurassic-Cretaceous Eromanga Basin unconformable overlies the Permo-Triassic Cooper Basin. P1 = Poonarunna-1. B) Sample well locations in the southern Cooper-Eromanga Basin (B5 = Bookabourdie-5, M4 = Moorari-4, L7/8 = Limestone Creek-7/8, J2 = Jackson-2, T1 = Thungo-1, W1 = Winna-1. GMI Ridge = Gidgealpa-Merrimelia-Innamincka Ridge, JNP

Ridge = Jackson-Naccowlah-Pepita Ridge. Poonarunna-1 is located outside of this map). 104

Figure 4.2: Stratigraphy and petroleum systems of the study area. A) Chronostratigraphic overview, lithology and petroleum system elements of the study area (modified after AGBA, 2015). B) Schematic petroleum system of the study area shows possible mixing of hydrocarbons during migration into the anticlinal traps (modified after Bowering & Harrison, 1986). 106

Figure 4.3: Selected cores and samples with remarkable sedimentary features. The sandy siltstones of the Murta Formation at Thungo-1 exhibit interbeds of rhythmic lamination (sample T1/24, varvites) as well as intense bioturbation (sample T1/26), both in combination with high organic matter content. The laminated and lenticular sandy successions of the Birkhead Formation at Bookabourdie-5 show organic-rich interbeds (samples B5/34, B5/35) and exhibit a lower degree of bioturbation. 121

Figure 4.4: Microscopic details of dispersed organic matter (DOM) from petrographic maceral analysis (left column: reflected light; right column: with fluorescence). a) DOM in a representative sample of the Murta Formation (Thungo-1, sample T1/24): "cutinite flames" (bright yellow in UV-light) and vitrinite in coarse siliciclastic matrix. b) DOM in a representative sample of the Birkhead Formation (Bookabourdie-5, sample B5/34): thick lamalginite (yellow/brown), "cutinite flames" (yellow/orange) and vitrinite in coarse siliciclastic matrix. 128

Figure 4.5: GC-FID/GC-MS chromatograms with signal intensities of molecular compounds from representative samples of both analyzed formations. a) Saturated hydrocarbons, hopanes and steranes (left: Murta Formation, sample W1/17; right: Birkhead Formation, sample P1/55). 132

Figure 4.6: Elemental composition, source-related Rock-Eval parameters and source-related biomarkers. a) The relation between total sulphur content (TS) and total organic carbon content (TOC) subdivided into Murta Formation (green circles) and Birkhead Formation samples (blue triangles). Classes of depositional environment (anoxic, oxic, fresh

WATER), PRESENT-DAY NORMAL MARINE LINE, AS WELL AS CRETACEOUS AND JURASSIC NORMAL MARINE PALEO-LINES (AFTER BERNER, 1984 AND BERNER & RAISWELL, 1984). B) SIMPLE DIFFERENTIATION OF KEROGEN TYPE (SOURCE OF ORGANIC MATTER) BASED ON ROCK-EVAL S_2 VS. TOC DISPLAYED AS "LANGFORD-PLOT" (CLASSIFICATION AFTER LANGFORD & BLANC-VALLERON, 1990) AND SEPARATED BY INDIVIDUAL WELLS (EXCLUDED SAMPLES / OUTSIDE DIAGRAM: T1/24, B5/34, P1/55, P1/56). C) HYDROGEN INDEX (HI) VS ROCK-EVAL T_{MAX} WITH KEROGEN TYPE CLASSIFICATION AND ONSET OF OIL/GAS WINDOWS AFTER ESPITALIÉ ET AL (1985). GREEN ELLIPSE = MURTA FM, BLUE ELLIPSE = BIRKHEAD FM. D) LOGARITHMIC CROSS PLOT OF PRISTANE/N-C_{17} AND PHYTANE/N-C_{18} RATIOS SHOWING THE DEPOSITIONAL MILIEU AND ORIGIN OF ORGANIC MATTER OF THE ANALYZED SAMPLES (AFTER CONNAN & CASSOU, 1980, MODIFIED AFTER PETERS ET AL., 1999). E) TERNARY DIAGRAM WITH RELATIVE CONTENT OF STERANE COMPOUNDS C_{27}, C_{28}, AND C_{29} FOR CLASSIFICATION OF ORGANIC MATTER ORIGIN (AFTER HUANG AND MEINSCHEIN, 1979). BOTH FORMATIONS YIELD TERRESTRIAL PALEO-DEPOSITIONAL MILIEU. F) CROSS-PLOT OF DBT/PHENANTHRENE VS PRISTANE/PHYTANE FOR THE CLASSIFICATION OF THE DEPOSITIONAL ENVIRONMENT (ZONATION AFTER HUGHES ET AL., 1995). THE MURTA FORMATION INDICATES LACUSTRINE TO FLUVIAL CONDITIONS, WHILE THE BIRKHEAD FORMATION PLOTS IN THE FLUVIAL/DELTAIC ZONE. 139

FIGURE 4.7: MATURITY-RELATED ROCK-EVAL PARAMETERS, MATURITY-RELATED BIOMARKERS AND HYDROCARBON POTENTIAL. A) THERMAL MATURITY EXPRESSED AS THE RELATION BETWEEN ROCK-EVAL T_{MAX} VS. VITRINITE REFLECTANCE. ONSET OF KEROGEN-DEPENDENT OIL WINDOW AFTER TISSOT & WELTE (1984). B) TERPANES MATURITY-RELATED RATIOS TS/TS+TM VS. C_{29}TS/C_{29}TS+C_{29} (AFTER PETERS ET AL., 2005). BOTH FORMATIONS SHOW RELATIVE LOW THERMAL MATURITY. C) CROSS-PLOT OF ISOMERIZATION RATIOS FOR C_{29} 20S/20S+20R VS. C_{29} BB/BB+AA STERANES (EQUILIBRIUM VALUES (DASHED LINES AFTER SEIFERT ET AL., 1981; SEIFERT & MOLDOWAN, 1986). D) SOURCE ROCK POTENTIAL ACCORDING TO THE LOGARITHMIC ILLUSTRATION OF THE GENETIC POTENTIAL (GP = S1+S2) VS. TOC BASED ON THE CLASSIFICATION AFTER HUNT (1996) AND PETERS & CASSA (1994). E) PRODUCED HYDROCARBONS BASED ON PRODUCTION INDEX (PI) VS. ROCK-EVAL TMAX. BOUNDARIES OF CONVERSION (ONSET GENERATION, PI = 0.1; PEAK OIL, PI = 0.5) AFTER LAW (1999); ONSET OF KEROGEN-DEPENDENT OIL WINDOW AFTER TISSOT &

WELTE (1984), SHAPES OF KEROGEN-DEPENDENT GENERATION CURVES ARE APPROXIMATED AND NOT DATABASED. 146

FIGURE 5.1: OVERVIEW MAP OF THE STUDY AREA WITH BASEMENT TOPOGRAPHY, MAIN STRUCTURAL ELEMENTS AND KEY WELL LOCATIONS. A) EROMANGA (LIGHT GREEN), COOPER (BROWN) AND WARBURTON (DARK GREEN) BASIN OUTLINES IN CENTRAL EASTERN AUSTRALIA. TASMAN LINE AFTER SCHEIBNER (1974) AND VEEVERS & POWELL (1984). B) OUTLINE OF THE COOPER BASIN AFTER STEWART ET AL. (2013) WITH COOPER BASEMENT TOPOGRAPHY AFTER HALL & PALU (2016) AND WITH MAIN STRUCTURAL FEATURES: THRUSTS AND BASEMENT LINEAMENTS MODIFIED AFTER APAK ET AL. (1997) AND PURDY ET AL. (2018); ANTICLINES AND TROUGHS MODIFIED AFTER HALL ET AL. (2015); MAGMATIC INTRUSIONS AFTER HOLGATE (2005) AND AFTER PURDY ET AL. (2018); HYDROTHERMAL PROVINCE AFTER HARDMAN ET AL. (2019); TOOKOONOOKA IMPACT AFTER BRON & GOSTIN (2012). WA = WESTERN AUSTRALIA, NT = NORTHERN TERRITORY, SA = SOUTH AUSTRALIA, QLD = QUEENSLAND, NSW = NEW SOUTH WALES, VIC = VICTORIA, TAS = TASMANIA, GMI = GIDGEALPA-MERRIMELIA-INNAMINCKA, DNC = DELLA-NAPPACOONGEE, DW = DULLINGARI-WOLLGOLLA, JNP = JACKSON-NACCOWLAH-PEPITA. 152

FIGURE 5.2: STRATIGRAPHIC OVERVIEW, PETROLEUM SYSTEM ELEMENTS AND TECTONICS OF THE STUDY AREA (MODIFIED AFTER AGBA, 2015, HALL ET AL., 2015B, 2019). A) STRATIGRAPHY OF THE COOPER BASIN. 1 = FIRST EROMANGA SUB-SEQUENCE (CUDDAPAN FORMATION, KINEMATIC ARROWS (PALEO-STRESS) MAINLY AFTER KULIKOWSKI ET AL. (2018). 159

FIGURE 5.3: HYDROCARBON FIELDS AND PETROLEUM SYSTEM OVERVIEW OF THE STUDY AREA. A) REGIONAL MAP WITH OUTLINE OF THE COOPER BASIN AND DISTRIBUTION OF ALL OIL- AND GAS FIELDS. B) ZOOM INTO THE SW COOPER BASIN, WHERE OIL- AND GAS FIELDS ARE ABUNDANT AND ARE MAINLY ASSOCIATED WITH ANTICLINES ALONG BASEMENT RIDGES (COMPARE FIGURE 5.1B). DNC = DELLA-NAPPACOONGEE, GMI = GIDGEALPA-MERRIMELIA-INNAMINCKA, JNP = JACKSON-NACCOWLAH-PEPITA, KNFZ = KARMONA-NACCOWLAH FAULT ZONE. C) SCHEMATIC PETROLEUM SYSTEM OVERVIEW SHOWING DISTRIBUTION OF HYDROCARBON FIELDS AND POSSIBLE MIGRATION INTO ANTICLINAL AND FAULT-RELATED TRAPS (MODIFIED AFTER BOWERING & HARRISON, 1986). 162

FIGURE 5.4: UPPER THERMAL BOUNDARY CONDITIONS AND PETROLEUM SYSTEM ELEMENTS (PSE) CHART. A) PALEO-WATER DEPTH (PWD) APPLIED IN THIS STUDY (MODIFIED AFTER DEIGHTON & HILL, 1998 AND DEIGHTON ET AL., 2003). B) SEDIMENT/WATER INTERFACE TEMPERATURE (SWIT) APPLIED IN THIS STUDY BASED ON WYGRALA (1989), SOUTHERN HEMISPHERE, AUSTRALIA, 27 °, WITH GLACIAL PERIOD BETWEEN 135 AND 115 MA (MODIFIED AFTER HEATHER ET AL., 1996; LADANT & DONNADIEU, 2016; ALLEY ET AL., 2019). C) PETROLEUM SYSTEM ELEMENTS (PSE) CHART. 168

FIGURE 5.5: TOTAL SUBSIDENCE WITH TEMPERATURE EVOLUTION (LEFT), CALIBRATED PRESENT-DAY TEMPERATURE BASED ON HORNER-CORRECTED BOTTOM HOLE TEMPERATURES (BHT) AND CALIBRATED THERMAL MATURITY OF FOUR SELECTED CALIBRATION WELLS LOCATED IN SOUTH AUSTRALIA. A) BEANBUSH-1, B) BURLEY-2, C) DULLINGARI-1, D) PANING-1. NOTE DIFFERENT SCALES OF X-AXIS. 172

FIGURE 5.6: TOTAL SUBSIDENCE WITH TEMPERATURE EVOLUTION (LEFT), CALIBRATED PRESENT-DAY TEMPERATURE BASED ON HORNER-CORRECTED BOTTOM HOLE TEMPERATURES (BHT) AND CALIBRATED THERMAL MATURITY OF FOUR SELECTED CALIBRATION WELLS LOCATED IN QUEENSLAND. A) ALKINA-1, B) MARENGO-1, C) SPRINGFIELD-1, D) WARNIE EAST-1. NOTE DIFFERENT SCALES OF X-AXIS. 174

FIGURE 5.7: SELECTED TIME-DEPENDENT PARAMETERS FOR THE ANALYSIS OF THE THERMO-TECTONIC EVOLUTION BASED ON EIGHT SIMULATED AND CALIBRATED KEY WELLS. A) TECTONIC SUBSIDENCE. B) SEDIMENTATION RATE (FOR TWO SELECTED WELLS ONLY, ALKINA-1, BURLEY-2). C) BASAL HEAT FLOW. D) TEMPERATURE GRADIENT. E) & F) HEATING RATE. G) TEMPERATURE AT TOP BASEMENT. 178

FIGURE 5.8: THERMAL EVOLUTION, MATURATION AND KEROGEN TRANSFORMATION OF THE ASSIGNED SOURCE ROCKS BASED ON FOUR CALIBRATED 1D MODELS (BEANBUSH-1, MARENGO-1, WARNIE EAST-1, AND BURLEY-2). A) SOURCE ROCK TEMPERATURE EVOLUTION. B) THERMAL MATURITY EVOLUTION. C) TRANSFORMATION RATIO EVOLUTION. TRANSLATION OF LAYER INDICES: (4) PATCHAWARRA FM, (5) MURTEREE SH, (6) EPSILON FM, (7) ROSENEATH SH, (8) DARALINGIE FM, (10) TOOLACHEE FM, (16) POOLOWANNA FM, (18) BIRKHEAD FM, (23) MURTA FM. 180

FIGURE 5.9: LAYER THICKNESS MAPS OF THE COOPER SEQUENCE. A) MERRIMELIA FM. B) PATCHAWARRA FM. C) MURTEREE SH. D) EPSILON FM. E) ROSENEATH SH. F) DARALINGIE FM. G) TOOLACHEE FM. H) ARRABURY FM. I) TINCHOO FM. TIRRAWARRA FM IS NOT SHOWN DUE TO ITS RELATIVELY SMALL THICKNESS.

Kinematic/tectonic indicators mainly based on Kulikowski et al. (2018). KNFZ = Karmona-Naccowlah Fault Zone. 182

Figure 5.10: Layer thickness maps of the Eromanga sequence. a) Hutton Sst incl. Poolowanna and Cuddapan formations. b) Birkhead Fm. c) Adori Sst. d) Westbourne Fm. e) Namur Sst. f) Wallumbilla Fm. g) Allaru Mdst. h) Mackunda Fm. i) Winton Fm. The relative thin layers of the Murta Fm, Cadna-owie Fm, and Toolebuc Fm are excluded. KNFZ = Karmona-Naccowlah Fault Zone, BLB = Bulloo Lake Basin. 184

Figure 5.11: Impact of uplift and erosion on thickness of the Winton Fm. a) Assigned erosion map (after Mavromatidis & Hillis, 2005). b) Resulting preserved thickness of the Winton Fm at present day. Kinematic/tectonic indicators based on Kulikowski et al. (2018). KNFZ = Karmona-Naccowlah Fault Zone. 185

Figure 5.12: Calculated basal heat flow maps for selected time steps. a) 134 Ma. b) 125 Ma. c) 120 Ma. d) 108 Ma. e) 101 Ma. f) 99.5 Ma, peak of Middle Cretaceous hydrothermal activity. g) 95 Ma. h) 62 Ma. i) Present day, peak of Quaternary hydrothermal activity. 187

Figure 5.13: Calculated maximum temperature maps for selected surfaces. a) Top basement. b) Patchawarra Fm. c) Murteree Sh. d) Epsilon Fm. e) Roseneath Sh. f) Daralingie Fm. g) Toolachee Fm. h) Birkhead Fm. i) Murta Fm. White areas indicate non-deposition or complete erosion. Note different temperature scale for the top basement. 189

Figure 5.14: Calculated present-day thermal maturity maps for most of the assigned source rock intervals. a) Patchawarra Fm. b) Murteree Sh. c) Epsilon Fm. d) Roseneath Sh. e) Daralingie Fm. f) Toolachee Fm. g) Birkhead Fm. h) Westbourne Fm. i) Murta Fm. White areas indicate non-deposition or complete erosion. 191

Figure 5.15: Phases of tectonic evolution and evolution of depocentre activity in the SW domain of the Cooper Basin from Carboniferous to Jurassic (rotated). a) Initial basin opening. b) Main phase of basin formation with oblique rifting and establishment of pull-apart structure. c) Basin inversion and ridge formation. d) Continuation of pull-apart basin. e) Compression, wedging of Innamincka Dome and transition into piggyback

basin. f) Initiation of SSE directed shearing/dragging and opening of Bulloo Lake Basin (BLB). PT = Patchawarra Trough, NT = Nappamerri Trough, TT = Tenappera Trough, WT = Weena Trough, GMI = Gidgealpa-Merrimelia-Innamincka Ridge, R1, R2 = Riedel shears / ridges. 194

Figure 5.16 (continued): Large-scale neotectonic features identified in the Cooper subregion in relation to pre-existing structures. a) (Previous page) Satellite image (Google Earth) with outline of the Cooper Basin. b) (This page) Interpretation of major structural elements inferred from surface morphology, river deviations and present-day stress field (image was rotated to show resemblance of the present-day geomorphology with the sketches in Figure 5.15). BLB = Bulloo Lake Basin, CHS = Cooper Hot Spot, PT = Patchawarra Trough, NT = Nappamerri Trough, TT = Tenappera Trough, WT = Weena Trough, GMI = Gidgealpa-Merrimelia-Innamincka Ridge, Mesozoic volcanic province after Hardman et al. (2019). 197

Figure 5.17: Depocentre migration of the stacked Cooper and Eromanga basins based on layer thickness variations. a) Crossline through the main depocentres with age of deposition overlay. b) Crossline through the main depocentres with layer thickness overlay. c) Inline through the Nappamerri Trough with age of deposition overlay. d) Inline through the Nappamerri Trough with layer thickness overlay and comparison of accumulated thickness with burial depth. See location of 2D lines in Figure 5.16. BLS = Big Lake Suite granodiorite, CESZ = Central Eromanga Shear Zone, CHS = Cooper Hot Spot. 200

Figure 5.18: Thermal modeling / calibration scenarios and burial history discussion based on the vitrinite reflectance profile at Burley-2. a) Overview of compared heat flow trends with vitrinite reflectance calibration points and calculated thermal maturity including constant heat flow scenarios. b) Best-fit scenario used to calibrate the 3D model. c) Alternative calibration with additional heat flow peak in the Jurassic. d) Alternative calibration with additional heat flow peak in the Triassic combined with erosion. 203

Figure 5.19: 3D-sketch of the crust and upwelled mantle below the Cooper Basin. Magma chambers represent assumed Cooper Pluton as part of the

MAGMATIC NETWORK RELATED TO THE MESOZOIC VOLCANIC/HYDROTHERMAL PROVINCE (COOPER HOT SPOT). BLS = BIG LAKE SUITE GRANODIORITE, CESZ = CENTRAL EROMANGA SHEAR ZONE, GMI = GIDGEALPA-MERRIMELIA-INNAMINCKA RIDGE, JNP = JACKSON-NACCOWLAH-PEPITA RIDGE, KNFZ = KARMONA-NACCOWLAH FAULT ZONE. 207

FIGURE 6.1: SCHEMATIC RECONSTRUCTION OF THE REGIONAL GEOLOGICAL SETTING AND CORRESPONDING GEOMETRY OF THE LITHOSPHERE BELOW THE GIPPSLAND BASIN OVER TIME. A) SITUATION BEFORE THE INITIAL OPENING OF THE GIPPSLAND BASIN (PRE-RIFT). B) MANTLE UPWELLING, CRUSTAL STRETCHING AND MAJOR SUBSIDENCE DURING THE SYN-RIFT. C) OROGENIC COLLAPSE AND TASMAN SEA OPENING DURING THE EARLY POST-RIFT. D) PASSIVE MARGIN FORMATION, TRANSGRESSION OF THE TASMAN SEA AND OPENING OF THE BASS STRAIT. BB = BASS BASIN, CP = CAMPBELL PLATEAU, GB = GIPPSLAND BASIN, LAB = LITHOSPHERE-ASTHENOSPHERE BOUNDARY, LFB = LACHLAN FOLD BELT, LHR = LORD HOWE RISE, NEO = NEW ENGLAND OROGEN, NR = NORFOLK RIDGE, NZ = NEW ZEALAND, SAFZ = SOUTHERN AUSTRALIAN FRACTURE ZONE, TAS = TASMANIA, VIC = VICTORIA (CONTINENTAL AUSTRALIA). PLEASE FIND LOCATION AND EXTEND OF THE BLOCKS IN FIGURE 2.20. 214

FIGURE 6.2: COMPARISON OF THERMO-TECTONIC EVOLUTION OF THE TWO STUDY AREAS WITH OVERVIEW ABOUT PHASES OF INCREASED HYDROTHERMAL ACTIVITY, PERIODS OF HYDROCARBON GENERATION (BLUE = IMMATURE, GREEN = OIL MATURE, RED = GAS MATURE) AND VOLCANIC EVENTS (RED ASTERISKS). A) TECTONIC SUBSIDENCE OVER TIME IN THE CENTRAL DEEP, GIPPSLAND BASIN. B) BASAL HEAT FLOW OVER TIME IN THE CENTRAL DEEP, GIPPSLAND BASIN. C) TECTONIC SUBSIDENCE OVER TIME IN THE NAPPAMERRI TROUGH, EROMANGA BASIN (COOPER REGION). D) BASAL HEAT FLOW OVER TIME IN THE NAPPAMERRI TROUGH, EROMANGA BASIN (COOPER REGION). CIRCLES WITH NUMBERS 1-7 INDICATE STEPS OF THE CONNECTED THERMO-TECTONIC SEQUENCE DESCRIBED IN THE TEXT. 217

FIGURE 6.3: (PREVIOUS PAGE): RELATIONSHIP BETWEEN PRESENT-DAY TOPOGRAPHY, CRUSTAL STRUCTURE AND TECTONICS AROUND EASTERN AUSTRALIA. A) OVERVIEW SATELLITE IMAGE OF PRESENT-DAY EASTERN AUSTRALIA WITH OUTLINES OF THE STUDY AREAS AND MAIN TECTONIC FEATURES RELEVANT FOR THIS THESIS (IMAGE SOURCE: GOOGLE EARTH). KATI-TANDA (LAKE EYRE) AND KUNAMA NAMADGI (MOUNT KOSCIUSZKO) ARE MARKING THE LOWEST AND HIGHEST POINTS OF

CONTINENTAL AUSTRALIA, RESPECTIVELY. THE NAIL INDICATES THE POINT OF DEEPEST MOHO IN EASTERN AUSTRALIA. B) SECTION OF THE DEPTH-TO-MOHO MAP (FROM AITKEN ET AL., 2013) OF THE AREA AROUND THE BASS STRAIT. C) TOPOGRAPHY MAP OF THE EROMANGA BASIN (MODIFIED AFTER SANDIFORD ET AL., 2020). BLACK STIPPLED LINE: LITHOSPHERIC KEEL OF THE THOMSON OROGEN, WHITE STIPPLED LINE: JUMP OF HYDRAULIC HEAD AND ZONE OF HEAVY DEFORMATION WITHIN THE CENTRAL EROMANGA BASIN. ACT = AUSTRALIAN CAPITAL TERRITORY, CB = COOPER BASIN, CBMF = COOPER BASIN MASTER FAULT, CC = CURNAMONA CRATON, CESZ = CENTRAL EROMANGA SHEAR ZONE, CHS = COOPER HOT SPOT, EB = EROMANGA BASIN, FFS = FOSTER FAULT SYSTEM, FR = FLINDERS RANGES, GB = GIPPSLAND BASIN, ID = INNAMINCKA DOME, LWFS = LAKE WELLINGTON FAULT SYSTEM, OF = OLEPOLOKO FAULT, RFS = ROSEDALE FAULT SYSTEM, THZ = TORRENS HINGE ZONE, TL = TASMAN LINE. 221

LIST OF ABBREVIATIONS

Abbreviation	Definition	Comment
AB	Amadeus Basin	tectonic depression in Australia
ACT	Australian Capital Territory	Australian internal territory
AFMB	Albany-Fraser-Musgrave Belt (= AFO)	fold belt in Australia
AFO	Albany-Fraser Orogen (= AFMB)	fold belt in Australia
AG	Adelaide Geosyncline	tectonic depression in Australia
ANT	Antarctica	continent located at the South Pole
AOI	area of interest	geographic term
AUSMEX	Australia attached to Mexico	paleo-tectonic model
AUSWUS	Australia attached to Western United States	paleo-tectonic model
BB	Bass Basin	tectonic depression in Australia
BF	Birkhead Formation	petroleum source rock in Australia
BLB	Bulloo Lake Basin	tectonic depression in Australia
BLS	Big Lake Suite, granodiorite intrusion in the Warburton Basin	magmatic intrusion in Australia
CB	Cooper Basin	tectonic depression in Australia
CBMF	Cooper Basin Master Fault	tectonic lineament in Australia
CC	Curnamona Craton	cratonic block of Australia
CCS	carbon capture and storage	technical term, method
CEFS	Cape Everard Fault System	tectonic lineament in Australia
CESZ	Central Eromanga Shear Zone	tectonic lineament in Australia
CHS	Cooper Hot Spot	geological feature in Australia
CP	Campbell Plateau	submerged land in the Southern Pacific
CSB	Centralian Superbasin	tectonic depression in Australia
DEM	digital elevation model	geographic term
DFS	Darriman Fault System	tectonic lineament in Australia
DNC	Della-Nappacoongee ridge	positive tectonic feature in Australia
DO	Delamerian Orogen	fold belt in Australia
DOM	dispersed organic matter	geochemical term
EAN	East Antarctica	part of the Antarctic continent
EB	Eromanga Basin	tectonic depression in Australia
EGS	enhanced geothermal system	technical term, method
EWB	Eastern Warburton Basin	tectonic depression in Australia
FFS	Foster Fault System	tectonic lineament in Australia
Fm	stratigraphic formation	geological term
GAB	Great Artesian Basin	tectonic depression in Australia
GB	Gippsland Basin	tectonic depression in Australia
GC	Gawler Craton	cratonic block of Australia
GC*	gas chromatography	technical term, method
GC-FID	gas chromatography with coupled flame ionization detector	technical term, method

Abbreviation	Definition	Comment
GC-MS	gas chromatography coupled with mass spectrometry	technical term, method
GMI ridge	Gidgealpa-Merrimelia-Innamincka ridge	positive tectonic feature in Australia
Gp	stratigraphic group	geological term
HAS	hot sedimentary aquifer	technical term, method
HC	hydrocarbons	chemical term
ID	Innamincka Dome	positive tectonic feature in Australia
IFS	Innamincka Fault System	tectonic lineament in Australia
JNP	Jackson-Nackowlah-Pepita ridge	positive tectonic feature in Australia
KC	Kimberley Craton	cratonic block of Australia
KNFZ	Karmona-Naccowlah Fault Zone	tectonic lineament in Australia
LAB	lithosphere-asthenosphere boundary	geological term
LEB	Lake Eyre Basin	tectonic depression in Australia
LFB	Lachlan Fold Belt (= LO)	fold belt in Australia
LHR	Lord Howe Rise	submerged terrane in the Tasman Sea
LO	Lachlan Orogen (= LFB)	fold belt in Australia
LPG	liquefied petroleum gas	technical term, method
LRVE	locally refined volumetric elements	numerical gridding method
LWFS	Lake Wellington Fault System	tectonic lineament in Australia
MB	Murray Basin	tectonic depression in Australia
MC	Mawson Craton	cratonic block of Antarctica
MF	Murta Formation	petroleum source rock in Australia
MO	Musgravian Orogen	fold belt in Australia
Moho	Mohorovičić discontinuity	geological term
MPI-1	Methylphenantrene Index	geochemical term
NAC	North Australian Craton (= NAE)	cratonic block of Australia
NAE	North Australian Element (= NAC)	cratonic block of Australia
NC	New Caledonia	island in the Tasman Sea
NEO	New England Orogen	fold belt in Australia
NPR	North Phoenix Ridge	middle-oceanic ridge active during the Cretaceous
NR	Norfolk Ridge	submerged terrane in the Tasman Sea
NSW	New South Wales	Australian federal state
NT	Nappamerri Trough	tectonic depression in Australia
NT*	Northern Territory	Australian internal territory
NZ	New Zealand	two big islands in the Tasman Sea
OB	Officer Basin	tectonic depression in Australia
OEP	Odd-to-even predominance	geochemical term
OM	organic matter	geochemical term
OT	Otway Basin	tectonic depression in Australia
PA	Proto-Australia	paleo-tectonic plate configuration
PC	Pilbara Craton	cratonic block of Australia
PI	production index	geochemical term
PO	Paterson Orogen	fold belt in Australia
PSE	petroleum system elements	geological term

Abbreviation	Definition	Comment
PT	Patchawarra Trough	tectonic depression in Australia
QLD	Queensland	Australian federal state
RAI	Relative Acoustic Impedance (seismic attribute)	technical term, method
RFS	Rosedale Fault System	tectonic lineament in Australia
RMS	Root Mean Square amplitude (seismic attribute)	technical term, method
RO	Rudall Orogen	fold belt in Australia
RP	Rio de la Plata Craton	cratonic block of South America
SA	South Australia	Australian federal state
SAC	South Australian Craton (= SAE)	cratonic block of Australia
SAE	South Australian Element (= SAC)	cratonic block of Australia
SAFZ	South Australian Fracture Zone	tectonic lineament in Australia
SB	Surat Basin	tectonic depression in Australia
SCB	South China Block	cratonic block of SE Asia
SF	São Francisco Craton	Cartonic block of South America
SO	Sibao Orogen	fold belt in Australia
SPR	South Phoenix Ridge	middle-oceanic ridge active during the Cretaceous
SWEAT	Southwest United States attached to East Antarctica	paleo-tectonic model
TAFB	Trans-Australian Fold Belt	geological feature in Australia
TAR	terrigenous to aquatic ratio	geochemical term
TAS	Tasmania	cratonic block and federal state of Australia
TC	Tanzania Craton	cratonic block of Africa
TE	Tasman Element	continental crustal block of Australia
THZ	Torrens Hinge Zone	tectonic lineament in Australia
TL	Tasman Line	tectonic lineament in Australia
TR	Tasman Ridge	middle-oceanic ridge of Tasman Sea
TS	Tasman Sea	ocean to the east of Australia
TSC	Tasman Spreading Centre	triple point of continent separation during the Late Cretaceous
TT	Tenappera Trough	tectonic depression in Australia
VBM	volume-based modelling	technical term, method
VIC	Victoria	Australian federal state
WA	Western Australia	Australian federal state
WAE	West Australian Element	cratonic block of Australia
WAN	West Antarctica	part of the Antarctic continent
WB	Warburton Basin	tectonic depression in Australia
WT	Weena Trough	tectonic depression in Australia
WVP	Whitsunday Volcanic Province	volcanic province in Australia
WWB	Western Warburton Basin	tectonic depression in Australia
YC	Yilgarn Craton	cratonic block of Australia

LIST OF SYMBOLS AND UNITS

Symbol	Definition	Physical dimension	in SI base units (if available)
API gravity	measure for oil viscosity, given in °		-
bbl	barrel of oil	volume	0.159 m^3
Bcm	**billion** cubic meters, also Gcm	volume	1,000,000,000 m^3
BHT	bottom hole temperature, given in °C	temperature	K
boe	barrel of oil equivalent	volume	0.159 m^3
CO_2	carbon dioxide (chemical molecule)		-
Ga	**billion** years	time	3.1536e+16 s
Gbbl	**billion** barrels, also Bbbl	volume	158,987,294.928 m^3
Gboe	**billion** barrels of oil equivalent, also Bboe	volume	158,987,294.928 m^3
GJ	**giga**joule	work / energy	1e+12 kgm^2/s^2
GP	genetic potential	weight ratio	mg HC/g rock
Gt	**billion** tonnes	mass	1,000, 000,000,000 kg
h	thickness	length	m
h_c	thickness of the crust	length	m
HF	heat flow, given in mW = milliwatt	combined	mW/m^2
HI	hydrogen index	weight ratio	mgHC/gTOC
h_m	thickness of the lithospheric mantle	length	m
h_w	water depth	length	m
J	joule	work /energy	1 kgm^2/s^2
kt	**thousand** tonnes	mass	1,000,000 kg
kW	**kilo**watt	power	1,000 W
m/z	mass/charge ratio	combined	kg/As
Ma	**million** years	time	3,1536e+13 s
MD	measured depth	length	m
MJ	**mega**joule	work	1,000,000 kgm^2/s^2
MMbbl	million barrels; **M = mille = thousand**	volume	1,000,000 m3
MPa	**mega**pascal	pressure	1,000,000 Pa
Mt	**million** tonnes	mass	1,000,000,000 kg
MW	**mega**watt	power	1,000,000 W
mW	**milli**watt	power	0.001 W
OSI	oil saturation index	weight ratio	mgHC/gTOC
PJ	**peta**joule	work / energy	1e+15 kgm^2/s^2
PWD	paleo-water-depth	length	m
q	heat flow, given in mW = milliwatt	combined	mW/m^2
RC	calculated thermal maturity		%
Ro	vitrinite reflectance in oil		%
S1	free hydrocarbons released during Rock-Eval pyrolysis	weight ratio	mg HC/g rock
S2	thermally generated (“cracked”) hydrocarbons during Rock-Eval pyrolysis	weight ratio	mg HC/g rock

Symbol	Definition	Physical dimension	in SI base units (if available)
S3	generated carbon dioxide (CO_2) during Rock-Eval pyrolysis	weight ratio	mg HC/g rock
Sh_{max}	maximum horizontal stress, given in MPa	pressure	Pa
SWIT	sediment-water-interface temperature (=T_{swi}), given in °C	temperature	K
T_b	temperature at the base of the lithosphere, given in °C	temperature	K
TC	total carbon	weight ratio	wt.%
Tcf	**trillion** cubic feet	volume	28,316,846,592 m^3
Tcm	**trillion** cubic meters	volume	1e+12 m^3
TD	total depth	length	m
TIC	total inorganic carbon	weight ratio	wt.%
T_m	pyrolite melting temperature, given in °C	temperature	K
T_{max}	maximum temperature, given in °C	temperature	K
TOC	total organic carbon	weight ratio	wt.%
TR	transformation ratio (kerogen to petroleum)		%
T_s	surface temperature, given in °C	temperature	K
TS	total sulphur	weight ratio	wt.%
T_{swi}	sediment-water-interface temperature (=SWIT), given in °C	temperature	K
VR_r	vitrinite reflectance (random orientation)		%
β	stretching factor	dimensionless	-
λ	thermal conductivity	combined	W/m/K
ρ	specific density	combined	kg/m^3

LIST OF APPENDICES

APPENDIX 1 (CHAPTER 3) 261

APPENDIX 2 (CHAPTER 4) 263

APPENDIX 3 (CHAPTER 5) 305

1 INTRODUCTION

1.1 Primary energy demand and the geological subsurface

Reliable and affordable energy supply is the backbone of our civilization's development and of our economic prosperity. Steady population growth and increasing living standards are creating a constantly growing demand for energy resources of currently 13.9 Gboe (primary total annual energy consumption in 2019), which we use to heat our homes, fuel our cars and power our industry (BP, 2019, **Figure 1.1**).

Recently, the share of fossil fuels in the global energy mix yielded 85 % (BP, 2019) and remaining total proven reserves of crude oil (1,729.7 Gbbl, including condensates and natural gas liquids), natural gas (196.9 Tcm) and coal (1,054.7 Gt, BP 2019) could still deliver abundant energy for future generations. However, these reserves are limited and are not renewable.

Further, relatively cheap combustion of energy-efficient fossil fuels comes with a price for the global climate and for the habitability of our planet: it generates huge volumes of greenhouse gas (mainly carbon dioxide, CO_2), which contributes to human-caused global warming at accelerating rates since about a century. Although the anthropogenic impact on climate is thought to be irreversible on human time scale (Ciais et al., 2014), these emissions need to be substantially reduced to mitigate e.g., catastrophic sea level rise, extreme weather events, melting ice caps, desertification of habitats and extinction of entire food chains (IPCC, 2013).

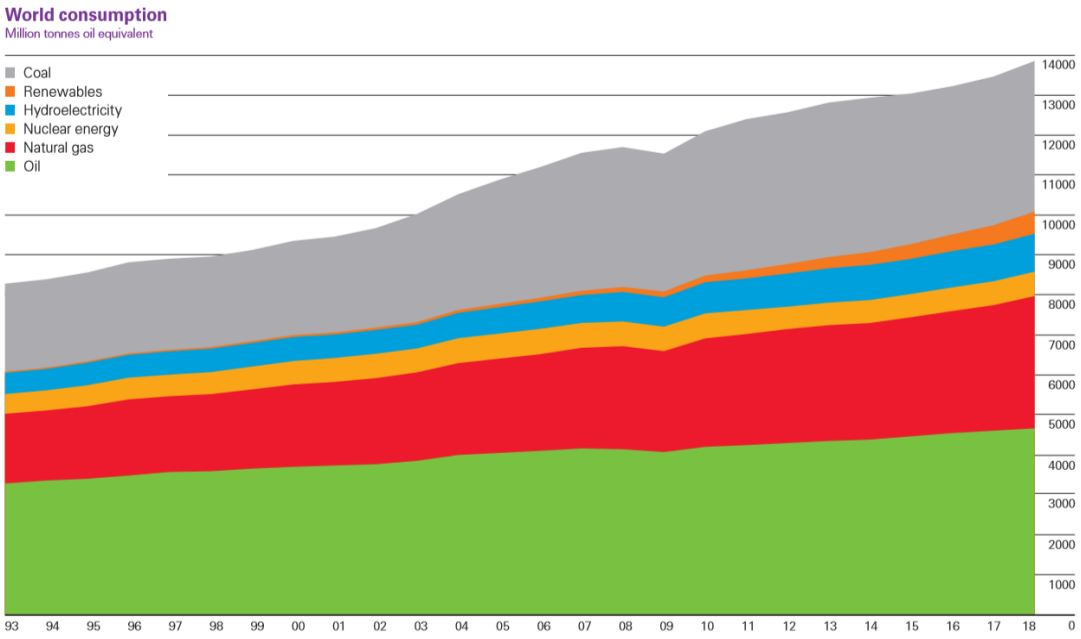

Figure 1.1: Global annual primary energy consumption by sector from 1993 to 2018 (BP, 2019).

Consequently, today's scientists, engineers and policymakers are supporting the Paris Agreement (UNFCCC, 2020) and are now facing a dual challenge – continue providing affordable energy for a developing society, while simultaneously meeting climate goals and reducing environmental impacts (ExxonMobil, 2019).

During the last years, global growth of oil and coal consumption constantly slowed, while shares of renewable energy sources and comparably clean natural gas were slightly increasing. Nevertheless, annual CO_2 emissions from fossil fuel combustion continued to increase and just reached an historic maximum of 33.9 Gt (BP, 2019; IEA, 2020a).

It required a global pandemic to reverse this trend. The Covid-19 crisis in 2020 caused a historic economic downturn with massive consequences for the global energy demand, which will likely drop by about 6 % during that year (IEA, 2020a). On 20 April 2020, exceeding oil storage capacity due to plummeting demand even caused temporarily negative oil prices for the first time in history. Further, global annual CO_2 emissions are expected to reach about 30 Gt at year-end 2020, which would be the lowest level since 2010, about 8 to 9 % lower than in 2019, and the largest year-to-year CO_2 emission reduction ever (IEA, 2020a, 2020b; Liu et al., 2020, **Figure 1.2**).

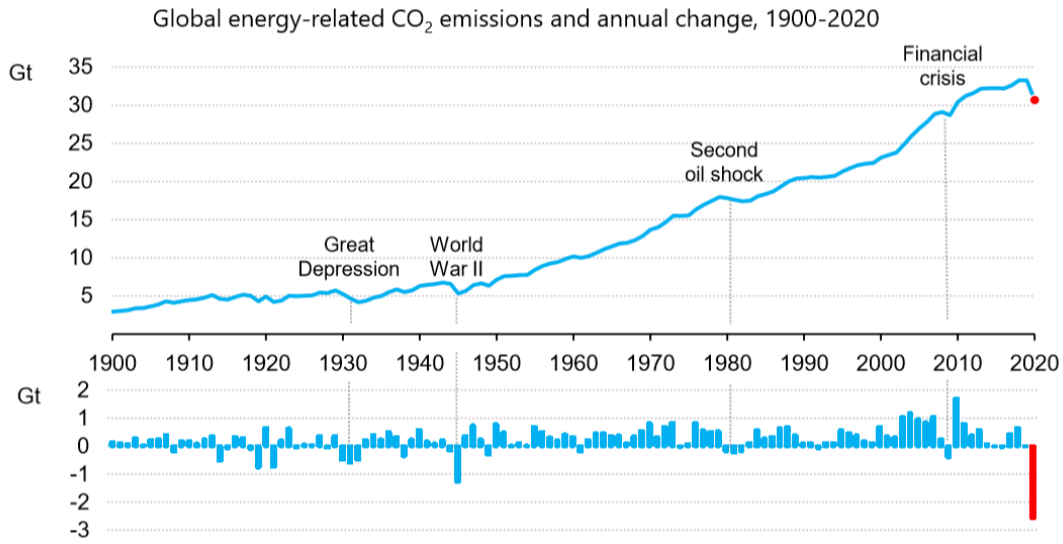

Figure 1.2: Global energy-related CO_2 emissions from 1900 to 2020 (IEA, 2020b).

Most likely, global markets will recover and energy demand will strongly rebound in the post-pandemic world (IEA, 2020a, 2020b). However, a more versatile, more flexible, more efficient and more sustainable use of the geological subsurface is required to realize longterm emission reductions.

Besides the extraction of raw materials, production of conventional, renewable and geothermal energy, the wide potential of the geological subsurface – particularly of sedimentary basins – includes intermediate gas storage (natural gas, hydrogen), and the permanent storage of CO_2 and nuclear waste (BGR, 2020). Especially, carbon capture and underground storage (CCS) technologies will play a decisive role in the future development of the geological subsurface and the energy infrastructure.

Consequently, a stronger commitment to climate goals and a deeper focus on the "vertical component" of our planet will be required to meet the dual challenge and to support a clean energy transition.

1.2 Australia's energy resources overview

Australia hosts abundant energy resources and is the world's largest coal exporter. Total proven non-renewable energy resources yield 6,277,275 PJ (thereof 3,519,155 PJ economically extractable) and are dominated by black coal (1,916,697 PJ) (AERA, 2020a, **Table 1.1**, **Figure 1.3**). Coal is the dominant source of primary energy consumption in Australia (40 %) and accounts for about 75 % of the domestic electricity

generation (GA, 2020a). Additional to 147.4 Gt of coal (all types combined, 14.0 % of global), proven fossil fuel reserves at end 2018 included 2.4 Tcm of natural gas (1.2 %, including coal seam gas / coal bed methane) and only 4 Gbbl of crude oil (0.2 % of global, including condensates and natural gas liquids) (BP, 2019).

In 2018, by exporting 91.8 Bcm liquefied petroleum gas (LPG, 21.3 % of global) mainly to the Asian/Pacific market, Australia was the world's second largest LPG exporter behind Qatar (104.8 Bcm, 24.3 %, BP, 2019).

Table 1.1: Australian non-renewable energy resources (AERA, 2020a). a. Includes Economic Demonstrated Resources and Subeconomic Demonstrated Resources; b. Includes reserves; c. Includes reserves and contingent resources; d. Recoverable coal resources; e. Recoverable resources at <US$130/kg; f. A conversion into energy content equivalent for thorium was not available at the time of publication; g. Excludes thorium resources. kt = thousand tonnes; LPG = liquefied petroleum gas; PJ = petajoule.

Resource	Unit	Economic Demonstrated Resources	Total Demonstrated Resources[a]
Crude oil	PJ	3286[b]	7066[c]
Condensate	PJ	7421[b]	16 463[c]
LPG	PJ	2633[b]	5957[c]
Shale oil	PJ	0[b]	0[c]
Oil shale	PJ	0[b]	0[c]
Conventional gas	PJ	77 253[b]	186 235[c]
Coal seam gas	PJ	45 895[b]	79 450[c]
Tight gas	PJ	39[b]	1748[c]
Shale gas	PJ	0[b]	12 252[c]
Black coal[d]	PJ	1 916 697	1 999 669
Brown coal[d]	PJ	754 855	3 250 352
Uranium[e]	PJ	711 076	718 083
Thorium	kt[f]	0	130
Total resources[g]		3 519 155	6 277 275

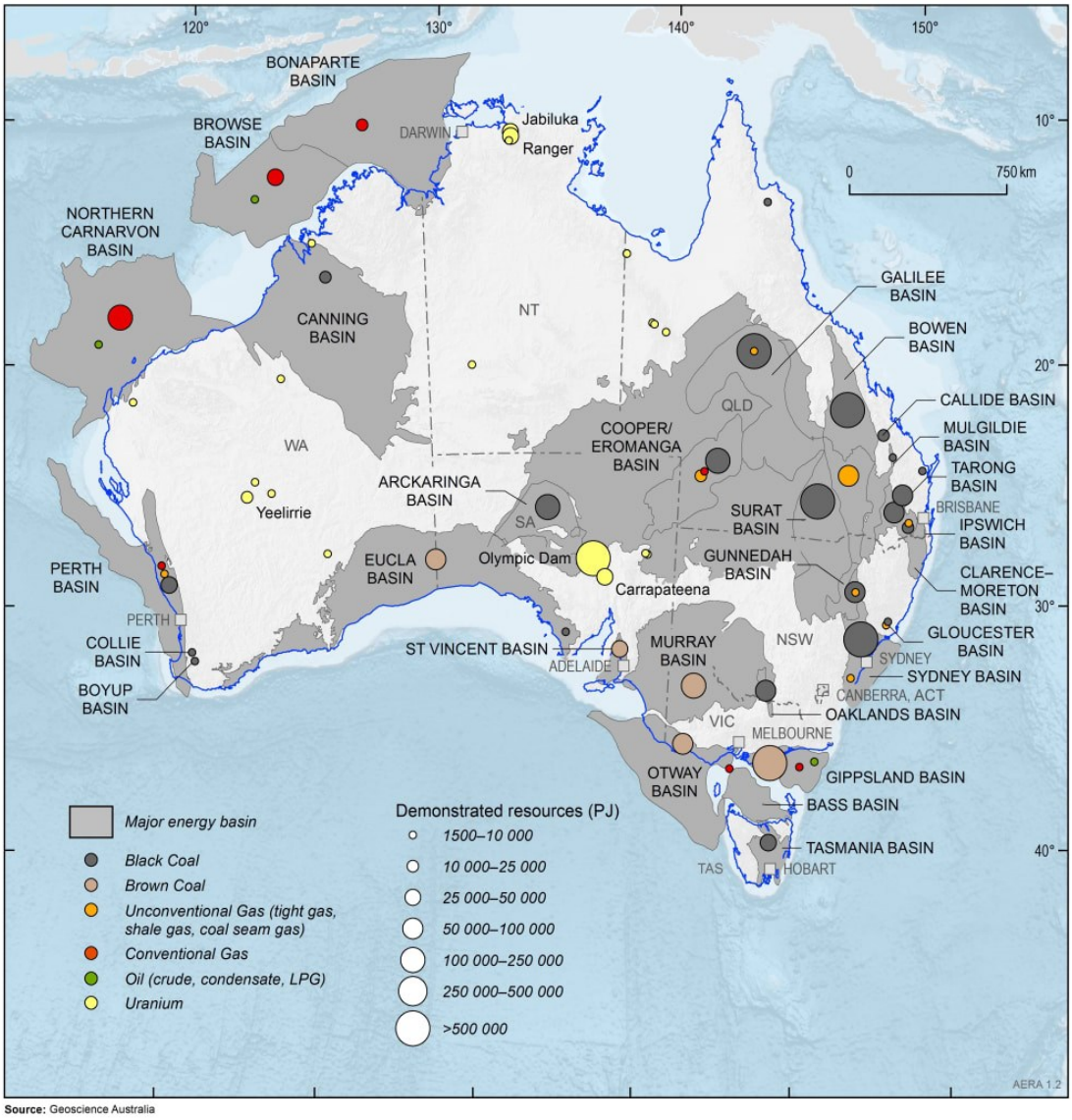

Figure 1.3: Distribution of Australia's major (containing more than 1,500 PJ) non-renewable energy resources (AERA, 2020a).

Renewable energy resources like hydro (8,018 MW annual capacity), wind (4,980 MW), solar (7,332 MW, large-scale and small-scale combined) and bioenergy (812 MW) have already established in the Australian energy mix (**Table 1.2**), while geothermal energy production (1.1 MW) is still in the early stages of development (AERA, 2020a, 2020b). Australia's future geothermal energy potential appears huge, but suitable areas are often located far from population centres (AERA, 2020a, **Figure 1.4**). Nevertheless, large areas in central east Australia and near Darwin in the north show elevated subsurface temperatures and might play important roles in future development of geothermal energy (AERA, 2020b, **Figure 1.5**).

Table 1.2: Renewable electricity generation capacity in Australia (AERA, 2020a). a. Large-scale electricity generation capacity. b. Large-scale electricity generation capacity (small-scale rooftop solar installation generation capacity). c. Includes bio generation capacity from bagasse, landfill gas and sewage, forest residues and other sources. MW = megawatt.

Energy resource	Capacity (MW)
Geothermal	1.1
Hydro	8018
Wind	4980[a]
Solar	310 (7022)[b]
Ocean	1
Bioenergy	812[c]
Total	14 122.1 (21 144.1)

Industry committment and public investments recently increased to make use of Australia's geological subsurface particularly for CCS. Sedimentary basins of Australia have an estimated capacity of injecting CO_2 at a rate of 300 Mt per year for at least 100 years and can therefore substantially support meeting global climate goals (Santos, 2020).

Further, besides large uranium resources for nuclear energy generation (AERA, 2020a, **Table 1.1**), Australia also hosts some noteable key mineral deposits for the energy transition (Cobalt, Lithium and rare earth metals, BP 2019).

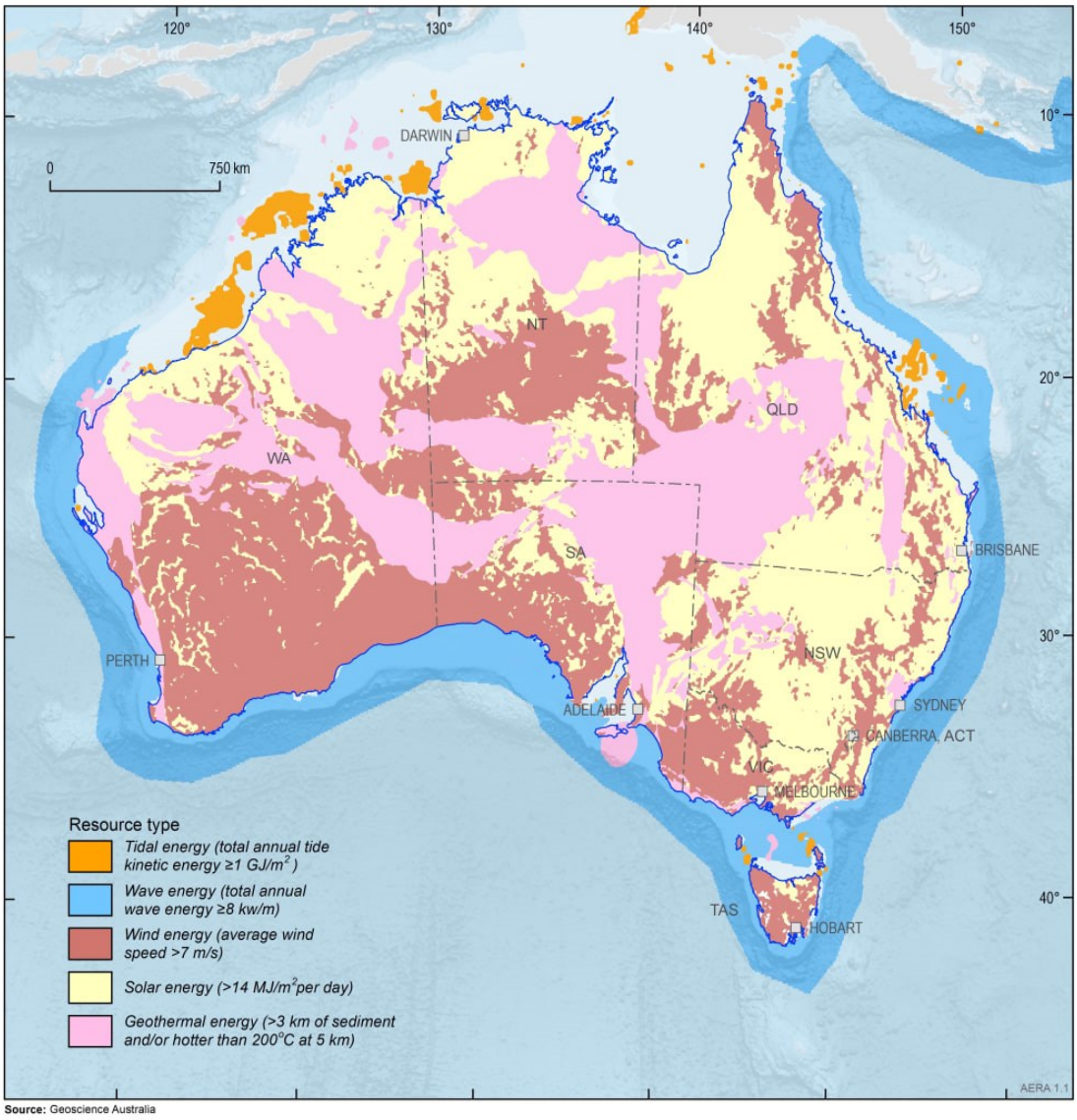

Figure 1.4: Distribution of Australia's renewable energy resources, excluding bio and hydro resources (AERA, 2020a).

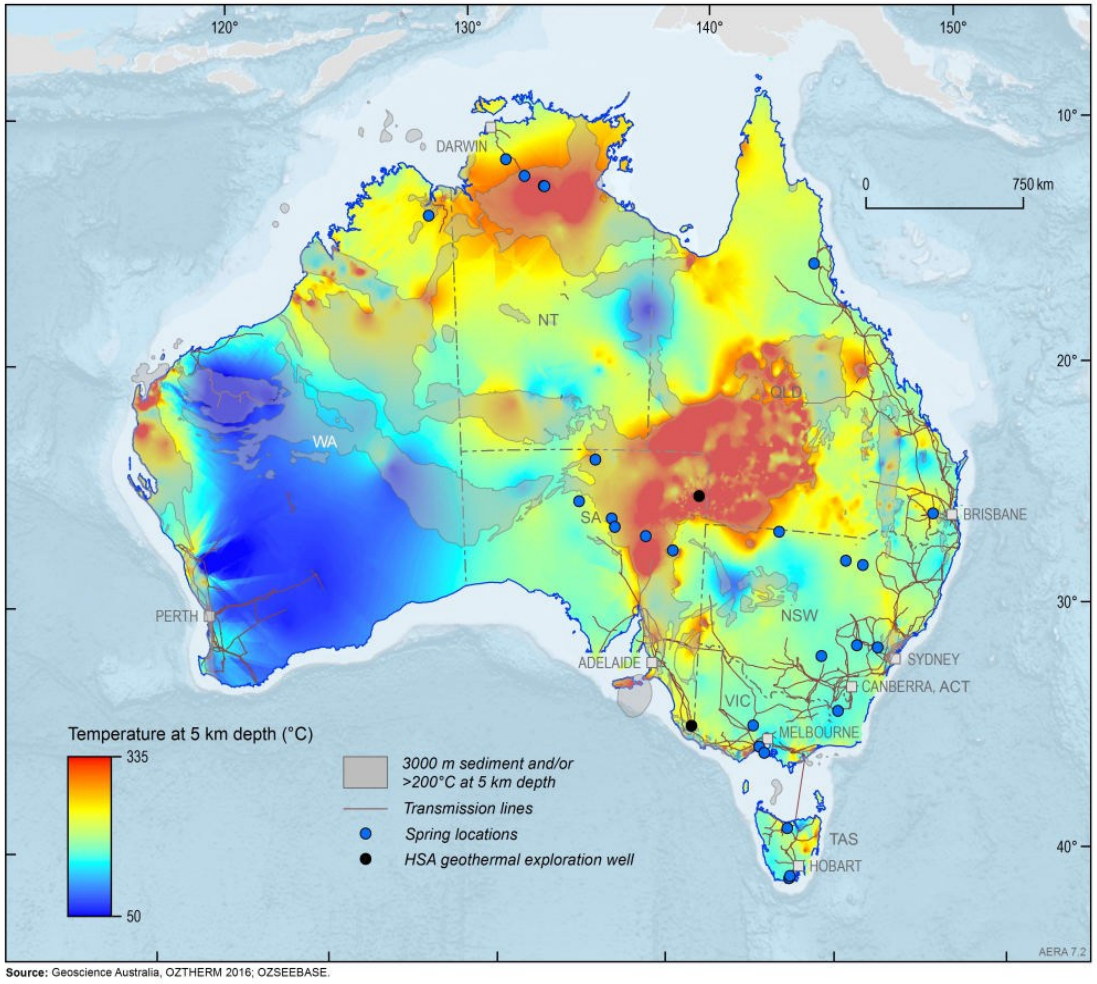

Figure 1.5: Predicted temperature at 5 km depth, showing HSA exploration wells, hot spring locations and areas with >3 km depth and/or 200 °C at 5 km depth (AERA, 2020b). HSA = hot sedimentary aquifer.

1.3 Petroleum systems and the global carbon cycle

A complete (conventional) petroleum system or hydrocarbon system (see **Figure 1.6**) is roughly defined by four main elements: a porous and permeable rock formation (reservoir), an overlying impermeable layer (seal), a three-dimensional structure (trap) and an underlying layer of organic-rich sediments (source rock, Hantschel & Kauerauf, 2009; Dembicki, 2017).

The depositional environment that is mainly determined by the degree of organic productivity, preservation potential and availability of oxygen is directly influencing the development of source rocks and their organic carbon content (e.g. Tissot & Welte, 1984; Peters et al, 2005a, 2005b). Most favorable conditions for the formation of source rocks occur in peat swamps and upwelling areas. Throughout geological history, numerous

source rocks (mainly coal and shale) formed along continental shelfs and within various sedimentary basins across the planet. Tectonic subsidence and subsurface temperature variations over time led to maturation and transformation of organic matter (kerogen and bitumen) into coal and hydrocarbons (oil and gas). The right timing of petroleum system processes like hydrocarbon expulsion, migration and trap formation decides if accumulations form in the subsurface or if oil and gas is leaking to the surface and escapes into the atmosphere (Peters & Cassa, 1994; Hantschel & Kauerauf, 2009).

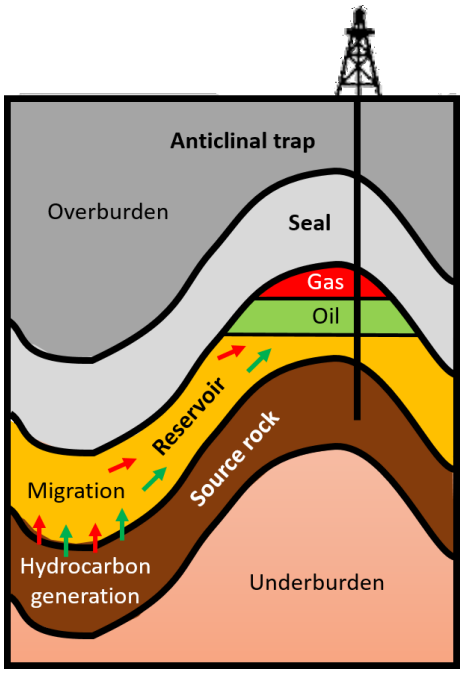

Figure 1.6: Scheme of a simple (conventional) petroleum system (modified after Dembicki, 2017).

Source rocks represent the most important element of a petroleum system and their quality can be assessed with numerous geochemical analytical methods (e.g., Tissot & Welte, 1984; Peters et al, 2005a, 2005b). One key parameter for source rock evaluation is the quantity of organic matter (kerogen and bitumen) expressed in total organic carbon (TOC) content, representing the ratio of all organic-matter related carbon atoms to the total mass of the rock matrix (Hantschel & Kauerauf, 2009). Additional information about source rock quality (including organic matter type, thermal maturity and hydrocarbon generation potential) is provided by organic geochemistry and programmed pyrolysis (or Rock-Eval pyrolysis, e.g., Espitalié et al., 1977; Horsfield, 1984; Espitalié, 1985; Peters & Cassa, 1994; Law, 1999). Obtained parameters can be used and combined to derive additional source rock properties and to support interpretation.

While kerogen classification primarily helps to reconstruct paleo-depositional environments and to determine specific kinetic models for kerogen transformation, maceral analysis complements these interpretations with information about thermal maturity (e.g., Tissot & Welte, 1984; Pepper & Corvi, 1995a). Vitrinite macerals, e.g., which represent remains of woody plant material, are abundant in coal, in coaly particles and occur as dispersed organic matter in most clastic rocks. Since its capability to reflect incident light systematically and irreversibly increases with time and temperature, vitrinite reflectance is the most widely used measure of coal rank and therefore of a rock's thermal maturation (e.g., Sweeney & Burnham, 1990; Peters et al., 2005a; Hantschel & Kauerauf, 2009). Consequently, comprehensive maturity vs. depth profiles can support the reconstruction of the subsidence history and the paleothermometry of sedimentary basins.

Before humans started to extract coal, crude oil and natural gas reserves from sedimentary basins, these sources of energy acted as natural carbon sinks and important long-term buffers of the delicately balanced global carbon cycle (**Figure 1.7**). Due to human activity since the industrial revolution (i.e., combustion of fossil fuels, agriculture) these buffers are rapidly reducing and the "Earth as a System" got out of equilibrium (Falkowski et al., 2000; Ciais et al., 2014). Even increased carbon uptake of oceans and vegetation as a natural response is not capable of absorbing excess carbon from anthropogenic emissions and land use change. Currently, the global carbon budget shows a surplus of about 0.4 Gt annually (Friedlingstein et al., 2019, **Figure 1.7**).

Today, gradually depleting hydrocarbon reservoirs provide suitable porous media combined with impermeable seals capable of hosting large volumes of CO_2 very similar to the oil and gas that was once trapped there for millions of years.

Current industry trends include not only increasing CO_2 cycling for enhanced recovery of oil and gas to boost efficiency (Suebsiri et al., 2006), but also large-scale removal of CO_2 from the atmosphere and injecting it into the geological subsurface for longterm storage. Additionally, short-term underground storage of natural gas and hydrogen for renewable energy systems becomes increasingly marketable (e.g., BGR, 2020).

In the context of the ongoing energy transition, the usage of sedimentary basins is currently changing from sources of energy to targets for excess atmospheric carbon and gas storage in order to meet the societal needs. Finally, remaining resources of oil and gas will be explored, developed and produced more efficiently and more environmentally-

friendly, while the infrastructure will change towards a system, which will increasingly incorporate reverse flow of carbon back into the geosphere.

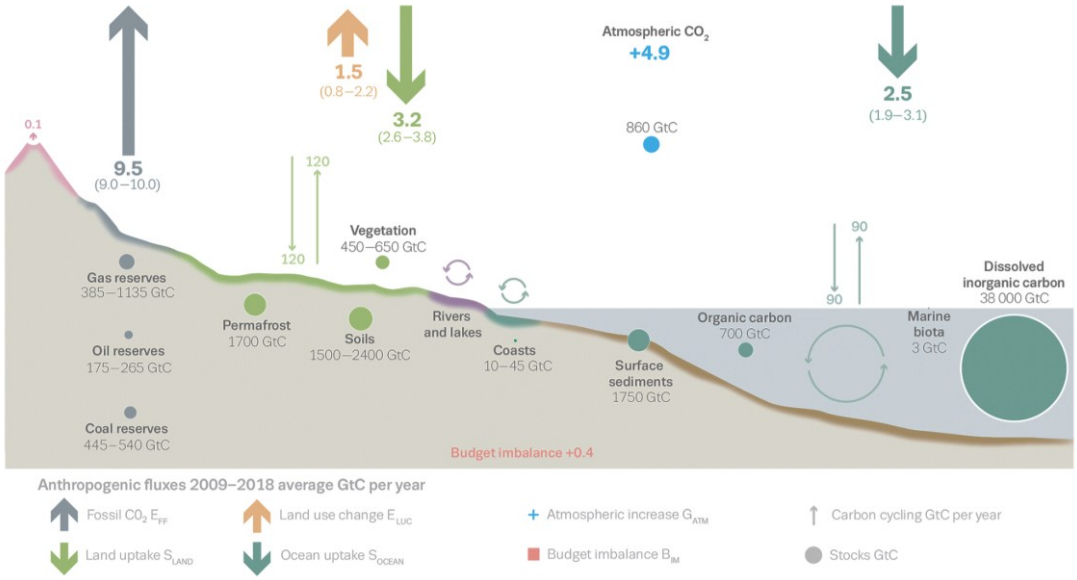

Figure 1.7: Schematic overall perturbation of the global carbon cycle caused by anthropogenic activities (Friedlingstein et al., 2019 and references therein). Values averaged globally for the decade 2009–2018.

1.4 Numerical basin and petroleum system modeling

Large-scale endogenous and exogenous processes like mantle-dynamics, plate tectonics, and climate are continuously influencing each other and are shaping the Earth's crust and its surface that humans are populating. These complex processes are controlling sea-level fluctuations, uplift and erosion rates, subsidence and sediment transport, the global carbon cycle, variances of the depositional environment as well as the heat flow and the temperature distribution within the crust and the sediments. The interaction of these processes accumulates in the formation of mountain ranges, oceans, and sedimentary basins (McKenzie, 1978; Littke et al., 2008; Allen & Allen, 2013).

Today, thanks to fast developing computer technology and accelerating processing capacity, integrated software programs can simulate many of these complex and interacting processes (e.g., Hantschel & Kauerauf, 2009; Galushkin, 2016). The related approach is generally summarized as "numerical basin and petroleum system modeling".

Originally, basin and petroleum system modeling software was developed to support the evaluation of hydrocarbon reserves in sedimentary basins. However, basin-scale geological studies aiming on the reconstruction of complex petroleum systems require thorough data acquisition, careful (computer-assisted) analysis, iterative modeling and quality control of already existing information, and deep comprehension of the spatial, chronological, physical and chemical interplay of numerous influencing parameters from micro- to macrometre-scale. Therefore, the systematic understanding of the geological, geochemical, thermal and structural evolution of a sedimentary basin and its uncertainties is needed before additional assumptions and new conclusions about the timing of petroleum system elements and processes throughout the respective sedimentary basin and the potentiality of prospective resources can be made (Tissot & Welte, 1984; Welte et al., 1997; Littke et al., 2008; Al-Hajeri et al., 2009, Hantschel & Kauerauf, 2009; Allen & Allen, 2013). Therefore, software development and scientific progress need to go hand in hand and should stimulate each other.

With accelerating computational power and increasing knowledge about the geological subsurface, the understanding and interpretation of geological, geophysical and geochemical data during the application of basin and petroleum system modeling is going well beyond industrial applications. Combined with knowledge in structural geology, petrophysics, paleothermometry and other related disciplines, this approach is capable of reconstructing the subsidence, exhumation and thermal history of sedimentary basins, fold belts and entire mountain ranges (e.g., Grobe et al., 2019; Karg & Littke, 2020).

A typical software-based basin modeling workflow includes processing of input data, model calibration and simulation, iterative scenario modelling and output analysis. Basic modeling exercises aim on reconstructing the burial history and thermal evolution of a sedimentary basin to predict source rock maturation as well as hydrocarbon expulsion, migration and trapping (e.g., Welte et al., 1997).

Today, various detailed kinetic models are available to simulate source rock maturation, transformation and hydrocarbon expulsion. Complex flow models help to predict fluid migration and accumulation of oil and gas, and comprehensive heat flow and crustal modeling tools support the reconstruction of the thermal evolution of the subsurface (Tissot & Welte, 1984; Taylor et al., 1998). The application of exploration risk assessment, prospect and play analysis as well as integration of more complex geophysical data (e.g., potential fields) increasingly complemented the broad capabilities of this modeling approach over the years (Hantschel & Kauerauf, 2009).

Basin modeling software for 1D/2D/3D and 4D applications is available from many different providers: BasinMod (Platte River Associates, Inc.), Genesis-Trinity (Zetaware), Genex,Temis 2D,3D (Beicip/IFP), JewelSuite (Baker Hughes), Migri, MigriX (Migris), Novva (Sirius Exploration Geochemistry Inc.), PBM-Pars Basin Modeler (Research Institute of Petroleum Industry), Permedia/Landmark (Halliburton), PetroMod (Schlumberger), Sigma2D (JNOC/TRC), and WinBury software.

In two chapters of this thesis, PetroMod from Schlumberger was used to reconstruct the subsidence history and the thermal evolution of sedimentary basins and to assess corresponding source rock maturation and the timing of hydrocarbon expulsion (see **Chapters 3** and **5**). While it still plays – and will further play – an important role during conventional and unconventional hydrocarbon exploration, also new integrated and multidisciplinary approaches related to resource efficiency and in the context of the energy transition are obvious. Numerical basin modelling can predict suitable conditions for geothermal energy generation (e.g., Ondrak et al., 1998; Beardsmore, 2004), assist the volume estimation of naturally released methane and CO_2 into the atmosphere over geologic time to improve our understanding of the global carbon cycle and to complement climate models (Kroeger et al., 2011; Berbesi et al., 2014). Further, the classic assessment of seal integrity could easily be extended by predicting underground storage conditions for nuclear waste (Fink et al., 2019), for hydrogen and CO_2 (e.g., Jimenez et al., 2003; O'Brien et al., 2008).

Finally, continuous exchange between industry and academia is required to realize the full potential of this powerful approach for the benefit of our modern society and it would be a fundamental error and misunderstanding to restrict the application of this brilliant technology only to the exploration of oil and gas.

1.5 Objectives and organization of the thesis

This thesis consists of six chapters. The first chapter contains the introduction to the topic by giving a short overview about the challenge of primary energy generation, energy resources of Australia, and the approach of numerical basin and petroleum system modeling. The second chapter provides a review of the **Tectonic evolution of Australia**. Each of the chapters **3**, **4** and **5** deals with a separate topic and describes performed research based on different methods in the form of independent research articles. In **Chapter 6**, concluding remarks and an outlook are given.

Chapter 3 was published as *Röth, J., Parent, A., Warren, C., Hall, L.S., Palmowski, D., Koronful, N., Husein, S.S., Sachse, V., Littke, R., (2021). Lithospheric evolution, thermo-tectonic history and source-rock maturation in the Gippsland Basin, Victoria, southeastern Australia*. In: Australian Journal of Earth Sciences, https://doi.org/10.1080/08120099.2021.1938219

This chapter mainly aims on understanding the evolution of the hyperextended crust below the offshore part of the Gippsland Basin in southeastern Australia and its unusually thick sedimentary fill. The study was motivated by the following key research question:

Is it possible to reconstruct the tectonic evolution and the thermal history of the Gippsland Basin based on McKenzie-type crustal layer modeling and thus to draw new conclusions about the timing of the overlying petroleum system?

For many years, the Gippsland Basin represented Australia's main offshore petroleum province. Some of its distal areas around the deep Bass Canyon are still underexplored and this important sedimentary basin recently became subject to new investigations. In cooperation with Schlumberger Aachen and Geoscience Australia (Australian Government), an extensive 3D dataset of the Gippsland Basin (i.e., 3DGEO, 2011) was modified and analyzed. Methods included the seismic interpretation of sedimentary horizons and the modification of the basement topography, mapping of major faults and magmatic features and the application of numerical McKenzie (pure shear) crustal layer models (McKenzie, 1978; Hantschel & Kauerauf, 2009).

The thermal history of the offshore Gippsland Basin was reconstructed by using a two-step inversion workflow, which calculates stretching of crust and lithospheric mantle from crustal layer thickness and tectonic subsidence and then converts stretching maps into basal heat flow maps. Scenario modeling and heat flow calibration was performed based on the existing digital regional-scale 3D basin model.

The resulting reconstruction of the regional subsidence history and the associated thermal evolution based on the dynamics of the underlying lithosphere provides direct implications for source rock maturation and hydrocarbon migration in the study area.

Although the basin opening mechanism is still a matter of debate and can still be considered as the main uncertainty, this work provides useful results for the tectonic and thermal evolution of the Gippsland Basin and offers a new concept for exploring similar geological settings.

Chapter 4 was submitted to International Journal of Earth Sciences as *Röth, J., Baniasad, A., Froidl, F., Ostlender, J., Boreham, C., Hall, L.S., Littke, R., (2021). The Birkhead and Murta formations - organic geochemistry and organic petrography of Mesozoic fluvio-lacustrine source rocks in the Eromanga Basin, central Australia*.

This study was motivated by a lack of knowledge about source rocks of the Mesozoic Eromanga petroleum system and uncertainties about their potential contribution to hydrocarbon occurrences in the Cooper region, which still represents Australia's main onshore petroleum province. To improve the understanding of potential petroleum source rocks in the study area, the following key research question was pursued:

What is the source rock potential of the Jurassic Birkhead and the Early Cretaceous Murta formations and do they contribute to the Eromanga petroleum system?

The majority of oil and gas accumulations in the stacked sedimentary basin system are associated with coals and carboniferous shales of the Carboniferous to Triassic Cooper Basin, which underlies the Eromanga sequence. However, potential contribution of Eromanga source rocks and evidence for oil mixing was found in previous studies (e.g., Michaelsen & McKirdy, 1989, 2001; McKirdy et al., 1997; Boreham et al., 1999; Michaelsen, 2002).

During a sampling campaign in 2018 performed in the core repositories of Queensland and South Australia, 55 core samples from eight petroleum wells were collected to investigate the source rock potential of the Middle Jurassic Birkhead Formation and the Early Cretaceous Murta Formation.

Applied methods included Rock-Eval pyrolysis, organic petrography and organic geochemical analysis to evaluate the paleo-depositional environment, petroleum generation potential, and thermal maturity of these two Mesozoic source rock formations.

Both source rock formations are expected to have locally contributed to hydrocarbon migration and charge of the Eromanga petroleum system dependent on regional heat flow variations and differences in burial depth.

The obtained data helps to extend the understanding of the Eromanga petroleum system and is suitable to complement the input for numerical modeling purposes in the study area.

Chapter 5 was submitted to MDPI Geosciences as *Röth, J., Littke, R., (2021). Down under and under cover: frequent hydrothermal activity and strike-slip tectonics in the Cooper Basin and central Eromanga Basin confirmed by subsidence history analysis and basin modelling*.

Besides being a major supplier for oil and gas, the Cooper region in central Australia is also known for its geothermal potential and it recently became an example for Australia's efforts to develop carbon capture and storage technology. However, the tectonic evolution and thermal history of the stacked Cooper and Eromanga sedimentary basins is still a controversial problem. Motivated by contributing to a better understanding of the regional thermo-tectonic history of the Cooper region, the following key research question was pursued:

What were the main tectonic drivers that formed the Cooper and Eromanga basins, how did the subsurface temperature develop and how did it influence source rock maturation and petroleum generation?

In cooperation with Geoscience Australia (Australian Government), an existing regional-scale 3D basin model (Hall & Palu, 2016) was modified, calibrated and analyzed. Comprehensive literature research, new input from recent studies (including obtained source rock data from **Chapter 5**) and remarkably detailed vitrinite reflectance profiles from the public domain database of the Australian Government (https://www.ga.gov.au/) helped to improve the model input.

To evaluate the subsidence history and the thermal evolution of the Cooper region, several well locations throughout the study area were selected to construct calibrated 1D petroleum system models. Resulting local heat flow trends were projected to regional heat flow maps and then used as input for the 3D model. The calculated output of the 3D model includes detailed maps for source rock maturation, maps for respective kerogen transformation and the subsurface temperature distribution throughout the entire basin history. Analysis of layer thickness maps and depocentre migration provided additional insights into the complex tectonic evolution.

Although many uncertainties remain, this study provides important new insights into the geological evolution of one of the most interesting sedimentary basins in Australia. At the end of this chapter, numerous uncertainties are discussed and newly interpreted tectonic and magmatic features are introduced, including a previously overlooked intracontinental shear zone and a continental hot spot.

Chapter 6 contains concluding remarks and additional findings based on this thesis and brings the different obtained results into a common context. This final chapter also provides suggestions for future investigations in the study areas and a short outlook into the future of basin and petroleum system modeling.

2 TECTONIC EVOLUTION OF AUSTRALIA

2.1 Overview

With ages of up to 4.6 Ga, parts of the Australian continent are probably not much younger than the Earth itself (Gradstein et al., 2020). Fragments of continental crust from Jacks Hill, Western Australia, date back to ages between 4 and 4.4 Ga and are thus amongst the oldest known rocks on Earth (Harrison, 2009). One of the oldest terrestrial rock fragments (about 4 Ga old felsite clast from Apollo 14 mission) was found on the surface of the Moon indicating that preservation potential of primary crust was very low due to constant meteorite bombardment (Bellucci et al., 2019). And if newly formed Hadean crust was not destroyed and ejected to outer space by impacts, it was quickly recycled in ancient Earth's magma ocean.

Geologic conditions became more constructive throughout the Archean and several generations of continental crust formed by multiple Wilson Cycles over time. Such cycles include phases of ocean opening and continent destruction alternating with phases of ocean closing and continent assembly (Wilson, 1966; Wilson et al., 2019).

Recurrent amalgamation of super-continents, successive periods of orogeny and episodes of continental break-up gradually shaped the Australian Continent from the Archean until present day and from west to east. The West Australian Element (WAE), the North Australian Element (NAE), the South Australian Element (SAE, consisting of the Gawler (GC) and Curnamona (CC) cratons, Tasmania (TAS) and the northern part of the Australian-Antarctic Mawson Craton, MC), and the assembled terranes of the Tasman Element (TE, often also called Terra Australis or Tasmanides) represent its main tectonic elements (**Figure 2.1**). These major crustal blocks consist of Archean cratons, Proterozoic orogens, Proterozoic basins and the Phanerozoic domain (**Figure 2.2**, Myers et al., 1996; Teasdale et al., 2001; Cawood & Korsch, 2008; Huston et al., 2012). The Tasman Line (TL) represents a major orogenic suture and separates the TE in the East from the other tectonic domains in the West (e.g., Teasdale, 2001; Huston et al., 2012).

Modern Australia is mainly surrounded by passive margins but the collision with New Guinea and a young subduction zone in the North influenced the entire continental plate throughout the Cainozoic until present day (Müller et al., 2000a; Huston et al., 2012).

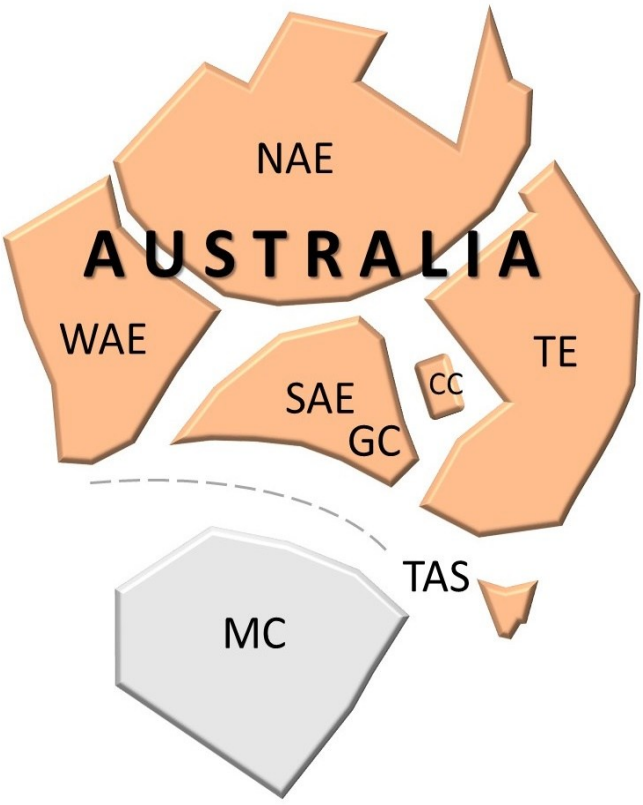

Figure 2.1: Schematic overview of main tectonic elements of the present-day Australian continent (after Myers et al., 1996; Teasdale et al., 2001, 2003; Cawood & Korsch, 2008; Huston et al., 2012). CC = Curnamona Craton, GC = Gawler Craton, MC = Mawson Craton, NAE = North Australian Element, SAE = South Australian Element, TAS = Tasmania, TE = Tasman Element, WAE = West Australian Element. Note: the Mawson Craton (today Antarctica) is displayed closer to Australia compared to reality.

2.2 Proterozoic Australia

Cratons and terranes of Australia were temporarily incorporated in two Archean supercratons (Vaalbara and Kenorland) and were involved in at least three supercontinent cycles (Nuna/Columbia, Rodinia, and Pangaea/Gondwana) through geologic history (**Figure 2.2**, Huston et al., 2012). The Archean Pilbara and Yilgarn cratons collided during the Paleoproterozoic to form the WAE already before the existence of the first supercontinent Nuna.

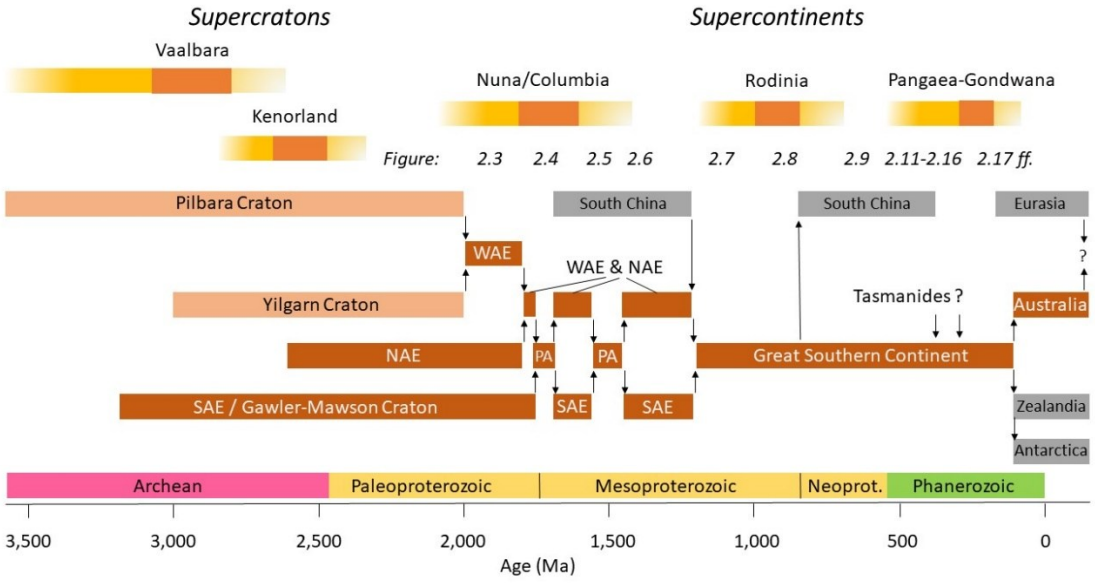

Figure 2.2: Chronologic overview of terranes and continental tectonic units, which participated in the assembly of Australia in geologic history and repeatedly formed supercratons and supercontinents (after Huston et al., 2012; modified after Li, 2002). WAE = West Australian Element, NAE = North Australian Element, SAE = South Australian Element, PA = Proto-Australia.

During Nuna's assembly (1950-1700 Ma), Australian cratons and terranes witnessed large-scale oblique convergence and mainly dextral transpressive deformation under the influence of the Halls Creek Orogeny (1820 Ma) and the Strangways Orogeny (1780-1730 Ma) in the North and the Kimban Orogeny (1845-1700 Ma) in the South (**Figure 2.3**, Myers et al., 1996). The Kimberley Craton joined the NAE, which merged with the WAE and the SAE to form Proto-Australia I (Cawood & Korsch, 2008). The today N-S directed Kimban Mobile Belt evolved during the Paleoproterozoic. It probably affected the Mt. Isa and Broken Hill blocks in the NAE as well as the eastern flank of the GC and the western flank of the CC and proceeded southward into East Antarctica (Drexel et al., 1993). Broken Hill (= CC) and Mt. Isa blocks were most likely connected (Henson et al., 2011). The Kimban Mobile Belt was repeatedly reactivated in the Neoproterozoic, Paleozoic and Mesozoic (Teasdale et al., 2001). During the existence of supercontinent Nuna, intracratonic deformation initiated the opening of the Mt. Isa and McArthur rifts and the Kimberley Basin (**Figure 2.4**, Myers et al., 1996).

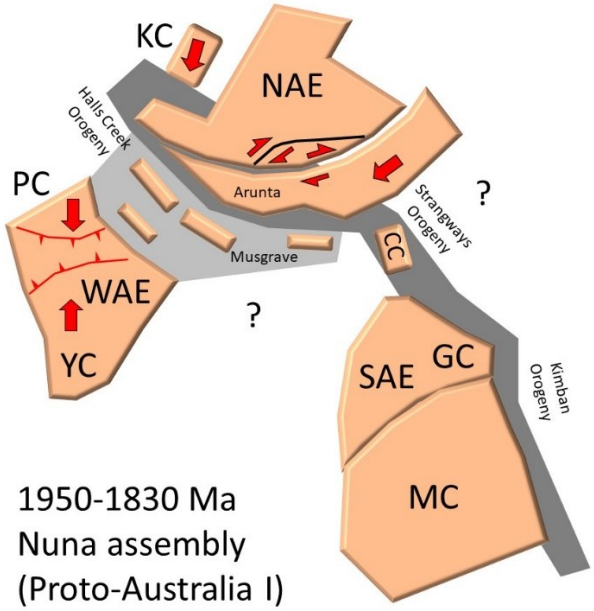

Figure 2.3: Simplified paleotectonic layout of main tectonic elements during the period of Nuna assembly / Proto-Australia I (after Myers et al., 1996; Teasdale et al., 2001, 2003; Cawood & Korsch, 2008; Huston et al., 2012). CC = Curnamona Craton, GC = Gawler Craton, KC = Kimberley Craton, MC = Mawson Craton, NAE = North Australian Element, PC = Pilbara Craton, SAE = South Australian Element, TAS = Tasmania, WAE = West Australian Element, YC = Yilgarn Craton.

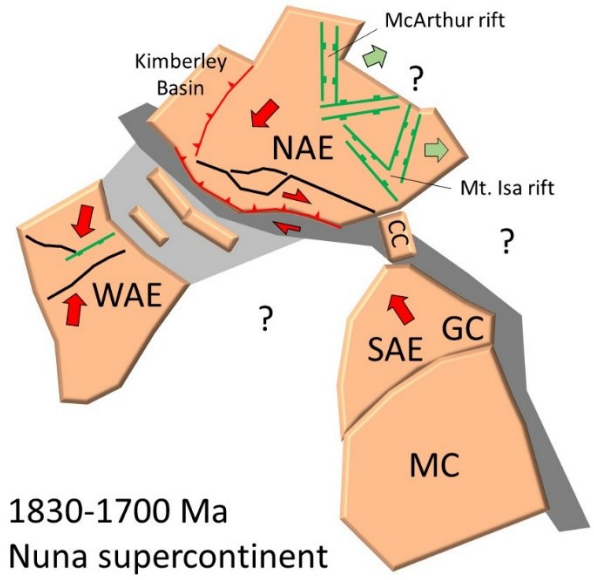

Figure 2.4: Simplified paleotectonic layout of main tectonic elements during the period of Nuna supercontinent (after Myers et al., 1996; Teasdale et al., 2001, 2003; Cawood & Korsch, 2008; Huston et al., 2012). CC = Curnamona Craton, GC = Gawler Craton, MC = Mawson Craton, NAE = North Australian Element, SAE = South Australian Element, TAS = Tasmania, WAE = West Australian Element.

The Mesoproterozoic disintegration of Nuna (1700-1300 Ma) was accompanied by the evolution of sedimentary basins (Bangemall, Birrindudu, McArthur, and Mount Isa) across Proto-Australia II (**Figure 2.5** and **Figure 2.6**, Myers et al., 1996; Huston et al., 2012) and repeated intracratonic deformation once more dominated by (NW-SE oriented) dextral transpressional stress regime (**Figure 2.6**, Myers et al., 1996). While the WAE and NAE remained united, the SAE veered away during the break-up of Nuna in the Mesoproterozoic (**Figure 2.5**) only to join the Rodinia supercontinent during the Albany-Fraser Orogeny (involving WAE and SAE), the Musgravian Orogeny (involving NAE and SAE) and the Rudall Orogeny (involving NAE and WAE, 1300-1000 Ma, **Figure 2.7**, Myers et al., 1996). The structural fabric of the Albany-Fraser Mobile Belt (= Albany-Fraser Orogen, AFO) was reactivated several times and later facilitated the separation of Australia from East Antarctica (Teasdale et al., 2003).

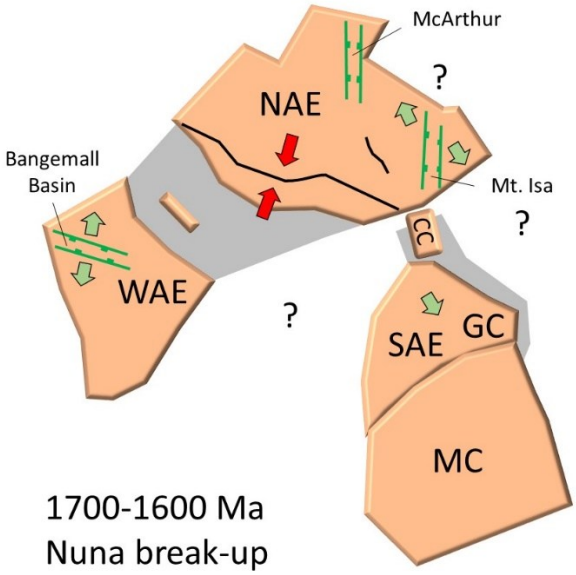

Figure 2.5: Simplified paleotectonic layout of main tectonic elements during the period of Nuna break-up (after Myers et al., 1996; Teasdale et al., 2001, 2003; Cawood & Korsch, 2008; Huston et al., 2012). CC = Curnamona Craton, GC = Gawler Craton, MC = Mawson Craton, NAE = North Australian Element, SAE = South Australian Element, TAS = Tasmania, WAE = West Australian Element.

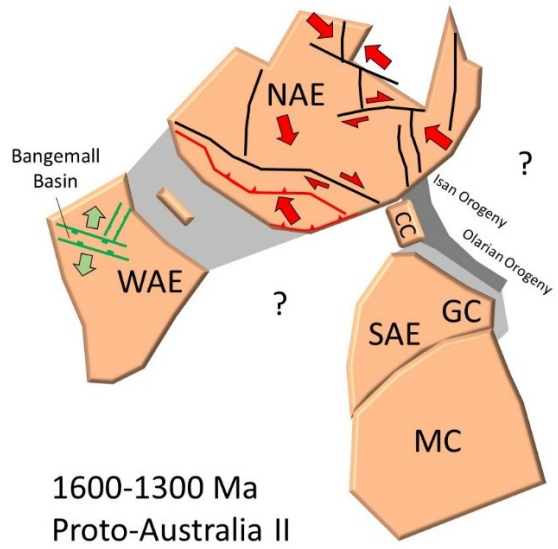

Figure 2.6: Simplified paleotectonic layout of main tectonic elements during the period of Proto-Australia II (after Myers et al., 1996; Teasdale et al., 2001, 2003; Cawood & Korsch, 2008; Huston et al., 2012). CC = Curnamona Craton, GC = Gawler Craton, MC = Mawson Craton, NAE = North Australian Element, SAE = South Australian Element, TAS = Tasmania, WAE = West Australian Element.

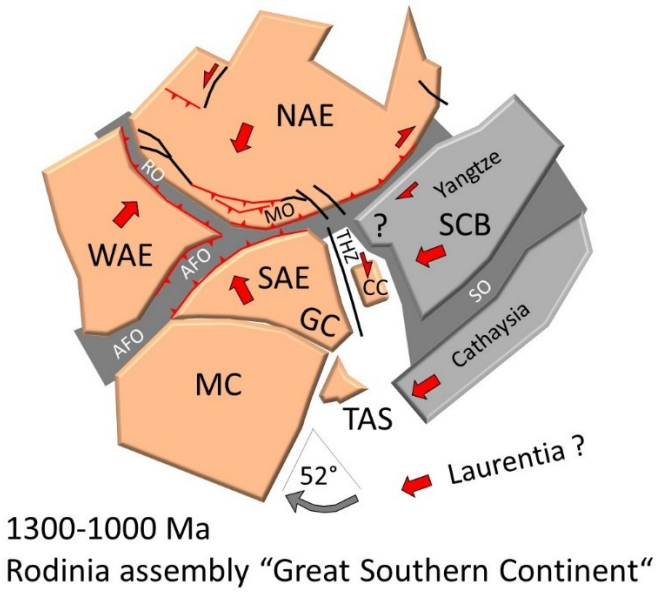

Figure 2.7: Simplified paleotectonic layout of main tectonic elements during the phase of Rodinia assembly (after Myers et al., 1996; Teasdale et al., 2001, 2003; Li & Powell, 2001; Li, 2002; Giles et al., 2004; Cawood & Korsch, 2008; Huston et al., 2012). AFO = Albany-Fraser Orogen, CC = Curnamona Craton, GC = Gawler Craton, MC = Mawson Craton, MO = Musgravian Orogen, NAE = North Australian Element, RO = Rudall Orogen, SAE = South Australian Element, SCB = South China Block, SO = Sibao Orogen, TAS = Tasmania (position speculative), THZ = Torrens Hinge Zone, WAE = West Australian Element.

Several opposing paleogeographic models exist that are placing the continental landmasses of Laurentia somewhere near or even connected with Australia during the Mesoproterozoic. These models are known as either AUSMEX (Australia attached to Mexico), AUSWUS (Australia attached to Western United States), or SWEAT (Southwest United States attached to East Antarctica) and commonly propose that the Albany-Fraser/Musgravian/Rudall orogenic belt somehow continues eastward into the Grenville Orogen during the assembly of Rodinia. These possible plate configurations are frequently debated within the scientific community (e.g., Burret & Berry, 2000; Karlstrom et al., 2001; Wingate et al., 2002; Pisarevsky et al., 2003), but often disregard or misplace the paleogeographic position of the South China Block (SCB). However, a rather unpopular paleogeographic reconstruction matches the Yangtze and Cathaysia blocks (together defined as the SCB) geometrically and chronologically quite well with the Tasman Line (TL) and delivers a reasonable explanation for this enigmatic tectonic feature (Li et al., 1995; Li & Powell, 2001; Li et al., 2002). This model also fits better with the required 52° counterclockwise rotation of the entire MC including the SAE during the assembly of Rodinia (**Figure 2.7**, Giles et al., 2004). Accordingly, the SCB was squeezed between Australia and Laurentia and the Torrens Hinge Zone (THZ) developed subparallel to the Kimban suture to compensate the resulting shear motion between the converging GC and the CC (Teasdale et al., 2001, 2003).

During the existence of the Rodinia supercontinent (**Figure 2.8**, 1000-750 Ma), large parts of Australia were covered by the shallow marine Centralian Superbasin (CSB) and its SE branch, the Adelaide Geosyncline (AG, 830-750 Ma). This episode of continent-wide NW-SE extension and crustal sagging was accompanied by significant strike-slip movement along the NNW-SSE oriented THZ, which defined the Adelaidian Basin (Teasdale et al., 2001, 2003). The suture between Australia and the SCB remained a zone of structural weakness and later provided the axis for their renewed separation. Contemporaneous to sedimentation in the AG, a proto-rift zone developed along the TL (Li & Powell, 2001). The episode of intracratonic rearrangements transitioned into the multiphase Adelaidian Orogeny (800-550 Ma, Betts et al., 2002; Teasdale et al., 2001) initiating the break-up of Rodinia (**Figure 2.9**, 750-540 Ma, Myers et al., 1996).

The early-stage Rodinia break-up in the Australian domain was characterized by NE-SW compression that reactivated old zones of weakness and led to the inversion and fragmentation of the CSB into smaller rift and foreland basins (e.g., Officer, Amadeus, Ngalia, and Georgina) and caused tilting and flexuring of crustal blocks along fold belts

throughout central Australia (Shaw et al., 1991; Myers et al., 1996). It is quite possible, that the CSB was internally sheared due to counterclockwise rotation of the NAE relative to its surrounding tectonic elements (see **Figure 2.8**).

In the following period (725-700 Ma), the eastern Australian margin was subject to SE extension, while NE-SW extension occurred in the AG (Preiss et al., 1993). This episode of rifting coincides with the initiation of the Paleo-Pacific Ocean (Powell et al., 1994) along the TL, which represents an important tectonic feature because it marks the eastern edge of thick Proterozoic crust in Australia and later predefined the construction of the Phanerozoic domain in eastern Australia (Teasdale et al., 2003). While the continental landmasses of the SCB and Laurentia drifted away to the north and the east, the Adelaidian Basin evolved into a passive margin (**Figure 2.9**, Myers et al., 1996).

The upcoming Pangaea-Gondwana assembly was pronounced by the Paterson Orogen (PO, 650-600 Ma) in Western Australia and was followed by a series of tectonic events throughout the Early and Middle Paleozoic (Huston et al., 2012, **Figure 2.10**). The NW-SE striking Trans-Australian Fold Belt (TAFB, **Figure 2.11**, Wopfner, 1997) established along deep crustal fracture zones and connected the Paterson suture with the THZ. The TAFB (or Paterson-THZ Shear Zone, after Teasdale et al., 2001) forms an s-shape and separates the WAE and the SAE from the NAE and the Tasman Geosynclinale, which later transformed into the Tasmanides (= Tasman Element). Throughout the remaining geological history of Australia, the TAFB and the TL were repeatedly reactivated and acted as transfer zones between the major tectonic elements (Myers et al., 1996).

An anticlockwise rotation of the NAE during the Rodinia break-up and associated dextral movement relative to the SAE is suggested (Powell et al., 1994), but contradicts with contemporaneous SW and NE directed thrusting and sinistral strike-slip tectonics observed along the Wunaamin Miliwundi (formerly known as King Leopold), Paterson, and Petermann orogens (Myers et al., 1996). A clockwise rotation of the NAE along the northern segment of the Tasman Line and the Paterson suture, creating extension in the East and sinistral transpression in the West, is more likely during this period (**Figure 2.9**, see also Li & Evans, 2011; Liu et al., 2018). During the transition between Rodinia break-up and Gondwana assembly from the Late Proterozoic to the Early Cambrian, southeastern Australia may have been extended southeastwards in a back-arc setting within the Palaeo-Pacific Ocean (Myers et al., 1996; Cawood, 2005).

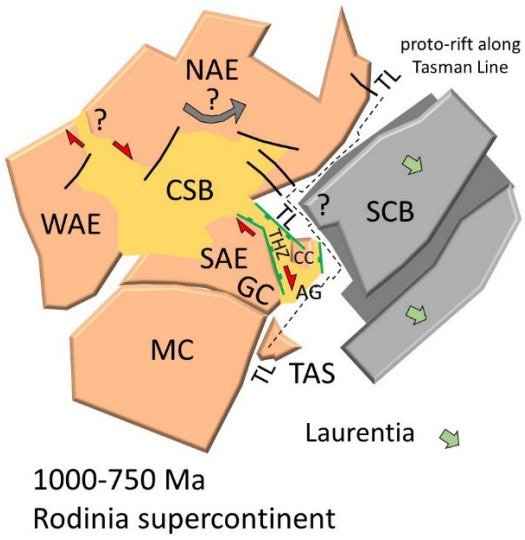

Figure 2.8: Simplified paleotectonic layout of main tectonic elements during the late Rodinia period (after Shaw et al., 1991; Myers et al., 1996; Li & Powell, 2001; Teasdale et al., 2001, 2003; Betts et al., 2002; Li, 2002; Cawood & Korsch, 2008; Huston et al., 2012). AG = Adelaidian Geosyncline, CC = Curnamona Craton, CSB = Centralian Superbasin, GC = Gawler Craton, MC = Mawson Craton, NAE = North Australian Element, SAE = South Australian Element, SCB = South China Block, TAS = Tasmania, TL = Tasman Line (after Teasdale, 2001), THZ = Torrens Hinge Zone, WAE = West Australian Element.

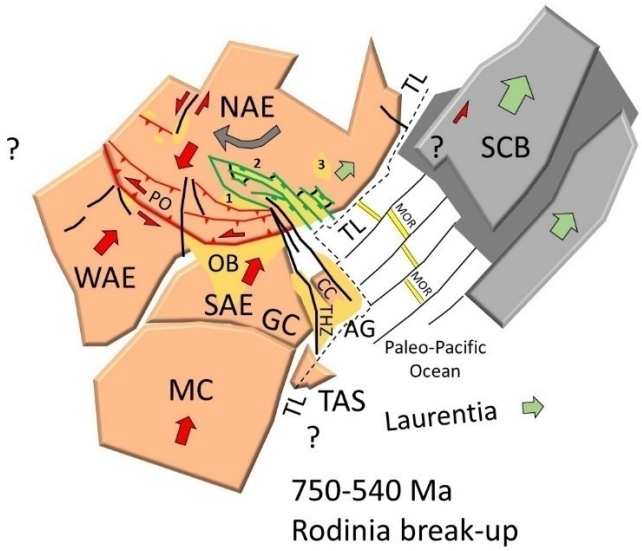

Figure 2.9: Simplified paleotectonic layout of main tectonic elements during the break-up of Rodinia (after Shaw et al., 1991; Preiss, 1993; Powell et al., 1994; Myers et al., 1996; Li & Powell, 2001; Teasdale et al., 2001, 2003; Betts et al., 2002; Li, 2002; Cawood & Korsch, 2008; Huston et al., 2012). 1 = Amadeus Basin, 2 = Ngalia Basin, 3 = Georgina Basin, AG = Adelaidian Geosyncline, CC = Curnamona Craton, GC = Gawler Craton, MC = Mawson Craton, NAE = North Australian Element, OB = Officer Basin, PO = Paterson Orogen, SAE = South Australian Element, SCB = South China Block, TAS = Tasmania, TL = Tasman Line (after Teasdale, 2001), THZ = Torrens Hinge Zone, WAE = West Australian Element.

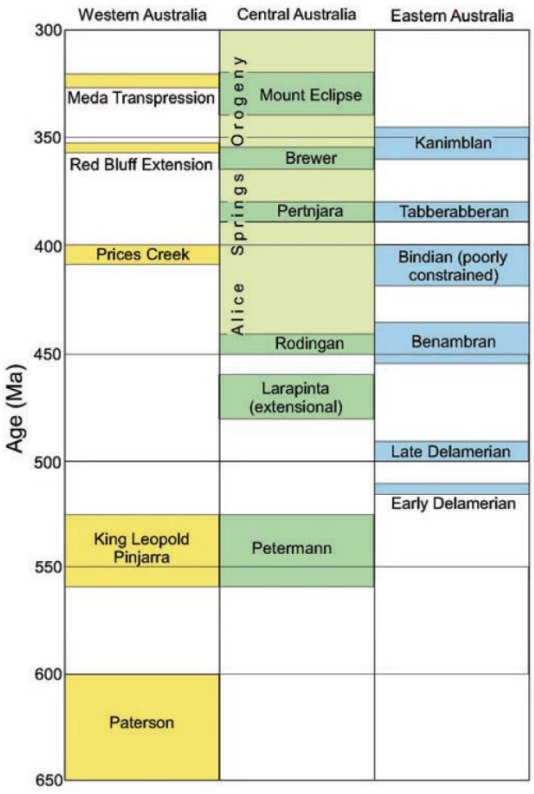

Figure 2.10: Overview of Neoproterozoic and Early-Middle Paleozoic tectonic events in western, central and eastern Australia (from Huston et al., 2012).

2.3 Paleozoic Australia

During the transition from the Neoproterozoic to the Phanerozoic, the evolution of Australia was characterized by multiple orogenic and basin forming episodes that culminated in the assembly of the Pangaea-Gondwana supercontinent (630-530 Ma, Cawood, 2005).

After the WAE collided with the NAE during the Paterson Orogeny, the Early Cambrian Petermann Orogeny caused the N-S oriented collision of the NAE with the SAE (550-530 Ma, **Figure 2.11**). Typical tectonic features of this period were widespread fault inversion, NW-SE dextral transpression, isolated pull-apart basins in the Musgrave Block (Central Australia), E-W oriented transpressional features and shear zones along the TAFB (Teasdale et al., 2001).

A relatively short episode of continental extension during the Cambrian (530-520 Ma, **Figure 2.12**) caused localized intracratonic NW-SE rifting and extension along the TL (Teasdale et al., 2001). The originally Mesoproterozoic Cork Fault re-established as a tectonic feature along the northern segment of the TL (Spampinato et al., 2015).

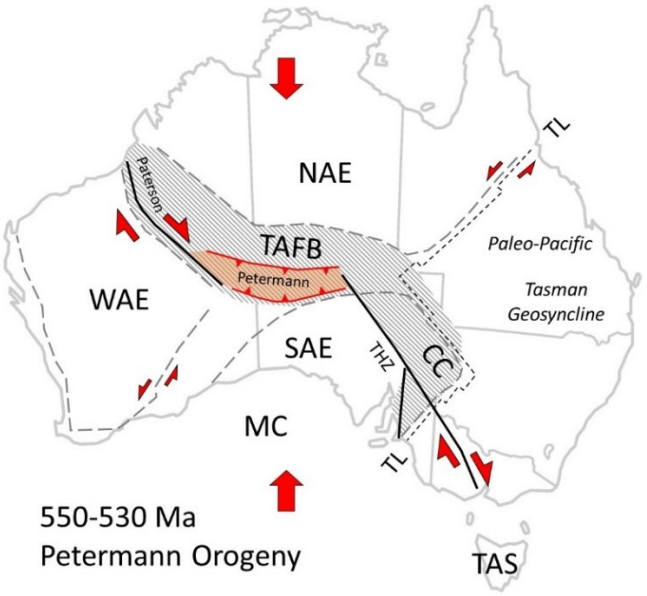

Figure 2.11: Simplified paleotectonic situation during the Petermann Orogeny (after Teasdale et al. 2001) and the Late Neoproterozoic Trans-Australian Fold Belt (TAFB, after Wopfner, 1997, also called Paterson-THZ Shear Zone after Teasdale et al., 2001). CC = Curnamona Craton, MC = Mawson Craton, NAE = North Australian Element, SAE = South Australian Element, TAS = Tasmania, THZ = Torrens Hinge Zone, TL = Tasman Line (after Teasdale et al., 2001), WAE = West Australian Element.

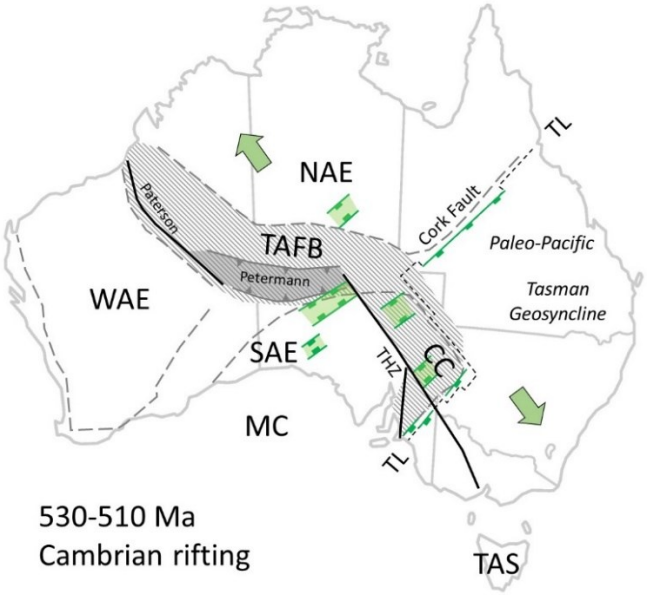

Figure 2.12: Simplified paleotectonic situation during the Cambrian rifting (after Teasdale et al. 2001). CC = Curnamona Craton, MC = Mawson Craton, NAE = North Australian Element, SAE = South Australian Element, TAFB = Trans-Australian Fold Belt (after Wopfner, 1997), TAS = Tasmania, THZ = Torrens Hinge Zone, TL = Tasman Line (after Teasdale et al., 2001), WAE = West Australian Element.

During the Late Cambrian Delamerian Orogeny (520-460 Ma, **Figure 2.13**) the focus of tectonic activity propagated again further to the east. Major NW-SE to NNW-SSE compressional deformation in the Adelaide Fold Belt occurred and transpressional deformation formed pop-up structures along the THZ and around the CC.

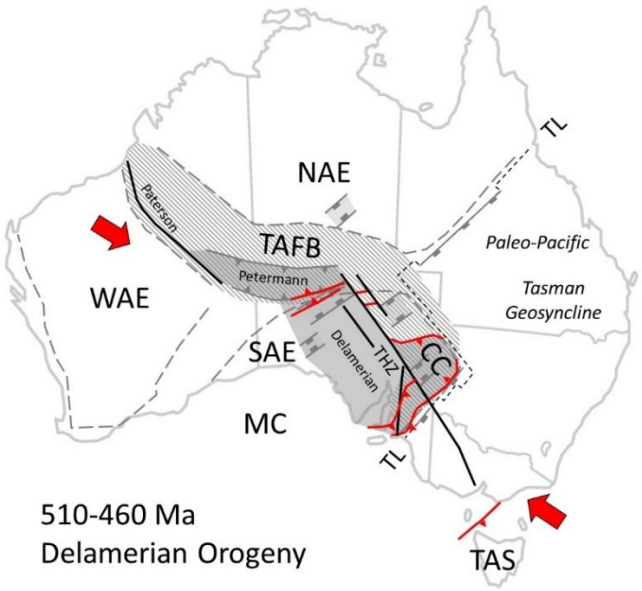

Figure 2.13: Simplified paleotectonic situation during the Delamerian Orogeny (after Teasdale et al. 2001). CC = Curnamona Craton, MC = Mawson Craton, NAE = North Australian Element, SAE = South Australian Element, TAFB = Trans-Australian Fold Belt (after Wopfner, 1997), TAS = Tasmania, THZ = Torrens Hinge Zone, TL = Tasman Line (after Teasdale et al., 2001), WAE = West Australian Element.

Late Ordovician NE-SW directed extension (460-440 Ma, **Figure 2.14**) reactivated the Proterozoic fold belts as major transfer zones and caused NW trending normal faults throughout the entire Australian Continent (Shaw et al., 1991; Myers et al., 1996; Teasdale et al., 2001). This period enabled the formation of the Warburton Basin as a part of the Larapintine Seaway, which connected the Tasman Geosyncline (Paleo-Pacific Ocean) in the east with the Proto-Indian Ocean in the west (Teasdale et al., 2001). The Warburton Basin filled mainly with turbidites in two major connected depocentres: the Western Warburton Basin (WWB) and the Eastern Warburton Basin (EWB).

The Alice Springs Orogeny (450-300 Ma, equivalent to the Kaledonian-Variscan Orogeny in Europe, **Figure 2.15**) caused major lithosphere-scale NNE-SSW compressional deformation of the Arunta Block in central Australia, which was accompanied by the formation of Devonian "foreland" basins in the Officer region (Musgrave Block). Sinistral strike-slip reactivation of E-W structures in Musgraves inverted Petermann-age short-lived pull-apart basins (Teasdale et al., 2001).

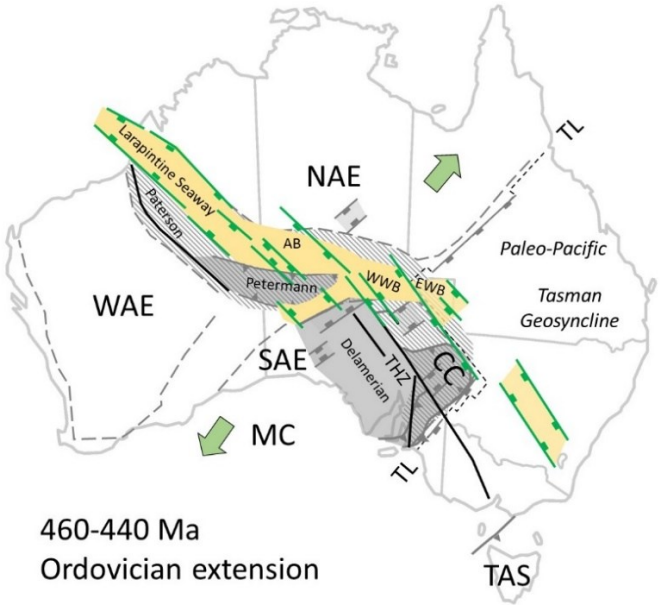

Figure 2.14: Simplified paleotectonic situation during the Ordovician extension (after Teasdale et al. 2001). AB = Amadeus Basin, CC = Curnamona Craton, EWB = Eastern Warburton Basin, MC = Mawson Craton, NAE = North Australian Element, SAE = South Australian Element, TAS = Tasmania, THZ = Torrens Hinge Zone, TL = Tasman Line (after Teasdale et al., 2001), WAE = West Australian Element, WWB = Western Warburton Basin.

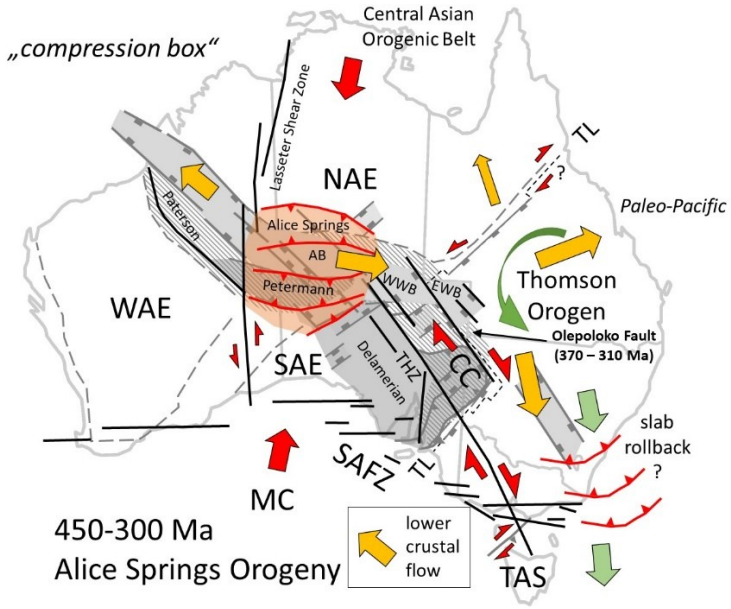

Figure 2.15: Simplified paleotectonic situation during the Alice Springs Orogeny (after Teasdale et al. 2001 and Klootwijk, 2013). AB = Amadeus Basin, CC = Curnamona Craton, EWB = Eastern Warburton Basin, MC = Mawson Craton, NAE = North Australian Element, SAE = South Australian Element, SAFZ = Southern Australian Fault Zone (after Teasdale et al., 2003), TAS = Tasmania, THZ = Torrens Hinge Zone, TL = Tasman Line (after Teasdale et al., 2001), WAE = West Australian Element, WWB = Western Warburton Basin. Olepoloko Fault after Wong et al. (2018).

Resulting from the collision with the Central Asian Orogenic Belt in the north and with the MC (Antarctica) in the south, the Australian continent was squeezed in a "compression box" (compare Klootwijk, 2013) and the intracontinental N-S directed Lasseter Shear Zone developed (Teasdale et al., 2001). Additionally, the Thomson Orogen approached from the east and collided with the NAE and the SAE as a "tectonic indenter". Similar to India and South China or Arabia and Anatolia, the Thomson Orogen performed an anticlockwise "tectonic escape" along the TL accompanied by mainly eastward lower crustal flow (i.e., Shaw et al., 1996; Klootwijk, 2013, see **Figure 2.15**). The tectonic escape of the Thomson Orogen was probably facilitated by northward subduction and slab rollback in the south and SE-directed crustal shear along the Olepoloko Fault, which was active between 370 and 310 Ma parallel to the middle segment of the TL (i.e., Wong et al. 2018, **Figure 2.15**). Obviously, the Olepoloko Fault compensated some transpressional stress away from the THZ and caused lateral offset and thrusting in the Warburton Basin during the Alice Springs Orogeny (compare Apak et al., 1995, 1997; Sun, 1997). Also during the Late Paleozoic, the Southern Australian Fault Zone (SAFZ) developed. The SAFZ comprises an array of E-W trending continental-scale lineaments (Teasdale et al., 2003, **Figure 2.15**) that initiated the separation of the MC from the SAE, which later resulted in the southward drift of Antarctica.

The Thomson Orogen is the central element of the Tasmanides – a series of exotic terranes that successively attached to Australia during the closure of a system of multiple back-arc basins in the Paleozoic (e.g., Myers et al., 1996; Foster & Goscombe, 2013) and produced rapid continental growth (e.g., Glen, 2005; Kemp et al., 2009; Fergusson & Henderson, 2015). Simplified, the Tasmanides subdivide into five orogenic domains geographically from west to east and chronologically from Cambrian to Triassic: Delamerian, Thomson, Lachlan, Mossman, and New England (**Figure 2.16**, Rosenbaum, 2018). The Delamerian Orogeny is predominantly associated with Cambrian collision events (**Figure 2.13**, Teasdale et al., 2001) and the Thomson Orogen is related to the Silurian Benambran Orogeny (Rosenbaum, 2018). The Lachlan Fold Belt (LFB, simultaneously with the Mossman Orogen in northern Queensland) is the result of multiple collisions lasting from Silurian to Carboniferous, and the New England Orogen (NEO) emerged during the Permo-Triassic Hunter-Bowen Orogeny (Rosenbaum, 2018).

The Tasmanides contributed to the final assembly of supercontinent Gondwana during multiple accretion events along the Terra Australis Orogen, an extensive peri-Gondwanan

subduction zone of the Paleo-Pacific Ocean that existed during the Late Paleozoic (**Figure 2.17**, Cawood, 2005; Fergusson & Henderson, 2015).

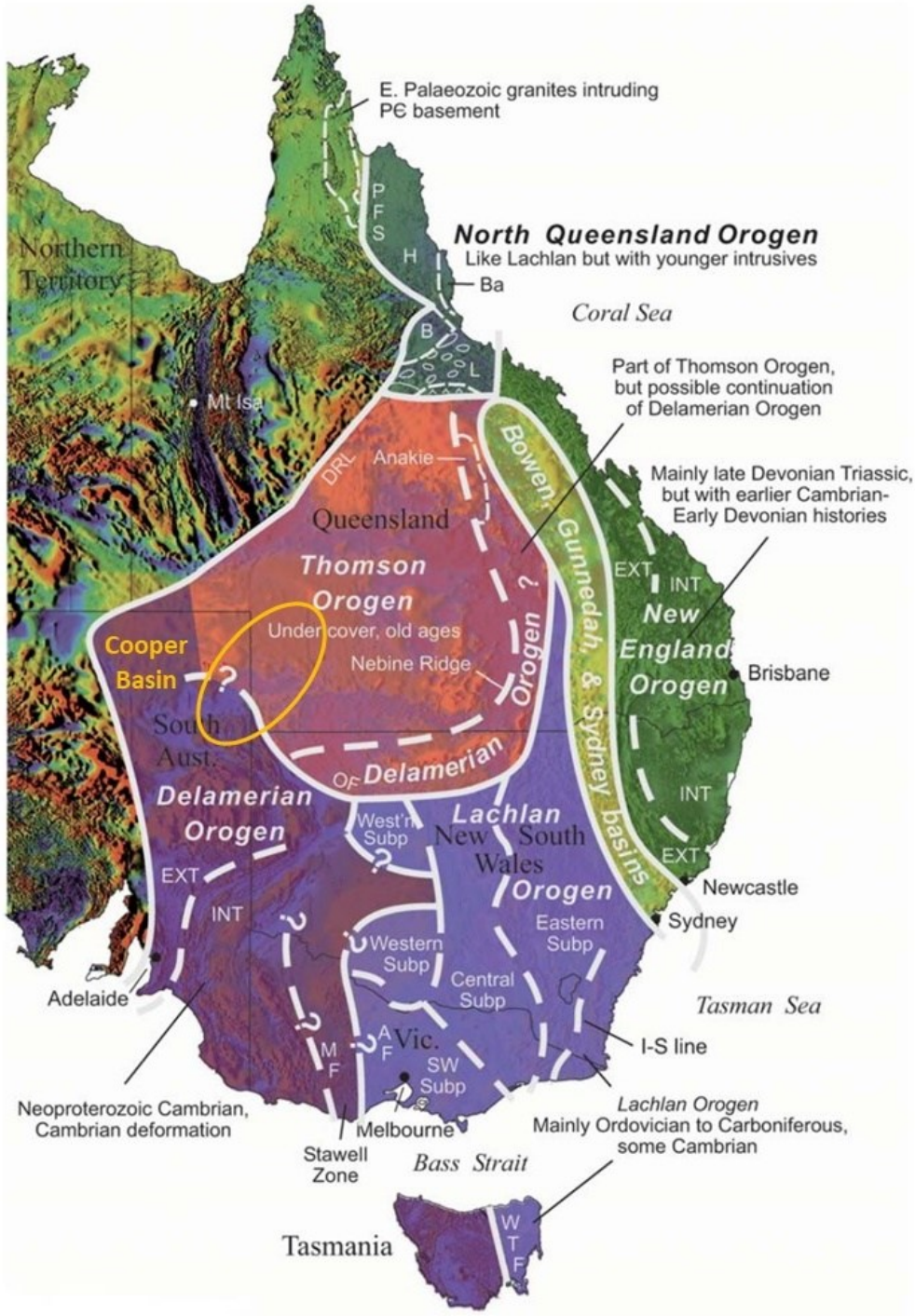

Figure 2.16: The Tasmanides in eastern Australia (after Rosenbaum, 2018). Underlying magnetic intensity map from Geoscience Australia (Milligan & Franklin, 2004). See original publication for additional abbreviations. Dark yellow ellipse shows approximate location of the Pennsylvanian-Triassic Cooper Basin.

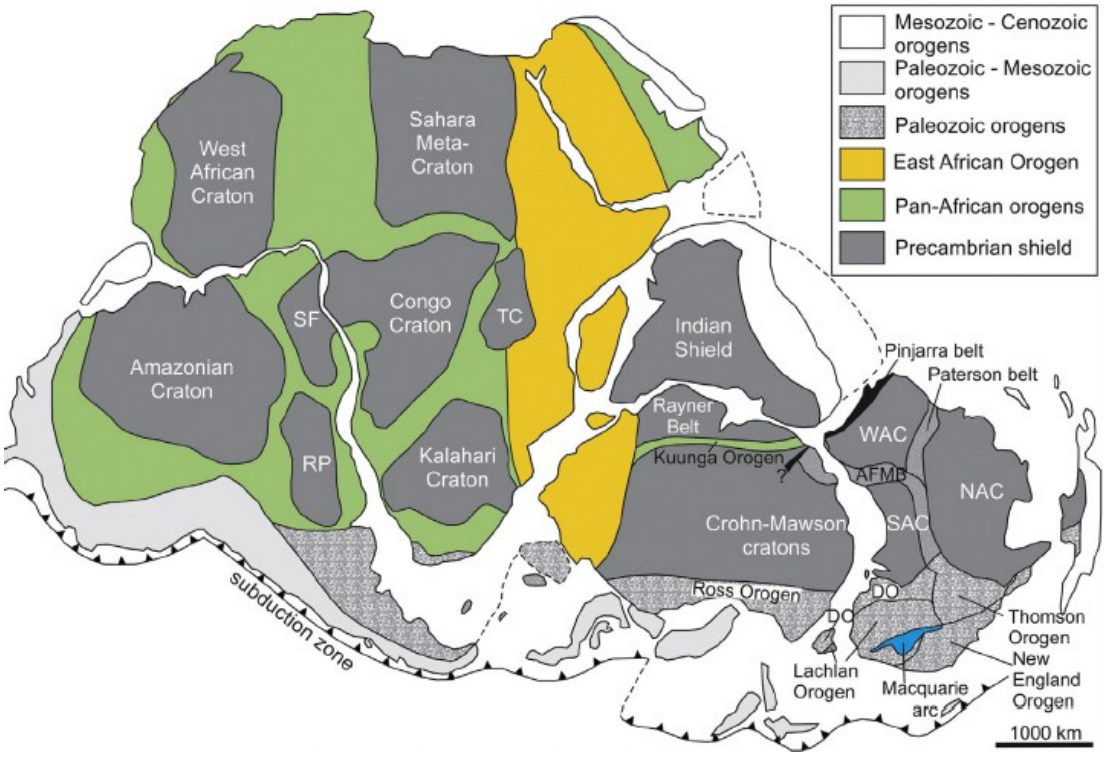

Figure 2.17: The layout of Gondwana during the Late Paleozoic (from Fergusson & Henderson, 2015). Cratons in Australia and Antarctica are from Myers et al. (1996) and Boger (2011) respectively. AFMB = Albany–Fraser–Musgrave Belt, DO = Delamerian Orogen, NAC = North Australian Craton, RP = Río de la Plata Craton, SAC = South Australian Craton, SF = São Francisco Craton, TC = Tanzania Craton, and WAC = West Australian Craton.

From the Pennsylvanian until the Middle Triassic, the Bowen, Gunnedah, and Sydney basins (see **Figure 2.16**) emerged as a system of N-S trending back-arc and rift basins along the eastern margin (e.g., Li et al., 2012; Rosenbaum, 2018), within which major coal deposits developed (see **Figure 1.3**). At the same time, sandstones, shales and coals of the intracontinental Cooper Basin (CB) covered the remains of the inverted EWB in central Australia (Apak et al., 1995, 1997) and the extensive Galilee Basin spread across large parts of the northwestern Tasmanides (Rosenbaum, 2018; compare **Figure 2.16** and **Figure 1.3**). The tectonic evolution and the lithostratigraphy of the CB is described in much detail in **Chapter 5**.

2.4 Mesozoic Australia

From Late Permian to Late Triassic, the Hunter-Bowen Orogeny (260-210 Ma) caused multiple phases of subduction roll-back along the eastern margin and basin inversion throughout central and eastern Australia (Li & Powell, 2001; Raza et al., 2009; Li et al., 2012). The resulting accretion of the NEO, the Gympie Terrane, and the Lord Howe Rise (LHR) marked the final stages of the last supercontinent cycle, before the breakup of Pangaea-Gondwana commenced in the Jurassic (Li & Powell, 2001; Huston et al., 2012). During these multiple accretion processes along the Tethys (Paleo-Pacific) margin, a set of conjugate (mainly dextral) strike-slip faults established throughout the Bass Strait (Collins & Vernon, 1992; Veevers & Morgan, 2000; Woollands & Wong, 2001; Teasdale et al., 2003).

In the Triassic and Jurassic, continuous westward convergence of the Pacific and Phoenix oceanic plates formed an Andean-type magmatic arc along the eastern margin of Gondwana (**Figure 2.18**, Müller et al., 2000a; Norvick et al., 2001; Hergt & Brauns, 2001; Teasdale et al., 2003; Salmon et al., 2012). Steady accumulation of hot mafic melts caused widespread thermal weakening and underplating of the continental crust along eastern Gondwana. Uplift and denudation of the magmatic arc enabled transport of massive amounts of volcanogenic debris towards the Eromanga (see detailed lithostratigraphy and tectonic evolution in **Chapter 4**) and Surat basins, representing elements of the Great Artesian Basin (GAB), a large system of foreland basins that developed in the interior of central eastern Australia during the Early Jurassic (Li & Powell, 2001).

During the Jurassic, the Neoproterozoic Southern Australian Fracture Zone (SAFZ) was reactivated along the southern margin (**Figure 2.18** & **Figure 2.19a**, Teasdale et al., 2003). Subsequently, relatively slow NW-SE directed trans-tensional tectonic activity along the SAFZ affected the entire southern Australian continental margin during the Jurassic and the Early Cretaceous (155-120 Ma). Representing the easternmost branches of the SAFZ, the Gippsland (see detailed lithostratigraphy and tectonic evolution in **Chapter 3**), Bass, Otway and Torquay basins emerged from the hinterland of the Mesozoic subduction zone, while Antarctica started separating in a clockwise rotation (**Figure 2.19b** & **Figure 2.20**; Collins & Vernon, 1992; Betts et al., 2002; Teasdale et al., 2003; Huston et al., 2012). The tectonic setting changed to NE-SW extension in the Early-Middle Cretaceous (120-100 Ma, **Figure 2.19c**) and the rift basins throughout the Bass Strait provided accommodation space for huge amounts of volcanic debris from the magmatic arc in the east (Hawlader, 1989; Bryan et al., 1997).

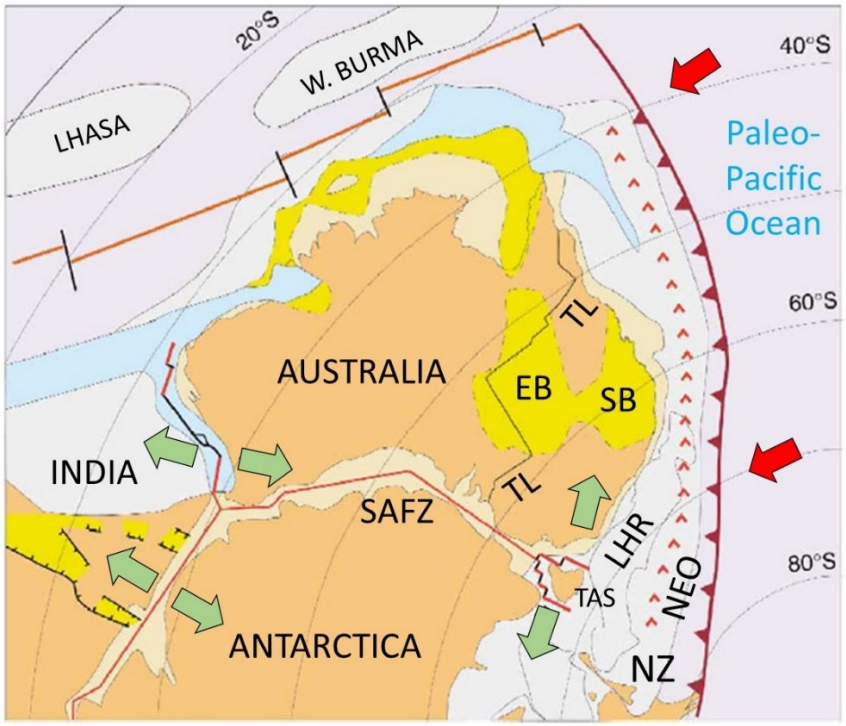

Figure 2.18: Middle Jurassic paleo-tectonic reconstruction just before Pangea breakup (175 Ma, modified after Li & Powell, 2001). Andean-type magmatic arc along the Paleo-Pacific Ocean with broad foreland basins over central eastern Australia. EB = Eromanga Basin, LHR = Lord Howe Rise, NEO = New England Orogen, NZ = New Zealand, SAFZ = Southern Australian Fracture Zone, SB = Surat Basin, TAS = Tasmania, TL = Tasman Line.

Starting in the Middle Cretaceous (from about 100 Ma, boundary Albian-Cenomanian), the continental assemblage of Australia, Antarctica and Zealandia (eastern Gondwana) underwent a rapid transition from a magmatic arc to a passive margin. This orogenic collapse initially featured NW-SE compression (lasting from 100 to 90 Ma, **Figure 2.19d**), which rotated towards E-W before the Tasman Sea opened along the Tasman Rift. The corresponding tectonic uplift caused substantial erosional unconformities throughout southeastern Australia, accompanied by exhumation of the Otway and Strzelecki Ranges and increasing sedimentation in the GAB (Teasdale et al., 2003).

The pre-extended lithosphere probably enabled rebound and uplift after loading (Hill et al., 1995), while the Tasman Spreading Centre (TSC) evolved at 96 Ma south of Tasmania and potentially contributed to transient doming of the mantle while slowly zipping northwards (**Figure 2.20**). In the following, the GAB was inverted and sedimentation in central Australia seized.

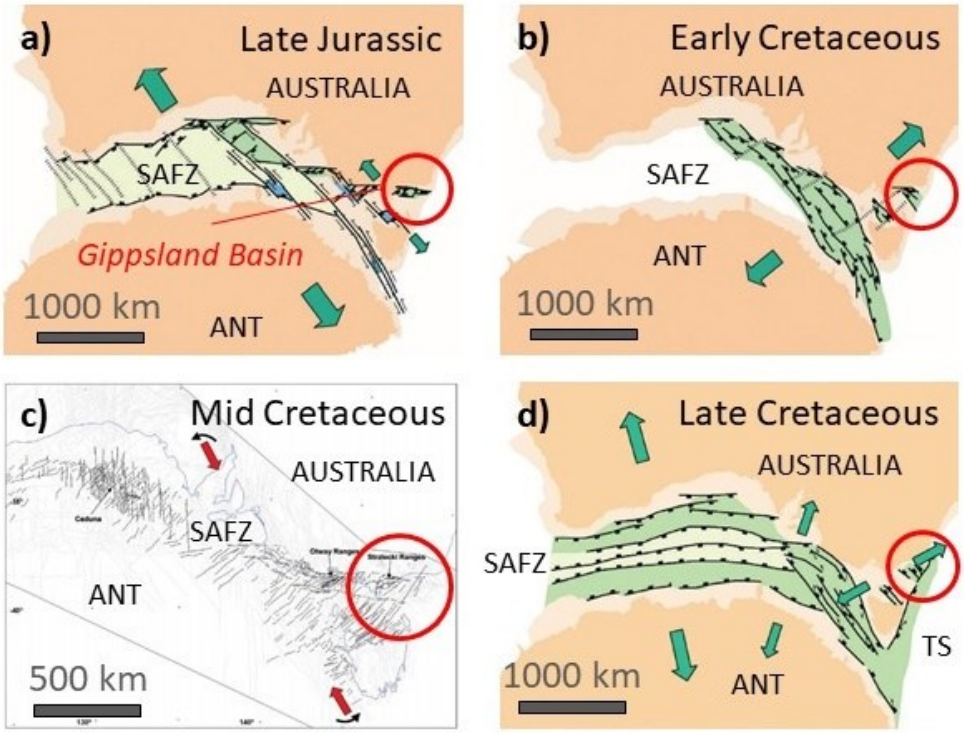

Figure 2.19: The key tectonic basin phases, which influenced the evolution of the southern margin of Australia during the Mesozoic (including the Gippsland Basin, see red circle; compiled and modified after Teasdale et al, 2003). Green and red arrows indicate the main tectonic stress direction during extensional and compressional basin phases, respectively. a) Late-Jurassic to Early Cretaceous NW-SE extension (onset Southern Ocean opening, 155 – 120 Ma); b) Early-Mid Cretaceous NE-SW extension (120 – 100 Ma); c) Mid-Cretaceous NW-SE compression (100 – 90 Ma); d) Late Cretaceous NNE-SSW extension (Tasman Sea spreading, 93 – 80 Ma);. ANT = Antarctica; SAFZ = Southern Australian Fault Zone; TS = Tasman Sea. All maps show top towards north. Please note different map scales.

This period of drastic vertical and horizontal tectonic reorganization was interpreted as a regional Cordilleran-type extensional orogenic collapse (e.g. Schwartz et al., 2016). Over a period of only 20-25 Ma (from Albian to Campanian), the regional geological setting changed dramatically from an active subduction zone to a triple junction of rift systems and further evolved to an open ocean basin with a passive margin. Crustal stretching, breakup, and seafloor spreading along the Tasman Ridge resulted in eastward drift of Zealandia and its fragmentation into the smaller landmasses of LHR, Norfolk Ridge and New Zealand (NZ, **Figure 2.20**, Woollands & Wong, 2001, Norvick et al., 2001; Mortimer, 2006, 2008). Tasman Sea spreading during the Late Cretaceous obeyed NNE-SSW extension (93-80 Ma, **Figure 2.19**), while the SAFZ facilitated opening of the Bight

Basin, separation of Antarctica and spreading of the Southern Ocean (Fitzgerald, 2002; Teasdale et al., 2003; Williams et al., 2011). During the Late Cretaceous and the Cainozoic, the extension of the Southern Ocean gradually increased, while Tasmania remained attached to Australia and the spreading direction between Australia and Antarctica rotated from NW-SE to N-S (Hill et al., 1998; Müller et al., 2000a, 2000b; Norvick et al., 2001; Huston et al., 2012).

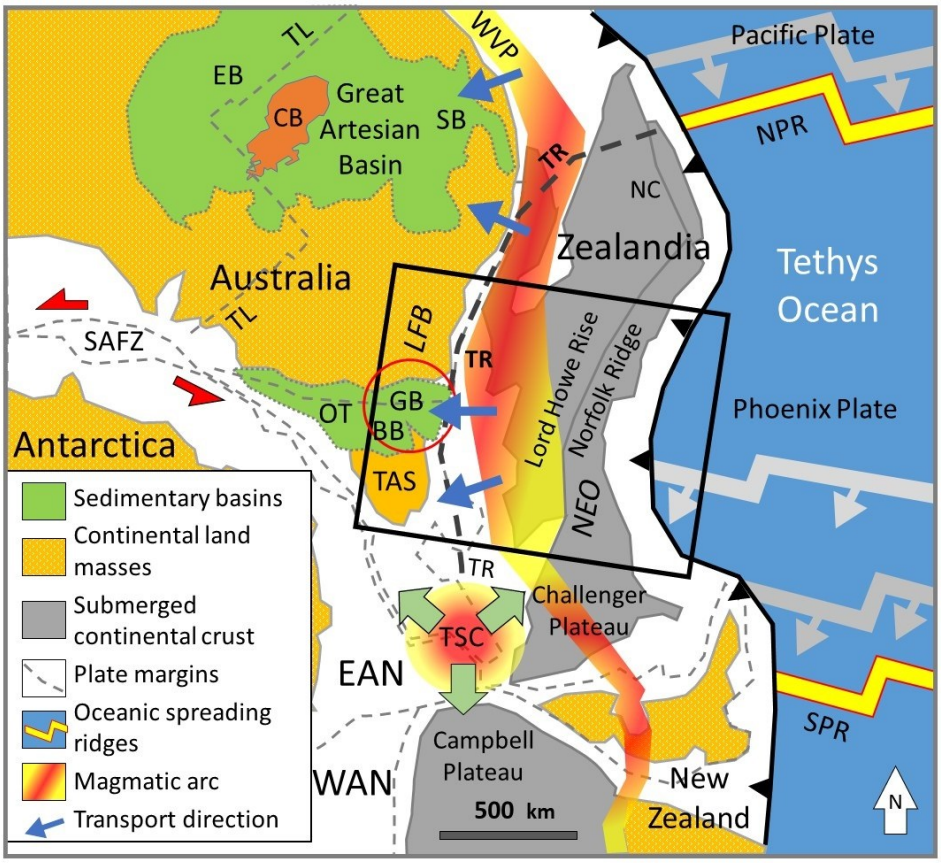

Figure 2.20: Reconstruction of the paleogeographic situation during the orogenic collapse and breakup of the eastern margin of Gondwana (Albian/Cenomanian boundary (100 Ma), modified after Bryan et al. 1997, Veevers et al. 2000, Norvick et al. 2001, Mortimer 2008, Kusky et al. 2014, Schwartz et al. 2016, Müller et al. 2016). Australia, Tasmania (TAS), Antarctica and Zealandia are still combined while the Phoenix and Pacific plates are subducted. BB = Bass Basin, CB = Cooper Basin (light brown polygon), EAN = East Antarctica, EB = Eromanga Basin, GB = Gippsland Basin (red circle), LFB = Lachlan Fold Belt, NC = New Caledonia, NEO = New England Orogen, NPR = North Phoenix Ridge, OT = Otway Basin, SAFZ = Southern Australian Fracture Zone, SB = Surat Basin, SPR = South Phoenix Ridge, TL = Tasman Line, TR = Tasman Ridge, TSC = Tasman Spreading Centre, WAN = West Antarctica, WVP = Whitsunday Volcanic Province. Black rectangle shows extent of **Figure 6.1**.

2.5 Cainozoic Australia

During the Eocene, renewed NW-SE compression caused local inversion and volcanism in southeastern Australia and first oceanic crust formed between the Australian and Antarctic continents (**Figure 2.21**, Li & Powell, 2001; Teasdale et al., 2003). As a consequence of reorganized tectonic forces and the accelerated northward movement of the Australian continent since the Ypresian, spreading of the Tasman Sea slowly seized (Gaina et al., 1998; Hill et al., 1998; Müller et al., 2000a, 2000b; Dyksterhuis & Müller, 2008; Huston et al., 2012).

In the meantime, the expanding Tasman Sea flooded main parts of the remaining fragments of Zealandia, the eastern Australian passive margin established and the Bass Strait opened. Due to regional rift-flank uplift in the Oligo-Miocene, the entire eastern Australian continental margin including Tasmania was elevated, and most of the Paleozoic basement was exposed at the surface (van der Beek et al., 1999).

At the same time, the Murray Basin (MB) opened and thin sandstones of the Lake Eyre Basin (LEB) covered the EB (**Figure 2.21**).

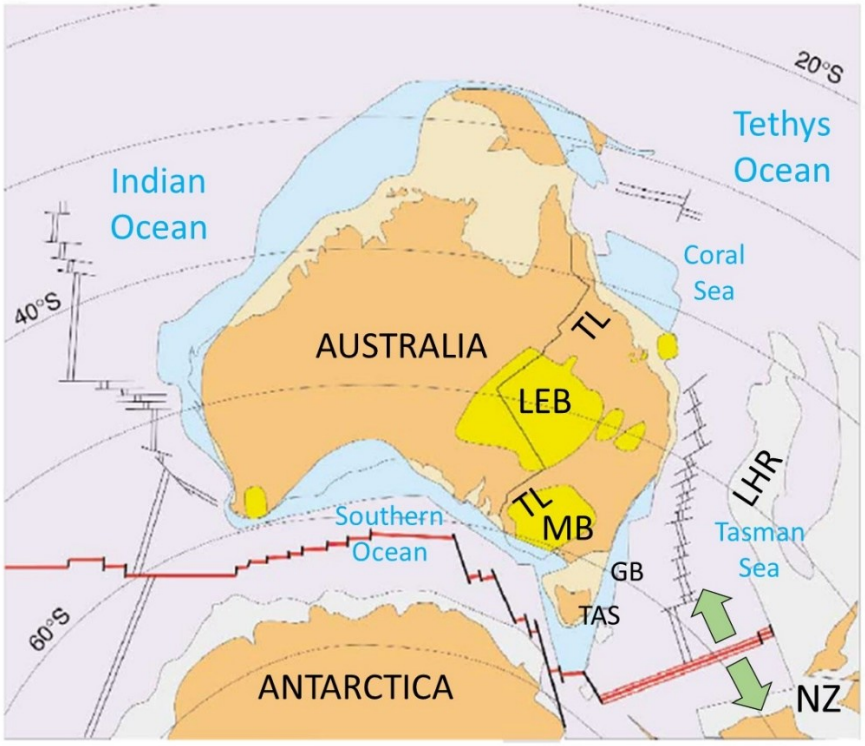

Figure 2.21: Middle Eocene paleo-tectonic reconstruction (45 Ma, modified after Li & Powell, 2001). GB = Gippsland Basin, LEB = Lake Eyre Basin, LHR = Lord Howe Rise, MB = Murray Basin, NEO = New England Orogen, NZ = New Zealand, SAFZ = Southern Australian Fracture Zone, TAS = Tasmania, TL = Tasman Line.

2.6 Present-day Australia

Numerous collisional and reorganizational processes in the north and in the east dominated the Neogene to present-day tectonic evolution of Australia (Müller et al., 2000a, 2000b, Norvick et al., 2001). Within the last 10 Ma, Cainozoic post-breakup compression caused major far-field shortening, right-lateral faulting, folding, uplift (e.g., Flinders, Otway, and Strzelecki ranges) and still impacts the present-day seismicity (Reynolds et al., 2003; Zhao & Müller, 2003; Hillis et al., 2008; Clark et al., 2011; Holford et al., 2011; Huston et al., 2012). A moderate relief characterizes the present-day topography of western, central and northern domains of Australia (**Figure 2.22**, Müller et al., 2012). The Eastern Highlands (Great Dividing Range) are stretching along the entire eastern continental margin, while the Eromanga/Lake Eyre and Murray basins represent wide depositional plains in central eastern Australia. Some areas in northeastern South Australia are even located below the sea level, with the endorheic Kati-tanda (Lake Eyre, elevation: -17 m, see green dot in **Figure 2.22**) representing the lowest point of the Australian continent. Kunama Namadgi (Mount Kosciuszko, +2,228 m, see red dot in **Figure 2.22**) in the Australian Alps marks the highest topographic elevation of Australia.

The Australian stress map (**Figure 2.23**, Hillis & Reynolds, 2000) shows three main directions of maximum horizontal stress (Sh_{max}). In the north and northwestern parts of the continent, Sh_{max} is oriented SW-NE, the southern margin features E-W directed Sh_{max} and in the southeast the stress is mainly aligned NW-SE. Trajectories seem to concentrate, rotate and merge within the Eromanga domain in central eastern Australia.

Present-day seismicity concentrates mainly in four distinct areas along the continental margins: the NW seismic zone, the SW seismic zone, the SE seismic zone, and the Flinders seismic zone (**Figure 2.24**, Hillis et al., 2008). Additional moderate and scattered seismic activity also occurs in central Australia (e.g., Tennant Creek), while the northeastern and the central southern parts of the continent are rather aseismic. An array of NNW-SSE aligned epicenters was recorded in the central EB and is probably associated with the Central Eromanga Shear Zone (CESZ), a previously overlooked tectonic feature, which is introduced in Chapter 5 (red ellipse in **Figure 2.24**).

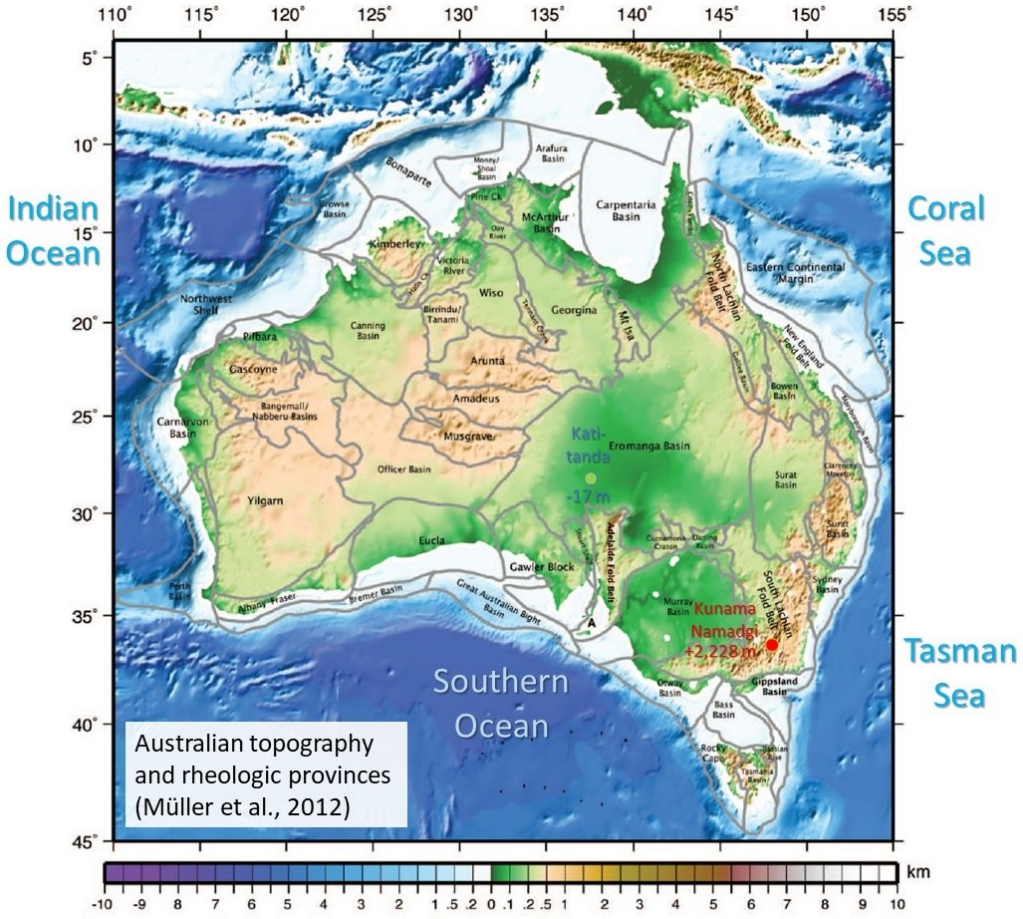

Figure 2.22: Topography and bathymetry map of present-day Australia with rheological provinces (grey outlines, from Müller et al., 2012) and with Kati-tanda (Lake Eyre) and Kunama Namadgi (Mount Kosciuszko) marking the lowest and highest points of continental Australia, respectively.

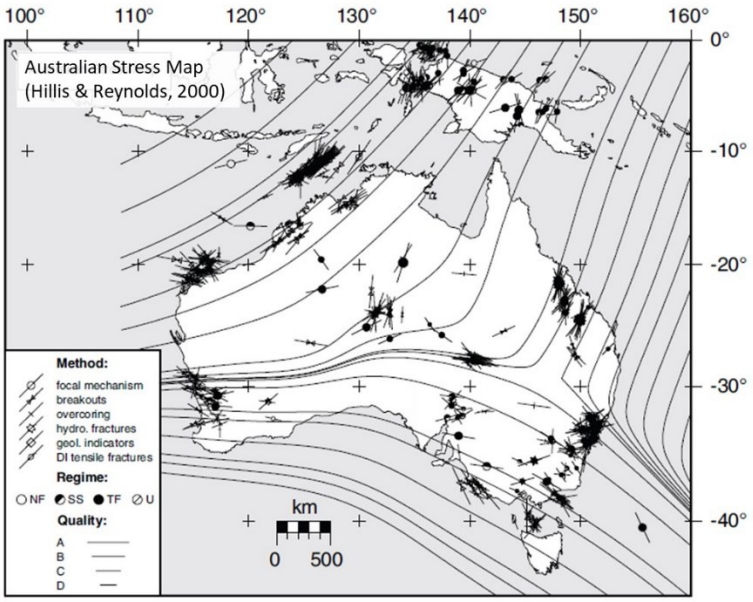

Figure 2.23: Stress trajectories based on the Australian stress map (Hillis & Reynolds, 2000).

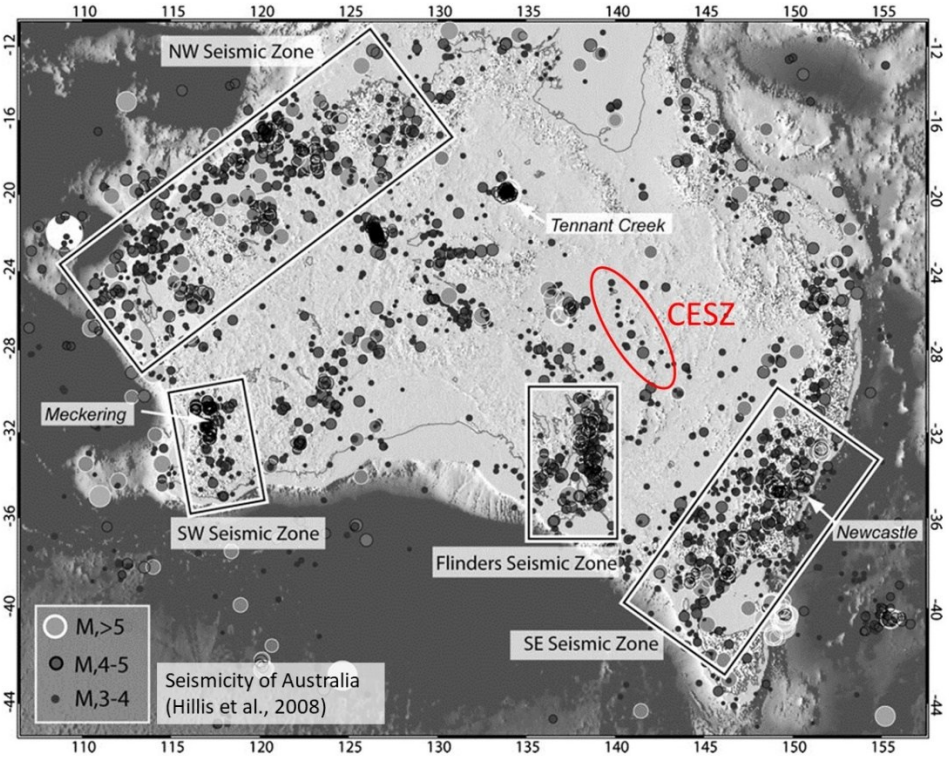

Figure 2.24: Present-day seismicity of Australia indicating the main seismic zones (modified after Hillis et al., 2008). Red ellipse shows aligned seismicity probably related to the Central Eromanga Shear Zone (CESZ), a newly interpreted tectonic feature (see Chapter 5).

The thickness of the present-day lithosphere below the Australian continent (**Figure 2.25**) shows highest values in the west, in the center and in the north (locally up to 250 km). Lowest values (between 70 and 100 km) are estimated for areas below the oceanic crust and for the eastern Australian continent (Kennett & Salmon, 2012). The transition from thick to thin lithosphere follows approximately the TL and the domain of thinned continental lithosphere is associated with the Tasmanides. While the GB is completely underlain by relatively thin lithosphere, the EB and the CB feature a more heterogeneous lithospheric geometry. Below the EB, the lithosphere is generally thinning eastwards, while beneath the CB, the lithosphere of the northeastern domain is obviously thicker than in the southwest (**Figure 2.25**). The depth to Moho beneath Australia is very heterogeneous (**Figure 2.26**, Aitken et al., 2013). Especially in the eastern part, large areas of the continental crust have been extended. The EB features thinned crust in the west (less than 25 km below the Warburton Basin) and in the center (around 30 km below the southwestern CB). Below the GB (locally less than 20 km), the crust was apparently stretched even more (**Figure 2.26**).

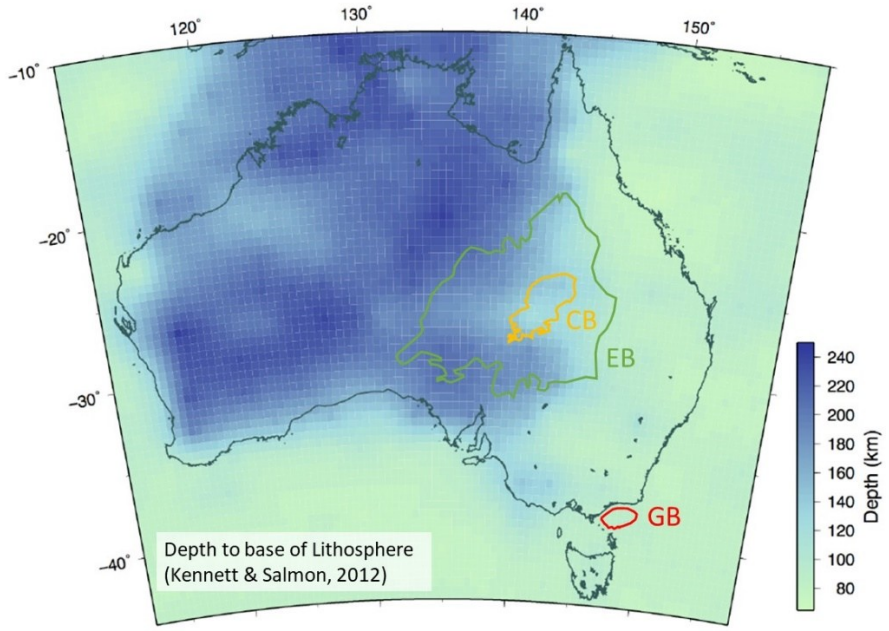

Figure 2.25: Depth to the base of the Lithosphere below Australia (Kennett & Salmon, 2012). Grid resolution: 0.5 x 0.5 degree. CB = Cooper Basin, EB = Eromanga Basin, GB = Gippsland Basin.

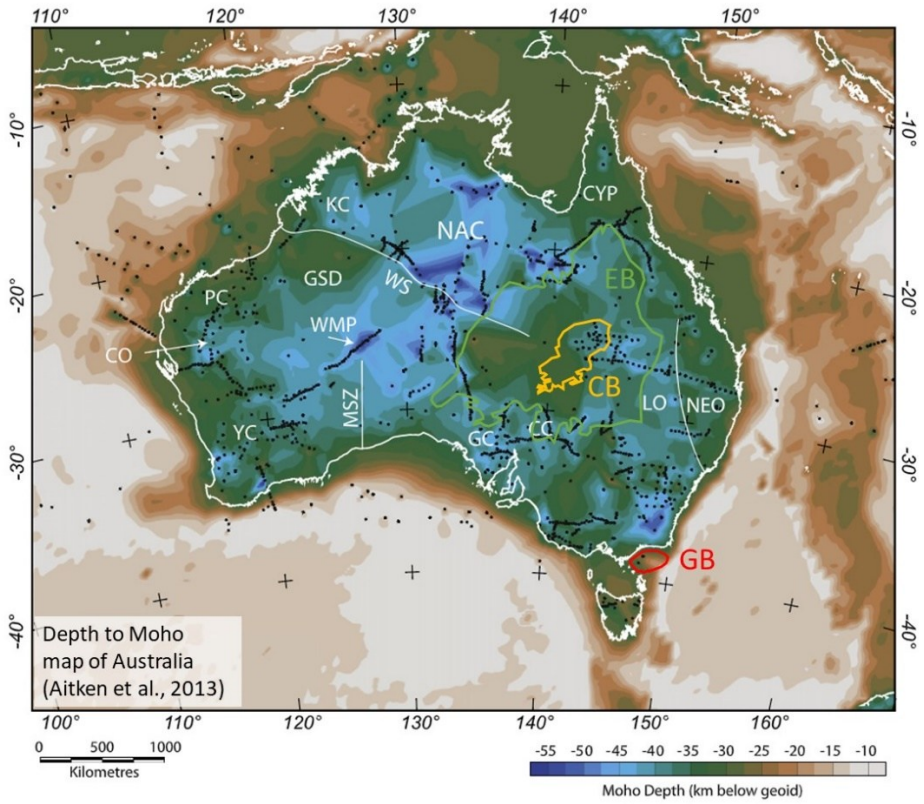

Figure 2.26: Depth to the Moho below Australia (mean Moho elevation, modified after Aitken et al., 2013). CB = Cooper Basin, CC = Curnamona Craton, EB = Eromanga Basin, GC = Gawler Craton, GB = Gippsland Basin, LO = Lachlan Orogen, NEO = New England Orogen. Refer to original publication for further abbreviations.

The gravity anomaly map of Australia (**Figure 2.27a**, Bacchin et al., 2008) shows the strongest variations within the central and eastern fold belts, along suture zones and along the passive margins, while anomalies in central eastern Australia are less pronounced.

In the Cooper region (**Figure 2.27b**) an arc-shaped chain of negative anomalies is visible, which corresponds with the Ella Belt (Purdy et al., 2018, see also **Chapter 4**) and a gravity low in the north resembles the Barrolka Trough, which is surrounded by gravity highs.

The GB (**Figure 2.27c**) features average gravity in the west, high values along the continental slope and very low values in the Bass Canyon, which represents the transition to oceanic crust.

On the magnetic anomaly map (**Figure 2.28a**, Milligan et al., 2010), cratonic domains and fold belts of Australia are well distinguishable by very strong small-scale and large-scale variations. However, a large region in central eastern and southeastern Australia, stretching from Mt. Isa to Tasmania, shows rather low variations of the magnetic intensity. The western boundary of this "magnetic normal zone" correlates with the Tasman Line and both study areas investigated in this thesis are located within this zone.

Magnetic lows in the Cooper region (**Figure 2.28b**) and in the GB (**Figure 2.28c**) roughly correspond with the main depocentres, whereas sporadic magnetic highs occur at the basin margins.

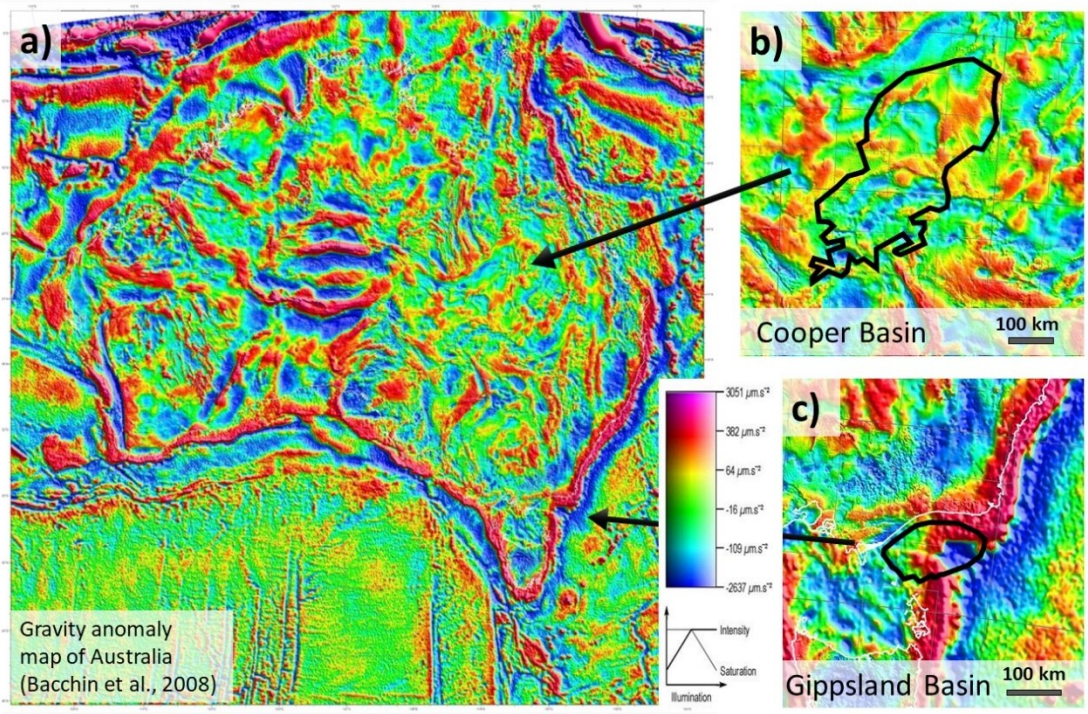

Figure 2.27: Gravity anomaly map of Australia (from Bacchin et al., 2008, Bouguer onshore, free-air offshore). a) Overview of the entire Australian continent and surroundings. b) Zoom into the area around the Cooper Basin. c) Zoom into area around the Gippsland Basin.

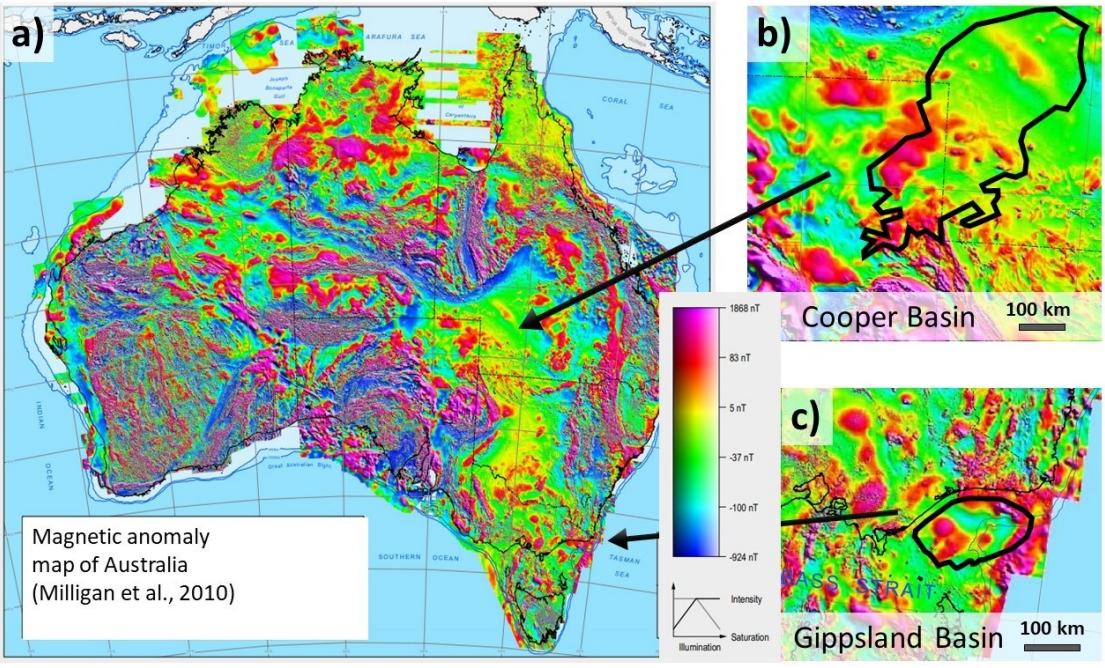

Figure 2.28: Magnetic anomaly map of Australia (from Milligan et al., 2010). a) Overview of the entire Australian continent and surroundings. b) Zoom into the area around the Cooper Basin. c) Zoom into area around the Gippsland Basin.

3 LITHOSPHERIC EVOLUTION, THERMO-TECTONIC HISTORY AND SOURCE ROCK MATURATION IN THE GIPPSLAND BASIN, VICTORIA, SOUTHEASTERN AUSTRALIA

Keywords: Gippsland Basin; petroleum system modelling; heat flow; lithosphere; crustal model; rifting; Gondwana breakup; Tasman Sea

Abstract

A fully integrated 3D basin model was built to study the lithospheric structural evolution and the thermal history of the offshore part of the Gippsland Basin to investigate the type, timing and magnitude of its initial opening mechanism and their effects on source rocks. The applied workflow included seismic interpretation of major faults and magmatic features, seismic reinterpretation of existing main stratigraphic boundaries and adjustment of the basement topography. Different scenarios for a McKenzie-type basal heat flow evolution were tested based on a two-step inversion approach, which translates the thickness changes of lithospheric layers into basal heat flow. Finally, a crustal layer model was assigned to the existing 3D numerical basin model and the effects on thermal maturation of petroleum source rocks were investigated. The results of the calibrated inversion model suggest intense lithospheric stretching and mantle upwelling during the Early Cretaceous, which caused initial breakup and massive subsidence of the Gippsland Basin. This syn-rift phase was accompanied by increasing basal heat flow from initially ~50 mW/m^2 to a maximum of 80 to 90 mW/m^2. The resulting upwelled Moho with an associated crustal thickness of locally only 8 km agrees with geophysical observations. Elevated paleogeothermal gradients between 50 and 60 °C/km prevailed from ca 120 to 80 Ma ago. Episodes of compression, uplift, erosion, and thermal subsidence resulted in fast and continuous cooling during the early post-rift and a constant basal heat flow of 45–50 mW/m^2 since the Eocene. Two main pulses of petroleum generation were identified in the Paleocene and in the Mio-Pliocene. This novel two-step crustal layer inversion method allows a detailed reconstruction of the thermal history of rift basins and, thus, can provide useful information about the maturation of petroleum source rocks.

3.1 Introduction

The main objective of this study is to investigate the lithospheric evolution and the thermal history of the Gippsland Basin offshore Victoria that contains large oil and gas fields. The study provides a numerical 3D model of the Gippsland Basin serves as a case study for the assessment of the thermal evolution of a McKenzie-type rift basin. The Gippsland Basin is located at the southeastern edge of the Australian margin between Victoria and Tasmania (**Figure 3.1a**) and can be subdivided into an offshore and an onshore part. The basin hosts giant oil and gas fields offshore and extensive lignite deposits onshore, although its deep-water region remains underexplored (Goldie Divko et al., 2010).

The Gippsland Basin measures approximately 450 km along the basin axis and extends approximately 150 km from its northern to its southern edge (**Figure 3.1b**). Bordered by the Bass Strait in the south and the mountain ranges of the Victorian Alps in the north, it comprises an area of more than 46,000 km^2 (Woollands & Wong, 2001). The basin widens and deepens from onshore at Port Phillip Bay (south of Melbourne) in the west towards the passive margin of the Tasman Sea in the east and represents a failed rift arm, whose east-west trending basin axis is oriented almost perpendicular to the shelf break. Water depths vary from less than 100 m to more than 3,000 m the offshore part of the basin that is filled with Lower Cretaceous to recent sediments, which reach a total thickness of up to 14 km in the Central Deep (Willcox et al., 1992; Bernecker et al., 2001; GA 2017a).

The focus of this study is limited to the prospective offshore part of the Gippsland Basin. Hydrocarbons have been produced commercially in this region since the mid 1960's at water depths between 45 m and 450 m (Woollands & Wong, 2001), and remaining reserves have been estimated at 400 Gbbl of liquids and 5 Tcf of gas (GA, 2014).

Although the productivity of the Gippsland Basin's petroleum system is proven at the top Latrobe Group, the area remains relatively underexplored at great depths due to high costs, uncertain facies distributions and inaccurate existing petroleum system models. A more quantitative database for thermal history modelling is required to better constrain depth-to-basement, the localization of breakup-related magmatic features and the chronological evolution of the heat flow.

This study models the lithospheric evolution and the thermal history of the prospective Gippsland Basin based on different crustal layer scenarios, with a two-step inversion

approach to calculate heat flow maps derived from lithospheric stretching. The obtained information is then used as additional input for an updated 3D numerical basin model to analyze the resultant thermal maturation and petroleum generation of and within petroleum source rocks. The focus here is both on the early, pre-Paleogene burial and temperature history and the post-Cretaceous phase of maximum burial and intense petroleum generation. The applied workflow serves as a case study for thermal modelling studies of rift basins and supports the general geological understanding of the interplay of dynamic basin-forming processes.

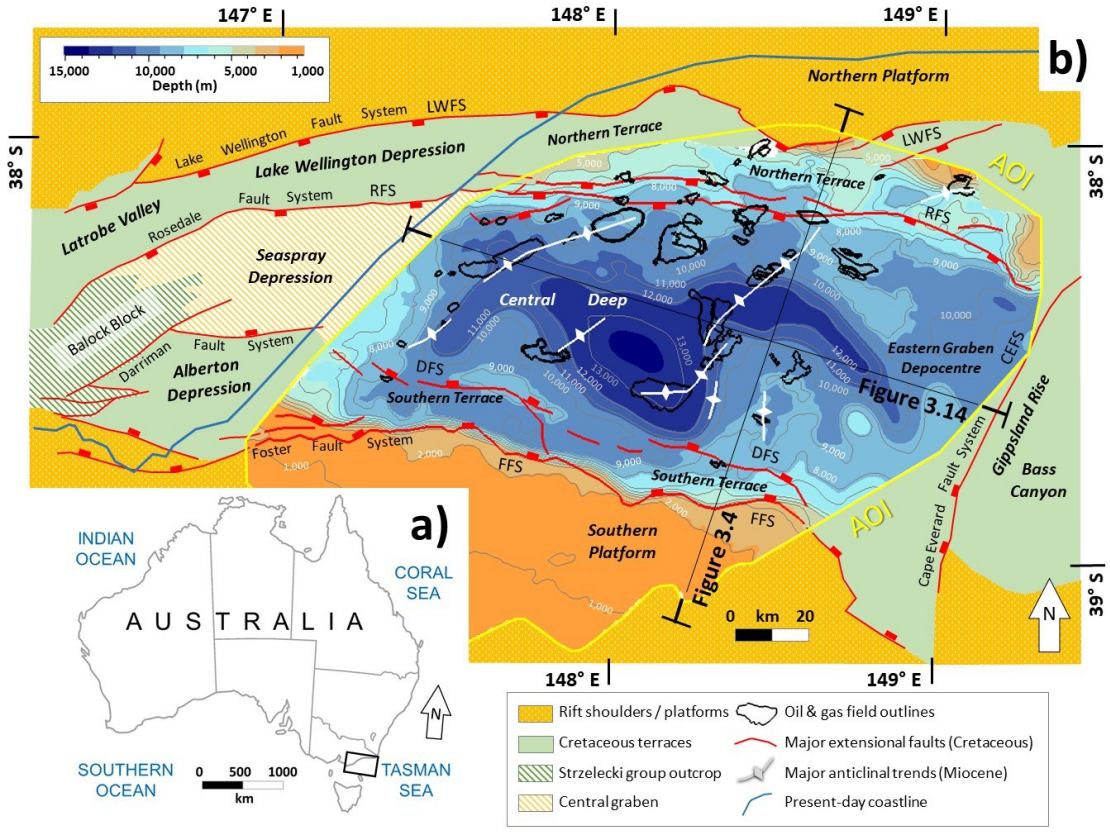

Figure 3.1: Geographic and structural overview of the study area. a) Overview map of Australia, surrounded by the Indian Ocean, the Southern Ocean, the Tasman Sea and the Coral Sea. The small black rectangle indicates the extent of Figure 3.1b. b) Structural elements of the Gippsland Basin (modified after Goldie Divko et al. 2010, basement topography within the AOI (grey isolines) after Power et al. 2001). The black lines indicate the orientation of 2D sections (Figure 3.4 & Figure 3.13).

3.1.1 Geological background and structural evolution

The Gippsland Basin represents the easternmost tectonic feature of the Southern Australian margin rift system, which has evolved in the context of the Pangaea-Gondwana breakup (Woollands & Wong, 2001). Its offshore part can be subdivided into

three main structural domains: the Northern and Southern platforms, and the Central Deep. The curved and complex east-west striking Lake Wellington Fault System (LWFS) in the north and the deeper, more continuous west-northwest–east-southeast-trending Foster Fault System (FFS) in the south represent the two main boundary fault systems (**Figure 3.1b**, Collins et al., 1992; Woollands & Wong, 2001; Divko et al., 2010). They are associated with intra-basinal second-order fault systems: the LWFS accompanied by the east-west-directed Rosedale Fault System (RFS), and the west-northwest–east-southeast-trending Darriman Fault System (DFS) trends parallel to the FFS. The interplay of these fault systems enabled the formation the Northern and the Southern Terraces.

The Central Deep opens towards the east until it is sharply interrupted by the Gippsland Rise, which is controlled by the prominent north-northeast-directed Cape Everard Fault System (CEFS) and offsets the Eastern Graben Depocentre against the abyssal plain of the Bass Canyon (**Figure 3.1b**, Woollands & Wong, 2001). Most of the oil and gas accumulations are trapped below southwest–northeast-trending anticlines, which correlate with Eocene and Neogene inversion trends (Holford et al., 2011; Teasdale et al., 2003).

The orogenic collapse of Eastern Gondwana commenced in the Middle Cretaceous (Albian-Cenomanian boundary) and initiated the opening of the Tasman Sea along the Tasman Rift (Bryan et al., 1997; Veevers, 2000, Norvick et al., 2001; Mortimer, 2008; Kusky et al., 2014; Schwartz et al., 2016; Müller et al., 2016; see also **Figure 2.20** and **Figure 6.1**).

The structural style of the Gippsland Basin was often described as an asymmetric rift (compare Wernicke, 1985; Etheridge et al., 1885, 1987; Hill et al., 1995) , whereas pre-existing basement structures may have strongly influenced the basin evolution and faulting of the sedimentary cover (Samsu et al., 2020).

3.1.1.1 Pre-rift (Paleozoic to Jurassic)

The Gippsland Basin overlies a Paleozoic crystalline basement (Collins & Vernon, 1992; Betts et al., 2002; Teasdale et al., 2003; Huston et al., 2012), which is characterised by large-scale conjugate (mainly dextral) strike-slip faults (Collins & Vernon, 1992; Veevers & Morgan, 2000).

In the Triassic and Jurassic, westward convergence of the Pacific and Phoenix oceanic plates formed a subduction zone with a volcanic/magmatic arc in the east (Müller et al.,

2000a, 2000b; Norvick et al., 2001; Hergt & Brauns, 2001; Teasdale et al., 2003; Salmon et al., 2012).

3.1.1.2 Syn-rift (Early Cretaceous)

Steady accumulation of hot mafic melts caused widespread thermal weakening and underplating of the continental crust. Relatively slow northwest–southeast-directed transtensional tectonic activity along the Southern Australian Fracture Zone (SAFZ) affected the entire southern Australian continental margin during the Jurassic and the Early Cretaceous and facilitated the initial opening of the Gippsland, Otway, Torquay and Bass Basins (Hawlader, 1989; Bryan et al., 1997).

In previous studies, the syn-rift of the Gippsland Basin is commonly related to the Upper Cretaceous Emperor and Golden Beach subgroups (e.g. Norvick et al., 2001) and the Strzelecki Group was simply defined as "economic basement" or as "stage 1 rifting" (Power et al., 2003). In this study, we defined the Strzelecki Group as the main syn-rift mega-sequence, because it agrees with the regional tectonic evolution and the amount of crustal stretching and crustal layer thickness much better explains the huge amount of thermal subsidence during the Late Cretaceous and Cenozoic.

3.1.1.3 Transition / orogenic collapse (Middle to Late Cretaceous)

Over a period of 20–25 m.y. (from Albian to Campanian), the regional geological setting changed from an active subduction zone to a triple junction of rift systems and further evolved to an open ocean basin with a passive margin. 96 Ma ago, the Tasman Spreading Centre evolved south of Tasmania and started unzipping northwards. Subsequent crustal stretching, breakup and seafloor spreading along the Tasman Ridge resulted in eastward drift of Zealandia and its fragmentation (Woollands & Wong, 2001; Norvick et al., 2001; Mortimer, 2006, 2008; Schwartz et al., 2016). This tectonic reorganisation caused regional uplift with up to 3 km of erosion (Otway Unconformity) prior to Tasman Sea spreading (Hill et al., 1995, 1998; Müller et al., 2000; Veevers, 2000; Geoscience Australia, 2017b) and resulted in the transition from syn-rift to post-rift in the Gippsland Basin.

3.1.1.4 Post-rift (Late Cretaceous–present day)

Continuous thermal subsidence since the Maastrichtian was amplified by relatively steady sediment supply and the lithosphere-asthenosphere boundary (LAB) gradually descended towards isostatic equilibrium. In the meantime, the expanding Tasman Sea flooded the Bass Strait, the eastern Australian passive margin established and the shoreface of the

Gippsland Basin migrated westward (see **Figure 3.2**). In contrast to previous studies, we incorporated the Emperor and Golden Beach subgroups ("stage 2 rifting" after Power et al., 2003) into the post-rift mega-sequence due to the much stronger observed extension, crustal stretching, and subsidence during the Early Cretaceous.

During the Oligo-Miocene, when the entire eastern Australian continental margin was uplifted and the Paleozoic basement was commonly exposed at the surface (van der Beek et al., 1999), the offshore Gippsland Basin remained subject to relatively continuous subsidence.

The Neogene to present-day tectonic evolution was dominated by collisional and reorganizational processes in the north and in the east (Müller et al., 2000a, 2000b; Norvick et al., 2001). Within the last 10 Ma, compression caused major far-field shortening, right-lateral faulting, folding and inversion across the Australian plate, still generating the highest seismic activity in southeastern Australia (Reynolds et al., 2003; Zhao & Müller, 2003; Clark et al., 2011; Holford et al., 2011; Huston et al., 2012).

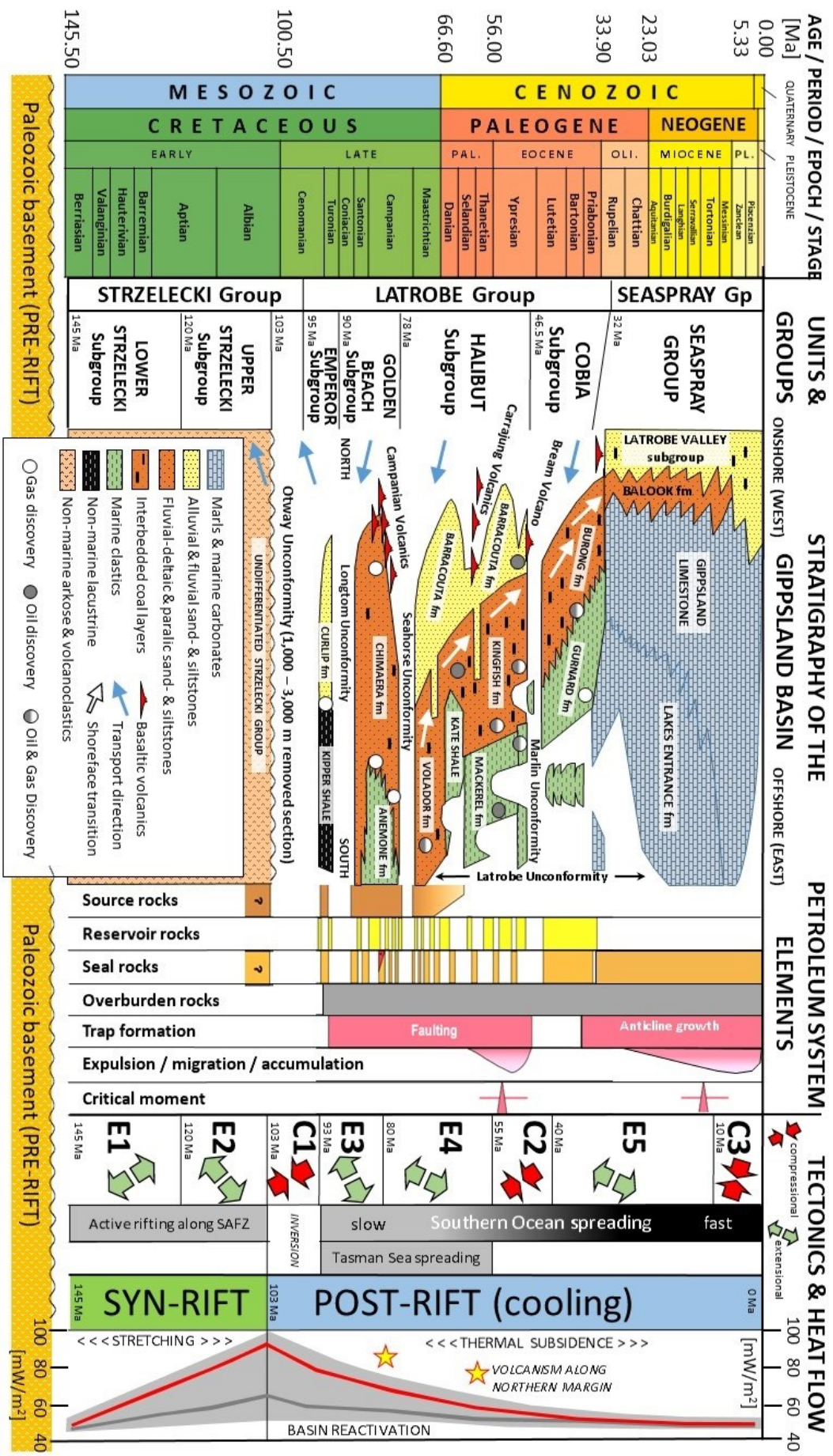
STRATIGRAPHY OF THE GIPPSLAND BASIN
AGE / PERIOD / EPOCH / STAGE [Ma]
UNITS & GROUPS
ONSHORE (WEST)
OFFSHORE (EAST)
PETROLEUM SYSTEM ELEMENTS
TECTONICS & HEAT FLOW
MESOZOIC
CENOZOIC
CRETACEOUS
PALEOGENE
NEOGENE
STRZELECKI Group
LATROBE Group
SEASPRAY Gp
SEASPRAY GROUP
COBIA Subgroup
HALIBUT Subgroup
GOLDEN BEACH Subgroup
EMPEROR Subgroup
UPPER STRZELECKI Subgroup
LOWER STRZELECKI Subgroup
LATROBE VALLEY subgroup
BALOOK fm
GIPPSLAND LIMESTONE
LAKES ENTRANCE fm
BURONG fm
GURNARD fm
KINGFISH fm
KATE SHALE
MACKEREL fm
VOLADOR fm
ANEMONE fm
CHIMAERA fm
KIPPER SHALE
CURLIP fm
BARRACOUTA fm
BARRACOUTA Volcanics
Carrajung Volcanics
Bream Volcano
Campanian Volcanics
Seahorse Unconformity
Longtom Unconformity
Marlin Unconformity
Latrobe Unconformity
Otway Unconformity (1,000 – 3,000 m removed section)
UNDIFFERENTIATED STRZELECKI GROUP
Marls & marine carbonates
Alluvial & fluvial sand- & siltstones
Fluvial-deltaic & paralic sand- & siltstones
Interbedded coal layers
Basaltic volcanics
Marine clastics
Transport direction
Non-marine lacustrine
Shoreface transition
Non-marine arkose & volcanoclastics
Gas discovery
Oil discovery
Oil & Gas Discovery
Source rocks
Reservoir rocks
Seal rocks
Overburden rocks
Trap formation
Expulsion / migration / accumulation
Critical moment
Faulting
Anticline growth
E1
E2
C1
E3
E4
C2
E5
C3
Active rifting along SAFZ
INVERSION
slow
Southern Ocean spreading
fast
Tasman Sea spreading
compressional
extensional
SYN-RIFT
POST-RIFT (cooling)
<<<STRETCHING>>>
<<<THERMAL SUBSIDENCE>>>
VOLCANISM ALONG NORTHERN MARGIN
BASIN REACTIVATION
Paleozoic basement (PRE-RIFT)
Paleozoic basement (PRE-RIFT)
[mW/m²]

Figure 3.2 (previous page): Stratigraphy, petroleum system elements and tectonic evolution of the Gippsland Basin (compiled and modified after Norvick et al. 2001, Bernecker & Partridge 2001, Woollands & Wong 2001, and Teasdale et al. 2003). The subdivision of major stratigraphic units and groups is displayed with representative lithology and relevant stratigraphic features. Important hydrocarbon occurrences are indicated as circles. The timing of petroleum system elements is shown in direct relation to tectonic processes and the thermal evolution. Large arrows indicate the main tectonic stress direction during extensional (E) and compressional (C) basin phases, respectively (according to Table 3.1). The illustrated heat flow trend with associated syn-rift and post-rift phases is derived from thermal modelling performed in this study. The red trend line is representative for the basin center, while the grey trend line corresponds with the Northern and Southern terraces. Stars indicate increased volcanic activity (Campanian and Carrajung volcanics).

3.1.2 Sedimentary evolution and stratigraphy

The sedimentary sequence can be subdivided into three major units: the Late Jurassic to Early Cretaceous Strzelecki Group, the Late Cretaceous to upper Eocene Latrobe Group and the Oligocene to present-day Seaspray Group (Nøttvedt et al., 1995; Bernecker & Partridge, 2001; Goldie Divko et al., 2010; Partridge et al., 2015).

3.1.2.1 Late Jurassic to Early Cretaceous Strzelecki Group (145–103 Ma)

The Tithonian to Neocomian lacustrine-dominated and heavily faulted lower Strzelecki Group corresponds with basin phase E1 (**Figure 3.2**) and unconformable overlies the Paleozoic pre-rift basement. Together with the overlying Barremian to Albian volcanic sandstones of the upper Strzelecki Group (= basin phase E2), it represents the syn-rift megasequence along the SAFZ (Hill et al., 1998; Woollands & Wong, 2001). The accumulation of mainly clastic and volcanic material is associated with an extensive westward draining braided river system and eruptive centers along the eastern Australian margin, whereas fine-grained flood plain deposits contain interbedded coal horizons towards the top of the succession (Norvick, 2005).

The top of the Strzelecki Group is marked by the Otway breakup unconformity (basin phase C1). While the total original thickness of the Strzelecki Group remains uncertain, the preserved section in the basin center is likely to exceed 7,000 m and may even include Late Jurassic sediment successions at the base.

3.1.2.2 Late Cretaceous to Eocene Latrobe Group (93–32 Ma)

The Latrobe Group hosts all currently known hydrocarbon accumulations in the Gippsland Basin (Woollands & Wong, 2001).

After the Albian–Cenomanian inversion (basin phase C1), the Gippsland Basin developed to an internally eastward draining depositional system in which coarse-grained erosional material entered from the uplifted basin margins and lacustrine shales of the Emperor (e.g. Kipper Shale) and Golden Beach subgroups covered the reactivated rift valley – separated by the basin-wide Longtom Unconformity.

Upper Santonian marine shales (Anemone Formation) demonstrate a first marine ingression from the east. A broadening retro-gradational coastal plain with associated deltas and barrier systems developed in the west and along the uplifted rift margins (Hill et al.,. 1998; Woollands & Wong, 2001; Norvick et al., 2001). This short-lived rift sequence (basin phase E3) coincides with the generation of oceanic crust below the abyssal plain beyond the CEFS (Norvick et al., 2001, O'Halloran & Johnstone, 2001). The following megasequence (basin phase E4) above the Seahorse Unconformity mainly consists of coastal-plain-dominated siliciclastic sag-phase deposits of the Halibut and Cobia subgroups.

During Eocene compression (basin phase C2) the northeastern part of the basin was uplifted, and sea-level fluctuations caused intense submarine channeling which is expressed by the Marlin Unconformity (Hill et al., 1998; Norvick et al., 2001; Woollands & Wong, 2001). Along the steep slopes of the Bass Canyon, turbidity currents and marly fans developed (Hill et al., 1998).

3.1.2.3 Oligocene to present-day Seaspray Group (32–0 Ma)

Continued Oligocene–Miocene post-rift subsidence (E5) corresponds with marine carbonates of the Seaspray Group (Hill et al., 1998; Goldie Divko et al., 2010). The basin-wide Latrobe Unconformity marks the transition from a clastic-dominated to a carbonate-dominated depositional environment that comprises the marine Lakes Entrance and the Gippsland Limestone subgroups.

The youngest tectonic inversion pulse (basin phase C3), which uplifted major structures several hundreds of meters along predefined reverse faults, is still ongoing (Teasdale et al., 2003). Major anticlinal structures became host for the large Barracouta, Tuna, Kingfish, Snapper and Halibut oil and gas accumulations, while the marly Lakes Entrance Formation acts as the regional seal (GA, 2014).

3.1.3 Magmatism and volcanism

Volcanic activity in the study area occurred only sporadically from the Late Cretaceous to the Cainozoic. Volcanic material was drilled in formations of the Campanian (70–80 Ma, along the Northern Terrace), the Eocene (55 Ma, Carrajung Volcanics and 46 Ma, Bream Volcanics in the Central Deep) and the Plio-Pleistocene (Sutherland, 1991; McPhail, 2000; Woollands & Wong, 2001; Teasdale et al., 2003; Meeuws et al., 2016a, 2016b).

3.1.4 Present-day heat flow

Generally, the present-day surface heat flow in the Bass Strait ranges between 55 and 60 mW/m^2 with local variations of about +/- 6 mW/m^2. A colder region toward the oceanic domain shows values below 55 mW/m^2 (Goutorbe et al., 2008; Holford et al., 2011). Elevated values in the basin center and along the northern margin are most likely due to the generation of radiogenic heat within the thick sedimentary cover (Goutorbe et al., 2008). Using corrected borehole temperature data to derive the present-day basal heat flow, values between 40 and 55 mW/m^2 can be expected in the study area, with higher values in the deeper parts of the basin (e.g., Holgate & Gerner, 2010).

3.2 Methods, data and modelling

The structural restoration (or "backstripping") of the dynamic evolution of a sedimentary basin is usually being performed by subdividing the modelling process into two separate steps: 1) backward modelling and 2) forward modelling. The basin geometry obtained by the backward modelling can be used in forward simulations to reproduce the chronological evolution of a sedimentary basin step by step and layer by layer (Al-Hajeri et al., 2009; Neumaier, 2015).

In this study, the traditional backstripping approach was extended by the reconstruction of the dynamic evolution of the lithosphere below the sedimentary succession. A new two-step inversion process, which includes (a) the inversion to lithospheric thickness maps, and (b) the conversion of lithospheric thickness maps to heat flow maps, enables reconstructing the thermal history of the study area. The basin modelling and calibration workflow was conducted using Schlumberger Petrel 2016.2 ® and PetroMod 2016.2.2 ® software.

The original 3D basin model was built by Geoscience Australia in conjunction with Schlumberger based on the public domain database of the Australian Government

(http://www.ga.gov.au) and was further modified for use in this study (**Figure 3.3**). The input data included the bathymetry (Whiteway, 2009), a 2D/3D merged seismic megacube, including key interpreted stratigraphic boundaries (3DGEO, 2011) and an associated velocity model (McLean & Blackburn, 2013), polygons (coastline, outlines of oil and gas fields) and about 900 exploration wells of which 9 were used for calibration of the modelling (i.e., Holgate & Gerner, 2010; Geoscience Australia, 2017c). Horizontal grid resolution of the modelling is 500 m by 500 m.The stratigraphic interpretation and age assignment were based on the geological timescale GTS 2012 (Gradstein et al., 2012), the regional chronostratigraphic table (Partridge et al., 2015; GA & Australian Stratigraphy Commission, 2017), public domain well completion reports and supporting geological information (e.g., Rahmanian et al., 1990; Masters, 1993).

The seven existing main sequence boundaries (from 3DGEO, 2011) were used as main input horizons in the 3D petroleum system model: top Paleozoic basement (modified after Power et al., 2001; see **Figure 3.1**), top Strzelecki Group (Otway Unconformity), top upper Emperor Subgroup (Longtom Unconformity), top Golden Beach Subgroup (Seahorse Unconformity), top Halibut Subgroup (Marlin Unconformity), top Cobia Subgroup (Latrobe Unconformity) and top Lakes Entrance Formation (see **Figure 3.2**). Additionally, the Mid Miocene unconformity horizon (from 3DGEO, 2011) was used and serves as the stratigraphic boundary between the lower and upper Seaspray Group. The seismic picks of the deeper horizons (especially Paleozoic basement and Strzelecki Group) are probably too shallow due to poor seismic data and lack of well control, which has direct implications on the uncertainty of calculated burial history and thermal modelling.

Based on these sequence boundaries, the depositional record was subdivided into 22 horizons and 5 unconformities (erosion / hiatus), resulting in 21 layers. Thickness ratios for the sublayer splitting within the main sequences were estimated based on well picks and biostratigraphic ages (**Table 3.1**). For each of the 21 layers, a corresponding facies map was assigned according to the available stratigraphic and regional paleogeographic information (Johnstone et al., 2001; Bernecker et al., 2001).

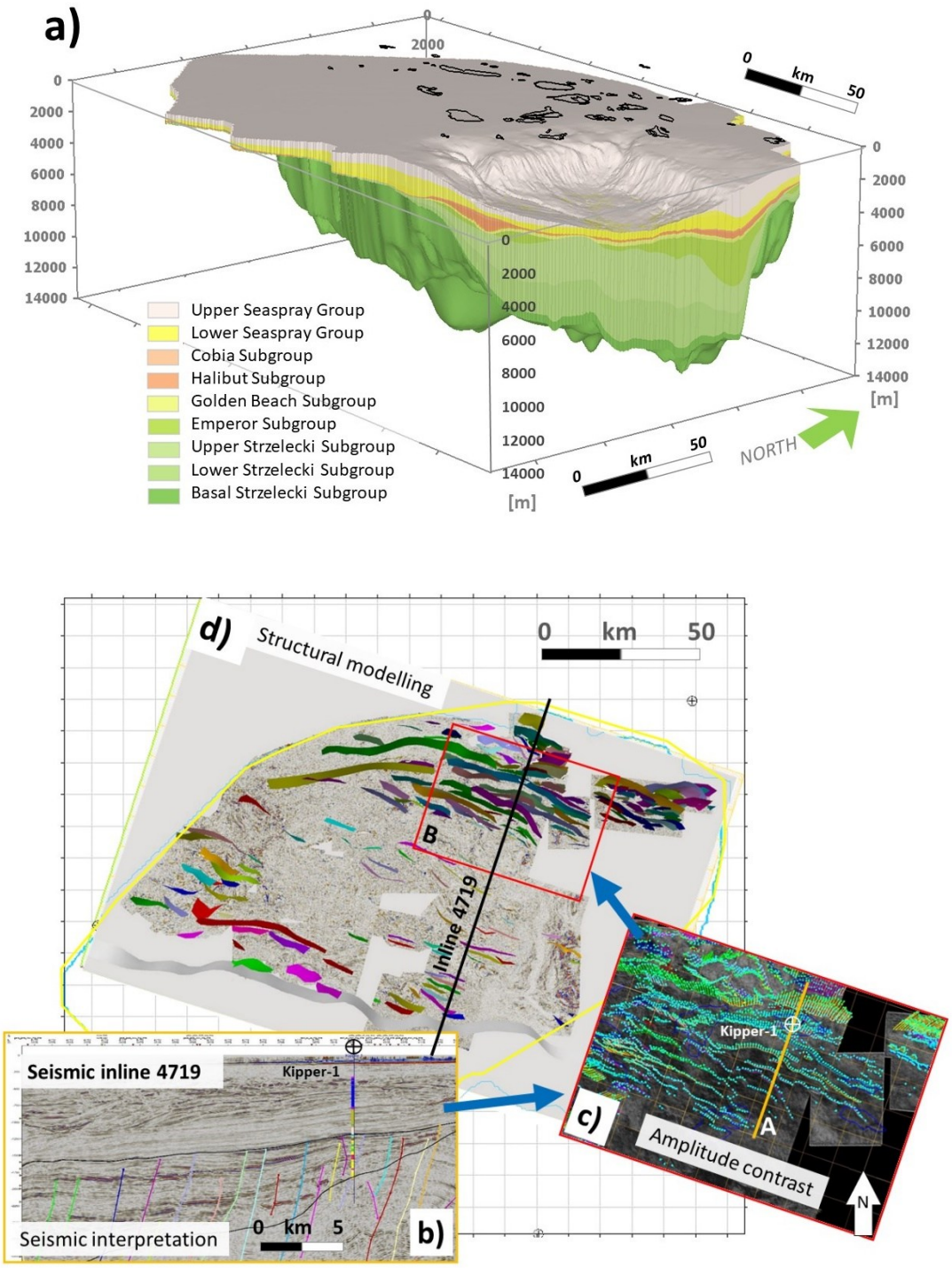

Figure 3.3: Overview of the model geometry and the applied workflow for fault interpretation. a) Geometry of the 3D basin model of the Gippsland Basin (vertical exaggeration factor = 5.00). Upper Cretaceous and Cenozoic post-rift successions rest unconformable on thick Lower Cretaceous syn-rift deposits. See Table 3.1 for detailed assignment and splitting of layers. Black polygons represent outlines of oil and gas fields. b) Manual grid-parallel picking of faults along 2D sections (scroll increment: 500 m). c) Quality control of fault interpretations with attribute volumes (e.g. amplitude contrast). d) Overview of all fault segments (edited and merged) selected for the fault framework in the structural model (~150 segments). Seismic inline 4719 is displayed in Figure 3.4 in more detail.

The facies maps were used to define individual paleo-water-depth maps (PWD) for each time step. The following PWD values were used to translate facies values into corresponding water depth values: onshore / coastal plain = 0 m, shoreface = 10 m, lower shoreface = 20 m, shallow marine = 50 m, marine = 100 m, open marine = 200 m. When conditions were fully terrestrial, a constant PWD = 0 m was assigned. Sediment-water-interface temperature maps (SWIT) were calculated from PWD maps based on the paleo-latitude of Australia.

Table 3.1: Layer splitting and split ratios as applied in the age assignment.

Layer name	# sublayers	Sublayer name	Sublayer [%]	Top Age [Ma]
Upper Seaspray	1	Upper Seaspray	100.00	0.00
Lower Seaspray	1	Lower Seaspray	100.00	10.00
Lakes Entrance	1	Lakes Entrance	100.00	15.60
Cobia	3	Cobia_UNasp	33.33	32.00
		Cobia_MNasp	33.33	34.00
		Cobia_LNasp	33.33	38.00
Halibut	7	Upper_Halibut_Pasp	12.50	46.50
		UH_UMdiv	12.50	50.50
		UH_LMdiv	12.50	54.30
		UH_ULbalmei	12.50	55.80
		KT_Paleocene	5.00	63.50
		LH_UFLong	15.00	66.00
		LH_LFlong	30.00	67.00
Golden Beach	3	Golden_Beach_Tlill	33.33	78.00
		GB_Nsen	33.33	80.60
		GB_Tapox	33.33	83.50
Emperor	2	Upper_Emperor	10.00	90.00
		Lower_Emperor	90.00	90.30
Strzelecki	3	Upper_Strzelecki	50.00	103.00
		Lower_Strzelecki	40.00	120.00
		Basal_Strzelecki	10.00	140.00

The following erosion events were assigned: Otway Unconformity (103–93 Ma, removed section = 1,000 m basin-wide), Seahorse Unconformity (78–68 Ma, with 20 m removed throughout most of the study area and up to 300 m in the southeast) and the Latrobe

Unconformity (32–31 Ma, after Johnstone et al., 2001). The Longtom and Marlin unconformities were modelled as hiatus only, because the actual amounts of erosion are unknown. In addition, the channel erosion of the complex Middle Miocene unconformity and the Marshal para-unconformity were not included.

The Pepper and Corvi kinetic model (Pepper & Corvi, 1995a, 1995b) was applied and the following values for original total organic carbon (TOC) and original hydrogen index (HI) were applied based on geochemical data from the GA well database:

- Lacustrine type I (TOC: 3 wt%, HI: 600 mgHC/gTOC): Kipper Shale (Emperor Subgroup, Lowry & Longley, 1991),
- Marine type II (TOC: 3 wt%, HI: 600 mgHC/gTOC): Anemone Formation (Golden Beach Subgroup),
- Non-marine type III (TOC: 2 wt%, HI: 300 mgHC/gTOC): lower coastal plain facies of Cobia, Upper Halibut, Lower Halibut, Golden Beach subgroups.

Given TOC contents are average values, generally able to generate and expel petroleum, if the thickness and distribution area of the source interval is sufficient (see Demaison & Huizinga, 1991).

The extended backstripping approach requires the geometric determination of the present-day lithosphere, comprising the sediments, crust, and upper mantle. The three-layer architecture of the lithosphere below the Gippsland Basin can be roughly described by the shape of four lithospheric reference horizons:

1) surface: topography or seafloor (bathymetry taken from Whiteway, 2009),
2) depth-to-basement: the interface between the sedimentary succession and the metamorphic or crystalline (pre-rift) basement (from 3DGEO, 2011; partly modified after Power et al., 2001; see **Figure 3.1b**),
3) "Moho": the boundary between the brittle crust and the elastic upper mantle (after Aitken et al., 2013),
4) Lithosphere-Asthenosphere Boundary (LAB): the 1,333 °C isotherm at the boundary between the lithosphere and the asthenosphere (after Kennett & Salmon, 2012).

This present-day lithospheric geometry is clearly an interpretation and thus contains significant uncertainty.

3.2.1 Seismic interpretation of faults, surfaces and magmatic features

To support the thermal modelling, major faults and magmatic features were interpreted along crosslines and inlines of the 2D and 3D merged seismic megacube (3DGEO, 2011). A series of attribute volumes was applied for quality control of the faults (structural smoothing for noise reduction, amplitude contrast, edge detection, see **Figure 3.3b** and **Figure 3.3c**). The structural framework model was defined based on about 150 merged and smoothed fault segments (**Figure 3.3d**). The existing main stratigraphic boundaries were slightly updated, depth-converted and tied to well tops by using the volume-based modelling (VBM) technique and the available velocity model (McLean & Blackburn, 2013).

Figure 3.4a and **Figure 3.4b** show an example of the seismic interpretation along inline 4719, which extends from the Southern Platform to the Northern Terrace. The interpreted syn-rift faults cut through the basement and locally create significant offset within the Latrobe Group due to Late Cretaceous transtensional reactivation (E3) and Eocene (C2) transpression and inversion (cf. Samsu et al., 2020). Although the post-rift sequence is interrupted by unconformities and intensely faulted in some areas, the typical steer's head geometry of the Gippsland Basin is visible.

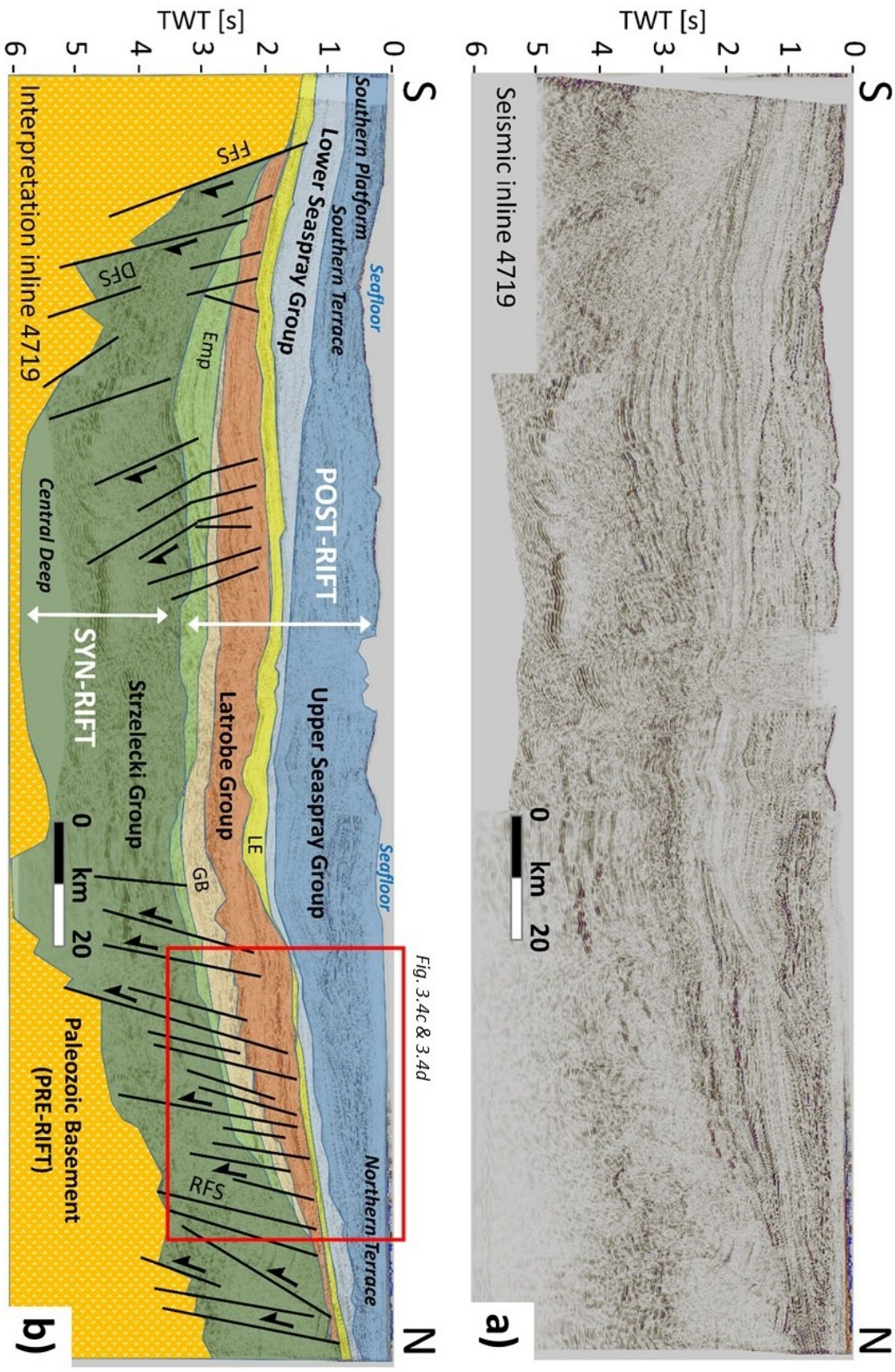

Figure 3.4: Example from seismic interpretation. a) Seismic inline 4719 from 3DGEO (2011, see Figure 3.1 for orientation). b) Seismic interpretation along inline 4719. Red rectangle indicates extent of Figure 3.4c & Figure 3.4d.

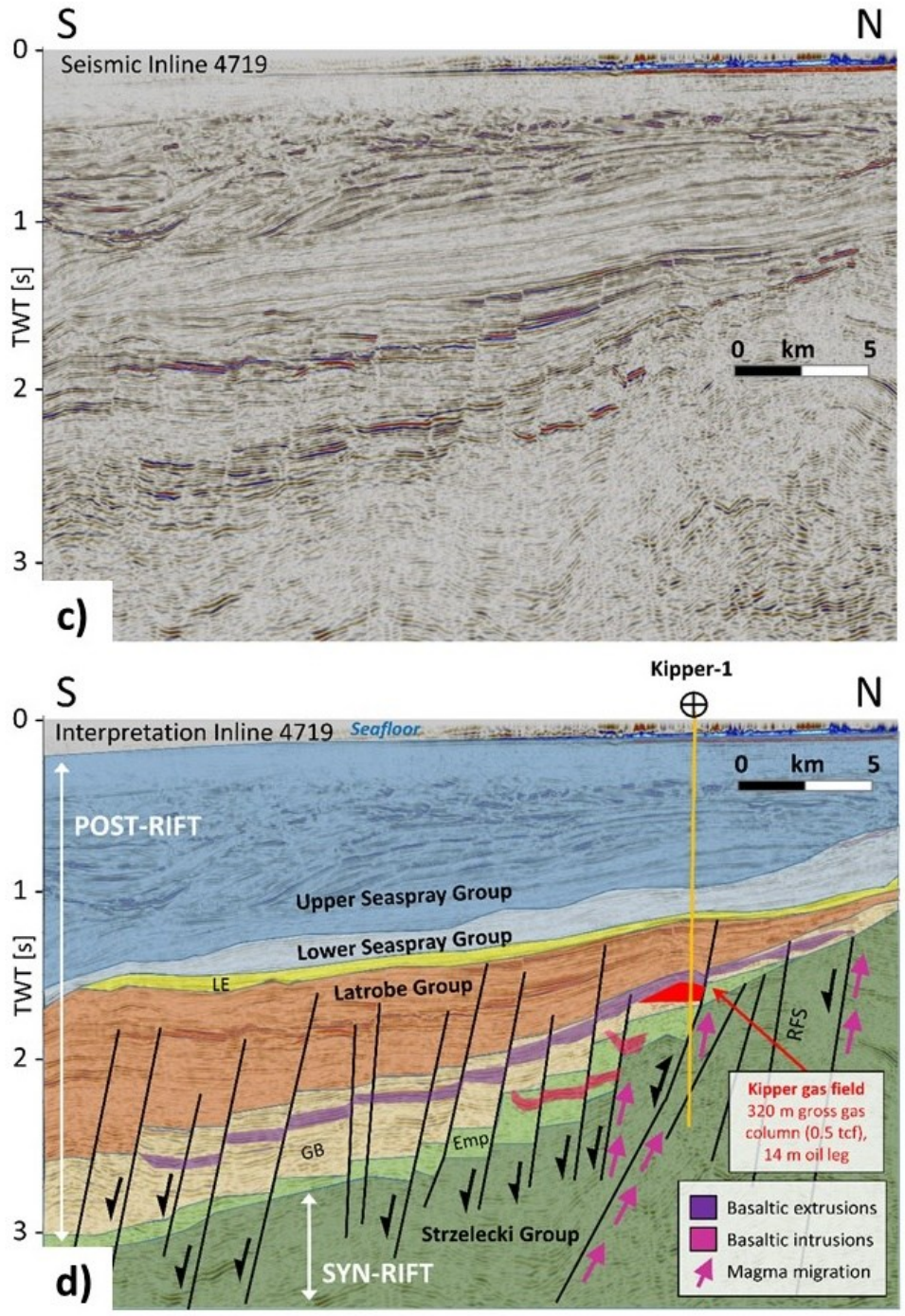

Figure 3.4 (continued): Example from seismic interpretation. c) Seismic inline 4719 from 3DGEO (2011). d) Seismic interpretation along inline 4719, zoom into the Kipper area. High-amplitude reflectors clearly crosscut the concordant strata. Basaltic lavas are intercalating with sediments of the Golden Beach subgroup (GB), while intrusive bodies were simultaneously trapped in the underlying Emperor subgroup (Emp). Both features were most likely fed by the same major faults, which reached deep into the crust and provided pathways for magma migration. Latrobe Group here summarizes Halibut and Cobia subgroups. Emp = Emperor subgroup; GB = Golden Beach subgroup; LE = Lakes Entrance subgroup; FFS = Foster Faults System; DFS = Darriman Fault System; RFS = Rosedale Fault System.

A zoom into inline 4719 reveals high-amplitude reflectors, which clearly crosscut the concordant strata in the Kipper area at the edge of the Northern Terrace (**Figure 3.4c** and **Figure 3.4d**). These are characteristic of magmatic intrusions (Planke et al., 2003) and confirm earlier observations (e.g., by McPhail, 2000; O'Halloran & Johnstone, 2001; Meeuws et al.; 2016a, 2016b). The magmatic features vary in thickness between 10 m and 100 m and many have been confirmed by drilling. The type can be interpreted from impedance: higher impedance relates to intrusions and subaerial flows, lower impedance generally relates to tuff, volcanic ash and weathered horizons. As shown in **Figure 3.4d**, extrusive and intrusive bodies are crosscutting and intercalated with the siliciclastic post- and syn-rift deposits. Further, the volcanic bodies appear in growth packages and in obvious spatial relationship to large faults (**Figure 3.5a** and **Figure 3.5b**). The type of volcanism can be described as fissure volcanism and is characterized by non-explosive eruptions of low viscosity basaltic material and a possible basinward (southward) flow. Deep-seated extensional and transtensional fault segments were reactivated by northeast-southwest-directed dextral movement along the RFS during the Late Cretaceous (E3), and gave way for ascending magma which migrated along the faults, intruding the Emperor Subgroup (sills, dikes, and funnels), and also covering the surface of the paleo-floodplain (subaerial lava-flows). The diameter of the intrusive bodies rarely exceeds 5 km, while the subaerial flows typically spread over distances of 10 to 20 km (**Figure 3.5a**) as interpreted from the seismic megacube, respectively.

Subaerial volcanic features (extrusions) were identified based on well intersections (e.g., Kipper-1, Manta-1, Moonfish-1, Stonefish-1, Sunfish-1 and Wirra-3, see **Figure 3.5**), and their distinct geometry was tracked along seismic crosslines and inlines supported by 3D-autotracking. The location and extent of maximum amplitude reflectors were mapped using seismic attribute volumes to indicate the subsurface magmatic intrusions (almost exclusively below reservoir level and therefore undrilled). The maximum impedance of the intrusions was highlighted using the seismic attributes of Relative Acoustic Impedance (RAI) and Root Mean Square amplitude (RMS). Three-dimensional "geobodies" were extracted from areas with maximum RAI and RMS values. The boundary polygons of the extracted "geobodies" (representing subsurface intrusions, **Figure 3.5a**) and the picked volcanic layers (representing subaerial lava flows, **Figure 3.5b**) were projected to the corresponding facies maps. Due to their relatively small size, volcanic and magmatic features are expected to have only local effects on heat flow and source rock maturation.

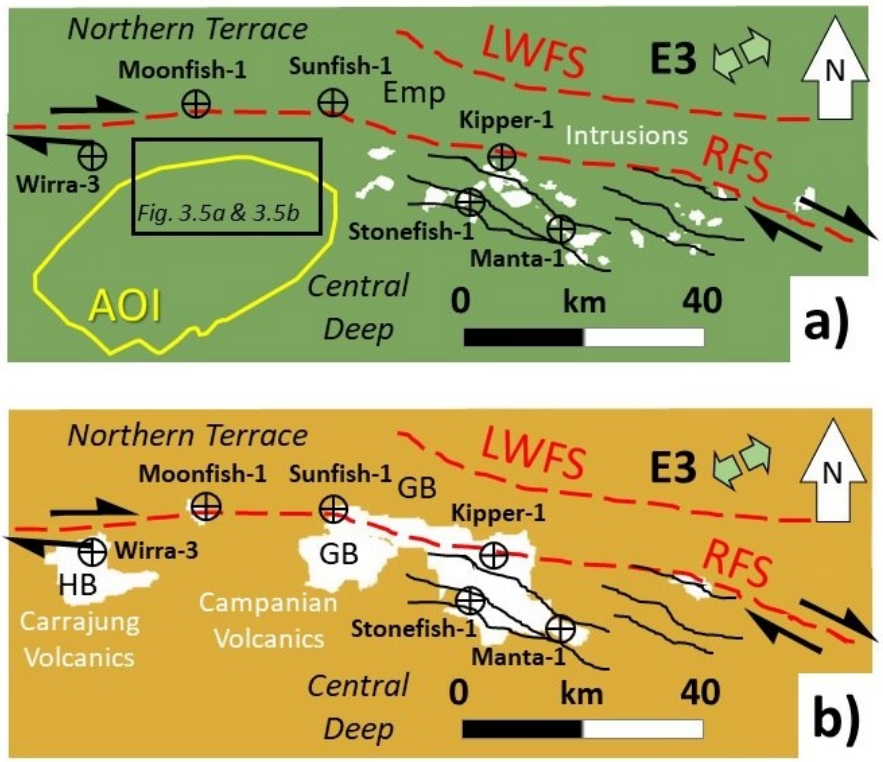

Figure 3.5: Mapped magmatic intrusions a) and subaerial flows b) along the edge of the Northern Terrace with selected well locations where volcanic material was intersected. The extracted 'geobodies' which represent the magmatic intrusions are aligned along large faults. Green extensional arrows (E3) indicate the paleo-stress direction. Corresponding transtensional fault activity (indicated by black kinematic arrows) probably triggered magmatism and volcanism along the Rosedale Fault System during the Campanian. The diameter of the mapped intrusive bodies ranges between 1 and 5 km. All mapped magmatic intrusions emplaced within the Emperor subgroup (Emp). The interpreted contemporaneous subaerial volcanic flows correspond to the Golden Beach (GB, Campanian Volcanics) and the Halibut (HB, Carrajung Volcanics) subgroups. AOI = Area of Interest; black rectangle: extent of Figure 3.5a & Figure 3.5b within the AOI; RFS = Rosedale Fault System; LWFS = Lake Wellington Fault System.

3.2.2 Fault modeling

The interpreted faults (**Figure 3.3**, **Figure 3.4** and **Figure 3.5**) are mainly extensional normal faults generally striking west-northwest–east-southeast and steeply dipping towards north-northeast along the southern margin and south-southwest along the northern margin. The extensional faults were active during the early stretching phases and especially in the eastern part of the Gippsland Basin, they have contributed to trapping of hydrocarbons since the Eocene.

Large fields around the Central Deep (e.g. Barracouta, Marlin, Snapper) are related to inversion anticlines generated during the Eocene inversion (Woollands & Wong, 2001)

indicating closed faults since then. Along the Northern Terrace in proximity to the RFS substantial east-west-directed lateral (most likely dextral) displacement can be observed (see **Figure 3.5**). Although the C2 compressional phase started already about 55 Ma ago, most rifting-related normal and strike-slip faults probably lost their permeability with a certain delay. The orientation of the fault strike is commonly subparallel to the northwest-southeast stress direction and certainly facilitated initial horizontal reactivation of the faults before their eventual closing and/or inversion.

Several scenarios of fault property (open vs. closed) evolution were tested and the following settings for the final simulation were applied: open faults from 145–45 Ma and closed faults from 45–0 Ma. This timing coincides with the Neogene phase of compression and inversion (C2), whereas no substantial extension occurred afterwards. The locally refined volumetric elements (LRVE) method was used prior to simulation. The LRVE method allows the incorporation of complicated faults by refining the grid along the fault surfaces.

3.2.3 Thermal modelling

In the McKenzie crustal model (McKenzie, 1978; 1981; **Figure 3.6**), uniform stretching is assumed resulting in isostatic compensation and upwelling of the asthenosphere (= initial rifting). Simultaneously ascending basaltic melts are trapped below the overlying granitic crust. This so-called ‘underplating’ process continuously increases the heat flow and accelerates stretching of the crust and mantle (= syn-rift phase). Once the uplifted isotherm begins to subside again, the solidifying mafic material with higher density will constantly pull down the lithosphere from below, causing another episode of subsidence, called thermal subsidence (= post-rift phase), during which the thermal and isostatic equilibrium is re-established and lithospheric thickening occurs (**Figure 3.6a** and **Figure 3.6b**, Hantschel & Kauerauf, 2009). The stretching-induced lithospheric thickness changes result in vertical isostatic movements of the lithosphere, enabling the geothermal gradient to be derived by fitting the tectonic subsidence at each location.

The applied method also accounts for the equilibrating effect of the sedimentary succession on the heat flow. The heat flow must change throughout the entire column of the lithosphere to establish steady-state thermal equilibrium after the deposition of new sediments and not just within the new deposits (Hantschel & Kauerauf, 2009). Therefore, the lag time required for the sediments to thermally equilibrate is incorporated in the calculation of the basal heat flow.

In this study, the geological control is increased using an alternative two-step approach for the McKenzie inversion. The basal heat flow is calculated by attaching crustal layers to the base of the model and solving the multi-1D heat flow equation ($q = -\lambda \nabla T$; where λ [W/m/K] is the thermal conductivity of the material, $\nabla T = T(x, t)$ is the temperature gradient [K/m], and $q = q(x, t)$ [mW/m2] is the magnitude and direction of the heat flow at point x and time t) with the given boundary conditions. The heat flow maps resulting from this inversion are then used as the lower thermal boundary condition for the model simulation. Thickness maps and heat flow maps were created with the PetroMod® McKenzie crustal heat flow tools.

3.2.3.1 Heat flow inversion from crustal layer thicknesses

The temperature distribution within a sedimentary basin are controlled by 1) basal heat flow (q), 2) sediment-water-interface temperature (T_{swi} or SWIT), and 3) radiogenic heat production. The heat flow (q [mW/m^2]) from the basement into the sediments is mainly determined by the average thermal conductivity (λ [W/m/K]) and the respective thickness of the mantle and the crustal layers (h [m]). **Figure 3.6c** illustrates the boundary value problem for the heat flow analysis of the lithosphere and within the sedimentary basin fill.

3.2.3.2 Two-step inversion from tectonic subsidence

The tectonic subsidence can be restored from total subsidence via backstripping of the isostatic sediment load. Since the subsidence over time at any location can be represented by a burial history plot at the top of the basement, tectonic subsidence is simply calculated for a basin filled with water, and total subsidence is calculated for a basin filled with sediments (higher density of sediments results in higher loads and greater subsidence). In McKenzie's model it is assumed that the thermal subsidence of the upper mantle during the post-rift phase is directly dependent on the magnitude of thinning during the syn-rift phase. Consequently, we applied the following two-step routine:

1) The mantle thickness is derived from the post-rift tectonic subsidence at each location and for each time step (see **Figure 3.7a** for well locations).
2) The incremental thickness changes of the crust are calculated by applying the results of the first step in combination with the inversion of the syn-rift tectonic subsidence (**Figure 3.7b**).

The resulting tectonic subsidence maps and stretching maps, can be used to invert the lithospheric layer thickness (taking smoothing of the ductile mantle into consideration) into basal heat flow maps for each time step.

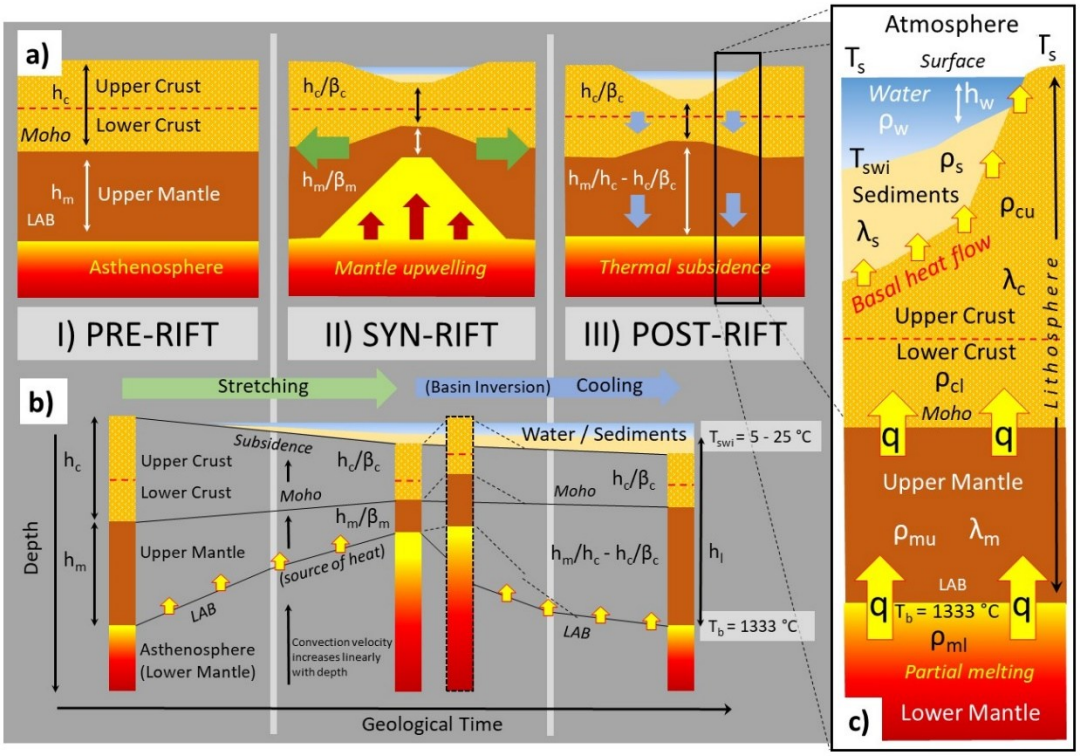

Figure 3.6: Cartoon of the three principal phases of the simplified McKenzie crustal model and involved relevant physical parameters (after McKenzie 1978 and Hantschel & Kauerauf 2009). a) The pre-rift phase (I) is characterized by low tectonic activity. It is followed by the syn-rift (II), during which deformation of the crust and upwelling of the asthenosphere occurs. A depression forms at the surface, which fills with water and sediments. Throughout the post-rift phase (III) cooling of the lithosphere results in thermal subsidence, facilitating accommodation space for additional sediment input. b) While the top of the lithosphere remains fixed, the Tb isotherm (Tb = temperature at the base of the lithosphere; Tb = ¾ Tm = 1,333 °C. Tm = pyrolite melting temperature) ascends and the heat flow (q) increases. A short interphase of post-rift inversion with uplift and erosion is possible before the isotherm drops again during the post-rift phase (III). The individual stretching factors (β) are describing the thickness variations (h) of the crust and the mantle over time. c) The layers of the lithosphere react differently to tectonic forces and temperature changes due to varying density (ρ) and thermal conductivity (λ). The heat flow (q) from the asthenosphere to the surface is controlled by the distance of the thermal boundaries (Ts = surface temperature; Tb = temperature at the base of the lithosphere) to each other. The heat transfer and the temperature distribution in the sedimentary basin itself are controlled by the basal heat flow, the water depth (hw) and the Tswi = sediment water interface temperature (SWIT).

Thermal calibration using a crustal layer model requires adjustment of the lithosphere thickness and the heat flow. The modelling also requires definition of the timing for the subsidence phases (syn-rift vs. post-rift) and the present-day geometry, present-day heat

flow, and present-day temperature, for the calibration window. The pre-rift thickness of crust and mantle are the other input variables for the crustal model. Individual pre-rift thickness value pairs (crust and mantle) need to be tested and the quality of the output needs to be iteratively verified by analyzing the stretching maps and the fit of the theoretical subsidence. A good fit is characterized by small subsidence differences (theoretical subsidence–tectonic subsidence ≈ 0).

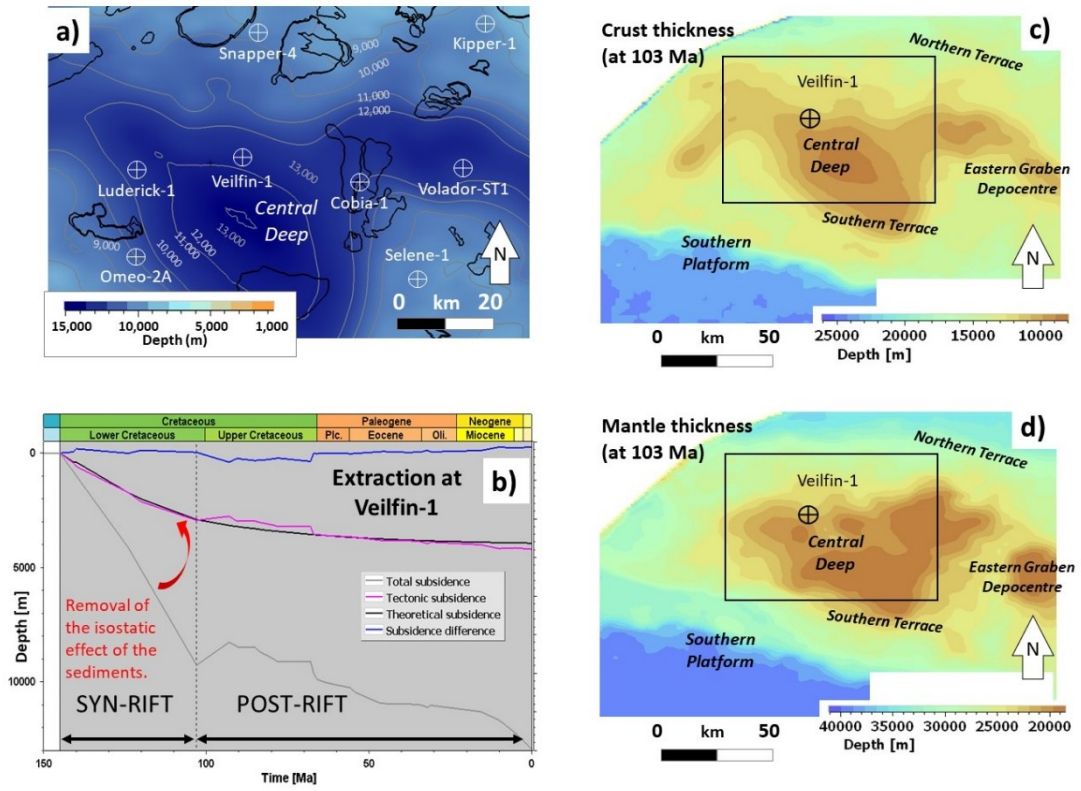

Figure 3.7: Fitting the theoretical subsidence to tectonic subsidence based on 1D-extractions. a) Overview of calibration boreholes used in this study located in the Central Deep of the Gippsland Basin (Archer-1 not shown, contours are depth-to-basement after Power et al., 2001). b) A representative extraction performed along the well path of Veilfin-1. Based on its gradient the total subsidence curve (sediment-filled basin) can be separated into two phases: syn-rift and post-rift. After removing the sediment load, the fit of the theoretical subsidence and the tectonic subsidence (basin filled with water) can then be achieved by fitting the stretching parameters (correct timing of rifting and selection of suitable pre-rift thickness; a good fit is characterized by small subsidence differences (theoretical subsidence – tectonic subsidence ≈ 0). c) Resulting thickness of the crust after stretching varies between 8 km in the Central Deep and 25 km below the rift shoulders (pre-rift thickness set to 25 km). d) The rift axis is underlain by a stretched mantle with minimum thickness values less than 20 km. Below the rift shoulders (e.g. Southern Platform) the upper mantle keeps its original thickness (pre-rift value set to 40 km). Please note that three different thickness scales are used in a), c) and d).

3.2.4 Scenarios for the crustal layer model

The scenario modelling was conducted assuming a symmetrical McKenzie-type (pure shear) rifting mechanism. This is a necessary simplification for the crustal layer inversion approach in which maximum stretching coincides with maximum heat flow. Related uncertainties will be discussed further below.

Four different crustal structure scenarios were analyzed (A, B, C, D), for which the uncertainty framework is given in **Table 3.2**). While several other settings were also tested, the differences between these four selected scenarios are exemples used here to illustrate the sensitivity of the various pre-rift settings.

3.2.4.1 Scenario A (30/95)

Scenario A represents a pre-rift lithospheric structure (crust: 30 km, upper mantle: 95 km) consistent with average continental lithosphere in isostatic equilibrium and the LAB located at ~125 km depth (i.e., Parsons & Sclater, 1977).

3.2.4.2 Scenario B (40/70)

Scenario B is based on the present-day crustal structure (crust: 40 km, upper mantle: 70 km). This is consistent with the present-day shape of the Moho below the remnants of the Lachlan Orogen, which measures up to 50 km below the Victorian Alps and up to 35 km below Tasmania (Aitken et al., 2013). Therefore, the second scenario assumes a thicker crust and a thinner lithosphere compared to the default values. This scenario is also consistent with the inferred geological setting at the time of initial rifting (double fold belt with a deep crustal root and an already upwelled mantle).

3.2.4.3 Scenario C (25/50)

In Scenario C, the pre-rift thickness of the upper mantle was reduced to 50 km and the crustal pre-rift thickness is only 25 km. These values were chosen to represent lithospheric structure further away from the collision zone (back-arc environment), where no crustal thickening has occurred, but the LAB is elevated either due to partial melting and enhanced convection in the asthenospheric mantle wedge or earlier extensional tectonic processes in that area.

3.2.4.4 Scenario D (25/30)

In scenario D, a thin crust (25 km) is assigned and the pre-rift thickness of the upper mantle is reduced further (30 km), representing a very thin lithosphere already prior to rifting.

An overview of the applied settings is given in the **Appendices**. Example thickness maps for the crust and the mantle below the Gippsland Basin at the end of the syn-rift (103 Ma) are illustrated in **Figure 3.7c** and **Figure 3.7d** (pre-rift thickness for the crust = 25 km; pre-rift thickness for the mantle = 40 km).

3.2.5 Well data calibration and thermal conductivity

The quality of the modelling was controlled by calibrating the calculated results against measured present-day temperature (Horner-corrected borehole temperature), thermal maturity (vitrinite reflectance profiles, %Ro), and lithology (porosity, permeability) from the well database (GA, 2017b). Compaction was calibrated only against porosity and permeability and a detailed pressure calibration was not performed in this study. The applied thermal conductivity values in this study are the result of the lithology proportioning of each individually assigned lithology. Measured values for thermal conductivity of the sediments are only available for the onshore sector (e.g., Harrison et al., 2012).

3.3 Results and interpretation

Only the calculated heat flow maps of scenario C were assigned for the final simulation of the 3D basin model since it provided the most plausible output by resulting in realistic stretching factors and matching best to the present-day geometry. The comparison of the individual heat flow trends and corresponding stretching maps of all four scenarios are described in the following.

3.3.1 Crustal layer modelling results

The crustal layer thickness of the described scenarios (A, B, C and D) were used to create the corresponding heat flow maps. The lithospheric stretching and corresponding heat flow trends were then estimated at nine representative borehole locations in the center of the 3D basin model: Archer-1, Cobia-1, Kipper-1, Luderick-1, Omeo-2a, Selene-1, Snapper-4, Veilfin-1 and Volador-1 ST1 (see **Figure 3.7a**). The calculated output of all four scenarios is tabulated for comparison with ranges from previous references as shown in **Table 3.2**. The tabulated data are only shown for the area around the Central Deep, where maximum lithospheric stretching and associated subsidence occurred, because only small variations in thickness and heat flow were computed at the rift shoulders. Scenario C provided the best match to the calibration data from the four scenarios, so it was used in the remaining workflow.

Table 3.2: Calibration matrix for the result analysis of the inversion to lithospheric layer thickness (step 1) and inversion to heat flow (step 2). Calculated output, which fits the calibration window in bold and italic. Thickness of the entire lithosphere includes the sedimentary column in the Central Deep (~7 km at after stretching (103 Ma); ~13 km at present day). Value ranges for calibration are taken from literature or derived from literature values: 1) Aitken et al., 2013; 2) Kennett & Salmon, 2012; 3) Allen & Allen, 2013; 4) Green et al., 1995; 5) Holgate & Gerner, 2010.

Scenario	Input (geometry)		Inversion to lithospheric layer thickness (step 1)			
	Pre-rift thickness [km]		Stretching β [-]	Thickness after stretching [km]	Present-day thickness [km]	Calibration window [km]
A	Crust	30	2.0 - 3.5	~ 9	~ ***9***	5 - 20 [1)]
	Mantle	95	1.5 - 3.5	~ 24	~ 90	40 - 70
	Lithosphere	125	n.d.	~ 40	~ 113	70 - 90 [2)]
B	Crust	40	1.4 - 1.9	~ 20	~ ***20***	5 - 20 [1)]
	Mantle	70	1.5 - 3.5	~ 18	***60 - 70***	40 - 70
	Lithosphere	110	n.d.	~ 38	~ 103	70 - 90 [2)]
C	Crust	25	2.0 - 3.5	~ 8	~ ***8***	5 - 20 [1)]
	Mantle	50	2.0 - 5.0	~ 13	~ ***57***	40 - 70
	Lithosphere	75	n.d.	~ 28	~ ***78***	70 - 90 [2)]
D	Crust	25	2.0 - 3.5	~ 8	~ ***8***	5 - 20 [1)]
	Mantle	30	2.0 - 7.0	~ 7.5	~ ***40***	40 - 70
	Lithosphere	55	n.d.	~ 22.5	~ 61	70 - 90 [2)]

Scenario	Input (tectonic phases)	Inversion to heat flow (step 2)	
	Basin phase	Calculated heat flow [mW/m^2]	Calibration window [mW/m^2]
A	Syn-rift start (145 Ma)	~ 32	40 - 60 [3)]
	Rifting maximum (103 Ma)	~ 62	70 - 100 [3) 4)]
	Present-day (0 Ma)	~ 36	40 - 55 [4) 5)]
B	Syn-rift start (145 Ma)	~ 35	40 - 60 [3)]
	Rifting maximum (103 Ma)	~ 54	70 - 100 [3) 4)]
	Present-day (0 Ma)	~ 38	40 - 55 [4) 5)]
C	Syn-rift start (145 Ma)	~ ***45***	40 - 60 [3)]
	Rifting maximum (103 Ma)	~ ***85***	70 - 100 [3) 4)]
	Present-day (0 Ma)	~ ***42***	40 - 55 [4) 5)]
D	Syn-rift start (145 Ma)	~ ***58***	40 - 60 [3)]
	Rifting maximum (103 Ma)	~ 94	70 - 100 [3) 4)]
	Present-day (0 Ma)	~ ***52***	40 - 55 [4) 5)]

3.3.1.1 Scenario A (30/95)

The modelled results of scenario A (**Figure 3.8a**) estimate that the present-day LAB is located at a depth of ~113 km. This large total lithospheric thickness (sediments + crust + mantle) is primarily the result of a thick pre-rift mantle (95 km), which reaches thermal equilibrium at a present-day thickness of about 90 km. The present-day crustal thickness reaches a minimum of ~9 km below the Central Deep corresponding to stretching values between 2.5 and 3.5. Heat flow increases from 32 to 62 mW/m^2 during stretching maximum, and later decreases to 36 mW/m^2 by the present. These low stretching and heat flow values lead to temperatures that are too low to match calibration data.

3.3.1.2 Scenario B (40/70)

The results from scenario B (**Figure 3.8b**) are similar to scenario A even though the present-day lithospheric thickness (~103 km) input to the model is larger than the observed present-day thickness of 80 +/- 10 km, and the modelled present-day crustal thickness (~20 km) is much greater than observed. Modelled crustal stretching yields values below 2.0, while modelled mantle stretching rarely exceeds 3.0. The calculated basal heat flow increases from 35 to 54 mW/m^2 later decreasing a present-day values of 38 mW/m^2. The modelled temperatures remain below measured values as was the case for scenario A, implying the modelled mantle upwelling remains insufficient to replicate the basin's evolution. The heat flow peak calculated for this scenario is even lower than that in scenario A since the effect of increased initial crustal thickness counteracts the reduction in initial mantle thickness.

3.3.1.3 Scenario C (25/50)

Scenario C, with pre-rift crust and upper mantle thicknesses of 25 and 50 km respectively, was designed to test the effect of a thinner lithosphere on the basal heat flow (**Figure 3.8c**). Overall, the thickness inversion delivered model results consistent with observed lithospheric structure and heat flow measurements. The calculated present day crustal thickness map reaches a minimum of ~8 km and the mantle thickness after cooling estimates constant values around 57 km. Addition of the present-day depth to basement (minimum 13 km) and the lithospheric layer thicknesses (8 km + 57 km), gives a depth of the LAB (~78 km) that falls within the reference case range given in **Table 3.2**. The stretching maps show a good fit with beta values between 2.5 and 3.0 for the crust (maximum = 3.3) and between 2.0 and 5.0 for the mantle, respectively. Beta values are, as expected, higher than for the onshore Gippsland area (Hegarty et al., 1986; Power et

al., 2001). The calculated basal heat flow shows a typical trend of a McKenzie-type rift: starting from 45 mW/m^2, peaking at 85 mW/m^2 and (following exponential cooling) finishing at 42 mW/m^2 at present day. The estimated values for the lithosphere thickness and heat flow fall within the reference ranges for scenario C suggesting it provides the most plausible result for the lithospheric and thermal evolution of the Gippsland Basin. Nevertheless, in many parts of the study area the measured present-day heat flow is still slightly higher than suggested by scenario C.

3.3.1.4 Scenario D (25/30)

Scenario D, with pre-rift crust and upper mantle thicknesses of 25 km and 30 km respectively, was designed to test the effect of a further reduction in mantle thickness (**Figure 3.8d**). The resulting present-day crustal thickness map and the corresponding beta distribution remained similar to the results of scenario C. The reduction of the initial mantle thickness resulted in a modelled LAB at ~61 km, which is far less than the present day estimated depth of 80 +/- 10 km. The calculated basal heat flow increases from 58 to 94 mW/m^2 and later decreases to 52 mW/m^2 at present day. The resulting mantle stretching yields unusually high beta factors between 6.0 and 7.0 throughout large parts of the basin. Stretching factors above 3.5 generally represent already separation of the lithosphere due to seafloor spreading (i.e. England, 1983).

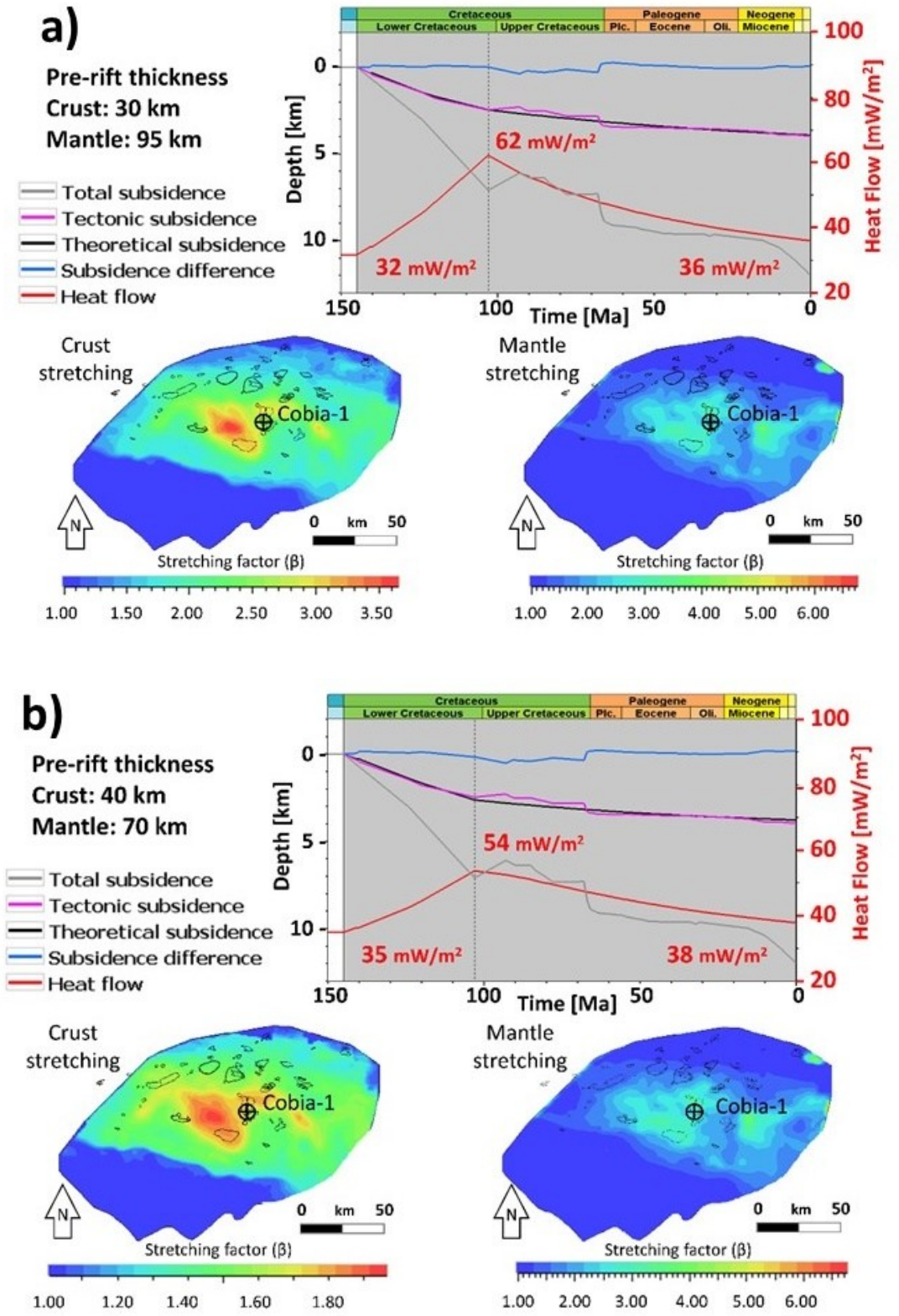

Figure 3.8: Tectonic subsidence fit, resulting stretching maps after lithospheric layer thickness inversion and calculated heat flow trends extracted at Cobia-1. Inversion results for (a) Scenario A, (b) Scenario B, (c) Scenario C, and (d) Scenario D. Note that stretching maps have different scales.

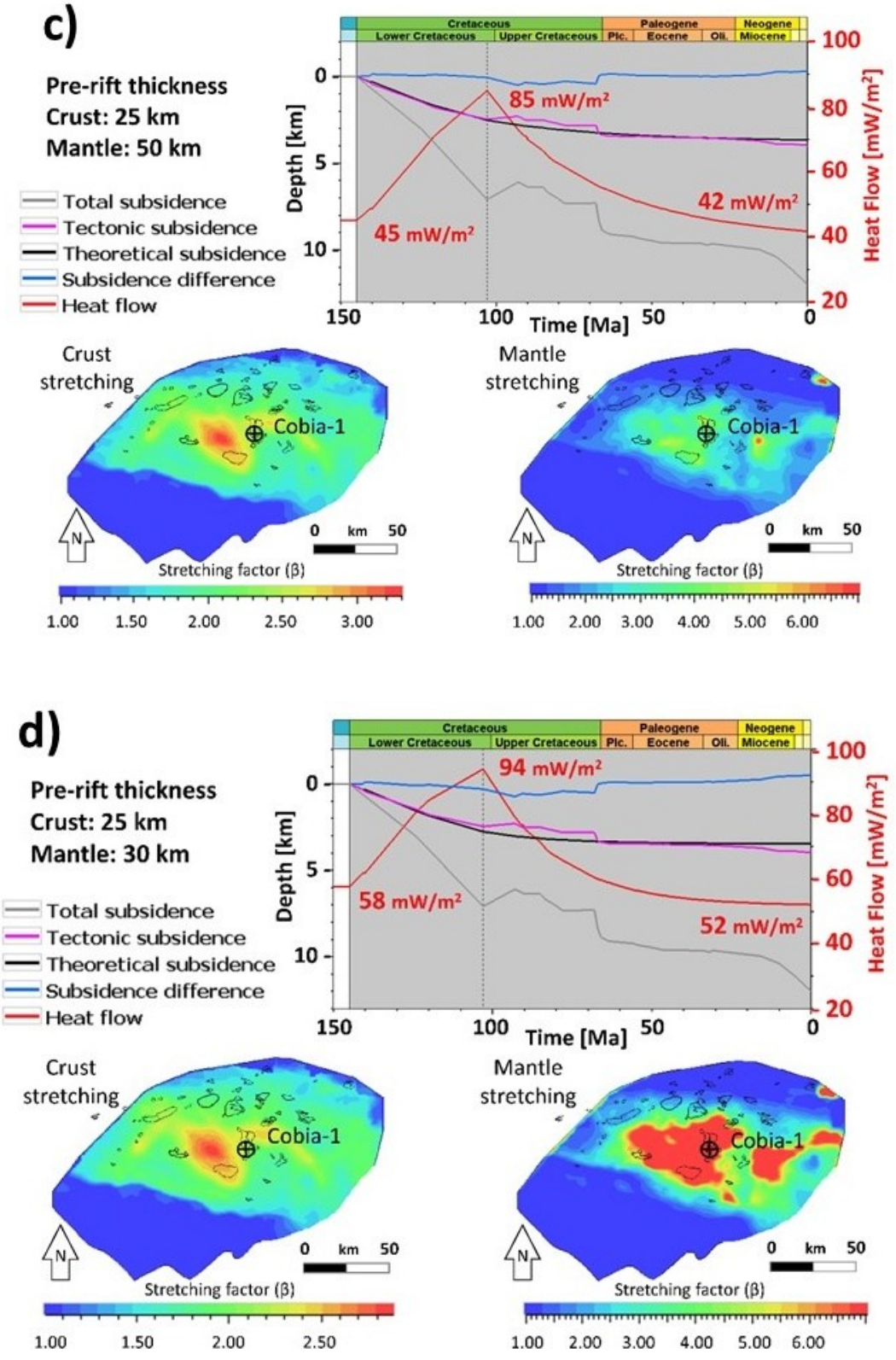

Figure 3.8 (continued): Tectonic subsidence fit, resulting stretching maps after lithospheric layer thickness inversion and calculated heat flow trends extracted at Cobia-1. Inversion results for (a) Scenario A, (b) Scenario B, (c) Scenario C, and (d) Scenario D. Note that stretching maps have different scales.

3.3.1.5 Simulation of the crustal layer model

Plausible pre-rift thickness value pairs were chosen for all four scenarios, and each scenario provided a fit of the modelled tectonic and theoretical subsidence (acceptable subsidence difference in **Figure 3.8**). The scenario models were simulated to see if they lie in the range of the reference case estimates of the main variables taken from the literature. However, as the results of scenarios A and B did not match present day observations of both, crustal structure and heat flow (**Table 3.2**), these were not considered for the final simulation. The modelled crustal stretching factors and the present-day crustal layer thicknesses of scenario C are the closets to the observed geological conditions. Consequently, only the resulting basal heat flow maps of scenario C were assigned for the simulation run of a final 3D basin model (simulator settings are provided in the **Appendices**). The simulation of the basin model was performed to understand the influence of the crustal layer model on the maturation of source rocks in the Gippsland Basin and to test the usefulness of the crustal modelling workflow in the context of petroleum system analysis.

3.3.2 Burial history and temperature evolution

Figure 3.9a displays the present-day geometry of the top horizon of the Strzelecki Group with the calculated maximum temperature overlay and 1D-extractions along six well loctions for comparison of the results with selected well data (**Figure 3.9b;** Omeo-2A, Luderick-1, Snapper-4, Kipper-1, Archer-1, and Volador-1 ST1; it should be noted that the well data reaches depths of only 3–4 km and deeper values are thus extrapolated). This temperature/vitrinite reflectance calibration is thus only valid for the upper part of the sedimentary succession. The estimated maximum temperature varies between 35 °C at the platforms and 185 °C in the center of the troughs. The match of the present-day temperature is generally satisfactory and a maximum geothermal gradient of 28 °C/km can be estimated.

The comparison with vitrinite reflectance thermal maturity data shows varying results in different parts of the basin. Satisfactory matches with calibration data were achieved throughout the basin center (e.g. Omeo-2A, Luderick-1, and Volador-ST1), whereas some locations in the south are ‘over-estimated’ (Archer-1), and the Northern Terrace is ‘under-estimated’ (Snapper-4 and Kipper-1), since the maturation gradient is too low compared to the measured data. A good (theoretical) calibration for each well is shown as orange dashed lines in **Figure 3.9**.

As model in the pseudo burial history extracted at the location of Cobia-1 (**Figure 3.10a**), the highest subsidence rate over a longer period occurred during the syn-rift phase (145–103 Ma). The lowermost successions of the Strzelecki Group reached depth levels of 7 to 8 km and maximum temperatures of up to 300 °C. Between 120 and 100 Ma a paleogeothermal gradient of about 50 °C/km was established. The inversion after the rifting maximum not only resulted in the removal of (at least) 1 km of the upper Strzelecki Group (Otway Unconformity) but also shifted relatively hot sediments closer to the surface providing an increased geothermal gradient of ~50 °C/km also for the early post-rift period between 90 and 80 Ma. Contrastingly, the present-day geothermal gradient in the basin center ranges between 25 and 28 °C/km. Most formations in the offshore areas (except for the lower parts of the Strzelecki Group) reached their maximum temperature only at present day due to continuous burial during the post-rift phase.

In the center of the Gippsland Basin the modelling suggests source rock beds in the Kipper Shale and the Golden Beach Subgroup underwent significant kerogen transformation (TR > 10 %) during the Paleocene (**Figure 3.10b**). The critical moment (TR > 50 %) for the Kipper Shale occurred in the early Eocene, while the successions of the Golden Beach Subgroup surpassed its critical moment only in the Miocene. The Lower Halibut source rocks just started to generate substantial amounts of petroleum in the Miocene to Pliocene.

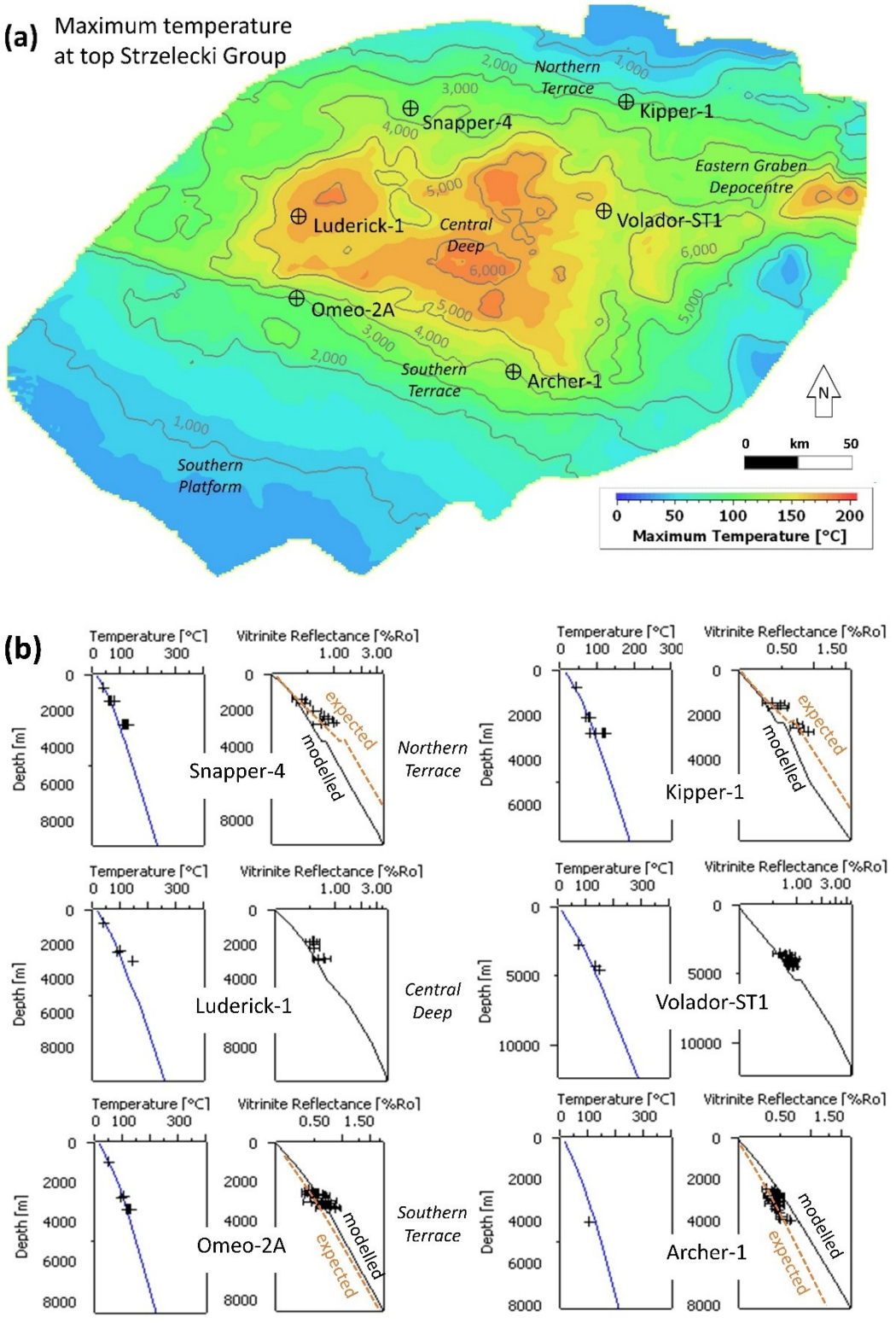

Figure 3.9: Comparison of the modelled temperature evolution of scenario C with selected well data. (a) Map of estimated maximum temperature at the top of the Strzelecki Group with depth isolines and well locations. Thermal maxima of about 185 °C are located within the deep troughs. (b) Plots of modelled temperature (blue) and vitrinite reflectance (black) of scenario C at selected well locations compared with well data (cross). Expected trends (drawn as orange dashed lines) at the northern and southern terraces are discussed in the text.

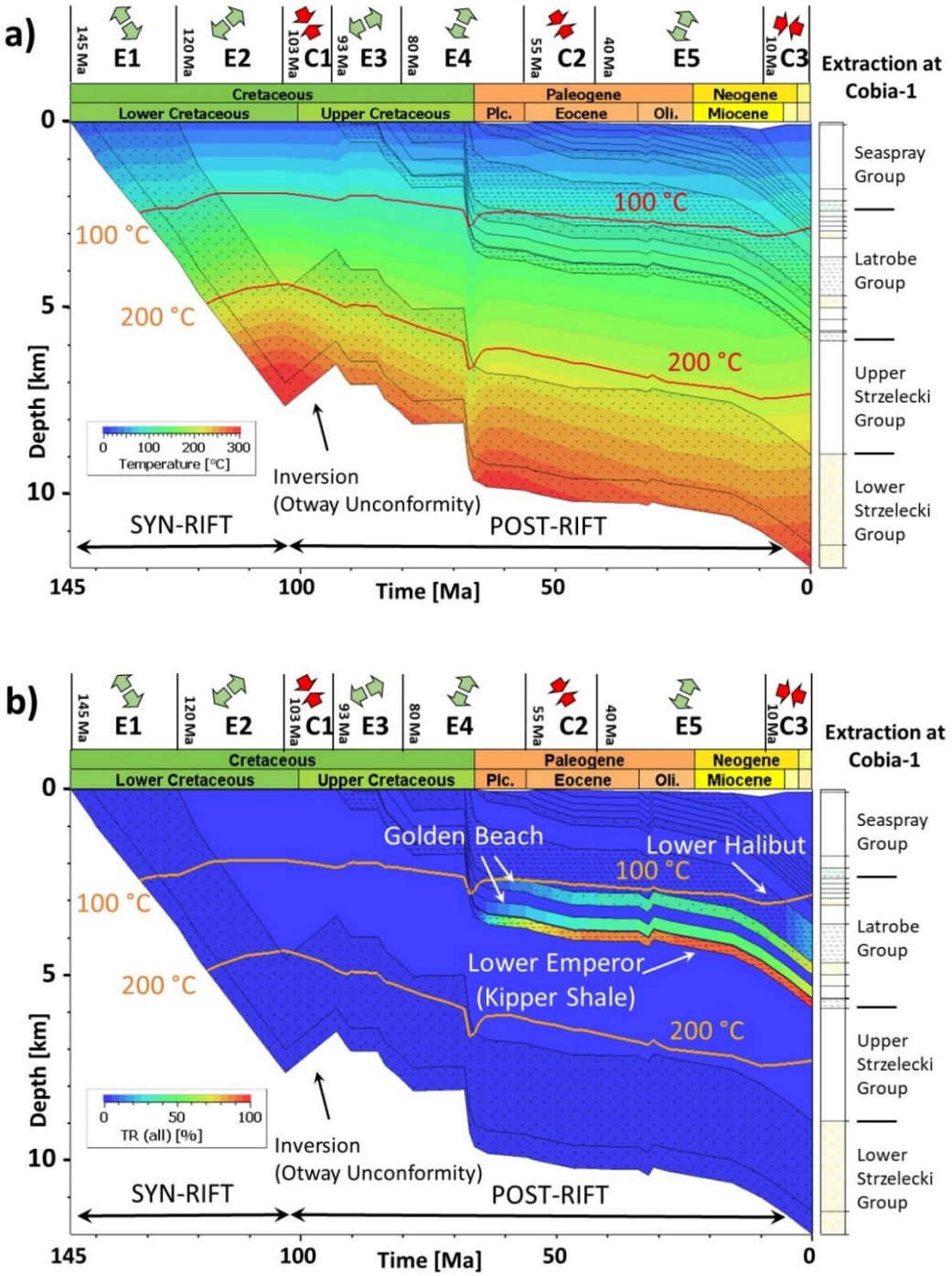

Figure 3.10: Burial history plots with a) maximum temperature overlay extracted at Cobia-1 (see Figure 3.7 for borehole location) based on scenario C). The highest geothermal gradient was established after the basin inversion between about 93 Ma and 80 Ma. All formations except the Lower Strzelecki Group reached their individual maximum temperature at present day. b) Transformation ratio (TR) over time extracted at Cobia-1 based on scenario C. The Kipper Shale and the Golden Beach source rocks initiate significant kerogen transformation during the Paleocene (TR > 10 %). The critical moment (TR > 50 %) for the Kipper Shale occurred already in the early Eocene, while the Golden Beach subgroup surpassed its critical moment in the Miocene. The Lower Halibut source rocks just started to generate substantial amounts of petroleum in the Mio-/Pliocene.

3.3.3 Basal heat flow evolution and lithospheric layer dynamics

The modelled evolution of the basal heat flow since the Early Cretaceous started with moderate values around 45 mW/m^2 at the onset of rifting. After approximately 5 Ma, the heat flow increased to levels around 48 mW/m^2 with a tendency towards higher values in the basin center due to mantle upwelling (**Figure 3.11a**).

Ongoing mantle upwelling during the syn-rift phase provided gradually increasing basal heat flow with values between 50 and 60 mW/m^2 along the terraces and between 80 and 90 mW/m^2 throughout the basin center at the end of the Albian with corresponding paleogeothermal gradients between 50 and 60 °C/km. As shown in **Figure 3.11b**, the model suggests that the Southern Platform and the Northern Terrace remained relatively unaffected by the thermal pulse, while the highest basal heat flow occurs in the Central Deep and in the Eastern Graben. At the rift maximum (ca 103 Ma) up to ~7 km of the Strzelecki sedimentary succession had accumulated in the deepest troughs, while the thickness of the crust measured only ~8 km below the center of the Gippsland Basin, resulting in a total maximum lithospheric thickness of 28 km.

Throughout the period of exhumation (ca 103-93 Ma) the subsurface temperatures remained elevated (see **Figure 3.10**). The post-rift phase already began featured by initial thickening, cooling and subsidence of the LAB, whereas the shape of the upwelled Moho prevailed. While the basal heat flow decreased to 60-75 mW/m^2 (**Figure 3.11c**), the elevated paleogeothermal gradient remained until 80 Ma.

During the Late Cretaceous, the modelled basal heat flow in the basin center dropped but remained constant at the margins (**Figure 3.11d**). Heat flow values in the Central Deep and the Eastern Graben rarely exceeded 50 mW/m^2, while the terraces and the Southern Platform maintained values of about 45 mW/m^2.

After continuous thermal subsidence until present day, the modelled basal heat flow stabilized at values between 40 and 45 mW/m^2 in the deepest parts (**Figure 3.11e**) with a corresponding geothermal gradient not higher than 30 °C/km.

Throughout the area of interest, the present-day depth-to-Moho is estimated to ranges between 15 and 35 km (Aitken et al., 2013) and features the lowest values along the assumed rift axis. Subtracting the sedimentary column, present-day crustal thickness values between 5 and 20 km can be derived. The LAB is estimated at depths of 80 +/- 10 km (Kennett & Salmon, 2012).

3.3.4 Present-day surface heat flow

The calculated heat flow takes the radiogenic heat of the sediments into account (**Figure 3.11f**). At present day, the surface heat flow of the Gippsland Basin shows values of about 45 mW/m^2 at the margins, 50 mW/m^2 in the central parts, and the highest values (50–60 mW/m^2) in the Eastern Graben and the Bass Canyon.

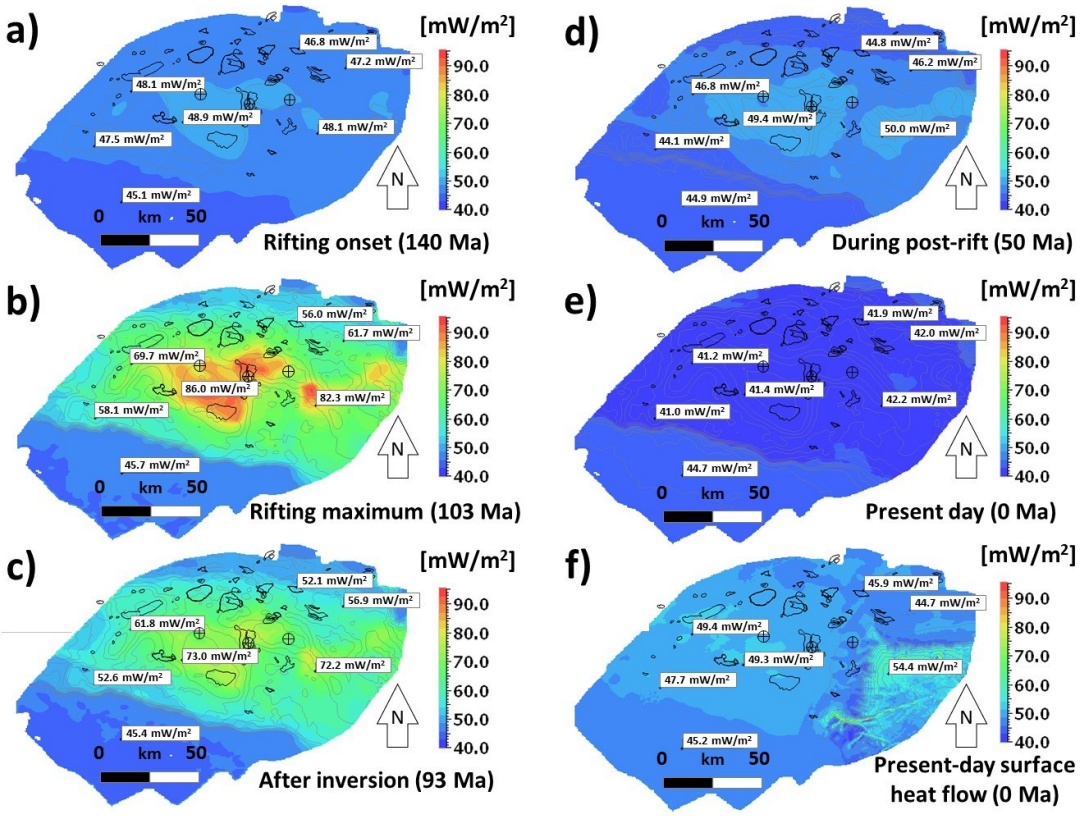

Figure 3.11: The evolution of the calculated heat flow for the offshore Gippsland Basin based on the crustal layer model of scenario C. a) Basal heat flow shortly after onset of rifting and initial subsidence (140 Ma, Lower Strzelecki formation). b) Basal heat flow after rapid subsidence at rifting maximum (103 Ma, Upper Strzelecki formation). c) Basal heat flow shortly after the uplift and erosion, which occurred at the transition between syn-rift and post-rift (93 Ma, Lower Emperor formation). d) Basal heat flow after substantial cooling during the early post-rift (50 Ma, Upper Halibut formation). e) The present-day basal heat flow. f) Surface heat flow at present day (0 Ma). Shown values were picked at the lower left corner of the labels. Crosshairs indicate borehole locations of Veilfin-1, Cobia-1 and Volador-ST1 (from West to East, compare Figure 3.14).

3.3.5 Source rock thermal maturity and kerogen transformation

The evolution of heat flow and temperature over time directly influenced the thermal maturity and transformation of the source rocks. **Figure 3.12** and **Figure 3.13** show present-day modelled maturity maps based on the Easy%Ro algorithm (Sweeney & Burnham, 1990; see Froidl et al., 2020 for comparison with Easy%RoDL and Basin%Ro) and transformation ratio (TR) maps, respectively. Values for six representative source rock intervals are displayed, ordered by the age of deposition (from lower Emperor Subgroup Kipper Shale (a) to lower Halibut *upper F. longus zone* (f)). The maps indicate the spatial distribution and extent of the kitchen areas of the respective source rock intervals using scenario C.

The Kipper Shale (lower Emperor Subgroup) is the deepest confirmed source rock of the study area within the Latrobe Group (Lowry & Longley, 1991). Its lowermost interval shows modelled values above 0.55 %Ro (early oil window) throughout the entire Central Deep, along the Southern Terrace and in large parts of the Eastern Graben Depocenter (**Figure 3.12a**). While the thermal maturity gradually increases from the margins to the center, the Central Deep features two kitchen areas with values above 1.30 %Ro (wet gas window). Maximum values of about 1.55 %Ro were modelled between the Kingfish and the Cobia fields. A smaller kitchen area for wet gas is located between the Bream and the Barracouta fields. In the easternmost part of the Eastern Graben Depocenter the Kipper Shale entered the late oil window (> 1.00 %Ro). The entire Central Deep and large parts of the Eastern Graben Depocenter are characterized by transformation ratios above 90 % (**Figure 3.13a**), indicating substantial petroleum expulsion. No kerogen transformation was predicted throughout the entire Northern Terrace.

The uppermost interval of the Kipper Shale is mainly located in the oil window and shows only a small area which entered the wet gas window between the Kingfish and Cobia fields (**Figure 3.12b**). The Eastern Graben Depocenter is predominantly immature (< 0.55 %Ro) and shows no transformation. In the Central Deep, transformation ratios generally exceed 50 %, while the main kitchen area is located around the Cobia Field with maximum values up to 97 % (**Figure 3.13b**).

The source rock intervals of the Golden Beach Subgroup are featured by a concentric maturity increase from the margins to the Cobia area, where predicted values do not exceed the late oil window, while the extent of the oil kitchen gets generally smaller (**Figure 3.12c** and **Figure 3.12d**). Limited petroleum expulsion is also demonstrated by generally low transformation ratios of the Golden Beach source rocks. Values above 50

% are only predicted for the Cobia area (**Figure 3.13c** and **Figure 3.13d**). Although the Golden Beach *T. apoxyeximus zone* is located deeper, the overlying Golden Beach *T. lillii zone* features a higher maximum (75 % TR vs. 84 % TR) due to varying assigned kinetics.

The lower Halibut Subgroup is represented by a relatively small oil kitchen, which is restricted to the Central Deep and mainly corresponds to the early oil window (**Figure 3.12e** and **Figure 3.12f**). During deposition of the Halibut Subgroup, the local maturity maximum shifted westward from the Cobia area to the trough between the Bream and the Barracouta fields, indicating a shift of the depocentre during the Cainozoic. But there is only local oil generation and expulsion in the Cobia area (**Figure 3.13e** and **Figure 3.13f**).

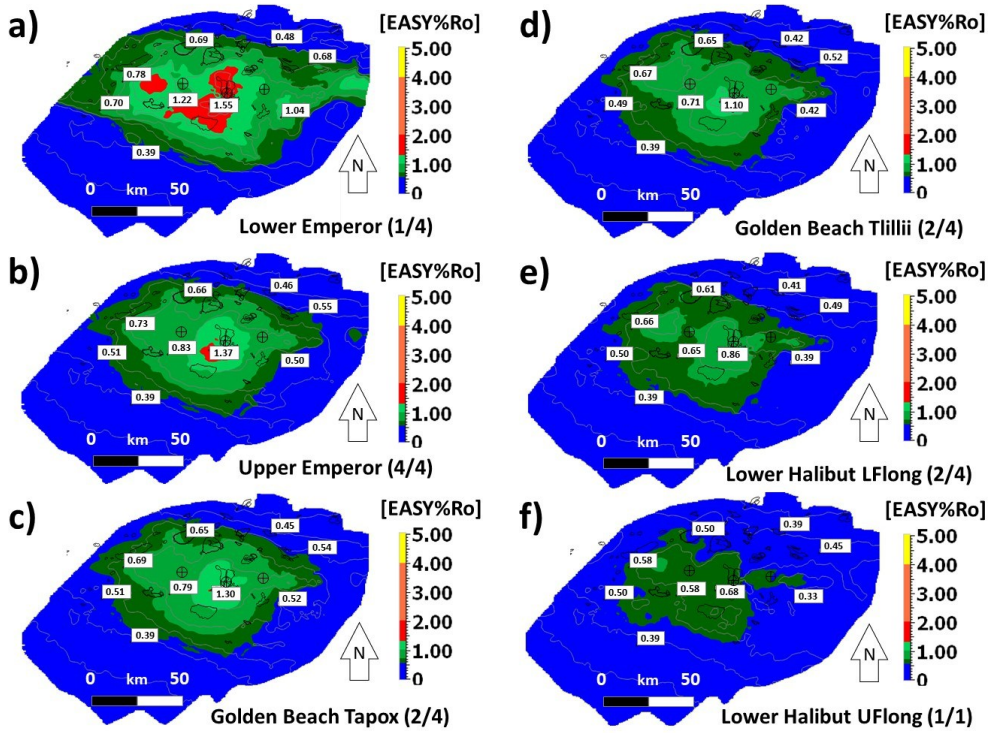

Figure 3.12: Thermal maturity variations at the tops of the assigned source rock sublayers based on scenario C (at present day; vitrinite reflectance, Easy%Ro after Sweeney & Burnham 1990). a) At the bottom of the Emperor subgroup (Kipper Shale, deposited before 90.3 Ma). b) At the top of the Emperor subgroup (Kipper Shale, deposited before 90.0 Ma). c) In the middle of Golden Beach *T. apoxyeximus zone* (deposited before 83.50 Ma). d) In the middle of Golden Beach *T. lillii zone* (deposited before 78.0 Ma). e) In the middle of lower Halibut *lower F. longus zone* (deposited before 67.0 Ma). f) In the middle of lower Halibut *upper F. longus zone* (deposited before 66.0 Ma). The shown source rock intervals represent sublayers already and were again subdivided for more detailed analysis; numbers in brackets indicate the number of the displayed sublayer (from 1 = bottom to 4 = top). Shown values were picked at the lower left corner of the labels. Crosshairs indicate borehole locations of Veilfin-1, Cobia-1 and Volador-ST1 (from West to East, compare Figure 3.14).

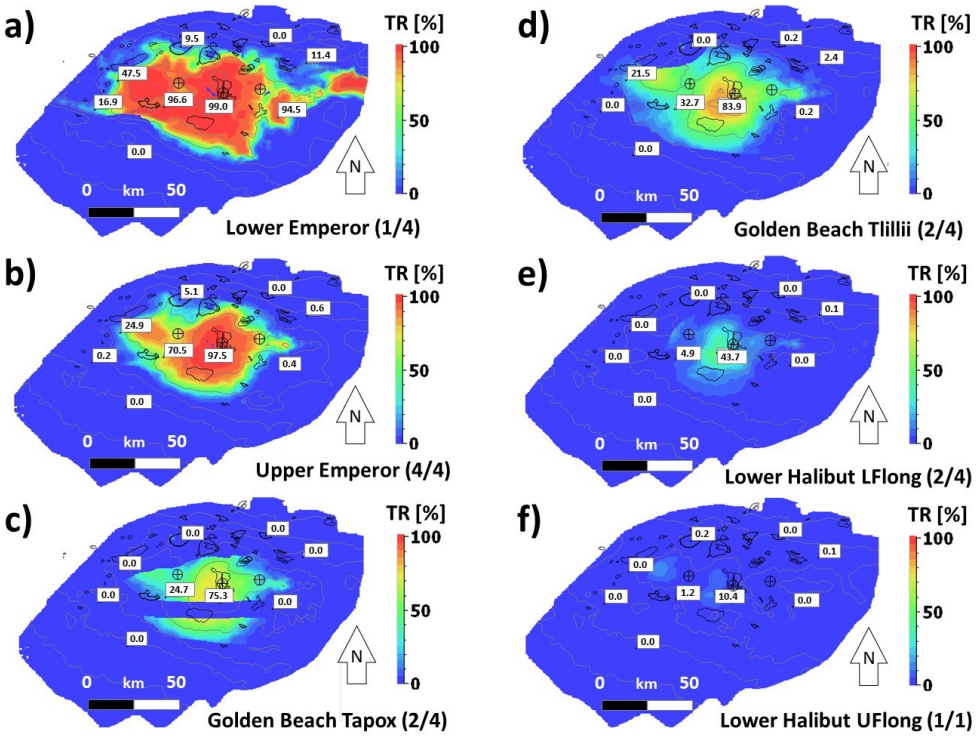

Figure 3.13: The spatial variation of the magnitude of kerogen transformation (TR = transformation ratio) at the tops of the assigned source rock sublayers based on scenario C (at present day). a) At the bottom of the Emperor subgroup (Kipper Shale, deposited before 90.3 Ma). b) At the top of the Emperor subgroup (Kipper Shale, deposited before 90.0 Ma). c) In the middle of Golden Beach T. apoxyeximus zone (deposited before 83.50 Ma). d) In the middle of Golden Beach T. lillii zone (deposited before 78.0 Ma). e) In the middle of lower Halibut *lower F. longus zone* (deposited before 67.0 Ma). f) In the middle of lower Halibut *upper F. longus zone* (deposited before 66.0 Ma). The shown source rock intervals represent sublayers already and were again subdivided for more detailed analysis; numbers in brackets indicate the number of the respective sublayer (from 1 = bottom to 4 = top). Shown values were picked at the lower left corner of the labels. Crosshairs indicate borehole locations of Veilfin-1, Cobia-1 and Volador-ST1 (from West to East, compare Figure 3.14).

The modelled present-day thermal maturity of the Gippsland Basin is shown along a cross-section subparallel to the rift axis (**Figure 3.14**). A general trend can be observed: from higher maturity values in the west compared to the east. Nearshore and below the shelf the onset of the early oil window (0.55 %Ro) lies at around 3 km, while it drops to depths of around 5 km at shelf break and throughout the Bass Canyon. The beginning of the wet gas window (1.3 %Ro) is distributed more irregularly and is in depths of approximately 5 km in the west and around 7 km in the east, respectively. Overall, the maturity trends proceed subparallel to the bathymetry.

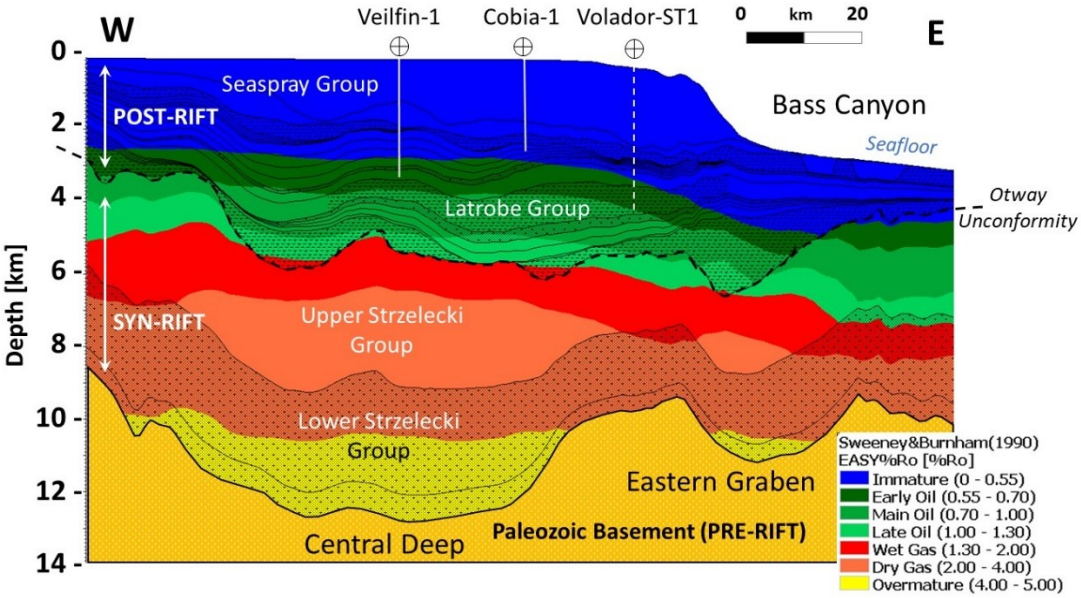

Figure 3.14: Present-day maturity of the sedimentary fill of the Gippsland Basin from west to east based on scenario C (see Figure 3.1 for orientation of the section; vitrinite reflectance, Easy%Ro after Sweeney & Burnham 1990). In the west (shelf areas), higher maturity levels are generally encountered at shallower depths compared to the east (deep water). Note that none of the wells reaches down to the lowermost formations of the Latrobe Group (i.e. Emperor). The stippled line at borehole Volador-ST1 indicates that the well path is a few km away from the shown section.

3.3.6 Thermal evolution of source rocks and critical moment

As modelled here, the deposition of all confirmed source rocks in the study area postdates the stretching-related thermal event at the Albian-Cenomanian boundary. Corresponding elevated geothermal gradients therefore only affected the sediments of the Strzelecki Group. Therefore, the evolution of the formation temperature, as well as the thermal maturity and the transformation of these source rock intervals was rather related to subsidence during the post-rift than to elevated basal heat flow.

Due to increased sedimentation rates during deposition of the lower Halibut formations (up to 2.4 mm/year, i.e., at Cobia-1) all underlying formations were subject to fast burial in the Late Cretaceous (**Figure 3.10**). This event is demonstrated in the time plots for temperature, maturity and transformation ratio at three well locations in the basin center (**Figure 3.15**).

Modelled source rocks experienced a temperature shift close to the K/T boundary (ca 66 Ma) due to a short sea-level drop affecting surface temperatures, during which the lower Emperor Subgroup and the Golden Beach Formation already exceeded temperatures

above 100 °C in the Cobia area (**Figure 3.15a**). Throughout the Paleogene, the formation temperatures remained rather constant, before they started to increase in the Miocene. The lower Halibut intervals surpassed 100 °C by the Miocene-Pliocene, while the lower Emperor source rock intervals had reached values around 150 °C at the same time.

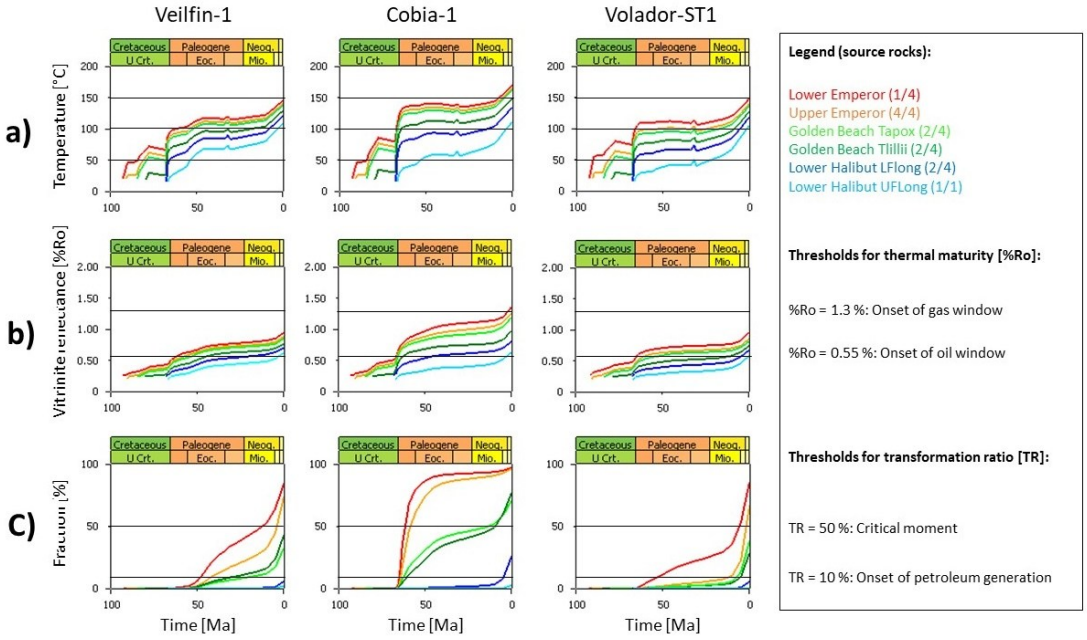

Figure 3.15: Evolution of temperature a), thermal maturity b) and transformation ratio c) at three selected calibration boreholes based on scenario C at three selected boreholes in the basin center (see Figure 3.7 & Figure 3.14 for borehole locations). Thresholds for thermal maturation and kerogen transformation are given as horizontal lines.

The relative steady temperature increase over time caused successive thermal maturation and shifted one source rock after another into the oil window (**Figure 3.15b**). The lower Emperor and Golden Beach subgroups reached modelled vitrinite reflectance values above 0.55 %Ro in the Paleocene, while the lower Halibut *lower F. longus* and the *upper F. longus zones* entered the oil window during Eocene and at present day, respectively. Today, most source rock intervals are located within the oil window throughout the Central Deep, except in the Cobia area, where the lower Emperor (Kipper Shale) just entered the wet gas window (see also present-day maturity map in **Figure 3.12**).

The modelling of the transformation ratio (**Figure 3.15c**) indicates that (1) already in the Paleocene, potential source rocks in the Emperor and Golden Beach intervals would have started to generate petroleum (TR > 10 %) in the Cobia area with the Emperor Subgroup passing through its critical moment (TR = 50 %) and reaching values around 90 % in the Eocene. (2) Another phase of rapid increase of the transformation ratio occurred since the Miocene and is probably still ongoing today. At Veilfin-1 and Volador-ST1, petroleum generation initiated within the Golden Beach Subgroup and even shifted its source rock intervals beyond the critical moment in the Cobia area (ca 15 Ma).

3.4 Discussion and uncertainties of the model

The thermo-tectonic evolution of the Gippsland Basin records the dynamic story of the geological past of the southeastern Australian continental margin. Based on the applied McKenzie-type crustal model (**Figure 3.6**) the dynamics of the lithosphere below the Gippsland Basin and its surroundings can be reconstructed (**Figure 3.7** and **Figure 3.8**).

Although modelling uncertainties can be reduced by careful data evaluation and interpretation, digital sedimentary basin models remain rough approximations, which involve intrinsic uncertainties, such as the resolution of the model grid (500 m x 500 m). The most relevant uncertainties and simplifications – related to both, input parameters and modelling assumptions – are discussed below and summarized in **Table 3.3**.

Table 3.3: List of most relevant uncertainties, their characteristics and impact on the model and its results. Some suggestions for improvement in future studies are given.

Uncertainties & simplifications	Characteristics	Possible effects on the model input and results	Suggested applications for improvement
seismic 2D/3D megacube	varying quality, incomplete coverage	locally only interpolations of horizons, faults, facies possible	reprocessing of existing data, additional surveys
missing well control	undrilled deep strata (e.g., Strzelecki Group and crystalline basement)	stratigraphy and facies of syn-rift sediments unclear	potential field inversion for facies interpretation and geometry, consider few deep exploration wells
rheological impact of volcanic and magmatic facies	incomplete interpretations due to gaps in the seismic	facies replacement influences backstripping only where associated facies were assigned	include additional 3D seismic surveys in the megacube
thermal impact of magmatism	volcanics and intrusions were only modelled as facies	locally underestimated thermal maturity due to insufficient heat flow along the Northern Terrace	include intrusion model to determine effect on thermal maturity
thermal conductivity and radiogenic heat production	no calibration data available, values based on customized lithology mixing	calculated heat flow underestimated/overestimated during thermal modelling	include measurements of thermal conductivity and radiogenic mineral content in the calibration process
layer splitting	geometry of sublayers may not reflect true geometry	imprecise volumes and distribution of sublayers (incl. source rock intervals)	double-check layer geometry after splitting with well tops/seismic
paleo-elevation	no paleo-elevation was assigned for the Early Cretaceous (PWD = 0 m)	overestimated surface temperatures ergo underestimated thermal gradient during syn-rift	investigate paleo-isostasy to determine local paleo-relief
amount of erosion	magnitude of Otway Unconformity unclear	higher amounts of erosion would decrease heat flow maximum	include more thermal calibration data from the Early Cretaceous
basement topography	basement topography based on geophysical data only	deviations from true geometry affect stretching and heat flow maps	refined basement interpretation based on long-offset seismic
crustal composition	crystalline basement includes only granite facies	true facies variations would induce a more heterogeneous thermal field	potential field inversion for facies interpretation and geometry refinement
timing of syn-rift	Early Cretaceous considered as single syn-rift phase, second extension phase ignored	5 % of additional stretching could add a second heat flow peak in late Cretaceous	test impact of second syn-rift phase on heat flow trend
crustal extension model	McKenzie pure shear model was applied for crustal layer calibration	strict coupling of lithospheric stretching and heat flow (max subsidence = max heat flow)	build alternative workflow based on Wernicke simple shear crustal model
magnitude of strike-slip tectonics	stretching is translated in subsidence, not in horizontal movement	block movement along transform faults is ignored	currently very challenging to simulate translateral motion in basin modelling applications
paleo-heat flow and paleo-temperature	conservative thermal calibration applied	calculated temperature and source rock maturation underestimated	Include more low-temperature paleothermochronometry in future studies (i.e., fission tracks)

3.4.1 Basin architecture, stratigraphy and facies distribution

Considerable uncertainties during modelling of horizons, faults and facies maps occur when well control is lacking, and seismic resolution is limited. Particularly, the interpretation of deeper horizons is challenging and triggers additional uncertainties (i.e., simplified layer splitting and spatial distribution of source rock intervals).

For example, in this study the assigned facies and the sub-layering of the Strzelecki Group – the thickest and lowermost layer – are only rough approximations. Furthermore, the fine-grained flood plain deposits with interbedded coal horizons at the top of the Strzelecki Group (Norvick, 2005) were neglected since reliable spatial information about the presence and type of this potential source rock interval is missing. The assignment of a source rock interval within the Strzelecki Group therefore could be implemented, when more data are available.

3.4.2 Paleo-elevation and amount of erosion

The Albian-Cenomanian inversion (Otway Unconformity, C1) marks the most distinct erosion event in the study area but the amount of removed section remains poorly constrained (e.g. 1–3 km proposed by Hill et al., 1995, 1.5–2.7 proposed by Aghaei et al., 2017). During modelling, varying amounts of erosion were tested, and a match with maturity profiles was attempted by applying an inclined erosion map for the Otway Unconformity with erosion amounts between 500 m in the south and 1,500 m in the north.

A paleo-water depth of 0 m was assigned to all continental facies. Since surface temperature decrease with increasing elevation above sea level (~1°C / 100 m), and pre-rift and syn-rift elevation can be expected for the Gippsland Basin, the modelled Cretaceous surface temperatures represent maximum values.

3.4.3 Mapping of faults

Not all faults were captured during seismic interpretation, since substantial offset is only visible on large faults and the seismic coverage is not continuous. Due to gaps in the seismic record, some fault segments remain isolated and may represent only parts of a larger fault system. Further, the scale of the interpreted faults is dependent on the model resolution.

3.4.4 Magmatism and volcanism

Large areas of the Northern Terrace feature igneous rock formations, but most exploration wells reach maximum depth above the volcanic sequences (with exceptions, e.g., in the Kipper area). Furthermore, gaps in the seismic record, the variety of their seismic response and different geometries impede the identification of extrusive bodies. In many cases, volcanic subaerial flows cannot be safely distinguished from other lithologies in the seismic data, although well logs are available. Consequently, only very few extrusive volcanic successions could be interpreted with high confidence (**Figure 3.5**). The interpretation of intrusions was only successful throughout a restricted part of the Northern Terrace. It is very likely that additional intrusions were emplaced further to the west and to the east but have been overlooked either due to poor seismic signal or due to gaps in the seismic cube.

The impact of localized magmatism on the thermal history of the Gippsland Basin is believed to have been rather limited (Meeuws et al., 2016a) and an intrusion model was dismissed for this study. However, as soon as the localization of igneous features is more complete, it could be useful to test an additional scenario, which simulates the emplacement of intrusions along the Northern Terrace and provides locally elevated heat flow. Indeed, additional small-scale source-rock maturation due to magmatism could be the key to understand the charge of the Kipper Gas Field and surrounding fields, where the model fails to predict accumulations (**Figure 3.16**).

However, the assignment of the interpreted volcanic features also adds additional uncertainties to the backstripping of the layers, since the facies replacement (basalt vs. sandstone or siltstone) introduces sudden variations in petrophysical properties. Associated changes in density and permeability have direct implications on compaction and pressure distribution within the model.

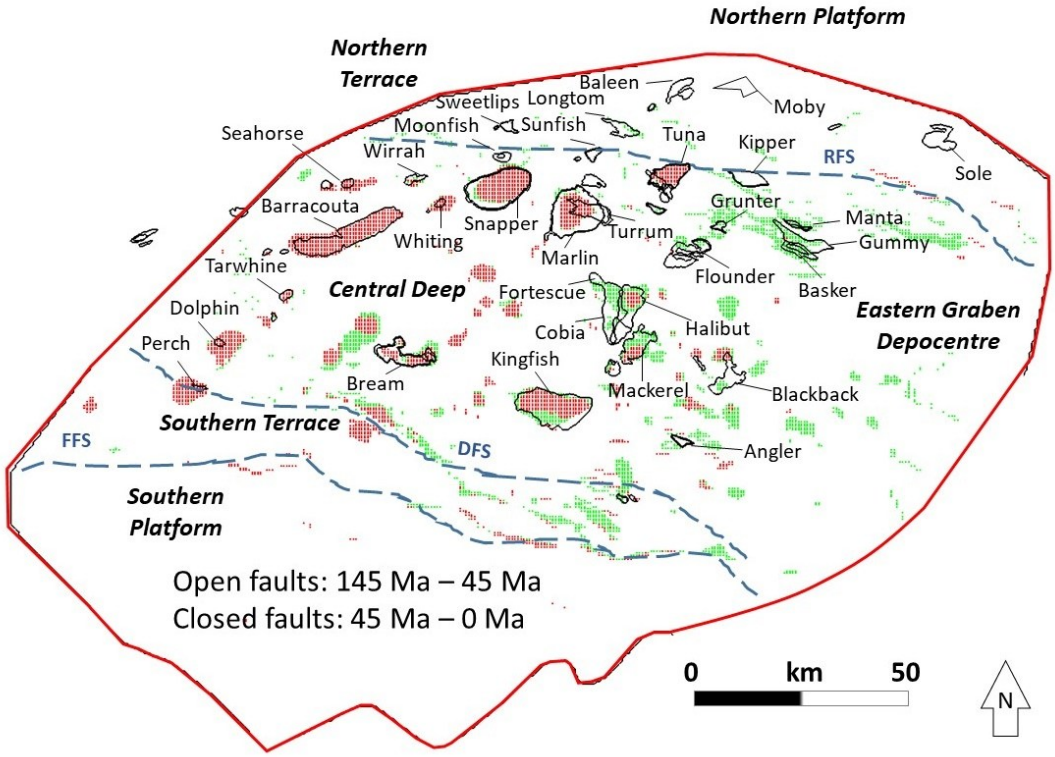

Figure 3.16: Comparison of all modelled accumulations with the known reservoirs (black polygons) with open faults from 145 Ma to 45 Ma and closed faults from 45 Ma until 0 Ma. Most of the large known accumulations are filled and the match is generally sufficient. Some "new" oil accumulations are modelled in the South, East and Northeast. Fields of the Northern Terrace (Baleen, Moby, Kipper and Sole) are not charged. Model resolution / grid cell size: 500 m * 500 m. DFS = Darriman Fault System. FFS = Foster Fault System. RFS = Rosedale Fault System.

3.4.5 Crustal geometry and composition

The dynamic geometry and composition of the lithosphere over time has direct influence on variations of the heat flow and can be considered as the major sensitivity factor in this study. Aside from the basement composition (which has direct implications on local variations in thermal conductivity and radiogenic heat production), related uncertainties include both, the present-day geometry and pre-rift thickness of the lithospheric layers (bathymetry, basement topography, Moho and the LAB). While the present-day crustal geometry was derived from geophysical studies (Power et al., 2001; Whiteway, 2009; 3DGEO, 2011; Kennett & Salmon, 2012; Aitken et al., 2013), the estimation of the thickness of the crust and the upper mantle prior to stretching is rather challenging and represents the key element of the applied methodology.

The basement topography applied in this study was derived from two existing interpretations with different velocity models (3DGEO, 2011 vs. Power et al., 2001) and

remains ambiguous due to the limited seismic data quality, especially in the Central Deep. Further refinement of the basement topography could be achieved by the analysis and inversion of gravity and magnetic data (e.g., Moore & Wong, 2001, 2002).

The crustal layer model suggests that during the late Jurassic, the lithosphere below the eastern margin of Gondwana was ~70 km thick (at least behind the collision zone). The crustal thickness varied between ~50 km below southeast Australia and ~35 km below Tasmania, while it measured probably only ~25 km below the SAFZ – the area where the Gippsland Basin subsequently formed (see **Figure 3.7**). However, these values do not include possible paleo-elevation (as discussed above), which should be added to the crustal thickness and would affect the isostatic and geometric evolution of the lithosphere.

3.4.6 Crustal extensional model

Although the structural style of the Gippsland Basin can also be described as an asymmetric simple shear extensional model (Wernicke, 1985; Etheridge et al., 1985, 1987), for simplification a symmetric McKenzie-type pure shear extensional model has been assumed for this study. Indeed, in earlier studies the northern margin of the Bass Strait was interpreted as a zone of weakness and focus area of maximum extension, whereas maximum vertical offset can be observed in the south along the Foster Fault System (Hill et al., 1995).

The application of a Wernicke-model (Wernicke, 1985) would shift the axis of maximum stretching (and therefore the thermal focus) away from the basin center towards the north. This asymmetric scenario would provide additional heat to the Northern Terrace and could improve the thermal calibration (**Figure 3.9**). For the realization of such an approach a more detailed analysis of the crustal structure (refined shape of the Moho, localization of a possible basal detachment) is required.

A presumptive right-lateral (dextral) opening mechanism of the Gippsland Basin in the Late Jurassic to Early Cretaceous would explain the fast subsidence and the extraordinary thick basin fill. However, the assumption of a pure pull-apart basin contradicts the observed amount of crustal stretching and an oblique opening mechanism is very likely.

3.4.7 Timing and magnitude of extension

In earlier studies, two separate episodes of syn-rift and post-rift have been described for the Gippsland Basin: the first syn-rift mega-sequence corresponds to the lower Strzelecki Group and the first post-rift is represented by the upper Strzelecki Group., while the

second syn-rift affected the Emperor and Golden Beach subgroups, followed by the second post-rift megasequence (e.g. Norvick et al., 2001; Power et al., 2001).

The total amount of stretching was estimated to ~36 %, but the two separate episodes of rifting show very different amounts of crustal extension: whereas ~31 % is associated to the first syn-rift phase, only 5 % occurred during the proposed second rifting event (Power et al., 2001). It remains unclear, to which extent the observed strike-slip tectonics influenced the deformation of the study area. This uncertainty is difficult to assess using the method applied here, since the back-stripping approach does not take the transtensional and transpressional motion of blocks into account.

The corresponding peak of the basal heat flow has been substantially higher during the formation of the Strzelecki Group compared to the second syn-rift phase. Consequently, for thermal modelling in this study the two dominant extensional phases E1 and E2 are summarized to represent only one major syn-rift phase, and the minor extensional phase E3 is regarded only as a short interphase of basin reactivation during one major post-rift phase, which started approximately with the basin inversion around 103 Ma and is still ongoing until present day. Further, the amount of reported crustal extension (after Power et al., 2001) correlates well with the crustal stretching map of scenario C (**Figure 3.8c**). Earlier proposed crustal stretching factors of $\beta = 1.40$ (Hegarty et al., 1986) can only be confirmed for the Northern Terrace, but not for the basin center.

3.4.8 Paleo-heat flow and paleo-temperature

Thermal history reconstructions based on onshore outcrops (e.g. Barker et al., 1998) suggest a geothermal pulse associated to the initial breakup of the Otway Rift and the Gippsland Basin during the mid Cretaceous followed by dike intrusions in the Strzelecki Formation between 100 Ma and 85 Ma. The locally outcropping Strzelecki host rock formations were buried to depths between 2 and 3 km and were already heated up to 100–135 °C at the time of the intrusions. These findings are supported by paleogeothermal gradients of up to 60 °C/km (according to analysis of vitrinite reflectance and apatite fission tracks; Green et al., 1995) for the period when the Gippsland Basin was initially inverted (C1, Otway Unconformity). Generated hydrocarbons during that episode of rapid burial and contemporaneous heating are most probably not preserved. Continuous cooling and regional thermal subsidence since the Late Cretaceous resulted in a constant decrease and stabilization of the regional heat flow until present day (Green et al., 1995).

Considering the stretching maps and the calculated heat flow trends acquired from thermal modelling, the most plausible output was provided by scenario C (pre-rift thickness crust: 25 km, mantle: 50 km; **Figure 3.8c**). The LAB was relatively close to the surface before the initial subsidence (75 km). By adding up the calculated thickness maps (Strzelecki Group + crust + mantle) during the rift maximum (103 Ma time step), the LAB below the Gippsland Basin reached its shallowest position at depth levels around 38 km (**Table 3.2**). This corresponds to basal heat flow maxima between 80 and 90 mW/m^2 in the deep troughs and provides geothermal gradients of ~50 °C/km during the late syn-rift phase, which confirms the reported paleo-temperatures of 100-135 °C at 2 - 3 km depth between ca 100 Ma and ca 85 Ma (Barker et al., 1998). Considering scenario C as the lower end member, which is characterized by rather conservative mantle stretching and a low corresponding estimation for the basal heat flow, even a syn-rift related geothermal gradient of up to 60 °C/km (Green et al., 1995) is possible.

3.4.9 Source rock thermal maturity and kerogen transformation

All known source rock intervals are located within the late Cretaceous Emperor and Golden Beach to Eocene Halibut subgroups and therefore postdate the rift-related heat flow peak. The maturation of the younger sediments is related to burial due to thermal subsidence (see **Figure 3.10** and **Figure 3.11**).

The results of the final model do not fit the migration and distribution of oil and gas in various parts of the basin, e.g. it leaves (mainly gas) fields uncharged along the Northern Terrace (**Figure 3.16**). Certainly, the results are the product of multiple simplifications and assumptions in such a large-scale approach and the uncertainty in the modelling approach itself. Especially the thermo-tectonic uncertainties related to the assumed opening mechanism and the simplified crustal structure have a major effect on the temperature field.

The modelling of the paleo-temperature for the offshore Strzelecki Group suggests that the base of the Strzelecki Group reached temperatures above 100 °C at ca 130 Ma and above 200 °C ca 120 Ma, respectively. Maximum temperatures of up to 300 °C were established at the end of the syn-rift at around 103 Ma (**Figure 3.10**). Sediments of the Mid Strzelecki Group surpassed the 100 °C isotherm at 115–105 Ma and entered temperatures above 200 °C around the K/T-boundary (ca 66 Ma). The uppermost successions of the upper Strzelecki Group reached temperatures above 100 °C only during the Maastrichtian and are located today at their maximum temperatures with locally up to

185 °C (**Figure 3.15**). The temperature history of the Strzelecki Group therefore suggests that petroleum generation from the older successions has been initiated mainly during the Early Cretaceous and even the middle Strzelecki Group is located in the gas window since the Albian, thus, its generation potential is already exhausted. Generated hydrocarbons from the lower Strzelecki Group most probably escaped to the surface or prior accumulations were eroded during the basin inversion and transition.

However, significant transformation of kerogen from the upper Strzelecki most probably did not occur before the Maastrichtian. Gas generation and migration most likely initiated during the Miocene. Such a pulse of additional gas from source rock intervals of the upper Strzelecki Group could also explain the missing gas accumulations in the model along the Northern Terrace (**Figure 3.16**).

The focus of this study is on the temperature evolution and the crustal layer inversion. Pressure calibration within the sedimentary cover was not conducted and consequently modelled migration results and accumulations should be regarded with caution. Nevertheless, based on the above discussion it is suggested focusing on investigating the presence, geochemistry and spatial distribution of upper Strzelecki source rock intervals in the offshore sector. Resulting facies maps should be added to the basin model and would essentially improve the understanding of the thermo-tectonic history of the study area and the present petroleum system.

3.5 Conclusions

The thermo-tectonic history of the Gippsland Basin is strongly coupled with the dynamics of the underlying mantle. By attaching a crustal layer model underneath a fully integrated 3D basin model and applying a new two-step inversion approach, it was possible to calculate the evolution of the basal heat flow and simulate the temperature distribution of the study area from the Early Cretaceous until present day.

The results of the calibrated inversion model suggest intense lithospheric stretching and mantle upwelling during the Early Cretaceous, which caused initial breakup and massive subsidence of the Gippsland Basin. This syn-rift phase was accompanied by increasing basal heat flow from initially ~50 mW/m^2 to a maximum of 80–90 mW/m^2. The resulting upwelled Moho with an associated crustal thickness of locally only 8 km agrees with geophysical observations. Elevated paleogeothermal gradients between 50 and 60 °C/km prevailed from ca 120 to 80 Ma ago. Episodes of compression, uplift, erosion, and thermal

subsidence resulted in fast and continuous cooling during the early post-rift and a rather constant basal heat flow of 45–50 mW/m^2 since the Eocene.

Late Cretaceous source rocks reached petroleum generation during two phases during the Cainozoic, i.e., the Paleocene and the Mio-/Pliocene, respectively. Maturation and petroleum generation is related to fast and deep burial rather than variability in basal heat flow. As soon as Early Cretaceous (Strzelecki) source rocks will be confirmed and sampled in the offshore sector, our provided heat flow trend should be tested on the corresponding calibration data.

Finally, this study provides a confident paleo-heat flow trend for the Gippsland Basin, which is agrees with and is complementing existing data of the study area. The modelling results still contain considerable uncertainty but show potential to decrease the risk for future exploration in the Gippsland Basin and neighboring regions.

The basin modelling workflow and especially the crustal modelling approach based on a McKenzie-type rift basin also reveals limitations and uncertainties, which still require additional examination. Primarily, it is advised to refine the McKenzie model based on a more detailed uncertainty analysis and a focus on the thermal evolution of the Northern Terrace.

Finally, it could be beneficial to construct an alternative crustal modelling approach based on asymmetric rifting (simple shear, after Wernicke, 1985) representing a crustal detachment in the south (Foster and Darriman fault systems) and a northwards shifted basin axis (parallel and in proximity to the Rosedale Fault System). The resulting heat flow maps should then be compared with the results of the symmetric rift model (pure shear, after McKenzie, 1978) of this study.

3.6 Copyright / data availability statement

Half of the data were derived from public domain resources: The data that support the findings were derived from the following resources available in the public domain (please also see additional sources in the reference list):

- Australian Government, Geoscience Australia: http://www.ga.gov.au/
- State Governments, Earth Resources: http://www.dpi.vic.gov.au/earth-resources/oil-gas
- Commonwealth Scientific and Industrial Research Organization, CSIRO: http://www.csiro.au/

The other half of the data are subject to third party restrictions: The data that support the findings of this study are available from Schlumberger. Restrictions apply to the availability of these data, which were used under license for this study. Data are available from the authors with the permission of Schlumberger.

4 The Birkhead and Murta formations – organic geochemistry and organic petrography of Mesozoic fluvio-lacustrine source rocks in the Eromanga Basin, central Australia

Keywords: Eromanga Basin, Birkhead Formation, Murta Formation, thermal maturity, petroleum potential, fluvio-lacustrine shale, organic petrology, organic geochemistry

Abstract

Due to a historic focus on the underlying Cooper Basin and a growing demand for primary energy in Australia, a reassessment of the Eromanga Basin in central and eastern Australia is necessary including a more detailed characterization of the Jurassic-Cretaceous petroleum system elements. The Jurassic Birkhead Formation and the Cretaceous Murta Formation are considered the most important source rocks of the Eromanga petroleum system. To study the petroleum generation potential of these two formations, a set of 55 rock cores from eight petroleum exploration wells was analyzed. The sample set was subject to a chain of organic geochemical and petrographic analyses to evaluate organic richness, hydrocarbon potential (Rock-Eval S_1 and S_2), maceral composition, thermal maturity (e.g., vitrinite reflectance), and saturated and aromatic biomarker composition.

The investigated fluvio-lacustrine siltstones and carbonaceous shales exhibit low to excellent TOC content, very low sulphur and low inorganic carbon content. Thermal maturity of both formations is at the onset of the oil window (immature to early mature). The Cretaceous Murta Formation shows good hydrocarbon generation potential and, in part, high production indices, while the Jurassic Birkhead Formation generally shows low kerogen to bitumen conversion and a good to very good hydrocarbon generation potential. Dispersed, rather coarse organic matter of terrigenous origin in fine-grained siliciclastic matrix with well-preserved plant-remnants including “cutinite flames” is typical. Liptinite (mainly lamalginite) content is generally higher in the Murta Formation (including the occurrence of Botryococcus green algae), while vitrinite is clearly dominant in the Birkhead Formation. The Birkhead solvent extracts exhibit a more heterogeneous distribution of n-alkanes with distinct maxima in the long-chain hydrocarbon range, whereas shorter-chain n-alkanes dominate the Murta extracts. Both formations are expected to have locally contributed to the migration and charge of the Eromanga petroleum system.

Based on their quality and quantity of incorporated organic matter, sufficient petroleum generation potential and locally increased thermal maturity, we consider the Murta and Birkhead formations as potential source rocks of the Eromanga petroleum system.

4.1 Introduction and objectives

The Cooper Region within the Eromanga Basin (**Figure 4.1a**) is a mature petroleum province in Australia. Recent studies aimed to determine the ultimate potential of the region, assess unconventional resources (e.g. coal bed methane), presence of source rock reservoirs, geothermal and other overlooked opportunities (Hall et al., 2015a, 2015b). However, petroleum generation potential and biomarker composition of Eromanga petroleum source rocks remained partly undefined. This study aims on reducing these uncertainties.

The geologic succession of central eastern Australia is characterized by several superimposed sedimentary basins: Paleozoic sequences of the Warburton Basin and sediments of the Late Carboniferous to Triassic Cooper Basin are covered by the Jurassic to Cretaceous Eromanga Basin and the Cainozoic Lake Eyre Basin. Combined, these stacked basins represent Australia's most significant onshore petroleum province. Anticlinal traps, which formed along basement ridges, accommodate most of the associated gas- and oilfields (**Figure 4.1b**; Hall et al., 2015b and references therein).

The majority of the region's initially discovered hydrocarbons were originally attributed to Permian shales and coals within the Cooper Basin (O'Neil, 1998; Boreham et al., 1999; O'Neil & Alexander, 2006; Hall et al., 2016 and references therein; APPEA, 2020). The source rock potential of the overlying Eromanga Basin, notably carbonaceous shales and siltstones of the Middle Jurassic Birkhead Formation and the Early Cretaceous Murta Formation (**Figure 4.2a**), and recognition of the phenomenon of oil mixing, came into focus relatively late as a result of detailed geochemical and petrographic studies (e.g., Vincent et al., 1985; Michaelsen & McKirdy, 1989, 2001; McKirdy et al., 1997; Michaelsen, 2002; Deighton et al., 2003; Arouri et al., 2004). Throughout the study area – measuring approximately 127,000 km2 (South Australia and Queensland combined, considering the outline of the Cooper Basin defined by AGBA, 2013, see **Figure 4.1**) – the burial depths and thermal maturity levels of Jurassic and Cretaceous formations were considered too low to be responsible for significant oil generation. However, source rock pods with locally elevated thermal maturity, increased organic matter content, and/or early oil generation from labile organic matter were overlooked. Reconstruction of their burial and thermal history (Deighton & Hill, 1998; Deighton et al., 2003) provided the first insights into the hydrocarbon generation potential and expulsion of several Eromanga source rocks.

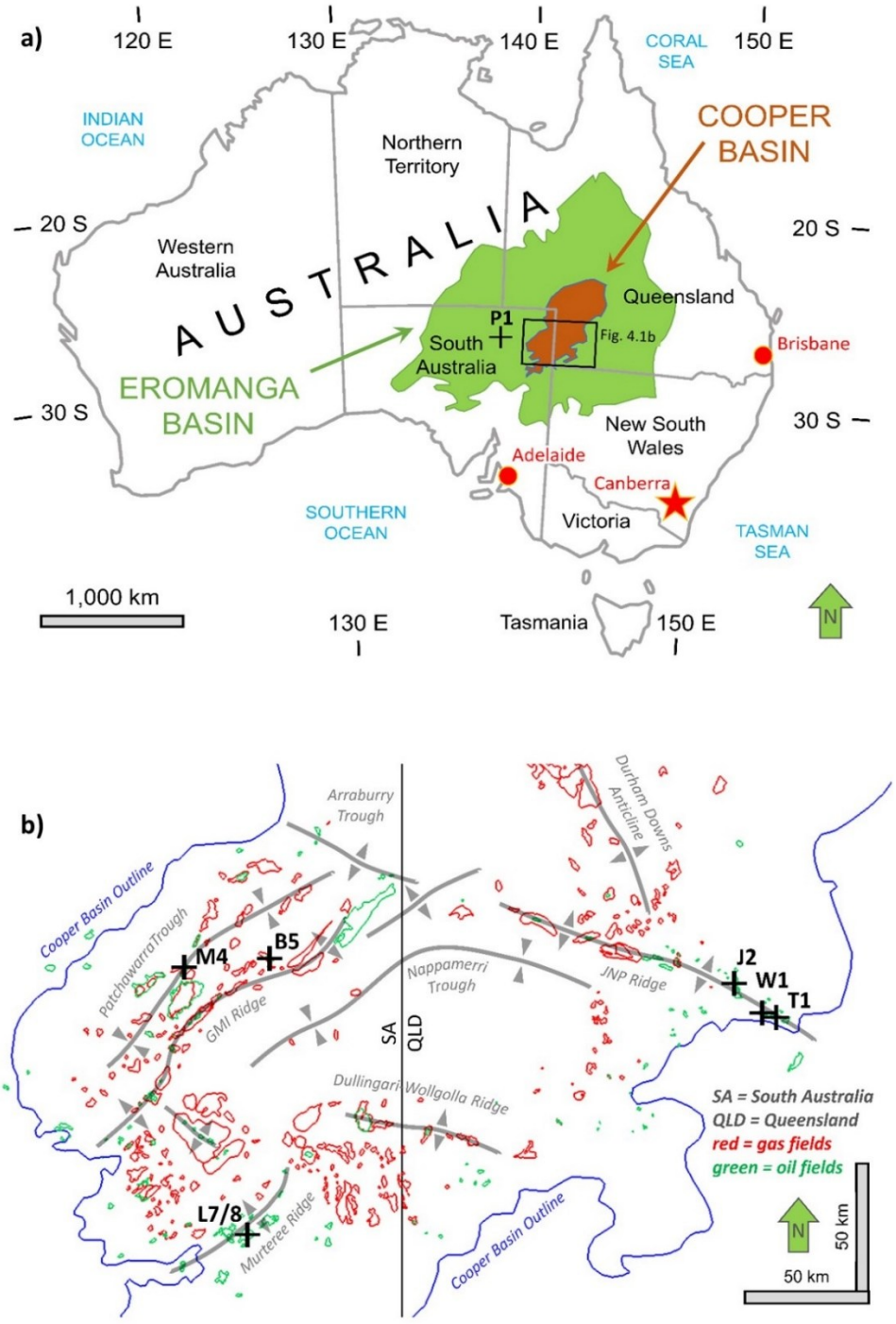

Figure 4.1: Overview of the study area and sample locations. A) The location of the study area at the border between South Australia and Queensland. The Jurassic-Cretaceous Eromanga Basin unconformable overlies the Permo-Triassic Cooper Basin. P1 = Poonarunna-1. B) Sample well locations in the southern Cooper-Eromanga Basin (B5 = Bookabourdie-5, M4 = Moorari-4, L7/8 = Limestone Creek-7/8, J2 = Jackson-2, T1 = Thungo-1, W1 = Winna-1. GMI Ridge = Gidgealpa-Merrimelia-Innamincka Ridge, JNP Ridge = Jackson-Naccowlah-Pepita Ridge. Poonarunna-1 is located outside of this map).

However, amounts of paleo-deposition and subsequent erosion due to Late Cretaceous basin inversion are probably more variable than previously assumed and lateral variations of thermal maturity might be underestimated. According to previous research (e.g., Powell et al., 1989; Boult et al., 1997), the Murta and Birkhead formations are not considered as unconventional targets (e.g. shale oil), but represent potential source rock intervals that contributed to the charge of the Eromanga petroleum system.

A collection of 55 rock cores covering the above two formations from eight petroleum exploration wells (Bookabourdie-5 (B5), Jackson-2 (J2), Limestone Creek-7 (L7), Limestone Creek-8 (L8), Moorari-4 (M4), Poonarunna-1 (P1), Thungo-1 (T1), and Winna-1 (W1), see well locations in **Figure 4.1**) was sampled in August 2018 from the core repositories of South Australia and Queensland state governments (SA Ref. No. 4857, QLD Ref. No. 27146). In this article a comprehensive study on two important petroleum source rocks in the Eromanga Basin is presented, applying multiple geochemical and petrographic methods (elemental analysis, organic petrography, programmed pyrolysis, gas chromatography, and gas chromatography-mass spectrometry) - for the first time with data from South Australia and Queensland combined.

Oil expulsion from the Birkhead and Murta formations has often been discussed (e.g. Vincent et al., 1985, Michaelsen & McKirdy, 1989; Arouri et al., 2004; Hallmann et al, 2006 and references therein), but never been successfully confirmed by previously built kinetic models (Boreham et al., 1999) and potential migration pathways for the generated hydrocarbons were probably underestimated. In this study, we are investigating the source rock potential of the Birkhead and Murta formations and discussing their contribution to oil accumulations within the Eromanga Basin (see **Figure 4.2b**).

We evaluated source rock properties such as organic richness (total organic carbon (TOC)), hydrocarbon generation potential (Rock-Eval S_1 and S_2), sulphur content, maceral composition, thermal maturity (T_{max}, vitrinite reflectance (VRr %)), and selected 17 subsamples to assess the saturated and aromatic biomarker composition. Based on the data set we discuss similarities and differences of the two source rock formations and argue about their relative contribution to oil occurrences in the Eromanga Basin.

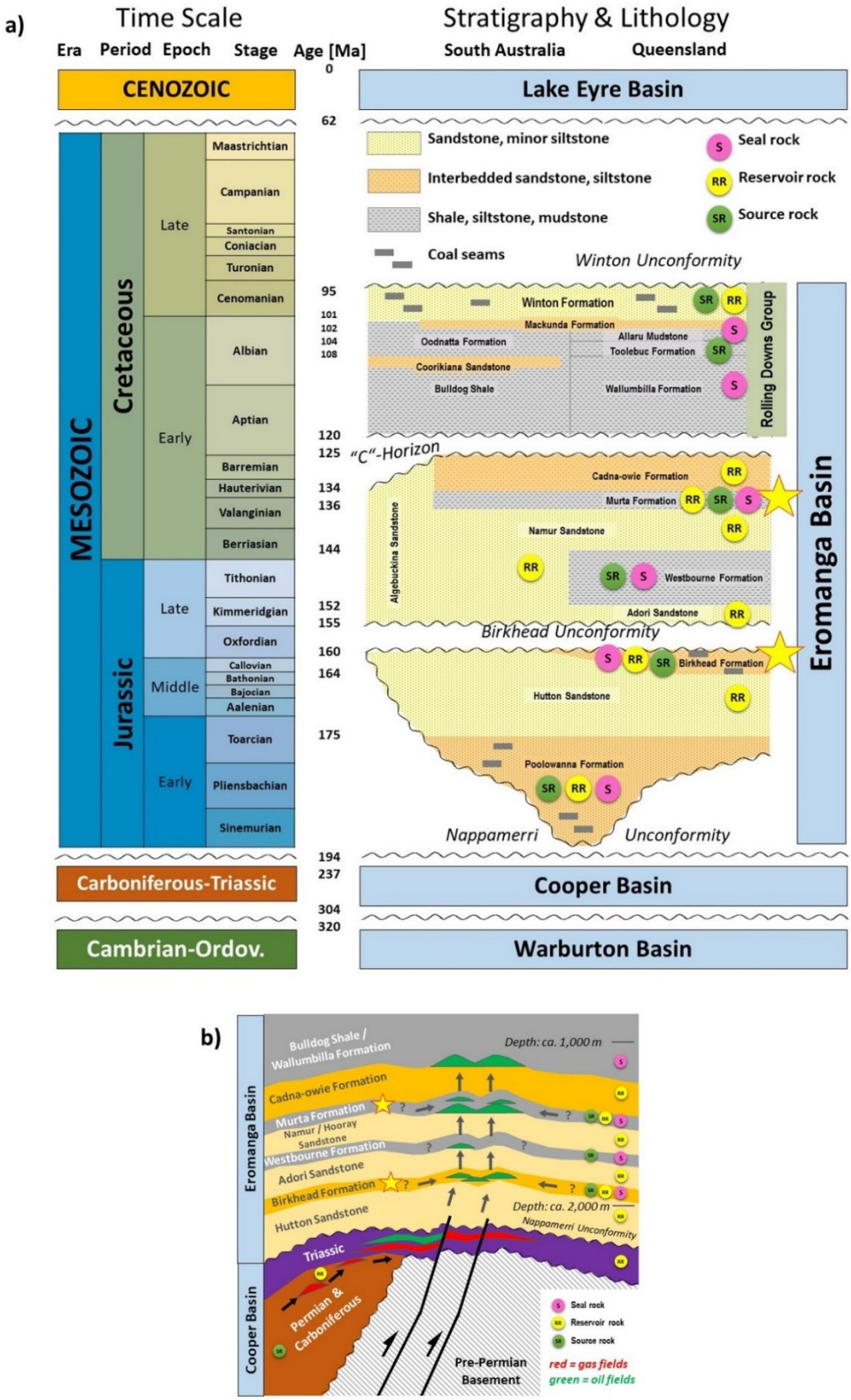

Figure 4.2: Stratigraphy and petroleum systems of the study area. A) Chronostratigraphic overview, lithology and petroleum system elements of the study area (modified after AGBA, 2015). B) Schematic petroleum system of the study area shows possible mixing of hydrocarbons during migration into the anticlinal traps (modified after Bowering & Harrison, 1986).

Since 2009, local exploration activities increasingly focussed on unconventional reservoirs (tight gas in the Gidgealpa Group, deep dry coal seam gas in the Patchawarra and Toolachee formations, shale gas plays in the Roseneath shale, and mixed lithotype hybrid plays in the Murteree shale (Goldstein et al., 2012; Menpes et al., 2013; Greenstreet & Dello, 2015). Although the Cooper and Eromanga basins feature the largest datasets of all sedimentary basins onshore Australia (Gravestock et al., 1998; Carr et al., 2016), the area is still relatively under-explored (Greenstreet & Dello, 2015; Hall et al., 2016). By determining the petroleum generation potential, thermal maturity and paleo-depositional environment of the Birkhead and Murta source rock formations, this study helps to reduce remaining uncertainties for oil and gas exploration in the Eromanga Basin and to improve the estimation of its ultimate petroleum potential.

4.2 Geological setting and petroleum system

The system of stacked sedimentary basins in central eastern Australia developed during multiple cycles of westward subduction and periodic crustal accretion along the eastern Australian continental margin. Smaller-scale superimposing Paleozoic to Triassic sedimentary basins (e.g. Warburton, Cooper, Galilee, Bowen basins) were blanketed by the widespread successions of the Early Jurassic to Late Cretaceous intra-cratonic Great Artesian Basin (GAB). The GAB covers an area of around 1,700,000 km^2 (about one fifth of Australia) and represents one of the largest artesian aquifer systems in the world (Gravestock et al., 1998; Smerdon et al., 2012; GA, 2020b). Besides representing an important source of fresh water for the outback of central eastern Australia, the strong groundwater flow potentially influenced the migration of oil and gas in the region.

Alternating aquiferous sandstones and confining shales and siltstone interbeds of the GAB formed in three major depressions: the Carpentaria Basin in the north, the Surat Basin in the east and the Eromanga Basin in the center and in the west (Gravestock et al., 1998). The area of the central and western Eromanga Basin is mainly overlain by the relative thin (100–200 m) Cainozoic cover of the endorheic Lake Eyre Basin (Draper, 2002; Smerdon et al., 2012). The sub-horizontal Eromanga Basin attains its maximum present-day thickness of more than 2 km in the basin depocenter where it directly overlays the Pennsylvanian to Middle Triassic Cooper Basin (Smerdon et al., 2012; Cook et al., 2013; GA, 2020c; **Figure 4.2a**).

Following the Triassic Nappamerri Unconformity, the Eromanga Basin formed due to renewed subsidence starting in the Late Triassic. It is stratigraphically divided into four sub-sequences, which are separated by distinct unconformities (Hall et al., 2015b).

1) The Late Triassic Cuddapan Formation consists of erosional remnants and fluvial deposits and is the precursor of the extensive sedimentary blanket of the Eromanga Basin. Continuous sedimentation only re-established in the Early Jurassic.
2) The Early Jurassic to Early Cretaceous fluvio-lacustrine succession includes the coal-bearing sandstones of the Poolowanna formation, the widespread Hutton Sandstone and the Birkhead Formation. After a minor interruption (Birkhead Unconformity, see Wainman et al., 2018), the fluvio-lacustrine sub-sequence continues with the Adori Sandstone, the Algebuckina Sandstone on the South Australian side and its Queensland counterparts: Westbourne Formation, Namur Sandstone and Murta Formation.
3) The Early Cretaceous marginal marine to shallow marine sub-sequence includes the regional sand sheet of the Cadna-owie Formation, as well as the Bulldog Shale, the Coorikiana Sandstone and the Oodnatta Sandstone in South Australia and the Wallumbilla, Toolebuc and Allaru formations in Queensland and finishes with regional Mackunda Formation (**Figure 4.2a**).
4) Above a sharp boundary, the non-marine Late Cretaceous Winton Formation comprises the uppermost sub-sequence of the Eromanga Basin.

4.2.1 The Birkhead Formation

The organic-rich silty and sandy successions of the Birkhead Formation were first defined by Exon (1966) and are the equivalent of the Walloon Coal Measures (or Walloon Formation), which are prevalent in the neighboring Surat and Clarence-Moreton basins (Reeves, 1947). Throughout the central Eromanga Basin the Birkhead Formation overlies the more widespread Middle Jurassic upper Hutton Sandstone and is assigned to the Middle-Late Jurassic PJ4.2 – PJ5 palynozones (Paton, 1986; Alexander et al., 2006) which corresponds to the Callovian to Oxfordian stages (164-160 Ma).

The Birkhead Formation features a maximum thickness of about 150 m in the Patchawarra and Nappamerri troughs and predominantly consists of dark grey and brown siltstone, interbedded with mudstone, fine to medium-grained sandstone and contains thin (< 0.3 m), lenticular coal seams. West of the Birdsville Track Ridge the Birkhead

Formation laterally interfingers with the Algebuckina Sandstone (Alexander et al., 2006), while the upper boundary is defined by an unconformity against the overlying Namur and Adori sandstones (Draper, 2002; AGBA, 2015).

The boundary between the Hutton Sandstone and the Birkhead Formation is described as the "top-of-porosity" (Paton, 1986; Watts, 1987; McIntyre et. Al, 1989). This petrological change is featured by a provenance shift characterized by the first appearance of labile, lithic fragments sourced from a volcanic arc located along the eastern Australian margin, which superpose the craton-sourced quartz-arenites of the Hutton Sandstone (Watts, 1987; Veevers et al., 1991; Boult, 1993; Boult et al., 1997).

The shift of the depositional environment is also expressed in facies change from northerly draining low sinuosity braided fluvial (Hutton Sandstone) to easterly flowing high sinuosity meandering deltaic to fluvio-lacustrine environments (Birkhead Formation) (Veevers, 1984; Paton, 1986; McIntyre et. Al, 1989; Lanzilli, 1999). This sudden drainage reorientation and decrease of energy in the fluvial system was probably caused by intensifying arc activity, increasing influx of volcanogenic sediment and induced isolation from the sea (Lanzilli, 1999; Watts, 1987; Salomon et. Al, 1990). While the resulting floodplain of "Lake Birkhead" (Mackie & Gumley, 1995; Boult et al., 1997) was fluvial, paleo-depositional conditions may have been temporarily brackish at the connection between the Eromanga Basin and the Carpentaria Basin (Burger, 1986). From bottom to top, the Birkhead Formation can be internally subdivided into three units, each measuring about 30 m in thickness (Paton, 1986):

- Unit 1 (basal Birkhead Formation): meandering fluvial,
- Unit 2 (mid Birkhead Formation): coal swamp to lacustrine,
- Unit 3 (top Birkhead Formation): meandering to braided fluvial.

Organic matter content of the Birkhead Formationis highly variable with an estimated average of 2.5 wt.% TOC and a yield of 10.8 kg/t hydrocarbons (Jenkins, 1989). While a dominance of "hydrogen-rich" type III kerogen was determined earlier (Khorasani, 1987), more recent studies indicate rather type II kerogen or mixed kerogen types with associated hydrogen indices mostly varying between 150 and 500 mgHC/gTOC (McKirdy et al., 1986a; Michaelsen, 2002 and references therein; Boreham & Summons, 1999; Mahlstedt & Horsfield, 2016).

Thermal maturity distribution suggests oil and gas maturity levels in the Nappamerri Trough and in large areas of Queensland, but expulsion was reported to be very low (Deighton et al., 2003) indicating a relatively late onset of the specific oil-window. Only some oil discoveries along the Naccowlah-Jackson Ridge (Queensland) were attributed to Jurassic sources (Vincent et al., 1985). Large uncertainties remain due to limited availability of suitable drill core material.

4.2.2 The Murta Formation

The fluvio-lacustrine successions of the Late Jurassic to Early Cretaceous Namur Sandstone are locally overlain by the fine-grained and organic-rich Murta Formation (Gravestock et al., 1995; Draper, 2002; Alexander et al., 2006). This unit interfingers with the Algebuckina Sandstone in the west (South Australia) and the Hooray Sandstone in the east (Queensland) and is covered by the Cadna-owie Formation (Alexander & Sansome, 1996). It is assigned to the Early Cretaceous (Neocomian) PK1.2 – PK2.1 (Alexander et al., 2006) corresponding to the Valanginian to Hauterivian stages (140-134 Ma).

The Murta Formation features a maximum thickness of about 90 m in the Nappamerri Trough and consists of dark grey siltstone, interbedded with shale, pale grey very fine to fine-grained sandstone and minor medium and coarse-grained sandstone, locally with reservoir quality (Bowering, 1982; Alexander et al., 2006). Fine-grained lacustrine turbidites with recognizable Bouma sequences and slumps indicate slope deposition (Ambrose et al., 1986).

Sedimentation occurred in varied lacustrine paleo-depositional environments including open lacustrine, lacustrine fan delta, distributary channel and lacustrine shoreline under fresh to brackish-marine influence (Mount, 1981, 1982; Ambrose et al., 1986; Moore et. al, 1986) (Zoellner, 1988; Wecker, 1989; Gorter, 1994; Alexander & Sansome, 1996). Land plant spores, pollen and the occurrence of *Botryococcus* green algae (e.g. Michaelsen & McKirdy, 1989) underline the interpretation of "Lake Murta" (Alexander et al., 2006). A microtidal environment established within this lake, occasionally interrupted by incised channels, in which reservoir sands developed (Gorter, 1994). A localized, southward propagating marine transgression originating from the neighboring Carpentaria Basin towards the upper Murta Formation is possible (Veevers et al., 1991). From the base to the top, the Murta Formation can be subdivided into four units (Ambrose et al., 1982, Ambrose et al., 1986):

- Unit 1: upward-coarsening lacustrine delta sequence / delta-front
- Unit 2: shallow-water silt and fine sand
- Unit 3: progradational fan sequence / shallowing trend with shoreline bar
- Unit 4: fining-upward towards offshore / deep-water lacustrine environment

The organic matter content of the MF ranges from 0.5 to 2.5 wt.% TOC and is characterized by mixed kerogen sources with corresponding HI values between 80 and 460 mgHC/gTOC (Boreham & Summons, 1999; Powell et al., 1991; Draper, 2002). Thermal maturity measurements indicate that the MF locally reached the oil window (0.5-0.6 VR_r %; Powell et al., 1989). In this context, the only oil discovery attributed to the Murta Formation – the Dullingari-Murta field (Robinson & Butler, 1989) seems to underrepresent the real numbers.

4.2.3 Petroleum systems

Several episodes of petroleum generation from multiple source rocks are accountable for hydrocarbon fields in the study area (McKirdy et al., 2001; Michaelsen & McKirdy, 2001). The Cooper Basin is predominantly hosting gas accumulations (including tight gas and dry coal seam gas), while oil reservoirs are common within the overlying Eromanga Basin (Draper, 2002). The composition of the liquid hydrocarbons varies from light oil-condensates to waxy oils with API gravities ranging between 34 ° and 53 ° (Boreham & Summons, 1999).

Different source-reservoir couplets comprise predominantly Cooper sources and corresponding migration into reservoirs of both, the Cooper and the Eromanga basin, mixed reservoirs in the Eromanga Basin charged by Cooper and Eromanga source rocks, as well as minor contribution by pre-Permian sources (Bowering & Harrison, 1986; Boreham & Summons, 1999, see **Figure 4.2**).

Reservoired hydrocarbons exclusively originate from terrigenous organic matter of fluvio-lacustrine shales, siltstones and coals. Corresponding source rock material was found in successions of the Cooper and Eromanga basins at different stratigraphic levels, although quantity and quality are variable (Boreham & Hill, 1998; Gravestock et al., 1998; Gray & Draper, 2002; Deighton et al., 2003; Jadoon et al., 2016; Hall et al., 2016a). Oil-prone and effective source rocks (Poolowanna, Birkhead, Westbourne and Murta formations) exist within the Eromanga Basin (Draper, 2002; Michaelsen & McKirdy,

2006), with the Birkhead and Murta formations representing the most significant ones (Boreham & Summons, 1999).

Together with the Winton formation, the entire Jurassic to early Cretaceous formations of the Eromanga Basin (from Poolowanna to Cadna-owie) feature reservoir properties with varying quality with the Hutton and the Hooray sandstone representing the most significant reservoir rocks (Draper, 2002; Deighton et al., 2003). The fine-grained and low-permeable Early Cretaceous marginal marine to shallow marine sub-sequence (from Wallumbilla to Mackunda formation) represents the thickest and most effective regional seal of the study area (Deighton et al., 2003). Major targets in the study area are anticlinal traps and fault-controlled traps (Draper, 2002).

4.3 Materials and analytical methods

During the sampling campaign in August 2018, first author Joschka Röth performed the core selection at the regional drill core repositories in Adelaide (Government of South Australia, SA sampling Ref. No. 4857) and Brisbane (Government of Queensland, QLD sampling Ref. No. 27146). 55 core samples of the Murta and Birkhead formations from eight petroleum wells were taken (see **Figure 4.1** for names and locations, see **Table 4.1** for depth and formation). The particular core intervals were selected based on the availability of sufficient and representative rock material, their proximity to known oil fields, expected thermal maturity and estimated organic matter content according to earlier studies (e.g. Michaelsen & McKirdy, 1989; Boreham & Summons, 1999) and according to the database of Geoscience Australia. Representative fine-grained rock samples (size: quarter core; thickness: varying between 1 and 2 cm) were then removed and documented. Sandy interbeds were excluded from the sampling, which resulted in irregular spacing. Additional spot samples were taken from those interbeds where organic particles were recognized and where dark brown to black rocks with fine laminations were present.

At the Institute of Geology and Geochemistry of Petroleum and Coal (RWTH Aachen University, Germany), the core samples were studied by various organic geochemical and organic petrographical methods. From all 55 original samples, we prepared powdered material for the organic geochemical analysis and polished sections (see Zieger and Littke, 2019) for the organic petrographical analysis. We selected 17 subsamples for molecular organic geochemistry.

Table 4.1: Overview of the complete sample set used in this study. Rock-Eval pyrolysis and petrographic determination of thermal maturity was performed on all samples (results summarized in Table 4.2). Asterisks indicate samples, which underwent molecular organic geochemical analysis due to high TOC (at least two samples per well, see Table 4.4). MD = measured depth. TD = total depth.

State	Well name / location	MD [m]	Sample ID	Formation	Lithology	Comments
Queensland	Jackson-2	1,104,59	**J2/02**	Murta	Sandy siltstone	Appraisal well, oil shows, TD: 1,549.3 m, TD date: 07-MAR-1982
	X: 641029	1,105,53	**J2/03**	Murta	Sandy siltstone	
	Y: 6945534	1,108,87	**J2/04**	Murta	Fine sandstone	
		1,110,33	**J2/05***	Murta	Sandy siltstone	
		1,111,60	**J2/06***	Murta	Sandy siltstone	
		1,111,65	**J2/07**	Murta	Sandy siltstone	
		1,116,15	**J2/08**	Murta	Fine sandstone	
		1,116,52	**J2/09**	Murta	Fine sandstone	
	Winna-1	999,91	**W1/10**	Murta	Sandy siltstone	Exploration well, oil shows, TD: 1,380.0 m, TD date: 19-OCT-1985
	X: 653100	1,005,37	**W1/11***	Murta	Silty shale	
	Y: 6932009	1,009,91	**W1/12**	Murta	Sandy siltstone	
		1,010,87	**W1/13**	Murta	Silty shale	
		1,010,96	**W1/14**	Murta	Silty shale	
		1,011,05	**W1/15**	Murta	Silty shale	
		1,011,08	**W1/16**	Murta	Silty shale	
		1,011,52	**W1/17***	Murta	Sandy siltstone	
		1,013,83	**W1/18**	Murta	Sandy siltstone	
		1,016,34	**W1/19**	Murta	Sandy siltstone	
		1,017,34	**W1/20**	Murta	Sandy siltstone	
	Thungo-1	1,009,46	**T1/21**	Murta	Sandy siltstone	Exploration well, oil shows, TD: 1,424.0 m, TD date: 21-MAR-1986
	X: 655771	1,010,76	**T1/22**	Murta	Sandy siltstone	
	Y: 6931634	1,011,35	**T1/23**	Murta	Sandy siltstone	
		1,017,70	**T1/24***	Murta	Sandy siltstone	
		1,022,41	**T1/25**	Murta	Sandy siltstone	
		1,023,20	**T1/26***	Murta	Sandy siltstone	
		1,024,97	**T1/27**	Murta	Fine sandstone	
		1,026,40	**T1/28**	Murta	Silty shale	
		1,026,45	**T1/29***	Murta	Silty shale	
		1,031,16	**T1/30**	Murta	Sandy siltstone	
		1,032,94	**T1/31**	Murta	Sandy siltstone	
		1,033,64	**T1/32**	Murta	Sandy siltstone	

Table 4.1 (continued):

State	Well name / location	MD [m]	Sample ID	Formation	Lithology	Comments
South Australia	Bookabourdie-5	2,120.07	**B5/33**	Birkhead	Sandy siltstone	Appraisal well, oil shows, TD: 2,365.1 m, TD date: 08-DEC-1985
	X: 448764	2,120.49	**B5/34***	Birkhead	Sandy siltstone	
	Y: 6954111	2,122.17	**B5/35***	Birkhead	Fine sandstone	
	Moorari-4	2,155.24	**M4/36**	Birkhead	Sandy siltstone	Development well, oil/gas, TD: 2,954.1 m, TD date: 15-JAN-1982
	X: 414502	2,156.15	**M4/37***	Birkhead	Sandy siltstone	
	Y: 6951619	2,159.75	**M4/38**	Birkhead	Sandy siltstone	
		2,160.12	**M4/39**	Birkhead	Sandy siltstone	
		2,160.18	**M4/40***	Birkhead	Sandy siltstone	
		2,160.45	**M4/41**	Birkhead	Sandy siltstone	
	Limestone-Creek-8	1,199.97	**L8/42***	Murta	Sandy siltstone	Development well, oil shows, TD: 1,306.4 m, TD date: 04-MAR-1988
	X: 440972	1,200.64	**L8/43**	Murta	Sandy siltstone	
	Y: 6844654	1,205.45	**L8/44***	Murta	Sandy siltstone	
	Limestone-Creek-7	1,206.00	**L7/45***	Murta	Sandy siltstone	Development well, oil shows, TD: 1,303.6 m, TD date: 29-JUL-1987
	X: 440787	1,210.76	**L7/46***	Murta	Sandy siltstone	
	Y: 6845289	1,216.00	**L7/47**	Murta	Sandy siltstone	
	Poonarunna-1	1,584.30	**P1/48**	Birkhead	Shale	Exploration well, dry, TD: 1,699.3 m, TD date: 06-OCT-1964
	X: 786875	1,587.80	**P1/49**	Birkhead	Shale	
	Y: 6910113	1,596.10	**P1/50**	Birkhead	Shale	
		1,601.30	**P1/51**	Birkhead	Fine sandstone	
		1,602.03	**P1/52**	Birkhead	Fine sandstone	
		1,621.11	**P1/53**	Birkhead	Sandy siltstone	
		1,622.78	**P1/54**	Birkhead	Sandy siltstone	
		1,625.07	**P1/55***	Birkhead	Sandy siltstone	
		1,625.44	**P1/56***	Birkhead	Silty shale	

4.3.1 Organic petrography

The polished sections were embedded in epoxy resin perpendicular to bedding with indicated top and bottom to preserve the original orientation of the laminations and the particles. Vitrinite reflectance (VRr %) was measured with a Zeiss Axio Scope.A1 microscope under reflected light with a Zeiss Epiplan-NEOFLUAR 50x/1.0 oil immersion objective and a 10x ocular (= 500 x magnification) equipped with a camera and Hilgers Fossil software for data evaluation. Since the measurements were performed on a certain number of randomly oriented particles the short notation term VR_r is used (Taylor et al., 1998). Details of the procedure are described in Zieger and Littke (2019). To determine the thermal maturity of the in-situ organic particles, only the autochthonous, low-reflecting vitrinite population was measured. Abundant particles of inertinite and reworked vitrinite were excluded from our analysis, with a preference for large vitrinites.

Qualitative maceral identification was based on Taylor et al. (1998). A selection of 17 subsamples (featuring the highest TOC and covering at least two samples from each well) was analysed with Zeiss Axio Imager.M2m microscope and an Epiplan-NEOFLUAR 50x/1.0 oil objective. Since TOC content of most of the samples is below 10 wt.%, quantitative maceral group counting (500 points, after Taylor et al., 1998) was only performed on the most organic rich sample B5/34 (16.83 wt.% TOC) both in incident white light (for vitrinite and inertinite) and in fluorescence mode for liptinite. For selected other samples, maceral group content was estimated based on evaluation of 20 pictures, each 300 micrometers in diameter. Each picture was evaluated both in reflected and fluorescent light. Finally the resultant percentages were rounded to numbers without decimals for each sample and normalised to organic particles only (see **Table 4.2**).

Table 4.2: Overview of Rock-Eval pyrolysis results (S1, S2, oil saturation index OSI, production index PI, and hydrogen index HI) sorted after formation and including elemental composition (TOC, TIC, and TS) and vitrinite reflectance (VRr mean, with standard deviation s). Samples with asterisk underwent molecular organic geochemical analysis (see Table 4.4).

Formation	Sample ID	TOC [%]	TIC [%]	TS [%]	S1 [mg HC/g rock]	S2 [mg HC/g rock]	OSI [mg HC/g rock]	PI [-]	HI [mg HC/g TOC]	Tmax [°C]	VRr mean [%]	VRr s [%]
Murta Formation	**J2/02**	0.86	0.02	0.09	0.05	0.55	5.77	0.08	64	437	0.56	0.052
	J2/03	0.98	0.02	0.10	0.07	0.75	6.95	0.08	76	440	0.56	0.062
	J2/04	2.29	0.02	0.07	0.20	0.99	8.70	0.17	43	433	0.59	0.059
	J2/05*	4.29	0.02	0.07	2.34	1.59	54.40	0.60	37	425	0.63	0.077
	J2/06*	2.86	0.03	0.13	5.16	5.03	180.13	0.51	176	432	0.58	0.071
	J2/07	1.97	0.02	0.11	2.45	3.48	124.47	0.41	176	430	0.53	0.058
	J2/08	1.78	0.02	0.12	0.82	4.78	45.75	0.15	268	437	0.53	0.051
	J2/09	2.25	0.01	0.12	0.91	5.14	40.42	0.15	229	432	0.57	0.072
	W1/10	0.75	0.01	0.11	0.28	0.90	37.76	0.24	120	431	0.55	0.045
	W1/11*	4.57	0.02	0.14	5.31	9.70	116.13	0.35	212	430	0.54	0.034
	W1/12	0.86	0.01	0.09	0.83	1.96	96.12	0.30	228	436	0.54	0.042
	W1/13	1.44	0.01	0.11	0.53	3.13	36.56	0.14	217	437	0.58	0.057
	W1/14	2.15	0.01	0.20	0.40	2.90	18.55	0.12	135	431	0.56	0.052
	W1/15	3.10	0.02	0.17	0.37	2.14	11.92	0.15	69	430	0.58	0.047
	W1/16	1.99	0.02	0.17	0.32	3.09	15.85	0.09	155	434	0.59	0.053
	W1/17*	1.10	0.01	0.11	4.29	2.29	388.75	0.65	208	428	0.56	0.049
	W1/18	2.03	0.26	0.16	1.15	3.96	56.73	0.23	195	436	0.62	0.058
	W1/19	1.38	0.01	0.10	0.53	1.46	38.62	0.27	106	435	0.59	0.068
	W1/20	2.10	0.01	0.11	2.00	3.18	95.25	0.39	152	430	0.60	0.065
	T1/21	1.24	0.01	0.10	1.00	1.88	80.77	0.35	152	437	0.57	0.057
	T1/22	1.91	0.01	0.11	0.86	3.87	45.21	0.18	203	436	0.54	0.038
	T1/23	1.13	0.01	0.08	0.78	1.90	69.23	0.29	168	436	0.56	0.040
	T1/24*	9.31	0.02	0.20	12.94	22.85	139.04	0.36	245	427	0.52	0.047
	T1/25	1.50	0.01	0.08	0.24	1.46	15.89	0.14	97	433	0.63	0.054
	T1/26*	3.89	0.01	0.12	1.56	7.61	40.11	0.17	196	432	0.53	0.035
	T1/27	0.50	3.33	0.05	0.17	0.98	34.44	0.15	196	436	0.55	0.048
	T1/28	1.56	0.01	0.10	0.21	3.38	13.67	0.06	217	437	0.57	0.059
	T1/29*	2.62	0.03	0.12	0.45	5.55	17.23	0.08	212	435	0.59	0.065
	T1/30	1.71	0.01	0.12	0.27	2.66	15.75	0.09	156	432	0.66	0.055
	T1/31	0.98	0.01	0.08	0.10	1.13	10.26	0.08	115	433	0.70	0.084
	T1/32	2.38	0.01	0.11	0.35	6.15	14.67	0.05	258	433	0.58	0.059
	L8/42*	2.71	0.01	0.13	0.29	3.25	10.77	0.08	120	433	0.65	0.065
	L8/43	1.83	0.02	0.10	0.17	1.48	9.10	0.10	81	430	0.73	0.053
	L8/44*	5.86	0.10	0.07	0.86	1.63	14.75	0.35	28	425	0.62	0.080
	L7/45*	2.85	0.05	0.11	0.67	3.40	23.37	0.16	119	431	0.61	0.055
	L7/46*	1.59	0.10	0.07	0.74	1.47	46.60	0.34	92	429	0.56	0.051
	L7/47	1.18	0.02	0.08	0.36	1.56	30.60	0.19	132	429	0.61	0.058

Table 4.2 **(continued):**

Formation	Sample ID	TOC [%]	TIC [%]	TS [%]	S1 [mg HC/g rock]	S2 [mg HC/g rock]	OSI [mg HC/g rock]	PI [-]	HI [mg HC/g TOC]	Tmax [°C]	VRr mean [%]	VRr s [%]
Birkhead Formation	**B5/33**	2.68	0.02	0.10	1.07	6.59	39.91	0.14	246	433	0.57	0.053
	B5/34*	16.83	0.03	0.33	5.49	61.24	32.60	0.08	364	432	0.65	0.045
	B5/35*	3.49	0.02	0.15	0.96	8.09	27.53	0.11	232	433	0.65	0.065
	M4/36	0.98	0.02	0.08	0.43	2.94	43.78	0.13	300	434	0.56	0.048
	M4/37*	3.59	0.02	0.13	1.35	11.51	37.61	0.10	321	427	0.56	0.046
	M4/38	1.87	0.02	0.10	0.66	3.61	35.19	0.15	193	428	0.55	0.035
	M4/39	1.41	0.02	0.08	0.61	2.86	43.28	0.18	203	430	0.58	0.044
	M4/40*	1.93	0.02	0.10	0.51	3.55	26.70	0.13	184	431	0.57	0.054
	M4/41	1.91	0.02	0.11	0.56	3.89	29.20	0.13	203	432	0.55	0.046
	P1/48	1.41	0.05	0.09	0.25	5.76	17.89	0.04	408	436	0.57	0.032
	P1/49	1.85	0.05	0.11	0.39	8.07	20.88	0.05	436	439	0.54	0.043
	P1/50	0.99	0.03	0.10	0.12	3.92	12.08	0.03	396	435	0.63	0.040
	P1/51	2.56	0.03	0.12	0.41	8.27	16.02	0.05	323	437	0.58	0.049
	P1/52	2.66	0.03	0.13	0.45	8.67	16.84	0.05	326	434	0.56	0.051
	P1/53	2.41	0.03	0.13	0.54	7.58	22.22	0.07	315	437	0.51	0.044
	P1/54	2.26	0.03	0.12	0.51	7.07	22.54	0.07	313	436	0.51	0.028
	P1/55*	9.07	0.19	0.19	2.21	33.31	24.33	0.06	367	430	0.61	0.045
	P1/56*	9.24	0.03	0.18	2.74	34.27	29.66	0.07	371	436	0.61	0.036

4.3.2 Bulk organic geochemistry

Total organic carbon (TOC wt.%), total inorganic carbon (TIC wt.%), total carbon (TC wt.% = TOC + TIC), and sulphur content expressed as total sulphur (TS wt.%) of all powder samples were determined with an Elementar liquiTOC II instrument and with a LECO S-200 Sulfur Analyser, respectively. The source rock quality, quantity and thermal maturity of the whole sample set was then analysed with a Vinci Rock-Eval 6 instrument by using the cycle of analysis and indices based on Tissot & Welte (1984) and by applying the non-isothermal bulk rock method (Béhar et al., 1984).

From the TOC values and the peaks of Rock-Eval S_1 (free hydrocarbons) and S_2 (thermally generated "cracked" hydrocarbons) the evaluation parameters Hydrogen Index (HI [mg HC/g TOC] = S_2/TOC x 100), Genetic Potential (GP [mg HC/g rock] = $S_1 + S_2$) and Production Index (PI [-] = $S_1/S_1 + S_2$) are derived. The evaluation and interpretation of our elemental analysis (TOC, TIC, TS) and the results of the Rock-Eval pyrolysis

(T_{max}, S_1, S_2, etc.) followed the traditional approaches described by Espitalié et al. (1977), Tissot & Welte (1984), Peters & Cassa (1994), and Law (1999). Results of organic geochemistry are listed in **Table 4.2**.

4.3.3 Molecular organic geochemistry

Detailed geochemical analysis was performed on 17 subsamples of the two formations (Birkhead: six samples; Murta: eleven samples) by following standard workflows for organic matter extraction (Guo et al., 2020) and for subsequent fractionation (Schwarzbauer & Jovančićević, 2020). Gas chromatography (GC) measurements with coupled flame ionization detector (GC-FID) and gas chromatography with coupled mass spectrometry (GC-MS) analysis were conducted on aliphatic and aromatic fractions by following standard procedures (recently described in detail by Fang et al., 2019).

Compound identifications are based on reference materials, comparison with selected molecular ions, retention properties and elution orders of published gas chromatograms. Separation of co-eluted compounds, e.g. C_{27} ααα 20R and C_{29} βα diasteranes 20R was conducted using relative mass-to-charge ratios, i.e. m/z 372 and 400. Biomarker ratios are based on the integration of peak areas derived from specific ion chromatograms. The moleculesrelevant for this study are listed in **Table 4.3**.

Table 4.3: List of identified biomarker peaks used in this study (most relevant peaks are shown in Figure 4.5; see Table 4.4 for resulting molecular ratios).

Peak ID		Saturated hydrocarbons
Pr		Pristane
Ph		Phytane
n-Cxx		normal alkanes

Peak ID		Hopanes (mass-to-charge ratio m/z = 191)
C_{19}		C_{19} tricyclic diterpane
C_{23}		C_{23} tricyclic diterpene
T_S		18α(H)-22,29,30-trisnorneohopane
T_M		17α(H)-22,29,30-trisnorhopane
C_{29}		17α,21β(H)-30-norhopane
C_{29} T_S		18α,21β(H)-30-norneohopane
C_{30}		17α(H),21β(H)-hopane
C_{30} M		17β(H),21α(H)-moretane
C_{31}	homohopanes	17α(H),21β(H)-30-homohopane (22S + 22R)
C_{32}		17α(H),21β(H)-30,31-dihomohopane (22S + 22R)
C_{33}		17α(H),21β(H)-30,31 ,32-trishomohopane (22S + 22R)
C_{34}		17α(H),21β(H)-30,31 ,32 ,33-tetrahomohopane (22S + 22R)
C_{35}		17α(H),21β(H)-30,31 ,32 ,33 ,34-pentahomohopane (22S + 22R)

Peak ID		Steranes (mass-to-charge ratio m/z = 217)
C_{27} dia		13β(H),17α(H)-diasterane (20S)
		13β(H),17α(H)-diasterane (20R)
C_{27}		5α(H),14α(H),17α(H)-cholestane (20S)
		5α(H),14β(H),17β(H)-cholestane (20R)
		5α(H),14β(H),17β(H)-cholestane (20S)
		5α(H),14α(H),17α(H)-cholestane (20R)
C_{28}		24-methyl-5α(H),14α(H),17α(H)-cholestane (20S)
		24-methyl-5α(H),14β(H),17β(H)-cholestane (20R)
		24-methyl-5α(H),14β(H),17β(H)-cholestane (20S)
		24-methyl-5α(H),14α(H),17α(H)-cholestane (20R)
C_{29}	C29 ααα	24-ethyl-5α(H),14α(H),17α(H)-cholestane (20S)
		24-ethyl-5α(H),14α(H),17α(H)-cholestane (20R)
	C29 αββ	24-ethyl-5α(H),14β(H),17β(H)-cholestane (20R)
		24-ethyl-5α(H),14β(H),17β(H)-cholestane (20S)

Table 4.3 **(continued):**

Peak ID		Aromatic hydrocarbons (TIC = total ion chromatogram)
N		naphtalene
MN		β,α methylnaphthalene
DBT		dibenzothiophene
Phen		phenanthrene
MP		3,2,9,1 methylphenanthrene

Peak ID		Aromatic hydrocarbons (mass-to-charge ratio m/z = 170)
TMN	1,3,7-	1,3,7-trimethylnaphtalene
	1,2,5-	1,2,5-trimethylnaphtalene

Peak ID		Aromatic hydrocarbons (mass-to-charge ratio m/z = 184)
TeMN	1,3,6,7-	1,3,6,7-tetramethylnaphtalene
	1,2,5,6-	1,2,5,6-tetramethylnaphtalene
	1,2,3,5-	1,2,3,5-tetramethylnaphtalene

4.4 Results

A detailed source rock evaluation includes determination of organic richness (quantity), kerogen type, maceral composition molecular signatures (quality), and thermal maturity (Peters & Cassa, 1994). The investigated rock samples represent non-marine siltstones, fine-grained sandstones and carbonaceous shales. Both studied formations can be macroscopically characterized as fluvio-lacustrine siliciclastics (**Figure 4.3**). Typical features are fine, often wavy laminations of interbedded sand, silt and clay, as well as lenticular bedding and bioturbation. In the following, the detailed results of our investigations are summarized (see also **Table 4.2** and **Table 4.4**).

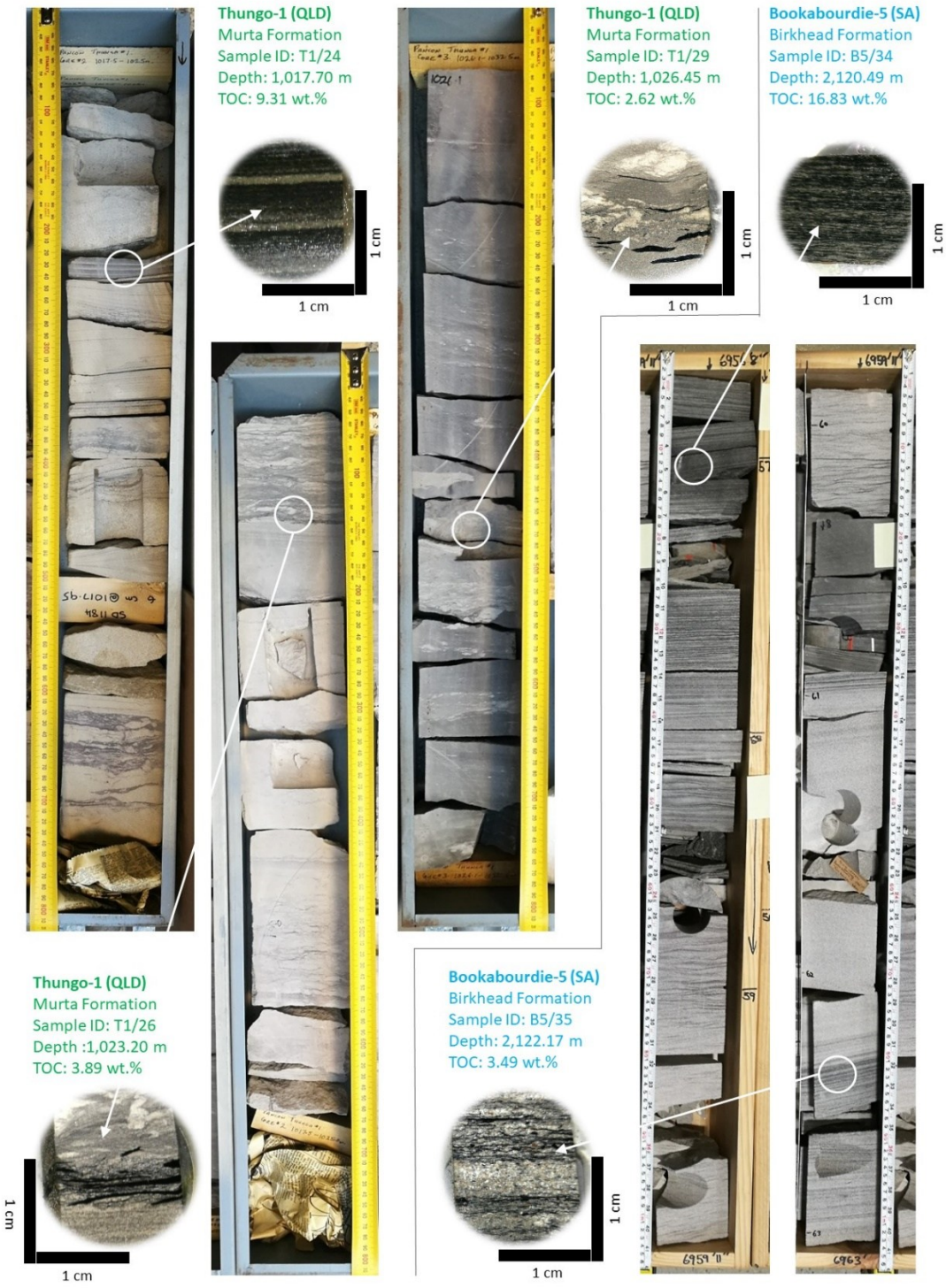

Figure 4.3: Selected cores and samples with remarkable sedimentary features. The sandy siltstones of the Murta Formation at Thungo-1 exhibit interbeds of rhythmic lamination (sample T1/24, varvites) as well as intense bioturbation (sample T1/26), both in combination with high organic matter content. The laminated and lenticular sandy successions of the Birkhead Formation at Bookabourdie-5 show organic-rich interbeds (samples B5/34, B5/35) and exhibit a lower degree of bioturbation.

Table 4.4: Results of molecular organic geochemistry sorted after formation and distinguished between GC-FID and GC-MS (see Table 4.3 for abbreviations). Source-related biomarker ratios are in italic, all remaining parameters are maturity-related. A) Peters et al., 2005a; b) Connan & Cassou, 1980; c) Peters et al., 1999; d) Peters et al., 2005b; e) Scalan & Smith, 1970; f) ten Haven & Rullkötter, 1988; g) Fan et al., 1987; h) Seifert & Moldowan, 1980; i) Moldowan et al., 1985; j) Seifert et al., 1981; Seifert & Moldowan, 1986; k) Hughes et al., 1995; l) Maslen et al., 2011; m) Radke et al., 1982.

		GC-FID molecular ratios					
Formation	**Sample ID**	**Pr/Ph** [a]	**Pr/n-C_{17}** [b,c]	**Ph/n-C_{18}** [b,c]	**n-C_{17}/n-C_{27}** [a]	**TAR** [d]	**OEP** [e]
Murta	**J2/05**	*2.55*	*0.32*	*0.10*	*3.99*	*0.17*	1.01
	J2/06	*3.10*	*0.28*	*0.10*	*40.64*	*0.01*	1.12
	W1/11	*2.32*	*0.32*	*0.13*	*20.12*	*0.02*	1.00
	W1/17	*2.50*	*0.39*	*0.14*	*3.62*	*0.16*	1.03
	T1/24	*3.44*	*0.28*	*0.09*	*581.52*	*0.00*	1.08
	T1/26	*6.74*	*0.34*	*0.11*	*65.22*	*0.01*	1.05
	T1/29	*3.62*	*0.54*	*0.16*	*2.12*	*0.34*	1.09
	L8/42	*2.73*	*0.20*	*0.06*	*16.35*	*0.03*	1.19
	L8/44	*1.93*	*0.18*	*0.09*	*2.48*	*0.19*	1.04
	L7/45	*3.26*	*0.22*	*0.07*	*38.33*	*0.02*	1.10
	L7/46	*3.09*	*0.24*	*0.07*	*65.04*	*0.01*	1.07
Birkhead	**B5/34**	*5.21*	*0.84*	*0.18*	*1.41*	*0.57*	1.07
	B5/35	*4.55*	*1.11*	*0.23*	*1.26*	*0.39*	1.05
	M4/37	*6.67*	*1.26*	*0.21*	*4.04*	*0.18*	1.04
	M4/40	*9.92*	*1.40*	*0.22*	*0.69*	*0.85*	1.13
	P1/55	*6.02*	*1.65*	*0.24*	*0.31*	*1.91*	1.04
	P1/56	*6.37*	*1.68*	*0.24*	*0.37*	*1.52*	1.04

Table 4.4 (continued): Hopanes (see Table 4.3 for abbreviations). Source-related biomarker ratios are in italic, all remaining parameters are maturity-related. A) Peters et al., 2005a; b) Connan & Cassou, 1980; c) Peters et al., 1999; d) Peters et al., 2005b; e) Scalan & Smith, 1970; f) ten Haven & Rullkötter, 1988; g) Fan et al., 1987; h) Seifert & Moldowan, 1980; i) Moldowan et al., 1985; j) Seifert et al., 1981; Seifert & Moldowan, 1986; k) Hughes et al., 1995; l) Maslen et al., 2011; m) Radke et al., 1982.

		GC-MS molecular fractions, ratios and indices					
		Hopanes					
Formation	Sample ID	C_{19}/C_{23} [a]	C_{29}/C_{30} [f g]	$T_S/(T_S+T_M)$ [a]	$C_{29}T_S/(C_{29}T_S+C_{29})$ [a]	$C_{30}M/C_{30}+C_{30}M$ [h]	$C_{31}22S/(22S+22R)$ [h]
Murta	**J2/05**	*4.38*	*0.65*	0.35	0.20	0.20	0.56
	J2/06	*7.33*	*0.56*	0.31	0.30	0.15	0.51
	W1/11	*13.16*	*0.61*	0.27	0.24	0.18	0.56
	W1/17	*5.46*	*0.69*	0.27	0.21	0.19	0.55
	T1/24	*10.17*	*0.68*	0.26	0.18	0.27	0.54
	T1/26	*5.24*	*1.03*	0.13	0.14	0.30	0.58
	T1/29	*2.26*	*0.64*	0.23	0.19	0.20	0.61
	L8/42	*3.12*	*0.60*	0.11	0.15	0.28	0.57
	L8/44	*2.52*	*0.58*	0.27	0.22	0.23	0.60
	L7/45	*5.35*	*0.67*	0.23	0.21	0.22	0.57
	L7/46	*3.24*	*0.62*	0.29	0.31	0.22	0.46
Birkhead	**B5/34**	*13.17*	*0.60*	0.12	0.11	0.13	0.59
	B5/35	*4.94*	*0.66*	0.16	0.15	0.11	0.58
	M4/37	*8.05*	*0.66*	0.25	0.23	0.17	0.60
	M4/40	*3.05*	*0.50*	0.31	0.29	0.16	0.58
	P1/55	*14.87*	*0.52*	0.18	0.16	0.14	0.58
	P1/56	*16.81*	*0.58*	0.21	0.19	0.13	0.58

Table 4.4 (continued): Steranes and aromatics (see Table 4.3 for abbreviations). Source-related biomarker ratios are in italic, all remaining parameters are maturity-related. A) Peters et al., 2005a; b) Connan & Cassou, 1980; c) Peters et al., 1999; d) Peters et al., 2005b; e) Scalan & Smith, 1970; f) ten Haven & Rullkötter, 1988; g) Fan et al., 1987; h) Seifert & Moldowan, 1980; i) Moldowan et al., 1985; j) Seifert et al., 1981; Seifert & Moldowan, 1986; k) Hughes et al., 1995; l) Maslen et al., 2011; m) Radke et al., 1982.

		GC-MS molecular fractions, ratios and indices							
		Steranes					**Aromatics**		
Formation	**Sample ID**	**C_{27} [%] [a) i)]**	**C_{28} [%] [a) i)]**	**C_{29} [%] [a) i)]**	**C_{29} αββ/αββ+ααα [j)]**	**C_{29} ααα 20S/20S+20R [j)]**	**DBT/Phen [k) l)]**	**MPI-1 [m)]**	**R_C [m)]**
Murta	**J2/05**	*18.03*	*11.40*	*70.58*	0.43	0.34	*0.06*	0.40	0.64
	J2/06	*20.37*	*10.90*	*68.73*	0.31	0.29	*0.24*	0.43	0.66
	W1/11	*21.29*	*18.46*	*60.25*	0.32	0.36	*0.39*	0.37	0.62
	W1/17	*19.03*	*13.59*	*67.39*	0.44	0.38	*0.32*	0.39	0.63
	T1/24	*15.37*	*14.14*	*70.49*	0.46	0.30	*0.54*	0.35	0.61
	T1/26	*20.17*	*12.63*	*67.20*	0.40	0.34	*0.35*	0.35	0.61
	T1/29	*14.47*	*10.15*	*75.39*	0.25	0.32	*0.35*	0.34	0.60
	L8/42	*18.39*	*16.58*	*65.03*	0.27	0.20	*0.27*	0.28	0.57
	L8/44	*25.98*	*10.46*	*63.55*	0.35	0.27	*0.22*	0.30	0.58
	L7/45	*15.55*	*14.07*	*70.38*	0.37	0.24	*0.26*	0.31	0.59
	L7/46	*23.44*	*14.00*	*62.55*	0.37	0.37	*0.19*	0.30	0.58
Birkhead	**B5/34**	*22.17*	*12.24*	*65.59*	0.49	0.44	*0.38*	0.33	0.60
	B5/35	*13.99*	*13.50*	*72.50*	0.47	0.43	*0.31*	0.35	0.61
	M4/37	*15.02*	*12.21*	*72.77*	0.44	0.43	*0.51*	0.14	0.49
	M4/40	*12.47*	*10.48*	*77.05*	0.42	0.42	*0.48*	0.14	0.49
	P1/55	*11.51*	*15.63*	*72.86*	0.44	0.43	*0.65*	0.24	0.54
	P1/56	*9.70*	*12.08*	*78.21*	0.43	0.45	*0.63*	0.24	0.54

4.4.1 Organic richness and carbonate content (TOC, TIC, TC, $CaCO_3$)

TOC values vary between 0.5 and 16.8 % considering all samples from both formations (Murta Formation avg.: 2.3 %; Birkhead Formation avg.: 3.7 %). Provided averages (see **Table 4.2**) should be regarded with caution, since the sampling process was focussed on the richest beds and was not conducted along a constant interval.. Further, the analysed core only cover sections of the formations, but not their entire thickness. From all 55 samples only seven samples contain less than 1.0 % and most of the TOC values are ranging between 1.0 and 5.0 %.

Extraordinary high TOC values were measured on carbonaceous samples of the Birkhead Formation (B5/34: TOC = 16.8 %, P1/55: TOC = 9.1 %; P1/56: TOC = 9.2 %). The maximum value for the Murta Formation was determined for sample T1/24 (TOC = 9.3 %).

Measured TIC values mainly fall in the range of 0.01 to 0.05 %. (Murta Formation avg.: 0.12 %; Birkhead Formation avg.: 0.04 %). From the TIC values, the carbonate content of the rock samples can be derived. While most samples do not contain more than 0.4 % $CaCO_3$, the maximum TIC value corresponds with the minimum TOC and TS values (T1/27, TOC = 0.50 %, TS = 0.05 %, TIC = 3.33 %) and yields 27.73 % $CaCO_3$.

4.4.2 Sulphur content (TS)

Total sulphur contents are low between 0.05 and 0.33 % (Murta Formation avg.: 0.11 %; Birkhead Formation avg.: 0.13 %) and show a linear relationship with the TOC content. The minimum TS value corresponds with the minimum TOC value (T1/27: TOC = 0.5 %, TS = 0.05 %) and the maxima also correlate (B5/34: TOC = 16.8 %, TS = 0.3 %). The overall TS/TOC ratio scatters around 1:78.

4.4.3 Rock-Eval pyrolysis

Fundamental parameters (S_1, S_2, GP, PI, HI, Tmax) can be derived from the Rock-Eval pyrolysis and are used to characterize and quantify the hydrocarbon potential of organic-rich sediments. HI values are generally higher for the Birkhead Formation (184-436, average about 300 mgHC/gTOC) than the Murta Formation (28-268, average about 150 mgHC/gTOC). Obtained data are presented in **Table 4.2** and is discussed in more detail further below. Representative Rock-Eval pyrograms are provided in the supplementary information.

4.4.4 Thermal maturity (Vitrinite reflectance VR_r; Rock-Eval T_{max};)

Vitrinite reflectance (VR_r) and Rock-Eval T_{max} are indicators for the level of thermal maturity in rock samples (Hartkopf-Fröder et al., 2015). The relationship between both parameters is usually linear (see Hackley & Cardott, 2016; Yang & Horsfield, 2020 for a non-linear correlation). Kerogen-specific onsets of the oil window (Tissot & Welte, 1984) are used to determine potential hydrocarbon generation from source rocks. The obtained values of both investigated formations are very similar ranging between 425 and 440 °C T_{max} (avg. for both: 433 °C) and between 0.5 and 0.7 % VR_r, respectively (Murta Formation avg.: 0.58 % VR_r; Birkhead Formation avg.: 0.57 % VR_r). Representative VR_r measurements are provided in the **Appendices**.

4.4.5 Organic petrography

Based on the analysis of the cores and the polished sections, we characterize the samples as carbonaceous sandy siltstones and silty shales (**Figure 4.4**, **Table 1.1**). Both formations show laminated sediment structures with varying intensity of bioturbation. Organic matter occurs in various types and sizes – as dispersed organic matter (DOM) in coarse mineral detritus (**Figure 4.4a** and **Figure 4.4b**) or as fine particles in fine-grained siliciclastic matrix (**Figure 4.4c**). Well-preserved plant-remnants are often macroscopically recognizable (compare **Figure 4.3**).

The observed maceral group composition (vitrinite, liptinite, and inertinite; siliciclastic matrix subtracted) of the examined samples is displayed as a ternary diagram in **Figure 4.4d**. All samples exhibit relative high amounts of vitrinite and liptinite. While vitrinite is dominant in the Birkhead Formation (vitrinite 63-85 %, liptinite 10-37 %), the liptinite content is generally higher in the Murta Formation (vitrinite 37-80 %, liptinite 20-60 %). Further, the presence of inertinite is generally low. In Birkhead Formation samples inertinite is mainly absent but was observed occasionally in samples from the Murta Formation. Based on **Figure 4.4d** the two examined formations can be roughly distinguished by two separate clusters (Murta Formation: liptinite >> vitrinite >> inertinite; Murta Formation: vitrinite >> liptinite >> inertinite). Three samples of the Murta Formation (W1/17, T1/26, and T1/27) plot in the cluster of the Birkhead Formation featuring a high vitrinite to liptinite ratio (80/20) and contain no inertinite.

In UV-induced fluorescent light, we identified cutinite, lamalginite and telalginite. While smaller, squeezed lamalginite is abundant in the Murta Formation (**Figure 4.4c**), relative thick laminated fragments occur in the Birkhead Formation (**Figure 4.4b**). In both

formations we found well-preserved flame-shaped cutinite particles (**Figure 4.4a** and **Figure 4.4b**) present in those samples with the highest TOC values (T1/24 (Murta Formation), TOC = 9.3 wt.%; B5/34 (Birkhead Formation), TOC = 16.8 wt.%). While the fluorescence color of the "cutinite flames" (remnants of leafs/cuticles from higher land plants) appears in bright yellow in the Murta Formation (**Figure 4.4a**), it appears darker and turns into orange in the Birkhead Formation (**Figure 4.4b**). This color change reflects the difference in depth and in thermal maturity between the two investigated sets of samples (T1/24 (Murta Formation), VR_r = 0.52 %, shallower; B5/34 (Birkhead Formation), VR_r = 0.65 %, deeper). Sporadic occurrence of bright yellow to light orange fluorescent telalginite derived from *Botryococcus* algae in the Murta Formation (also observed by Michaelsen & McKirdy, 1989) was confirmed in some samples (**Figure 4.4c**).

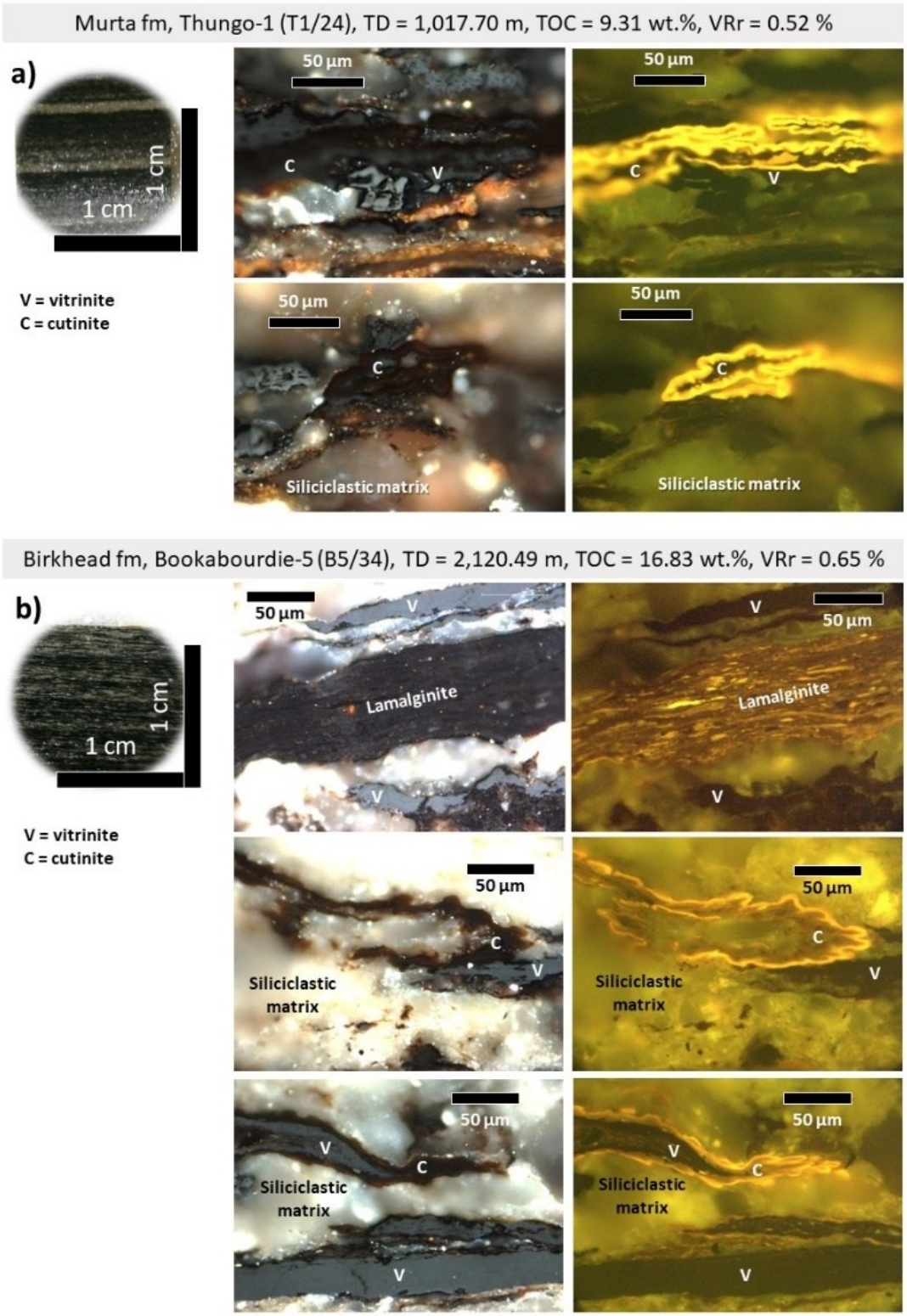

Figure 4.4: Microscopic details of dispersed organic matter (DOM) from petrographic maceral analysis (left column: reflected light; right column: with fluorescence). a) DOM in a representative sample of the Murta Formation (Thungo-1, sample T1/24): "cutinite flames" (bright yellow in UV-light) and vitrinite in coarse siliciclastic matrix. b) DOM in a representative sample of the Birkhead Formation (Bookabourdie-5, sample B5/34): thick lamalginite (yellow/brown), "cutinite flames" (yellow/orange) and vitrinite in coarse siliciclastic matrix.

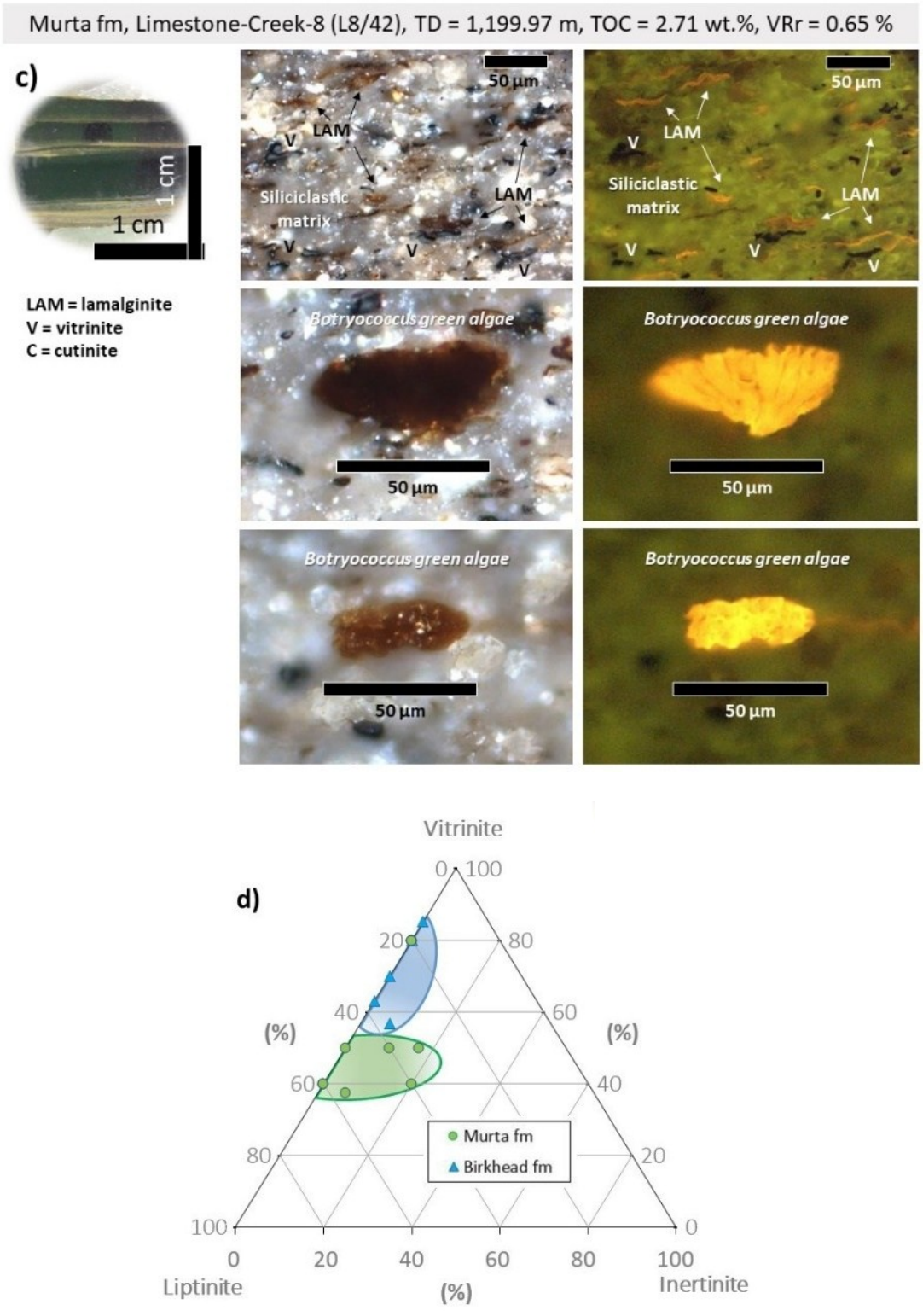

Figure 4.4 (continued): c) DOM in the Murta Formation (Limestone-Creek-8, sample L8/42): abundant particles of fine lamalginite (orange/brown), vitrinite, and fragments and aggregates of Botryococcus green algae (dark yellow) in fine siliciclastic matrix. d) Maceral composition of selected samples displayed in a ternary diagram (siliciclastic matrix subtracted): both formations contain little to no inertinite. The vitrinite content is generally higher in the Birkhead Formation, while liptinite (including cutinite, lamalginite, and telalginite) dominate in the Murta Formation.

4.4.6 Normal alkanes and acyclic isoprenoids

Figure 4.5a shows the distribution of n-alkanes and isoprenoids of selected samples from the Murta and Birkhead formations. Whereas short-chain n-alkanes (n-C_{16} to n-C_{20}) are dominant in the Murta Formation, the Birkhead Formation features a more heterogeneous distribution of saturated hydrocarbons with additional distinct maxima in the long-chain range (n-C_{25} to n-C_{27}).

Pristane to phytane (Pr/Ph) ratios are generally high with moderate values for the Murta Formation (1.93-6.74; avg.: 3.21) and very high values for the Birkhead Formation (4.55-9.92; avg.: 6.45). The Birkhead Formation also contains more isoprenoids related to n-alkanes. Both corresponding ratios yield higher ranges for the Birkhead Formation (Pr/n-C_{17}: 0.84-1.68; avg.: 1.32; Ph/n-C_{18}: 0.18-0.24; avg.: 0.22) compared to the Murta Formation (Pr/n-C_{17}: 0.18-0.54; avg.: 0.30; Ph/n-C_{18}: 0.06-0.16; avg.: 0.10), respectively.

The n-C_{17}/n-C_{27} and terrigenous to aquatic ratios (TAR = (n-C_{27}+n-C_{29}+n-C_{31})/(n-C_{15}+n-C_{17}+n-C_{19})) show very similar diverging trends. The n-C_{17}/n-C_{27} ratio ranges from 0.31 to 1.41 in the Birkhead Formation (except sample M4/37; avg.: 1.35) and from 2.12 to 65.22 in the Murta Formation (except sample T1/24; avg.: 76.31). TARs of the Birkhead Formation range from 0.18 to 1.91 (avg.: 0.90), while the Murta Formationfeatures TARs less than 0.34 (avg.: 0.09). Sample T1/24 represents an extreme outlier with TAR = 0.00 and n-C_{17}/n-C_{27} = 581.52. Odd-to-even predominance (OEP; after Scalan & Smith, 1970; calculated according to Peters et al., 2005b) is very similar in both formations and varies between 1.0 and 1.2 (Murta Formation avg.: 1.07; Birkhead Formation avg.: 1.06). A correlation between TAR and Pr/Ph (as proposed by Hackley et al., 2020) was not observed.

4.4.7 Alicyclic isoprenoids

Hopane and sterane compounds were detected in all samples in high concentrations permitting peak area calculation without strong background interference. The distribution of hopanes and steranes in selected samples from both formations shows a remarkable intensity of pentacyclic triterpanes and C_{29} steranes (**Figure 4.5a**).

The C_{19}/C_{23} tricyclic terpane ratio ranges between 2.03 and 13.16 (Murta Formation, avg.: 5.66) and between 3.05 and 16.81 (Birkhead Formation, avg.: 10.15), respectively. The C_{29}/C_{30} hopane ratios of both formations fall in the same range between 0.50 and 0.69 (except sample T1/26 with a ratio of 1.03; Murta Formation avg.: 0.67; Birkhead Formation avg.: 0.59). Maturity-related terpanes ratios show very similar results for both

formations ($T_S/(T_S+T_M)$; Birkhead Formation: 0.12-0.31; avg.: 0.21; Murta Formation: 0.11-0.35; avg.: 0.25; and $C_{29}T_S/(C_{29}T_S+C_{29}H)$; Birkhead Formation: 0.11-0.29; avg.: 0.19; Murta Formation: 0.14-0.31; avg.: 0.21). The moretane to hopane ratio ($C_{30}M/(C_{30}+C_{30}M)$) is generally lower in the Birkhead Formation (0.11-0.17; avg.: 0.14) than in the Murta Formation (0.15-0.30; avg.: 0.22). Calculated C_{31} 22S/(22S+22R) ratios range from 0.58 to 0.60 in the Birkhead Formation (avg.: 0.59) and from 0.46 to 0.61 in the Murta Formation (avg.: 0.56), respectively.Ranging from 60 to 78 %, C_{29} regular steranes dominate the relative distribution of the homologue series of $C_{27}/C_{28}/C_{29}$ sterane compounds. The isomerization ratios of asymmetric centers in the C_{29} steranes (C_{29} ααα 20S/(20S+20R) and C_{29} αββ/(αββ+ααα)) show a broader scatter for the Murta Formation (0.20-0.38; avg.: 0.31; and 0.25-0.46; avg. 0.36) and a narrow range at generally higher values for the Birkhead Formation (0.42-0.45; avg.: 0.43; and 0.42-0.49; avg.: 0.45).The common salinity indicator gammacerane and the angiosperm biomarker oleanane (compare Moldowan et al., 1994) were both not identified.

4.4.8 Aromatic compounds

Evaluation of phenanthrene (Phen) and its methyl homologues, i.e. 3-, 2-, 9-, and 1-methylphenanthrene as well as dibenzothiophene (DBT, after Hughes et al., 1995; Maslen et al., 2011) resulted in DBT/Phen ratios ranging from 0.06 to 0.54 in the Murta Formation (avg.: 0.29) and from 0.31 to 0.65 in the Birkhead Formation (avg.: 0.49; compare **Figure 4.5b**). Values of the Methylphenantrene Index (MPI-1, after Radke et al., 1982) range between 0.14 and 0.35 for the Birkhead Formation (avg.:0.24), and from 0.28 to 0.43 in the Murta Formation (avg.: 0.35) resulting in calculated thermal maturity (R_C, after Radke et al., 1982) varying between 0.49 and 0.61 for the Birkhead Formation (avg.: 0.54) and between 0.57 and 0.66 for the Murta Formation (avg.: 0.61).

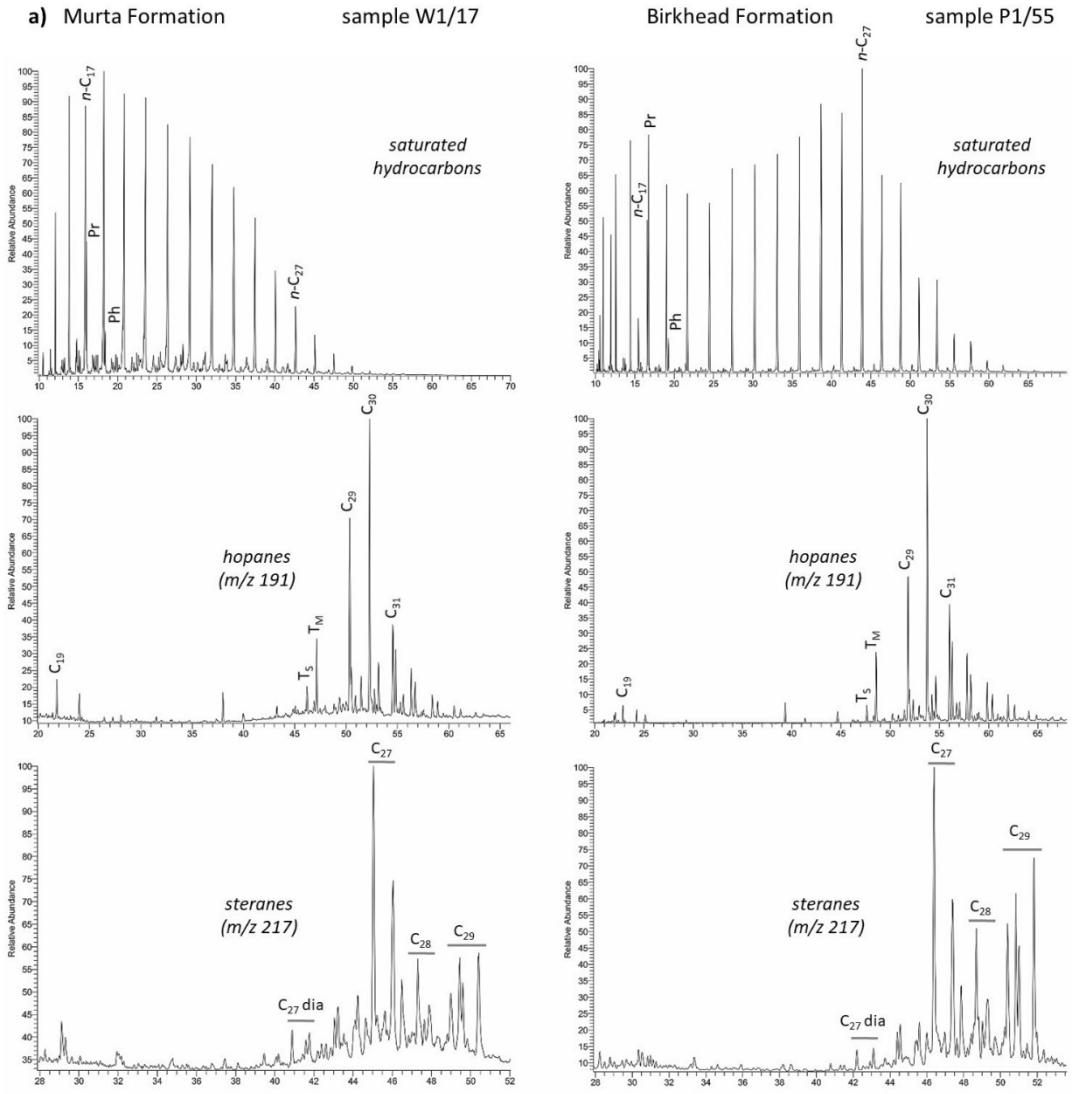

Figure 4.5: GC-FID/GC-MS chromatograms with signal intensities of molecular compounds from representative samples of both analyzed formations. a) Saturated hydrocarbons, hopanes and steranes (left: Murta Formation, sample W1/17; right: Birkhead Formation, sample P1/55).

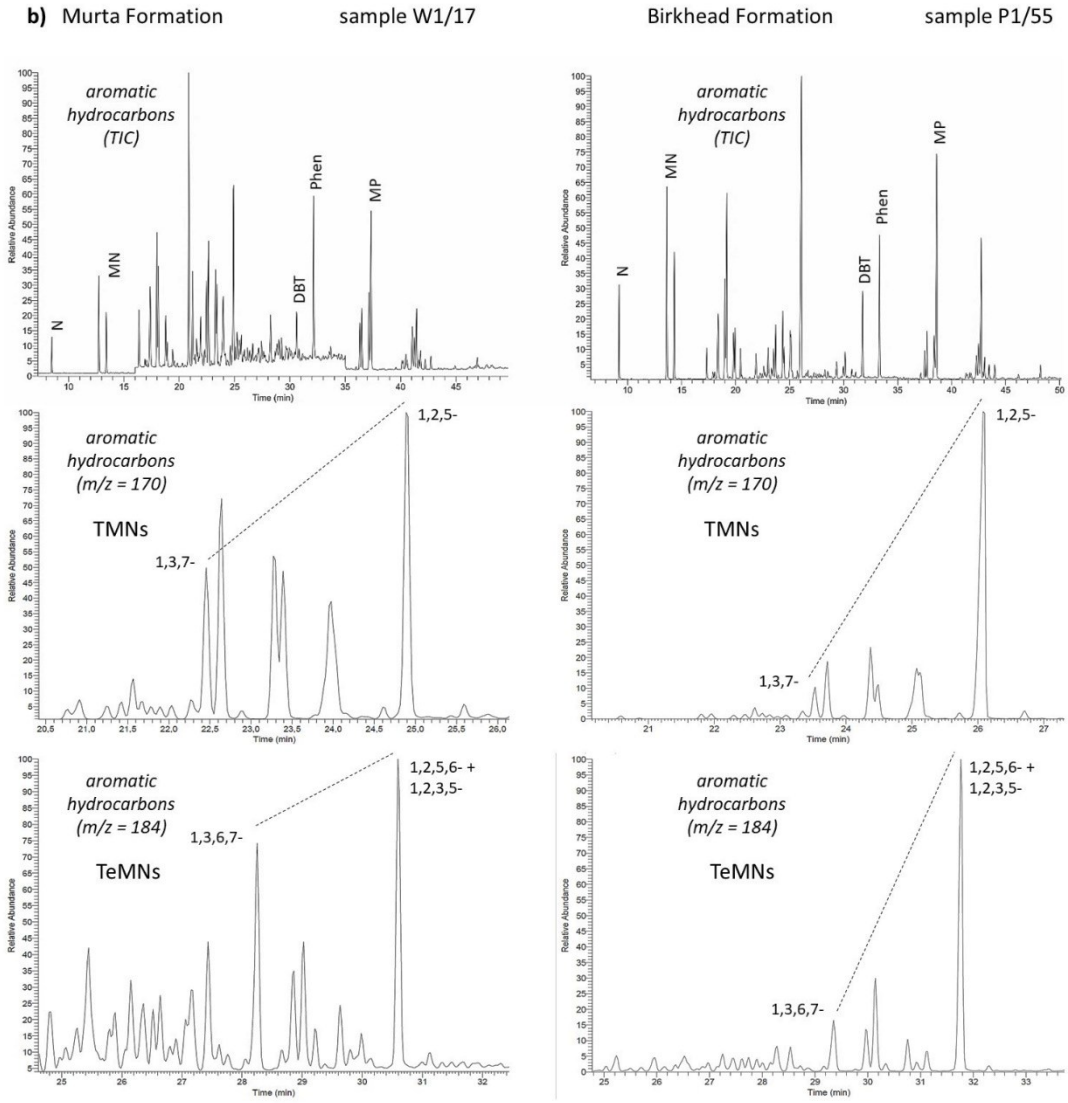

Figure 4.5 (continued): GC-FID/GC-MS chromatograms with signal intensities of molecular compounds from representative samples of both analyzed formations. b) Aromatic hydrocarbons, tri-methylnaphthalenes (TMNs) and tetra-methylnaphthalenes (TeMNs) (left: Murta Formation, sample W1/17; right: Birkhead Formation, sample P1/55). Stippled lines (slopes between the peaks) are explained in the discussion section under 'thermal maturity'. Only the most important biomarkers are labelled (abbreviations / peak IDs explained in Table 4.3).

4.5 Discussion

Evaluation and interpretation of the organic geochemical and organic petrographical data includes thorough comparison with existing data and classification based on established interpretation schemes. Results of each individual parameter must be regarded with caution since biochemical and thermal processes are sometimes counteracting. Thus, only the combination of multiple parameters allows reliable conclusions.

The two fluvio-lacustrine formations are not comparable with successions of typical marine or lacustrine shales or cyclothems and the analysed core sections are not continuous. Therefore, the observed heterogeneity of the two potential source rocks and the limited core data do not allow providing representative net/gross ratios. Even combined length at single well locations (see **Table 4.1**) is rarely representative for the entire formation thickness (values derived from the regional numerical 3D model of Hall & Palu (2016): Birkhead Formation: maximum thickness = 150 m, average thickness = 80 m; Murta Formation: maximum thickness = 90 m, average thickness = 20 m). Further, sampling was conducted with focus on fine-grained organic-rich material - and due to exclusion of the sandy interbeds - not along constant sampling intervals. Therefore no true geochemical logs can be provided.

In the following, we systematically discuss our results in the context of paleo-depositional environment (section **4.5.1**), thermal maturity (section **4.5.2**) and source rock potential (section **4.5.3**).

4.5.1 Biological precursors and paleo-depositional environment

The carbon and sulphur cycles are strongly interrelated in sedimentary systems. According to Berner (1984) and Berner & Raiswell (1984), a generally positive relationship between TOC and TS exists in environments with oxygenated bottom waters, but not in anoxic settings. Further, sulphur contents are much higher in marine as well as brackish water than in freshwater sediments. Sulphur is mainly bound to iron sulphides, pyrite and marcasite as well as organic sulphur formed during early diagenesis; it declines with decreasing availability of dissolved sulphate. Therefore, TS/TOC ratios are usually much higher in marine water than in sulphate-depleted freshwater. Thus, modern "normal", non-anoxic, marine sediments have TOC/TS ratios close to 2.8:1. The overall TOC/TS ratio of both analysed formations scatters, however, around 70:1 (**Figure 4.6a**). This trend clearly matches with freshwater conditions and supports the presence of

sulphate-depleted waters during deposition of the Birkhead Formation and the Murta Formation without any brackish water period.

The maximum TIC value of 3.3 % (T1/27) converts to 27.7 % $CaCO_3$ and corresponds with the minimum TOC and minimum TS values (TOC = 0.5 %, TS = 0.05 %). Under the microscope, amorphous crystalline material is visible, which occupies most of the intergranular space between the silt and fine sand grains (about 60 µm diameter) and which can be characterized as phreatic carbonate cement. This exceptional interval therefore either represents a (eogenetic) calcrete horizon due to temporarily high evaporation rates during deposition of the Murta Formation, or it was caused by mesogenetic calcite cementation (compare e.g. Schulz-Rojahn, 1993). The otherwise very low TIC values in all other samples are expected for deposition in fresh water.

Langford & Blanc-Valleron (1990) developed a diagram to classify the three main kerogen types (type I = algal/lacustrine; type II = planktonic/marine; and type III = land plants/terrigenous) based on the relationship between S_2 and TOC. In the "Langford plot" (**Figure 4.6b**) the Murta Formation samples scatter around the boundary between type II and type III kerogen with a preference towards type III, while the Birkhead samples predominantly yield type II kerogen.

As displayed in the classification scheme after Espitalié et al. (1985), kerogen types can also be determined based on the relationship between HI and Rock-Eval T_{max} (**Figure 4.6c**). While the range of measured T_{max} is very similar for both formations (all samples are scattering around the onset of the indicated oil window), the HI of the Birkhead Formation yields generally higher compared to the Murta Formation. Poonarunna-1 (Birkhead Formation) samples feature HI maxima and Jackson-2 (Murta Formation) samples show minimum values. Here – similar to the "Langford plot" (**Figure 4.6b**) – the Birkhead Formation also represents type II kerogen, while the Murta Formation indicates mixed sources of type II and type III kerogens. Contrary, the heterogeneous n-alkane chromatograms of the Birkhead Formation are reflecting a mix of algal/bacterial type I/II with waxy type III), while the Murta Formation appears more homogenous in the short-chain range (**Figure 4.5a**).

As pointed out by Connan & Cassou (1980), the Pr/n-C_{17} and Ph/n-C_{18} ratios help to distinguish kerogen types and depositional environments. In a log/log diagram (modified after Peters et al., 1999 with customized axis minima) the Murta Formation plots with some unusually low values at the boundary between type III and mixed type II/III kerogen

(**Figure 4.6d**). With predominantly Pr/n-C_{17} > 1, the Birkhead Formation data indicate type III kerogen and deposition under oxidizing, swampy conditions (Lijmbach, 1975). These interpretations have to be used with caution, since both ratios decrease with thermal maturity and increase with biodegradation (Peters et al, 2005b). However, the presence of abundant n-alkanes and the absence of a distinct hump in the chromatograms related to unresolved complex mixture (UCM) indicates that no significant biodegradation occurred (Hedges et al., 2000; **Figure 4.5a**).

With TAR = 0.00 and n-C_{17}/n-C_{27} = 581.52, sample T1/24 represents an extreme outlier and implies purely aquatic conditions. Indeed, macroscopically recognizable and undisturbed varvites (see **Figure 4.3**) indicate deposition in a low-energy environment. Further, the occurrence of *Botryococcus* algae (e.g. found in sample T1/42) represents planktonic green algae colonies in fresh to brackish water and is common in terrestrial/lacustrine petroleum source rocks (Moldowan & Seifert, 1980; McKirdy et al., 1986b; Glikson et al., 1989; Metzger & Largeau, 2005; Blumenberg et al., 2019). According to Peters et al. (2005a), the TAR is sensitive to thermal maturation which leads to a preferential loss of long-chain hydrocarbons. Further, a mix of aquatic and land-derived OM often features disproportionate weights assigned to the long-chain land-plant input. Fresh-water algal material (e.g. from *Botryococcus* algae) might even increase the signal of C_{27}-C_{31} n-alkanes (Moldowan et al., 1985; Derenne et al., 1988).

The C_{19}/C_{23} tricyclic terpane ratio is also sensitive to differences in OM input (Peters et al., 2005a). C_{19} and C_{20} tricyclic diterpanes originate from higher land plants (e.g. Alberdi et al., 2001), whereas extended tricyclic terpanes (C_{21}+) derive from algae and bacteria (Ourisson et al., 1982; Moldowan et al., 1983; Zumberge, 1987). Sources of OM can therefore be distinguished by low (marine < 1) and high (terrigenous > 1) C_{19}/C_{23} values. All analysed samples exhibit C_{19}/C_{23} ratios >> 1 and thus indicate an exclusively terrigenous origin for both formations.

To differentiate between terrigenous and marine sourced oils, the C_{29}/C_{30} hopane ratio serves as a lithological parameter. Clastic source rocks commonly show values below 0.75, while carbonate source rocks feature C_{29}/C_{30} ratios > 1 (Fan et al., 1987; ten Haven & Rullkötter, 1988). Except for sample T1/26, all obtained values match with (non-marine) clastic source rocks.

The ternary diagram with relative distribution of the homologue sterane compounds $C_{27}/C_{28}/C_{29}$ (after Huang & Meinschein, 1979) shows a clear dominance of C_{29} steranes

and indicates OM input from terrestrial sources (**Figure 4.6e**). Particularly the Birkhead Formation shows a very high C_{29} steranes signal, representing predominant OM origin from higher land plants.

Hughes et al. (1995) introduced the zonation of depositional environments based on the relationship between Pr/Ph and DBT/Phen ratios. The DBT/Phen ratio helps discriminating between carbonate- and clay-rich lithofacies (Hughes et al., 1995; Maslen et al., 2011). According to this classification, all samples belong to the clay-rich series (**Figure 4.6f**). While the Murta Formation formed under oxic/terrigenous fluvio-lacustrine conditions (Zones 3/4), the Birkhead Formation incorporates predominantly oxic/terrigenous OM in a fluvio-deltaic/swampy milieu (Zone 4). With only one exception (T1/26), the two formations can be clearly distinguished; indicating two different mixes of OM. Highest Pr/Ph ratios occur at Moorari-4 (6.7, 9.9), followed pairwise by samples of Poonarunna-1 (6.0, 6.4) and Bookabourdie-5 (4.5, 5.2), respectively. With high, but varying input from higher land plants, all Birkhead Formation samples are therefore attributable to the terrigenous (fluvial/deltaic) zone. Samples of Thungo-1 (3.4, 3.6, and 6.7) reveal the highest Pr/Ph ratios within the Murta Formation subsamples, followed by Limestone Creek-7 (3.1, 3.3). Remaining Murta Formation samples are scattering around Pr/Ph ratios between about 2 and 3. Samples from Thungo-1 and Limestone Creek-7 therefore represent terrigenous (fluvial/deltaic) conditions, while the remaining Murta Formation samples reflect more aquatic (lacustrine) depositional environments. Absence of gammacerane (a typical salinity indicator after Sinninghe Damsté et al., 1995) in all samples also indicates fresh-water conditions.

Relative distribution of macerals (**Figure 4.4d**) and corresponding HI values (**Table 4.2**, **Figure 4.6c**) indicate bacterially enriched terrigenous OM present in the Murta Formation. Earlier studies found evidence of mixed algal OM with terrestrial organic detritus that accumulated in a fresh-water to brackish lacustrine environment (Ambrose et al., 1986; Michaelsen & McKirdy, 1989). While this is in principal agreement with our results, we see little evidence of brackish conditions (see very low S/TOC ratios). Increased oxidation related to fluctuating water levels and varying flow velocity, a high degree of bioturbation and relative slow deposition and burial are possible reasons for the reduced HI of the Murta Formation.

Dominance of vitrinite in the Birkhead Formation (**Figure 4.4d**) clearly indicates terrigenous kerogen (type III). The rather high HI values are consistent with earlier

observations (e.g. Khorasani, 1987) and are related to a terrigenous organic facies containing abundant hydrogen-rich liptinite, mainly represented by cutinite and sporinite (e.g. Jenkins, 1989; Hawkins et al., 1989). Additionally, microbial decay of vitrinite could have added biomass of archaea and bacteria modifying HI values (**Table 4.2**, **Figure 4.6c**) of the Birkhead Formation (Powell, 1986; Boreham & Summons, 1999). The rather undisturbed laminations observed on the core (**Figure 4.3**) indicate a relative quiet water body and a lesser degree of bioturbation during deposition of the Birkhead Formation.

Although we could not assign our results to the individual Birkhead Formation units after Paton (1986), we can confirm a calm, oxic, and purely terrestrial paleo-depositional environment that matches with earlier published high sinuosity meandering deltaic to fluvio-lacustrine conditions (e.g. Veevers, 1984; McIntyre et al., 1989; Lanzilli, 1999) representing the "Lake Birkhead" floodplain (Mackie & Gumley, 1995; Boult et al., 1997). Brackish paleo-depositional conditions (Burger, 1986), however could not be confirmed based on this study.

Featuring a relative dynamic and predominantly oxic fluvio-lacustrine paleo-depositional environment with sporadic occurrence of fresh-water *Botryococcus* green algae, the Murta Formation represents the Australian example of common fluvio-lacustrine lowermost Cretaceous deposits such as the English Purbeckian and German Wealden facies (Blumenberg et al., 2019). Since we found no evidence for deep-water/offshore sedimentation in our results, we assign the investigated Murta Formation samples to the lower successions of the Murta Formation (Units 1 & 2 after Ambrose et al., 1982, Ambrose et al., 1986), which mainly represent shallow water and fluvio-lacustrine/deltaic conditions. Similarly, also for the Murta Formation fluvio-lacustrine paleo-depositional conditions of the proposed "Lake Murta" were confirmed by our study (compare Gorter, 1994; Alexander et al., 2006).

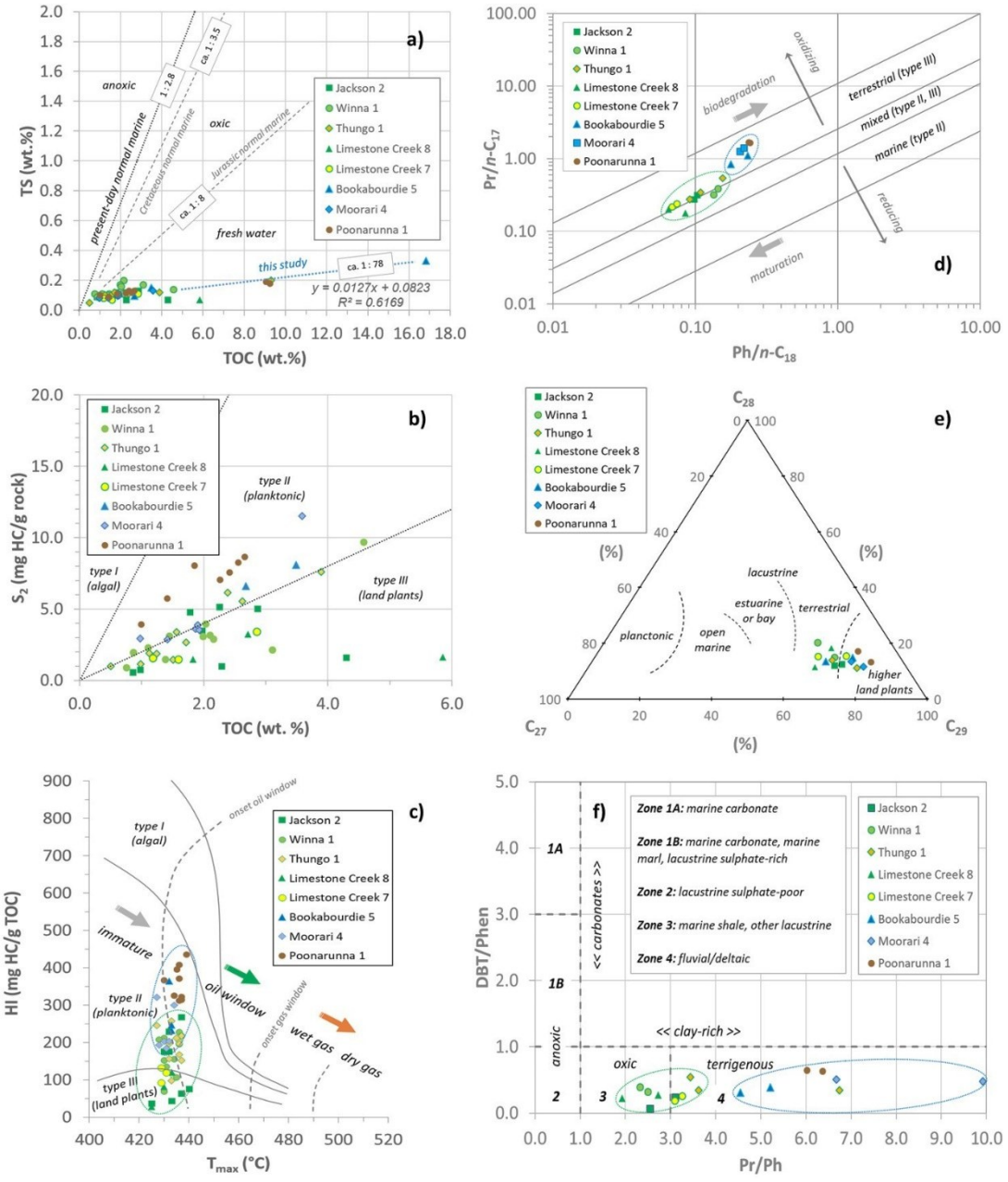

Figure 4.6: Elemental composition, source-related Rock-Eval parameters and source-related biomarkers. a) The relation between total sulphur content (TS) and total organic carbon content (TOC) subdivided into Murta Formation (green circles) and Birkhead Formation samples (blue triangles). Classes of depositional environment (anoxic, oxic, fresh water), present-day normal marine line, as well as Cretaceous and Jurassic normal marine paleo-lines (after Berner, 1984 and Berner & Raiswell, 1984). b) Simple differentiation of kerogen type (source of organic matter) based on Rock-Eval S_2 vs. TOC displayed as "Langford-plot" (classification after Langford & Blanc-Valleron, 1990) and separated by individual wells (excluded samples / outside diagram: T1/24, B5/34, P1/55, P1/56). c) Hydrogen Index (HI) vs Rock-Eval T_{max} with kerogen type classification and onset of oil/gas windows after Espitalié et al (1985). Green ellipse = Murta Fm, blue ellipse = Birkhead fm. d) Logarithmic cross plot of pristane/n-C_{17} and phytane/n-C_{18} ratios showing the depositional milieu and origin of organic matter of the analyzed

samples (after Connan & Cassou, 1980, modified after Peters et al., 1999). e) Ternary diagram with relative content of sterane compounds C_{27}, C_{28}, and C_{29} for classification of organic matter origin (after Huang and Meinschein, 1979). Both formations yield terrestrial paleo-depositional milieu. f) Cross-plot of DBT/phenanthrene vs pristane/phytane for the classification of the depositional environment (zonation after Hughes et al., 1995). The Murta Formation indicates lacustrine to fluvial conditions, while the Birkhead Formation plots in the fluvial/deltaic zone.

4.5.2 Thermal maturity

As displayed in **Figure 4.7a**, the samples of both formations cluster between 0.5 and 0.7 VR_r % and from 425 to 440 °C T_{max}, respectively. In case of the vitrinite-rich Birkhead and Murta formations, vitrinite reflectance works very well as maturity parameter (Hartkopf-Fröder et al., 2015). Based on the typical onsets of the respective oil windows (after Tissot & Welte, 1984) all samples are located at the transition from immature state to the onset of the oil window for type II of type III kerogen. However, only Birkhead Formation samples from Poonarunna-1 are located inside the given (early) oil window. All other Birkhead Formation samples are immature. Scatter within individual boreholes is large; therefore no clear regional maturity trends can be deduced. "Suppression" of vitrinite reflectance is unlikely, because both formations contain abundant non-fluorescing vitrinite. As compared to coals, in such environments vitrinite reflectance shows more scatter, but the same average values and depth trends (Scheidt & Littke, 1989). Furthermore, the ranges of HI and T_{max} values correspond well with the expected range in such environments (Zieger et al., 2020).

The HI is an indirect maturity indicator and helps distinguishing kerogen types and to understand their respective maturation pathways and the potential of hydrocarbon generation (Espitalié et al, 1985; Law, 1999). **Figure 4.6c** demonstrates the relationship between HI and Tmax and shows two different trends for both formations, respectively. While the samples of the Murta Formation feature relative low HI values and show an apparent mix of mainly immature type II and type III kerogen at the transition to the type II specific oil window, the Birkhead Formation samples feature generally higher HI values and exclusively plot in the field of type II kerogen. Due to the relatively early onset of oil generation from type II kerogen, all the samples of Poonarunna-1 are located in the early oil window.

Maturity-related biomarker ratios of the subsamples deliver partly contradicting interpretations. Values between 1.0 and 1.2 for the odd-to-even predominance (OEP) ratio of n-alkanes are surprisingly low in all samples with those from Poonarunna-1 (Birkhead

Formation) and Winna-1 (Murta Formation) being closest to OEP = 1.0 indicating the highest maturity.

Terpane ratios Ts/(Ts+Tm) and C_{29}Ts/(C_{29}Ts+C_{29} hopane) typically increase with maturity (Peters et al., 2005a). Whereas the Birkhead Formationsubsamples vary by location with Moorari-4 being more mature than Poonarunna-1 and with Bookabourdie-5, being the least mature, no obvious relationship is visible for the Murta Formation (**Figure 4.7b**). Typically, the moretane to hopane ratio (C_{30}M/(C_{30}M+C_{30}H)) decreases with increasing maturity from 0.8 to 0.05 (Seifert & Moldowan, 1980). Measured values point towards higher maturity of the Birkhead Formationcompared to the Murta Formation, which is not in accordance with vitrinite reflectance and Rock-Eval pyrolysis data. Progressing thermal maturation also causes a stereochemical arrangement of the C_{31} homohopane towards an endpoint mixture of the C_{31} 22S/(22S+22R) ratio between 0.58 and 0.62 (Seifert & Moldowan, 1980). All calculated ratios of the Birkhead Formationsamples (0.58-0.60) are close to these values, while the Murta Formationsamples are scatter between 0.46 and 0.61, with only three samples having values greater than 0.58.

C_{29} ααα 20S/(20S+20R) and C_{29} αββ/(αββ+ααα) are common biomarker parameters used to evaluate immature to early mature rock samples. Equilibrium ratios are at 0.55 and 0.71, respectively, roughly equivalent to the transition from the early to the main oil window (R_o ~ 0.8-0.9 %; Seifert et al., 1981; Seifert & Moldowan, 1986; Peters et al., 2005a). As displayed in **Figure 4.7c**, the Birkhead Formationplots in a small area entirely within the early oil window, while the Murta Formationshows a broader scattering at the transition from immature to early mature. Biomarker-based thermal maturity seems to be generally slightly higher and more homogeneous in the Birkhead Formationthan in the Murta Formation.

The Methylphenantrene Index (MPI-1, after Radke et al., 1982) correlates with thermal maturity and allows the calculation of equivalent vitrinite reflectance (R_C). The obtained R_C values of the Murta Formationfall between 0.58 and 0.66 with local variations providing higher values for the Jackson-Naccowlah-Pepita Ridge compared to the Murteree Ridge and with Jackson-2 presenting the highest values. Oil staining of individual samples from Jackson-2 and Winna-1 proves petroleum generation and migration there. Thus, a variable but mostly low thermal maturity at the onset of petroleum is confirmed; subtle differences should not be over-interpreted, since this parameter is better suitable for higher maturities (Radke et al. 1982).

Multiple maturity-related parameters are in accordance with a narrow zone around the transition from immature to the early oil window (compare VR_r %, Rock-Eval Tmax, and C_{29} steranes). Poonarunna-1 seems to represent the high maturity end-member with all samples generally matching with the early oil window. Several parameters indicate a slightly higher thermal maturity for Birkhead Formationthan for Murta Formation (**Figure 4.6c**, **Figure 4.7a**, **Figure 4.7c**, and **Figure 4.7e**), but not Pr/n-C_{17} and Ph/n-C_{18} ratios, which show the opposite trend. Although distributions of tri-methylnaphthalenes (TMNs) and tetra-methylnaphthalenes (TeMNs) indicate low maturity for both formations (compare van Aarssen et al., 1999), according to the steepness of the slope between the peaks (**Figure 4.5b**), the Murta Formationshows a more advanced isomerization towards thermodynamically more stable substitutes compared to the Birkhead Formation.

The majority of analysed samples represents low thermal maturity based on VR_r (immature to early oil window, ~ 0.55 VR_r %) and the measured TOC and derived HI values are therefore expected to be not much different from the original TOC and original HI values during deposition. Our results confirm that the Birkhead Formation does not generate substantial amounts of petroleum below 0.55 VR_r % (Wecker, 1989); accordingly petroleum expulsion is expected to be very limited (Deighton et al., 2003). The sample locations of the Murta Formationare situated along two ridges associated with deep-seated inverted faults – the Jackson-Naccowlah-Pepita and the Murteree ridges, which represent important tectonic features of the stacked basin system (Apak e al., 1997). Episodes of sedimentation and post-sedimentary uplift and erosion caused multiple unconformities (e.g. Winton Unconformity) in the area and could therefore influence thermal maturity. While volcanic/magmatic influence near the sampled wells is unlikely, hydrothermal circulation along deep faults could also provide focused alterations of the temperature field. In future studies, detailed thermal modelling could help to constrain the thermo-tectonic evolution of the Eromanga Basin and the underlying Cooper Basin.

4.5.3 Petroleum generation potential

To identify the origin of hydrocarbons in source rock samples the Oil Saturation Index (OSI = S_1 x 100/TOC) was introduced by Jarvie (2012). A value of OSI = 100 serves as the boundary between rock samples containing indigenous and/or nonindigenous hydrocarbons. During programmed pyrolysis, most samples generated indigenous

hydrocarbons, but exceptional pyrolysis results of a few core samples from Jackson-2 (J2/05, J2/06, and J2/07) and Winna-1 (W1/17) indicate staining from deeper source rocks or generation and expulsion within the formation.

Unusually high n-C_{17}/n-C_{27} ratios and TARs close to zero in many Murta Formation samples could be an additional indicator of non-expulsion or staining from nearby petroleum sources. Contamination from drilling mud seems unlikely, since water-based products (South Australia: NaCl polyacrylamide, Queensland: KCl polymer, according to well completion reports) were applied and clean core samples (no cuttings) were investigated. Interestingly, there is no clear correlation between n-C_{17}/n-C_{27} and PI (compare **Table 4.2** and **Table 4.4**). Contamination from younger 'marine' formations (e.g. Toolebuc Formation) can also be excluded, since oleanane as well as C_{30} desmethyl and methylsteranes (Boreham & Powell, 1987) are absent in all samples.

The relationship between generation potential (GP = S_1 + S_2) and TOC can be illustrated using the log/log-diagram of Peters & Cassa (1994) and Hunt (1996). This plot (**Figure 4.7d**) reveals poor to very good GP for the Murta (1 – 36 mg HC/g rock) and fair to excellent GP for the Birkhead (3 – 67 mg HC/g rock; see **Table 4.5**). The correlation between GP and TOC is stronger for the latter formation.

Moderate to high PI values of most Murta samples (mainly between 0.1 and 0.5) are unexpected and may be due to indigenous oil generated from early-mature lamalginiteThis is in agreement with earlier observations which reported an early onset of oil generation at approximately 0.45 VR_r % (e.g. Wecker, 1989). In contrast, the minor occurrence of *Botryococcus* algae might not suffice for measurable oil generation. Further, for such *Botryococcus* facies, kinetic studies (e.g. Ziegs et al., 2015) indicate late oil generation, which does not fit to the situation observed here. Further, considering the underlying Birkhead Formation to be oil-mature in the area of the Jackson-Naccowlah-Pepita Ridge (e.g. Vincent et al., 1985), generation and upward migration of Birkhead oil is possible.

Birkhead Formation samples originating from Bookabourdie-5 and Moorari-4 show initial generation, but remain below PI = 0.2 (**Figure 4.7e**). Assuming the presence of similar kerogen also near the Jackson-Naccowlah-Pepita Ridge, slightly higher thermal maturity could cause expulsion and migration of Birkhead oil into overlying strata including the Murta Formation. To detect and quantify oil mixing from different source rocks, separate oil samples are required. We therefore suggest combining organic

geochemical analysis of oil samples with isotope analysis in future studies (e.g. Boreham & Summons, 1999) to be able to discuss oil migration effects. However, as long as the source for contamination remains uncertain, even lateral self-charging of the Murta Formationis a valid assumption.

Based on maceral composition, a better petroleum generation potential can be expected for the liptinite-rich Murta Formation as compared to the vitrinite-rich Birkhead Formation (**Table 4.5**). Also n-alkane distribution suggests algal-derived kerogen for the Murta. However, Rock-Eval HI values tend to be higher in the Birkhead Formation (**Figure 4.6**), although there is some overlap. This discrepancy is in our opinion mainly related to the lower TOC values in the Murta and thus mineral-matrix effects during Rock-Eval pyrolysis (Peters, 1986; Michaelsen, 2002), but partly also to i) differences in thermal maturity, and ii) presence of submicroscopic liptinite and per-hydrous vitrinite in the Birkhead Formation, which could not be petrographically identified.

Interestingly, all samples from Poonarunna-1 show very low conversion levels (PI < 0.1); although the respective oil window for type II kerogen (Tissot & Welte, 1984) was entered already (compare **Figure 4.7a** and **Figure 4.7c**). However, Poonarunna-1 is located outside the Cooper depocenter and probably represents a somewhat different organic facies. Indeed, the high HI values of the P1 samples might indicate incorporation of type I kerogen, which is known for a relative late oil generation at approximately 0.7 VR_r %. Exceptional HI values above 700 mg TOC/g rock in particular Birkhead Formation samples observed by Mahlstedt & Horsfield (2016) support this argument.

The average organic richness of the Birkhead Formation (3.7 % TOC: **Table 4.2**) is higher than earlier reported (2.5 % TOC: Jenkins, 1989), but this could be due to the focus on organic-rich beds during sampling. Hydrogen indices from the Birkhead Formation (184-436 mg HC/g TOC, avg. = 305 mg HC/g TOC) generally fall into the expected range (150 and 500 mg HC/g TOC; McKirdy et al., 1986b; Michaelsen, 2002; Boreham & Summons, 1999; Mahlstedt & Horsfield, 2016).

The organic richness of the Murta Formation (0.5–9 % TOC; HI = 28–268) turned out to be greathigher than previously reported (0.5–2.5 % TOC: Michaelsen & McKirdy, 1989; Draper, 2002), while the corresponding HI values (range = 28–268, avg. 153) appear slightly lower than those recorded by other workers (80–553: Michaelsen & McKirdy, 1989, 2006; Powell et al., 1991; Boreham & Summons, 1999). In **Table 4.5**, we summarize the main source rock properties of the Birkhead and Murta formations.

Based on the results of this study and in contrast to some earlier publications, we consider the Murta and Birkhead formations as efficient source rocks of the Eromanga petroleum system, although located comparably shallow. We conclude that organic matter content and petroleum generation potential of both formations are generally sufficient for oil expulsion when thermal maturation has reached the early oil window. Lateral variations of thermal maturity are primarily related to strong differences of burial depth and variable a mounts of Late Cretaceous erosion in the study area. Based on our preliminary modelling results (described in a separate study currently under review), localized Middle Cretaceous magmatism in the Nappamerri Trough also might have influenced thermal maturity of the Jurassic and Early Cretaceous source rocks. Therefore, corresponding oil migration from and accumulations of the Murta and Birkhead source rocks are expected in overlying sandstone intervals mainly along inversion structures (large faults and ridges) and near intrusive bodies of the Eromanga basin.

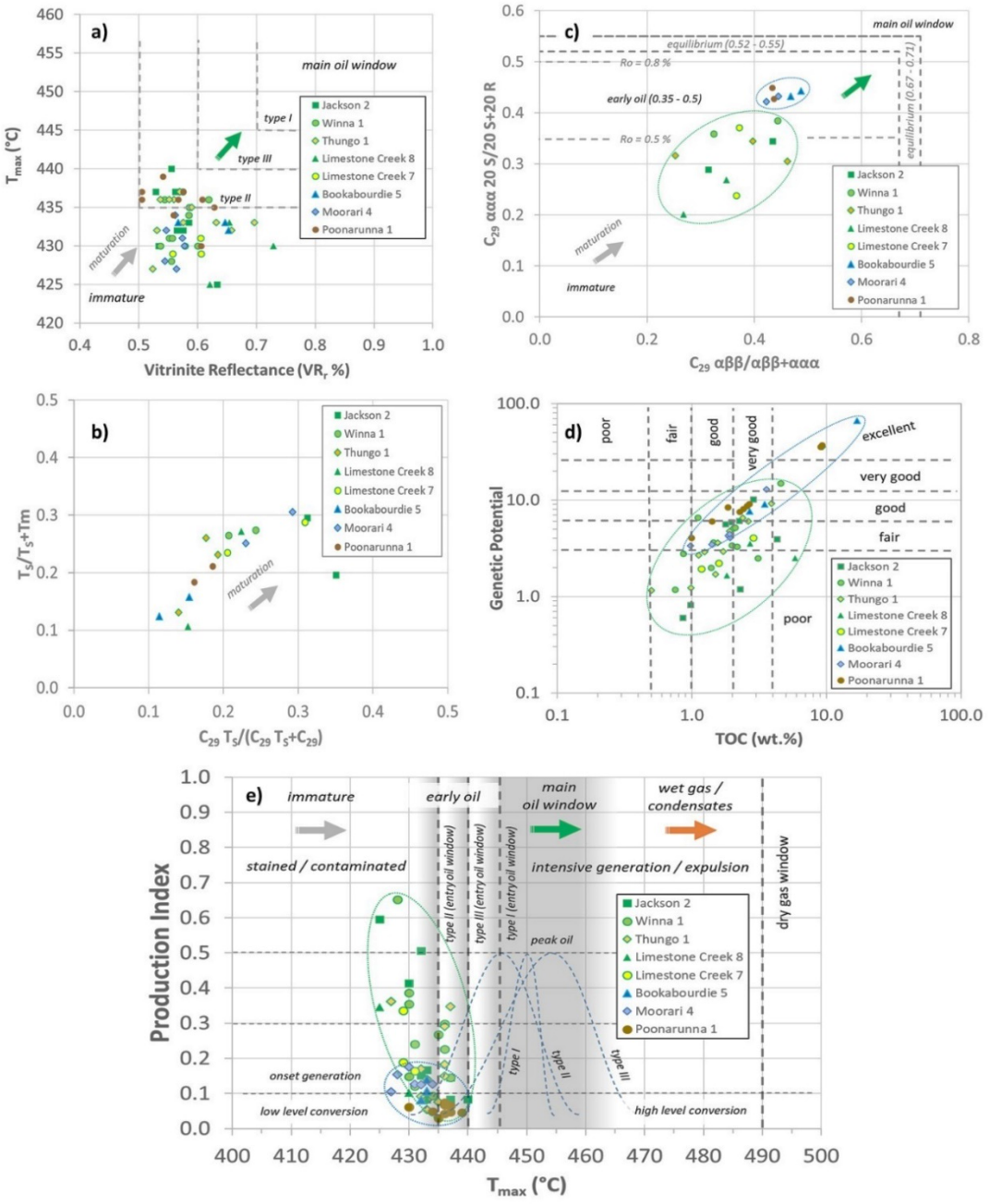

Figure 4.7: Maturity-related Rock-Eval parameters, maturity-related biomarkers and hydrocarbon potential. a) Thermal maturity expressed as the relation between Rock-Eval T_{max} vs. vitrinite reflectance. Onset of kerogen-dependent oil window after Tissot & Welte (1984). b) Terpanes maturity-related ratios Ts/Ts+Tm vs. C_{29}Ts/C_{29}Ts+C_{29} (after Peters et al., 2005). Both formations show relative low thermal maturity. c) Cross-plot of isomerization ratios for C_{29} 20S/20s+20R vs. C_{29} ββ/ββ+αα steranes (equilibrium values (dashed lines after Seifert et al., 1981; Seifert & Moldowan, 1986). d) Source rock potential according to the logarithmic illustration of the genetic potential (GP = S1+S2) vs. TOC based on the classification after Hunt (1996) and Peters & Cassa (1994). e) Produced hydrocarbons based on Production Index (PI) vs. Rock-Eval Tmax. Boundaries of conversion (onset generation, PI = 0.1; peak oil, PI = 0.5) after Law (1999); onset of kerogen-dependent oil window after Tissot & Welte (1984), shapes of kerogen-dependent generation curves are approximated and not databased.

4.6 Conclusions

New organic petrographic and organic geochemical data on a set of overall 55 rock samples provided information on the source rock potential and the biomarker composition of the siliciclastic fluvio-lacustrine Murta and Birkhead formations. Both source rock intervals are members of the *Early Jurassic to Early Cretaceous fluvio-lacustrine succession* (194-130 Ma) within the central Eromanga Basin and reveal several petrographical and geochemical similarities, but also compositional differences.

The silt- and fine sandstones of the Middle Jurassic Birkhead Formation and the Early Cretaceous Murta Formation formed in an isolated intracontinental setting in fresh-water paleo-depositional conditions. Very low total sulphur, low total inorganic carbon, absence of gammacerane, low dibenzothiophene/phenanthrene ratios and very high pristane/phytane ratios clearly indicate an oxic, non-marine paleo-depositional environment.

Table 4.5: Summary of the main source rock characteristics of the Murta and Birkhead formations.

Parameter / Formation	Birkhead	Murta
Depositional environment	meandering fluvial, floodplain	fluvio-lacustrine
Total organic carbon content (TOC)	1.0-16.8 wt.% (average: 3.7 wt.%)	0.5-9.3 wt.% (average: 2.2 wt.%)
Vitrinite reflectance (VR_r)	0.54-65 % (early oil window)	0.52-73 % (early oil window)
Rock-Eval T_{max}	427-439 °C	425-440 °C
Relative maceral group content	vitrinite > liptinite > inertinite	liptinite > vitrinite > inertinite
Pristane/Phytane ratio (Pr/Ph)	4.55-9.92 (terrigenous)	1.93-6.74 (oxic/terrigenous)
Typical saturate chromatogram maxima	*n*-C_{15} to *n*-C_{17}, and *n*-C_{25} to *n*-C_{27}	*n*-C_{16} to *n*-C_{20}
Hydrogen Index (HI)	184-436 mg HC/g TOC (average: 300 mg HC/g TOC)	28-268 mg HC/g TOC (avg. 150 mg HC/g TOC)
Kerogen types	mixed type II/III, mixed type I/III	mixed type II/III
Generation potential (GP)	fair to very good	poor to very good
Production index (PI)	0.03-0.18	0.05-0.65
Approximate onset of oil window	> 440 °C / > 0.7 VR_r %	< 425 °C / < 0.45 VR_r %

Both formations contain abundant fair to excellent organic matter quantities from mixed sources and reveal fair to very good petroleum generation potential. Mixtures of type II and type III kerogen prevail, which is, however, mainly derived from higher land plants with varying microbial contribution. Liptinite (mainly as lamalginite and cutinite) and vitrinite macerals are abundant in both formations. Pristane/n-C_{17} and Phytane/n-C_{18}

ratios and predominance of C_{29} regular steranes also indicate predominant terrigenous origin of organic matter.

Based on vitrinite reflectance, Rock-Eval T_{max}, odd-to-even predominance ratios, maturity-related hopane ratios, and isomerization of C_{29} steranes, both formations are thermally immature to early mature. Different kerogen composition and extremely varying production indices suggest individual onsets of the specific oil generation window. Oil staining of individual samples from Jackson-2 and Winna-1 proves petroleum generation and migration.

The results of this study provide new geochemical and petrographical data and adds novel observations about the paleo-depositional environments and the petroleum generation potential of the Murta and Birkhead formations. The obtained source rock data is suitable for geological integration and serve to complement existing numerical petroleum system models of the Cooper Basin, in which the Eromanga Basin only represents overburden and source rock properties were not assigned yet (i.e., Hall & Palu, 2016). Finally, it could be of great importance for the understanding of this major petroleum province to use this data for oil-source correlation and lateral continuity studies in the near future.

5 DOWN UNDER AND UNDER COVER: FREQUENT HYDROTHERMAL ACTIVITY AND STRIKE-SLIP TECTONICS IN THE COOPER BASIN AND CENTRAL EROMANGA BASIN CONFIRMED BY SUBSIDENCE HISTORY ANALYSIS AND BASIN MODELLING

Keywords: Cooper Basin Master Fault, Central Eromanga Shear Zone, Cooper Hot Spot, pull-apart basin, strike-slip tectonics, hydrothermal activity, thermal evolution, source rock maturation

Abstract

The Cooper subregion within the central Eromanga Basin is the Swiss army knife among Australia's sedimentary basins. Besides important oil and gas resources, it hosts abundant coal bed methane, important groundwater resources, features suitable conditions for enhanced geothermal systems, and is a potential site for carbon capture and storage. However, after seven decades of exploration, various uncertainties remain concerning its tectonic and thermal evolution.

In this study, the public-domain 3D model of the Cooper and Eromanga stacked sedimentary basins was modified and used to perform numerical basin modelling and subsidence history analysis to better understand the complex geologic history. Calibrated 1D/3D numerical models provide maps for heat flow, temperature, thermal maturity and sediment thickness.

According to calibrated vitrinite reflectance profiles, a major hydrothermal/magmatic event at about 100 Ma ago with associated basal heat flow up to 150 mW/m^2 caused intense source rock maturation and petroleum generation and probably overprinted most previous hydrothermal events in the study area. This event correlates with sedimentation rates up to 200 m/Ma and was apparently accompanied by extensive crustal shear. Structural style and depocentre migration analysis suggest that the Carboniferous-Triassic Cooper Basin initially has been a lazy-s shaped triplex pull-apart basin controlled by the Cooper Basin Master Fault, before it was inverted into a piggyback basin and then blanketed by the Jurassic-Cretaceous Eromanga sequence. The interpreted Central Eromanga Shear Zone governed the tectonic evolution since the Triassic until today. It repeatedly induced NNW-SSE directed deformation along the western edge of the Thomson Orogen and is characterized by present-day seismicity and succinct neotectonic features.

We hypothesize that throughout the basin evolution, alternating tectonic stress caused frequent thermal weakening of the crust and facilitated the establishment of the Cooper Hot Spot, which recently increased again its activity below the Nappamerri Trough.

5.1 Introduction

Since the 1950's, the intracontinental Cooper Basin (CB) in conjunction with the overlying Eromanga Basin (EB) in central eastern Australia (**Figure 5.1a**) constitutes Australia's most important onshore petroleum province (Gravestock et al., 1998, Draper, 2002). With a combined sediment thickness of up to 5,000 m and with an area of ca 127,000 km^2 the CB is covering parts of NE South Australia and SW Queensland (Stewart et al., 2013; Hall et al., 2015b).

Although intensely studied, the region recently became again subject of numerous investigations aiming on the reassessment of its ultimate petroleum potential including source rock characterization and identification of new unconventional hydrocarbon targets (i.e., Goldstein et al., 2012, Hall et al., 2015a, 2015b, 2016a, 2016b, 2019). Objectives also comprise development of enhanced geothermal systems (EGS), hydrogeological studies and identification of carbon capture and underground storage potential (CCS) to improve Australia's domestic energy market and water supply (i.e., Radke et al., 2009; Siégel et al., 2012, 2014; Meixner et al., 2014; Khair et al., 2015a, 2015b; Smith et al., 2015; Carr et al., 2016; Golding et al., 2016).

The study area in central eastern Australia (represented by the outline of the CB after Stewart et al., 2013; **Figure 5.1b**) comprises at least four superimposed sedimentary basin sequences: 1) the Paleozoic Warburton Basin (WB), 2) the Late Carboniferous to Triassic CB, 3) the Jurassic to Cretaceous EB, and 4) the Cainozoic Lake Eyre Basin (LEB). Several attempts have been made to reconstruct the subsidence history and thermal evolution (Gallagher & Lambeck, 1989; Moussavi-Harami, 1996; Deighton & Hill, 1998; Duddy & Moore, 1999; Zwingmann et al., 2001; Deighton et al., 2003; Mavromatidis & Hillis, 2005; Mavromatidis, 2006a, 2007; McLaren & Dunlap, 2006; Meixner et al., 2012). However, conclusions of these studies are often contradicting and the debate on the responsible tectonic opening mechanism of the superimposed basins (intracratonic vs. foreland vs. rift-related, etc.) is still ongoing (e.g., Hall et al., 2015b, 2016b; Wainman et al., 2018, Hardman et al., 2019).

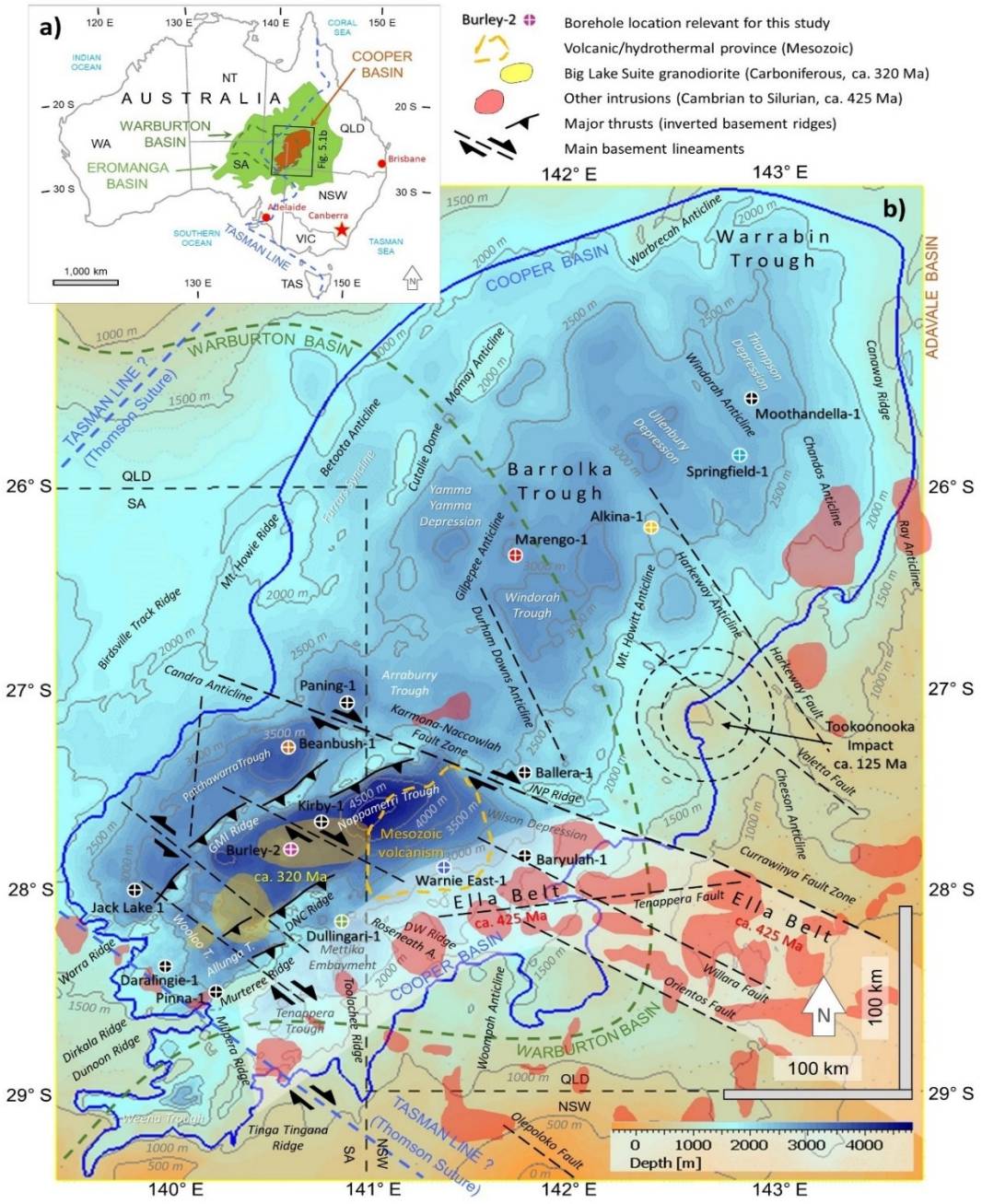

Figure 5.1: Overview map of the study area with basement topography, main structural elements and key well locations. a) Eromanga (light green), Cooper (brown) and Warburton (dark green) basin outlines in central eastern Australia. Tasman Line after Scheibner (1974) and Veevers & Powell (1984). b) Outline of the Cooper Basin after Stewart et al. (2013) with Cooper basement topography after Hall & Palu (2016) and with main structural features: thrusts and basement lineaments modified after Apak et al. (1997) and Purdy et al. (2018); anticlines and troughs modified after Hall et al. (2015); magmatic intrusions after Holgate (2005) and after Purdy et al. (2018); hydrothermal province after Hardman et al. (2019); Tookoonooka Impact after Bron & Gostin (2012). WA = Western Australia, NT = Northern Territory, SA = South Australia, QLD = Queensland, NSW = New South Wales, VIC = Victoria, TAS = Tasmania, GMI = Gidgealpa-Merrimelia-Innamincka, DNC = Della-Nappacoongee, DW = Dullingari-Wollgolla, JNP = Jackson-Naccowlah-Pepita.

Initial exploration activities in the study area began in 1945. Drilled by Santos in 1959, wildcat well Innamincka-1 for the first time intersected the entire Cooper sequence and revealed first hydrocarbon shows in Mesozoic and Permian rocks. In 1963, first commercial gas was found at Gidgealpa-2 and in the following years, further hydrocarbon discoveries were made mainly in anticlinal structures and along basement ridges (O'Neil, 1998; O'Neil & Alexander, 2006).

Since 2009, exploration activities are focusing on development of unconventional resources (Goldstein et al., 2012; Menpes et al., 2013) and total petroleum prospectivity (Hall et al., 2019), but also include assessment of ground water, EGS and CCS (i.e., Radke et al., 2009; Smith et al., 2015; Carr et al., 2016; Golding et al., 2016).

In 2015, about 160 oil fields (84 in Queensland, 82 in South Australia) and nearly 250 gas fields (158 of which in Queensland, 98 in South Australia) were producing (Hall et al., 2016b). Conventional and unconventional plays of the Cooper-Eromanga basin couplet contain 447 MMbbl of oil, 160 MMbbl of condensates, 220 MMbbl of liquefied petroleum gas (LPG), and 10.2 Tcf (2.9 Tcm) of natural gas (combined remaining identified and produced, as of December 2014, AERA, 2020a).

Multi-1D and pseudo-3D petroleum system models provided first insights into the hydrocarbon generation potential and timing of expulsion and retained volumes (Hall et al., 2016b, 2019). The publicly available *Cooper Basin regional petroleum system model* (Hall & Palu, 2016) includes regional-scale 3D interpretations of main stratigraphic surfaces, updated stratigraphic ages, erosion estimates, facies maps and property maps of Permo-Triassic source rocks (thickness, TOC and original HI). This data set serves as the most detailed available framework for regional scale resource assessment and petroleum system analysis (Hall et al., 2015b; Kuske et al., 2015) and was recently used for a regional-scale prospectivity study (Hall et al., 2019).

Subsurface temperature variations and thermal pulses throughout the geologic history are still poorly understood. This is due to local abnormally high present-day heat flow, inconclusive apatite and zircon fission track data and some gaps in otherwise remarkably comprehensive vitrinite reflectance profiles (e.g., Middleton, 1979; Gallagher, 1988; Duddy & Moore, 1999). Further, proposed unconformities due to episodes of erosion, Cretaceous glaciation, and probable effects of the enigmatic Tookoonooka meteorite impact (e.g., Burger & Senior, 1979; Gostin & Therriault, 1997; Bron & Gostin, 2012; Wainman et al., 2018; Alley et al., 2019) have been either overlooked and/or were not yet

considered in existing reports and models. Numerous evidence for strike-slip tectonics and considerable amounts of compression and uplift have been reported (Kantsler et al., 1983; Kuang, 1985; Finlayson et al., 1988; Apak et al., 1995, 1997; Mavromatidis, 2006b; Grant-Woolley et al., 2014; Kulikowski & Amrouch, 2017; Kulikowski et al., 2018), but were probably underestimated in recent prospectivity and modelling studies. Recently, revision of well data and interpretation of gravity maps and new 3D seismic surveys revealed widespread magmatic intrusions and volcanic flows in the basin center (e.g., Holgate, 2005; Meixner et al., 2012; Purdy et al., 2018; Hardman et al., 2019).

For improved exploration of hydrocarbons, geothermal systems and groundwater and for a safe CCS assessment in the Cooper and Eromanga basins it is fundamental to understand the tectonic evolution of the region. Especially the impact of the thermal history on the timing of source rock maturation and hydrocarbon generation and the faults' slip tendency and permeability require detailed examination.

In this study, the thermo-tectonic evolution of the Cooper-Eromanga couplet is reconstructed based on the existing 3D petroleum system model (Hall & Palu, 2016), the well database of Geoscience Australia (GA, 2017b) and additional input data. Source rock data from the Jurassic Birkhead and the Cretaceous Murta formations were integrated (see **Chapter 4**) and 1D burial history modelling was performed. Basal heat flow trends and amounts of erosion were constrained based on identified unconformities, calibrated thermal maturity (vitrinite reflectance) profiles and Horner-corrected borehole temperature. Reconstructed thermo-tectonic evolution scenarios and their implications on the petroleum system are summarized and discussed. The applied workflow, which combines basin modelling, thermal calibration, subsidence history analysis and a reality-check with the present-day tectonic situation is easily applicable in other sedimentary basins worldwide, when sufficient data are available.

5.2 Geological background

Multiple cycles of westward subduction and periodic crustal accretion along the eastern continental margin created stacked sedimentary basins in central eastern Australia (e.g., Warburton, Cooper, Galilee, Bowen basins). These Palaeozoic to Triassic sedimentary basins are blanketed by widespread sedimentary sequences of the Early Jurassic to Late Cretaceous intra-continental Great Artesian Basin (GAB). Together with the Carpentaria Basin in the North and the Surat Basin in the East, the EB represents one of three major depressions of the GAB (Gravestock et al., 1998; GA, 2020b). In the study area it directly

overlays the Pennsylvanian to Middle Triassic CB and features its maximum present-day thickness of locally more than 2 km (Smerdon et al., 2012). Sporadically, 100–200 m of Cainozoic sandstones of the endorheic LEB are covering the eastern and central EB (Draper, 2002; Smerdon et al., 2012). The GAB including the EB undoubtedly represents a large intra-continental sag basin (Apak et al., 1997; Cook et al., 2013) and the WB is broadly accepted as a metamorphic overprinted back-arc-basin (e.g., Roberts et al., 1990). However, the tectonic evolution and structural type of the CB remains controversial (e.g., Hall et al., 2015b).

The CB unconformable overlies a Palaeozoic basement (Warburton Unconformity), which predominantly consists of the Early Palaeozoic WB in South Australia and the Late Palaeozoic Thomson Beds on the Queensland side (Gravestock et al., 1998; Draper, 2002; Siégel et al., 2018). The NW-striking Karmona-Naccowlah Fault Zone (KNFZ, often also referred to as Jackson-Naccowlah-Pepita (JNP) trend) divides the basement topography of the CB into a high NE domain and a deeper, more complex SW domain (**Figure 5.1b**, McKellar, 2013).

The main depocentres in the NE domain (Windorah Trough, Ullenburry and Thompson depressions) form a rather smooth relief and are separated by gentle NNW- and NNE-striking anticlines (Draper, 2002). In comparison, the three relatively deep, NE-trending and subparallel oriented Patchawarra (PT), Nappamerri (NT) and Tenappera (TT) troughs in the SW domain are generally better defined and are divided by distinct NE-aligned basement ridges (Gidgealpa-Merrimelia-Innamincka (GMI), Della-Nappacoongee (DNC) and Murteree ridges (Gravestock & Jensen-Schmidt, 1998). The basement ridges are associated with major thrusts and are laterally displaced by NW-striking lineaments (Apak et al., 1997). These lineaments are oriented subparallel to the KNFZ and often feature an apparent dextral shear sense probably originating from repeated strike-slip tectonics during the Proterozoic and Paleozoic (Teasdale et al., 2001).

The basement of the SW CB also comprises numerous magmatic features. For example, the arcuate Ella Belt hosts plutonic bodies of Cambrian to Silurian age (Purdy et al., 2018). This chain of S-type granitic intrusions proceeds subparallel to the Currawinya Fault Zone (the eastward extension of the KNFZ) and bends towards SW to form a line with the Metticka Embayment, the Tenaperra Trough (TT) and the Weena Trough (WT). Additional sequences of probably Silurian intrusive bodies were identified along the Tasman Line (TL) further southwest and near the transition to the Adavale Basin in the east of the study area (**Figure 5.1b**, Holgate, 2005). The Late Carboniferous Big Lake

Suite (BLS, age: 320 +/-10 Ma) represents a second generation of S-type magmatic activity in the study area (Middleton, 1979, 2014; Beardsmore, 2004). These high-heat producing granodiorites are restricted to the NT in South Australia (**Figure 5.1b**), are oriented subparallel to the Ella Belt, and are associated with a prominent geothermal anomaly with corresponding temperatures of about 270 °C at depths of only 4 to 5 km (e.g., Holgate, 2005; Meixner et al., 2012).

5.2.1 Cooper Basin

The CB developed from Late Carboniferous to Middle Triassic and was filled with glacial, fluvio-deltaic and lacustrine sediments (Apak et al., 1997; Draper, 2002; Cook et al., 2013). The fully terrestrial stratigraphy of the CB (**Figure 5.2a**) subdivides into 1) the Late Carboniferous to Late Permian *Gidgealpa Group* (Gp) and 2) the Late Permian to Middle Triassic *Nappamerri Gp*:

1) Sedimentation of the *Gidgealpa Gp* (304-252 Ma) initiated after the Alice Springs Orogeny with the deposition of the terminoglacial Merrimelia Formation during the late Pennsylvanian and continued with the proglacial outwash and fluvial successions of the Tirrawarra Sandstone in the earliest Permian. Terrestrial sedimentation prevailed until the Capitanian and is represented by locally more than 1 km thick alternating (often coal-bearing) fluvio-deltaic, fluvio-lacustrine and floodplain deposits of the Patchawarra Formation, Murteree Shale, Epsilon Formation, Roseneath Shale and Daralingie Formation. The Gidgealpa Gp is interrupted by the Late Permian Daralingie Unconformity (Capitanian to Wuchiapingian, 263-258 Ma), caused by an early pulse of the Hunter-Bowen Orogeny and separates the Daralingie Formation from the coal-bearing meandering fluvial Toolachee Formation (Draper, 2002; Hall et al., 2019; GA, 2020c).
2) The *Nappamerri Gp* (252-237 Ma) initiates with the braided fluvial and floodplain deposits of the Arrabury Formation on the Queensland side and its South Australian equivalents Callamurra, Paning and Wimma Sandstone members. Sandy shales of the meandering fluvial Tinchoo Formation represent the uppermost successions of the Nappamerri Gp. Throughout the remaining Triassic period, the study area was subject to folding, uplift and erosion associated with the final pulse of the Hunter-Bowen Orogeny and represented by the widespread Nappamerri Unconformity (237-200 Ma, Draper, 2002; Carr et al., 2016; Hall et

al., 2019; GA, 2020c). Volcanic material intersected at various wells (e.g., Kappa-1, Lambda-1, Orientos-2, Warnie East-1) provides a broad range of possible ages (e.g., Murray, 1994; Hardman et al., 2019; personal communication with Ian R. Duddy), but most features seem to be of effusive origin and are often chronologically and stratigraphically correlating with the Nappamerri Unconformity.

5.2.2 Eromanga Basin

The evolution of the EB (194-95 Ma) started due to renewed subsidence since the Jurassic. Its stratigraphy (**Figure 5.2b**) divides into four sub-sequences (Hall et al., 2015b).

1) The chronologically isolated Late Triassic *Cuddapan Formation* (210-203 Ma, **Figure 5.2a**) represents the precursor of the extensive sedimentary blanket of the Eromanga sequence and consists of fluvial deposits and erosional remnants. More frequent and basin-wide sedimentation re-established only in the Early Jurassic.
2) The *Early Jurassic to Early Cretaceous fluvio-lacustrine* succession (194-130 Ma) comprises the carbonaceous sandstones of the Poolowanna Formation, the fluvial Hutton Sandstone and the fluvio-lacustrine Birkhead Formation. After the Birkhead Unconformity (160-155 Ma, see Wainman et al., 2018), siliciclastic sedimentation resumes with the Adori Sandstone, Westbourne Formation, Namur Sandstone and fluvio-lacustrine Murta Formation on the Queensland side and their South Australian equivalent, the Algebuckina Sandstone.
3) The shallow marine Cadna-owie Formation introduces the *Early Cretaceous marginal marine to shallow marine* sub-sequence (130-101 Ma). The distinct seismic "C"-horizon marks a short-lived unconformity (Lavering, 1991; Dixon & Hodgkinson, 2011) that coincides with the Tookoonooka structure (125 Ma, Bron, 2010; Bron & Gostin, 2012), a large meteorite impact crater located at the eastern edge of the study area (**Figure 5.1b**). Its crater diameter measures approximately 60 km and the impact was accompanied by a twin, the Talundilly meteorite, which hit the surface about 300 km further north just outside the study area (Bron & Gostin, 2012). Following the Cadna-owie Unconformity (125-120 Ma), the Wyandra Sandstone Member, the shallow marine Wallumbilla, Toolebuc and Allaru formations in Queensland and their South Australian equivalents (Bulldog Shale, Coorikiana and Oodnatta sandstones) formed. This Aptian-Albian

transgressive sequence finishes with the basin-wide marginal marine siltstones of the Mackunda Formation.

4) The fluvial Late Cretaceous *Winton Formation* (101-95 Ma) represents the uppermost sub-sequence of the EB and features the highest sedimentation rate of all formations in the study area. Expressed by the distinct Winton Unconformity (95-62 Ma), the formation was quickly buried and heated, then rapidly uplifted, extensively eroded and deeply weathered throughout the remaining Late Cretaceous period.

5.2.3 Lake Eyre Basin

During the Cainozoic, the endorheic LEB formed, throughout which only occasional sedimentation, frequent ablation and re-deposition of thin fluvial, lacustrine and aeolian sands occurred (Draper, 2002). The Middle Cretaceous Winton Fm remained exposed to weathering at many places.

5.2.4 Petroleum systems

Hydrocarbon production in the study area is concentrated on fault-controlled traps and anticlines (Draper, 2002) around the depocentres of the SW CB (**Figure 5.3a**). In South Australia the Moomba area within the NT, the Patchawarra Trough (PT), the Mettika Embayment as well as the GMI, DNC, Murteree and Dullingari-Wollgolla ridges host abundant oil and gas fields, while there have been only very little discoveries in the deep NT. Producing fields in Queensland are mainly limited to the JNP Ridge and the Durham Downs Anticline. Many small oil and gas fields are located in the TT and along the southeastern basin margin (**Figure 5.3b**). The Arrabury Trough as well as the remaining northern part of the NE CB features only very few scattered hydrocarbon discoveries (**Figure 5.3a**).

The Cooper Basin is predominantly hosting gas, while oil is common in the Eromanga Basin (**Figure 5.3c**, Bowering & Harrison, 1986; Draper, 2002). Main commercial reservoirs including tight gas and dry coal seam gas in the Cooper Basin are located in the Patchawarra and Toolachee formations. The Merrimelia, Epsilon and Daralingie formations as well as the Tirrawarra Sandstone provide additional sporadic reservoirs (Gravestock et al., 1998; Gray & Draper, 2002). While the Winton Formation and most layers of the fluvio-lacustrine succession provide good reservoir properties, the Hutton

and the Hooray sandstones represent the most significant reservoir rocks of the Eromanga Basin (Draper, 2002; Deighton et al., 2003).

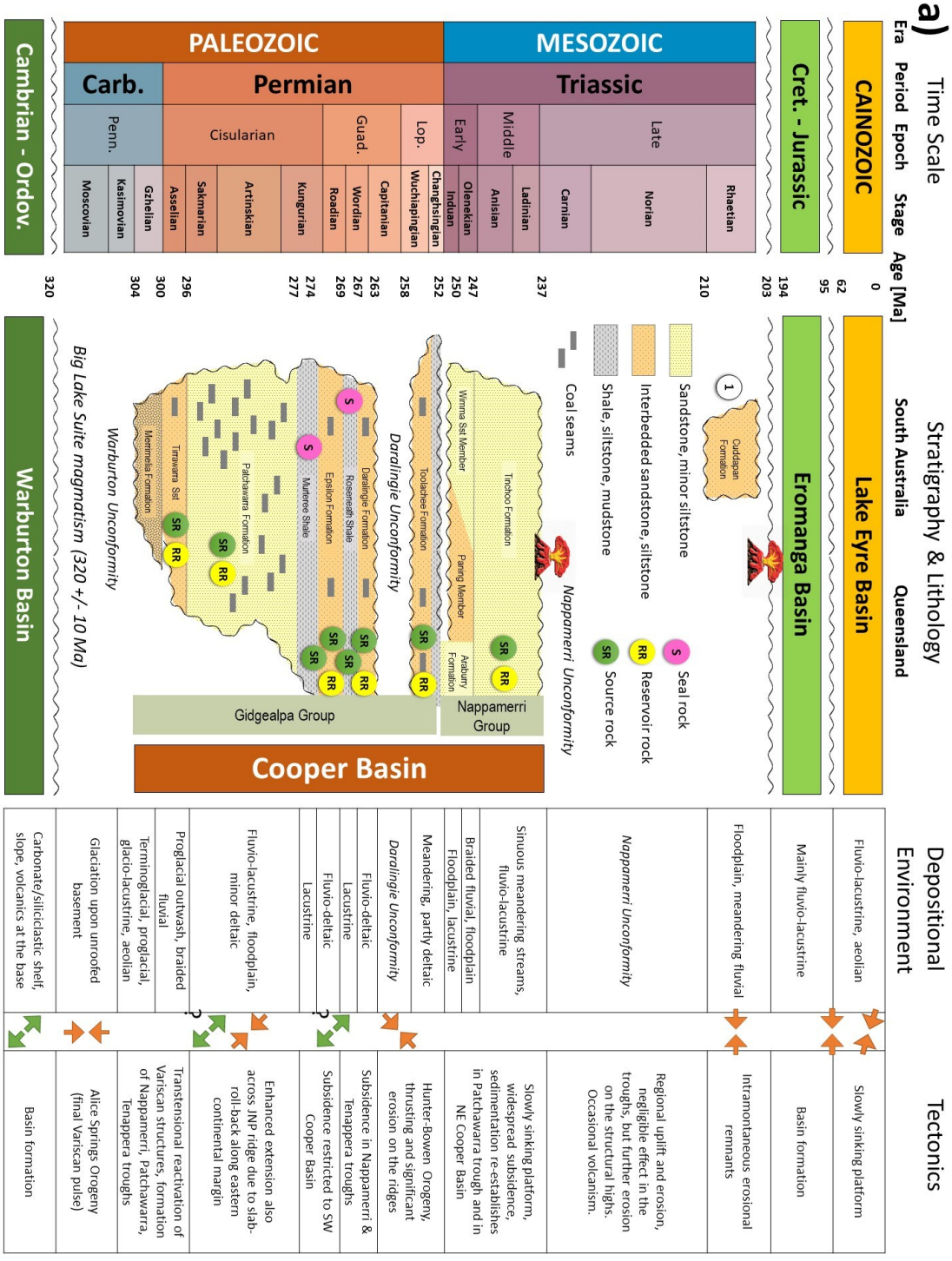

Figure 5.2: Stratigraphic overview, petroleum system elements and tectonics of the study area (modified after AGBA, 2015, Hall et al., 2015b, 2019). a) Stratigraphy of the Cooper Basin. 1 = First Eromanga sub-sequence (Cuddapan Formation, Kinematic arrows (paleo-stress) mainly after Kulikowski et al. (2018).

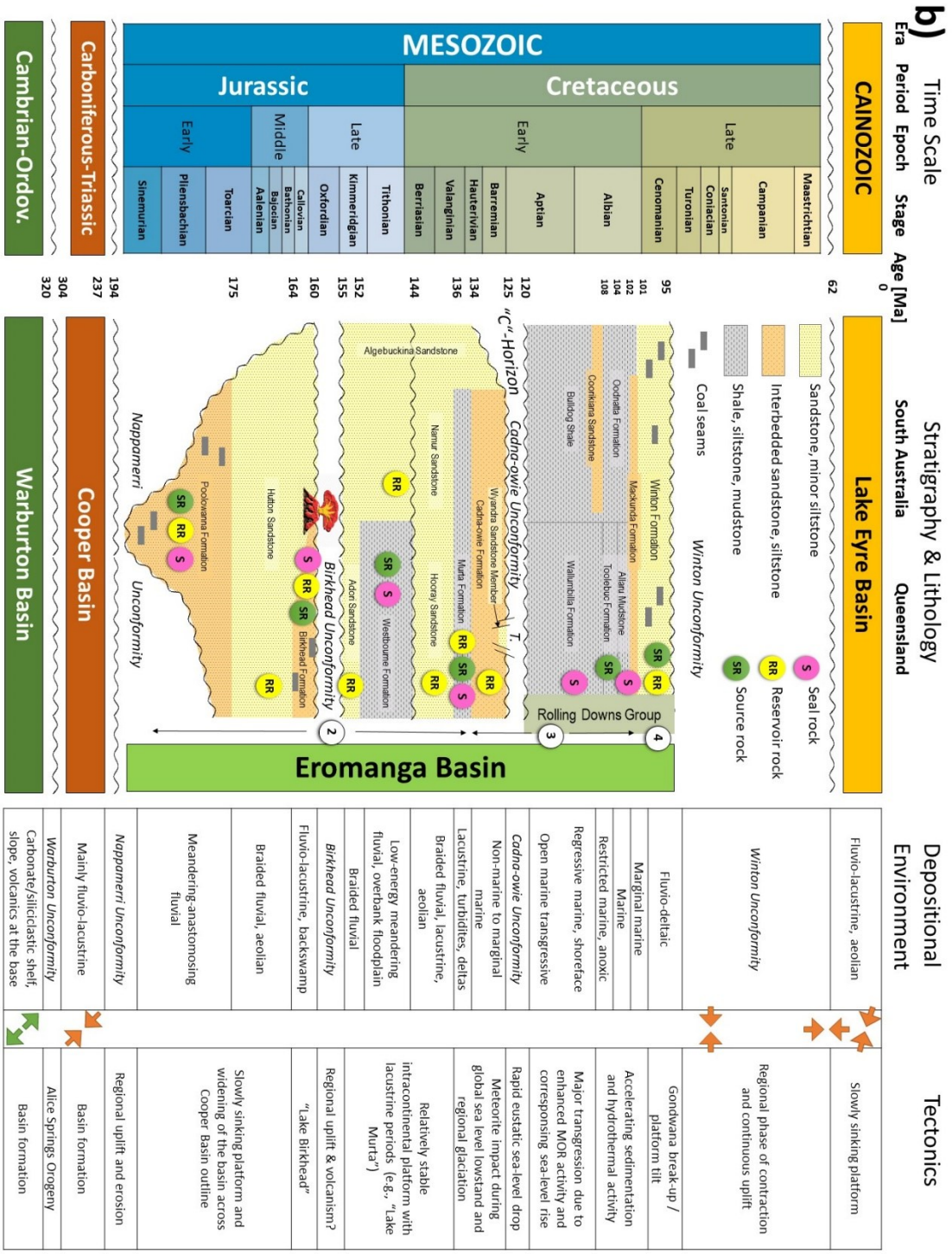

Figure 5.2: Continued. Stratigraphic overview, petroleum system elements and tectonics of the study area (modified after AGBA, 2015, Hall et al., 2015b, 2019). **b)** Stratigraphy of the Central Eromanga Basin. T = Tookoonooka meteorite impact (Bron, 2010), 2 = second Eromanga sub-sequence (fluvio-lacustrine), 3 = third Eromanga sub-sequence (marine), 4 = fourth Eromanga sub-sequence (Winton Formation). Kinematic arrows (paleo-stress) mainly after Kulikowski et al. (2018).

Throughout the Cooper Basin, the Murteree Shale seals the Patchawarra Formation and the Roseneath Shale provides the seal to the Epsilon Formation. The Nappamerri Gp represents the basin-wide seal to the underlying Gidgealpa Gp (Gravestock et al., 1998; Gray & Draper, 2002). The Poolowanna, Birkhead, Westbourne and Murta formations provide local seals and the fine-grained members of the Rolling Downs Gp (Wallumbilla to Mackunda formation) represent the thickest and most effective regional seal of the study area (Deighton et al., 2003).

Trapped hydrocarbons originate exclusively from terrigenous organic matter of fluvio-lacustrine shales, siltstones and coals (Boreham & Hill, 1998; Deighton et al., 2003; Hall et al., 2016a). The majority have been attributed to coals and shales of the Cooper sequence (Draper, 2002), but minor contribution by EB rocks (i.e., Birkhead and Murta formations) and pre-Permian sources is evident (Bowering & Harrison, 1986; Yew & Millis, 1989; Boreham & Summons, 1999).

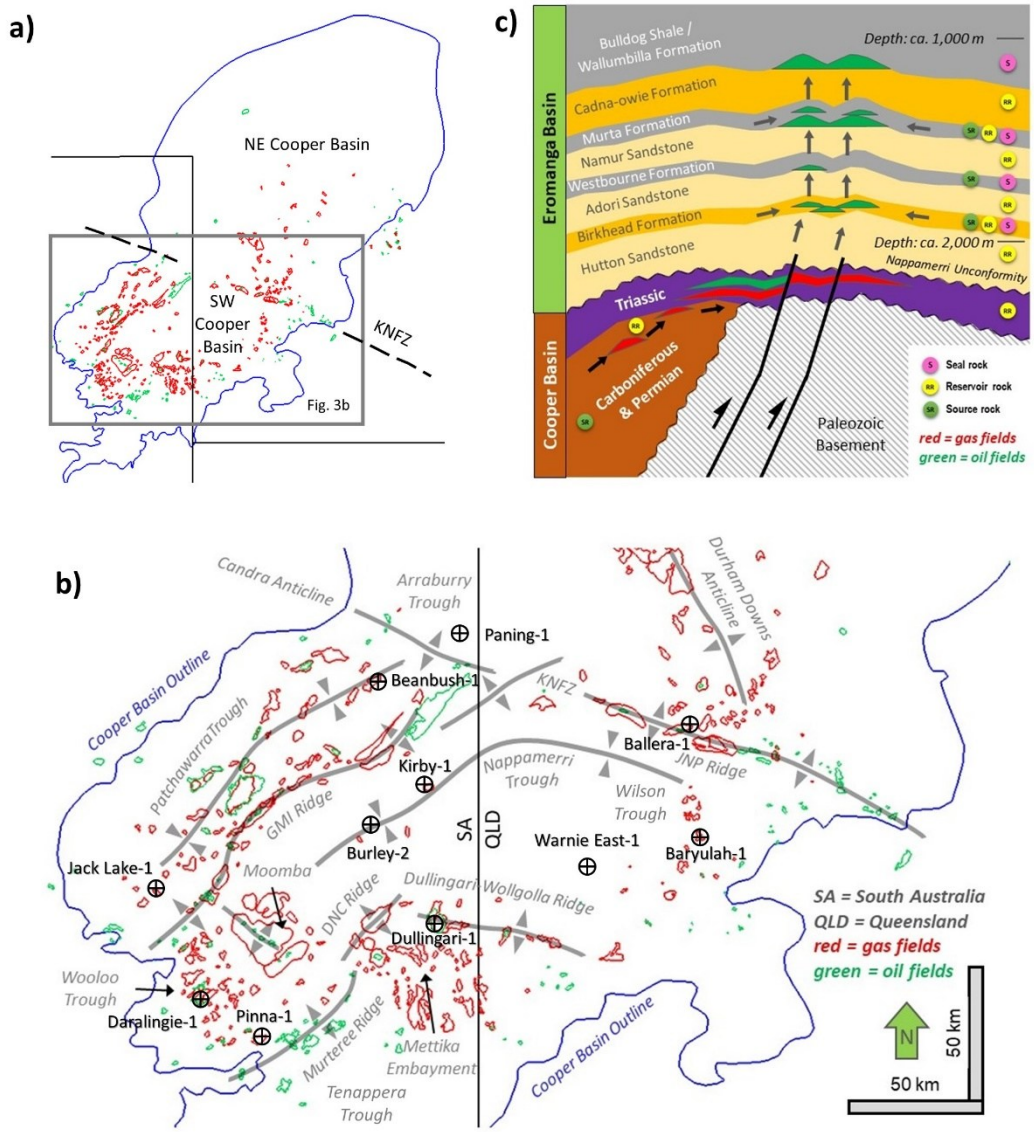

Figure 5.3: Hydrocarbon fields and petroleum system overview of the study area. a) Regional map with outline of the Cooper Basin and distribution of all oil- and gas fields. b) Zoom into the SW Cooper Basin, where oil- and gas fields are abundant and are mainly associated with anticlines along basement ridges (compare Figure 5.1b). DNC = Della-Nappacoongee, GMI = Gidgealpa-Merrimelia-Innamincka, JNP = Jackson-Naccowlah-Pepita, KNFZ = Karmona-Naccowlah Fault Zone. c) Schematic petroleum system overview showing distribution of hydrocarbon fields and possible migration into anticlinal and fault-related traps (modified after Bowering & Harrison, 1986).

5.3 Materials and methods

Petroleum well data (well headers, formation tops, completion reports, etc.) and corresponding calibration data from public domain data bases (e.g., Holgate & Gerner, 2010; GA, 2017b; PEPS-SA, 2018; QPED, 2020) serve as input for 1D petroleum system models. Heat flow maps and source rock maturation maps were created based on

integrating calibrated 1D models with the available regional-scale 3D petroleum system model (Hall & Palu, 2016). The geometry is based on 20 depths maps and includes an interpretation of the pre-Permian basement and the digital elevation model (DEM, after Whiteway, 2009). Layer thickness maps derived from this model and complementary literature serve as additional data for analyzing the basin history.

5.3.1 Stratigraphic input

Formation tops from public domain data bases and corresponding horizons of the 3D model were assigned with top and bottom layer ages based on combined chronostratigraphic information from the Geoscience Australia Stratigraphic Units Database (GA, 2020c) and supporting literature (Moussavi-Harami, 1996; Alexander et al., 1998, 2005; NGMA, 2001; DMITRE, 2001, 2009; Gray et al., 2002; Mavromatidis & Hillis, 2005; Turner et al., 2009; Radke et al., 2012; McKellar, 2013; AGBA, 2015; Hall et al., 2015b, 2016b, 2019; Wainman et al., 2018; Alley, 2019; plus unpublished results from Moussavi-Harami used in Hall et al., 2019; see **Table 5.1**). Whenever possible and useful, the stratigraphic nomenclature of Queensland was used as a standard.

Selected layers were split by age or based on thickness to obtain additional horizons for the 3D model. The uppermost layer (constrained by the surface topography and the Top Winton Fm) was subdivided into Quaternary, Eyre Fm and Namba Fm. Similarly, the Toolebuc layer was subdivided into Toolebuc Fm and Wallumbilla Fm; the Murta layer was split into Murta Fm and Namur Sst, the Nappamerri Gp was subdivided into Tinchoo Fm and Arrabury Fm; and the glacial sediments were subdivided into Tirrawarra Fm and Merrimelia Fm. In total, 37 events (numbered from bottom (0 = pre-Permian basement) to top (36 = Quaternary) were defined, thereof 28 sedimentary layers (deposition events) and 8 unconformities (defined as erosion or hiatus).

Table 5.1: Overview of assigned layers and their ages used as input for the numerical models (modified after Hall et al., 2019).

Province	Short name	Seismic horizon	Top age [Ma]	Horizon / top name	Average preserved thickness / amount of erosion [m]	Event type	Key references
Lake Eyre Basin	(36)	DEM	0	Surface / Quaternary	~ 35	Deposition	Whiteway (2009)
	(35)		2	Namba Unconformity	< 50	Erosion	Moussavi-Harami (unpublished results); Radke et al. (2012)
	(34)		*12*	Namba Formation	~ 90	Deposition	Alley (1998), Moussavi-Harami (unpublished results); Radke et al. (2012)
	(33)		*24*	Eyre Unconformity	< 50	Erosion	Moussavi-Harami (unpublished results); Radke et al. (2012)
	(32)		*42*	Eyre Formation	~ 60	Deposition	Alley (1998), Moussavi-Harami (unpublished results); Radke et al. (2012)
Eromanga Basin	(31)		*62*	Winton Unconformity	100 -1,200	Erosion	Moussavi-Harami (unpublished results); Mavromatidis & Hillis (2005)
	(30)	A	95	Winton Formation	~ 530	Deposition	DMITRE (2001)
	(29)		101	Mackunda Formation	~ 135	Deposition	Gray et al. (2002); Radke et al. (2012)
	(28)		102	Allaru Mudstone	~ 240	Deposition	Gray et al. (2002); Alexander et al. (2006); Radke et al. (2012)
	(27)		104	Toolebuc Formation or Oodnadatta Format	~ 80	Deposition	Gray et al. (2002); Radke et al. (2012)
	(26)		*108*	Wallumbilla Formation / Bulldog Shale	~ 235	Deposition	Hall et al. (2019)
	(25)		*120*	Cadna-owie Unconformity	n.d.	Hiatus	Burger & Senior (1979); Bron et al. (2012); Gostin & Therriault (1997); Turtle et al. (2003)
	(24)	C	125	Cadna-owie Formation, including Wyandra Sst	~ 70	Deposition	NGMA (2001); Gray et al. (2002); DMITRE (2009); Radke et al. (2012); Lavering (1991)
	(23)		134	Murta Formation, Hooray Sst, or Algebuckina Sst	~ 20	Deposition	Gray et al. (2002); Radke et al. (2012)
	(22)		*136*	Namur Sst, incl. McKinlay Mbr	*~ 75*	Deposition	*H*all et al. (2019)
	(21)		144	Westbourne Formation	*~ 85*	Deposition	Gray et al. (2002); Radke et al. (2012)
	(20)		152	Adori Sandstone	*~ 75*	Deposition	Gray et al. (2002); Alexander et al. (2006)
	(19)		155	Birkhead Unconformity	*n.d.*	Hiatus	Wainman et al. (2018), Turner et al. (2009), Radke et al. (2012)
	(18)		160	Birkhead Formation	~ 80	Deposition	Gray et al. (2002); Radke et al. (2012)
	(17)	H	164	Hutton Sst	~ 375	Deposition	DMITRE (2001); Gray et al. (2002); Radke et al. (2012)
	(16)		185	Poolowanna Fm	n.d.	Deposition	*H*all et al. (2019)
	(15)		194	Cuddapan Unconformity	n.d.	Hiatus	Moussavi-Harami (unpublished results)
	(14)		*203*	Cuddapan Formation	n.d.	Deposition	Hall et al. (2015b, 2019)

Table 5.1 (continued):

Province	Short name	Seismic horizon	Top age [Ma]	Horizon / top name	Average preserved thickness / amount of erosion [m]	Event type	Key references
Cooper Basin	(13)		*210*	Nappamerri Unconformity	< 180	Erosion	Moussavi-Harami (unpublished results); McKellar (2013); Hall et al. (2015b)
	(12)	N	237	Tinchoo Fm / Top Nappamerri Gp	~ 125	Deposition	DMITRE (2001); Hall et al. (2015b)
	(11)		247	Arrabury Fm	~ 190	Deposition	DMITRE (2001); Hall et al. (2015b)
	(10)	P	252	Toolachee Formation / Top Permian	~ 190	Deposition	NGMA (2001); DMITRE (2009); Hall et al. (2015b,2016b)
	(9)		258	Daralingie Unconformity	75 - 350	Erosion	Moussavi-Harami (unpublished results); Hall et al. (2015b)
	(8)		263	Daralingie Formation	~ 80	Deposition	DMITRE (2001); Hall et al. (2015b,2016b)
	(7)		267	Roseneath Shale	~ 120	Deposition	Hall et al. (2015b, 2016b)
	(6)		269	Epsilon Formation	~ 130	Deposition	Hall et al. (2015b, 2016b)
	(5)		274	Murteree Shale	~ 80	Deposition	Hall et al. (2015b, 2016b)
	(4)		277	Patchawarra Formation	~ 420	Deposition	DMITRE (2001); Hall et al. (2015b,2016b)
	(3)		296	Tirrawarra Sst	~ 75	Deposition	DMITRE (2001); Hall et al. (2015b, 2016b)
	(2)		300	Merrimelia Formation	~ 300	Deposition	DMITRE (2001); Hall et al. (2015b, 2016b)
WB / Adavale Basin	(1)		304	Warburton Unconformity	n.d.	Hiatus	
	(0)	Z	320	Top pre-Permian "basement", equivalent in age to the Devonian Adavale Basin and the Big Lake Suite granodiorites	n.d.		NGMA (2001); DMITRE (2009); Hall et al. (2015b,2016b)

For the 3D model, only the erosion map for the Winton Unconformity (from Hall & Palu, 2016) was assigned, since all other unconformities are based on either contradicting information or the amount of eroded thickness is negligible. Only for selected 1D models (e.g. Burley-2, Warnie East-1), the Namba, Eyre, Nappamerri and Daralingie unconformities were assigned with relative small values. Nevertheless, the remaining unconformities were assigned as hiatus events, which serve as placeholders to allow easy changes of the input during future modelling.

If available, facies information for the layers of the 1D models was taken from interpreted electro-facies (Sun & Camac, 2004; see Hall et al., 2016a, 2016b) and, if required, complemented with additional data from well completion reports and the chronostratigraphic chart. A simplified facies assignment with standard or mixed lithologies was used for the 3D model. Thermal conductivity values for each layer (1D and 3D) were customized based on existing measurements (from Beardsmore, 2004, **Table 5.2**).

Table 5.2: Overview of main lithologies, corresponding thermal conductivity values (from Beardsmore, 2004) and assignment of petroleum system elements.

Province	Short name	Top age [Ma]	Bottom age [Ma]	Layer name (South Australia equivalents when different to Queensland)	Dominant rock type	Thermal conductivity at 20 °C [WmK]	Assigned PSE
Lake Eyre Basin	(35)	0	2	Quaternary	Sandstone	3.95 (standard sandstone)	Overburden
	(33)	12	24	Namba Fm	Sandstone	2.64 +/- 0.63	Overburden
	(32)	42	62	Eyre Fm	Sandstone	2.19 +/- 0.65	Overburden
Eromanga Basin	(30)	95	101	Winton Fm	Sandstone	2.01 +/- 0.53	Overburden
	(29)	101	102	Mackunda Fm	Siltstone	2.93 +/- 0.56	Seal rock
	(28)	102	104	Allaru Mdst (Oodnadatta Fm)	Shale	1.95 +/- 0.13	Seal rock
	(27)	104	108	Toolebuc Fm (Coorikiana Sst)	Shale	2.54 +/- 0.52 (2.65 +/- 0.66)	Seal rock
	(26)	108	120	Wallumbilla Fm (Bulldog Shale)	Shale	2.10 +/- 0.13 (2.72 +/- 0.64)	Seal rock
	(24)	125	134	Cadna-owie Fm, incl. Wyandra Sst	Siltstone	2.08 +/- 0.18	Reservoir
	(23)	134	136	Murta Fm, Hooray Sst (Algebuckina Sst)	Siltstone	4.24 +/- 0.02	Source rock
	(22)	136	144	Namur Sst, incl. McKinlay Mbr	Sandstone	3.94 +/- 0.57	Reservoir
	(21)	144	152	Westbourne Fm	Shale	4.00 +/- 0.60	Seal rock
	(20)	152	155	Adori Sst	Sandstone	4.12 +/- 0.56	Reservoir
	(18)	160	164	Birkhead Fm	Siltstone	4.85 +/- 1.06	Source rock
	(17)	164	185	Hutton Sst	Sandstone	5.00 +/- 0.84	Reservoir
	(16)	185	194	Poolowanna Fm (only in 1D)	Sandstone	2.99 +/- 0.69	Source rock
	(14)	203	210	Cuddapan Fm (only in 1D)	Sandy shale	taken from Poolowanna Fm	Reservoir
Cooper Basin	(12)	237	247	Tinchoo Fm	Sandy shale	2.30 +/- 0.24	Reservoir
	(11)	247	252	Arrabury Fm	Siltstone / sand	2.30 +/- 0.24	Reservoir
	(10)	252	258	Toolachee Fm	Siltstone / shale	1.29 +/- 0.36	Source rock
	(8)	263	267	Daralingie Fm	Fine sandstone	1.64 +/- 0.31	Source rock
	(7)	267	269	Roseneath Shale	Siltstone / shale	2.45 +/- 0.15	Source rock
	(6)	269	274	Epsilon Fm	Fine sandstone	1.55 +/- 0.29	Source rock
	(5)	274	277	Murteree Shale	Siltstone / shale	2.60 +/- 0.13	Source rock
	(4)	277	296	Patchawarra Fm	Sand & coal	1.61 +/- 0.31	Source rock
	(3)	296	300	Tirrawarra Sst	Fine sandstone	4.35 +/- 0.59	Reservoir
	(2)	300	304	Merrimelia Fm	Conglomerate	4.01 +/- 1.47	Reservoir
WB	(0)	320	n.d.	Paleozoic Basement	Gneiss	2.70 (standard)	Underburden

5.3.2 Boundary conditions

Paleo-water depth (PWD, **Figure 5.4a**) trends (modified after Deighton & Hill, 1998; Deighton et al., 2003) were used to constrain the sediment-water interface temperature (SWIT, **Figure 5.4b**), which represents the upper thermal boundary. Automatically calculated values (after Wygrala, 1989; southern hemisphere, Australia, 27 °) were manually adjusted considering the present-day annual average surface temperature of 22-24 °C (BOM, 2015) and the Antarctic episode of glaciation during Early Cretaceous (Ladant & Donnadieu, 2016; Alley et al., 2019) with estimated annual average temperature of 5 °C from 135 Ma to 115 Ma.

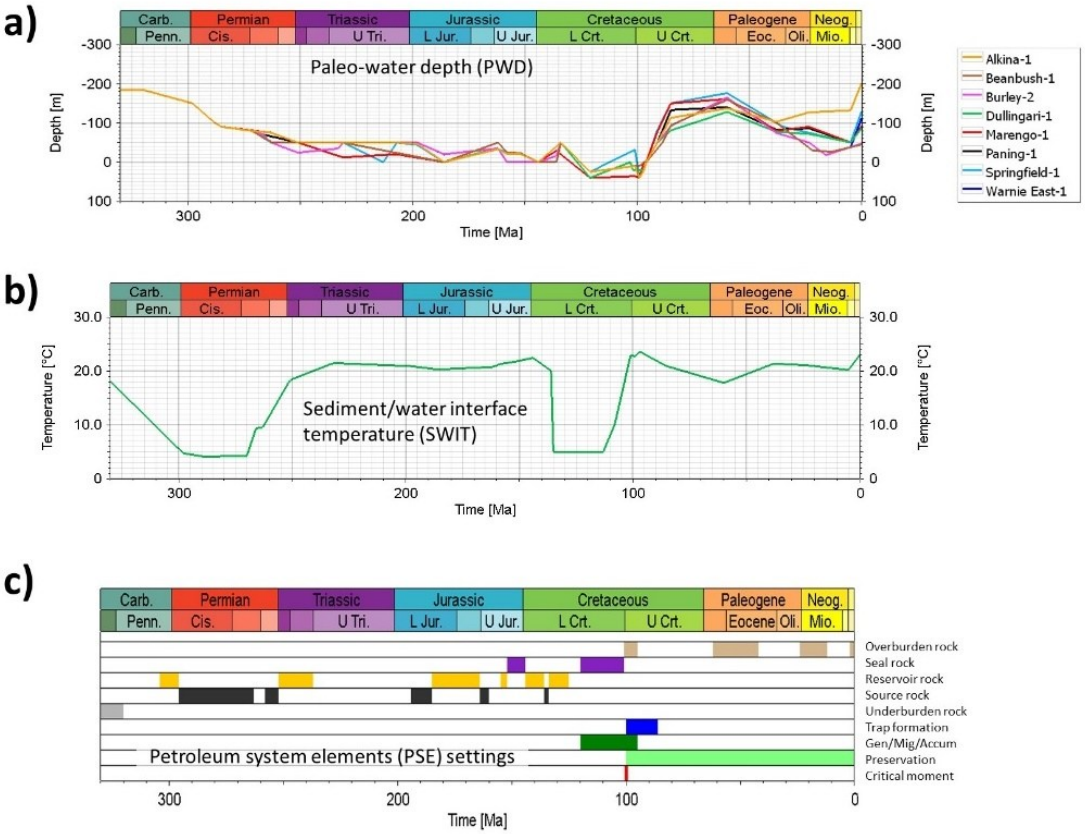

Figure 5.4: Upper thermal boundary conditions and petroleum system elements (PSE) chart. a) Paleo-water depth (PWD) applied in this study (modified after Deighton & Hill, 1998 and Deighton et al., 2003). b) Sediment/water interface temperature (SWIT) applied in this study based on Wygrala (1989), Southern hemisphere, Australia, 27 °, with glacial period between 135 and 115 Ma (modified after Heather et al., 1996; Ladant & Donnadieu, 2016; Alley et al., 2019). c) Petroleum system elements (PSE) chart.

5.3.3 Petroleum system settings and source rock assignment

Several formations simultaneously represent source as well as reservoir rocks (see **Figure 5.2**) and petroleum generation potential can be highly variable (see Hall et al., 2016a, 2019 and references therein). **Table 5.2** includes the simplified assignment for the petroleum system elements (PSE) used in this study. The PSE chart in **Figure 5.4c** also shows the timing of related processes such as petroleum generation, migration and accumulation, critical moment, trap formation and preservation, which will be further examined in the results and discussion sections. Assigned source rock properties (kinetic models, TOC content, and hydrogen index based on Pepper & Dodd, 1995; Pepper & Corvi, 1995a, 1995b, Gray & Draper, 2002; Michaelsen & McKirdy, 2001, 2006; Hall et al., 2016a; plus complementary data from **Chapter 4**) are summarized in **Table 5.3**.

Table 5.3: Overview of source rock properties and assignment of kinetic models. Values from Hall et al. (2016a) and references therein. [1)]TOC and HI values of Birkhead and Murta formations complemented by the results of Chapter 4).

Province	Source rock formation	Kerogen type	Assigned kinetic model	Reported avg. TOC [%]	Assigned TOC [%]	Reported avg. HI [mg HC/g rock]	Assigned HI [mg HC/g rock]
Eromanga Basin	Toolebuc Fm	-	not assigned in this study	-	-	-	-
	Murta Fm[1)]	II/III	Pepper & Corvi (1995a), TII(B)	0.6 - 2.2	1.7	150	150
	Westbourne Fm	-	not assigned in this study	-	-	-	-
	Birkhead Fm[1)]	II/III, I/III	Pepper & Corvi (1995a), TII(B)	2.5 - 3.7	3.0	300	300
	Poolowanna Fm	II, II/III	Pepper & Corvi (1995a), TII(B)	0.6 - 17.9	15	> 250	250
Cooper Basin	Toolachee Fm	II/III, III	Pepper & Corvi (1995a), TIIIH(DE)	21	21	190	190
	Daralingie Fm	II/III, III	Pepper & Corvi (1995a), TIIIH(DE)	18.9	18.9	200	200
	Roseneath Sh	III	Pepper & Corvi (1995a), TIII-IV(F)	6.4	6.4	130	130
	Epsilon Fm	II/III, III	Pepper & Corvi (1995a), TIIIH(DE)	26	26	210	210
	Murteree Sh	III	Pepper & Corvi (1995a), TIII-IV(F)	5.6	5.6	140	140
	Patchawarra Fm	II/III, III	Pepper & Corvi (1995a), TIIIH(DE)	24.7	24.7	216	216

5.3.4 Heat flow and thermal modelling

Bottom hole temperature (BHT) (Holgate & Gerner, 2010) and vitrinite reflectance data (GA, 2017b; PEPS-SA, 2018; QPED, 2020) were used for thermal calibration of the 1D

petroleum system models based on the Easy%RoDL algorithm (Burnham, 2019). Further, thermal history was constrained based on existing information from literature (e.g., Middleton et al., 2014; Hall et al., 2015b, 2016a, 2016b and references therein).

5.4 Results

In the following, an overview is given about the simulation results focusing on reconstructed subsidence history and calibrated thermal history. Although other thermal history scenarios are possible and may also lead to good calibration matches, only the results of the best match are summarized here. Alternative scenarios and other factors affecting the thermal history of the study area are debated in the discussion section below.

5.4.1 Calibration of bottom hole temperature and thermal maturity

Table 5.4 shows the best matching heat flow trends as the calibration results for eight representative 1D models. The trends reveal a background heat flow that is varying between 60 to 80 mW/m^2 throughout the study area. Area-wide elevated values occurred between 125 Ma and 85 Ma and peaked at 99.5 Ma with local maxima reaching from 85 to 150 mW/m^2. A renewed heat flow increase since 2 Ma can be observed with locally varying intensity between 62 and 110 mW/m^2. The calibrated trends were used to create heat flow maps for each time step and the resulting heat flow maps were assigned to the 3D model.

The calibration results of four representative South Australian wells (Beanbush-1, Burley-2, Dullingari-1, and Paning-1) are displayed in **Figure 5.5a-d**. All four wells are located in the SW CB area. The subsidence history plots show the temperature variation with depth and time. The indicated 100 °C isolines serve as a rough orientation for the onset of the oil generation window and is generally located at depths of around 2 km. During the Early Cretaceous glaciation, the temperature gradient was temporarily lower due to low surface temperatures and the 100 °C threshold dropped below 2 km, only to quickly ascend to shallow depths of only 800–1,200 m during the Middle Cretaceous. The regional subsurface temperature maximum in the Middle Cretaceous was the result of the fast subsidence in combination with simultaneously increasing basal heat flow. Regional uplift and cooling followed during the Upper Cretaceous and resulted in a rather stable temperature distribution throughout the Cainozoic.

Table 5.4: Overview of assigned basal heat flow trends for the eight selected calibration wells. Regional Middle Cretaceous peak (99.5 Ma) in bold letters.

Age [Ma]	Alkina-1	Beanbush-1	Burley-2	Dullingari-1	Marengo-1	Paning-1	Springfield-1	Warnie East-1
0.00	82.00	62.00	110.00	75.00	87.00	66.00	78.00	85.00
2.00	60.00	60.00	60.00	75.00	65.00	60.00	70.00	60.00
80.00	60.00	60.00	60.00	75.00	65.00	60.00	70.00	60.00
85.00	62.00	61.00	61.00	78.00	68.00	62.00	72.00	62.00
90.00	64.00	63.00	62.00	81.00	72.00	65.00	76.00	64.00
91.00	67.00	64.00	63.00	82.00	74.00	68.00	78.00	66.00
93.00	71.00	66.00	70.00	83.00	79.00	71.00	79.00	68.00
97.00	80.00	70.00	78.00	85.00	90.00	78.00	81.00	72.00
98.00	85.00	75.00	95.00	86.00	98.00	80.00	82.00	75.00
98.50	90.00	80.00	120.00	87.00	105.00	82.00	83.00	80.00
99.00	95.00	85.00	145.00	88.00	115.00	85.00	84.00	85.00
99.50	**105.00**	**90.00**	**150.00**	**90.00**	**120.00**	**90.00**	**85.00**	**90.00**
100.50	95.00	85.00	95.00	85.00	85.00	80.00	80.00	85.00
125.00	65.00	65.00	65.00	77.00	70.00	60.00	72.00	65.00
135.00	60.00	60.00	60.00	75.00	65.00	60.00	70.00	60.00
200.00	60.00	60.00	60.00	75.00	65.00	60.00	70.00	60.00
237.00	60.00	60.00	60.00	75.00	65.00	60.00	70.00	60.00
240.00	60.00	60.00	60.00	75.00	65.00	60.00	70.00	60.00
290.00	60.00	60.00	60.00	75.00	65.00	60.00	70.00	60.00
310.00	60.00	60.00	60.00	75.00	65.00	60.00	70.00	60.00
330.00	60.00	60.00	60.00	75.00	65.00	60.00	70.00	60.00

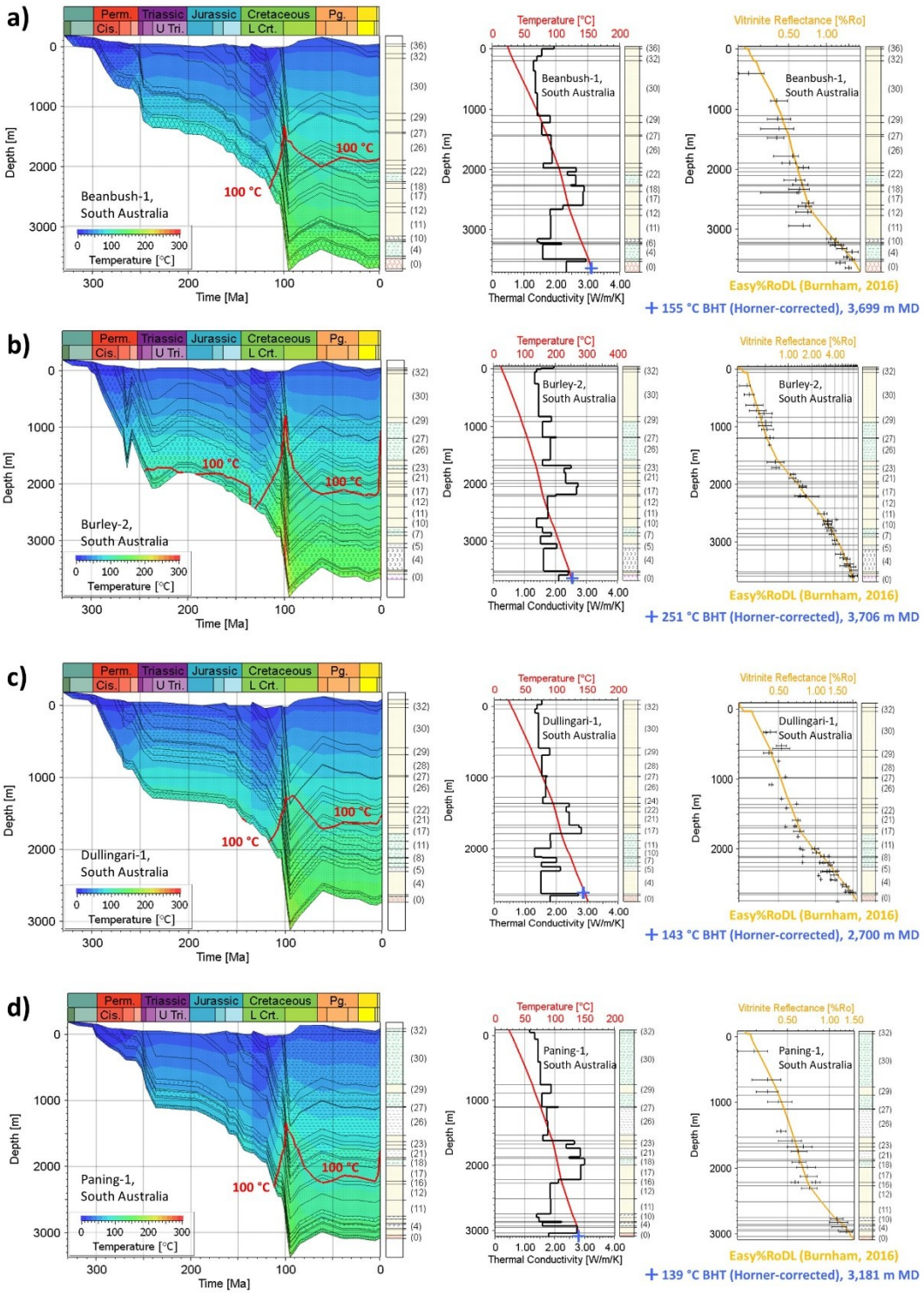

Figure 5.5: Total subsidence with temperature evolution (left), calibrated present-day temperature based on Horner-corrected bottom hole temperatures (BHT) and calibrated thermal maturity of four selected calibration wells located in South Australia. a) Beanbush-1, b) Burley-2, c) Dullingari-1, d) Paning-1. Note different scales of x-axis.

The present-day temperature calibration is based on Horner-corrected BHT measurements (values are given in **Figure 5.5** and **Figure 5.6**) and generally matches with present-day heat flow values above the global average (60 mW/m^2). Thermal conductivity values shown in the temperature/depth plots (in **Figure 5.5** and **Figure 5.6**) are the calculated results based on the input values (after Beardsmore, 2004, see **Table 5.2**), the assigned rock type (composition, initial porosity, etc.), the subsidence history (compaction) and the current temperature at each individual well location. While at Beanbush-1, Dullingari-1 and Paning-1 the recent heat flow increase since 2 Ma is moderate (see **Table 5.4**), at Burley-2 a present-day heat flow of 110 mW/m^2 was applied to match the exceptionally high BHT of about 251 °C at a comparably shallow depth of only 3,706 m (**Figure 5.5b**).

Vitrinite reflectance profiles, can be subdivided into three sections. The upper (youngest) section is represented by the events 22 to 36 (Namur Sst until Quaternary, compare **Table 5.1**) and mainly features values of 0.2–0.7 %Ro along a steep gradient. In the middle section (events 11 to 21, Nappamerri Gp to Westbourne Fm), values are mostly in a range between 0.7 and 1.0 %Ro or locally scattering around 1.0 %Ro. The lower (oldest) section, represented by events 0 to 10 (basement to Toolachee Fm), shows a less steep maturity gradient with values between 1.0 and 1.5 %Ro and has locally (e.g., Burley-2) even reached the dry gas window (vitrinite reflectance > 2.0 %Ro). For Burley-2 a paleo-heat flow peak of 150 mW/m^2 in the Middle Cretaceous (see **Table 5.4**) is required to match the overmature lower section (3.0–6.0 %Ro, see **Figure 5.5b**). The thermal maturity profiles of the other three South Australian wells can be matched with a Middle Cretaceous heat flow peak of 90 mW/m^2.

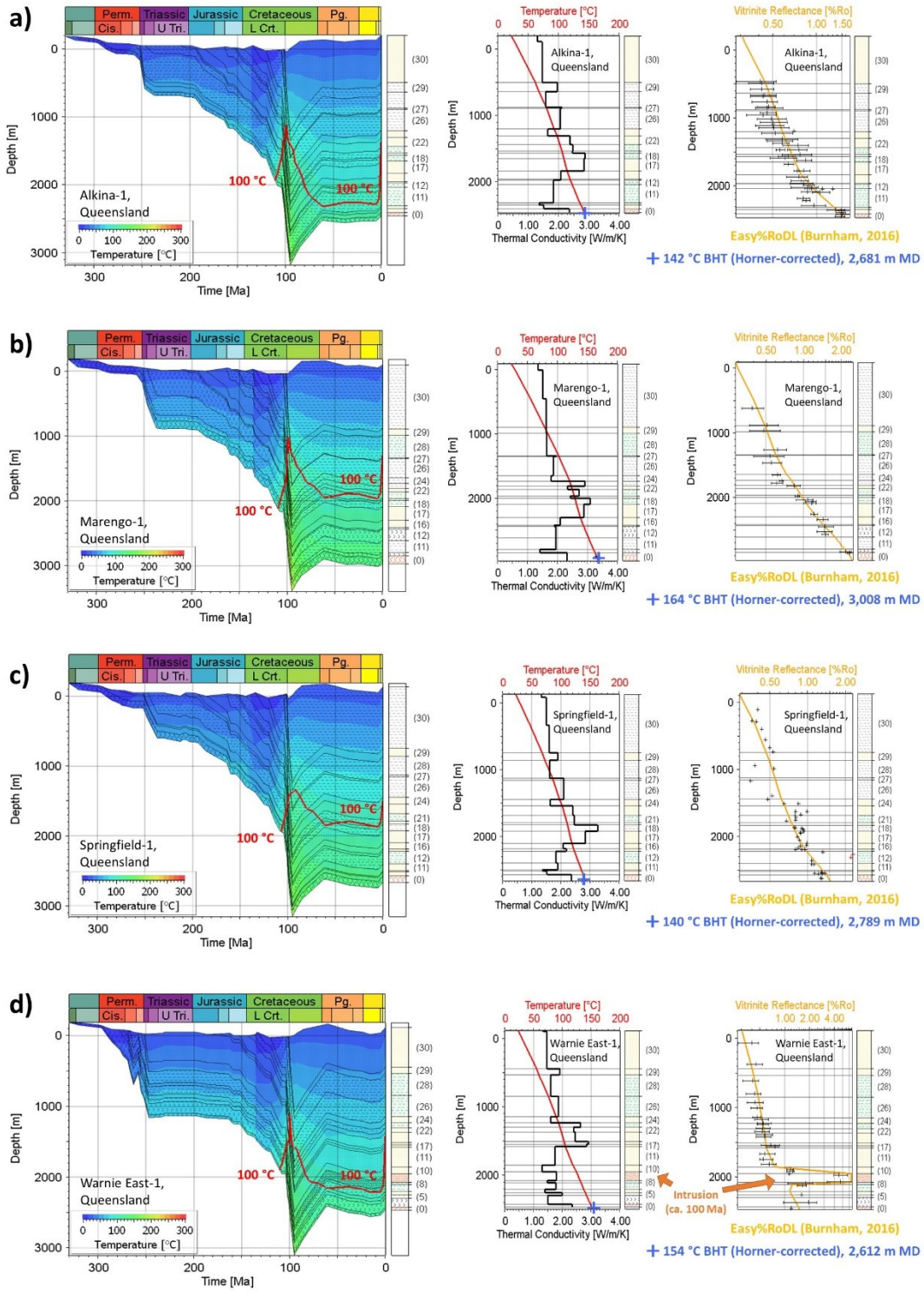

Figure 5.6: Total subsidence with temperature evolution (left), calibrated present-day temperature based on Horner-corrected bottom hole temperatures (BHT) and calibrated thermal maturity of four selected calibration wells located in Queensland. a) Alkina-1, b) Marengo-1, c) Springfield-1, d) Warnie East-1. Note different scales of x-axis.

Figure 5.6a-d shows the calibration results of four representative wells (Alkina-1, Marengo-1, Springfield-1, Warnie East-1) located on the Queensland side of the study area. Except Warnie East-1, these wells are located in the high NE domain of the CB. In comparison with the South Australian wells (**Figure 5.5**), the subsidence history is slightly different in two ways. Primarily, because in the deeper SW domain continuous and significant sedimentation already occurred during the Permian (see **Figure 5.5**) and substantial sedimentation and subsidence in the NE domain started only in the Early Triassic (**Figure 5.6**). Secondly, the amounts of Late Cretaceous uplift and erosion are generally higher in the NE domain (compare **Figure 5.5** and **Figure 5.6**). However, the variation of the 100 °C threshold over time and the general thermal history is very similar throughout the entire study area.

Present-day temperatures of the wells drilled in Queensland scatter around 150 °C at depths of 2,500 m with associated present-day basal heat flow of 78 to 85 mW/m^2 (see **Table 5.4**). Alkina-1 and Marengo-1 require a relative high Middle Cretaceous heat flow peak of 105 mW/m^2 and 120 mW/m^2 to match their thermal maturity profiles, respectively (compare **Table 5.4** and **Figure 5.6a** and **Figure 5.6b**).

The lower section of the maturity profiles of Springfield-1 (**Figure 5.6c**) and Warnie East-1 (**Figure 5.6d**) are matching with rather low Middle Cretaceous heat flow peaks of 85 mW/m^2 and 90 mW/m^2, respectively. Further, both wells feature extraordinary high thermal maturity values within a narrow part of their lower sections. The cause for the thermal maturity increase of the Tinchoo Fm at Springfield-1 could be due to erroneous measurements or the well just missed a nearby intrusion body (two red calibration points in **Figure 5.6c**). Actually, at Warnie East-1 a basaltic sill was intersected, which is stratigraphically correlating with the Daralingie Fm and was dated 100 +/-6 Ma based on K-Ar pyroxene age (**Figure 5.6d**, personal communication with Ian R. Duddy). To match the thermal maturity calibration with the outliers at Warnie East-1 a simple increase of the paleo-heat flow is inapplicable. An intrusion model with facies replacement (basalt vs. sandstone within the Daralingie Fm), associated with short-term temperature increase (> 400 °C), fast cooling and an assigned intrusion age of 100 Ma delivers the best match for this exceptional borehole.

5.4.2 Tectonic subsidence and sedimentation rate

A collection of time plots (**Figure 5.7**) shows calculated tectonic subsidence, sedimentation rate and thermal evolution and reveals some correlations between these parameters.

Tectonic subsidence (**Figure 5.7a**) initiated in the Early Permian throughout the SW domain and started to extend over the entire study area during the Late Permian to Early Triassic. From Upper Triassic to Upper Cretaceous, all wells follow very similar trends and reach their maximum tectonic subsidence after deposition of the Winton Fm (95 Ma). The NT (represented by Burley-2) generally features the fastest and strongest tectonic subsidence during the Palaeozoic and Mesozoic, while Alkina-1 and Warnie East-1 exhibit the strongest uplift in the Cainozoic.

Sedimentation rates of Alkina-1 and Burley-2 are displayed in **Figure 5.7b**. Both wells show strong variations during the Cooper sequence, but share a very similar development during the Eromanga sequence. The most remarkable event is the deposition of the Mackunda and Winton formations during the Middle Cretaceous with high sedimentation rates of up to 200 m/Ma.

5.4.3 Evolution of basal heat flow and temperature

The extraordinary "depositional event" around 100 Ma ago coincides with elevated temperature throughout the basin, which was enhanced by a short-lived "hydrothermal event" (compare **Figure 5.7c** and **Table 5.4**). The intensity of the Middle Cretaceous hydrothermal event (up to 150 mW/m^2) most likely provided enough thermal energy to overprint all past thermal events, which complicates pre-Cretaceous thermal history reconstruction. A renewed relatively fast heat flow increase (up to 110 mW/m^2; peak I in **Figure 5.7c**) is currently developing since the Quaternary, but still shows a lower intensity compared to the Middle Cretaceous hydrothermal event (peak II). The relevance of possible older heat flow peaks (III-VII, **Figure 5.7c**) is debated in the discussion section.

While the calculated temperature gradient lies between 25 and 42 °C/km throughout most of the geological history, it locally doubled at peak I (52 °C/km at Burley-2) and even tripled at peak II (74 °C/km at Burley-2; **Figure 5.7d**). The corresponding heating rates were rather constant and rarely exceeded 10 °C/Ma (**Figure 5.7e**), except for the Middle Cretaceous hydrothermal event, during which the temperature suddenly increased by locally 100 °C/Ma between 100.5 and 99.5 Ma (**Figure 5.7f**). The subsequent cooling

rates were even stronger (up to 150 °C/Ma at Burley-2) between 99.5 Ma and 98.5 Ma before the temperature slowly equilibrated again. Resulting temperature evolution at the basement/sediment interface (**Figure 5.7g**) shows two plateaus and two main peaks. After a slow and steady increase throughout the Permo-Triassic, the first plateau lasts from Early Triassic until Early Cretaceous with corresponding temperatures ranging between 50 and 100 °C. The second plateau features temperatures between 100 °C and 150 °C from Late Cretaceous until Quaternary. The Quaternary peak (I) corresponds with maximum temperatures up to 250 °C and the second peak (II) locally generated maximum temperatures as high as 320 °C (calculated at Burley-2).

5.4.4 Evolution of source rock thermal maturity and transformation ratio

In **Figure 5.8**, the consequences of the Middle Cretaceous fast subsidence and simultaneous hydrothermal activity for the petroleum source rocks of the study area are illustrated. The evolution of formation temperature (**Figure 5.8a**), thermal maturity (**Figure 5.8b**) and transformation ratio (**Figure 5.8c**) is shown based on four representative well locations. One well from each state was selected, which represents the general thermal evolution on either side (SA: Beanbush-1, QLD: Marengo-1). Further, two wells near the main depocentre (Warnie East-1 and Burley-2) show remarkably high thermal maturity. Not all source rock intervals are present in all wells and the stratigraphy in the SW domain (Warnie East-1 and Burley-2) is more complete.

Similar to the basement (**Figure 5.7g**), the temperature evolution of the source rocks is mainly characterized by two plateaus separated by the main peak at 100 Ma (**Figure 5.8a**). Permian as well as Eromanga source rock intervals exceeded temperatures above 100 °C only after 120 Ma. Permian source rock intervals temporarily reached maximum temperatures of 170 °C at Beanbush-1 and 200 °C at Marengo-1. At Warnie East-1, Toolachee and Daralingie formations reached 261 and 269 °C, respectively right before the Daralingie Fm was replaced by the basaltic intrusion. At Burley-2 the Permian source rocks witnessed even higher temperatures, i.e., the Patchawarra Fm was exposed to 295 °C at 100 Ma ago. Due to their shallower stratigraphic position, Eromanga source rocks generally feature lower paleo-temperatures than the Permian successions. However, local maxima exceeded 150 °C at some locations (i.e., Marengo-1, Burley-2) and caused a distinct step during the thermal maturation process.

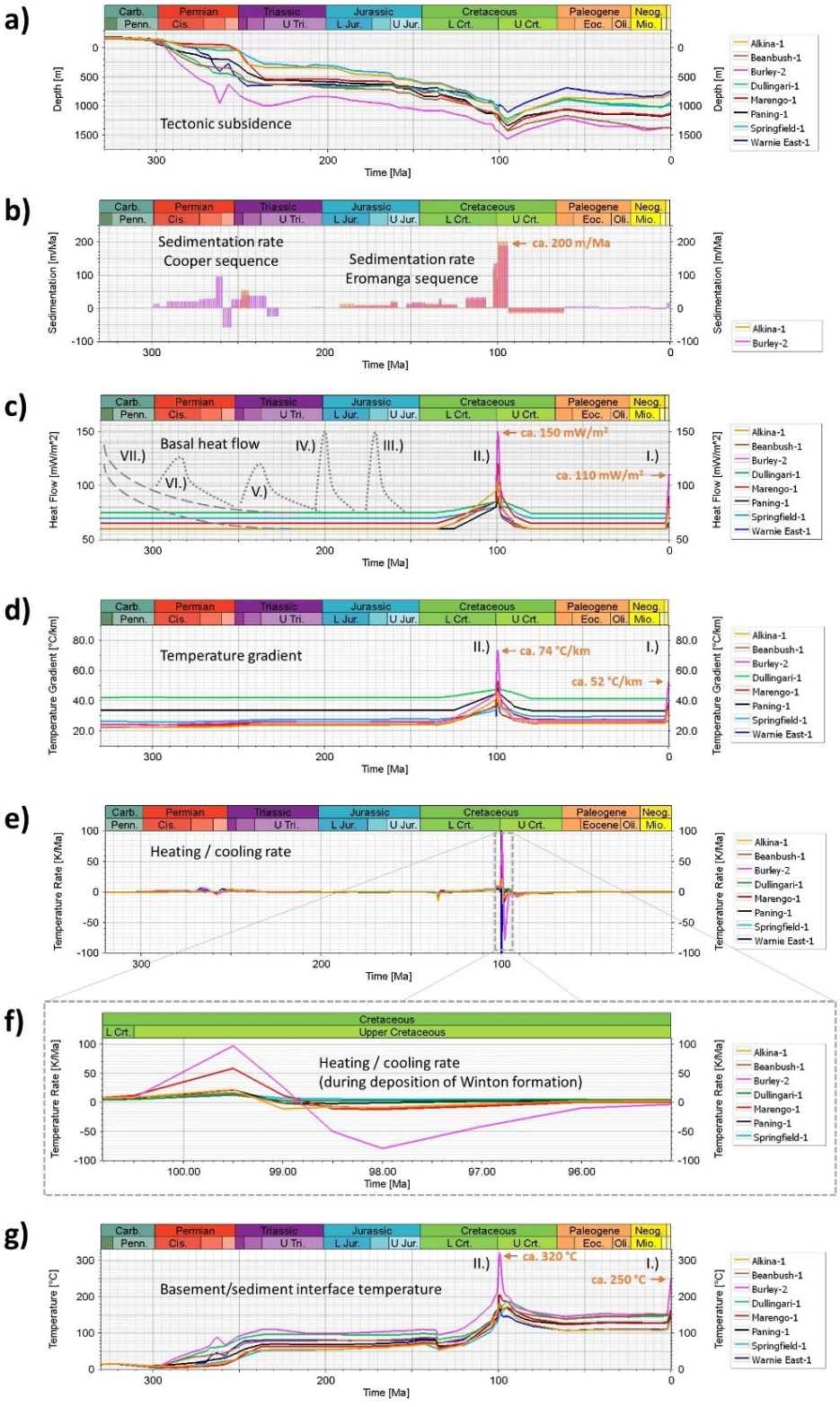

Figure 5.7: Selected time-dependent parameters for the analysis of the thermo-tectonic evolution based on eight simulated and calibrated key wells. a) Tectonic subsidence. b) Sedimentation rate (for two selected wells only, Alkina-1, Burley-2). c) Basal heat flow. d) Temperature gradient. e) & f) Heating rate. g) Temperature at top basement.

Thermal maturity of all source rock intervals (**Figure 5.8b**) remained below 0.5 %Ro until 120 Ma ago. Maturation then started to increase and quickly accelerated until its irreversible maximum since 100 Ma. At about that time, Eromanga source rocks entered the oil window at Beanbush-1 (> 0.5 %Ro) and thermal maturity of Permian source rocks jumped to values between 1.0 and 1.5 %Ro. At Marengo-1, thermal maturity of the Toolachee Fm jumped beyond 2.0 %Ro and Eromanga source rocks range between 0.8 and 1.4 %Ro since 100 Ma. The thermal evolution of Permian and Eromanga source rocks at Warnie East-1 is very similar to Beanbush-1. However, the intrusion at 100 Ma provided additional heat for the Late Permian source intervals, which were closest to (or even replaced by) the intrusion body. Due to this intrusion effect, the Daralingie and Toolachee formations feature exceptional vitrinite reflectance values between 3.5 and 4.0 %Ro. Calculated vitrinite reflectance at Burley-2 generally features the highest values compared to all other analysed locations because of the exceptionally high heat flow at 100 Ma. This hydrothermal effect shifted the Eromanga source rocks to values between 0.9 and 1.8 %Ro and all Permian source rocks beyond 3.0 %Ro. In contrast to the intrusion effect observed at Warnie East-1, the thermal maturity sequence is in line with stratigraphic age.

Kerogen transformation from the source rock intervals initiated at 120 Ma and then jumped because of the exceptionally high heating rate during the Mid Cretaceous event (**Figure 5.8c**). The transformation ratio (TR) passed the critical moment (TR > 50 %) somewhere near 100 Ma for most of the formations. At Marengo-1 and Burley-2 all source rock intervals yield TRs above 75 %. Only at locations where the background heat flow is lower (i.e., Beanbush-1, Warnie East-1), TR of the shallow and/or gas-prone intervals mainly remained below 50 %.

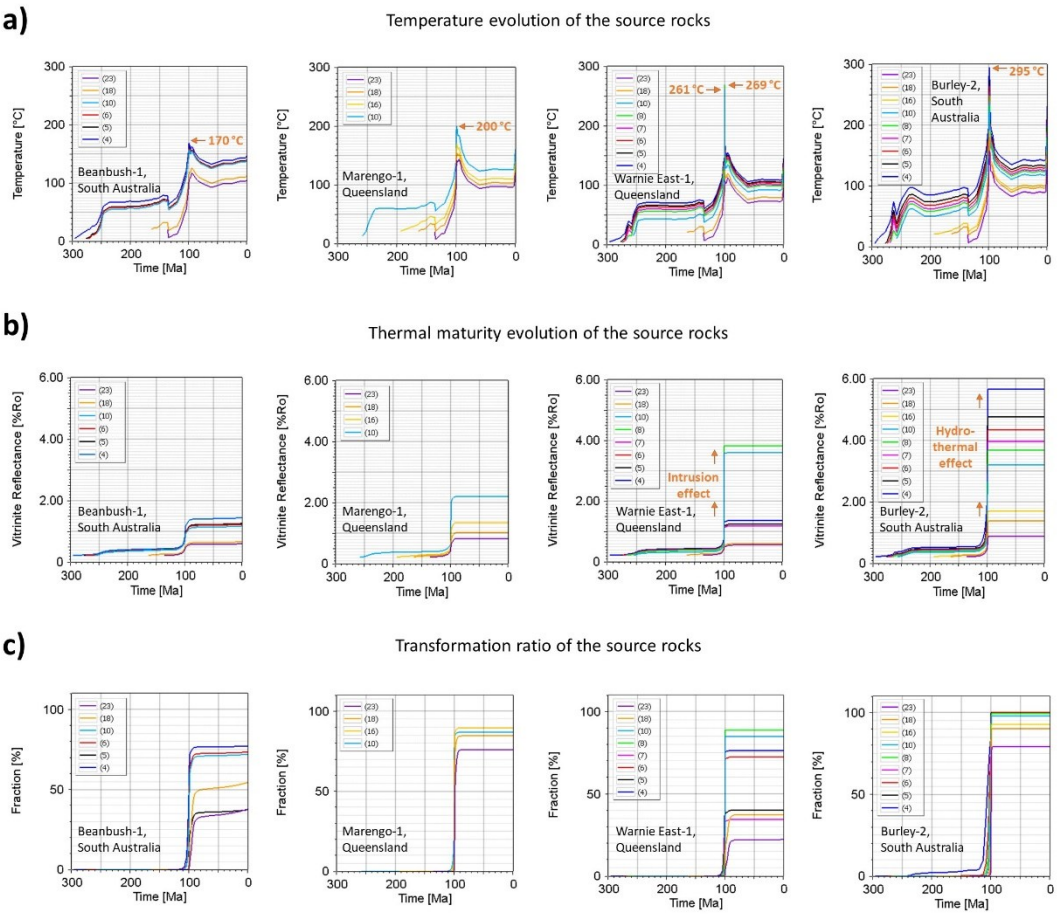

Figure 5.8: Thermal evolution, maturation and kerogen transformation of the assigned source rocks based on four calibrated 1D models (Beanbush-1, Marengo-1, Warnie East-1, and Burley-2). a) Source rock temperature evolution. b) Thermal maturity evolution. c) Transformation ratio evolution. Translation of layer indices: (4) Patchawarra Fm, (5) Murteree Sh, (6) Epsilon Fm, (7) Roseneath Sh, (8) Daralingie Fm, (10) Toolachee Fm, (16) Poolowanna Fm, (18) Birkhead Fm, (23) Murta Fm.

5.4.5 Layer thickness and depocentre migration

Figure 5.9 shows the thickness maps of the most relevant layers of the Cooper sequence to illustrate the spatial distribution and magnitude of sedimentation over time. During an NS-oriented stress regime (compare **Figure 5.2a**), deposition of the glacial outwash of the Pennsylvanian Merrimelia Fm (as well as the Early Permian Tirrawarra Fm) was restricted to the PT, NT and WT in the SW domain (**Figure 5.9a**). Subsequently, the NT established as the main depocentre during the deposition of the entire Gidgealpa Gp (**Figure 5.9b-f**).

However, the Patchawarra Fm represents the thickest and most dynamic depositional event of the Cooper sequence (**Figure 5.9b**). During a period of alternating extensional and compressional NW-SE directed stress, obviously a SW-NE directed "rift axis" established in the NT, upon which more than 800 m of sandstone and coal accumulated. In addition, the WT was subject to continued subsidence. Parallel to the temporary Nappamerri half-graben, the NE-SW oriented GMI Ridge acted as a hinge line, where NT and PT were separated by outcropping basement highs. Intermittent sedimentation in the NE domain beyond the KNFZ only occurred during the Patchawarra Fm along the prolongation of the temporary Nappamerri rift axis (**Figure 5.9b**).

In the following, minor but steady deposition concentrated in the NT and the TT, separated in the south by the Murteree Ridge (**Figure 5.9c-f**). While the NT always remained the primary depocentre, the other two parallel-oriented secondary Permian troughs exhibit a very different timing: Whereas during the Early Permian, the PT represented the secondary depocentre (**Figure 5.9a-b**), the TT became dominant during the Late Permian (**Figure 5.9c-f**). Noteworthy sedimentation in the PT re-established only during the early and Middle Triassic (Nappamerri Gp, **Figure 5.9h-i**). After the Daralingie Unconformity, sedimentation still focused on the central NT (**Figure 5.9g**), but then gradually and equally extended throughout the entire basin (**Figure 5.9h-i**).

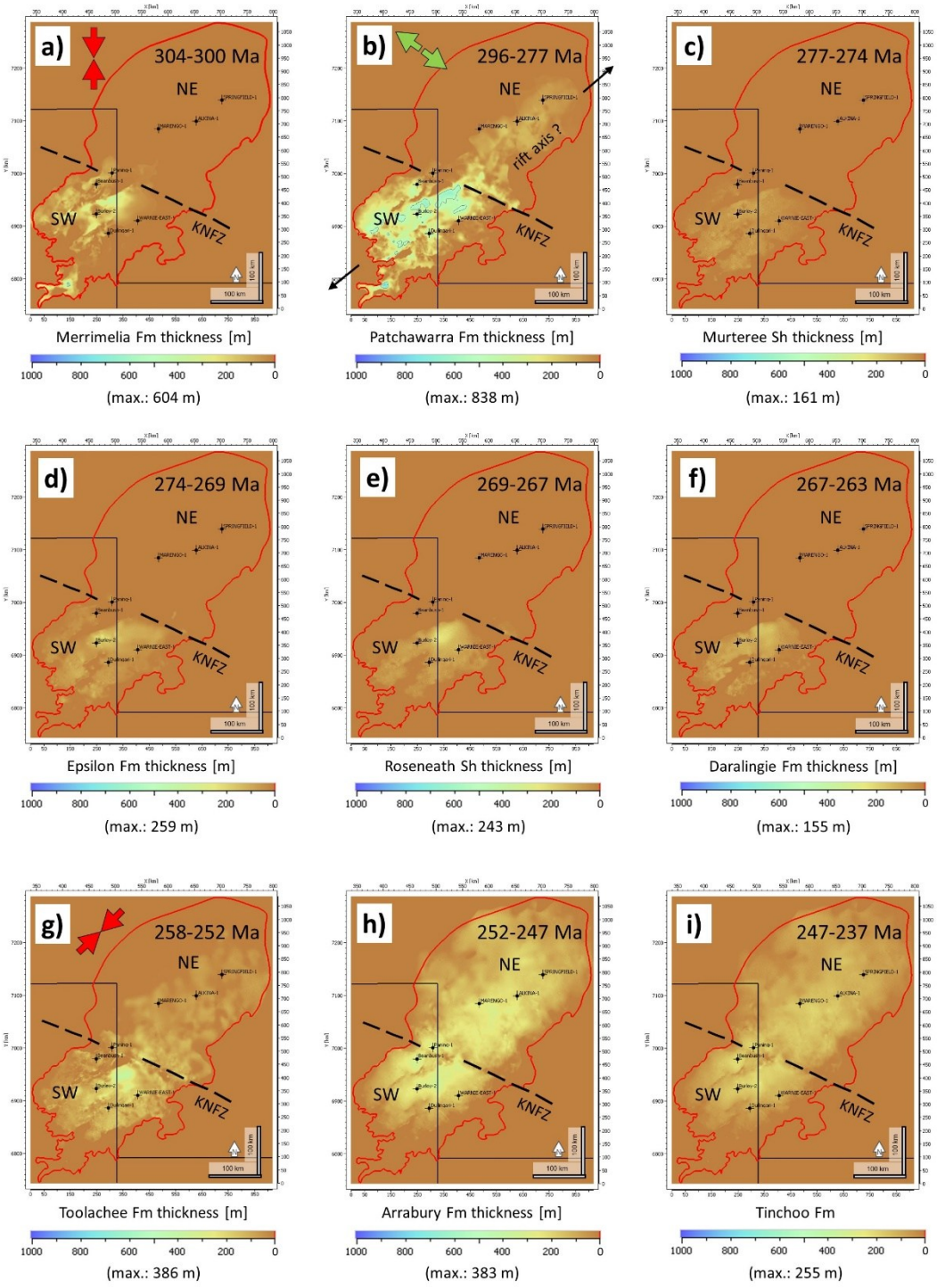

Figure 5.9: Layer thickness maps of the Cooper sequence. a) Merrimelia Fm. b) Patchawarra Fm. c) Murteree Sh. d) Epsilon Fm. e) Roseneath Sh. f) Daralingie Fm. g) Toolachee Fm. h) Arrabury Fm. i) Tinchoo Fm. Tirrawarra Fm is not shown due to its relatively small thickness. Kinematic/tectonic indicators mainly based on Kulikowski et al. (2018). KNFZ = Karmona-Naccowlah Fault Zone.

The sediment input during the Eromanga sequence was not restricted anymore to the outline of the CB, but highest sedimentation rates still occurred within the established regional depression (**Figure 5.10**). With remarkable thickness variations, the Middle Jurassic Hutton Sst covered mainly the NE domain, but also filled several smaller depressions along the CB margin and beyond. Locally, over a distance of a few km, sediment thickness varies between 50 and 700 m. In the SE, a short-lived rhombic mini-basin (a precursor of the Bulloo Lake Basin, BLB) with a diameter of about 50 km was filled with up to 450 m of sediments (**Figure 5.10a**). Deposition of the Birkhead Fm extended over a major part of the Cooper area (**Figure 5.10b**), while the accumulation of the Adori sandstone concentrated in the SW domain (**Figure 5.10c**). The relatively thin Late Jurassic Westbourne Fm and the Namur Sst were deposited over most of the study area with relative constant thickness (**Figure 5.10d-e**).

During the fast deposition of the Early to Middle Cretaceous sedimentary blanket, the depocentre location was very dynamic. The largest thickness of the Wallumbilla Fm is recorded in the SW domain (**Figure 5.10f**), while the Allaru Mdst is thicker in the north (**Figure 5.10g**) and the layer thickness of the Mackunda Fm is again relatively constant throughout the study area (**Figure 5.10h**). During the deposition of the Wallumbilla Fm, the remains of the Tookoonooka impact crater (+/- 125 Ma) represented a temporary structural high (**Figure 5.10f**).

The Winton Fm features the highest sedimentation rate (**Figure 5.7b**), the largest original thickness (**Figure 5.10i**), the largest amount of post-sedimentary erosion (**Figure 5.11a**) and the largest preserved thickness (**Figure 5.11b**) of all formations. Initially, the study area was entirely covered by at least 300 m of Winton Fm sediments. New depocentres established in the NE domain and up to 1,300 m of fluvial sandstones accumulated in the Windorah Trough, the Ullenbury Depression and the Thompson Depression (**Figure 5.10i**).

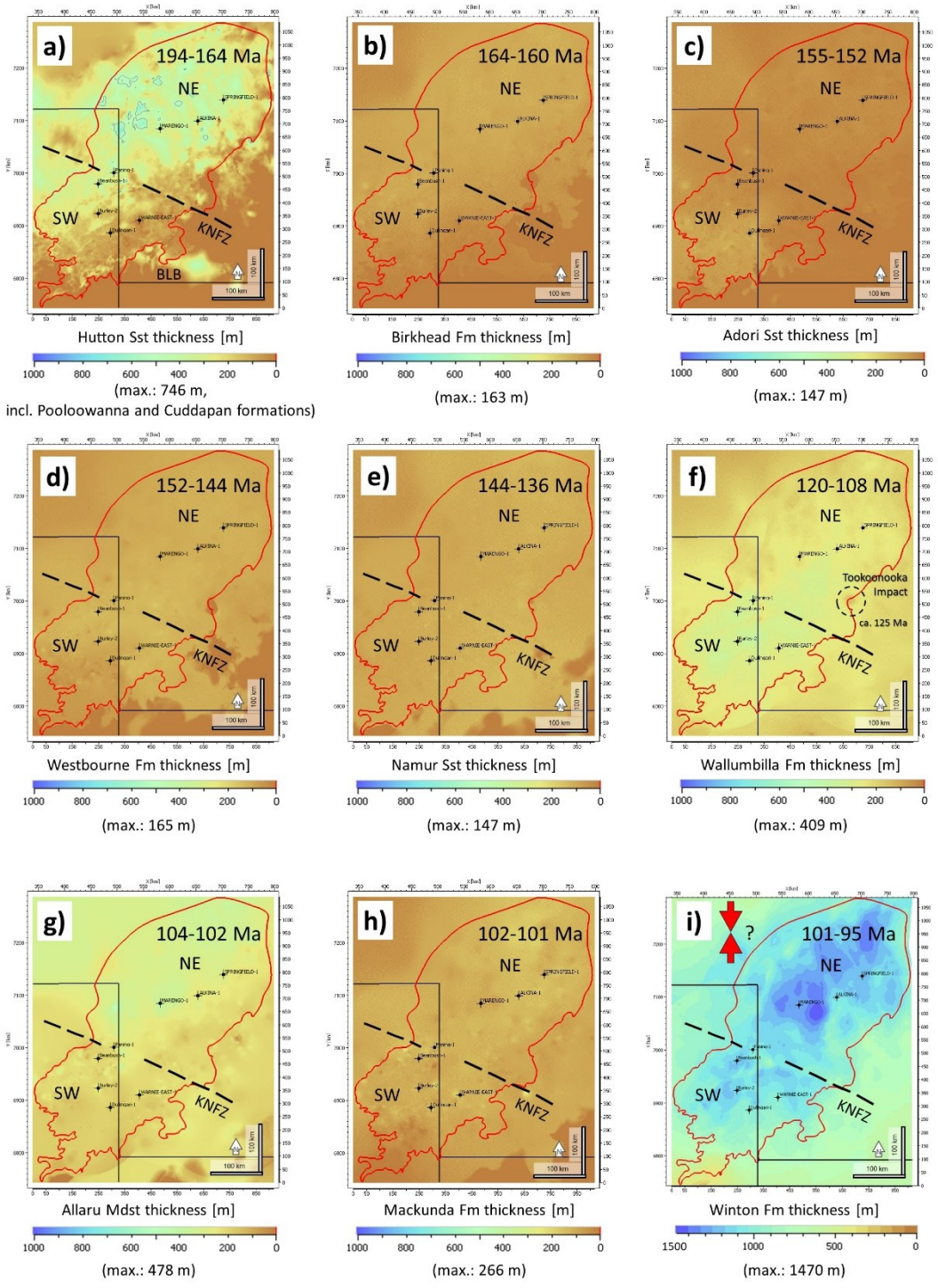

Figure 5.10: Layer thickness maps of the Eromanga sequence. a) Hutton Sst incl. Poolowanna and Cuddapan formations. b) Birkhead Fm. c) Adori Sst. d) Westbourne Fm. e) Namur Sst. f) Wallumbilla Fm. g) Allaru Mdst. h) Mackunda Fm. i) Winton Fm. The relative thin layers of the Murta Fm, Cadna-owie Fm, and Toolebuc Fm are excluded. KNFZ = Karmona-Naccowlah Fault Zone, BLB = Bulloo Lake Basin.

E-W directed compression and inversion resulted in widespread erosion of the Winton Fm with highest amounts along the Mt. Howitt Anticline (up to 870 m), along the GMI Ridge, the Murteree Ridge and along the northern and southern margins of the basin. Lowest amounts of erosion occurred in the PT and WT (**Figure 5.11a**).

The preserved thickness of the Winton Fm is highest in the Windorah Trough (up to 1,055 m), the Ullenbury Depression and the Thompson Depression. The PT and NT locally contain more than 900 m of Winton deposits (**Figure 5.11b**). Besides newly formed anticlines in the NE domain, the KNFZ, the GMI Ridge and the Murteree Ridge were re-activated during the Late Cretaceous. In addition, the area around Warnie East-1 established a smooth dome structure.

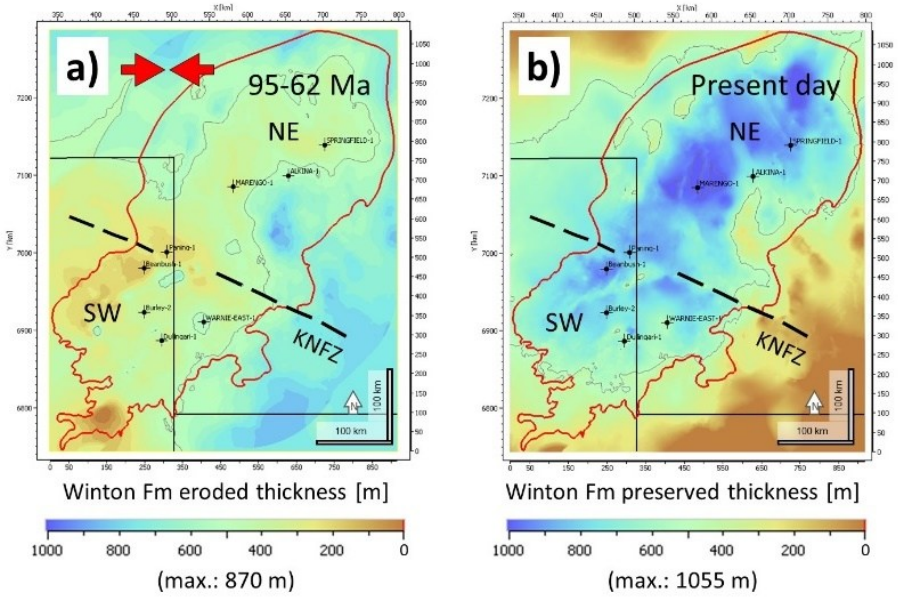

Figure 5.11: Impact of uplift and erosion on thickness of the Winton Fm. a) Assigned erosion map (after Mavromatidis & Hillis, 2005). b) Resulting preserved thickness of the Winton Fm at present day. Kinematic/tectonic indicators based on Kulikowski et al. (2018). KNFZ = Karmona-Naccowlah Fault Zone.

5.4.6 Basal heat flow maps

Heat flow trends from 15 calibrated 1D models (eight located in South Australia, seven in Queensland) were interpolated to generate heat flow maps for defined time steps. Together with PWD and SWIT maps, the heat flow maps were then assigned as boundary conditions to the 3D model to reconstruct the thermal history of the study area in 4D. A selection of resulting heat flow maps is displayed in **Figure 5.12**. Since a constant heat flow was assigned from the Pennsylvanian to the Early Cretaceous, the focus is on the two hydrothermal events in the Middle Cretaceous and at present-day. The intrusion model at Warnie East-1 was not applied in 3D leaving the heat flow and resulting temperatures underrepresented at this particular location.

Since about the time of deposition of the Murta Fm, heat flow started to increase mainly throughout the NT and in the NE domain. (**Figure 5.12a-d**). With accelerating sedimentation rate during the end of the Early Cretaceous, heat flow locally increased to values around 80 mW/m^2 (**Figure 5.12e**).

At the peak of hydrothermal activity during the deposition of the Winton Fm (peak II, **Figure 5.12f**), heat flow reached values around 100 mW/m^2 throughout most of the study area. Highest calculated heat flow values between 130 and 150 mW/m^2 occurred at 99.5 Ma mainly along the axis of the NT. In addition, the NE domain was temporarily heated up by values locally as high as 120 mW/m^2.

After the peak of Middle Cretaceous hydrothermal activity and before the regional uplift started, heat flow decreased relatively quickly to 70 to 90 mW/m^2 throughout the study area (**Figure 5.12g**). After tectonic stabilization in the Late Cretaceous and throughout most of the Cainozoic, heat flow equilibrated again between 60 and 75 mW/m^2 (**Figure 5.12h**).

The Quaternary hydrothermal pulse (peak I) mainly affects the NT with locally increased heat flow of 110 mW/m^2. While the NE domain is also affected to a lower degree with local maxima around 90 mW/m^2, the PT remains apparently unaffected (**Figure 5.12i**).

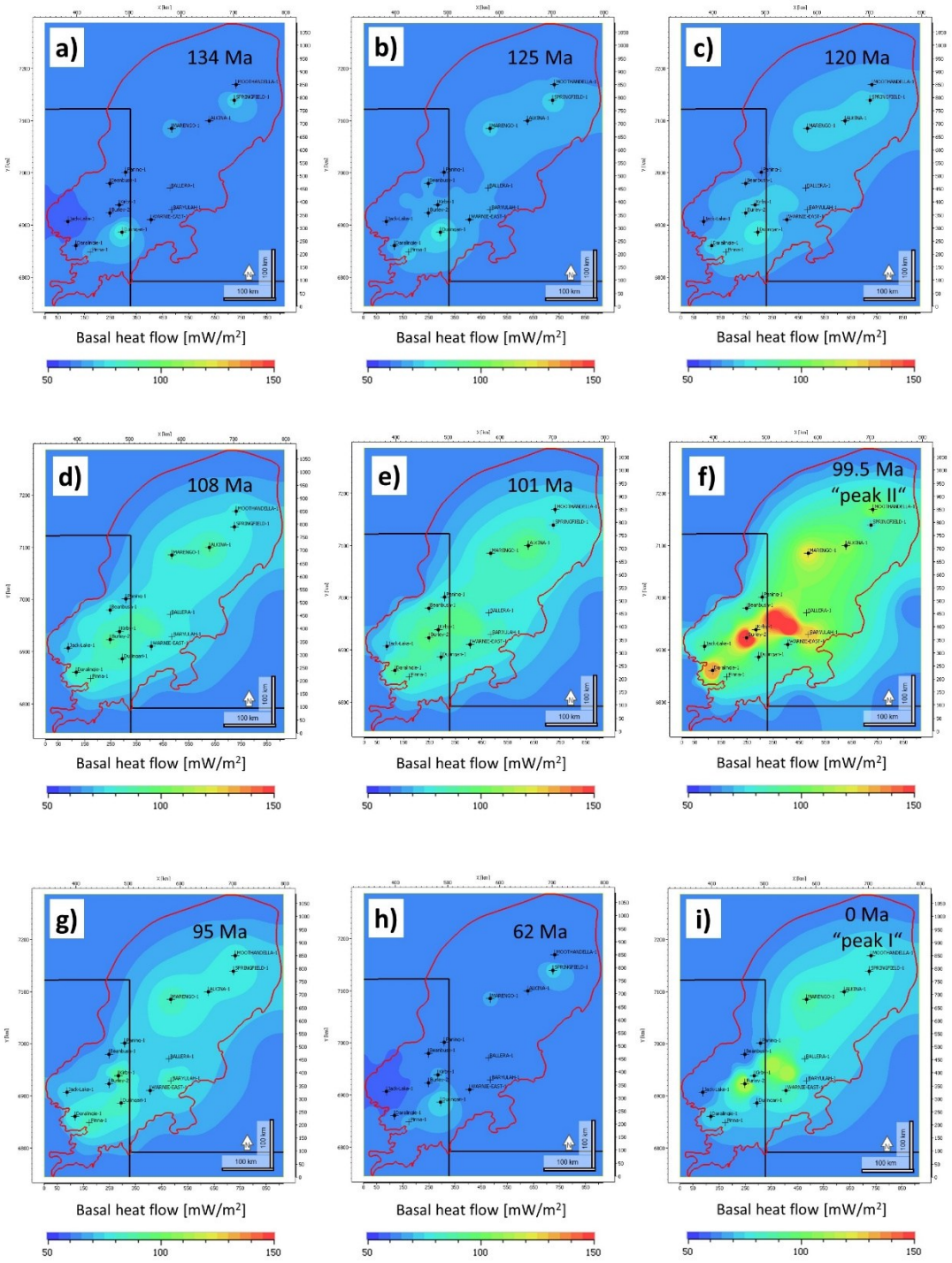

Figure 5.12: Calculated basal heat flow maps for selected time steps. a) 134 Ma. b) 125 Ma. c) 120 Ma. d) 108 Ma. e) 101 Ma. f) 99.5 Ma, peak of Middle Cretaceous hydrothermal activity. g) 95 Ma. h) 62 Ma. i) Present day, peak of Quaternary hydrothermal activity.

5.4.7 Maximum temperature maps

Figure 5.13 shows a compilation of maximum temperature maps for the top basement and the assigned source rock layers (except the Poolowanna Fm, which was merged with the Hutton Sst). The values represent the highest temperatures that these layers have witnessed and which were achieved during the Middle Cretaceous hydrothermal event at 99.5 Ma.

The maximum temperature at the top basement ranges between 150 and 190 °C in the NE domain and went up to 360 °C in the NT (**Figure 5.13a**). The respective maximum temperature of the source rocks of the Gidgealpa Gp (**Figure 5.13b-g**) was calculated as follows: Patchawarra Fm: 300 °C, Murteree Sh: 290 °C, Epsilon Fm: 280 °C, Roseneath Sh: 270 °C, Daralingie Fm: 250 °C, and Toolachee Fm: 215 °C. All these maxima were obtained in the NT, while the Patchawarra (**Figure 5.13b**) and Toolachee (**Figure 5.13g**) formations also witnessed maximum temperatures of up to 190 °C in the NE domain.

For the Birkhead (**Figure 5.13h**) and Murta (**Figure 5.13i**) formations maximum temperatures of 165 °C and 145 °C were calculated, both in the NT. Although the Westbourne Fm in between was not assigned as a source rock in this study, maximum temperatures were calculated anyway and yield values around 155 °C in the NT.. In the NE domain, all three relatively shallow source rock intervals did not exceed 140 °C.

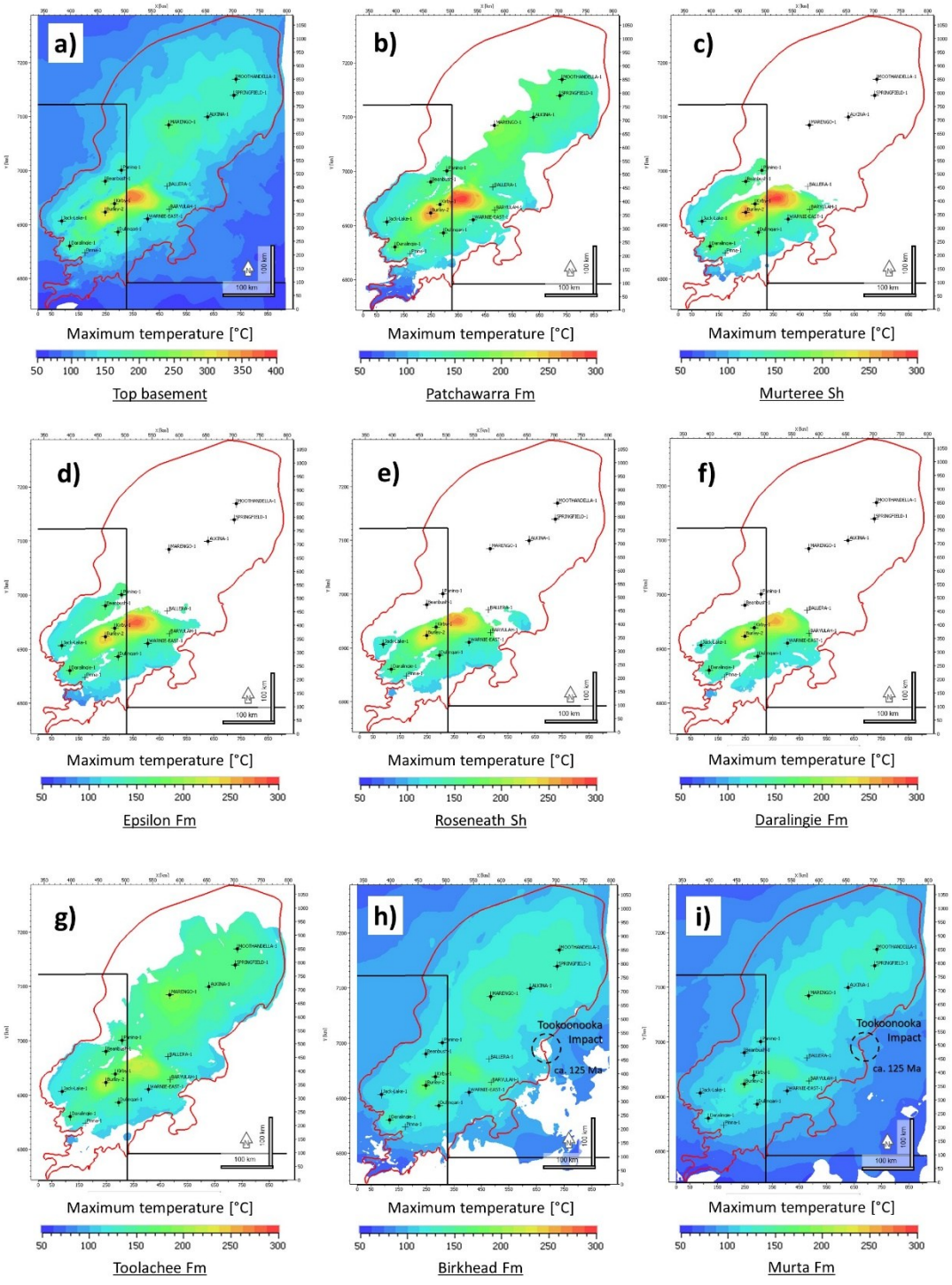

Figure 5.13: Calculated maximum temperature maps for selected surfaces. a) Top basement. b) Patchawarra Fm. c) Murteree Sh. d) Epsilon Fm. e) Roseneath Sh. f) Daralingie Fm. g) Toolachee Fm. h) Birkhead Fm. i) Murta Fm. White areas indicate non-deposition or complete erosion. Note different temperature scale for the top basement.

5.4.8 Thermal maturity maps

Resulting present-day thermal maturity for most assigned source rocks is shown in Figure 14. Poolowanna Fm is not shown, because it was merged with Hutton Sst and Westbourne Fm was added although not assigned with a kinetic model.

In the NT the Patchawarra Fm (**Figure 5.14a**) reached the dry gas window (2.0-4.0 %Ro) and is even overmature (> 4.0 Ro%) in its deepest/hottest parts. In the Barrolka Trough the wet gas window (1.3-2.0 %Ro) was entered. The Murteree Sh and the Epsilon Fm (**Figure 5.14b-c**) are located mainly in the dry gas window throughout the NT, while they only reached the early oil (0.55-0.7 %Ro) to late oil window (1.0-1.3 %Ro) in the PT and the TT. The Roseneath Sh and Daralingie Fm (**Figure 5.14d-e**) show very similar thermal maturity distribution with generally slightly lower values, except that they are absent in the PT. The Toolachee Fm (**Figure 5.14f**) was predominantly oil generating throughout the study area, but is also gas-mature in the Nappamerri and Barrolka troughs.

The calculated thermal maturity of the three Eromanga source rock intervals (Birkhead, Westbourne, and Murta formations, **Figure 5.14g-i**) correlates with the early oil window throughout most of the study area. Locally, in the Nappamerri and Barrolka troughs the main oil window was entered while they are predominantly immature in the PT and the TT.

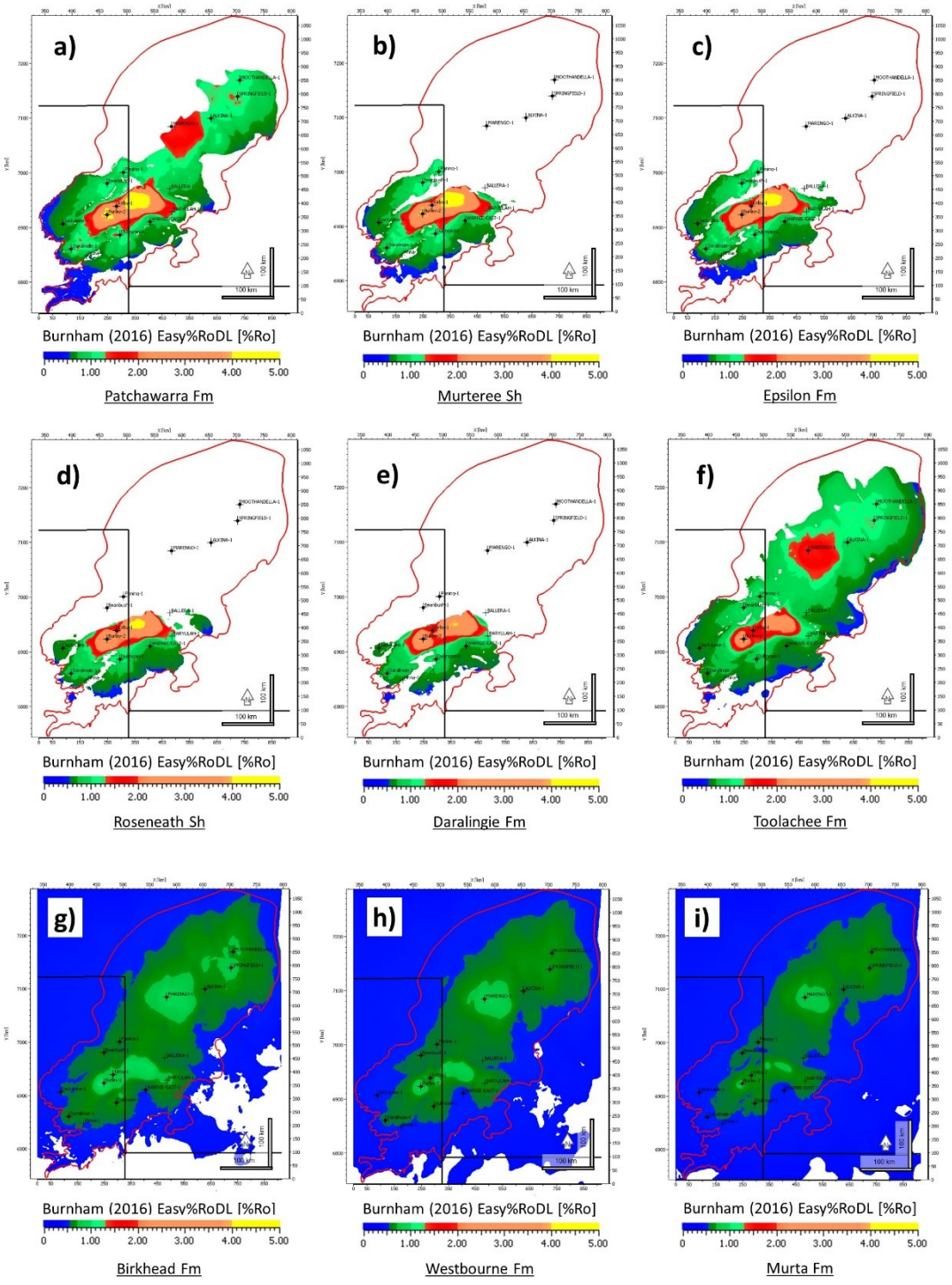

Figure 5.14: Calculated present-day thermal maturity maps for most of the assigned source rock intervals. a) Patchawarra Fm. b) Murteree Sh. c) Epsilon Fm. d) Roseneath Sh. e) Daralingie Fm. f) Toolachee Fm. g) Birkhead Fm. h) Westbourne Fm. i) Murta Fm. White areas indicate non-deposition or complete erosion.

5.5 Discussion and remaining uncertainties

One major uncertainty of the study area is the classification of the basin type and the determination of tectonic boundary conditions during the two different phases of basin formation. This uncertainty can be reduced by regarding basin phases separately, considering surficial structural features, and by analyzing their relationship with the regional thermal and tectonic evolution.

5.5.1 Permo-Triassic tectonics

Generally, investigating crustal geometry and shape of the Moho below the study area could help to identify the basin opening mechanism. The Moho depth in the Cooper region varies between 32 km in the SW domain and 40 km in the NE domain (Kennett et al., 2011) and corresponding crustal thickness is generally lower below the WB and higher towards the Cambrian to Devonian Thomson Fold Belt. It yields about 38 km below the Warrabin Trough and features less than 29 km below the NT (Hall et al., 2015b). An axis of crustal stretching ("rifting axis") is not clearly recognized, but it appears that the Moho shape in the SW domain of the CB mainly resembles the stretched eastern WB and is therefore associated with NW-SE directed extension.

Bouguer gravity variations in the study area (Bacchin et al., 2008) suggest that the CB was strongly influenced by movements along the JNP and GMI ridges, where also the faults with the largest vertical offset are located. Indeed, patterns of sedimentation and erosion during the Cooper sequence were governed by an array of three main depocentres separated by NE-striking ridges (GMI, DNC, and Murteree; compare **Figure 5.1b**, **Figure 5.3b** and **Figure 5.9**). These parallel-oriented fault zones apparently acted as Riedel shears and connected the ESE-striking KNFZ and the TL already during the Devonian-Carboniferous inversion and uplift of the WB. In the Pennsylvanian, kinematics were oriented N-S and probably formed a temporary shortcut for the TL that proceeded through the PT, the westernmost NT and the WT (**Figure 5.15a**), before NW-SE directed transtensional stress in the Permian caused stretching and subsidence on either side of the GMI Ridge hinge line and sinistral transtension along the KNFZ and the TL (**Figure 5.15b**). Together, these three tectonic features acted as the master fault, which facilitated the basin opening in a fault-bend or pull-apart basin style. Indeed, the observed rhomboidal geometry of the SW domain and the course of the master fault is characteristic for pull-apart basins (e.g., Mann et al., 1983; Noda, 2013).

Regarding the PT, NT and TT as one system of subparallel, elongated, rhomboidal releasing bends (each 50-60 km wide and 150-200 km long; length-to-width ratio, l/w = 3) results in one large rhomb with approximately l/w = 1 (length: +/- 200 km, width: +/- 200 km; **Figure 5.15c**). Pre-existing structures of the inverted WB simplified the opening of the CB by reverting strike-slip zones and converting former thrusts into oblique extensional slip planes (e.g., Apak et al., 1997). However, mature rhomboidal pull-apart basins generally show l/w = 3 (Aydin & Nur, 1982) rather than 1. To satisfy this geometric rule, a theoretical elongated system along the KNFZ can be assumed, which extended from the Cork Fault in the NW to the Bulloo Lake in the SE (total length: about 600 km). Permian sediments that would verify this layout were probably completely removed during episodes of uplift (e.g., Daralingie, Nappamerri unconformities).

Throughout the Permian, the NT established as the primary depocentre along the Cooper Basin Master Fault (CBMF), while the activity of the other troughs greatly varied over time (**Figure 5.15b-e**). Initiated as a deep oblique half-graben with a SW-NE oriented rift axis during the Patchawarra Fm, the NT was continuously the focus of subsidence and sediment accumulation until the Triassic (also see **Figure 5.9**). The deepest point was constantly located near the Innamincka Dome (ID), where the CBMF bends into the GMI Ridge. A smaller rhomboidal trough with a diameter of about 50 km occurred in the SE during the deposition of the Hutton Sst (**Figure 5.15f**, compare **Figure 5.10a**) and could be an indicator of renewed strike-slip tectonics during the Jurassic but with a different stress field.

The question about the style of the "Permian rifting" might therefore be answered with oblique strike-slip tectonics and a sinistral pull-apart mechanism. However, various still poorly studied unconformities within the Patchawarra Fm (Kantsler et al., 1983; Apak et al., 1997) as well as the uncertain magnitude of the Daralingie Unconformity testify to a more complex Permian tectonic history that requires additional examination, which is beyond the scope of this study. At least the Daralingie Unconformity was the result of a short-lived basin inversion (push-up phase, see Apak et al., 1997), which was characterized by thrusting, accentuation and erosion of the ridges, particularly the GMI and JNP. A straight line with low sediment thickness proceeded from the ID towards SSE, indicating an additional temporary ridge (**Figure 5.9g**, **Figure 5.15e**, and **Figure 5.15f**). From Middle to Late Permian, the CB can therefore be classified as a push-up or piggyback basin. The ID obviously represents a tectonic wedge, which was uplifted and

pushed between the NT and the PT due to NE-SW compression during the Daralingie Unconformity.

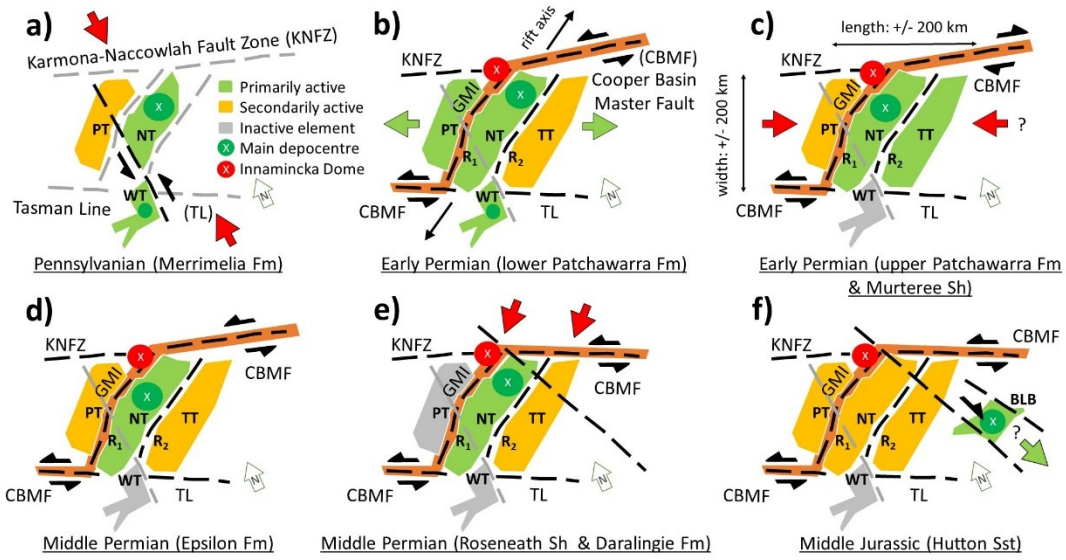

Figure 5.15: Phases of tectonic evolution and evolution of depocentre activity in the SW domain of the Cooper Basin from Carboniferous to Jurassic (rotated). a) Initial basin opening. b) Main phase of basin formation with oblique rifting and establishment of pull-apart structure. c) Basin inversion and ridge formation. d) Continuation of pull-apart basin. e) Compression, wedging of Innamincka Dome and transition into piggyback basin. f) Initiation of SSE directed shearing/dragging and opening of Bulloo Lake Basin (BLB). PT = Patchawarra Trough, NT = Nappamerri Trough, TT = Tenappera Trough, WT = Weena Trough, GMI = Gidgealpa-Merrimelia-Innamincka Ridge, R1, R2 = Riedel shears / ridges.

Except some erosional remnants of the Cuddapan Fm, no Late Triassic sediments are preserved. This stratigraphic gap was often connected with a basin-wide post-rift unconformity of an associated "Triassic rifting event" similar to the one observed in the Surat and Bowen basins (Green et al., 1997; Raza et al., 2009; Li et al., 2012). However, the low-angle Nappamerri Unconformity implies that the far-field effect of the Early Triassic subduction rollback and subsequent compression along the eastern continental margin during the dynamic Hunter-Bowen Orogeny (260-210 Ma; Li et al., 2012) was rather low. Especially in the south, minor uplift and erosion after the deposition of the Tinchoo Fm occurred, but the sediment distribution (see **Figure 5.9g-i**) as well as the thermal maturity profiles do not support very large amounts of uplift. Distinct steps in the

thermal maturity profiles would underline the hypothesis of strong Triassic post-rift erosion, but exist only locally (see **Figure 5.5** and **Figure 5.6**).

The NT acted as the main depocentre during the Toolachee Fm (**Figure 5.9g**). The small thickness variations and widespread sedimentation patterns during the Triassic (**Figure 5.9h** and **Figure 5.9i**) are representing a gentle basin-wide transition phase rather than continental rifting. Additionally, the Moho is not uplifted along an expected NE-SW directed rifting axis (compare Kennett et al., 2011). Nevertheless, temporary compression triggered localized uplift and erosion along the ridges and within the NT, but to a lesser extent compared to the Daralingie Unconformity.

5.5.2 Neotectonics and topography

Before discussing the tectonic processes during the Eromanga sequence, it is very insightful to analyze the present-day geomorphology and the present-day stress field. Although the sediments of the Australian Outback are intensely modified by wind and water, numerous geometric and topographic features become visible on satellite images thanks to missing vegetation (e.g., Google Earth, **Figure 5.16**).

The surface topography is generally higher (mainly above 100 m) and more dynamic on the Queensland side with the ID representing a local peak (about 260 m elevation). In South Australia, the topography is flat and generally lower (mainly ranging between 20 and 50 m) and even drops below the sea level (Lake Callabonna, -5 m; Kati-tanda / Lake Eyre, -17 m). The intermittent Cooper Creek and the Warburton River are draining towards SW to feed the endorheic Lake Eyre (Wakelin-King & White, 2011), the lowest point of the entire Australian Continent. The underlying tectonic features of the CB have a complex influence on the course of the rivers, especially the Cooper Creek. Its original SW course is remarkably deviated southward by the NNW-SSE oriented Durham Downs Anticline (apparent offset: about 150 km). The muddy sediments of the braided/anabranching river system are spreading across the Cooper floodplain (Wakelin-King & White, 2011), are occasionally splaying within the endorheic Lake Yamma Yamma and, after crossing the JNP Ridge, are filling the rhomboidal Wilson Depression. After passing some important waterholes (“billabongs”), the Cooper Creek then bends westward around the ID into the NT. Here, the river becomes single-thread, crosses the GMI Ridge and meanders towards NW into the PT, proceeds again towards SW to get deviated once more by the WNW-directed TL (apparent offset: about 100 km). Even the Bulloo River in the East follows a similar pattern. It generally flows in SW direction and

charges the endorheic and rhomboidal BLB, which obviously represents a rejuvenation of the Jurassic mini-basin (see **Figure 5.15f**). Similarities in shape and size with the Wilson Depression (rhomb with about 50 km in diameter) are certainly not random.

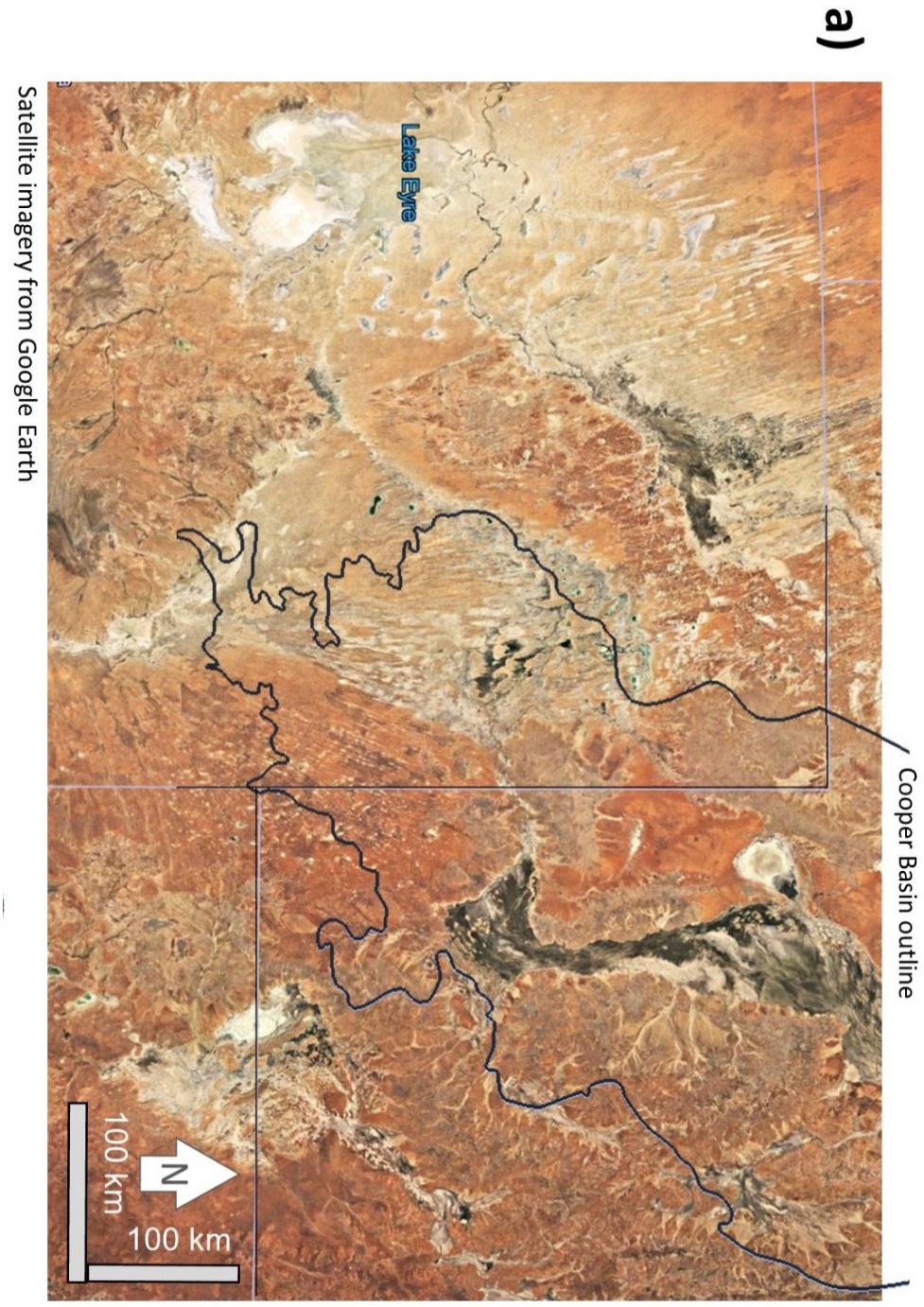

Figure 5.16: Large-scale neotectonic features identified in the Cooper subregion in relation to pre-existing structures. a) Satellite image (Google Earth) with outline of the Cooper Basin. b) Please find descriptin on the next page.

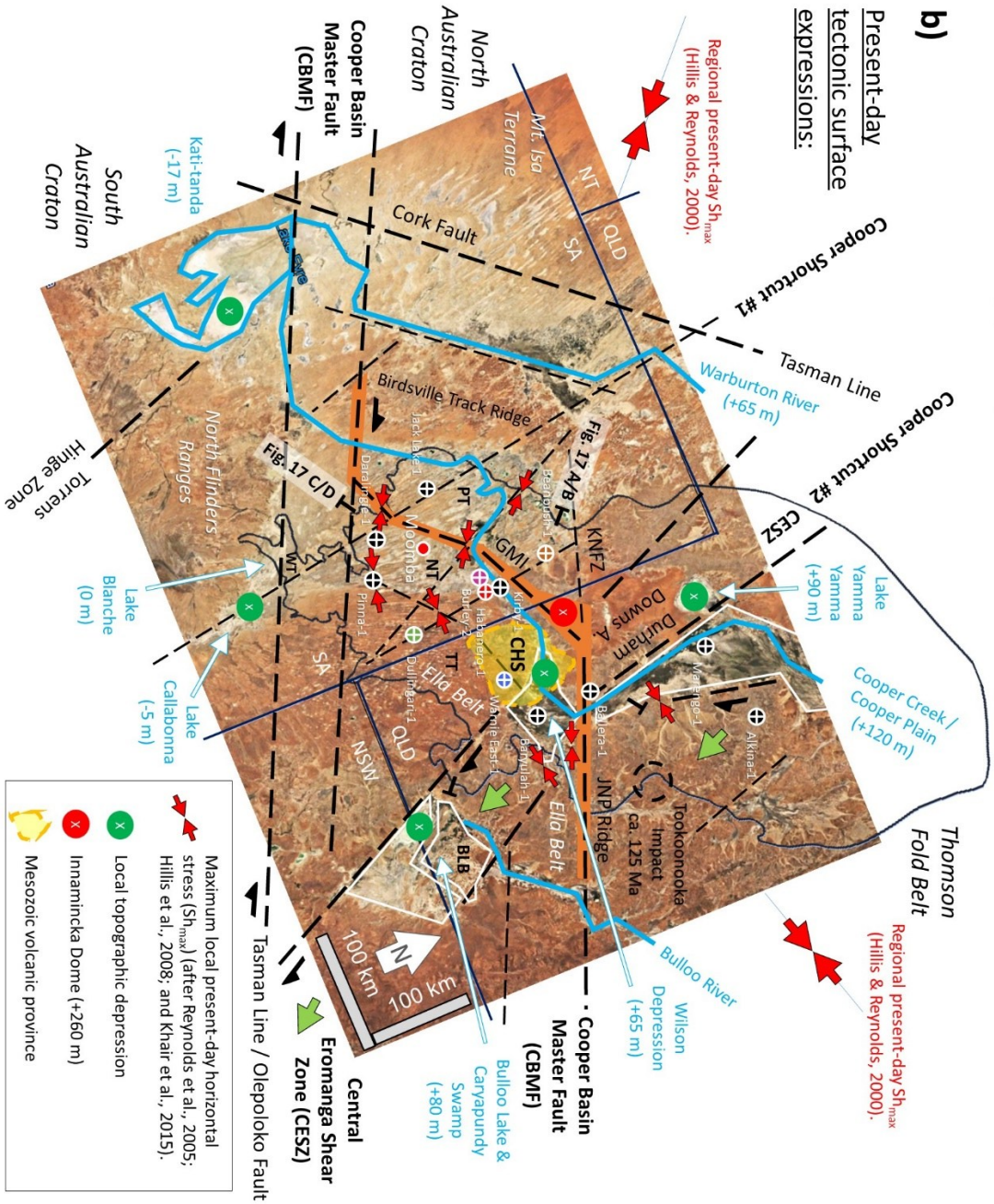

Figure 5.16 (continued): Large-scale neotectonic features identified in the Cooper subregion in relation to pre-existing structures. a) (Previous page) Satellite image (Google Earth) with outline of the Cooper Basin. b) (This page) Interpretation of major structural elements inferred from surface morphology, river deviations and present-day stress field (image was rotated to show resemblance of the present-day geomorphology with the sketches in Figure 5.15). BLB = Bulloo Lake Basin, CHS = Cooper Hot Spot, PT = Patchawarra Trough, NT = Nappamerri Trough, TT = Tenappera Trough, WT = Weena Trough, GMI = Gidgealpa-Merrimelia-Innamincka Ridge, Mesozoic volcanic province after Hardman et al. (2019).

It seems that the old shortcut of the TL, which proceeded subparallel to the Torrens Hinge Zone (THZ) during the Late Carboniferous (compare **Figure 5.15a** and **Figure 5.16a**), meanwhile propagated about 200 km eastward. At least since the Middle Cretaceous, the new shortcut (**Figure 5.16a**) obviously forms an active shear zone along the Durham Downs Anticline and crosscuts the CB just at its most interesting point. At this tectonic focal point, the deepest trough, the largest sediment thickness, the largest fault offset, the most prominent uplifted basement structure, the thinnest crust and a variety of volcanic and magmatic features coexist within a very small radius of only 50 km. In the following, this area is therefore called Cooper Hot Spot (CHS).

The present-day regional maximum horizontal stress (Sh_{max}) is oriented NW-SE on the South Australian side and it swings towards ENE-WSW on the Queensland side (Hillis & Reynolds, 2000; Reynolds et al., 2005; Hillis et al., 2008; Khair et al., 2015a, 2015b). The turning point of the stress field seems to be located not very far from the CHS, too. On the South Australian side, this stress distribution allows dextral movement of the North Australian Craton (NAC) vs. the South Australian Craton (SAC) along the TL and provides additional compression of the basement ridges within the CB. The stress field on the Queensland side is able to accentuate the Durham Downs Anticline, and is compatible with the interpreted dextral shear of the Thomson Fold Belt along the new shortcut due to SSE directed extensional forces that formed an array of small indent-linked strike-slip basins (e.g., Cooper Plain, Lake Yamma Yamma, Wilson Depression, and Bulloo Lake). Within these topographic lows, river deviations and endorheic lakes are common indicating neotectonic activity. Seismicity in the study area is low to moderate (magnitude M 3-4), but epicenters remarkably align with new shortcut (e.g., Hillis et al., 2008). Based on hydrology and lithospheric structure, this zone of deformation was recently described as the Innamincka Fault System (IFS, Sandiford et al., 2020). However, since this deformation zone is apparently intersecting the entire Central EB from the Georgina River to the Darling River, we suggest to summarize this large tectonic landscape as the Central Eromanga Shear Zone (CESZ, see **Figure 5.16**).

The CESZ probably dragged the originally rhomboidal SW domain constantly along its direction of shear and is obviously responsible for the southward flexure of the NT and TT. During the last 20 years, earthquakes also concentrated in the NT, but were probably related to induced seismicity from geothermal drilling projects (see Allen et al., 2019).

5.5.3 Jurassic and Cretaceous tectonics

During the Cooper sequence, the migration of the primary depocentre was restricted to a relative small radius within the NT (**Figure 5.15**). Deduced from the preserved layer thickness, sediment distribution in the study area changed in the Jurassic and the primary depocentre jumped across the GMI Ridge (**Figure 5.17a** and **Figure 5.17b**). Throughout the Cretaceous, the PT established as the primary depocentre in the SW domain and even Cainozoic sediments are thicker than in the NT.

The depocentre migration within the NT itself remained restricted to a rather small area (**Figure 5.17c** and **Figure 5.17d**). The location with the largest preserved sediment thickness repeatedly jumped back and forth between the KNFZ and the conjugate Central Nappamerri Fault (CNF). While the CNF was more active during the Cooper sequence, the KNFZ became obviously dominant during the Eromanga sequence, particularly during the Jurassic and the Middle Cretaceous. On the one hand, during the Permian and Triassic, the KNFZ was also the zone of strongest uplift (particularly during Late Permian and Late Triassic) and therefore original layer thickness was reduced by erosion. On the other hand, episodic depocentre migration towards the NE (during Late Permian, Jurassic, and Middle Cretaceous, see **Figure 5.17d**) was increasingly driven by activity of the CESZ. In the Cainozoic, subsidence was strongest in the SW domain upon the Wooloo Trough, while the JNP Ridge and the Durham Downs Anticline still represent uplifted areas being incorporated to the CESZ. Adding the maximum thickness of each individual layer in the NT results in accumulated thickness of about 5,424 m, which exceeds the maximum burial depth (4,663 m) by 761 m or 16.3 % (**Figure 5.17d**). Relative thick strata compared to burial depth due to depocentre migration is another strong indicator for dominant strike-slip tectonics (e.g., Noda, 2013).

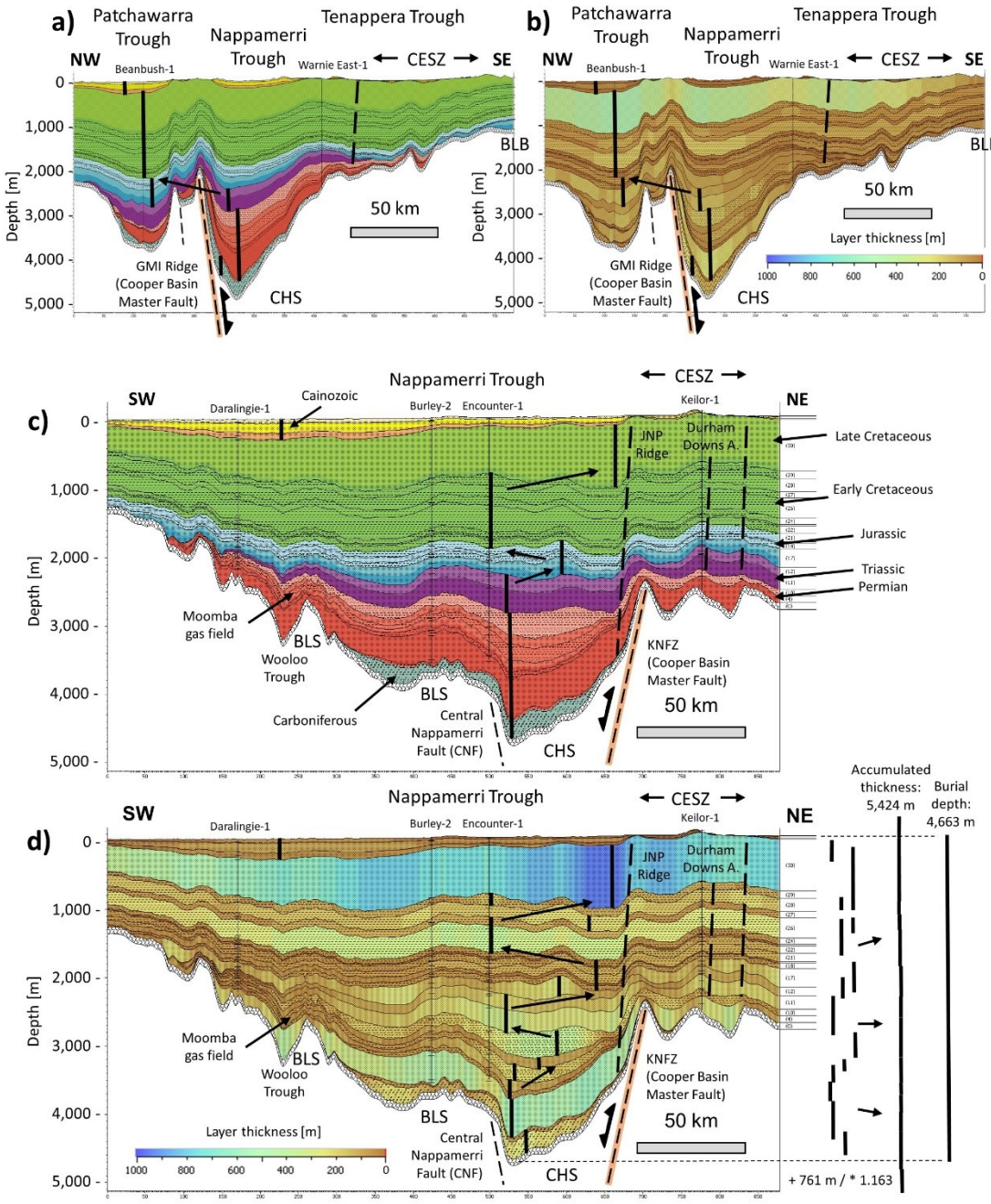

Figure 5.17: Depocentre migration of the stacked Cooper and Eromanga basins based on layer thickness variations. a) Crossline through the main depocentres with age of deposition overlay. b) Crossline through the main depocentres with layer thickness overlay. c) Inline through the Nappamerri Trough with age of deposition overlay. d) Inline through the Nappamerri Trough with layer thickness overlay and comparison of accumulated thickness with burial depth. See location of 2D lines in Figure 5.16. BLS = Big Lake Suite granodiorite, CESZ = Central Eromanga Shear Zone, CHS = Cooper Hot Spot.

The subsidence history during the Eromanga sequence (see **Figure 5.5** and **Figure 5.6**) was mainly the result of regional sagging and increasing sediment input from the uplifting magmatic arc along the eastern Australian continental margin in the context of the Gondwana breakup. However, the first and the last episode of the Eromanga sequence are outstanding: the very dynamic deposition of the Hutton Sst during the Middle Jurassic (**Figure 5.10a**) and the remarkably thick Winton Fm during the Middle Cretaceous (**Figure 5.10i**).

The rhomboidal BLB and other small and deep troughs in the NE domain (i.e., Yamma Yamma Depression) are indicating possible strike-slip tectonics during the Middle Jurassic (see **Figure 5.10a**) comparable with the observed present-day setting (**Figure 5.16a**). It is plausible that crustal shear along CESZ occurred already during the Middle Jurassic.

E-W directed maximum horizontal stress (Sh_{max}) probably acted after the deposition of the Winton Fm (Kulikowski et al., 2018; see **Figure 5.11**) and caused a regional episode of post-sedimentary uplift and erosion along preferably N-S oriented features, especially the Mount Howitt and Durham Downs anticlines, but also strongly uplifted the ID (see **Figure 5.11a** and **Figure 5.17a**).

The largest layer thickness is preserved along a SW-NE directed alignment of several depressions between the PT and the Warrabin Trough (**Figure 5.11b**). The corresponding subsidence pattern and a NW-SE oriented stretching axis would agree with a fixed Mt. Isa Terrane in the North and a southward moving Thomson Fold Belt. Paleo-stress field analysis (e.g., Müller et al., 2012) yielded 80-100 MPa of NS directed Sh_{max} for the study area in the Middle Cretaceous (around 100 Ma), which is generally compatible with N-S to NW-SE strike-slip motion along the CESZ.

Certainly, the study area was not only overfilled with debris from the east, but also strongly affected by tectonic far-field effects of the orogenic collapse and violent continental breakup along the eastern margin during the Middle Cretaceous (e.g., Bryan et al., 2012). It is therefore reasonable that the observed present-day setting (**Figure 5.16**) is predominantly the result of the stress reconfiguration during and directly after the deposition of the Winton Fm (N-S transpression and transtension followed by E-W compression and uplift). An additional period of possible small-scale reactivation of the CESZ happened during the Middle Miocene (Namba Fm, Müller et al., 2012).

Southward stretching and thinning of the Thomson Orogen along the CESZ could be the result of a combination of tectonic escape from westward indentation, southward mantle flow and sub-crustal delamination, which is obviously still ongoing today (see Sandiford et al., 2020).

5.5.4 Uncertainties of thermal history

Several hydrothermal and volcanic events were reported in the study area (i.e., Gallagher & Lambeck, 1989; Moussavi-Harami, 1996; Duddy & Moore, 1999; Mavromatidis & Hillis, 2005; Mavromatidis, 2006a, 2006b, 2007; Bryan et al., 2012; Middleton et al., 2014; Hardman et al., 2019) and amounts of erosion are rather low in the study area (except for the Winton Fm), while the fluctuating heat flow seems to have much greater influence on thermal maturity. However, determining the number, exact ages and magnitudes of thermal events in the study area is challenging. The input of the numerical models in this study considers only the two youngest heat flow peaks (**Table 5.4**, peak I and II in **Figure 5.7c**), because apparently the magnitude of the Middle Cretaceous event (peak II) has been high enough to overprint previous thermal events (III-VII in **Figure 5.7c**) throughout most of the study area (**Figure 5.5** and **Figure 5.6**). Additionally, the differences in the calibration results are too small to identify the exact timing and magnitude of thermal events prior to the Middle Cretaceous with the applied method.

Based on the 1D model along borehole Burley-2, a comparison of alternative thermal calibration scenarios is shown in **Figure 5.18**. To emphasize the effects of input variations on calibration, two end-member scenarios with background heat flow (60 mW/m^2) and with present-day heat flow (110 mW/m^2) are shown (**Figure 5.18a**). It is obvious that the background heat flow fits only the youngest sediments and the present-day heat flow would only match the values of the deepest layers. A constant heat flow trend can therefore be safely excluded.

To achieve a satisfying match of the calculated thermal maturity with the very detailed vitrinite profiles (**Figure 5.5** and **Figure 5.6**), numerous transient heat flow scenarios lead to similar results (compare **Figure 5.7c** and **Figure 5.18b-d**) with the oil window located at only 1.2 km and the gas window already at 2 km depth. The results of the best fit scenario (peak II, **Figure 5.18b**) can be replicated with additional peaks either in the Middle Jurassic (peak III, **Figure 5.18c**) or in the Middle Triassic (peak V, **Figure 5.18d**).

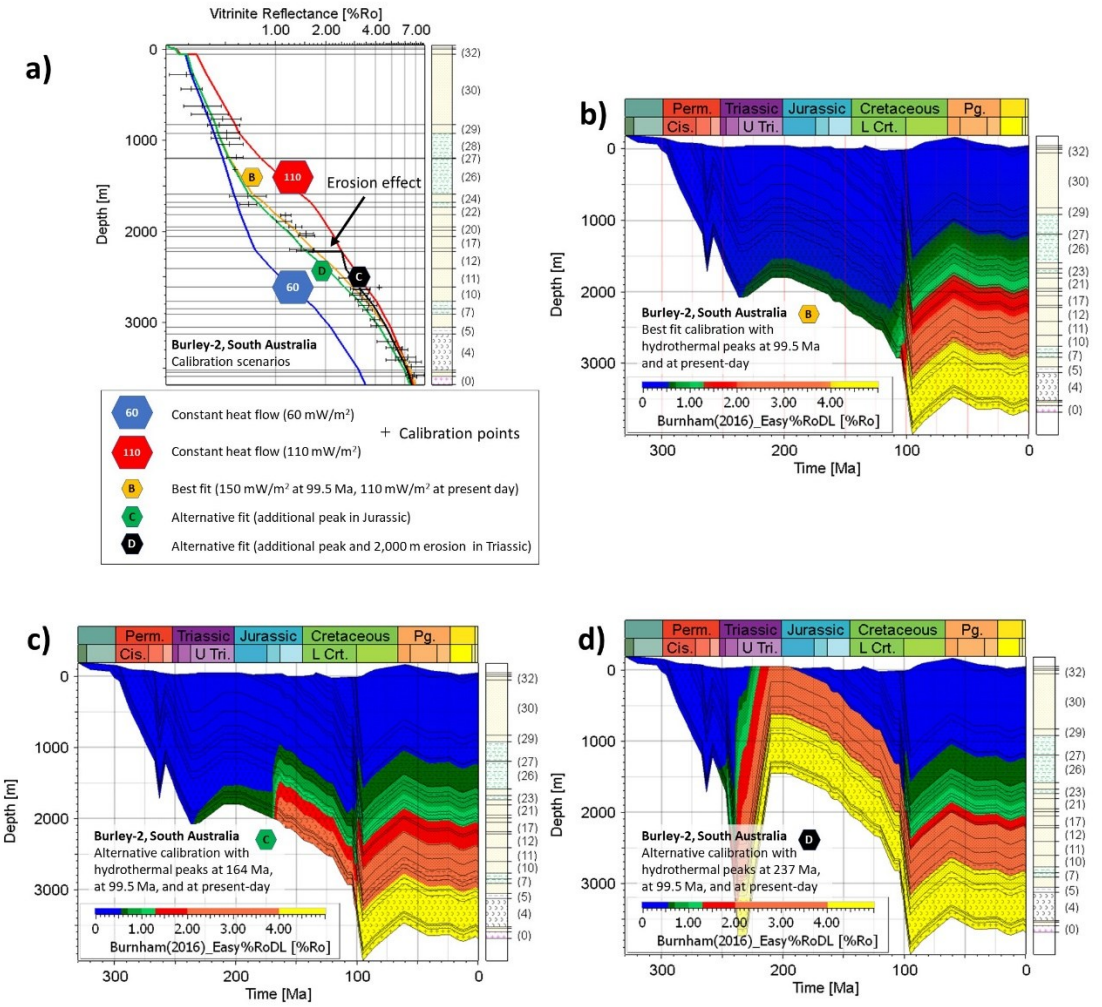

Figure 5.18: Thermal modeling / calibration scenarios and burial history discussion based on the vitrinite reflectance profile at Burley-2. a) Overview of compared heat flow trends with vitrinite reflectance calibration points and calculated thermal maturity including constant heat flow scenarios. b) Best-fit scenario used to calibrate the 3D model. c) Alternative calibration with additional heat flow peak in the Jurassic. d) Alternative calibration with additional heat flow peak in the Triassic combined with erosion.

5.5.5 Palaeozoic thermal evolution

Possible hydrothermal events due to Permian rifting (e.g., McLaren & Dunlap, 2006; Middleton et al., 2014; peak VI, see **Figure 5.7c**) cannot be excluded, but would only affect Permian sediments. Required amounts of heat flow and/or erosion to match vitrinite reflectance profiles would exceed those of scenario D (**Figure 5.18d**).

Emplacement of BLS granodiorite occurred prior to CB sedimentation (peak VII, see **Figure 5.7c**) and was therefore not directly responsible for thermal maturation. However,

its high radioactive heat generation (about 10 µW/m^3) is responsible for continuously enhanced heat flow into sediments directly above (Holgate, 2005, Meixner et al., 2012, Middleton et al., 2014).

5.5.6 Mesozoic thermal evolution

Peak III (150 mW/m^2 at 164 Ma) represents the so-called "Warnie Volcanic Province" with increased volcanic activity in the NT during the Middle Jurassic (Hardman et al., 2019). The same settings for the Triassic-Jurassic boundary (peak IV at 200 Ma, see Middleton et al., 2014) delivered similar results, but are not shown.

Peak V represents a theoretical Triassic post-rift unconformity with elevated heat flow and substantial uplift (120 mW/m^2 at 237 Ma plus 2 km of Tinchoo Fm erosion). The distinct step in the maturity profile shows a typical "erosion effect", but becomes only visible with unusually high amounts of removed section.

It should be noted, that all calibration scenarios still require peak II (150 mW/m^2 at 99.5 Ma) to match the middle section of the vitrinite profile, which emphasizes the dominance of the Middle Cretaceous hydrothermal event. Although hydrothermal activity probably lasted from Early to Late Cretaceous (128-86 Ma, Murray, 1994; Deighton & Hill, 1998; Middleton et al., 2014), the exact timing and magnitude of the peak is crucial. Small shifts in either direction (age or amount of heat flow) leads to large variations in the calibration quality.

At Warnie East-1, a Middle Cretaceous basaltic sill was intersected (K-Ar pyroxene age: 100 Ma, Murray, 1994, see **Figure 5.6**). This discovery was eponymous for the "Warnie Volcanic Province", where numerous volcanic features are often correlating with NW-SE oriented strike-slip faults and which were interpreted to be of Jurassic age (Hardman et al., 2019). The restriction to Jurassic age is problematic since additional volcanic material at other locations provides inconclusive or contradicting ages:

- At Kappa-1, undated basalt at the top of the Nappamerri Gp was intersected, directly overlain by Hutton Sst (Draper, 2002).
- Lambda-1 contains a Triassic weathered basalt flow or feeder vent (227 Ma, Murray, 1994) and is overlain by thermally unaffected Birkhead Fm.
- Orientos-2 hosts undated basalt overlain by Adori Sst, while volcanic material is absent in Orientos-1 (only 1 km apart, Draper, 2002).

Recent comprehensive 3D seismic mapping (Hardman et al., 2019) delivered no hard evidence for volcanic material of Jurassic age and interpretations could also represent sinter cones from different ages (including Cretaceous or younger). Often it remains unclear if mapped features show progressive onlap or intrusive relationships and until seismic interpretations are not correlated with dated core material, the Jurassic age will remain questionable.

It is quite possible that erratic volcanism occurred throughout the Triassic, in the Middle Jurassic and in the Middle Cretaceous. Since it apparently represents hot spot-related hydrothermal activity and volcanism from various ages, the hydrothermal area around the CHS could also be referred to as "Mesozoic Volcanic Province". Further, the age dating of Warnie East-1 (100 Ma) and Lambda-1 (227 Ma) suggests that volcanism frequently correlated with episodes of high fault activity (Winton Fm, Nappamerri Unconformity). Any Jurassic volcanism would also agree with increased tectonic activity before/during the deposition of the Hutton Sst (**Figure 5.10a** and **Figure 5.17**).

The intracontinental CHS could be a product of intraplate convective upwelling, but rather caused by very localized crustal shear and strong mantle flow around the lithospheric keel below the Thomson Orogen (Sandiford et al., 2020) than by convective upwelling from the subducting Pacific slab (Hardman et al., 2019). Future work in the study area should include additional mapping and age correlation of the volcanic features and adding them as intrusion bodies in the 3D basin model.

The Tookoonooka meteorite impact probably contributed to the Early Cretaceous glaciation of the Southern hemisphere, but impact-induced shock heating is expected to be restricted to the impact site (Turtle et al., 2003). There, much higher thermal maturity is expected for Mesozoic formations than calculated by our model (**Figure 5.14g-i**). During future thermal modelling of the study area such unique impact scenarios could be included.

5.5.7 Cainozoic to present-day thermal evolution

Erratic Mesozoic volcanism and transient heat flow peaks suggest that circulation of hot fluids in the subsurface is directly linked to fault activity and stress field variations. Consequently, high heat flow and volcanism imply episodes of increased fault permeability (dominant extensional horizontal stress) and low heat flow would indicate closed faults (dominant compressional horizontal stress). Indeed, after peak II, subsurface temperatures dropped dramatically due to compression and uplift (Moussavi-Harami,

1996; Bryan et al., 2012) and remained relatively low before hydrothermal activity increased again in the Plio-Pleistocene (peak I; Pitt, 1986; Gallagher, 1988).

Present-day heat flow and temperature distribution across Australia shows a remarkable anomaly in the CB (Holgate & Gerner, 2010, Hall et al., 2016b) with highest values in the NT. Despite the relative coarse resolution of constructed heat flow maps (**Figure 5.12**), modelling results of this work broadly agree with these previous studies. Recently, numerous EGS projects were attracted by the highly permeable fault zones in combination with high heat flow within the study area. Extraordinary high volumes of mud losses, e.g., at Habanero geothermal reservoir (Holl & Barton, 2015) suggest that conditions are locally excellent for geothermal energy production, but could be a high risk for other technologies, i.e., CCS.

Assuming the present-day geothermal gradient of locally up to 52 °C/km (e.g., at Burley-2) to be constant with depth implies partial melting of the crust at about 15 km (~750 °C) and the transition from lithosphere to asthenosphere at around 26 km (~1,333 °C). Although resolution of related geophysical surveys is coarse, thinned crust and locally abnormal lithospheric thickness below the SW domain are generally supporting this hypothesis (Kennett et al., 2011; Hall et al., 2016b; Rawlinson et al., 2017, Sandiford et al., 2020). The sketch in **Figure 5.19** schematically displays a magmatic network that connects the hot upwelled mantle and a hypothetic Cooper Pluton, from which magma occasionally finds its way into the sedimentary successions above.

Presumably, this magmatic system was frequently active throughout geologic history, was regularly feeding magmatic intrusions, and was responsible for circulating hot fluids within the network of faults and fractures. In reality, associated hydrothermal activity probably shows much higher regional variability than predicted by our relatively coarse model. Together with a higher number of calibration wells, detailed fault mapping and incorporating a corresponding structural model into the numerical basin model could provide a more detailed evolution and spatial distribution of heat flow and temperature.

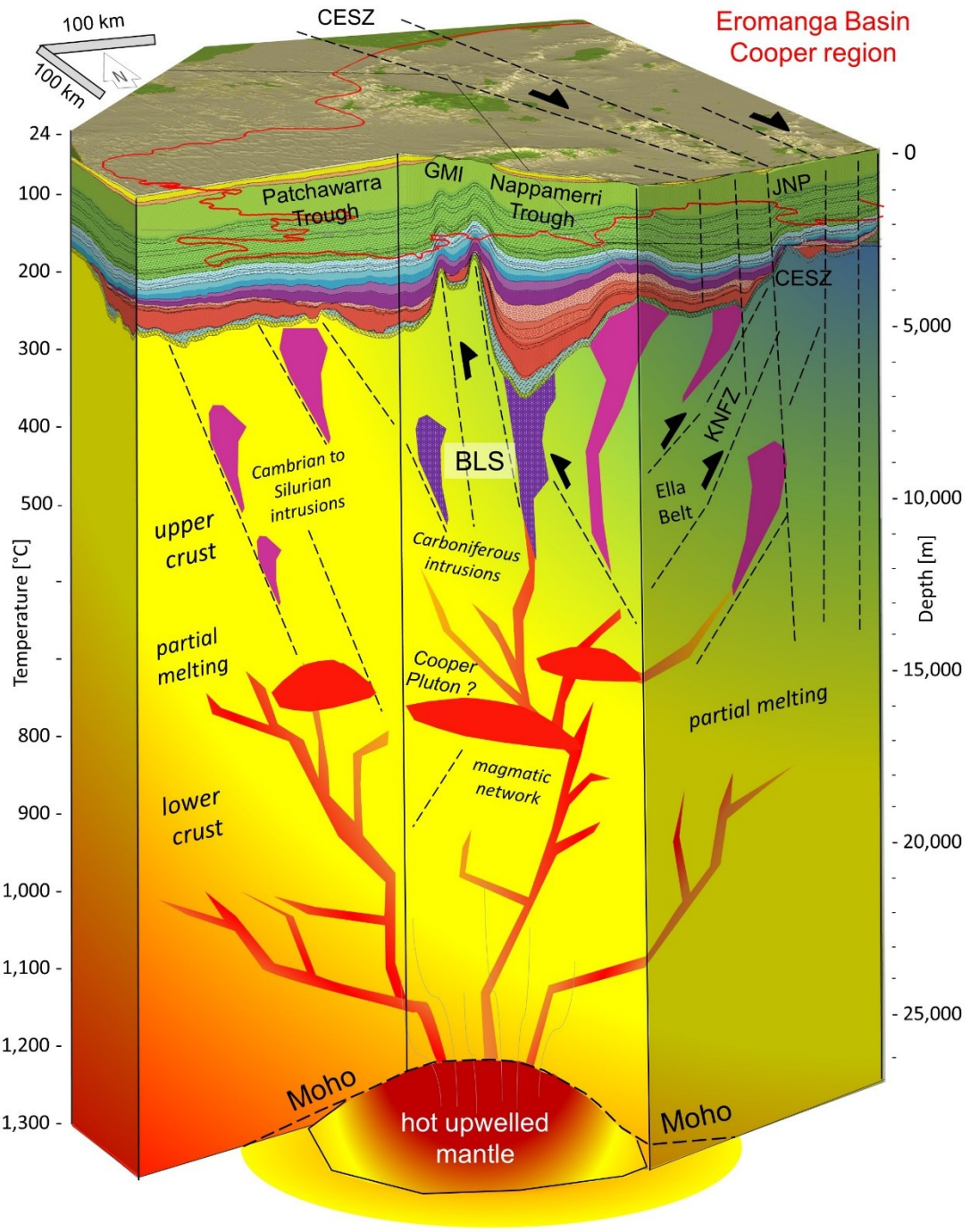

Figure 5.19: 3D-sketch of the crust and upwelled mantle below the Cooper Basin. Magma chambers represent assumed Cooper Pluton as part of the magmatic network related to the Mesozoic volcanic/hydrothermal province (Cooper Hot Spot). BLS = Big Lake Suite granodiorite, CESZ = Central Eromanga Shear Zone, GMI = Gidgealpa-Merrimelia-Innamincka Ridge, JNP = Jackson-Naccowlah-Pepita Ridge, KNFZ = Karmona-Naccowlah Fault Zone.

5.5.8 Implications on hydrocarbon generation and exploration outlook

Minor pulses of kerogen maturation and transformation occurred already in the Permian, at least in the basin center (compare McKirdy et al., 2001; Michaelsen & McKirdy, 2001), but simulation results indicate that extreme heating rate and high temperatures during peak II (**Figure 5.7**) were responsible for the vast majority of petroleum generation in the study area (**Figure 5.8**).

The high heating rates in combination with fast subsidence caused all source rocks to transform considerable amounts of their kerogen into oil and gas, simultaneously in a relative short period. During such rapid heating, petroleum expulsion and thus accumulation can occur faster from source rocks than at other times due to creation of overpressure and microfracturing (Leythaeuser et al., 1988; Littke et al., 1988; Kutovaya et al., 2019).

Based on calculated transformation ratio (**Figure 5.8** and **Figure 5.14**) huge volumes of hydrocarbons (especially gas) must have been generated especially in the NT and in the Windorah Trough within a relatively short period, but are not preserved (see locations of gas fields in **Figure 5.3**). It is plausible that during the fast maturation process, most of the generated hydrocarbons have been lost to the atmosphere, because faults were highly permeable and no traps existed in the deep basin center. Accumulations concentrate in a ring around the NT where heating was less and compartmentalization was possible due to anticlinal structures and tight sealing layers. It is therefore obvious, that besides further coal bed methane development, the NT is very suitable for enhanced geothermal system projects due to highly permeable faults and very high heat flow. However, for the same reasons, the NT is also a candidate for degassing hydrocarbons and carbon dioxide until present day and various waterholes in the area could represent active or intermittent vents. Isolated blocks with good sealing capacity (e.g., Moomba Gas Field) could also act as suitable targets for carbon capture and storage projects (Santos, 2020), but their individual tectonic history should be carefully examined.

Future work with the 3D model should therefore include calibration of pressure, porosity and permeability to determine exact timing of migration, accumulation and to quantify fault permeability and seal integrity. Combined with earlier studies (e.g., Hall et al., 2019), escaped volumes could then be quantified and their contribution to the Late Cretaceous greenhouse could be assessed. Further, a detailed structural model based on geomechanical and seismic data could help to understand the slip-tendency and permeability-history of faults and fractures in the study area.

5.6 Conclusions

The Cooper region within the central Eromanga Basin represents a central weak spot of the Australian continental crust that frequently compensated tectonic movements along the Tasman Line and Torrens Hinge Zone. It was strongly affected by far-field tectonic effects of the dynamic transformation of the eastern continental margin during the Cretaceous and is still tectonically and hydrothermally active today. The application of numerical basin and petroleum system modelling, analyses of burial history and depocentre migration provided important evidence for strong correlations between tectonics, hydrothermal/volcanic activity and petroleum source rock maturation in the Cooper Basin and the overlying Eromanga Basin.

Basin opening, depocentre migration and intermittent episodes of inversion in the Cooper region were governed by major overlapping strike-slip systems and basement ridges. The structural layout of the Cooper region is mainly characterized by the WNW trending Karmona-Naccowlah Fault Zone (KNFZ) and the Jackson-Naccowlah-Pepita (JNP) Ridge, which are subdividing the basement topography into the lower SW domain and the higher NE domain.

Ancient structures of the Eastern Warburton Basin controlled the evolution of the Cooper Basin Master Fault (CBMF) in the SW domain. Along the CBMF, a triplex lazy-s pull-apart basin opened during the Permian, which transformed into a push-up (piggyback) basin before it was blanketed by the Jurassic-Cretaceous Eromanga sequence.

The NE domain was influenced by the structure of the underlying Thomson Orogen, which was subject to frequent E-W indentation, ongoing ENE-WSW compression and SSE simple shear due to tectonic escape until today. Since the Jurassic, tectonic style and depocentre migration in the Cooper region was more and more controlled by the NNW-SSE-oriented Central Eromanga Shear Zone (CESZ), which caused southward flexure of the Nappamerri Trough and the CBMF. The crossing point of the CBMF and the CESZ marks the deepest point of the basement and features a Mesozoic volcanic province upon an inferred Cooper Hot Spot (CHS). The CHS is apparently related to punctual crustal thinning and an associated magma chamber (“pull-apart pluton”), which also caused multiple Palaeozoic intrusions nearby. Frequent and transient heat flow peaks due to hydrothermal events and occasional volcanism were obviously associated with/caused by episodes of increased fault activity throughout the Phanerozoic. Calibration of very detailed vitrinite reflectance profiles suggests an outstanding tectonic and hydrothermal

event in the Middle Cretaceous (about 100 Ma ago) with associated sedimentation rates of locally up to 200 m/Ma, heat flow up to 150 mW/m^2 and formation temperatures up to 300 °C (Patchawarra Fm), which probably overprinted all previous thermal events. The Middle Cretaceous event was characterized by oversupply of sediments during the Winton Fm, simultaneous substantial shearing along the CESZ and extraordinary hydrothermal fluid circulation through open faults and fractures. This remarkable event shifted Eromanga source rocks to thermal maturity between 0.9 and 1.8 %Ro, pushed all Permian source rocks beyond 3.0 %Ro and caused intense kerogen transformation beyond the critical value in the basin center (i.e., Nappamerri and Windorah troughs).

Today, the main oil window is located at 1.2 km, the gas window starts at 2 km and the dry gas window commences at about 3 km depth. No major oil or gas accumulations occur within the Nappamerri Trough, because most volumes of locally generated hydrocarbons probably escaped to the atmosphere already during the Middle Cretaceous. An unusually high present-day geothermal gradient and highly permeable faults make the Cooper subregion a suitable province for enhanced geothermal systems (EGS). By combining basin modelling, thermal modelling, subsidence history analysis and neotectonic analysis, the interdisciplinary approach performed in this study supports the understanding of the tectonic and thermal history of central eastern Australia and serves as an example workflow for other intracratonic sedimentary basins worldwide.

6 CONCLUDING REMARKS AND OUTLOOK

6.1 Summary of generated data and its relevance

In this thesis, two important Australian petroleum provinces were investigated. Generated data comprise the tectonic and thermal history of both, the Gippsland Basin, situated in the Bass Strait offshore Victoria, and the Cooper/Eromanga basin couplet, located in central eastern Australia. Calibrated heat flow trends for both study areas were obtained by applying basin and petroleum system modeling workflows on two individual 3D numerical basin models in two separate studies. In either case, the determined thermotectonic history (reconstructed based on fault interpretations, subsidence analysis, depocentre variation, interpreted volcanic/magmatic features, crustal layer modeling, borehole temperature and vitrinite reflectance profiles) had important influence on the thermal maturation of petroleum source rocks and resulting transformation and expulsion of hydrocarbons.

In a third independent study, samples of two potential petroleum source rocks of the Eromanga sequence were analysed by applying organic geochemical and organic petrographical methods and were evaluated based on their thermal maturity, petroleum potential and paleo-depositional environment. The results of this study are described in **Chapter 4** and reveal that both, the Jurassic Birkhead Fm and the Cretaceous Murta Fm, originated from an oxic/terrestrial paleo-depositional environment, exhibit fair to very good petroleum generation potential and have partly reached the transition to the early oil window (0.5-0.7 VR_r %, T_{max} 425-440 °C, see summarized results in **Table 4.5**). Many samples from the Murta Fm show unusually high production indices compared to their respective thermal maturity, which is the result either from relatively fragile kerogen or from a rapid and strong heating event.

Although not yet finally confirmed by this work, it is very likely that oil expulsion from the two investigated source rocks locally contributed to the charge of the Eromanga petroleum system. At least, the determined individual source rock properties of the Birkhead Fm (average HI = 300 mgHC/gTOC, average TOC = 3.7 wt.%) and the Murta

Fm (average HI = 150 mgHC/gTOC, average TOC = 2.2 wt.%) were used to complement the input data of the Cooper/Eromanga modeling study and therefore provided new insight into the thermal maturation and petroleum generation history.

At first sight, both study areas differ substantially. The smaller GB is situated at the continental shelf, relatively deep (filled with up to 14 km of sediment), quite cold (about 50 mW/m^2 present-day basal heat flow), and witnessed the highest sedimentation rates during the Early Cretaceous to Middle Cretaceous. Contrastingly, the much larger Cooper/Eromanga region occupies the central eastern interior of the Australian continent, is relatively shallow (sediment fill: about 4.5 km), unusually hot (present-day basal heat flow varies between 60 and 110 mW/m^2), and featured two episodes of increased subsidence and sediment accumulation in the Permian and in the Middle Cretaceous.

However, results and observations from the two independent modeling studies also reveal some remarkable similarities. Although the main depocentres of both study areas are separated by a horizontal distance of more than 1,000 km, the GB and the EB show notable resemblance in their thermal and tectonic history during the Cretaceous. Both sedimentary basins have recorded accelerating tectonic subsidence and increasing sedimentation rate during the Early Cretaceous and were strongly affected and transformed by the orogenic collapse of the eastern Australian margin, which contributed to the final breakup of supercontinent Pangaea-Gondwana (see **Figure 2.20**).

Some simulator options used for numerical basin modelling performed in **Chapter 3** are available in Appendix 1. The remaining data related to this study are only available on request and only with the permission of Schlumberger due to copyright reasons (see copyright statement at the end of **Chapter 3**).

Detailed results of the organic geochemical and organic petrographic analyses performed in **Chapter 4** are available in Appendix 2.

The input data used for 1D numerical basin modelling in **Chapter 5** is available in the Appendix 3.

6.2 Conclusions from numerical modelling and structural analysis

Chapter 3 dealt with the key research question if "*it is possible to reconstruct the tectonic evolution and the thermal history of the Gippsland Basin based on McKenzie-type crustal layer modeling and thus to draw new conclusions about the timing of the overlying petroleum system?"*

Based on a fully integrated numerical 3D model and the application of an innovative two-step crustal layer inversion workflow, it was indeed possible to calibrate a databased and logical tectonic evolution and to reconstruct the corresponding thermal history of the GB.

The structure and the stratigraphic record of the GB described in the third chapter of this thesis represent important evidence for a complex multi-phase tectonic evolution, during which the continental assemblage of Australia, Antarctica and Zealandia disintegrated and large parts of Eastern Gondwana underwent a drastic transition from a magmatic arc to a passive margin. This orogenic collapse culminated in the Middle Cretaceous (Albian-Cenomanian boundary, about 103 Ma ago, see references and detailed description in **Chapter 3**) with associated maximum basal heat flow of about 90 mW/m^2 and initiated the opening of the Tasman Sea along the Tasman Rift. Simplified 3D cartoons in **Figure 6.1** demonstrate this evolution in four steps: pre-rift (a), syn-rift (b), transition (c), and late post-rift (d) based on the obtained results from crustal layer modelling.

Concluding, the results from numerical modelling show that the dynamic tectonic and thermal history of the GB was directly coupled with stretching and heating of the crust and mantle upwelling during the Early Cretaceous and subsequent thermal subsidence from the Late Cretaceous until present day. Combined with extensive literature research, seismic interpretation of faults and magmatic features, and based on a purpose-built calibration matrix (see **Table 3.2**), this study also confirms that the GB initially evolved as an intracratonic rift system along the SAFZ and transitioned into an aulacogen during the opening of the Tasman Rift. It then submerged as part of the newly formed passive continental margin during the transgression of the Tasman Sea.

Since an idealized McKenzie-approach and other simplifications were applied, a number of uncertainties remain (see **Table 3.3**). For example, it turned out that the area of maximum subsidence does not necessarily correlate with the area of maximum heating. This mismatch can have several reasons, but most likely, the GB opened as an asymmetric oblique rift due to simple shear (Wernicke crustal extension model) rather than symmetrically due to pure shear (McKenzie crustal extension model).

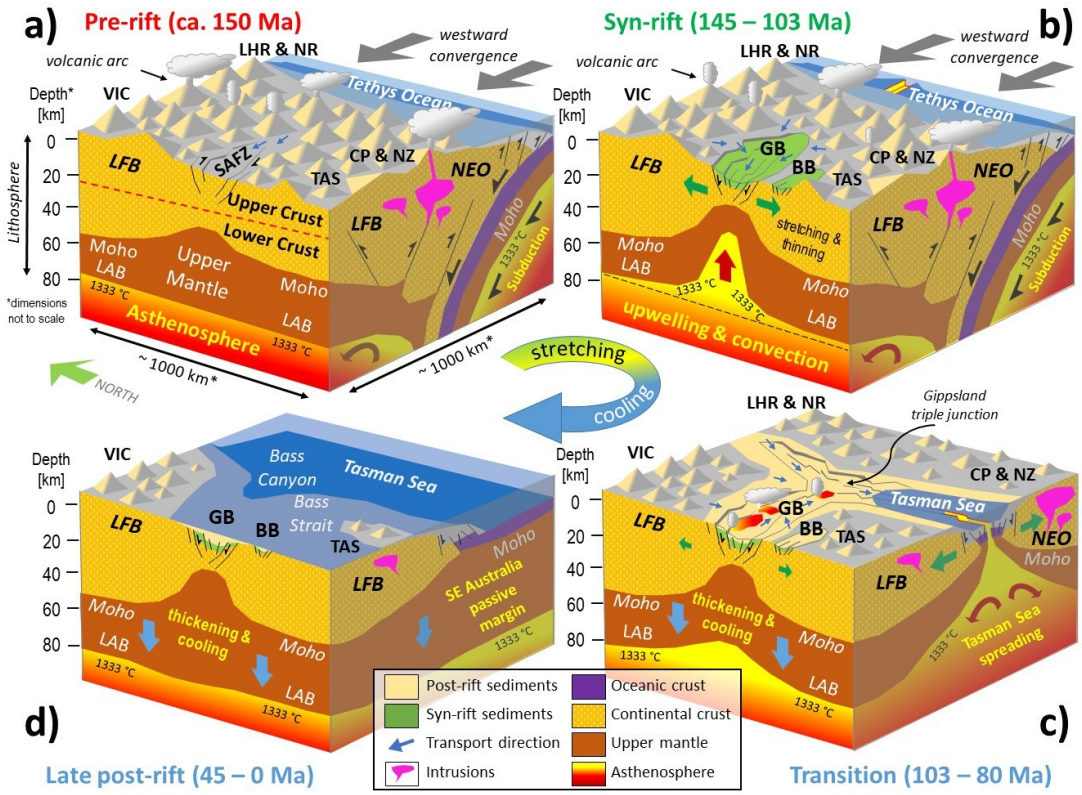

Figure 6.1: Schematic reconstruction of the regional geological setting and corresponding geometry of the lithosphere below the Gippsland Basin over time. a) Situation before the initial opening of the Gippsland Basin (pre-rift). b) Mantle upwelling, crustal stretching and major subsidence during the syn-rift. c) Orogenic collapse and Tasman Sea opening during the early post-rift. d) Passive margin formation, transgression of the Tasman Sea and opening of the Bass Strait. BB = Bass Basin, CP = Campbell Plateau, GB = Gippsland Basin, LAB = Lithosphere-Asthenosphere Boundary, LFB = Lachlan Fold Belt, LHR = Lord Howe Rise, NEO = New England Orogen, NR = Norfolk Ridge, NZ = New Zealand, SAFZ = Southern Australian Fracture Zone, TAS = Tasmania, VIC = Victoria (continental Australia). Please find location and extend of the blocks in **Figure 2.20**.

Middle Cretaceous uplift and erosion along the magmatic arc of Eastern Gondwana (including the GB) caused westward transport of massive amounts of eroded material towards the fluvio-lacustrine foreland basins, particularly the central EB. Sedimentation concentrated, where the EB overlies the Pennsylvanian to Late Triassic CB, especially in the Nappamerri Trough. While the eastern margin was uplifted and eroded, the continental interior not only received the resulting erosional products, but also experienced a phase of accelerated tectonic subsidence. Temporarily, the paleo-depositional conditions in the EB changed from terrestrial to marine, representing a short-lived Middle Cretaceous marine transgression, before the entire continental platform was uplifted again, exposed to weathering and was subject to minor sedimentation processes since the Late Cretaceous.

In **Chapter 5**, it was mainly investigated "w*hat were the main tectonic drivers that formed the Cooper and Eromanga basins, how did the subsurface temperature develop and how did it influence source rock maturation and petroleum generation?*

To answer these questions, numerical basin modeling and subsidence history analysis was performed based on a public-domain 3D model of the Cooper and Eromanga stacked sedimentary basins. Maps for sediment thickness, temperature, heat flow and thermal maturity were generated and calibrated based on remarkably detailed vitrinite reflectance profiles (see **Figure 5.5** and **Figure 5.6**).

Resulting heat flow trends indicate a major hydrothermal/magmatic event in the Middle Cretaceous (about 100 Ma ago) with associated maximum basal heat flow up to 150 mW/m^2. This event was also characterized by accelerating tectonic subsidence probably due to extensive crustal shear and correlates with highest sedimentation rates in the Eromanga sequence.

Structural interpretation and depocentre migration analysis suggest that the underlying Carboniferous-Triassic CB initially opened as a pull-apart basin, before it was inverted into a piggyback basin and then covered by the Jurassic-Cretaceous Eromanga sequence.

The Carboniferous to Permian initial opening of the CB was not the first event associated with strike-slip tectonics in central Australia. Already during Palaeozoic and Archean times, several tectonic episodes shaped the Australian continent by large-scale transtensional and transpressional movements often along the TL and the THZ (see **Chapter 2**).

The CB formed near the junction of the TL and the THZ (a pivotal point of Paleozoic Australian tectonics) and it continuously compensated the tectonic movements in this very dynamic intracratonic setting throughout its entire geologic evolution. The Cambrian to Silurian intrusions along the Ella Belt (Purdy et al., 2018, **Figure 5.1b**) as well as the Carboniferous BLS granodiorites (Middleton et al., 2014, **Figure 5.1b**) can be associated with NW-SE to NNW-SSE directed compressional (push-up) episodes during the Petermann, Delamarian and Alice Springs orogenies, respectively. Apparently, the layout and rheology of these intrusions later controlled the development and structure of the CB (compare **Figure 5.1** and **Figure 5.15**).

6.3 Influence of tectonics on heat flow

For the analysis of the timing of the petroleum systems, it is crucial to implement the correct sequence of depositional and erosional events and to apply suitable thermal boundary conditions during modeling. Therefore, based on extensive literature research and data evaluation, the tectonostratigraphy of the GB (**Figure 3.2**) and the Cooper/Eromanga basin couplet (**Figure 5.2**) is presented in much detail in this thesis and was used as input data for the numerical models.

The resulting output of both individual 3D basin models is described in much detail in the respective chapters **3** and **5**, but combining both datasets and bringing them into an overall context shows that the thermotectonic history of both study areas is strongly connected and they probably even communicated with each other.

The tectonic subsidence and the corresponding heat flow of the two main depocentres (GB: Central Deep, EB: Nappamerri Trough) from the Early Cretaceous until present day are shown in **Figure 6.2**. In the GB, the tectonic subsidence (**Figure 6.2a**, compare **Figure 3.7**) was relatively fast and continuous throughout the entire Early Cretaceous until about 103 Ma (first blue stippled line) due to substantial stretching of the crust and the upper mantle associated with a typical syn-rift phase. The temporary maximum burial at 103 Ma was followed by a period of inversion, exhumation, transition and post-rift thermal subsidence until the end of Late Cretaceous. Due to continuous thermal subsidence of the lithosphere and the development of a passive margin setting throughout the Cainozoic, the tectonic subsidence reached its final maximum at present day.

The corresponding basal heat flow trend in the Central Deep (**Figure 6.2b**, compare **Figure 3.2**) shows a typical peak at rifting maximum with values of about 90 mW/m^2 synchronous with the (temporary) burial maximum. While pre-rift and late post-rift values are mainly below the global average (60 mW/m^2), the period of increased heat flow around the rifting maximum corresponds well with the phase of reported increased hydrothermal activity between 120 and 85 Ma.

Remarkably, during uplift and exhumation of the GB (between 103 and 90 Ma), the tectonic subsidence in the EB accelerated and reached its maximum at about 95 Ma (right blue stippled line in **Figure 6.2c**; compare **Figure 5.7**). Inversion and exhumation occurred in the EB only after 95 Ma - with a delay of eight million years compared to the GB. Another five million years later, subsidence in the GB already started again, while uplift in the EB lasted until the end of the Late Cretaceous.

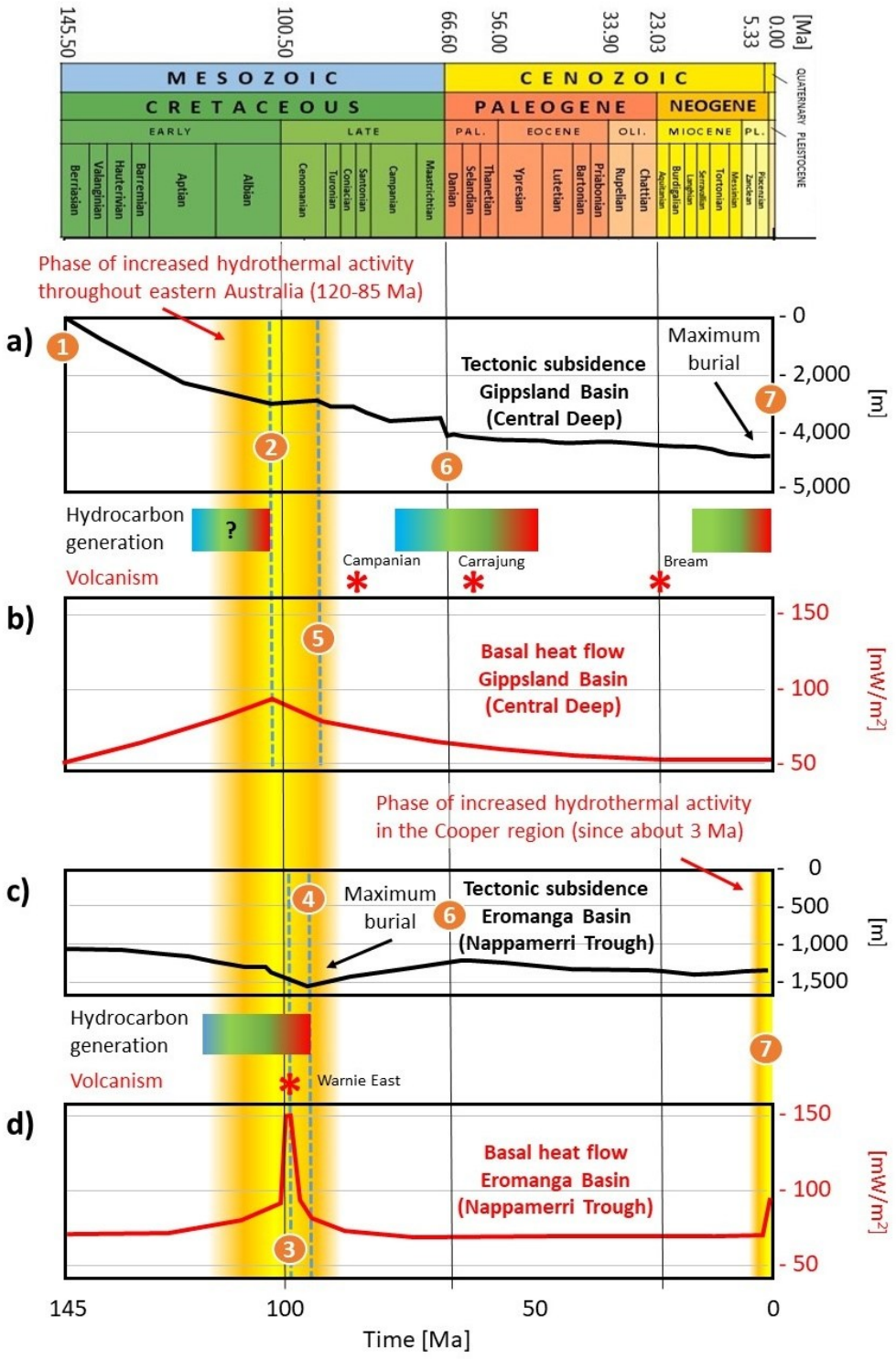

Figure 6.2: Comparison of thermo-tectonic evolution of the two study areas with overview about phases of increased hydrothermal activity, periods of hydrocarbon generation (blue = immature, green = oil mature, red = gas mature) and volcanic events (red asterisks). a) Tectonic subsidence over time in the Central Deep, Gippsland Basin. b) Basal heat flow over time in the Central Deep, Gippsland Basin. c) Tectonic subsidence over time in the Nappamerri Trough, Eromanga Basin (Cooper region). d) Basal heat flow over time in the Nappamerri Trough, Eromanga Basin (Cooper region). Circles with numbers 1-7 indicate steps of the connected thermo-tectonic sequence described in the text.

A phase of increased hydrothermal activity and elevated subsurface temperatures between 120 and 85 Ma was also reported for the EB. However, with values of up to 150 mW/m^2, the determined maximum of the basal heat flow in the EB (left blue stippled line in **Figure 6.2d**, compare **Figure 5.7**) is substantially higher than in the GB. With an age of about 99.5 Ma, it predates the moment of maximum subsidence in the EB (95 Ma) by four to five million years, but postdates the thermal maximum in the GB (103 Ma) by another three to four million years.

Obviously (and unlike to the GB), heating and subsidence in the Middle Cretaceous are not directly coupled in the EB and the comparison of tectonic subsidence and heat flow evolution of both study areas reveals an overall chronologically connected thermo-tectonic sequence of two communicating sedimentary basins (corresponding numbers also given in **Figure 6.2**):

1) 145 Ma: start syn-rift in the GB,
2) 103 Ma: rifting maximum, heat flow maximum and start of inversion in the GB,
3) 99.5 Ma: heat flow maximum in the EB,
4) 95 Ma: maximum subsidence and beginning inversion of the EB,
5) 90 Ma: post-rift subsidence in the GB, continuous uplift in the EB,
6) 66 Ma: start passive margin formation in the GB, ending uplift in the EB,
7) 0 Ma: maximum subsidence in the GB, renewed hydrothermal activity in the EB,

In a combined context, all these events are obviously expressing overall lithospheric stretching during the Early Cretaceous and subsequent multiple periods of tilting of the eastern Australian continental platform during the Middle and Late Cretaceous (e.g., Bryan et al., 2012). The thermo-tectonic activities in the EB seem to be slightly delayed reactions to the drastic movements in the east. It is also quite possible that some fragments of the Strzelecki Fm were exhumed and eroded in the GB, were transported northwestwards into the EB and then incorporated into the Winton Fm during the breakup of Eastern Gondwana.

Once established, the boundaries of Proterozoic Australian crustal fragments remained important zones of crustal weakness. These zones (e.g., SAFZ, TL, and THZ) intermittently reactivated as lines along which continental crust assembled, pulled and sheared (e.g., Myers et al., 1996). An additional intracontinental shear zone was identified via depocentre variation analysis conducted in the context of this thesis (see Chapter 5). The interpreted Central Eromanga Shear Zone (CESZ, see **Figure 5.16**) periodically

governed the tectonic evolution in central eastern Australia since the Triassic until today. It repeatedly induced NNW-SSE directed deformation along the western edge of the Thomson Orogen and is characterized by moderate present-day seismicity and succinct neotectonic features.

At times, major transcurrent faulting and volcanism occurred simultaneously. In the EB, magmatic intrusions correlate with the thermal maximum and a phase of increased tectonic activity at 99.5 (e.g., Warnie East-1, compare **Figure 5.6d** and **Figure 6.2d**). In the GB, magmatic intrusions and volcanic features formed during short tectonic reactivation periods during the post-rift (e.g., Campanian volcanics at Kipper-1, compare **Figure 3.4**, **Figure 3.5** and **Figure 6.2b**) and are spatially correlating with major strike-slip faults. It is possible, that volcanoes pierced the offshore GB also during the Early to Middle Cretaceous, but corresponding evidence has yet to be found in the deeply buried syn-rift sequence.

A large zone of periodical hydrothermal activity and associated erratic volcanism was identified in the EB (compare Hardman et al., 2019). Apparently, throughout the evolution of the Cooper and Eromanga basins, alternating tectonic stress caused frequent thermal and structural weakening of the crust and facilitated the establishment of the CHS (see **Figure 5.19**) in the Nappamerri Trough. The CHS represents a zone of very high present-day basal heat flow (> 100 mW/m^2), which increased again its activity since the Quaternary - probably triggered by increasing activity of the nearby CESZ.

On a continental scale (**Figure 6.3**), these recent thermal and tectonic features can be explained by a relatively deep and fixed crustal root of the Australian Alps (Moho depth > 50 km, see **Figure 6.3b**) and a general northward movement of Proterozoic Australia (NAE, WAE, and SAE combined). The eastern Australian continent, represented by the Tasmanides, is situated in between and is apparently subject to large-scale crustal stretching (Moho depth often about 30 km; Aitken et al., 2013) and corresponding heating (compare **Figure 1.5** and **Figure 2.26**), which locally is even causing subsidence below the sea level (Kati-tanda / Lake Eyre). Crustal shearing concentrates along the CESZ, which shows obvious neotectonic features characterized by dextral shear, (**Figure 5.16**) and is generally directed towards the Kunama Namadgi (Mount Kosciuszko), which is not only the highest topographic point of Australia, but also corresponds with the locally increased Moho depth of the orogenic root of the LFB (**Figure 6.3b**). Similarly, the crustal movement along the TL is also affected by the CC, which obviously represents

another cold and rigid block, which is unable to move due to its deep crustal root (compare **Figure 6.3** with **Figure 1.5** and **Figure 2.26**).

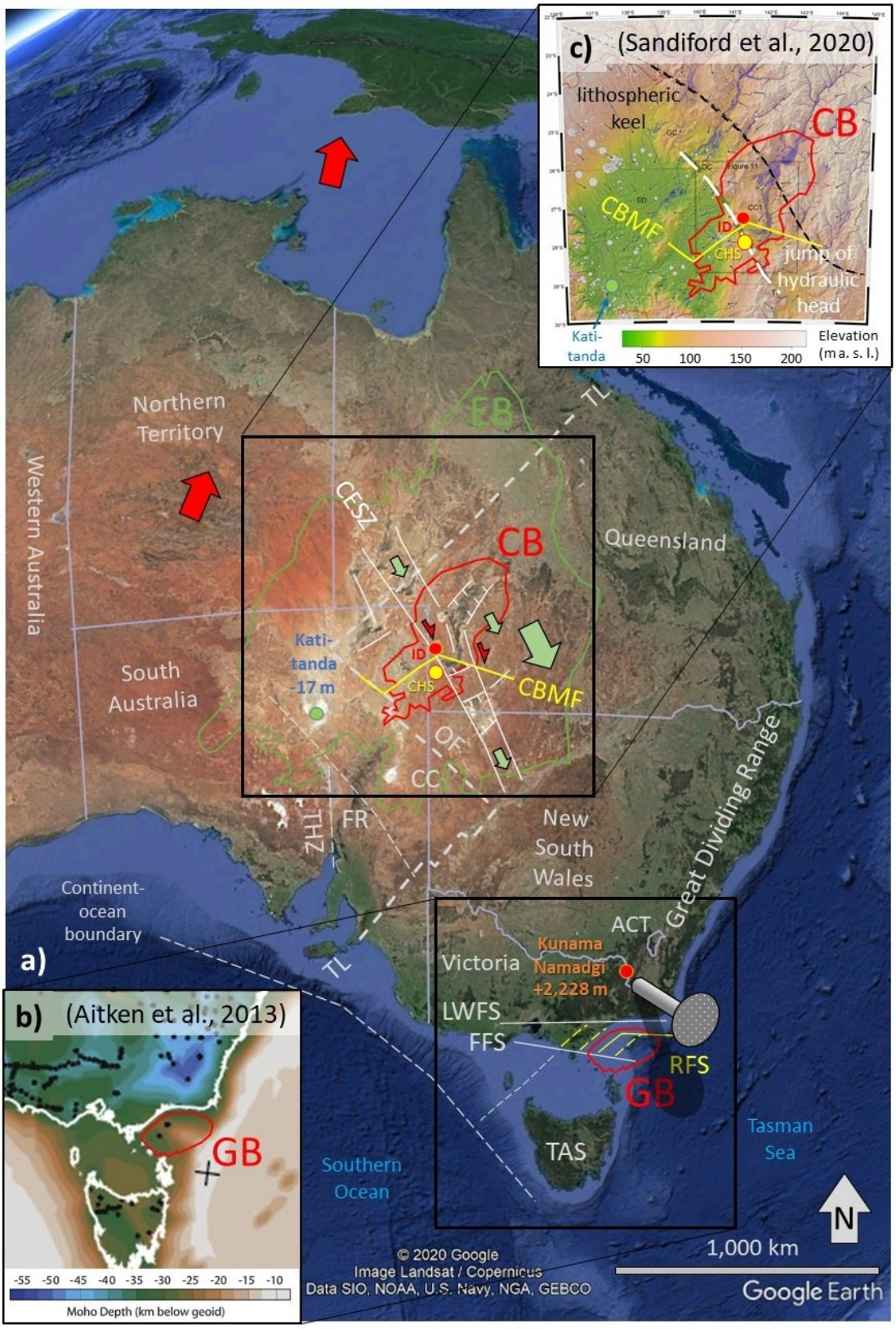

Figure 6.3: Please find the figure caption on the next page.

Figure 6.3: (previous page): Relationship between present-day topography, crustal structure and tectonics around eastern Australia. a) Overview satellite image of present-day eastern Australia with outlines of the study areas and main tectonic features relevant for this thesis (image source: Google Earth). Kati-tanda (Lake Eyre) and Kunama Namadgi (Mount Kosciuszko) are marking the lowest and highest points of continental Australia, respectively. The nail indicates the point of deepest Moho in eastern Australia. b) Section of the depth-to-Moho map (from Aitken et al., 2013) of the area around the Bass Strait. c) Topography map of the Eromanga Basin (modified after Sandiford et al., 2020). Black stippled line: lithospheric keel of the Thomson Orogen, white stippled line: jump of hydraulic head and zone of heavy deformation within the central Eromanga Basin. ACT = Australian Capital Territory, CB = Cooper Basin, CBMF = Cooper Basin Master Fault, CC = Curnamona Craton, CESZ = Central Eromanga Shear Zone, CHS = Cooper Hot Spot, EB = Eromanga Basin, FFS = Foster Fault System, FR = Flinders Ranges, GB = Gippsland Basin, ID = Innamincka Dome, LWFS = Lake Wellington Fault System, OF = Olepoloko Fault, RFS = Rosedale Fault System, THZ = Torrens Hinge Zone, TL = Tasman Line.

To emphasize the above-described tectonic model, a big nail was hammered into **Figure 6.3a**. The local crustal structure in the area around the Bass Strait together with a slight southward movement of Tasmania probably also explains the recently increased subsidence in the GB. Further, lower crustal flow along the western flank of the lithospheric keel below the northeastern CB (**Figure 6.3c**, see Sandiford et al., 2020) caused not only thermal weakening and concentrated crustal shear along the CESZ, but probably also provided conditions for recurring hydrothermal activity and contributed to the establishment of the CHS.

6.4 Effects on source rock maturation

Both study areas comprise a working petroleum system and the determined heat flow trends represent important boundary conditions for the respective petroleum system analysis. As demonstrated in chapters three and five, transient basal heat flow peaks generally correspond with periods of crustal stretching and have important influence on the temperature field and therefore on thermal maturation of the petroleum source rocks. However, it turned out that at times thermal subsidence as well as the paleo-climate and locally magmatic activity considerably affected subsurface temperatures.

Modeling results show that Late Cretaceous petroleum source rocks in the GB underwent two main phases of thermal maturation and kerogen transformation (**Figure 3.13**). After their deposition in the Late Cretaceous, a first pulse of maturation occurred from the Paleocene to the Eocene and a second pulse started in the Neogene and is still ongoing today. Both pulses were associated with continuous post-rift thermal subsidence rather

than with abnormal basal heat flow (see **Figure 6.2a** and **Figure 6.2b**). However, the Middle Cretaceous heat flow peak in the GB would have caused strong maturation and expulsion from hypothetical Early Cretaceous source rocks, which were not yet drilled in the deeply buried syn-rift sequence. Although the preservation potential is questionable due to subsequent erosion, there could be some additional volumes still waiting for their discovery especially in the underexplored deeper waters.

The numerical model of the GB failed to predict several gas fields along the Northern Terrace (**Figure 3.16**). This could be due to the multiple intrusions, which were only interpreted as structural features as part of this work, but which were not yet implemented as effective intrusion models.

The temperature evolution in the Cooper region features an extreme hydrothermal event during the Middle Cretaceous (**Figure 6.2d**), which apparently overprinted all previous thermal pulses (see **Figure 5.7c**). Results from numerical modeling show that a rapid temperature increase caused relatively fast thermal maturation and kerogen transformation of all Paleozoic source rocks. This event also caused rapid maturation and obviously also petroleum expulsion from the Jurassic Birkhead and the Early Cretaceous Murta formations. As described in detail in chapter 4, respective core samples from relatively shallow depths (1,000-2,200 m) were collected and analysed with organic geochemical and organic petrographic methods. Although most samples of these two potential source rock layers turned out to be mainly immature to early mature, many samples have already expelled surprisingly high amounts of hydrocarbons.

However, the thermal and tectonic activities during the Middle Cretaceous were probably so strong (very high heat flow combined with increased fluid circulation and many open faults), that large amounts of the generated hydrocarbons escaped to the atmosphere. At least in the main depocentre, where the highest thermal maturity is present (**Figure 5.14**), almost no hydrocarbon accumulations are preserved (**Figure 5.3**).

The recently developing thermal pulse, which affects the Cooper region since the Quaternary is not yet strong enough to have any additional influence on thermal maturation of the already strongly matured source rocks.

6.5 Lateral movements of the crust and limits of modelling

While the methodology of basin and petroleum system modelling can easily simulate vertical movements (subsidence and uplift) of grid cells, it translates lateral movements

only into corresponding stretching factors. However, these stretching factors are again based on vertical subsidence and do not represent real lateral block movement. Although, recent software solutions include the individual movement of separated blocks in 2D and 3D on top of each other to reconstruct fold-and-thrust belts (i.e., TecLink), a solution for three-dimensional strike-slip movement is still missing.

Both study areas investigated in this thesis exhibit considerable amounts of movement along strike-slip faults and even along shear zones, which were partly unrecognized before. However, such tectonic features may have important influence on local stress distribution, fluid migration, fault properties, seal integrity, the heterogeneity of heat flow and the corresponding temperature field.

Additionally, strike-slip motion of crustal blocks and lateral fault offset can be considerably larger than the amounts of vertical subsidence and uplift in a sedimentary basin itself. This also can create a space problem, since continuous lateral displacement along curved fault planes requires compaction and expansion (or addition or subtraction) of single grid cells, while the total model volume should remain constant. Anyway, reconstructing dynamics of strike-slip tectonics will be an interesting challenge for geoscientists and software developers for the nearest future.

Therefore, a basin modeler should always keep such limitations in mind and should be aware of the multitude of uncertainties (as comprehensively discussed in **Chapter 3**), which can affect input data, interpretations and conclusions.

6.6 Relevance of obtained knowledge and outlook

The conducted research in the scope of this thesis showed that the approach of basin and petroleum system modeling offers great potential for structural interpretation and petroleum exploration when combined with comprehensive geological data and profound background knowledge. Additionally, this work provided new comprehensive data about the thermal and tectonic evolution of two important sedimentary basins of Australia. Further, it was possible to evaluate the paleo-depositional environment, kerogen composition, thermal maturity and transformation of corresponding source rocks, to classify hitherto enigmatic structural elements and to identify so far unrecognized neotectonic features. Finally, the applied workflow enhanced the individual geological understanding of the two investigated complex geological settings, but also revealed some remarkable similarities.

Furthermore, in the context of increasing anthropogenic carbon emissions, accelerating climate change and the current transformation of the energy landscape, the range of possible applications of basin modelling has additional development potential, e.g., with respect to geothermal energy and storage of gases and liquids in sedimentary rocks. Geologists, geophysicists, drilling and reservoir engineers investigate the subsurface and it is crucial to combine forces to meet societal demands of the future. It will be of particular importance for Australia to manage successfully its energy transition away from coal towards an energy mix, which includes more natural gas, hydrogen and geothermal energy. Another important step is to develop further the huge CCS potential of Australia's sedimentary basins. The near future will show, if industry, governments and academia will be able to merge their knowledge and experience to expand the method of numerical basin modelling, which combines knowledge from different disciplines and forces researchers to think quantitatively and to gain knowledge on physical and chemical parameters and processes.. We should expand this methodology into an instrument for the large-scale assessment of geothermal applications and underground gas storage, to contribute to improved understanding of the global carbon cycle and to support a recovery from its current disequilibrium.

7 REFERENCES

3DGEO (2011). [Web page] 3D geological model of the Gippsland Basin. http://earthresources.efirst.com.au/product.asp?pID=1085&cID=54&c=19819. (Last accessed: 26.02.2019).

AERA, Australian Government, Geoscience Australia, Australian Energy Resources Assessment (2020a). [Web page] Executive summary. https://aera.ga.gov.au/. (Last accessed: 14.10.2020).

AERA, Australian Government, Geoscience Australia, Australian Energy Resources Assessment (2020b). [Web page] Geothermal. https://aera.ga.gov.au/#!/geothermal. (Last accessed: 14.10.2020).

AGBA, Australian Government, Bioregional Assessment (2013). [Web page] Australian geological provinces (Vol 2, 2013.01 ed., scale 1:2,500,000). Bioregional Assessment Source Dataset. Geoscience Australia, Canberra, Australia. http://data.bioregionalassessments.gov.au/dataset/13ad6933-ee80-4c51-a97b-bac1e8bef16d. (Last accessed: 22.04.2020).

AGBA, Australian Government, Bioregional Assessment (2015). [Web page] Stratigraphy of the Cooper subregion, showing geological ages, units, rock types and basin associations. https://www.bioregionalassessments.gov.au/assessments/11-context-statement-cooper-subregion/1132-stratigraphy-and-rock-type. (Last accessed: 22.04.2020).

Aghaei, H., Hall, M., Wagstaff, B., & Tait, A. (2017). Stratigraphic reconstruction of the Strzelecki Group outcrops in west Gippsland: new data on the present-day thickness and amount of erosion. Australian Journal of Earth Sciences, 64(2), 251–264. https://doi.org/10.1080/08120099.2016.1278033.

Aitken, A. R. A., Salmon, M. L., & Kennett, B. L. N. (2013). Australia's Moho: a test of the usefulness of gravity modelling for the determination of Moho depth. Tectonophysics, 609, 468-479. https://doi.org/10.1016/j.tecto.2012.06.049.

Alberdi, M., Moldowan, J. M., Peters, K. E., & Dahl, J. E. (2001). Stereoselective biodegradation of tricyclic terpanes in heavy oils from the Bolivar Coastal Fields, Venezuela. Organic Geochemistry, 32(1), 181-191.

Alexander, E. M., & Sansome, A. (1996). Lithostratigraphy and environments of deposition. In: Alexander, E.M. & Hibburt, J.E. (Eds). The petroleum geology of South Australia. Vol. 2: Eromanga Basin, Report Book 96/20 (101–110). Department of Mines and Energy South Australia.

Alexander, E. M., Gravestock, D. I. Cubitt, C. & Chaney, A. (1998). Chapter 6: Lithostratigraphy and environments of deposition, in D. I. Gravestock, J. E.Hibburt, and J. F. Drexel, eds., The petroleum geology of South Australia: Cooper Basin: Adelaide, Australia, South Australia Department of Primary Industries and Resources, v. 4, p. 69–115.

Alexander, E. M., Sansome, A. & Cotton, T. B. (2006). Chapter 5: Lithostratigraphy and environments of deposition, in T. B. Cotton, M. F. Scardigno, and J. E. Hibburt, eds., The petroleum geology of South Australia, 2nd ed.: Eromanga Basin: Adelaide, Australia, South Australia Department of Primary Industries and Resources, v. 2, 129 p.

Al-Hajeri, M. M., Al Saeed, M., Derks, J., Fuchs, T., Hantschel, T., Kauerauf, A.,Neumaier, M., Schenk, O., Swientek, O., Tessen, N., Welte, D., Wygrala, B., Kornpihl, D., & Peters, K. (2009). Basin and petroleum system modeling. Oilfield Review, 21(2), 14-29.

Allen, P. A., & Allen, J. R. (2013). Basin analysis: Principles and application to petroleum play assessment (3rd ed.). John Wiley & Sons. ISBN: 978-0-470-67376-8

Allen, T. I., Griffin, J. D., Leonard, M., Clark, D. J., & Ghasemi, H. (2019). The 2018 National Seismic Hazard Assessment of Australia: quantifying hazard changes and model uncertainties. Earthquake Spectra, 8755293019900777.

Alley, N. F. (1998). Cainozoic stratigraphy, palaeoenvironments and geological evolution of the Lake Eyre Basin. Palaeogeography, Palaeoclimatology, Palaeoecology, 144(3-4), 239-263.

Alley, N. F., Hore, S. B., & Frakes, L. A. (2019). Glaciations at high-latitude Southern Australia during the Early Cretaceous. Australian Journal of Earth Sciences, 1-51.

Ambrose, G., Suttill, R., & Lavering, I. (1982). A review of the Early Cretaceous Murta Member in the southern Eromanga Basin. In Eromanga Basin Symposium 1982. Petroleum Exploration Society of Australia (PESA).

Ambrose, G., Suttill, R., & Lavering, I. (1986). The geology and hydrocarbon potential of the Murta Member (Mooga Formation) in the Southern Eromanga Basin. Contributions to the geology and hydrocarbon potential of the Eromanga Basin: Geological Society of Australia Special Publication, 12, 71-84.

Apak, S. N., Stuart, W. J., & Lemon, N. M. (1995). Compressional control on sediment and facies distribution SW Nappamerri Syncline and adjacent Murteree High, Cooper Basin. The APPEA Journal, 35(1), 190-202.

Apak, S. N., Stuart, W. J., Lemon, N. M., & Wood, G. (1997). Structural Evolution of the Permian–Triassic Cooper Basin, Australia: Relation to Hydrocarbon Trap Styles. AAPG Bulletin, 81(4), 533–555.

APPEA, Australian Petroleum Production & Exploration Association (2020). [Web page] APPEA Annual Production Statistics 2013. http://www.appea.com.au/?attachment_id=5432. (Last accessed: 07.02.2020).

Arouri, K. R., McKirdy, D. M., Schwark, L., Leythaeuser, D., & Boult, P. J. (2004). Accumulation and mixing of hydrocarbons in oil fields along the Murteree Ridge, Eromanga Basin, South Australia. Organic geochemistry, 35(11-12), 1597-1618.

Aydin, A., & Nur, A. (1982). Evolution of pull- apart basins and their scale independence. Tectonics, 1(1), 91–105. https://doi.org/10.1029/TC001i001p00091.

Bacchin, M., Milligan, P. R., Wynne, P., & Tracey, R. (2008). Gravity anomaly map of the Australian region, scale 1: 5 000 000. Geoscience Australia, Canberra.

Barker, C. E., Bone, Y., & Lewan, M. D. (1998). Fluid inclusion and vitrinite-reflectance geothermometry compared to heat-flow models of maximum paleotemperature next to dikes, western onshore Gippsland Basin, Australia. International Journal of Coal Geology, 37(1), 73-111.

Beardsmore, G. (2004). The influence of basement on surface heat flow in the Cooper Basin. Exploration Geophysics, 35(4), 223-235.

Béhar, F., Pelet, R., & Roucache, J. (1984). Geochemistry of asphaltenes. Organic Geochemistry, 6, 587-595.

Bellucci, J. J., Nemchin, A. A., Grange, M., Robinson, K. L., Collins, G., Whitehouse, M. J., ... & Kring, D. A. (2019). Terrestrial-like zircon in a clast from an Apollo 14 breccia. Earth and Planetary Science Letters, 510, 173-185. https://doi.org/10.1016/j.epsl.2019.01.010

Berbesi, L. A., di Primio, R., Anka, Z., Horsfield, B., & Wilkes, H. (2014). Methane leakage from evolving petroleum systems: Masses, rates and inferences for climate feedback. Earth and Planetary Science Letters, 387, 219-228.

Bernecker, T., & Partridge, A. (2001). Emperor and Golden Beach subgroups: the onset of Late Cretaceous sedimentation in the Gippsland Basin, SE Australia. In: Hill, K.C. & Bernecker, T. (eds.), Eastern Australasian Basins Symposium 2001. A refocused

Energy perspective for the future. PESA Petroleum Exploration Society of Australia, Special Publication, Melbourne, 2001.

Bernecker, T., Woollands, M.A., Wong, D., Moore, D.H., & Smith, M.A. (2001). Southeast Australia – Hydrocarbon prospectivity of the deep-water Gippsland Basin, Victoria, Australia. APPEA Journal – Australian Petroleum Production and Exploration Association, 41(1), 91-114.

Berner, R. A. (1984). Sedimentary pyrite formation: an update. Geochimica et Cosmochimica Acta, 48(4), 605-615.

Berner, R. A., & Raiswell, R. (1984). C/S method for distinguishing freshwater from marine sedimentary rocks. Geology, 12(6), 365–368.

Betts, P. G., Giles, D., Lister, G. S., & Frick, L. R. (2002). Evolution of the Australian lithosphere. Australian Journal of Earth Sciences, 49(4), 661-695.

BGR, Bundesanstalt für Geowissenschaften und Rohstoffe (2020). [Web page] Subsurface use / CO2 storage. https://www.bgr.bund.de/EN/Themen/Nutzung_tieferer_Untergrund_CO2Speicherung/nutzung_tieferer_untergrund_co2speicherung_node_en.html. (Last accessed: 14.10.2020).

Blumenberg, M., Zink, K. G., Scheeder, G., Ostertag-Henning, C., & Erbacher, J. (2019). Biomarker paleo-reconstruction of the German Wealden (Berriasian, Early Cretaceous) in the Lower Saxony Basin (LSB). International Journal Earth Sciences, 108, 229–244. https://doi.org/10.1007/s00531-018-1651-5.

BOM, Australian Government, Bureau of Meteorology (2015). [Web page] Mean monthly and mean annual temperature data, http://www.bom.gov.au/jsp/ncc/climate_averages/temperature/index.jsp. (Last accessed: 03.11.2020).

Boreham, C. J., & Hill, A. J. (1998). Source rock distribution and hydrocarbon geochemistry. Petroleum Geology of South Australia, 4, 129-42.

Boreham, C. J., & Powell, T. G. (1987). Sources and preservation of organic matter in the Cretaceous Toolebuc Formation, eastern Australia. Organic Geochemistry, 11(6), 433-449.

Boreham, C. J., & Summons, R. E. (1999). New insights into the active petroleum systems in the Cooper and Eromanga Basins, Australia. The APPEA Journal, 39(1), 263-296.

Boreham, C. J., Horsfield, B., & Schenk, H. J. (1999). Predicting the quantities of oil and gas generated from Australian Permian coals, Bowen Basin using pyrolytic methods. Marine and Petroleum Geology, 16(2), 165-188.

Boult, P. J. (1993). Membrane seal and tertiary migration pathways in the Bodalla South oilfield, Eromanga Basin, Australia. Marine and Petroleum Geology, 10(1), 3-13.

Boult, P. J., Ryan, M. J., Michaelsen, B. H., McKirdy, D. M., Tingate, P. R., Lanzilli, E., & Kagya, M. L. (1997). The Birkhead-Hutton (!) Petroleum System of the Gidgealpa Area, Eromanga Basin, Australia. In Conference on petroleum systems of SE Asia and Australasia, 1997 (213-236). Conference proceedings. Indonesian Petroleum Association. https://doi.org/10.29118/ipa.965.213.235.

Bowering, O. J. W. (1982). Hydrodynamics and hydrocarbon migration – a model for the Eromanga Basin. The APPEA Journal, 22(1), 227-236.

Bowering, O. J. W., & Harrison, D. M. (1986). The Merrimelia oil and gas field – a case history. In D. I. Gravestock, P. S. Moore, and G. M. Pitt (Eds.), Contributions to the geology and hydrocarbon potential of the Eromanga basins: Geological Society of Australia Special Publication 12, 183-194.

BP plc (2019). [Web page] BP Statistical Review of World Energy 2019. 68th edition. https://www.bp.com/content/dam/bp/business-sites/en/global/corporate/pdfs/energy-economics/statistical-review/bp-stats-review-2019-full-report.pdf. (Last accessed: 13.10.2020).

Bron, K. A. (2010). Accretionary and melt impactoclasts from the Tookoonooka impact event, Australia.

Bron, K. A., & Gostin, V. (2012). The Tookoonooka marine impact horizon, Australia: Sedimentary and petrologic evidence. Meteoritics & Planetary Science, 47(2), 296-318.

Bryan, S. E., Constantine, A. E., Stephens, C. J., Ewart, A., Schön, R. W., & Parianos, J. (1997). Early Cretaceous volcano-sedimentary successions along the eastern Australian continental margin: Implications for the break-up of eastern Gondwana. Earth and Planetary Science Letters, 153(1-2), 85-102. https://doi.org/10.1016/S0012-821X(97)00124-6.

Bryan, S. E., Cook, A., Allen, C. M., Siegel, C., Purdy, D., Greentree, J., & Uysal, T. (2012). Early-mid Cretaceous tectonic evolution of eastern Gondwana: from silicic LIP magmatism to continental rupture. Episodes, 35(1), 142-152.

Burger, D. (1986). Palynology, cyclic sedimentation, and palaeoenvironments in the Late Mesozoic of the Eromanga Basin. Geological Society Special Publication, 12, 53-70.

Burger, D., & Senior, B. R. (1979). A revision of the sedimentary and palynological history of the northeastern Eromanga Basin, Queensland. Journal of the Geological Society of Australia, 26(3-4), 121-133.

Burnham, A. K. (2019). Kinetic models of vitrinite, kerogen, and bitumen reflectance. Organic Geochemistry, 131, 50-59.

Burrett, C., & Berry, R. (2000). Proterozoic Australia–Western United States (AUSWUS) fit between Laurentia and Australia. Geology, 28(2), 103-106.

Carr, L K., Korsch, R.J., Palu. T.J. & Reese, B. (2016). Onshore Basin Inventory: the McArthur, South Nicholson, Georgina, Wiso, Amadeus, Warburton, Cooper and Galilee basins, central Australia. Record 2016/04. Geoscience Australia, Canberra.

Cawood, P. A. (2005). Terra Australis Orogen: Rodinia breakup and development of the Pacific and Iapetus margins of Gondwana during the Neoproterozoic and Paleozoic. Earth-Science Reviews, 69(3-4), 249-279.

Cawood, P. A., & Korsch, R. J. (2008). Assembling Australia: Proterozoic building of a continent. Precambrian Research, 166(1-4), 1-35.

Ciais, P., Sabine, C., Bala, G., Bopp, L., Brovkin, V., Canadell, J., ... & Jones, C. (2014). Carbon and other biogeochemical cycles. In Climate Change 2013: the physical science basis. Contribution of Working Group I to the Fifth Assessment Report of the Intergovernmental Panel on Climate Change (pp. 465-570). Cambridge University Press. https://www.ipcc.ch/site/assets/uploads/2018/02/WG1AR5_Chapter06_FINAL.pdf

Clark, D., McPherson, A., & Collins, C.D.N. (2011), Australia's seismogenic neotectonic record: A case for heterogeneous intraplate deformation. Geoscience Australia Record, 2011(11).

Collins, C.D.N., Cull, J.P., Colwell, J.B., & Willcox, J.B. (1992). The deep velocity structure beneath the Gippsland Basin from long-offset seismic data. Exploration Geophysics, 23(2), 69-74. https://doi.org/10.1071/EG992069.

Collins, W. J., & Vernon, R. H. (1992). Palaeozoic arc growth, deformation and migration across the Lachlan Fold Belt, south-eastern Australia. Tectonophysics, 214(1-4), 381-400. https://doi.org/10.1016/0040-1951(92)90206-L.

Connan, J., & Cassou, A. M. (1980). Properties of gases and petroleum liquids derived from terrestrial kerogen at various maturation levels. Geochimica et Cosmochimica Acta, 44(1), 1-23.

Cook, A. G., Bryan, S. E., & Draper, J. (2013). Post-orogenic Mesozoic basins and magmatism. In P. Jell (Ed.), Geology of Queensland (515-575). Geological Survey of Queensland, Australia.

Deighton, I. & Hill, A.J. (1998). Chapter 9: Thermal and burial history. In: Gravestock, D.I., Hibburt, J.E. & Drexel, J.F. (eds.), The Petroleum Geology of South Australia, Volume 4: Cooper Basin. South Australia Department of Primary Industries and Resources, Adelaide. Report Book, 1998/9, 143–155, https://sarigbasis.pir.sa.gov.au/WebtopEw/ws/samref/sarig1/image/DDD/PGSA004.pdf.

Deighton, I., Draper, J. J., Hill, A. J., & Boreham, C. J. (2003). A hydrocarbon generation model for the Cooper and Eromanga Basins. The APPEA Journal, 43(1), 433–451.

Demaison, G., & Huizinga, B. J. (1991). Genetic classification of petroleum systems. AAPG Bulletin, 75(10), 1626–1643.

Dembicki Jr., H. (2017). Practical petroleum geochemistry for exploration and production. Elsevier. 2017, pp. 342. https://doi.org/10.1016/C2014-0-03244-3.

Derenne, S., Largeau, C., Casadevall, E., & Connan, J. (1988). Comparison of torbanites of various origins and evolutionary stages. Bacterial contribution to their formation. Causes of the lack of botryococcane in bitumens. Organic Geochemistry, 12(1), 43-59. https://doi.org/10.1016/0146-6380(88)90114-3.

Direen, N. G., & Crawford, A. J. (2003). The Tasman Line: where is it, what is it, and is it Australia's Rodinian breakup boundary? Australian Journal of Earth Sciences, 50(4), 491-502.

Divko, L. M., O'Brien, G. W., Harrison, M. L., & Hamilton, P. J. (2010). Evaluation of the regional top seal in the Gippsland Basin: Implications for geological carbon storage and hydrocarbon prospectivity. The APPEA Journal, 50(1), 463-486. https://doi.org/10.1071/AJ09028.

Dixon, O., & Hodgkinson, J. (2011). The base of the Wallumbilla Formation in the Eromanga, Surat, Carpentaria and Laura Basins – regional correlation of a key stratigraphic surface, the C-Horizon. Queensland Geological Record 2011/04.

DMITRE, Department for Manufacturing, Innovation, Trade, Resources and Energy (2001). [Web page] Seismic mapping data sets over the Cooper Basin sector, South Australia 2001, https://sarig.pir.sa.gov.au/Map. (Last accessed: 03.11.2017).

DMITRE, Department for Manufacturing, Innovation, Trade, Resources and Energy (2009), Seismic mapping data sets over the Cooper Basin sector, South Australia 2009, https://sarig.pir.sa.gov.au/Map. (Last accessed: 03.11.2017).

Draper, J.J. (ed.) (2002). Geology of the Cooper and Eromanga Basins, Queensland. Queensland Government, Natural Resources and Mines, Queensland Mineral and Energy Review Series.

Drexel, J. F., Preiss, W. V., & Parker, A. J. (Eds.). (1993). The Geology of South Australia: The Precambrian (Vol. 54). Mines and Energy, South Australia, Geological Survey of South Australia.

Duddy, J.R., & Moore, M.E. (1999). Thermal history reconstruction in Cooper-Eromanga Basin wells using apatite and zircon fission track analysis and vitrinite reflectance. Geotrack report #668. PIRSA, Adelaide

Dyksterhuis, S., & Müller, R. D. (2008). Cause and evolution of intraplate orogeny in Australia. Geology, 36(6), 495-498.

England, P. (1983). Constraints on extension of continental lithosphere. Journal of Geophysical Research: Solid Earth, 88(B2), 1145-1152.

Espitalié, J., Deroo, G., & Marquis, F. (1985). La pyrolyse Rock-Eval et ses applications. Deuxième partie. Revue de l'Institut français du Pétrole, 40(6), 755-784.

Espitalié, J., Laporte, J. L., Madec, M., Marquis, F., Leplat, P., Paulet, J., & Boutefeu, A. (1977). Rapid method for source rocks characterization and for determination of petroleum potential and degree of evolution. Revue de l´Institut Francais du Petrole, 32(1), 23-42.

Etheridge, M. A., Branson, J. C., & Stuart-Smith, P. G. (1985). Extensional basin-forming structures in the Bass Strait and their importance for hydrocarbon exploration. The APPEA Journal, 25(1), 344-361. https://doi.org/10.1071/AJ84030.

Etheridge, M. A., Branson, J. C., & Stuart-Smith, P. G. (1987). The Bass, Gippsland and Otway basins, southeast Australia: a branched rift system formed by continental extension. Sedimentary Basins and Basin-Forming Mechanisms - Memoir 12, 147-162.

Exon, N. F. (1966). Revised Jurassic to Lower Cretaceous stratigraphy in the south-east Eromanga Basin, Queensland. Queensland Government Mining Journal, 67, 232–238.

ExxonMobil (2019). [Web page] 2019 Outlook for Energy: a perspective to 2040. https://corporate.exxonmobil.com/-/media/Global/Files/outlook-for-energy/2019-Outlook-for-Energy_v4.pdf. (Last accessed: 13.10.2020).

Falkowski, P., Scholes, R. J., Boyle, E. E. A., Canadell, J., Canfield, D., Elser, J., ... & Mackenzie, F. T. (2000). The global carbon cycle: a test of our knowledge of earth as a system. Science, 290(5490), 291-296. DOI: 10.1126/science.290.5490.291. https://science.sciencemag.org/content/290/5490/291.

Fan, P., King, J. D., & Claypool, G. E. (1987). Characteristics of biomarker compounds in Chinese crude oils. In R. K. Kumar, P. Dwivedi, V. Banerjie & V. Gupta, (Eds.), Petroleum Geochemistry and Exploration in the Afro-Asian Region, Balkema, Rotterdam, 197–202.

Fang, R., Littke, R., Zieger, L., Baniasad, A., Li, M., & Schwarzbauer, J. (2019). Changes of composition and content of tricyclic terpane, hopane, sterane, and aromatic biomarkers throughout the oil window: A detailed study on maturity parameters of Lower Toarcian Posidonia Shale of the Hils Syncline, NW Germany. Organic Geochemistry, 138, 103928.

Fergusson, C. L., & Henderson, R. A. (2015). Early Palaeozoic continental growth in the Tasmanides of northeast Gondwana and its implications for Rodinia assembly and rifting. Gondwana Research, 28(3), 933-953.

Fink, R., Frohn, V., Froidl, F., Littke, R., & Uffmann, A. K. (2019). Impact of burial history on petrophysical properties of Jurassic and Lower Cretaceous mudstones as potential nuclear waste storage sites in the Lower Saxony Basin, Northern Germany. Zeitschrift der Deutschen Gesellschaft für Geowissenschaften, 339-355.

Finlayson, D. M., Leven, J. H., & Etheridge, M. A. (1988). Structural styles and basin evolution in Eromanga region, eastern Australia. AAPG bulletin, 72(1), 33-48.

Fitzgerald, P. A. U. L. (2002). Tectonics and landscape evolution of the Antarctic plate since the breakup of Gondwana, with an emphasis on the West Antarctic Rift System and the Transantarctic Mountains. Royal Society of New Zealand Bulletin, 35, 453-469.

Foster, D. A., & Goscombe, B. D. (2013). Continental growth and recycling in convergent orogens with large turbidite fans on oceanic crust. Geosciences, 3(3), 354-388.

Friedlingstein, P., Jones, M., O'Sullivan, M., Andrew, R., Hauck, J., Peters, G., ... & Bakker, D. (2019). Global carbon budget 2019. Earth System Science Data, 11(4), 1783-1838. https://doi.org/10.5194/essd-11-1783-2019.

Froidl, F., Zieger, L., Mahlstedt, N., & Littke, R. (2020). Comparison of single-and multi-ramp bulk kinetics for a natural maturity series of Westphalian coals: Implications for modelling petroleum generation. International Journal of Coal Geology, 219, 103378. https://doi.org/10.1016/j.coal.2019.103378.

GA, Australian Government, Geoscience Australia (2014). [Web page] Regional geology of the Gippsland Basin. https://industry.gov.au/resource/LowEmissionsFossilFuelTech/Documents/GHG_Regional_Geology-Gippsland_Basin.pdf. (Last accessed: 26.02.2019).

GA, Australian Government, Geoscience Australia (2017a). [Web page] Gippsland Basin. http://www.ga.gov.au/scientific-topics/energy/province-sedimentary-basin-geology/petroleum/offshore-southern-australia/gippsland. (Last accessed: 26.02.2019).

GA, Australian Government, Geoscience Australia (2017b). [Web page] National Petroleum Wells Database, http://dbforms.ga.gov.au/www/npm.well.search. (Last accessed: 17.08.2020).

GA, Australian Government, Geoscience Australia (2020a). [Web page] Energy basics. https://www.ga.gov.au/scientific-topics/energy/basics. (Last accessed: 14.10.2020).

GA, Australian Government, Geoscience Australia (2020b). [Web page] Great Artesian Basin. http://www.ga.gov.au/scientific-topics/water/groundwater/gab. (Last accessed: 22.04.2020).

GA, Australian Government, Geoscience Australia (2020c). [Web page] Australian Stratigraphic Units Database. http://www.ga.gov.au/data-pubs/data-standards/reference-databases/stratigraphic-units. (Last accessed: 22.04.2020).

Gaina, C., Müller, D. R., Royer, J. Y., Stock, J., Hardebeck, J., & Symonds, P. (1998). The tectonic history of the Tasman Sea: a puzzle with 13 pieces. Journal of Geophysical Research: Solid Earth, 103(B6), 12413-12433.

Gallagher, K. L. (1988). The subsidence history and thermal state of the Eromanga and Cooper Basins. PhD thesis.

Gallagher, K., & Lambeck, K. (1989). Subsidence, sedimentation and sea- level changes in the Eromanga Basin, Australia. Basin Research, 2(2), 115-131.

Galushkin, Y. I. (2016). Non-standard Problems in Basin Modelling. Springer, Cham. 10.1007/978-3-319-33882-8.

Geoscience Australia and Australian Stratigraphy Commission (2017). [Web page] Australian Stratigraphic Units Database. http://www.ga.gov.au/data-pubs/datastandards/stratigraphic-units. (Last accessed: 26.02.2019).

Giles, D., Betts, P. G., & Lister, G. S. (2004). 1.8–1.5-Ga links between the north and south Australian cratons and the early–middle Proterozoic configuration of Australia. Tectonophysics, 380(1-2), 27-41.

Glen, R. A. (2005). The Tasmanides of eastern Australia. Special Publication-Geological Society of London, 246, 23.

Glikson, M., Lindsay, K., & Saxby, J. (1989). Botryococcus – a planktonic green alga, the source of petroleum through the ages: transmission electron microscopical studies of oil shales and petroleum source rocks. Organic geochemistry, 14(6), 595-608.

Golding, S.D., Dawson, G.K.W., Pearce, J.K., Farrajota, F., Mernagh, T., Boreham, C., Hall L.S., Palu, T.J. & Sommacal, S. (2016). Great Artesian Basin Authigenic Carbonates as Natural Analogues for Mineralisation Trapping. CO2CRC Project 1.5.2 ANLEC Project 7-1011-0189. CO2CRC Report No RPT16-5497.

Goldstein, B., Menpes, S., Hill, A., Wickham, A., Alexander, E., Jarosz, M., Pepicelli, D., Malavazos, M., Staritski, K., Taliangis, P., Coda, J., Hill, D. & Webb, M. (2012). [Web page] Roadmap for Unconventional Gas Projects in South Australia. South Australia Department for Manufacturing, Innovation, Trade, Resources and Energy, Energy Resources Division, https://www.energymining.sa.gov.au/__data/assets/pdf_file/0019/238033/Roadmap_Unconventional_Gas_Projects_SA_12-12-12_web.pdf. (Last accessed: 08.11.2020).

Gorter, J. D. (1994). Sequence stratigraphy and the depositional history of the Murta Member (upper Hooray Sandstone), southeastern Eromanga Basin, Australia: implications for the development of source and reservoir facies. The APPEA Journal, 34(1), 644-673.

Gostin, V. A., & Therriault, A. M. (1997). Tookoonooka, a large buried early Cretaceous impact structure in the Eromanga Basin of southwestern Queensland, Australia. Meteoritics & planetary science, 32(4), 593-599.

Goutorbe, B., Lucazeau, F., & Bonneville, A. (2008). Surface heat flow and the mantle contribution on the margins of Australia. Geochemistry, Geophysics, Geosystems, 9(5). https://doi.org/10.1029/2007GC001924.

Gradstein, F. M., Ogg, J. G., Schmitz, M. B., & Ogg, G. M. (Eds.). (2020). Geologic Time Scale 2020. Elsevier.

Gradstein, F. M., Ogg, J. G., Schmitz, M., & Ogg, G. (Eds.). (2012). The geologic time scale 2012 (1st ed.). Elsevier. ISBN: 9780444594259

Grant-Woolley, L., Kong, A., Schoemaker, B., Nasreddin, H., & Montague, E. T. (2014). Identification of strike-slip faults provides insights into the further development of mature Cooper Basin fields. In SPE Asia Pacific Oil & Gas Conference and Exhibition. Society of Petroleum Engineers.

Gravestock, D. I., & Jensen-Schmidt, B. (1998). Structural setting: in Gravestock DI, Hibburt JE and Drexel JF. Petroleum Geology of South Australia, 4, 47-67.

Gravestock, D. I., Gatehouse, C. G., Drexel, J. F., & Preiss, W. V. (1995). The Geology of South Australia (Volume 2: The Phanerozoic. Cooper Basin).

Gravestock, D.I., Hibburt, J.E. & Drexel, J.F. (eds.) 1998. Petroleum geology of South Australia, Volume 4: Cooper Basin. South Australia Department of Industries and Resources, Report Book, 1998/9.

https://sarigbasis.pir.sa.gov.au/WebtopEw/ws/samref/sarig1/image/DDD/PGSA004.pdf.

Gray, A. R. G., & Draper, J. J. (2002). Petroleum geology. Geology of the Cooper and Eromanga Basins (63-74). Queensland Department of Natural Resources and Mines, Brisbane, Australia.

Gray, A. R. G., M. McKillop, & J. L. McKellar, (2002). Eromanga Basin stratigraphy, in J. J. Draper, ed., Geology of the Cooper and Eromanga Basins: Brisbane, Australia, Queensland Department of Natural Resources and Mines, p. 30–56.

Green, P. F., Duddy, I. R., & Bray, R. J. (1995). Applications of thermal history reconstruction in inverted basins. In Buchanan, J. G., & Buchanan, P. G., (eds.), 1995, Basin Inversion, Geological Society Special Publication (88), pp. 149-165.

Green, P. M., Hoffmann, K. L., Brain, T. J., & Gray, A. R. G. (1997). The Surat and Bowen basins, southeast Queensland. Brisbane: Queensland Department of Mines and Energy.

Greenstreet, C., & Dello, L. (2015). Santos and the Cooper Basin: The next frontier. Gas Today, 32, 76-78. https://www.oilandgastoday.com.au/santos-and-the-cooper-basin-the-next-frontier/. (Last accessed: 03.11.2020).

Grobe, A., von Hagke, C., Littke, R., Dunkl, I., Wübbeler, F., Muchez, P., & Urai, J.L. (2019). Evolution of Oman's Mesozoic passive continental margin under the obducting Semail Ophiolite - a basin modeling study of pressure, temperature and tectonically expelled fluids in the Jebel Akhdar, Oman. Solid Earth, 10, 149-175.

Guo, Q., Littke, R., Sun, Y., & Zieger, L. (2020). Depositional history of low-mature coals from the Puyang Basin, Yunnan Province, China. International Journal of Coal Geology, 221, 103428.

Hackley, P. C., & Cardott, B. J. (2016). Application of organic petrography in North American shale petroleum systems: A review. International Journal of Coal Geology, 163, 8-51.

Hackley, P. C., Dennen, K. O., Garza, D., Lohr, C. D., Valentine, B. J., Hatcherian, J. J., ... & Dulong, F. T. (2020). Oil-source rock correlation studies in the unconventional Upper Cretaceous Tuscaloosa marine shale (TMS) petroleum system, Mississippi and Louisiana, USA. Journal of Petroleum Science and Engineering, 190, 107015.

Hall, L. S., Hill, A., Troup, A., Korsch, R., Radke, B., Nicoll, R. S., Palu, T., Wang, L. & Stacey, A. (2015b). [Web page] Cooper Basin architecture and lithofacies: regional hydrocarbon prospectivity of the Cooper Basin, Part 1. Record 2015/31. Geoscience Australia, Canberra. http://dx.doi.org/10.11636/Record.2015.031. (Last accessed: 03.11.2020).

Hall, L. S., Hill, T., Wang, L., Edwards, D., Kuske, T., Troup, A., & Boreham, C. J. (2015a). Unconventional gas prospectivity of the Cooper Basin. The APPEA Journal, 55(2), 428-428.

Hall, L. S., Palu, T. J., Murray, A. P., Boreham, C. J., Edwards, D. S., Hill, A. J., & Troup, A. (2019). Hydrocarbon prospectivity of the Cooper Basin, Australia. AAPG Bulletin, 103(1), 31-63.

Hall, L.S. & Palu, T.J. (2016). [Web page] Cooper Basin regional petroleum systems model. Geoscience Australia, Canberra. http://pid.geoscience.gov.au/dataset/ga/100740. (Last accessed: 03.11.2020).

Hall, L.S., Boreham, C.J., Edwards, D.S., Palu, T.J., Buckler, T., Hill, A.J. & Troup, A. (2016a). [Web page] Cooper Basin source rock geochemistry: regional hydrocarbon prospectivity of the Cooper Basin, Part 2. Record 2016/06. Geoscience Australia, Canberra. http://dx.doi.org/10.11636/Record.2016.006. (Last accessed: 03.11.2020).

Hall, L.S., Palu, T.J., Murray, A.P., Boreham, C.J., Edwards, D.S., Hill, A.J. and Troup, A. (2016b). [Web page] Cooper Basin petroleum systems analysis: regional hydrocarbon prospectivity of the Cooper Basin, Part 3. Record 2016/29. Geoscience Australia, Canberra. http://dx.doi.org/10.11636/Record.2016.029. (Last accessed: 03.11.2020).

Hallmann, C. O. E., Arouri, K. R., McKirdy, D. M., & Schwark, L. (2006). A new perspective on exploring the Cooper/Eromanga petroleum province – Evidence of oil charging from the Warburton basin. The APPEA Journal, 46(1), 261-282.

Hantschel, T., & Kauerauf, A. I. (2009). Fundamentals of basin and petroleum systems modelling: Berlin, Springer-Verlag, 476 p., doi:10.1007/978-3-540-72318-9.

Hardman, J. P., Holford, S. P., Schofield, N., Bunch, M., & Gibbins, D. (2019). The Warnie volcanic province: Jurassic intraplate volcanism in Central Australia. Gondwana Research, 76, 322-347.

Harrison, B., Taylor, D., Tingate, P., & Sandiford, M. (2012). Heat flow modelling and thermal history of the onshore Gippsland Basin: upside potential for unconventional gas and geothermal resources. Eastern Australasian Basins Symposium IV(1-15), Brisbane.

Harrison, T. M. (2009). The Hadean crust: evidence from> 4 Ga zircons. Annual Review of Earth and Planetary Sciences, 37, 479-505.

Hartkopf-Fröder, C., Königshof, P., Littke, R., & Schwarzbauer, J. (2015). Optical thermal maturity parameters and organic geochemical alteration at low grade diagenesis to anchimetamorphism: a review. International Journal of Coal Geology, 150, 74-119.

Hawkins, P. J., Almond, C. S., Carmichael, D. C., Smith, R. J., & Williams, L. J. (1989). Kerogen Characterisation, and Organic and Mineral Diagenesis of Potential Source Rocks in Jurassic Units, Southern Eromanga Basin, Queensland. In: Proceedings of the Cooper and Eromanga Basins Conference (1989). Petroleum Exploration Society of Australia (PESA).

Hawlader, H.M. (1989). Petrology, diagenesis, and reservoir potential of the Surat Basin sandstones with special reference to hydrocarbon exploration. Doctoral dissertation, Macquarie Univ., N.S.W., Australia, 572 pp.

Hedges, J. I., Eglinton, G., Hatcher, P. G., Kirchman, D. L., Arnosti, C., Derenne, S., ... & Michaelis, W. (2000). The molecularly-uncharacterized component of nonliving organic matter in natural environments. Organic geochemistry, 31(10), 945-958.

Hegarty, K. A., Duddy, I., Green, P. F., Gleadow, A. J. W., Fraser, I., & Weissel, J.K. (1986). Regional evolution of the tectonic and thermal history of the Gippsland Basin. In: Second South-eastern Australia Oil Exploration Symposium. Petroleum Exploration Society of Australia, Melbourne, 65-74.

Henson, P., Kositcin, N., & Huston, D. (2011). Broken Hill and Mount Isa: Linked but not rotated: Geoscience Australia. AUSGEO News, 102, 13-17.

Hergt, J. M., & Brauns, C. M. (2001). On the origin of Tasmanian dolerites. Australian Journal of Earth Sciences, 48(4), 543-549.

Hill, K. C., Hill, K. A., Cooper, G. T., O'Sullivan, A. J., O'Sullivan, P. B., & Richardson, M. J. (1995). Inversion around the Bass basin, SE Australia. Geological Society, London, Special Publications, 88(1), 525-547.

Hill, P. J., Exon, N. F., Keene, J. B., & Smith, S. M. (1998). The continental margin off east Tasmania and Gippsland: structure and development using new multibeam sonar data. Exploration Geophysics, 29(3/4), 410-419. https://doi.org/10.1071/EG998410.

Hillis, R. R., & Reynolds, S. D. (2000). The Australian stress map. Journal of the Geological Society, 157(5), 915-921.

Hillis, R. R., Sandiford, M., Reynolds, S. D., & Quigley, M. C. (2008). Present-day stresses, seismicity and Neogene-to-Recent tectonics of Australia's 'passive' margins: intraplate deformation controlled by plate boundary forces. Geological Society, London, Special Publications, 306(1), 71-90.

Holford, S. P., Hillis, R. R., Hand, M., & Sandiford, M. (2011). Thermal weakening localizes intraplate deformation along the southern Australian continental margin. Earth and Planetary Science Letters, 305(1), 207-214. https://doi.org/10.1016/j.epsl.2011.02.056.

Holgate, F. L. (2005). Exploration and evaluation of the Australian geothermal resource. PhD thesis. The Australian National University.

Holgate, F., & Gerner, E. (2010). [Web page] Oz Temp Well temperature data. Geoscience Australia, Canberra. http://www.ga.gov.au/metadata-gateway/metadata/record/gcat_70604. (Last accessed: 26.02.2019).

Holl, H., & Barton, C. (2015). Habanero field—structure and state of stress. In Proceedings World Geothermal Congress (pp. 19-25).

Horsfield, B. (1984). Pyrolysis studies and petroleum exploration. In: Brooks, J. & Welte, D.H. (eds), Advances in petroleum geochemistry. Academic, London, Vol. 1, pp. 247–298.

Huang, W.-Y., & Meinschein, W. G. (1979). Sterols as ecological indicators. Geochimica et Cosmochimica Acta, 43(5), 739-745. http://dx.doi.org/10.1016/0016-7037(79)90257-6.

Hughes, W. B., Holba, A. G., & Dzou, L. I. P. (1995). The ratios of dibenzothiophene to phenanthrene and pristane to phytane as indicators of depositional environment and lithology of petroleum source rocks. Geochimica et Cosmochimica Acta, 59(17), 3581-3598.

Hunt, J. M., (1996). Petroleum geochemistry and geology (2nd Edition). Freeman and Company, New York.

Huston, D.L., Blewett, R.S., & Champion, D.C. (2012). Australia through time: a summary of its tectonic and metallogenic evolution. Episodes Journal of International Geoscience, 35(1), 23-43. https://doi.org/10.18814/epiiugs/2012/v35i1/004.

IEA, International Energy Agency (2020a). [Web page] Global Energy Review 2020, IEA, Paris. https://www.iea.org/reports/global-energy-review-2020. (Last accessed: 13.10.2020).

IEA, International Energy Agency (2020b). [Web page] Global Energy Review 2020. The impacts of the COVID-19 crisis on global energy demand and CO2 emissions. Press release 30 April 2020. https://iea.blob.core.windows.net/assets/74921671-51f5-4b5d-b88f-cd58b24ae23f/GER2020_PRESS_final.pdf. (Last accessed: 14.10.2020).

IPCC, Intergovernmental Panel on Climate Change (2013). Climate Change 2013: The Physical Science Basis. Contribution of Working Group I to the Fifth Assessment Report of the Intergovernmental Panel on Climate Change [Stocker, T.F., D. Qin, G.-K. Plattner, M. Tignor, S.K. Allen, J. Boschung, A. Nauels, Y. Xia, V. Bex and P.M. Midgley (eds.)]. Cambridge University Press, Cambridge, United Kingdom and New York, NY, USA, 1535 pp.

Jadoon, Q. K., Roberts, E., Blenkinsop, T., & Wust, R. (2016). Organic petrography and thermal maturity of the Permian Roseneath and Murteree shales in the Cooper Basin, Australia. International Journal of Coal Geology, 154, 240-256.

Jarvie, D. M. (2012). Shale resource systems for oil and gas: Part 2—Shale-oil resource systems. In J. A. Breyer (Ed.), Shale reservoirs – Giant resources for the 21st century: AAPG Memoir (97, 89–119).

Jenkins, C. C. (1989). Geochemical correlation of source rocks and crude oils from the Cooper and Eromanga Basins. In Proceedings of the Cooper and Eromanga Basins Conference 1989. Petroleum Exploration Society of Australia (PESA).

Jimenez, J. A., & Chalaturnyk, R. J. (2003). Are Disused Hydrocarbon Reservoirs Safe for Geological Storage of CO2?. In Greenhouse Gas Control Technologies-6th International Conference (pp. 471-476). Pergamon.

Johnstone, E. M., Jenkins, C. C., & Moore, M. A. (2001). An integrated structural and palaeogeographic investigation of Eocene erosional events and related hydrocarbon potential in the Gippsland Basin. In: Hill, K.C. & Bernecker, T. (eds.), Eastern Australasian Basins Symposium 2001. A refocused Energy perspective for the future, PESA Petroleum Exploration Society of Australia, Special Publication, Melbourne, 2001, 403-412.

Kantsler, A. J., Prudence, T. J., Cook, A. C., & Zwigulis, M. (1983). Hydrocarbon habitat of the Cooper/Eromanga Basin, Australia: Australian Petroleum Exploration Association Journal, v. 23, p. 75–92.

Karg, H., & Littke, R. (2020). Tectonic control on hydrocarbon generation in the northwestern Neuquén Basin, Argentina. AAPG Bulletin, 104(10), 2173-2208.

Karlstrom, K. E., Åhäll, K. I., Harlan, S. S., Williams, M. L., McLelland, J., & Geissman, J. W. (2001). Long-lived (1.8–1.0 Ga) convergent orogen in southern Laurentia, its extensions to Australia and Baltica, and implications for refining Rodinia. Precambrian Research, 111(1-4), 5-30.

Kemp, A. I. S., Hawkesworth, C. J., Collins, W. J., Gray, C. M., & Blevin, P. L. (2009). Isotopic evidence for rapid continental growth in an extensional accretionary orogen: The Tasmanides, eastern Australia. Earth and Planetary Science Letters, 284(3-4), 455-466.

Kennett, B. L. N., & Salmon, M. (2012). AuSREM: Australian seismological reference model. Australian Journal of Earth Sciences, 59(8), 1091-1103. https://doi.org/10.1080/08120099.2012.736406.

Kennett, B., M. Salmon, & E. Saygin, AusMoho Working Group (2011). AusMoho: The variation of Moho depth in Australia: Geophysical Journal International, v. 187, no. 2, p. 946–958, doi:10.1111/j.1365-246X.2011.05194.x.

Khair, H. A., Cooke, D., & Hand, M. (2015a). Seismic mapping and geomechanical analyses of faults within deep hot granites, a workflow for enhanced geothermal system projects. Geothermics, 53, 46-56.

Khair, H. A., Cooke, D., & Hand, M. (2015b). Paleo stress contribution to fault and natural fracture distribution in the Cooper Basin. Journal of Structural Geology, 79, 31-41.

Khorasani, G. K. (1987). Recent organic geochemical evaluation of the central Eromanga basin. The APPEA Journal, 27(1), 106-111.

Klootwijk, C. (2013). Middle–late Paleozoic Australia–Asia convergence and tectonic extrusion of Australia. Gondwana Research, 24(1), 5-54.

Kroeger, K. F., di Primio, R., & Horsfield, B. (2011). Atmospheric methane from organic carbon mobilization in sedimentary basins - the sleeping giant? Earth-Science Reviews, 107(3-4), 423-442.

Kuang, K. S. (1985). History and style of Cooper? Eromanga Basin structures. Exploration Geophysics, 16(3), 245-248.

Kulikowski, D., & Amrouch, K. (2017). Combining geophysical data and calcite twin stress inversion to refine the tectonic history of subsurface and offshore provinces: A case study on the Cooper- Eromanga Basin, Australia. Tectonics, 36(3), 515-541.

Kulikowski, D., Amrouch, K., Cooke, D., & Gray, M. E. (2018). Basement structural architecture and hydrocarbon conduit potential of polygonal faults in the Cooper-Eromanga Basin, Australia. Geophysical Prospecting, 66(2), 366-396.

Kuske, T.J., Hall, L.S., Hill, A.J., Troup, A.J., Edwards, D.S., Boreham, C.J. & Buckler, T. (2015). Source rocks of the Cooper Basin. Search and Discovery Article #90217, AAPG/SEG International Conference & Exhibition, Melbourne, Australia, September 13-16, 2015.

Kusky, T. M., Windley, B. F., Wang, L., Wang, Z., Li, X., & Zhu, P. (2014). Flat slab subduction, trench suction, and craton destruction: comparison of the North China, Wyoming, and Brazilian cratons. Tectonophysics, 630, 208-221.

Kutovaya, A., Kroeger, K. F., Seebeck, H., Back, S., & Littke, R. (2019). Thermal Effects of Magmatism on Surrounding Sediments and Petroleum Systems in the Northern Offshore Taranaki Basin, New Zealand. Geosciences, 9(7), 288.

Ladant, J. B., & Donnadieu, Y. (2016). Palaeogeographic regulation of glacial events during the Cretaceous supergreenhouse. Nature communications, 7(1), 1-9.

Langford, F. F., & Blanc-Valleron, M. M. (1990). Interpreting Rock-Eval pyrolysis data using graphs of pyrolizable hydrocarbons vs. total organic carbon. AAPG Bulletin, 74(6), 799–804.

Lanzilli, E. (1999). The Birkhead Formation: reservoir characterisation of the Gidgealpa south dome and sequence stratigraphy of the Eromanga Basin, Australia. Doctoral dissertation. University of Adelaide, Australia.

Lavering, I. H. (1991). Observations on the geological origin of the 'C'horizon seismic reflection, Eromanga Basin. BMR Journal of Australian Geology & Geophysics, 12, 5-12.

Law, C. A. (1999). Chapter 6 - Evaluating Source Rocks. In E. A. Beaumont & N. H. Foster (Eds.), Treatise of Petroleum Geology / Handbook of Petroleum Geology: Exploring for Oil and Gas Traps (1st ed.). AAPG. ISBN 978-1-58861-493-3

Leythaeuser, D., Littke, R., Radke, M., & Schaefer, R. G. (1988). Geochemical effects of petroleum migration and expulsion from Toarcian source rocks in the Hils syncline area, NW-Germany. In Organic Geochemistry in Petroleum Exploration (pp. 489-502). Pergamon.

Li, P. F., Rosenbaum, G., & Rubatto, D. (2012). Triassic asymmetric subduction rollback in the southern New England Orogen (eastern Australia): the end of the Hunter-Bowen Orogeny. Australian Journal of Earth Sciences, 59(6), 965-981.

Li, Z. X., & Evans, D. A. (2011). Late Neoproterozoic 40 intraplate rotation within Australia allows for a tighter-fitting and longer-lasting Rodinia. Geology, 39(1), 39-42.

Li, Z. X., & Powell, C. M. (2001). An outline of the palaeogeographic evolution of the Australasian region since the beginning of the Neoproterozoic. Earth-Science Reviews, 53(3-4), 237-277.

Li, Z. X., Li, X. H., Zhou, H., & Kinny, P. D. (2002). Grenvillian continental collision in south China: New SHRIMP U-Pb zircon results and implications for the configuration of Rodinia. Geology, 30(2), 163-166.

Li, Z. X., Zhang, L., & Powell, C. M. (1995). South China in Rodinia: part of the missing link between Australia–East Antarctica and Laurentia? Geology, 23(5), 407-410.

Lijmbach, G. W. M. (1975). On the origin of petroleum. In: Proceedings of the 9th World Petroleum Congress, Tokyo. London: Applied Sciences Publisher, Special Paper 1(2), 357-369). https://www.onepetro.org/conference-paper/WPC-16134.

Littke, R., Baker, D. R., & Leythaeuser, D. (1988). Microscopic and sedimentologic evidence for the generation and migration of hydrocarbons in Toarcian source rocks of different maturities. In Organic Geochemistry in Petroleum Exploration (pp. 549-559). Pergamon.

Littke, R., Bayer, U., Gajewski, D., & Nelskamp, S. (2008). Dynamics of complex intracontinental basins: the central European basin system. Springer Science & Business Media. ISBN 978-3-540-85085-4.

Liu, Y., Li, Z. X., Pisarevsky, S. A., Kirscher, U., Mitchell, R. N., Stark, J. C., ... & Hand, M. (2018). First Precambrian palaeomagnetic data from the Mawson Craton (East Antarctica) and tectonic implications. Scientific reports, 8(1), 1-12.

Liu, Z., Ciais, P., Deng, Z., Lei, R., Davis, S. J., Feng, S., ... & Guo, R. (2020). Near-real-time monitoring of global CO 2 emissions reveals the effects of the COVID-19 pandemic. Nature communications, 11(1), 1-12. https://doi.org/10.1038/s41467-020-18922-7.

Lowry, D. C., & Longley, I. M. (1991). A new model for the mid-Cretaceous structural history of the northern Gippsland Basin. The APPEA Journal, 31(1), 143–153. https://doi.org/10.1071/AJ90012

Mackie, S. I., & Gumley, C. M. (1995). The Dirkala South oil discovery: Focussing on cost-efficient reservoir delineation. The APPEA Journal, 35(1), 65-78.

Mahlstedt, N., & Horsfield, B. (2016). [Web page] Source rock evaluation and predicted petroleum compositions related to samples from the Adavale, Bowen, Cooper and Eromanga Basins, Queensland. GEOS4 REPORT 20161216 (ROUND 2). QDEX Report number CR 99555. Department of Natural Resources and Mines, Queensland, Australia. https://qdexguest.dnrm.qld.gov.au/portal/site/qdex/search?REPORT_ID=99555&COLLECTION_ID=999. (Last accessed: 08.02.2020).

Mann, P., Hempton, M. R., Bradley, D. C., & Burke, K. (1983). Development of pull-apart basins. The Journal of Geology, 91(5), 529-554.

Maslen, E., Grice, K., Métayer, P. L., Dawson, D., & Edwards, D. (2011). Stable carbon isotopic compositions of individual aromatic hydrocarbons as source and age indicators in oils from western Australian basins. Organic Geochemistry, 42(4), 387-398. http://dx.doi.org/10.1016/j.orggeochem.2011.02.005.

Masters, S. B. (1993). Detailed Sequence Stratigraphy of the Latrobe group, Gippsland Basin, Victoria. Doctoral dissertation, University of Adelaide.

Mavromatidis, A. (2006a). Burial/exhumation histories for the Cooper–Eromanga Basins and implications for hydrocarbon exploration, Eastern Australia. Basin Research, 18(3), 351-373.

Mavromatidis, A. (2006b). Combined analysis of different logs in quantification of exhumation and its implications for hydrocarbon exploration, a case study from Australia. Geologica Acta: an international earth science journal, 4(3), 355-370.

Mavromatidis, A. (2007). Exhumation study in the Cooper-Eromanga Basins, Australia and the implications for hydrocarbon exploration. Energy Sources, Part A: Recovery, Utilization, and Environmental Effects, 29(7), 631-648.

Mavromatidis, A., & Hillis, R. (2005). Quantification of exhumation in the Eromanga Basin and its implications for hydrocarbon exploration. Petroleum Geoscience, 11(1), 79-92.

McIntyre, S. M., Jamal, F. G., Pidcock, C. L., & Kabir, M. I. (1989). The Gidgealpa oil and gas field: a case history. In B. J. O'Neil (Ed.), The Cooper & Eromanga Basins, Australia (Proceedings of the Cooper and Eromanga Basins Conference, 1989). Petroleum Exploration Society of Australia (PESA).

McKellar, J. L. (2013). The Cooper Basin. Geology of Queensland: Brisbane, Australia, Geological Survey of Queensland, 204-212.

McKenzie, D. (1978), Some Remarks on the Development of Sedimentary Basins, Earth and Planetary Science Letters, 40, 25-32. https://doi.org/10.1016/0012-821X(78)90071-7.

McKenzie, D. (1981). The variation of temperature with time and hydrocarbon maturation in sedimentary basins formed by extension. Earth and Planetary Science Letters, 55(1), 87-98. https://doi.org/10.1016/0012-821X(81)90089-3.

McKirdy, D. M., Cox, R. E., Volkman, J. K., & Howell, V. J. (1986a). Botryococcane in a new class of Australian non-marine crude oils. Nature, 320(6057), 57-59.

McKirdy, D. M., Emmett, J. K., Mooney, B. A., Cox, R. E., & Watson, B. L., (1986b). Organic geochemical facies of the Cretaceous Bulldog Shale, western Eromanga Basin, South Australia. In: Gravestock, D.I., Moore, P.S. and Pitt, G.M. (Eds), Contributions to the geology and hydrocarbon potential of the Eromanga Basin (Special Publication, 12:287-304). Geological Society of Australia.

McKirdy, D. M., Michaelsen, B. H., Kagya, M. L. N., & Ryan, M. J. (1997). Biomarker signatures of oils from the Patchawarra Trough, Cooper/Eromanga Basin, South Australia. In 18th International Meeting on Organic Geochemistry Abstracts (18th IMOG, pp. 415-416). Maastricht, The Netherlands.

McKirdy, D. M., Yu, X., Leythaeuser, D., Schwark, L., & Arouri, K. R., (2001). A pilot study of secondary migration and reservoir filling in the Cooper/Eromanga Basin, South Australia. In 20th International Meeting on Organic Geochemistry Abstracts (20th IMOG, pp. 425-426). Nancy, France.

McLaren, S., & Dunlap, W. J. (2006). Use of 40Ar/39Ar K- feldspar thermochronology in basin thermal history reconstruction: an example from the Big Lake Suite granites, Warburton Basin, South Australia. Basin Research, 18(2), 189-203.

McLean, M. A., & Blackburn, G. J. (author.) & Victorian Geological Carbon Storage Initiative (issuing body) (2013). [Web page] A new regional velocity model for the Gippsland Basin. Melbourne, Victoria Department of Primary Industries. http://earthresources.efirst.com.au/product.asp?pID=1114&cID=59&c=75918. (Last accessed: 07.04.2020).

McPhail, A. (2000). A Petrographic and Geochemical Study of Gippsland Basin Volcanics. University of Adelaide, National Centre for Petroleum Geology and Geophysics.

Meeuws, F. J., Holford, S. P., Foden, J. D., & Schofield, N. (2016a). Distribution, chronology and causes of Cretaceous–Cenozoic magmatism along the magma-poor rifted southern Australian margin: Links between mantle melting and basin formation. Marine and Petroleum Geology, 73, 271-298. https://doi.org/10.1016/j.marpetgeo.2016.03.003.

Meeuws, F. J., Reynolds, P., Holford, S. P., Foden, J. D., & Schofield, N. (2016b). Characterizing extrusive and intrusive magmatism at the Kipper Field, Gippsland Basin, using 3D seismic data. In: ASEG Extended Abstracts 2016: 25th International Geophysical Conference and Exhibition. Australian Society of Exploration Geophysicists, 976-982. https://doi.org/10.1071/ASEG2016ab271.

Meixner, A. J., Kirkby, A. L., & Horspool, N. (2014). Using constrained gravity inversions to identify high-heat-producing granites beneath thick sedimentary cover in the Cooper Basin region of central Australia. Geothermics, 51, 483-495.

Meixner, A. J., Kirkby, A. L., Lescinsky, D. T., & Horspool, N. (2012). The Cooper Basin 3D map version 2: thermal modelling and temperature uncertainty. Geoscience Australia Record, 60.

Menpes, S., Hill, A., & Pepicelli, D. (2013). Characteristics of the Gidgealpa Group composite resource play in the Cooper Basin, South Australia. In Unconventional Resources Technology Conference Abstracts (pp. 2621-2630). SEG Society of Exploration Geophysicists, AAPG American Association of Petroleum Geologists, SPE Society of Petroleum Engineers.

Metzger, P., & Largeau, C. (2005). Botryococcus braunii: a rich source for hydrocarbons and related ether lipids. Applied Microbiological Biotechnology 66, 486–496. https://doi.org/10.1007/s00253-004-1779-z.

Michaelsen, B. H. (2002). Geochemical perspectives on the petroleum habitat of the Cooper and Eromanga Basins, central Australia (Doctoral dissertation). University of Adelaide, Australia.

Michaelsen, B. H., & McKirdy, D. M. (1989). Organic facies and petroleum geochemistry of the lacustrine Murta Member (Mooga Formation) in the Eromanga Basin, Australia. In B. J. O'Neil (Ed.), The Cooper & Eromanga Basins, Australia (Proceedings of the Cooper and Eromanga Basins Conference, 1989). Petroleum Exploration Society of Australia (PESA).

Michaelsen, B. H., & McKirdy, D. M. (2001). Migration and mixing of oils in the Cooper and Eromanga Basins, Central Australia. In: Hill, K.C. & Bernecker, T. (editors): Eastern Australian Basins Symposium 2001. Petroleum Exploration Society of Australia Special Publication. Melbourne, 25–28 Nov 2001, pp. 289–300.

Michaelsen, B. H., & McKirdy, D. M. (2006). Source rock distribution and hydrocarbon geochemistry. In T. B. Cotton, M. F. Scardigno, & J. E. Hibburt (Eds.), Petroleum Geology of South Australia Series. The petroleum geology of South Australia (Vol. 2: Eromanga Basin (2nd ed.). Department of Primary Industries and Resources. South Australia.

Middleton, A. W., Uysal, I. T., Bryan, S. E., Hall, C. M., & Golding, S. D. (2014). Integrating 40Ar–39Ar, 87Rb–87Sr and 147Sm–143Nd geochronology of authigenic illite to evaluate tectonic reactivation in an intraplate setting, central Australia. Geochimica et Cosmochimica Acta, 134, 155-174.

Middleton, M. F. (1979). Correlation between well log and surface resistivity measurements? A case study in the Eromanga Basin, Queensland. Exploration Geophysics, 10(2), 176-178.

Milligan, P. R., & Franklin, R. (2004). Magnetic anomaly grid of Australia.[Digital Dataset]. Geoscience Australia, Canberra.

Milligan, P. R., Franklin, R., Minty, B. R. S., Richardson, L. M., & Percival, P. J. (2010). Magnetic Anomaly Map of Australia: Canberra, Geoscience Australia, scale: 1: 15,000,000.

Moldowan, J. M., & Seifert, W. K. (1980). First discovery of botryococcane in petroleum. Journal of the Chemical Society, Chemical Communications, 19, 912-914.

Moldowan, J. M., Dahl, J., Huizinga, B. J., Fago, F. J., Hickey, L. J., Peakman, T. M., & Taylor, D. W. (1994). The molecular fossil record of oleanane and its relation to angiosperms. Science, 265(5173), 768-771. https://doi.org/10.1126/science.265.5173.768.

Moldowan, J. M., Seifert, W. K., & Gallegos, E. J. (1983). Identification of an extended series of tricyclic terpanes in petroleum. Geochimica et Cosmochimica Acta, 47(8), 1531-1534.

Moldowan, J. M., Seifert, W. K., & Gallegos, E. J. (1985). Relationship between petroleum composition and depositional environment of petroleum source rocks. AAPG bulletin, 69(8), 1255-1268.

Moore, D. H., & Wong, D. (2001). Down and out in Gippsland: using potential fields to look deeper and wider for new hydrocarbons. In: Hill, K.C. & Bernecker, T. (eds.), Eastern Australasian Basins Symposium 2001. A refocused Energy perspective for the future, PESA Petroleum Exploration Society of Australia, Special Publication, Melbourne, 2001.

Moore, D. H., & Wong, D. (2002). Eastern and Central Gippsland Basin, Southeast Australia: Basement Interpretation and Basin Links. Victorian Initiative for Minerals and Petroleum Report 69, Department of Natural Resources, and Environment.

Moore, P., Hobday, D., Mai, H., & Sun, Z. (1986). Comparison of selected non-marine petroleum-bearing basins in Australia and China. APEA journal, 26(1), 285-309.

Mortimer, N. (2006). Zealandia. ASEG Extended Abstracts, 2006(1), 1-4. https://doi.org/10.1071/ASEG2006ab119.

Mortimer, N., (2008). Zealandia. In: Spencer, J.E. & Titley, S.R. (eds.), Ores and orogenesis: Circum-Pacific tectonics, geologic evolution, and ore deposits. Arizona Geological Society Digest 22, 227–233.

Mount, T. J. (1981). Dullingari North 1, an oil discovery in the Murta Member of the Eromanga Basin. APEA Journal, 21(1), 71-77.

Mount, T. J. (1982). Geology of the Dullingari Murta oilfield. In Eromanga Basin Symposium (1982). Petroleum Exploration Society of Australia (PESA).

Moussavi-Harami, R. (1996). Burial history, in E. M. Alexander and J. E. Hibburt, eds., Petroleum geology of South Australia: Eromanga Basin: Adelaide, Australia, South Australia Department of Mines and Energy, v. 2, p. 125–140.

Müller, R. D., Dyksterhuis, S., & Rey, P. (2012). Australian paleo-stress fields and tectonic reactivation over the past 100 Ma. Australian Journal of Earth Sciences, 59(1), 13-28.

Müller, R. D., Gaina, C., & Clark, S. (2000a). Seafloor spreading around Australia. In: Veevers, J. (eds.), Billion-year earth history of Australia and neighbours in Gondwanaland. School of Geosciences, The University of Sydney, 2000, 18-28.

Müller, R. D., Gainã, C., Tikku, A., Mihut, D., Cande, S. C., & Stock, J. M. (2000b). Mesozoic/Cenozoic tectonic events around Australia.

Müller, R.D., Flament, N., Matthews, K.J., Williams, S.E., & Gurnis, M. (2016). Formation of Australian continental margin highlands driven by plate–mantle interaction. Earth and Planetary Science Letters, 441, 60-70. http://dx.doi.org/10.1016/j.epsl.2016.02.025.

Murray, C. G. (1994). Basement cores from the Tasman fold belt system beneath the Great Artesian Basin in Queensland. Department of Minerals and Energy, Queensland.

Myers, J. S., Shaw, R. D., & Tyler, I. M. (1996). Tectonic evolution of Proterozoic Australia. Tectonics, 15(6), 1431-1446.

Neumaier, M. (2015). Structural Restoration and Basin and Petroleum Systems Modeling: Case Studies from the Monagas Fold and Thrust Belt, Venezuela and the Moroccan Atlantic Margin. Doctoral dissertation, Library of the RWTH Aachen University.

NGMA, National Geoscience Mapping Accord (2001). [Web page] Cooper and Eromanga Basins, Australia, seismic mapping data sets: Custodian—Department for Manufacturing, Innovation, Trade, Resources and Energy on behalf of the National Geoscience Mapping Accord, https://sarig.pir.sa.gov.au/Map. (Last accessed: 03.11.2020).

Noda, A. (2013). Strike-slip basin–its configuration and sedimentary facies. Mechanism of Sedimentary Basin Formation. Intech, 27-57.

Norvick, M. S. (2005). [Web page] Plate tectonic reconstructions of Australia's southern margins: Final report. Canberra: Petroleum and Marine Division, Geoscience Australia Record. https://trove.nla.gov.au/version/32923035. (Last accessed: 08.11.2020).

Norvick, M. S., Smith, M. A., & Power, M. R. (2001). The plate tectonic evolution of eastern Australasia guided by the stratigraphy of the Gippsland Basin. In: Hill, K.C. & Bernecker, T. (eds.), Eastern Australasian Basins Symposium 2001. A refocused Energy perspective for the future, PESA Petroleum Exploration Society of Australia, Special Publication, Melbourne, 2001, 15-23.

Nøttvedt, A., Gabrielsen, R. H., & Steel, R. J. (1995). Tectonostratigraphy and sedimentary architecture of rift basins, with reference to the northern North Sea. Marine and Petroleum Geology, 12(8), 881-901. https://doi.org/10.1016/0264-8172(95)98853-W.

O'Brien, G. W., Tingate, P. R., Divko, L. G., Harrison, M. L., Boreham, C. J., Liu, K., ... & Skladzien, P. (2008). First order sealing and hydrocarbon migration processes, Gippsland Basin, Australia: Implications for CO2 geosequestration.

O'Halloran, G. J., & Johnstone, E. M. (2001). Late Cretaceous rift volcanics of the Gippsland Basin, SE Australia–new insights from 3D seismic. In: Hill, K.C. & Bernecker, T. (eds.), Eastern Australasian Basins Symposium 2001. A refocused Energy perspective for the future, PESA Petroleum Exploration Society of Australia, Special Publication, Melbourne, 353-361.

O'Neil, B. J., & Alexander, E. M. (2006). History of petroleum exploration and development. In T. B. Cotton, M. F. Scardigno, & J. E. Hibburt (Eds.), Petroleum Geology of South Australia Series. The petroleum geology of South Australia, Vol. 2: Eromanga Basin (2nd ed.). South Australia. Department of Primary Industries and Resources.

O'Neil, B.J. (1998). Chapter 2: History of Petroleum Exploration and Development. In: Gravestock, D.I., Hibburt, J.E. & Drexel, J.F. (eds.), The Petroleum Geology of South Australia. Volume 4: Cooper Basin. South Australia Department of Primary Industries and Resources, Adelaide. Report Book, 1998/9, 7–36. https://sarigbasis.pir.sa.gov.au/WebtopEw/ws/samref/sarig1/image/DDD/PGSA004.pdf.

Ondrak, R., Wenderoth, F., Scheck, M., & Bayer, U. (1998). Integrated geothermal modeling on different scales in the Northeast German basin. Geologische Rundschau, 87(1), 32-42.

Ourisson, G., Albrecht, P., & Rohmer, M. (1982). Predictive microbial biochemistry – from molecular fossils to procaryotic membranes. Trends in Biochemical Sciences, 7(7), 236-239.

Parsons, B., & Sclater, J. G. (1977). An analysis of the variation of ocean floor bathymetry and heat flow with age. Journal of geophysical research, 82(5), 803-827.

Partridge, A.D., Bernecker, T., Kelman, A.P., Khider, K., Le Poidevin, S., & Mantle, D. J. (2015). [Web page] Gippsland Basin, Biozonation and Stratigraphy, 2015, Chart 40. Geoscience Australia. https://d28rz98at9flks.cloudfront.net/76687/Chart_40_Gippsland_Basin_2015.pdf. (Last accessed: 07.04.2020).

Paton, I. M. (1986). Contributions to the Geology and Hydrocarbon Potential of the Eromanga Basin. Geological Society of Australia Special Publication, 12, 195-201.

Pepper, A. S., and P. J. Corvi, (1995a). Simple kinetic models of petroleum formation. Part I: Oil and gas generation from kerogen: Marine and Petroleum Geology, v. 12, no. 3, p. 291–319, doi:10.1016/0264-8172(95)98381-E

Pepper, A. S., and P. J. Corvi, (1995b). Simple kinetic models of petroleum formation. Part III: Modelling an open system: Marine and Petroleum Geology, v. 12, no. 4, p. 417–452, doi:10.1016/0264-8172(95)96904-5.

Pepper, A. S., and P. J. Dodd, (1995). Simple kinetic models of petroleum formation. Part II: Oil-gas cracking: Marine and Petroleum Geology, v. 12, no. 3, p. 321–340, doi: 10.1016/0264-8172(95)98382-F.

PEPS-SA, Department of State Development South Australia (2018). [Web page] Legacy Petroleum and geothermal attribute database (Legacy PEPS-SA), 2020, https://energymining.sa.gov.au/petroleum/data_and_publications/peps-sa. (Last accessed 17.08.2020).

Peters, K. E., & Cassa, M. R. (1994). Applied source rock geochemistry: Chapter 5: Part II. Essential elements. In L. B. Magoon & W. G. Dow (Eds.), The petroleum system – from source to trap. AAPG Memoir 60.

Peters, K. E., Fraser, T. H., Amris, W., Rustanto, B., & Hermanto, E. (1999). Geochemistry of crude oils from eastern Indonesia. AAPG Bulletin, 83(12), 1927-1942.

Peters, K. E., Walters, C. C., & Moldowan, J. M. (2005a). The Biomarker Guide, Volume 1: Biomarkers and Isotopes in the Environment and Human History (2nd ed.). Cambridge University Press, New York. ISBN 0521781582, https://doi.org/10.1017/CBO9780511524868.

Peters, K. E., Walters, C. C., & Moldowan, J. M. (2005b). The Biomarker Guide, Volume 2: Biomarkers and Isotopes in Petroleum Exploration and Earth History (2nd ed.). Cambridge University Press, New York. ISBN 0521837626, https://doi.org/10.1017/CBO9781107326040.

Pisarevsky, S. A., Wingate, M. T., Powell, C. M., Johnson, S., & Evans, D. A. (2003). Models of Rodinia assembly and fragmentation. Geological Society, London, Special Publications, 206(1), 35-55.

Pitt, G. M. (1986). Geothermal gradients, geothermal histories and the timing of thermal maturation in the Eromanga-Cooper Basins. GRAVESTOCK, DI, MOORE, PS, & PITT, GM (Editors), 323-351.

Planke, S., Jamtveit, B., Malthe-Sørenssen, A., Myklebust, R., Svensen, H., Rasmussen, T., Rey, S. S., & Berndt, C. (2003). Volcanic Processes and Deposits on Rifted Margins and in Sedimentary Basins. Extended abstract. 8th International Congress of the Brazilian Geophysical Society, Rio de Janeiro, 14. September 2003.

Powell, C. M., Preiss, W. V., Gatehouse, C. G., Krapez, B., & Li, Z. X. (1994). South Australian record of a Rodinian epicontinental basin and its mid-Neoproterozoic

breakup (~ 700 Ma) to form the Palaeo-Pacific Ocean. Tectonophysics, 237(3-4), 113-140.

Powell, T. G. (1986). Petroleum geochemistry and depositional setting of lacustrine source rocks. Marine and Petroleum Geology, 3(3), 200-219.

Powell, T. G., Boreham, C. J., McKirdy, D. M., Michaelsen, B. H., & Summons, R. E. (1989). Petroleum geochemistry of the Murta Member, Mooga Formation, and associated oils, Eromanga Basin. The APPEA Journal, 29(1), 114–129.

Powell, T. G., Boreham, C. J., Smyth, M., Russell, N., & Cook, A. C. (1991). Petroleum source rock assessment in non-marine sequences: pyrolysis and petrographic analysis of Australian coals and carbonaceous shales. Organic Geochemistry, 17(3), 375-394.

Power, M. R., Hill, K. C., Hoffmann, N., Bernecker, T., & Norvick, M. (2001). The Structural and Tectonic Evolution of the Gippsland Basin: Results From 2D Section Balancing and 3D Structural Modeling. In: Hill, K.C. & Bernecker, T. (eds.), Eastern Australasian Basins Symposium 2001. A refocused Energy perspective for the future, PESA Petroleum Exploration Society of Australia, Special Publication, Melbourne, 373 – 384.

Preiss, W. V., Belperio, A. P., Cowley, W. M., & Rankin, L. R. (1993). Neoproterozoic. The Geology of South Australia, 1, 171-203.

Purdy, D. J., Hegarty, R., & Doublier, M. P. (2018). Basement geology of the southern Thomson Orogen. Australian Journal of Earth Sciences, 65(7-8), 893-916.

QPED, Department of Natural Resources and Mines Queensland Government (2020). [Web page] Queensland petroleum exploration data (QPED), https://www.data.qld.gov.au/dataset/queensland-borehole-series. (Last accessed 17.08.2020).

Radke, B. (2009). Hydrocarbon and Geothermal Prospectivity of Sedimentary Basins in Central Australia Warburton, Cooper, Pedirka, Galilee, Simpson and Eromanga Basins. Record 2009/25, Geoscience Australia, Canberra, http://www.ga.gov.au/corporate_data/69150/Rec2009_025.pdf.

Radke, B. M., Kellett, J. R. Ransley, T. R. & Bell, J. G. (2012). Lexicon of the lithostratigraphic and hydrogeological units of the Great Artesian Basin and its Cenozoic cover: A technical report to the Australian Government from the CSIRO Great Artesian Basin Water Resource Assessment: Canberra, Australia, Commonwealth Scientific and Industrial Research Organisation Water for a Healthy Country Flagship, 175 p.

Radke, M., Welte, D. H., & Willsch, H. (1982). Geochemical study on a well in the Western Canada Basin: relation of the aromatic distribution pattern to maturity of organic matter. Geochimica et Cosmochimica Acta, 46(1), 1-10. http://dx.doi.org/10.1016/0016-7037(82)90285-X.

Rahmanian, V. D., Moore, P. S., Mudge, W. J., & Spring, D. E. (1990). Sequence stratigraphy and the habitat of hydrocarbons, Gippsland Basin, Australia. Geological Society, London, Special Publications, 50(1), 525-544. https://doi.org/10.1144/GSL.SP.1990.050.01.32.

Rawlinson, N., Davies, D. R., & Pilia, S. (2017). The mechanisms underpinning Cenozoic intraplate volcanism in eastern Australia: Insights from seismic tomography and geodynamic modeling. Geophysical Research Letters, 44(19), 9681-9690.

Raza, A., K. Hill, & R. J. Korsch, (2009). Mid Cretaceous uplift and denudation of the Bowen and Surat basins, eastern Australia: Relationship to Tasman Sea rifting from apatite fission track and vitrinite reflectance data: Australian Journal of Earth Sciences, v. 56, no. 3, p. 501–531, doi:10.1080/08120090802698752.

Reeves, F. (1947). Geology of Roma District, Queensland, Australia. AAPG Bulletin, 31(8), 1341-1371.

Reynolds, S. D., Coblentz, D. D., & Hillis, R. R. (2003). Influences of plate-boundary forces on the regional intraplate stress field of continental Australia. Geological Society of America Special Papers, 372, 59-70. https://doi.org/10.1130/0-8137-2372-8.59.

Reynolds, S. D., Mildren, S. D., Hillis, R. R., Meyer, J. J., & Flottmann, T. (2005). Maximum horizontal stress orientations in the Cooper Basin, Australia: implications for plate-scale tectonics and local stress sources. Geophysical Journal International, 160(1), 331-343.

Roberts, D. C., Carroll, P. G., & Sayers, J. (1990). The Kalladeina Formation–a Warburton Basin Cambrian carbonate play. The APPEA Journal, 30(1), 166-183.

Robinson, P. A., & Butler, G. F. (1989). Development of the Dullingari Murta Oil Field. In Proceedings of the Cooper and Eromanga Basins Conference (1989). Petroleum Exploration Society of Australia (PESA).

Rosenbaum, G. (2018). The Tasmanides: Phanerozoic tectonic evolution of eastern Australia. Annual Review of Earth and Planetary Sciences, 46, 291-325.

Salmon, M., Kennett, B. L. N., & Saygin, E. (2012). Australian seismological reference model (AuSREM): Crustal component. Geophysical Journal International, 192(1), 190-206. https://doi.org/10.1093/gji/ggs004.

Salomon, J. A., Keenihan, S. L., & Calcraft, A. P. (1990). Bodalla South Field. In J. A. Salomon, S. L. Keenihan, & A. P. Calcraft (Eds.), TR: Structural Traps I: Tectonic Fold Traps (AAPG Special Volumes, pp. 129-155). American Association of Petroleum Geologists.

Samsu, A., Cruden, A. R., Micklethwaite, S., Grose, L., & Vollgger, S. A. (2020). Scale matters: The influence of structural inheritance on fracture patterns. Journal of Structural Geology, 130, 103896. https://doi.org/10.1016/j.jsg.2019.103896

Sandiford, M., Lawrie, K. & Brodie, R.S. (2020). Hydrogeological implications of active tectonics in the Great Artesian Basin, Australia. Hydrogeol J 28, 57–73. https://doi.org/10.1007/s10040-019-02046-4.

Santos (2020). [Web page] Santos welcomes 1.9 billion dollars technology-neutral investment to reduce carbon emissions. Media Release. 17 September 2020. https://www.santos.com/wp-content/uploads/2020/09/200917-Release-Santos-welcomes-1.9-billion-technology-neutral-investment-to-reduce-carbon-emissions.pdf. (Last accessed: 14.10.2020).

Scalan, E. S., & Smith, J. E. (1970). An improved measure of the odd-even predominance in the normal alkanes of sediment extracts and petroleum. Geochimica et Cosmochimica Acta, 34(5), 611-620. https://doi.org/10.1016/0016-7037(70)90019-0.

Scheibner, E. (1974). Fossil fracture zones (transform faults), segmentation and correlation problems in the Tasman Fold Belt System. In The Tasman Geosyncline–A Symposium in Honour of Professor Dorothy Hill, Queensland Division Geological Society of Australia, Brisbane (pp. 65-96).

Scheidt, G., & Littke, R. (1989). Comparative organic petrology of interlayered sandstones, siltstones, mudstones and coals in the Upper Carboniferous Ruhr basin, Northwest Germany, and their thermal history and methane generation. Geologische Rundschau, 78(1), 375-390.

Schulz-Rojahn, J. P. (1993). Calcite-cemented zones in the Eromanga Basin: clues to petroleum migration and entrapment? The APPEA Journal, 33(1), 63-76. https://doi.org/10.1071/AJ92006.

Schwartz, J. J., Stowell, H. H., Klepeis, K. A., Tulloch, A. J., Kylander-Clark, A. R. C., Hacker, B. R., & Coble, M. A. (2016). Thermochronology of extensional orogenic collapse in the deep crust of Zealandia. Geosphere, 12(3), 647–677. https://doi.org/10.1130/GES01232.1.

Schwarzbauer, J., & Jovančićević, B. (2020). Principal Analytical Procedures in Organic Geochemistry. In Introduction to Analytical Methods in Organic Geochemistry (pp. 135-145). Springer, Cham.

Seifert, W. K., & Moldowan, J. M. (1980). The effect of thermal stress on source-rock quality as measured by hopane stereochemistry. Physics and Chemistry of the Earth, 12(0), 229-237. http://dx.doi.org/10.1016/0079-1946(79)90107-1.

Seifert, W. K., & Moldowan, J., M. (1986). Use of biological markers in petroleum exploration. In R. B. Johns (Ed.), Method in geochemistry and geophysics (Vol. 24, pp. 261-290). Amsterdam: Elsevier.

Seifert, W. K., Moldowan, J. M., & Jones, R. W. (1981). Application of biologic markers in combination with stable carbon isotopes to source rock/oil correlations, Prudhoe Bay, Alaska. AAPG Bulletin, 65(5), 990-991.

Shaw, R. D., Etheridge, M. A., & Lambeck, K. (1991). Development of the Late Proterozoic to Mid- Paleozoic, intracratonic Amadeus Basin in central Australia: A key to understanding tectonic forces in plate interiors. Tectonics, 10(4), 688-721.

Shaw, R.D., Wellman, P., Gunn, P., Whitaker, A.J., Tarlowski, C., Morse, M., (1996). Guide to using the Australian crustal elements map. Australian Geological Survey Organisation Record 1996/30.

Siégel, C., Bryan, S. E., Allen, C. M., Purdy, D. J., Cross, A. J., Uysal, I. T., & Gust, D. A. (2018). Crustal and thermal structure of the Thomson Orogen: constraints from the geochemistry, zircon U–Pb age, and Hf and O isotopes of subsurface granitic rocks. Australian Journal of Earth Sciences, 65(7-8), 967-986.

Siégel, C., Bryan, S., Purdy, D., Allen, C., Schrank, C., Uysal, T., ... & Beardsmore, G. (2012). Evaluating the role of deep granitic rocks in generating anomalous temperatures in south-west Queensland. In Geological Survey of Queensland: Digging Deeper 10 Seminar extended abstracts [Queensland Geological Record 2012/14]: (pp. 95-102). Geological Survey of Queensland, Department of Natural Resource and Mines.

Siégel, C., Schrank, C. E., Bryan, S. E., Beardsmore, G. R., & Purdy, D. J. (2014). Heat-producing crust regulation of subsurface temperatures: A stochastic model re-evaluation of the geothermal potential in southwestern Queensland, Australia. Geothermics, 51, 182-200.

Sinninghe Damsté, J. S., Kenig, F., Koopmans, M. P., Koster, J., Schouten, S., Hayes, J. M., & de Leeuw, J. W. (1995). Evidence for gammacerane as an indicator of water column stratification. Geochimica et Cosmochimica Acta, 59(9), 1895-1900.

Smerdon, B. D., Ransley, T. R., Radke, B. M., & Kellett, J. R. (2012). Water resource assessment for the Great Artesian Basin. A report to the Australian government from the CSIRO Great Artesian Basin water resource assessment. CSIRO Water for a Healthy Country Flagship, Australia. Australian Government.

Smith, M., Karim, F., Sparrow, A., Cassel, R. & Hall, L. (2015). Context statement for the Cooper subregion. Product 1.1 for the Cooper subregion from the Lake Eyre Basin Bioregional Assessment. Department of the Environment, Bureau of Meteorology, CSIRO and Geoscience Australia, Australia, http://data.bioregionalassessments.gov.au/doc/BA-LEB-COO-110-ContextStatement-20150903.pdf

Spampinato, G. P., Ailleres, L., Betts, P. G., & Armit, R. J. (2015). Imaging the basement architecture across the Cork Fault in Queensland using magnetic and gravity data. Precambrian Research, 264, 63-81.

Suebsiri, J., Wilson, M., & Tontiwachwuthikul, P. (2006). Life-cycle analysis of CO2 EOR on EOR and geological storage through economic optimization and sensitivity analysis using the Weyburn Unit as a case study. Industrial & engineering chemistry research, 45(8), 2483-2488. https://pubs.acs.org/doi/10.1021/ie050909w.

Sun, X. (1997). Structural style of the Warburton Basin and control in the Cooper and Eromanga Basins, South Australia. Exploration Geophysics, 28(3), 333-339.

Sun, X., and B. Camac, (2004). [Web page] Cooper Basin electrofacies mapping, Adelaide, Australia, South Australia Department of State Development, Resources and Energy, https://sarig.pir.sa.gov.au/Map. (Last accessed: 25.04.2017).

Sutherland, F. L. (1991). Cainozoic volcanism, eastern Australia: a predictive model based on migration over multiple 'hotspot' magma sources. The Cainozoic in Australia: A Reappraisal of the Evidence. Geological Society of Australia Special Publication, 18, 15-43.

Sweeney, J. J., & Burnham, A. K. (1990). Evaluation of a simple model of vitrinite reflectance based on chemical kinetics (1). AAPG Bulletin, 74(10), 1559-1570.

Taylor, G. H., Teichmüller, M., Davis, A., Diessel, C. F. K., Littke, R., & Robert, P. (1998). Organic petrology. Berlin, Stuttgart: Gebrüder Borntraeger. https://doi.org/10.1017/S001675689946332.

Teasdale, J. P., Pryer, L. L., Stuart-Smith, P. G., Romine, K. K., Etheridge, M. A., Loutit, T. S., & Kyan, D. M. (2003). Structural framework and basin evolution of Australia's southern margin. APPEA Journal, 43(1), 13-37. https://doi.org/10.1071/AJ02001.

Teasdale, J., Pryer, L., Etheridge, M., Romine, K., Stuart-Smith, P., Cowan, P., ... & Henley, P. (2001). Officer Basin SEEBASE Project. Report for Primary Industries and Resources SA.

ten Haven, H. L. and Rullkötter, J. (1988). The diagenetic fate of taraxer-14-ene and oleanane isomers. Geochimica et Cosmochimica Acta, 52, 2543–8.

Tissot, B. P., & Welte, D. H. (1984). From kerogen to petroleum. In B. P. Tissot & D. H. Welte (Eds.), Petroleum formation and occurrence (pp. 160-198). Berlin, Heidelberg: Springer.

Turner, S., Bean, L. B., Dettmann, M., McKellar, J. L., McLoughlin, S., & Thulborn, T. (2009). Australian Jurassic sedimentary and fossil successions: current work and future prospects for marine and non-marine correlation. GFF, 131(1-2), 49-70.

Turtle, E. P., Pierazzo, E., & O'Brien, D. P. (2003). Numerical modeling of impact heating and cooling of the Vredefort impact structure. Meteoritics & Planetary Science, 38(2), 293-303.

UNFCCC, United Nations Framework Convention on Climate Change (2020). [Web page] The Paris Agreement. https://unfccc.int/process-and-meetings/the-paris-agreement/the-paris-agreement. (Last accessed: 13.10.2020).

van Aarssen, B. G., Bastow, T. P., Alexander, R., & Kagi, R. I. (1999). Distributions of methylated naphthalenes in crude oils: indicators of maturity, biodegradation and mixing. Organic Geochemistry, 30(10), 1213-1227. https://doi.org/10.1016/S0146-6380(99)00097-2.

van der Beek, P. A., Braun, J., & Lambeck, K. (1999). Post- Palaeozoic uplift history of southeastern Australia revisited: Results from a process- based model of landscape evolution. Australian Journal of Earth Sciences, 46(2), 157-172. https://doi.org/10.1046/j.1440-0952.1999.00701.x.

Veevers, J. J. (2000). Change of tectono-stratigraphic regime in the Australian plate during the 99 Ma (mid-Cretaceous) and 43 Ma (mid-Eocene) swerves of the Pacific. Geology, 28(1), 47-50. https://doi.org/10.1130/0091-7613(2000)28<47:COTRIT>2.0.CO;2.

Veevers, J. J., & Morgan, P. (Eds.). (2000). Billion-year earth history of Australia and neighbours in Gondwanaland. Gemoc Press.

Veevers, J. J., & Powell, C. M. (1984). Epi-Adelaidean: regional shear. In: Veevers J. J. (ed.) Phanerozoic Earth History of Australia, pp. 278–284. Clarendon Press, Oxford

Veevers, J. J., Powell, C. M., & Roots, S. R. (1991). Review of seafloor spreading around Australia. I. Synthesis of the patterns of spreading. Australian Journal of Earth Sciences, 38(4), 373-389.

Veevers, J.J. (1984). Phanerozoic Earth history of Australia. Oxford University Press. ISBN 0198544596

Vincent, P. W., Mortimore, I. R. & McKirdy, D. M. (1985). Hydrocarbon generation, migration and entrapment in the Jackson-Naccowlah area, ATP 259P, Southwestern Queensland. The APPEA Journal, 25(1), 62-84.

Wainman, C. C., McCabe, P. J., & Crowley, J. L. (2018). Solving a tuff problem: Defining a chronostratigraphic framework for Middle to Upper Jurassic nonmarine strata in eastern Australia using uranium–lead chemical abrasion–thermal ionization mass spectrometry zircon dates. AAPG Bulletin, 102(6), 1141-1168.

Wakelin-King, G. A., & White, S. Q. (2011). Potential GeoHeritage Values Of Australian Desert Landscapes. A report to the Commonwealth Department of Sustainability, Environment, Water, Population and Communities. Wakelin Associates Pty. Ltd. https://environment.gov.au/system/files/resources/806716b9-dff5-48cb-b7d9-fae6ef053ad4/files/desert-geoheritage.pdf.

Watts, K. J. (1987). The Hutton Sandstone-Birkhead Formation transition, ATP 269P (1), Eromanga Basin. The APPEA Journal, 27(1), 215-229.

Wecker, H. R. B. (1989). The Eromanga Basin. The APPEA Journal, 29(1), 379-397.

Welte, D. H., Horsfield, B., & Baker, D. R. (Eds.). (1997). Petroleum and basin evolution: insights from petroleum geochemistry, geology and basin modeling. Springer Science & Business Media. ISBN 978-3-642-60423-2.

Wernicke, B. (1985). Uniform-sense normal simple shear of the continental lithosphere. Canadian Journal of Earth Sciences, 22(1), 108-125. https://doi.org/10.1139/e85-009

Whiteway, T. (2009). [Web page] Australian Bathymetry and Topography Grid, June 2009. Scale 1:5000000. Geoscience Australia, Canberra. http://www.ga.gov.au/corporate_data/67703/Rec2009_021.pdf. (Last accessed: 26.02.2019).

Willcox, J. B., Colwell, J. B., & Constantine, A. E. (1992). New ideas on Gippsland Basin regional tectonics. Gippsland Basin Symposium, Melbourne, 1992. Petroleum Exploration Society of Australia (PESA).

Williams, S. E., Whittaker, J. M., & Müller, R. D. (2011). Full- fit, palinspastic reconstruction of the conjugate Australian- Antarctic margins. Tectonics, 30(6).

Wilson, J. T. (1966). Did the Atlantic close and then re-open?. Nature, 211(5050), 676-681.

Wilson, R. W., Houseman, G. A., Buiter, S. J. H., McCaffrey, K. J. W., & Doré, A. G. (2019). Fifty years of the Wilson Cycle concept in plate tectonics: an overview. Geological Society, London, special publications. 470(1), 1-17.

Wingate, M. T., Pisarevsky, S. A., & Evans, D. A. (2002). Rodinia connections between Australia and Laurentia: no SWEAT, no AUSWUS?. Terra Nova, 14(2), 121-128.

Wong, S. C. T., Collins, W. J., Hack, A. C., & Huang, H. Q. (2018). Provenance and structure of the Yancannia Formation, southern Thomson Orogen: implications for the tectono-stratigraphic evolution of the Cambro-Ordovician western Tasmanides. Australian Journal of Earth Sciences, 65(7-8), 1097-1121.

Woollands, M. A., & Wong, D. (2001). [Web page] Petroleum Atlas of Victoria, Australia. The State of Victoria, Department of Natural Resources and Environment, Special Publications, 208. http://earthresources.efirst.com.au/product.asp?pID=9&cID=6. (Last accessed: 07.04.2020).

Wopfner, H. (1997). Australien (Vol. 4). Springer.

Wygrala, B. P., (1989). Integrated study of an oil field in the southern Po basin, northern Italy, Ph.D. dissertation, University of Cologne, Cologne, Germany, 217 p.

Yang, S., & Horsfield, B. (2020). Critical review of the uncertainty of Tmax in revealing the thermal maturity of organic matter in sedimentary rocks. International Journal of Coal Geology, 103500.

Yew, C. C., & Mills, A. A. (1989). The occurrence and search for Permian oil in the Cooper Basin, Australia.

Zhao, S. & Müller, R. D. (2003). Three-dimensional finite-element modelling of the tectonic stress field in continental Australia. In: Hillis, R.R., & Müller, R.D. (Eds.), Evolution and Dynamics of the Australian Plate, Geological Society of America Special Papers, 372, 71-89. https://doi.org/10.1130/0-8137-2372-8.71.

Zieger, L., Littke, R., Hartkopf-Fröder, C., & Schwarzbauer, J. (2020). Comparative geochemical and pyrolytic study of coals, associated kerogens, and isolated vitrinites at the limit between subbituminous and bituminous coal. International Journal of Coal Geology, 103517. https://doi.org/10.1016/j.coal.2020.103517.

Ziegs, V., Mahlstedt, N., Bruns, B., & Horsfield, B. (2015). Predicted bulk composition of petroleum generated by Lower Cretaceous Wealden black shales, Lower Saxony Basin, Germany. International Journal of Earth Sciences, 104(6), 1605-1621.

Zoellner, E. (1988). Geology of the Early Cretaceous Murta Member (Mooga Formation) in the Cooper Basin area, South Australia and Queensland. Doctoral dissertation. Flinders University of South Australia.

Zumberge, J. E. (1987). Terpenoid biomarker distributions in low maturity crude oils. Organic Geochemistry, 11, 479–96.

Zwingmann, H., Tingate, P. R., Lemon, N. M., & Hamilton, P. J. (2001). K-Ar dating, petrographic and thermal modelling constraints on illite origin in the Cooper Basin, South Australia.

QLD Ref. No. 27146: Local reference number of the sampled core material at the drill core reference library in Brisbane, Queensland. https://www.business.qld.gov.au/industries/mining-energy-water/resources/geoscience-information/exploration-incentives/drillcore

SA Ref. No. 4857: Local reference number of the sampled core material at the drill core reference library in Adelaide, South Australia. https://energymining.sa.gov.au/minerals/geoscience/drill_core_reference_library

8 APPENDICES

APPENDIX 1 (CHAPTER 3) 261

APPENDIX 2 (CHAPTER 4) 263

APPENDIX 3 (CHAPTER 5) 305

APPENDIX 1 (CHAPTER 3)

Appendix 1.1: Settings for thermal modelling (PetroMod crustal layer pre-processor).

Parameter	Value
Input	
Syn-rift from [Ma]	145,00
Syn-rift to [Ma]	103,00
Post-rift from [Ma]	103,00
Post-rift to [Ma]	0,00
Upper crust facies	granite (continental)
Lower crust facies	diorite (continental)
Upper mantle facies	upper mantle (lithosphere)
Pre-rift thickness crust	*variable*
Pre-rift thickness mantle	*variable*
Stretching maps	automatic calculation
Thermal properties	
Base temperature [°C]	1.333
Stretching model	
Uniform stretching model	off / crust and mantle decoupled
Time steps syn-rift	20
Time steps post-rift	100
Resolution (vertical cell number)	300
Stretching map sampling	
Stretching sampling factor (X)	2
Stretching sampling factor (Y)	2
Fitting	
Stretching factor precision (decimals)	2
Maximum iterations	1.000
Syn-rift weight	2
Post-rift weight	5
Use syn-rift and final tectonic subsidence only	off
Smoothing	
Filter width crust [grid points]	1
Filter width mantle [grid points]	5
Inversion routine	2-step inversion
Calculate strain rates	off
Crustal thickness ratios [%]	Upper crust 50 / lower crust 50

Appendix 1.2: Simulator settings.

Parameter	Applied value / option
Simulation method	parallel run
Run control	
Temperature run	2D/3D temperature
Pressure run	2D/3D pressure
All time steps	enabled
Optimization	use previous run (max 2)
Sampling	1 x 1
Stepsize x	582.182 m
Stepsize y	404.638 m
Output on sampled grid	
Calculation steps	10 / 10
Max time step duration	10 Ma
Min migration steps per time step	10
Number of CPU cores for parallel run	8
Migration method	Combined Darcy flow / IP
Processes & Tools	Default settings (except for faults)
Fault method	Locally refined volumetric elements (LRVE)

APPENDIX 2 (CHAPTER 4)

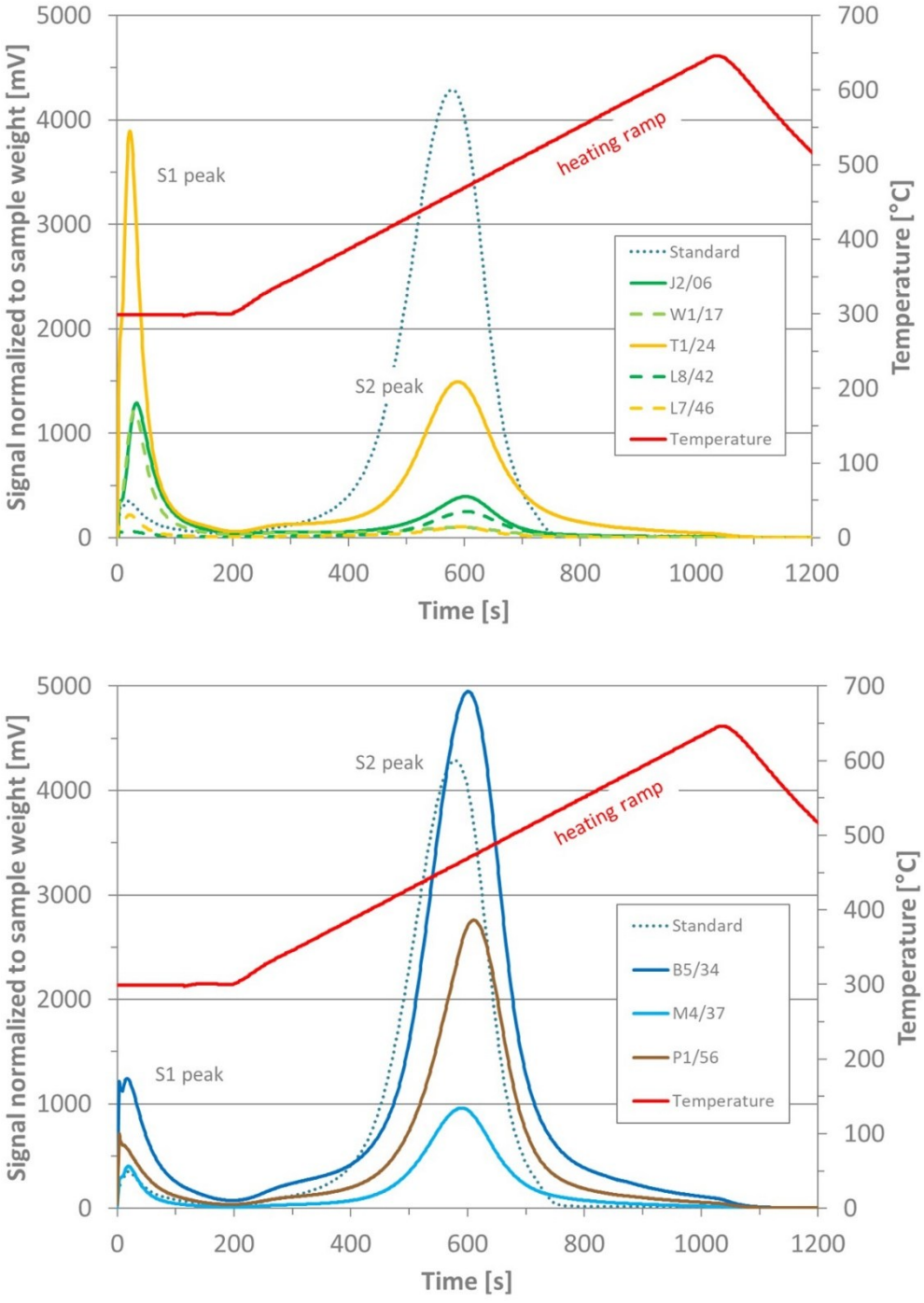

Appendix 2.1: Representative Rock-Eval pyrograms for the Murta (above) and the Birkhead (below) formations with signal intensity normalized to sample weight. A standard with the following properties was used: TOC = 7.65 wt. %, S1 = 2.51 mg HC/g rock, S2 = 50.6 mg HC/g rock, Tmax = 426 °C.

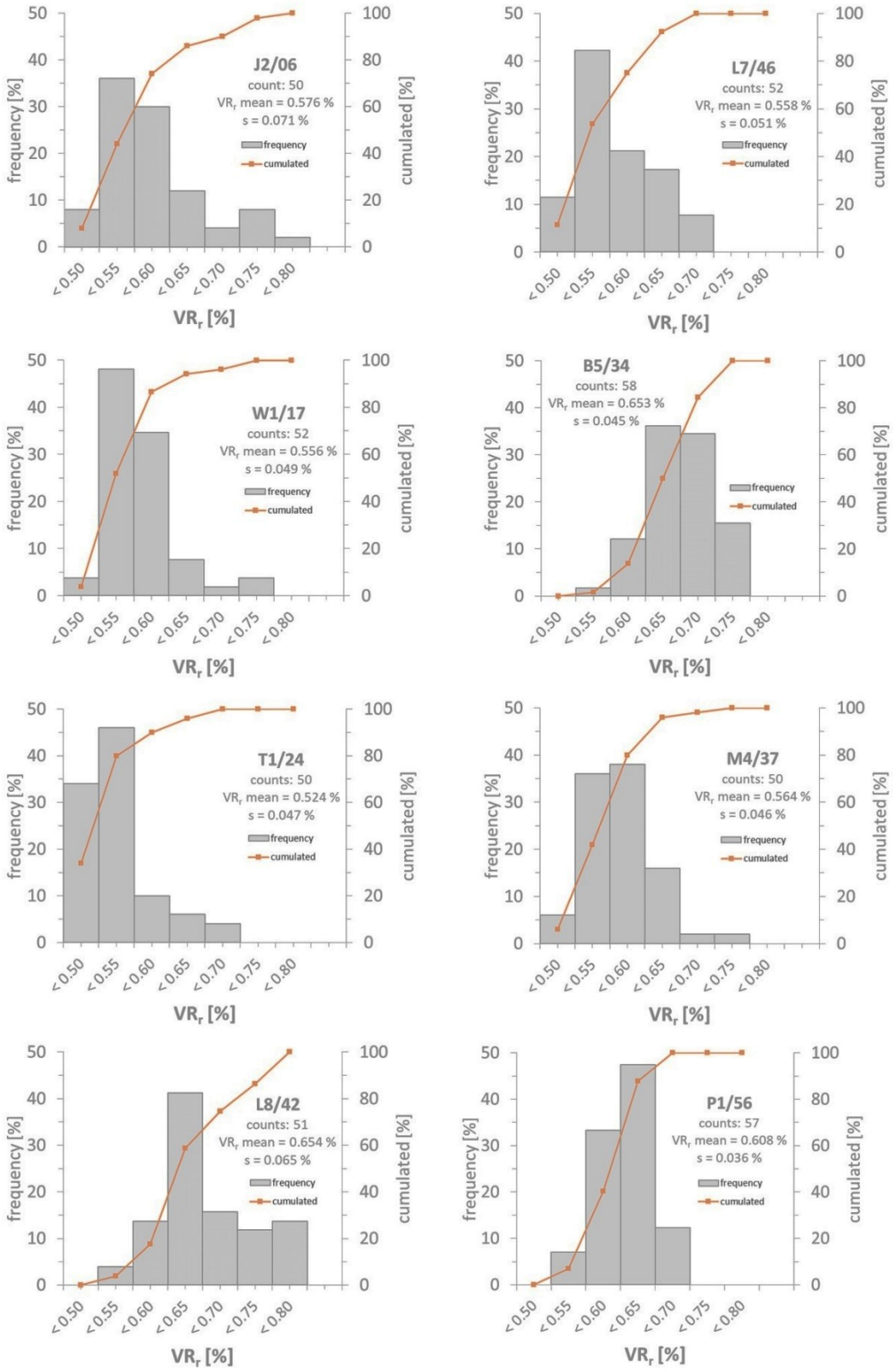

Appendix 2.2: Representative measurements of randomly oriented vitrinite reflectance (VR_r %) for petrographical determination of thermal maturity with frequency classes. Samples B5/34, M4/37, and P1/56 represent Birkhead Formation. Remaining samples are from Murta Formation.

Appendix 2.3: Measured GC peak areas, Murta Formation.

Compound / Sample ID	**18/1405**	**18/1406**	**18/1411**	**18/1417**	**18/1424**
n-alkanes					
n-C15	149239400	260973430	1718124865	97629909	6881504
n-C17	1317578036	446441522	662102183	331485347	12639310
Pristane	415112283	123208685	213597212	129525245	3490545
n-C18	1585136738	406706153	683644235	360843291	11098355
Phytane	162867999	39749630	92060174	51863325	1015683
n-C19	1723161507	391691815	623297168	399356124	7448627
n-C21	1590816579	168375417	382785249	413576969	1902051
n-C22	1455282516	92717800	262124958	378146923	749318
n-C23	1366750392	64195648	183773236	367114125	287119
n-C24	1174245244	38622335	132364659	312348535	107273
n-C25	853377005	33229979	93142063	232082332	59959
n-C27	329834521	10984303	32913688	91630612	21735
n-C29	152844758	3679673	10875997	31528133	11172
n-C31	51384714	1124387	2235361	5399804	7035

Compound / Sample ID	**18/1426**	**18/1429**	**18/1442**	**18/1444**	**18/1445**	**18/1446**
n-alkanes						
n-C15	188598154	71867095	73942873	57325652	82324290	38928281
n-C17	158289768	106632008	51368226	120132376	100801281	115624865
Pristane	54227794	57505584	10409489	21477805	22171610	27853321
n-C18	73751670	102105637	58739776	130437179	99421969	121495660
Phytane	8041899	15871556	3810631	11135215	6810267	9014060
n-C19	29838812	93143000	53559026	155562103	72407979	89979737
n-C21	9972870	72887629	15387094	204555057	25302447	33049015
n-C22	7479915	59047658	7164093	217918013	17770676	25097646
n-C23	6306286	60476602	5603780	234280465	14028601	20551040
n-C24	4866488	55878379	4106869	205331440	8572563	13365107
n-C25	4162929	64036502	4729770	154732863	6019860	7706110
n-C27	2427060	50211283	3142317	48385270	2629702	1777837
n-C29	1604549	26574111	1184148	13095475	1076376	599126
n-C31	602253	15095252	523647	2807492	569590	127074

Appendix 2.3 (continued): Measured GC peak areas, Murta Formation.

Compound / Sample ID	**18/1405**	**18/1406**	**18/1411**	**18/1417**	**18/1424**
mass to charge ratio: m/z = 191 (hopanes)					
C19 tricyclic diterpane	2222925	214291	322250	435205	2194374
C20 tricyclic diterpane	1832500	141355	214518	346114	1114115
C21 tricyclic diterpane	239228	29398	36859	81433	198601
C22 tricyclic diterpane	233440	15467	14144	31389	210869
C23 tricyclic diterpane	507933	29249	24494	79682	215717
C24 tetracyclic terpane (TET)	1302638	44606	50068	312198	561095
Ts 18α(H)-trisnorhopane	1689266	143677	301791	279367	381594
Tm 17α(H)-trisnorhopane	3126819	316186	797717	773573	1082283
C29 Tm 17α(H)21β(H)-norhopane	7645356	255679	271947	2180132	1901166
C29 Ts 18α(H)-norneohopane	1868547	107355	87331	568344	407713
C30 17α(H)-diahopane	742203	17116	19568	225478	110311
C29 normoretane	1546400	68332	63060	460756	548489
C30 17α(H)-hopane	11813009	457933	447073	3181567	2815629
17α(H)-30-nor-29-homohopane	649990	48357	32084	175245	116662
C30 moretane	2341526	69124	82467	613282	755932
C31 22S 17a(H) homohopane	4004268	172196	183005	1110133	1197030
C31 22R 17a(H) homohopane	3113392	162562	141948	890649	1000197
Gammacerane	238593	34231	21439	107674	99544
C32 22S 17a(H) bishomohopane	1892120	60559	84333	596547	692918
C32 22R 17a(H) bishomohopane	1512450	60834	79235	503614	669168
C33 22S 17a(H) trishomohopane	947937	22201	38375	379579	425398
C33 22R 17a(H) trishomohopane	729424	23242	32053	253341	377222
C34 22S 17a(H) extended hopane	590930	18086	24242	229367	290819
C34 22R 17a(H) extended hopane	444678	15675	13733	165567	263102
C35 22S 17a(H) extended hopane	248557	0	0	119250	168398
C35 22R 17a(H) extended hopane	189696	0	0	74599	154979

Appendix 2.3 (continued): Measured GC peak areas, Murta Formation.

Compound / Sample ID	**18/1426**	**18/1429**	**18/1442**	**18/1444**	**18/1445**	**18/1446**
mass to charge ratio: m/z=191 (hopanes)						
C19 tricyclic diterpane	432129	1082811	116883	213127	142039	71026
C20 tricyclic diterpane	272280	899449	65946	170994	83997	39248
C21 tricyclic diterpane	92896	890762	25118	35825	32546	9876
C22 tricyclic diterpane	26301	99107	8918	28940	18920	4492
C23 tricyclic diterpane	82453	479793	37507	84728	70081	21942
C24 tetracyclic terpane (TET)	326789	1561839	71452	163389	84353	19737
Ts 18α(H)-trisnorhopane	184910	4140579	60044	191230	108771	20860
Tm 17α(H)-trisnorhopane	1224186	13754361	502038	512405	354123	51527
C29 Tm 17α(H)21β(H)-norhopane	2591796	40098676	796545	954657	794579	126722
C29 Ts 18α(H)-norneohopane	421872	9570231	143489	275167	205013	56588
C30 17α(H)-diahopane	94714	1495527	12903	84634	17067	6848
C29 normoretane	831724	11512819	321535	347310	308909	48741
C30 17α(H)-hopane	2507793	62375929	1330475	1641627	1185213	204480
17α(H)-30-nor-29-homohopane	116261	2227610	101895	102046	93565	12343
C30 moretane	743734	12641969	373529	373768	262671	44001
C31 22S 17a(H) homohopane	824421	19913837	482023	845549	511353	58012
C31 22R 17a(H) homohopane	594232	12975119	362527	558929	388086	67956
Gammacerane	37845	2275962	39422	90738	64897	10311
C32 22S 17a(H) bishomohopane	416522	7547602	137400	326393	132187	24955
C32 22R 17a(H) bishomohopane	358598	5061611	109339	280110	113279	25864
C33 22S 17a(H) trishomohopane	219766	4200404	52281	135073	50301	10776
C33 22R 17a(H) trishomohopane	148914	3045295	38498	101282	53446	11183
C34 22S 17a(H) extended hopane	119912	2710388	33983	77300	0	0
C34 22R 17a(H) extended hopane	93656	2008209	24414	59036	0	0
C35 22S 17a(H) extended hopane	0	0	0	35284	0	0
C35 22R 17a(H) extended hopane	0	0	0	31579	0	0

Appendix 2.3 (continued): Measured GC peak areas, Murta Formation.

Compound / sample ID	**18/1405**	**18/1406**	**18/1411**	**18/1417**	**18/1424**
mass to charge ratio: m/z=217 (steranes)					
C21 sterane	852374	26980	27167	87359	174825
C22 sterane	169699	10683	11910	20785	102959
C27 βα 20S diasterane	301933	8003	6744	75936	60154
C27 βα 20R diasterane	257159	7643	3840	65413	41988
C27 αα 20S cholestane	289539	8854	4986	94698	43355
C27 ββ 20R cholestane	126718	2159	7333	9411	14227
C27 ββ 20S cholestane	268905	6175	10331	93255	58756
C27 αα 20R cholestane	196967	4513	1898	44001	47203
C29 dia	2067664	28817	36205	609163	418174
C29 dia	1456176	21216	32211	493751	314033
C28 αα 20S ergostane	94990	2019	3166	33716	36297
C28 ββ 20R ergostane	79535	3953	7818	41093	26623
C28 ββ 20S ergostane	217502	2342	6102	62420	39680
C28 αα 20R ergostane	165738	3302	4196	35149	47807
C29 αα 20S stigmastane	682785	12213	16145	189072	141247
C29 ββ 20R stigmastane	992065	14067	13682	239270	258989
C29 ββ 20S stigmastane	507834	8920	8811	139601	87335
C29 αα 20R stigmastane	1271115	38025	30835	286968	262440

Compound / sample ID	**18/1426**	**18/1429**	**18/1442**	**18/1444**	**18/1445**	**18/1446**
mass to charge ratio: m/z=217 (steranes)						
C21 sterane	64021	286874	30594	48513	31467	12658
C22 sterane	34623	119535	10900	19897	20559	6856
C27 βα 20S diasterane	32926	277068	12549	37798	21298	6427
C27 βα 20R diasterane	23710	203248	7206	30009	16270	5198
C27 αα 20S cholestane	44587	533625	1867	43233	15260	3361
C27 ββ 20R cholestane	38342	118547	16179	16618	11003	2404
C27 ββ 20S cholestane	32736	172198	11826	31507	11870	5303
C27 αα 20R cholestane	11098	294889	17912	43718	3932	3897
C29 dia	186440	1384289	26477	194257	39414	11739
C29 dia	161056	1041177	28513	150741	19050	11256
C28 αα 20S ergostane	16382	132533	2567	7494	4421	1882
C28 ββ 20R ergostane	30401	154470	9962	15100	14144	1923
C28 ββ 20S ergostane	19834	158346	15394	16577	12621	2472
C28 αα 20R ergostane	12757	339806	15167	15229	6893	2663
C29 αα 20S stigmastane	84030	1398600	25915	51378	23377	7739
C29 ββ 20R stigmastane	106175	1026601	37142	77426	47728	7774
C29 ββ 20S stigmastane	61632	444465	8102	37428	21999	7075
C29 αα 20R stigmastane	170568	2963080	97808	164186	97296	17346

Appendix 2.3 (continued): Measured GC peak areas, Murta Formation.

Compound / Sample ID	**18/1405**	**18/1406**	**18/1411**	**18/1417**	**18/1424**
mass to charge ratio: m/z=142 (aromatics)					
β-Methylnaphthalene	11490502	22041145	71969415	12691551	71075616
α-Methylnaphthalene	5789036	11723587	41970081	7619076	41265076
mass to charge ratio: m/z=178 (aromatics)					
Phenanthrene	21346045	49352369	100217604	27643973	68390350
mass to charge ratio: m/z=184 (aromatics)					
Dibenzothiopene	1383917	11889407	39435049	8903728	37125193
mass to charge ratio: m/z=192 (aromatics)					
3-Methylphenantrene	4189084	12345270	23105848	7316453	14077291
2-Methylphenantrene	6826460	15621535	29174394	9479657	17203928
9-Methylphenantrene	7420879	21239084	37451279	12241303	21445569
1-Methylphenantrene	12421348	27861428	74833201	25290551	42995715

Compound / Sample ID	**18/1426**	**18/1429**	**18/1442**	**18/1444**	**18/1445**	**18/1446**
mass to charge ratio: m/z=142 (aromatics)						
β-Methylnaphthalene	179077197	110138554	268923879	29152959	79103025	4952826
α-Methylnaphthalene	89138716	57169816	130351729	14920841	40082092	2680318
mass to charge ratio: m/z=178 (aromatics)						
Phenanthrene	74921533	49897967	112894181	26319704	59272122	7852194
mass to charge ratio: m/z=184 (aromatics)						
Dibenzothiopene	25935000	17217710	30839798	5888435	15466332	1459471
mass to charge ratio: m/z=192 (aromatics)						
3-Methylphenantrene	16240060	9850766	14860133	3829010	8799847	1052397
2-Methylphenantrene	20305265	12369589	20005847	5478809	12353478	1605648
9-Methylphenantrene	26708499	16338726	29101477	7460078	17143088	2157939
1-Methylphenantrene	53521106	32570096	44422039	12267575	26225668	3476341

Appendix 2.4: Measured GC peak areas, Birkhead Formation.

Compound / Sample ID	**18/1434**	**18/1435**	**18/1437**	**18/1440**	**18/1455**	**18/1456**
n-alkanes						
n-C15	150460261	11879417	187515102	67447592	82078778	26986100
n-C17	130805977	8427342	168727358	37057282	92686263	28607599
Pristane	109417400	9324920	212411188	51986549	153214044	48010966
n-C18	118192730	8780989	154467292	23853728	105568391	31776620
Phytane	21005223	2050669	31827579	5242331	25461932	7542760
n-C19	117644899	8913839	101977592	20706054	118619158	36410421
n-C21	109465308	8073974	46211152	22939616	152040388	40545546
n-C22	98143394	7985905	37670561	26879958	170117113	45678209
n-C23	100134445	8377898	36576535	35421245	199056130	51795534
n-C24	91123507	7834750	36018390	36574122	217348611	55695200
n-C25	96321496	8058025	41646288	50701868	271679635	68970703
n-C27	92624150	6684198	41764259	53927064	299968742	77749272
n-C29	77342682	3464133	28044750	38411096	170817728	42627012
n-C31	56856638	1269513	14619420	14514129	88983131	19839186

Appendix 2.4 (continued): Measured GC peak areas, Birkhead Formation.

Compound / Sample ID	**18/1434**	**18/1435**	**18/1437**	**18/1440**	**18/1455**	**18/1456**
mass to charge ratio: m/z=191 (hopanes)						
C19 tricyclic diterpane	1612921	243237	1632814	356073	3874301	1027494
C20 tricyclic diterpane	143884	171610	819795	233329	372539	571934
C21 tricyclic diterpane	90909	38925	230967	63380	215381	63345
C22 tricyclic diterpane	25605	11266	55450	25480	87352	26840
C23 tricyclic diterpane	122487	49200	202745	116853	260512	61113
C24 tetracyclic terpane (TET)	653777	166631	839421	352518	4651648	1135930
Ts 18α(H)-trisnorhopane	219031	86618	881331	662416	3862323	1111042
Tm 17α(H)-trisnorhopane	1549587	462205	2625839	1507976	17133993	4144341
C29 Tm 17α(H)21β(H)-norhopane	3530849	1156028	5492142	3990322	38528358	9209192
C29 Ts 18α(H)-norneohopane	456008	210992	1638919	1650539	7371364	2096001
C30 17α(H)-diahopane	655828	111425	571871	506620	5519664	1510256
C29 normoretane	447753	103070	917424	612881	4029727	764284
C30 17α(H)-hopane	5847230	1753434	8318708	7964017	73643471	15982365
17α(H)-30-nor-29-homohopane	255481	101585	392660	520401	2675848	717192
C30 moretane	753923	191051	1403307	1286886	10483028	2057426
C31 22S 17a(H) homohopane	2554051	629449	2877706	2872848	28040842	6054366
C31 22R 17a(H) homohopane	1760021	465110	1947741	2080501	19897999	4307402
Gammacerane	89108	45756	147721	236242	2018748	409123
C32 22S 17a(H) bishomohopane	1748756	352722	1748693	1912084	18184842	4075876
C32 22R 17a(H) bishomohopane	1139182	272644	1218562	1405623	12503884	2778529
C33 22S 17a(H) trishomohopane	1049741	247841	1060154	1324731	9833758	2129808
C33 22R 17a(H) trishomohopane	694935	153303	678023	868503	7133877	1467323
C34 22S 17a(H) extended hopane	804628	116818	804745	878975	6851806	1395153
C34 22R 17a(H) extended hopane	517753	73367	443292	556827	4392053	864799
C35 22S 17a(H) extended hopane	497142	71089	330642	422470	3000281	596306
C35 22R 17a(H) extended hopane	490643	56641	222305	237442	2069824	462213

Appendix 2.4 (continued): Measured GC peak areas, Birkhead Formation.

Compound / Sample ID	**18/1434**	**18/1435**	**18/1437**	**18/1440**	**18/1455**	**18/1456**
mass to charge ratio: m/z=217 (steranes)						
C21 sterane	99230	33579	196563	75143	238236	75501
C22 sterane	137832	25527	90742	41699	205250	54702
C27 βα 20S diasterane	94457	15764	128499	75611	251830	59309
C27 βα 20R diasterane	75675	12939	86078	68472	244549	51881
C27 αα 20S cholestane	166454	25665	162402	125500	549864	99844
C27 ββ 20R cholestane	43130	9114	31855	31271	125900	22455
C27 ββ 20S cholestane	179692	13840	92387	77739	561727	88494
C27 αα 20R cholestane	33427	6885	36522	7436	134504	12203
C29 dia	1252608	159796	1364701	816449	4246622	913449
C29 dia	947449	122753	852202	571037	3146399	614016
C28 αα 20S ergostane	99144	8678	61348	22339	446330	62300
C28 ββ 20R ergostane	25519	21069	55359	91069	404860	79099
C28 ββ 20S ergostane	71535	16434	101264	61889	484579	88625
C28 αα 20R ergostane	37208	7377	44687	28114	527334	47723
C29 αα 20S stigmastane	289407	62529	388741	366169	2102196	447031
C29 ββ 20R stigmastane	344420	72639	408309	366738	2178635	417463
C29 ββ 20S stigmastane	264805	61821	287754	265013	1612684	361275
C29 αα 20R stigmastane	352133	90585	480530	497508	2791077	572014

Appendix 2.4 (continued): Measured GC peak areas, Birkhead Formation.

Compound / Sample ID	**18/1434**	**18/1435**	**18/1437**	**18/1440**	**18/1455**	**18/1456**
mass to charge ratio: m/z=142 (aromatics)						
β-Methylnaphthalene	39189279	114830192	62221185	43916344	352873400	266500697
α-Methylnaphthalene	23268320	68330189	39459125	27181258	223184707	166090177
mass to charge ratio: m/z=178 (aromatics)						
Phenanthrene	19905232	112006963	56595961	33232654	303282731	233980549
mass to charge ratio: m/z=184 (aromatics)						
Dibenzothiopene	7623390	34928065	28750234	15919716	196429318	148193900
mass to charge ratio: m/z=192 (aromatics)						
3-Methylphenantrene	3056748	21183425	7745114	4203189	60264802	46453321
2-Methylphenantrene	4803032	31493966	12921670	6999953	94967700	74207090
9-Methylphenantrene	5232839	37431695	16459070	9303514	108204453	84046845
1-Methylphenantrene	10969747	73577848	142775805	74496196	566736858	443325290

Appendix: 2.5: Coelution of C27 and C29 dia, Murta Formation.

Compound / Sample ID	**18/1405**	**18/1406**	**18/1411**	**18/1417**	**18/1424**
C27+C29dia	2194382	30976	43538	618574	432401
Ratio of (m/z=372/400)	0.05775	0.06969	0.16843	0.01521	0.03290
C27	126718	2159	7333	9411	14227
C29	2067664	28817	36205	609163	418174

Compound / Sample ID	**18/1426**	**18/1429**	**18/1442**	**18/1444**	**18/1445**	**18/1446**
C27+C29dia	224782	1502836	42656	210875	50417	14143
Ratio of (m/z=372/400)	0.17058	0.07888	0.37930	0.07881	0.21824	0.17001
C27	38342	118547	16179	16618	11003	2404
C29	186440	1384289	26477	194257	39414	11739

Appendix 2.6: Coelution of C27 and C29 dia, Birkhead Formation.

Compound / Sample ID	**18/1434**	**18/1435**	**18/1437**	**18/1440**	**18/1455**	**18/1456**
C27+C29dia	1295738	168910	1396556	847720	4372522	935904
ratio of (m/z=372/400)	0.03329	0.05396	0.02281	0.03689	0.02879	0.02399
C27	43130	9114	31855	31271	125900	22455
C29	1252608	159796	1364701	816449	4246622	913449

Appendix 2.7: Ratios of pristane, phytane, n-C17 and n-C18, Murta Formation.

Compound / Sample ID	Pr	n-C17	Ph	n-C18	Pr/Ph	Pr/n-C17	Ph/n-C18
18/1405	415112283	1317578036	162867999	1585136738	2.55	0.32	0.10
18/1406	123208685	446441522	39749630	406706153	3.10	0.28	0.10
18/1411	213597212	662102183	92060174	683644235	2.32	0.32	0.13
18/1417	129525245	331485347	51863325	360843291	2.50	0.39	0.14
18/1424	3490545	12639310	1015683	11098355	3.44	0.28	0.09
18/1426	54227794	158289768	8041899	73751670	6.74	0.34	0.11
18/1429	57505584	106632008	15871556	102105637	3.62	0.54	0.16
18/1442	10409489	51368226	3810631	58739776	2.73	0.20	0.06
18/1444	21477805	120132376	11135215	130437179	1.93	0.18	0.09
18/1445	22171610	100801281	6810267	99421969	3.26	0.22	0.07
18/1446	27853321	115624865	9014060	121495660	3.09	0.24	0.07
min					**1.93**	**0.18**	**0.06**
max					**6.74**	**0.54**	**0.16**
avg					**3.21**	**0.30**	**0.10**

Appendix 2.8: Ratios of pristane, phytane, n-C17 and n-C18, Birkhead Formation.

Compound / Sample ID	Pr	n-C17	Ph	n-C18	Pr/Ph	Pr/n-C17	Ph/n-C18
18/1434	109417400	130805977	21005223	118192730	5.21	0.84	0.18
18/1435	9324920	8427342	2050669	8780989	4.55	1.11	0.23
18/1437	212411188	168727358	31827579	154467292	6.67	1.26	0.21
18/1440	51986549	37057282	5242331	23853728	9.92	1.40	0.22
18/1455	153214044	92686263	25461932	105568391	6.02	1.65	0.24
18/1456	48010966	28607599	7542760	31776620	6.37	1.68	0.24
min					**4.55**	**0.84**	**0.18**
max					**9.92**	**1.68**	**0.24**
avg					**6.45**	**1.32**	**0.22**

Appendix 2.9: Terrigeneous to aquatic ratios (TAR), Murta Formation.

Compound / Sample ID	n-C15	n-C17	n-C19	n-C27	n-C29	n-C31	TAR
18/1405	149239400	1317578036	1723161507	329834521	152844758	51384714	0.167
18/1406	260973430	446441522	391691815	10984303	3679673	1124387	0.014
18/1411	1718124865	662102183	623297168	32913688	10875997	2235361	0.015
18/1417	97629909	331485347	399356124	91630612	31528133	5399804	0.155
18/1424	6881504	12639310	7448627	21735	11172	7035	0.001
18/1426	188598154	158289768	29838812	2427060	1604549	602253	0.012
18/1429	71867095	106632008	93143000	50211283	26574111	15095252	0.338
18/1442	73942873	51368226	53559026	3142317	1184148	523647	0.027
18/1444	57325652	120132376	155562103	48385270	13095475	2807492	0.193
18/1445	82324290	100801281	72407979	2629702	1076376	569590	0.017
18/1446	38928281	115624865	89979737	1777837	599126	127074	0.010
min							**0.00**
max							**0.34**
avg							**0.09**

Appendix 2.10: Terrigeneous to aquatic ratios (TAR), Birkhead Formation.

Compound / Sample ID	n-C15	n-C17	n-C19	n-C27	n-C29	n-C31	TAR
18/1434	150460261	130805977	117644899	92624150	77342682	56856638	0.569
18/1435	11879417	8427342	8913839	6684198	3464133	1269513	0.391
18/1437	187515102	168727358	101977592	41764259	28044750	14619420	0.184
18/1440	67447592	37057282	20706054	53927064	38411096	14514129	0.853
18/1455	82078778	92686263	118619158	299968742	170817728	88983131	1.908
18/1456	26986100	28607599	36410421	77749272	42627012	19839186	1.524
min							**0.18**
max							**1.91**
avg							**0.90**

Appendix 2.11: Odd-to-even preference ratios (OEP), Murta Formation.

Compound / Sample ID	n-C21	n-C22	n-C23	n-C24	n-C25	OEP
18/1405	1590816579	1455282516	1366750392	1174245244	853377005	1.01
18/1406	168375417	92717800	64195648	38622335	33229979	1.12
18/1411	382785249	262124958	183773236	132364659	93142063	1.00
18/1417	413576969	378146923	367114125	312348535	232082332	1.03
18/1424	1902051	749318	287119	107273	59959	1.08
18/1426	9972870	7479915	6306286	4866488	4162929	1.05
18/1429	72887629	59047658	60476602	55878379	64036502	1.09
18/1442	15387094	7164093	5603780	4106869	4729770	1.19
18/1444	204555057	217918013	234280465	205331440	154732863	1.04
18/1445	25302447	17770676	14028601	8572563	6019860	1.10
18/1446	33049015	25097646	20551040	13365107	7706110	1.07
min						**1.0**
max						**1.2**
avg						**1.1**

Appendix 2.12: Odd-to-even preference ratios (OEP), Birkhead Formation.

Compound / Sample ID	n-C21	n-C22	n-C23	n-C24	n-C25	OEP
18/1434	109465308	98143394	100134445	91123507	96321496	1.07
18/1435	8073974	7985905	8377898	7834750	8058025	1.05
18/1437	46211152	37670561	36576535	36018390	41646288	1.04
18/1440	22939616	26879958	35421245	36574122	50701868	1.13
18/1455	152040388	170117113	199056130	217348611	271679635	1.04
18/1456	40545546	45678209	51795534	55695200	68970703	1.04
min						**1.0**
max						**1.1**
avg						**1.1**

Appendix 2.13: C19 to C23 ratios, Murta Formation.

Compound / Sample ID	C19	C23	C19/C23
18/1405	2222925	507933	4.38
18/1406	214291	29249	7.33
18/1411	322250	24494	13.16
18/1417	435205	79682	5.46
18/1424	2194374	215717	10.17
18/1426	432129	82453	5.24
18/1429	1082811	479793	2.26
18/1442	116883	37507	3.12
18/1444	213127	84728	2.52
18/1445	142039	70081	5.35
18/1446	71026	21942	3.24
min			**2.26**
max			**13.16**
avg			**5.66**

Appendix 2.14: C19 to C23 ratios, Birkhead Formation.

Compound / Sample ID	C19	C23	C19/C23
18/1434	1612921	122487	13.17
18/1435	243237	49200	4.94
18/1437	1632814	202745	8.05
18/1440	356073	116853	3.05
18/1455	3874301	260512	14.87
18/1456	1027494	61113	16.81
min			**3.05**
max			**16.81**
avg			**10.15**

Appendix 2.15: C29 to C30 ratios, Murta Formation.

Compound / Sample ID	C29	C30	C29/C30
18/1405	7645356	11813009	0.65
18/1406	255679	457933	0.56
18/1411	271947	447073	0.61
18/1417	2180132	3181567	0.69
18/1424	1901166	2815629	0.68
18/1426	2591796	2507793	1.03
18/1429	40098676	62375929	0.64
18/1442	796545	1330475	0.60
18/1444	954657	1641627	0.58
18/1445	794579	1185213	0.67
18/1446	126722	204480	0.62
min			**0.56**
max			**1.03**
avg			**0.67**

Appendix 2.16: C29 to C30 ratios, Birkhead Formation.

Compound / Sample ID	C29	C30	C29/C30
18/1434	3530849	5847230	0.60
18/1435	1156028	1753434	0.66
18/1437	5492142	8318708	0.66
18/1440	3990322	7964017	0.50
18/1455	38528358	73643471	0.52
18/1456	9209192	15982365	0.58
min			**0.50**
max			**0.66**
avg			**0.59**

Appendix 2.17: Ts_Ts+Tm vs. C29Ts ratios, Murta Formation.

Compound / Sample ID	Ts	Tm	C29	C29 Ts	Ts/Ts+Tm	Ts/Ts+Tm AR	C29 Ts/C29 Ts+C29
18/1405	201479	215288	7645356	1868547	0.48	0.35	0.20
18/1406	10404	12619	255679	107355	0.45	0.31	0.30
18/1411	18824	29378	271947	87331	0.39	0.27	0.24
18/1417	15991	27183	2180132	568344	0.37	0.27	0.21
18/1424	35732	53378	1901166	407713	0.40	0.26	0.18
18/1426	13731	37336	2591796	421872	0.27	0.13	0.14
18/1429	291585	468078	40098676	9570231	0.38	0.23	0.19
18/1442	5408	15856	796545	143489	0.25	0.11	0.15
18/1444	13489	16914	954657	275167	0.44	0.27	0.22
18/1445	9516	14685	794579	205013	0.39	0.23	0.21
18/1446	3173	3830	126722	56588	0.45	0.29	0.31
min					**0.25**	**0.11**	**0.14**
max					**0.48**	**0.35**	**0.31**
avg					**0.39**	**0.25**	**0.21**

Appendix 2.18: Ts_Ts+Tm vs. C29Ts ratios, Birkhead Formation.

Compound / Sample ID	Ts	Tm	C29	C29 Ts	Ts/Ts+Tm	Ts/Ts+Tm AR	C29 Ts/C29 Ts+C29
18/1434	27007	84171	3530849	456008	0.24	0.12	0.11
18/1435	7808	17275	1156028	210992	0.31	0.16	0.15
18/1437	94140	144618	5492142	1638919	0.39	0.25	0.23
18/1440	40705	49139	3990322	1650539	0.45	0.31	0.29
18/1455	498947	1145637	38528358	7371364	0.30	0.18	0.16
18/1456	108423	226229	9209192	2096001	0.32	0.21	0.19
min					**0.24**	**0.12**	**0.11**
max					**0.45**	**0.31**	**0.29**
avg					**0.34**	**0.21**	**0.19**

Appendix 2.19: TC30 dia vs. C29Ts ratios, Murta Formation.

Compound / Sample ID	C29 Ts	C30 dia	C30 dia/C29 Ts
18/1405	1868547	742203	0.40
18/1406	107355	17116	0.16
18/1411	87331	19568	0.22
18/1417	568344	225478	0.40
18/1424	407713	110311	0.27
18/1426	421872	94714	0.22
18/1429	9570231	1495527	0.16
18/1442	143489	12903	0.09
18/1444	275167	84634	0.31
18/1445	205013	17067	0.08
18/1446	56588	6848	0.12
min			**0.08**
max			**0.40**
avg			**0.22**

Appendix 2.20: TC30 dia vs. C29Ts ratios, Birkhead Formation.

Compound / Sample ID	C29 Ts	C30 dia	C30 dia/C29 Ts
18/1434	456008	655828	1.44
18/1435	210992	111425	0.53
18/1437	1638919	571871	0.35
18/1440	1650539	506620	0.31
18/1455	7371364	5519664	0.75
18/1456	2096001	1510256	0.72
min			**0.31**
max			**1.44**
avg			**0.68**

Appendix 2.21: C30 moretane vs. C30 ratios, Murta Formation.

Compound / Sample ID	C30 moretane	C30	C30 moretane/C30
18/1405	2341526	11813009	0.20
18/1406	69124	457933	0.15
18/1411	82467	447073	0.18
18/1417	613282	3181567	0.19
18/1424	755932	2815629	0.27
18/1426	743734	2507793	0.30
18/1429	12641969	62375929	0.20
18/1442	373529	1330475	0.28
18/1444	373768	1641627	0.23
18/1445	262671	1185213	0.22
18/1446	44001	204480	0.22
min			**0.15**
max			**0.30**
avg			**0.22**

Appendix 2.22: C30 moretane vs. C30 ratios, Birkhead Formation.

Compound / Sample ID	C30 moretane	C30	C30 moretane/C30
18/1434	753923	5847230	0.13
18/1435	191051	1753434	0.11
18/1437	1403307	8318708	0.17
18/1440	1286886	7964017	0.16
18/1455	10483028	73643471	0.14
18/1456	2057426	15982365	0.13
min			**0.11**
max			**0.17**
avg			**0.14**

Appendix 2.23: C31 isomerization ratios, Murta Formation.

Compound / Sample ID	C31 20 S	C31 20 R	C31 22S/(22S+22R)
18/1405	4004268	3113392	0.56
18/1406	172196	162562	0.51
18/1411	183005	141948	0.56
18/1417	1110133	890649	0.55
18/1424	1197030	1000197	0.54
18/1426	824421	594232	0.58
18/1429	19913837	12975119	0.61
18/1442	482023	362527	0.57
18/1444	845549	558929	0.60
18/1445	511353	388086	0.57
18/1446	58012	67956	0.46
min			**0.46**
max			**0.61**
avg			**0.56**

Appendix 2.24: C31 isomerization ratios, Birkhead Formation.

Compound / Sample ID	C31 20 S	C31 20 R	C31 22S/(22S+22R)
18/1434	2554051	1760021	0.59
18/1435	629449	465110	0.58
18/1437	2877706	1947741	0.60
18/1440	2872848	2080501	0.58
18/1455	28040842	19897999	0.58
18/1456	6054366	4307402	0.58
min			**0.58**
max			**0.60**
avg			**0.59**

Appendix 2.25: C27, C28, C29 fractions, Murta Formation.

Compound / Sample ID	C27 αα 20S	C27 ββ 20R	C27 ββ 20S	C27 αα 20R	C27	fraction	%
18/1405	289539	126717.5999	268905	196967	882128.5999	0.1803	18.03
18/1406	8854	2158.760148	6175	4513	21700.76015	0.2037	20.37
18/1411	4986	7333.287586	10331	1898	24548.28759	0.2129	21.29
18/1417	94698	9410.73269	93255	44001	241364.7327	0.1903	19.03
18/1424	43355	14227.20682	58756	47203	163541.2068	0.1537	15.37
18/1426	44587	38342.27822	32736	11098	126763.2782	0.2017	20.17
18/1429	533625	118547.1352	172198	294889	1119259.135	0.1447	14.47
18/1442	1867	16179.27869	11826	17912	47784.27869	0.1839	18.39
18/1444	43233	16618.24452	31507	43718	135076.2445	0.2598	25.98
18/1445	15260	11002.84353	11870	3932	42064.84353	0.1555	15.55
18/1446	3361	2404.455504	5303	3897	14965.4555	0.2344	23.44
						min	**14.47**
						max	**25.98**
						avg	**19.28**

Appendix 2.25 (continued): C27, C28, C29 fractions, Murta Formation.

Compound / Sample ID	C28 αα 20S	C28 ββ 20R	C28 ββ 20S	C28 αα 20R	C28	fraction	%
18/1405	94990	79535	217502	165738	557765	0.113976305	11.40
18/1406	2019	3953	2342	3302	11616	0.109027671	10.90
18/1411	3166	7818	6102	4196	21282	0.184574095	18.46
18/1417	33716	41093	62420	35149	172378	0.135874743	13.59
18/1424	36297	26623	39680	47807	150407	0.141365382	14.14
18/1426	16382	30401	19834	12757	79374	0.126282675	12.63
18/1429	132533	154470	158346	339806	785155	0.101478448	10.15
18/1442	2567	9962	15394	15167	43090	0.165832004	16.58
18/1444	7494	15100	16577	15229	54400	0.104636665	10.46
18/1445	4421	14144	12621	6893	38079	0.14074983	14.07
18/1446	1882	1923	2472	2663	8940	0.140038788	14.00
						min	**10.46**
						max	**18.46**
						avg	**13.31**

Appendix 2.25 (continued): C27, C28, C29 fractions, Murta Formation.

Compound / Sample ID	C29 αα 20S	C29 ββ 20R	C29 ββ 20S	C29 αα 20R	C29	fraction	%	total
18/1405	682785	992065	507834	1271115	3453799	0.705765417	70.58	**4893692.600**
18/1406	12213	14067	8920	38025	73225	0.68728919	68.73	**106541.760**
18/1411	16145	13682	8811	30835	69473	0.602524017	60.25	**115303.288**
18/1417	189072	239270	139601	286968	854911	0.673872608	67.39	**1268653.733**
18/1424	141247	258989	87335	262440	750011	0.704924583	70.49	**1063959.207**
18/1426	84030	106175	61632	170568	422405	0.672039121	67.20	**628542.278**
18/1429	1398600	1026601	444465	2963080	5832746	0.753861352	75.39	**7737160.135**
18/1442	25915	37142	8102	97808	168967	0.650270045	65.03	**259841.279**
18/1444	51378	77426	37428	164186	330418	0.635548486	63.55	**519894.245**
18/1445	23377	47728	21999	97296	190400	0.703767632	70.38	**270543.844**
18/1446	7739	7774	7075	17346	39934	0.625537917	62.55	**63839.456**
						min	**60.25**	
						max	**75.39**	
						avg	**67.41**	

Appendix 2.26: C27, C28, C29 fractions, Birkhead Formation.

Compound / Sample ID	C27 αα 20S	C27 ββ 20R	C27 ββ 20S	C27 αα 20R	C27	fraction	%
18/1434	166454	43129.87821	179692	33427	422702.8782	0.221673223	22.17
18/1435	25665	9114.11923	13840	6885	55504.11923	0.139937128	13.99
18/1437	162402	31854.65906	92387	36522	323165.6591	0.150228719	15.02
18/1440	125500	31271.39172	77739	7436	241946.3917	0.124664166	12.47
18/1455	549864	125900.3002	561727	134504	1371995.3	0.115103267	11.51
18/1456	99844	22454.94812	88494	12203	222995.9481	0.097016937	9.70
						min	**9.70**
						max	**22.17**
						avg	**16.80**

Appendix 2.26 (continued): C27, C28, C29 fractions, Birkhead Formation.

Compound / Sample ID	C28 αα 20S	C28 ββ 20R	C28 ββ 20S	C28 αα 20R	C28	fraction	%
18/1434	99144	25519	71535	37208	233406	0.122402432	12.24
18/1435	8678	21069	16434	7377	53558	0.135030567	13.50
18/1437	61348	55359	101264	44687	262658	0.122100767	12.21
18/1440	22339	91069	61889	28114	203411	0.1048086	10.48
18/1455	446330	404860	484579	527334	1863103	0.156304648	15.63
18/1456	62300	79099	88625	47723	277747	0.120837009	12.08
						min	**10.48**
						max	**15.63**
						avg	**13.21**

Appendix 2.26 (continued): C27, C28, C29 fractions, Birkhead Formation.

Compound / Sample ID	C29 αα 20S	C29 ββ 20R	C29 ββ 20S	C29 αα 20R	C29	fraction	%	total
18/1434	289407	344420	264805	352133	1250765	0.655924345	65.59	**1906873.878**
18/1435	62529	72639	61821	90585	287574	0.725032306	72.50	**396636.119**
18/1437	388741	408309	287754	480530	1565334	0.727670514	72.77	**2151157.659**
18/1440	366169	366738	265013	497508	1495428	0.770527234	77.05	**1940785.392**
18/1455	2102196	2178635	1612684	2791077	8684592	0.728592084	72.86	**11919690.300**
18/1456	447031	417463	361275	572014	1797783	0.782146054	78.21	**2298525.948**
						min	**65.59**	
						max	**78.21**	
						avg	**70.46**	

Appendix 2.27: C29 isomerization, Murta Formation.

Compound / Sample ID	C29 αα 20S	C29 ββ 20R	C29 ββ 20S	C29 αα 20R	ββ/αα+ββ	20 S/20 S+20 R
18/1405	682785	992065	507834	1271115	0.43	0.34
18/1406	12213	14067	8920	38025	0.31	0.29
18/1411	16145	13682	8811	30835	0.32	0.36
18/1417	189072	239270	139601	286968	0.44	0.38
18/1424	141247	258989	87335	262440	0.46	0.30
18/1426	84030	106175	61632	170568	0.40	0.34
18/1429	1398600	1026601	444465	2963080	0.25	0.32
18/1442	25915	37142	8102	97808	0.27	0.20
18/1444	51378	77426	37428	164186	0.35	0.27
18/1445	23377	47728	21999	97296	0.37	0.24
18/1446	7739	7774	7075	17346	0.37	0.37
				min	**0.25**	**0.20**
				max	**0.46**	**0.38**
				avg	**0.36**	**0.31**

Appendix 2.28: C29 isomerization, Birkhead Formation.

Compound / Sample ID	C29 αα 20S	C29 ββ 20R	C29 ββ 20S	C29 αα 20R	ββ/αα+ββ	20 S/20 S+20 R
18/1434	289407	344420	264805	352133	0.49	0.44
18/1435	62529	72639	61821	90585	0.47	0.43
18/1437	388741	408309	287754	480530	0.44	0.43
18/1440	366169	366738	265013	497508	0.42	0.42
18/1455	2102196	2178635	1612684	2791077	0.44	0.43
18/1456	447031	417463	361275	572014	0.43	0.45
				min	**0.42**	**0.42**
				max	**0.49**	**0.45**
				avg	**0.45**	**0.43**

Appendix 2.29: Dibenzothiophene (DBT) vs. Phenantrene (Phen), Murta Formation.

Compound / Sample ID	DBT	Phenan	Pr	Ph	DBT/ Phenan	Pr/Ph
18/1405	1383917	21346045	415112283	162867999	0.06	2.55
18/1406	11889407	49352369	123208685	39749630	0.24	3.10
18/1411	39435049	100217604	213597212	92060174	0.39	2.32
18/1417	8903728	27643973	129525245	51863325	0.32	2.50
18/1424	37125193	68390350	3490545	1015683	0.54	3.44
18/1426	25935000	74921533	54227794	8041899	0.35	6.74
18/1429	17217710	49897967	57505584	15871556	0.35	3.62
18/1442	30839798	112894181	10409489	3810631	0.27	2.73
18/1444	5888435	26319704	21477805	11135215	0.22	1.93
18/1445	15466332	59272122	22171610	6810267	0.26	3.26
18/1446	1459471	7852194	27853321	9014060	0.19	3.09
min					**0.06**	**1.93**
max					**0.54**	**6.74**
avg					**0.29**	**3.21**

Appendix 2.30: Dibenzothiophene (DBT) vs. Phenantrene (Phen), Birkhead Formation.

Compound / Sample ID	DBT	Phenan	Pr	Ph	DBT/ Phenan	Pr/Ph
18/1434	7623390	19905232	109417400	21005223	0.38	5.21
18/1435	34928065	112006963	9324920	2050669	0.31	4.55
18/1437	28750234	56595961	212411188	31827579	0.51	6.67
18/1440	15919716	33232654	51986549	5242331	0.48	9.92
18/1455	196429318	303282731	153214044	25461932	0.65	6.02
18/1456	148193900	233980549	48010966	7542760	0.63	6.37
min					**0.31**	**4.55**
max					**0.65**	**9.92**
avg					**0.49**	**6.45**

Appendix 2.31: Methylphenantrene Index (MPI), Murta Formation.

Compound / Sample ID	Phenan	3-MP	2-MP	9-MP	1-MP	MPI	Rc Radke
18/1405	21346045	4189084	6826460	7420879	12421348.00	0.40	0.64
18/1406	49352369	12345270	15621535	21239084	27861428.00	0.43	0.66
18/1411	100217604	23105848	29174394	37451279	74833201.00	0.37	0.62
18/1417	27643973	7316453	9479657	12241303	25290551.00	0.39	0.63
18/1424	68390350	14077291	17203928	21445569	42995715.00	0.35	0.61
18/1426	74921533	16240060	20305265	26708499	53521106.00	0.35	0.61
18/1429	49897967	9850766	12369589	16338726	32570096.00	0.34	0.60
18/1442	112894181	14860133	20005847	29101477	44422039.00	0.28	0.57
18/1444	26319704	3829010	5478809	7460078	12267575.00	0.30	0.58
18/1445	59272122	8799847	12353478	17143088	26225668.00	0.31	0.59
18/1446	7852194	1052397	1605648	2157939	3476341.00	0.30	0.58
min						**0.28**	**0.57**
max						**0.43**	**0.66**
avg						**0.35**	**0.61**

Appendix 2.32: Methylphenantrene Index (MPI), Birkhead Formation.

Compound / Sample ID	Phenan	3-MP	2-MP	9-MP	1-MP	MPI	Rc Radke
18/1434	19905232	3056748	4803032	5232839	10969747	0.33	0.60
18/1435	112006963	21183425	31493966	37431695	73577848	0.35	0.61
18/1437	56595961	7745114	12921670	16459070	142775805	0.14	0.49
18/1440	33232654	4203189	6999953	9303514	74496196	0.14	0.49
18/1455	303282731	60264802	94967700	108204453	566736858	0.24	0.54
18/1456	233980549	46453321	74207090	84046845	443325290	0.24	0.54
min						**0.14**	**0.49**
max						**0.35**	**0.61**
avg						**0.24**	**0.54**

Appendix 2.31: Methylnaphtalene ratios, Murta Formation.

Compound / Sample ID	2MN	1MN	2MN/1MN
18/1405	10529285	5654452	1.86
18/1406	21755368	11544421	1.88
18/1411	71023078	41553693	1.71
18/1417	12468035	7580489	1.64
18/1424	70602205	40398430	1.75
18/1426	176474507	88729288	1.99
18/1429	108923897	56865126	1.92
18/1442	266977268	129958494	2.05
18/1444	28859425	14878835	1.94
18/1445	77361933	39269714	1.97
18/1446	4779965	2677060	1.79
min			**1.64**
max			**2.05**
avg			**1.86**

Appendix 2.32: Methylnaphtalene ratios, Birkhead Formation.

Compound / Sample ID	2MN	1MN	2MN/1MN
18/1434	37871294	23182006	1.63
18/1435	113464143	68049748	1.67
18/1437	59249771	38697178	1.53
18/1440	43268362	27040446	1.60
18/1455	346597900	221636110	1.56
18/1456	260554494	164914902	1.58
min			**1.53**
max			**1.67**
avg			**1.60**

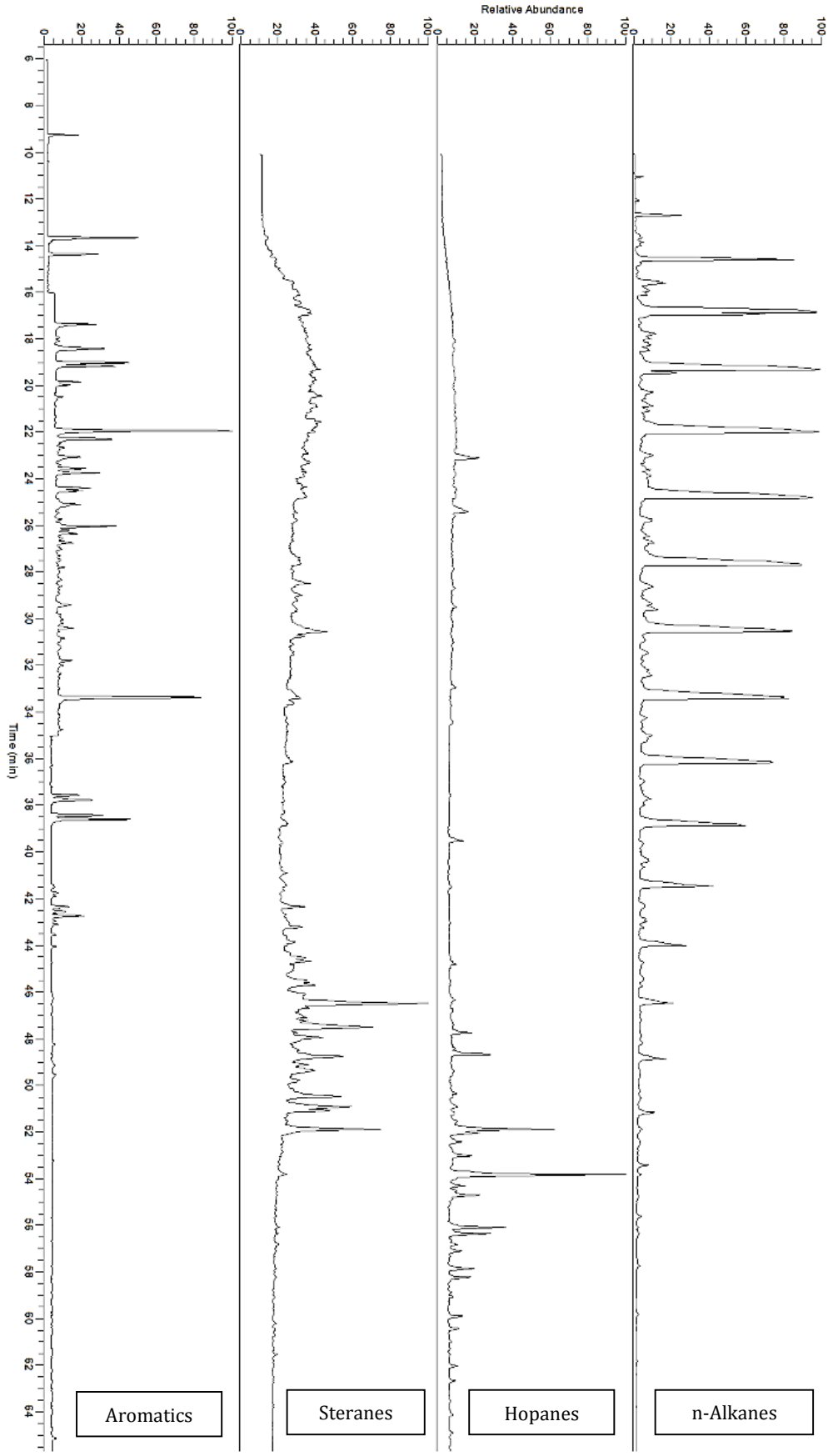

Appendix 2.33: Chromatograms of sample 18/1405.

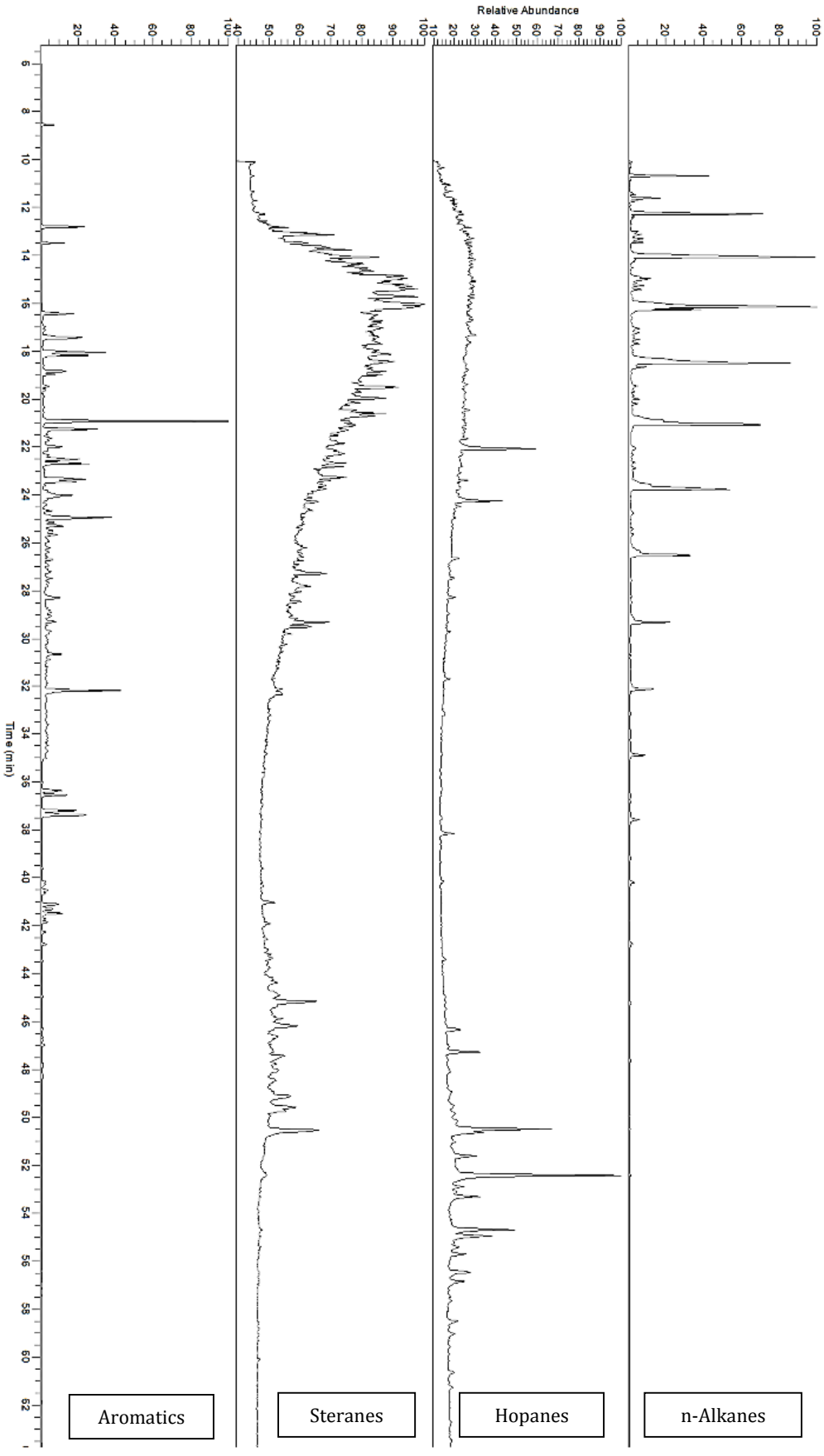

Appendix 2.34: Chromatograms of sample 18/1406.

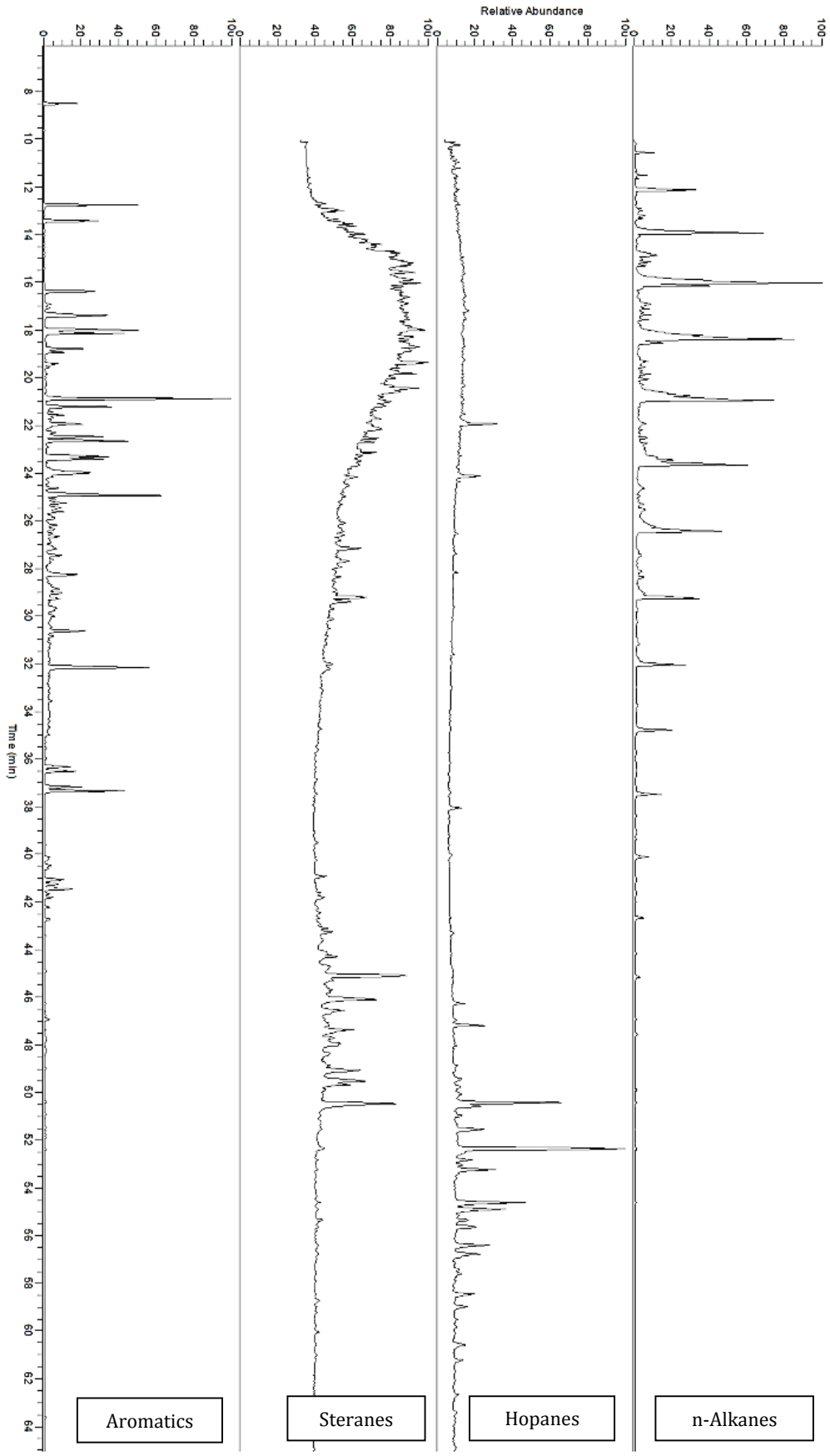

Appendix 2.35: Chromatograms of sample 18/1411.

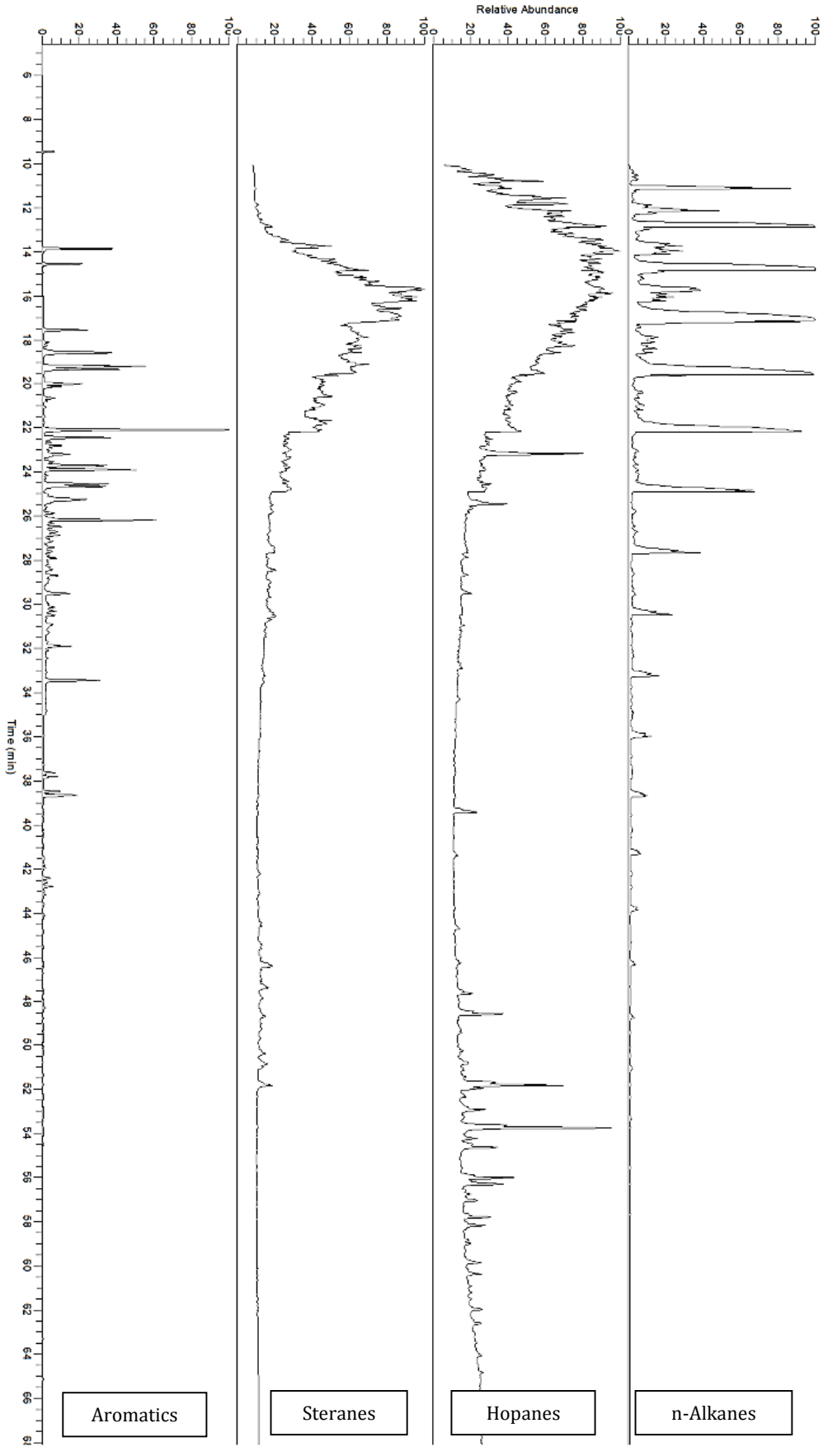

Appendix 2.36: Chromatograms of sample 18/1424.

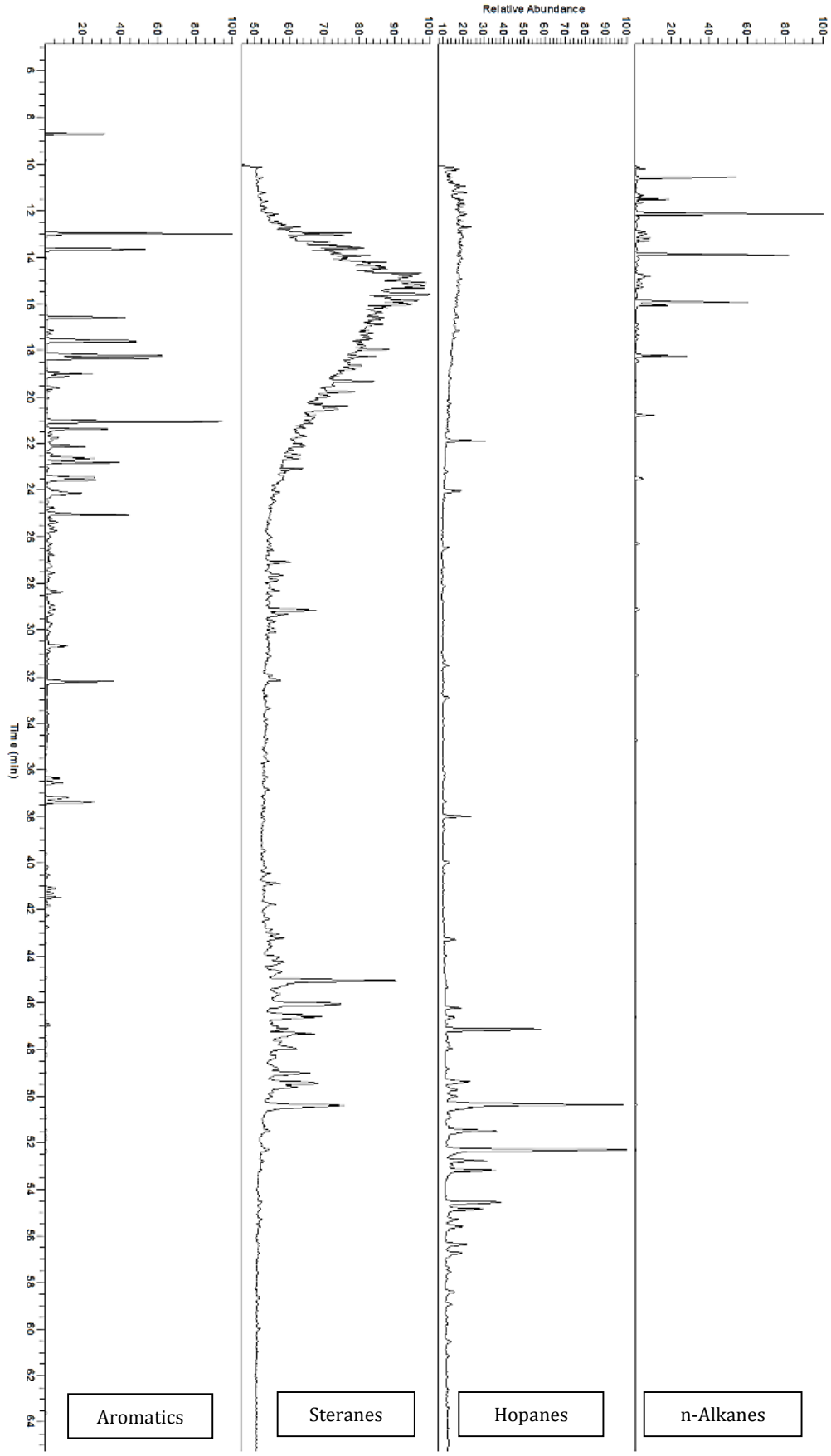

Appendix 2.37: Chromatograms of sample 18/1426.

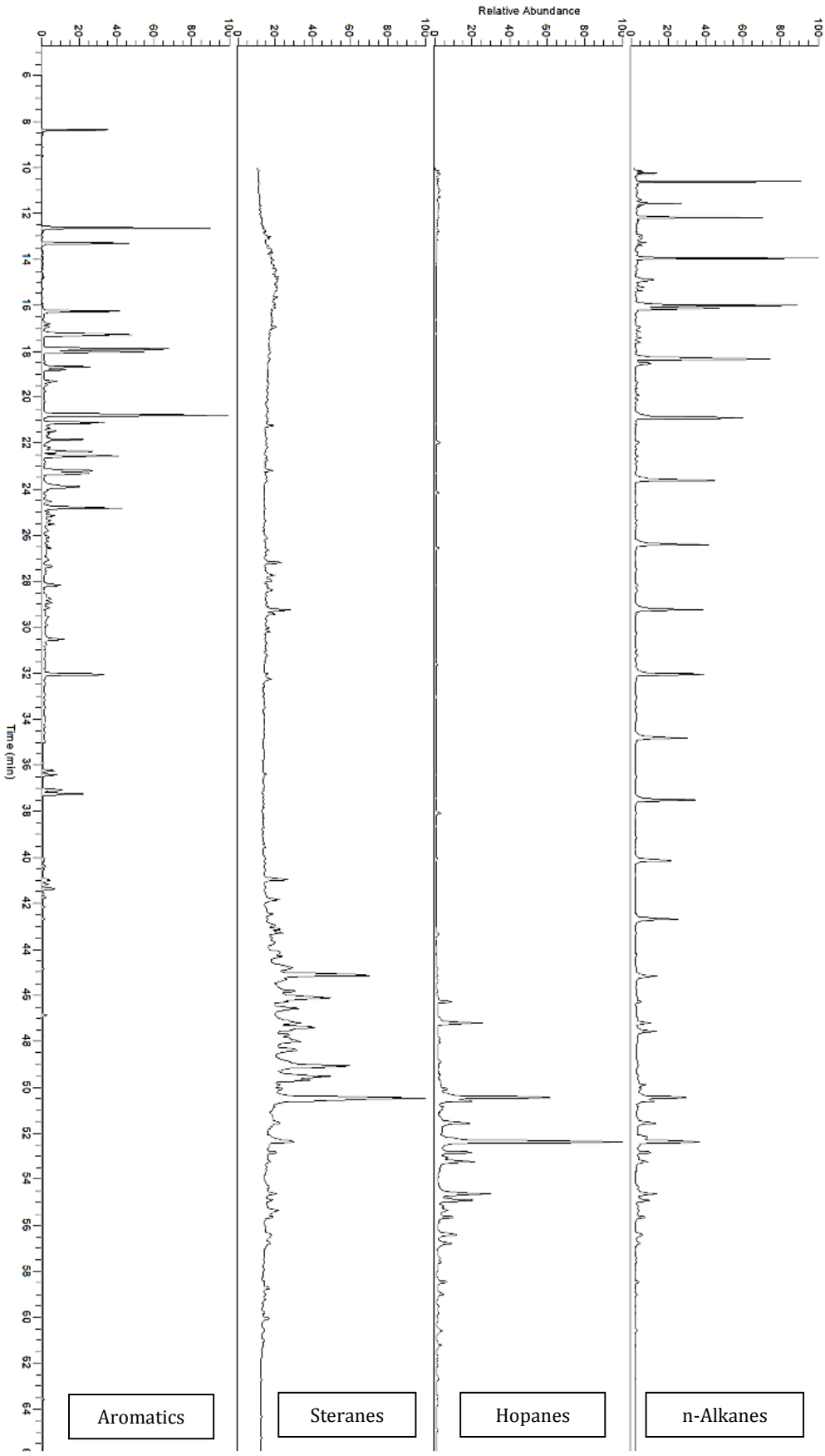

Appendix 2.38: Chromatograms of sample 18/1429.

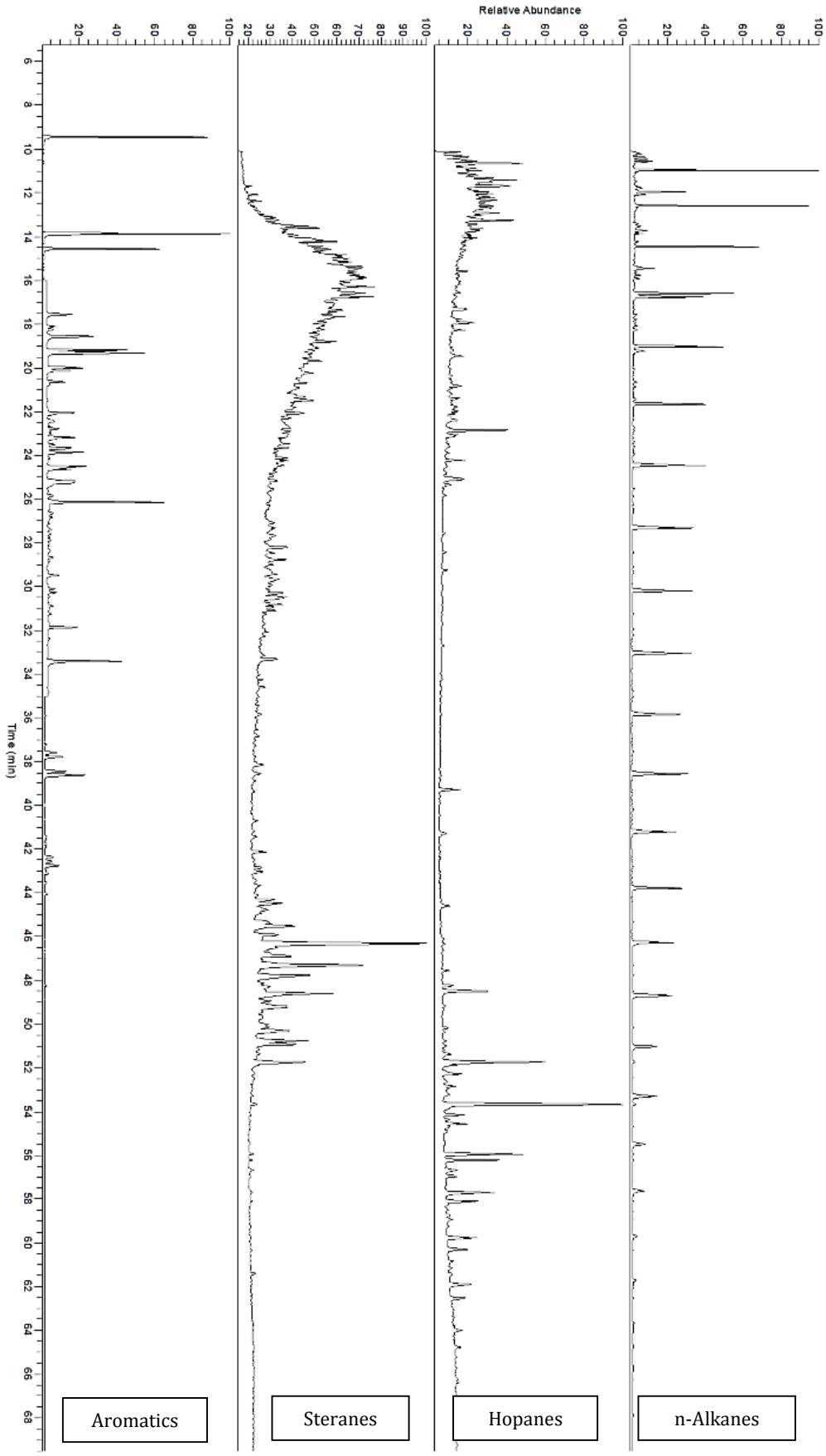

Appendix 2.39: Chromatograms of sample 18/1434.

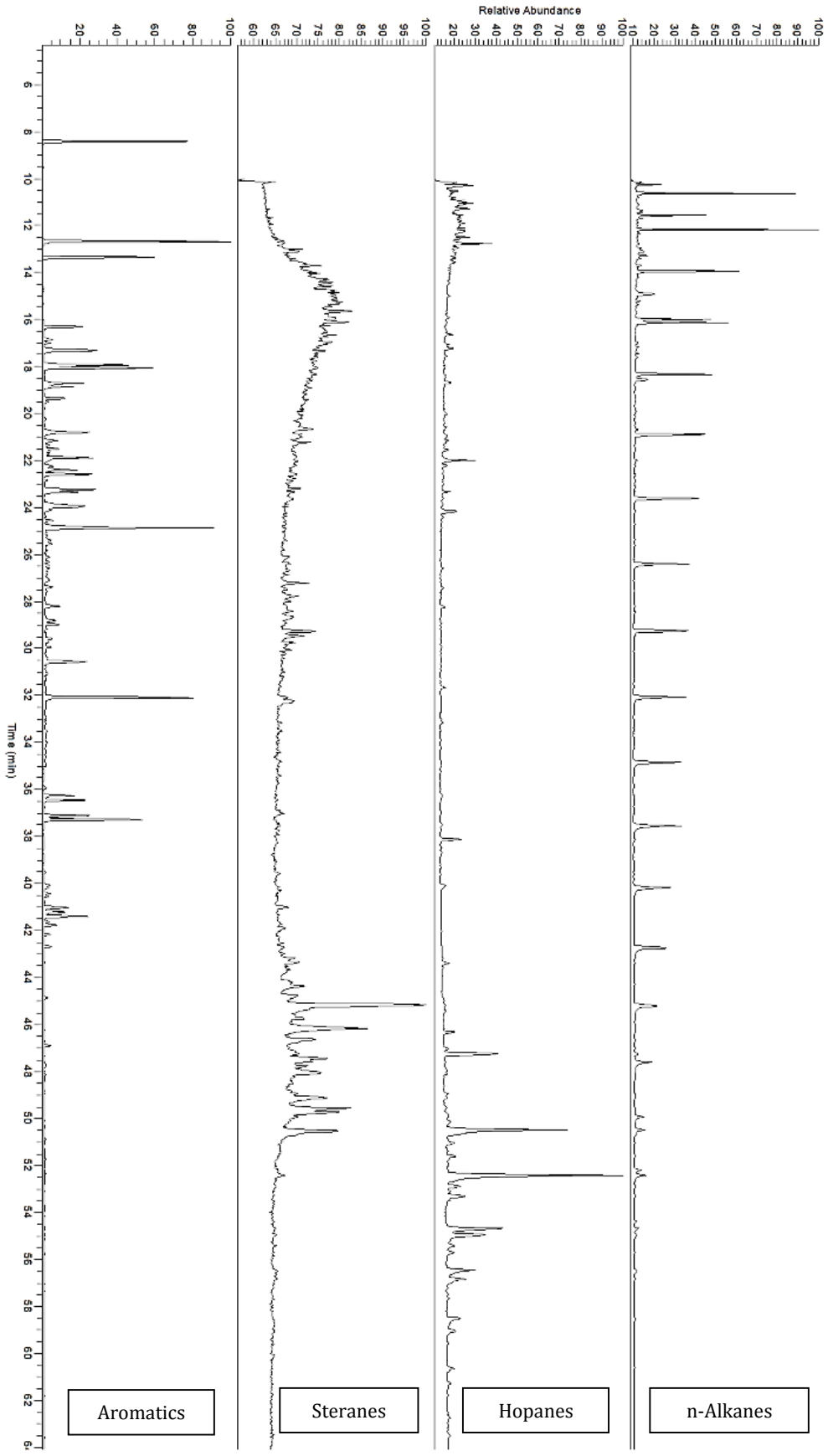

Appendix 2.40: Chromatograms of sample 18/1435.

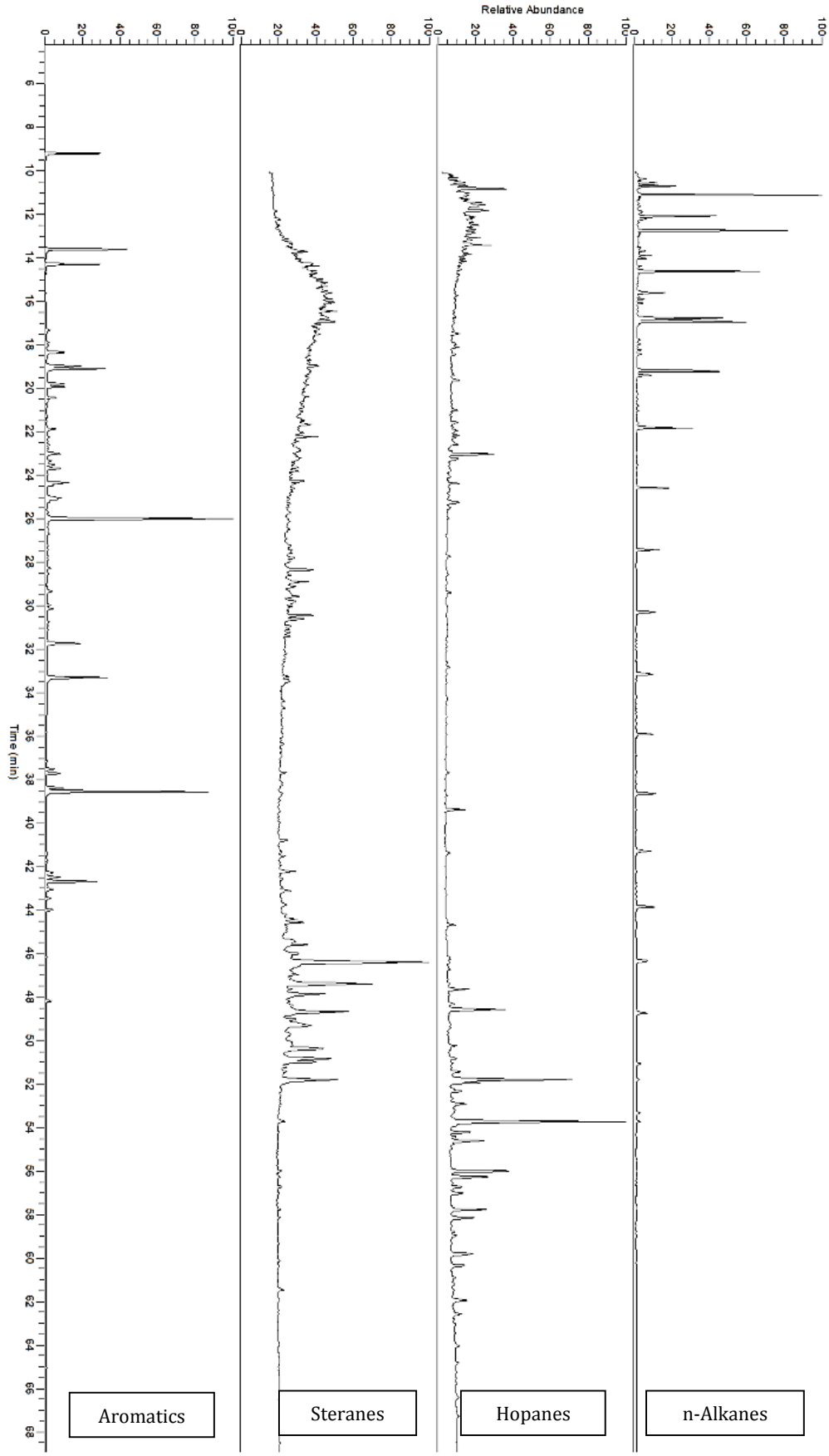

Appendix 2.41: Chromatograms of sample 18/1437.

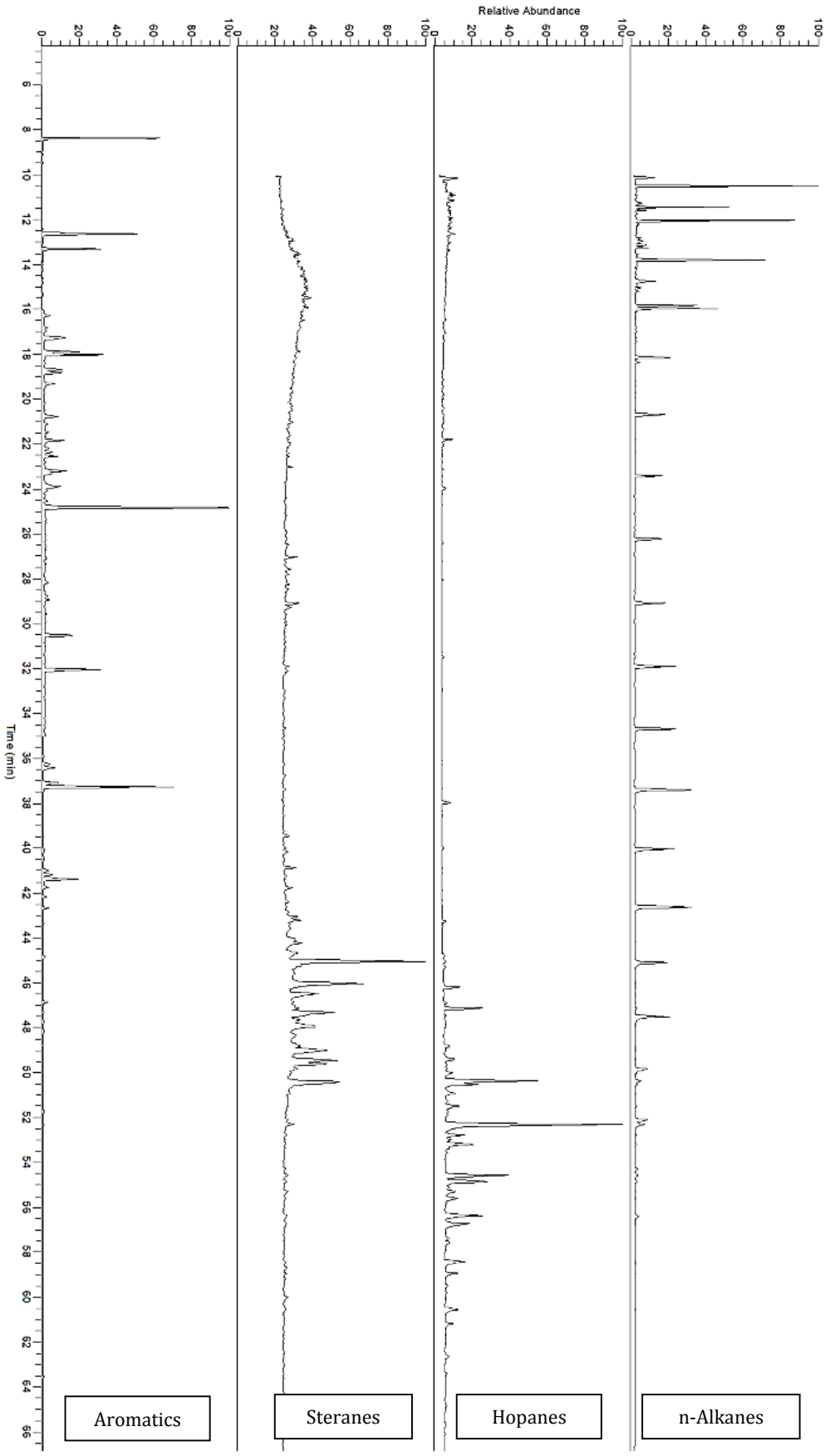

Appendix 2.42: Chromatograms of sample 18/1440.

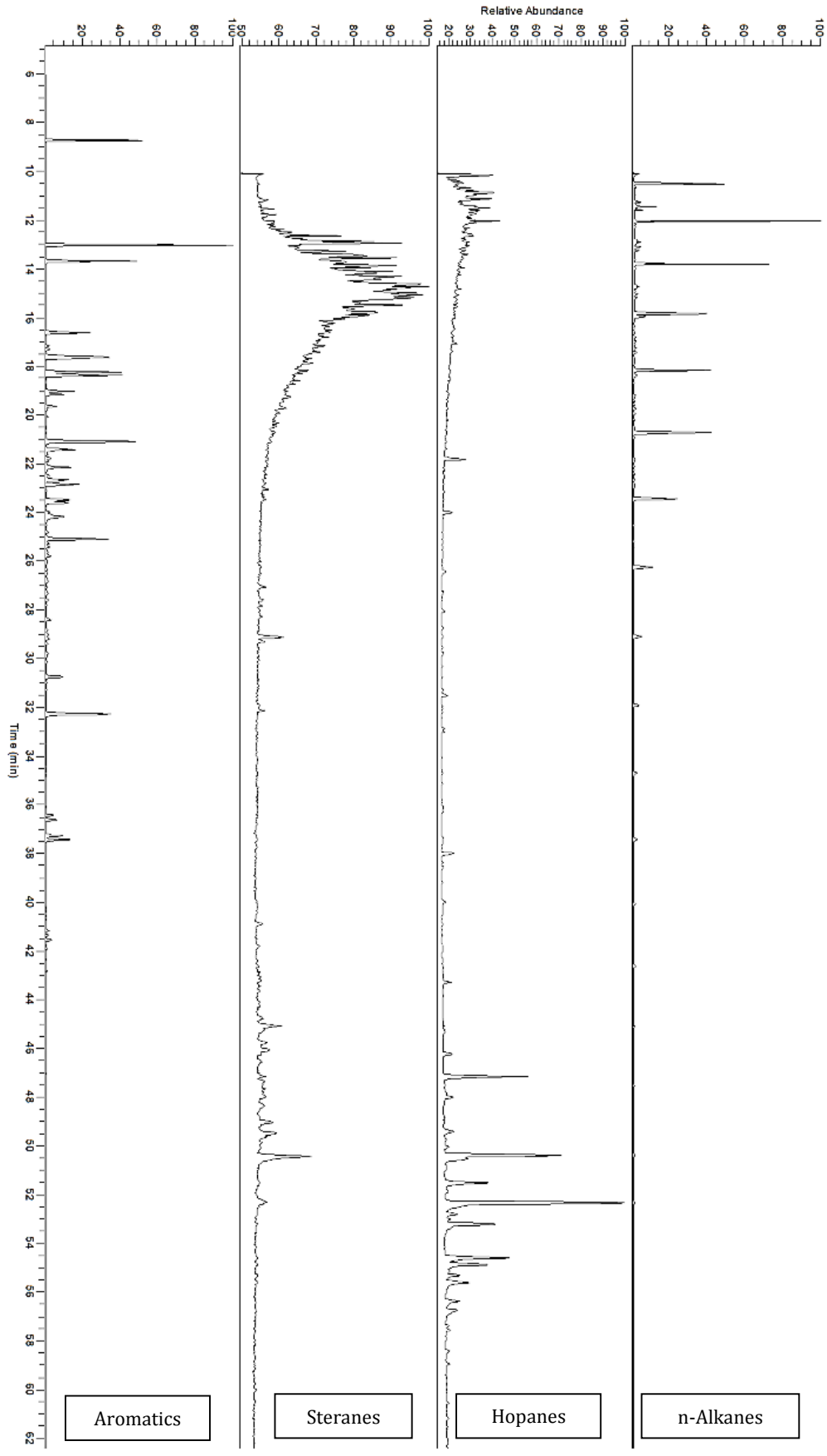

Appendix 2.43: Chromatograms of sample 18/1442.

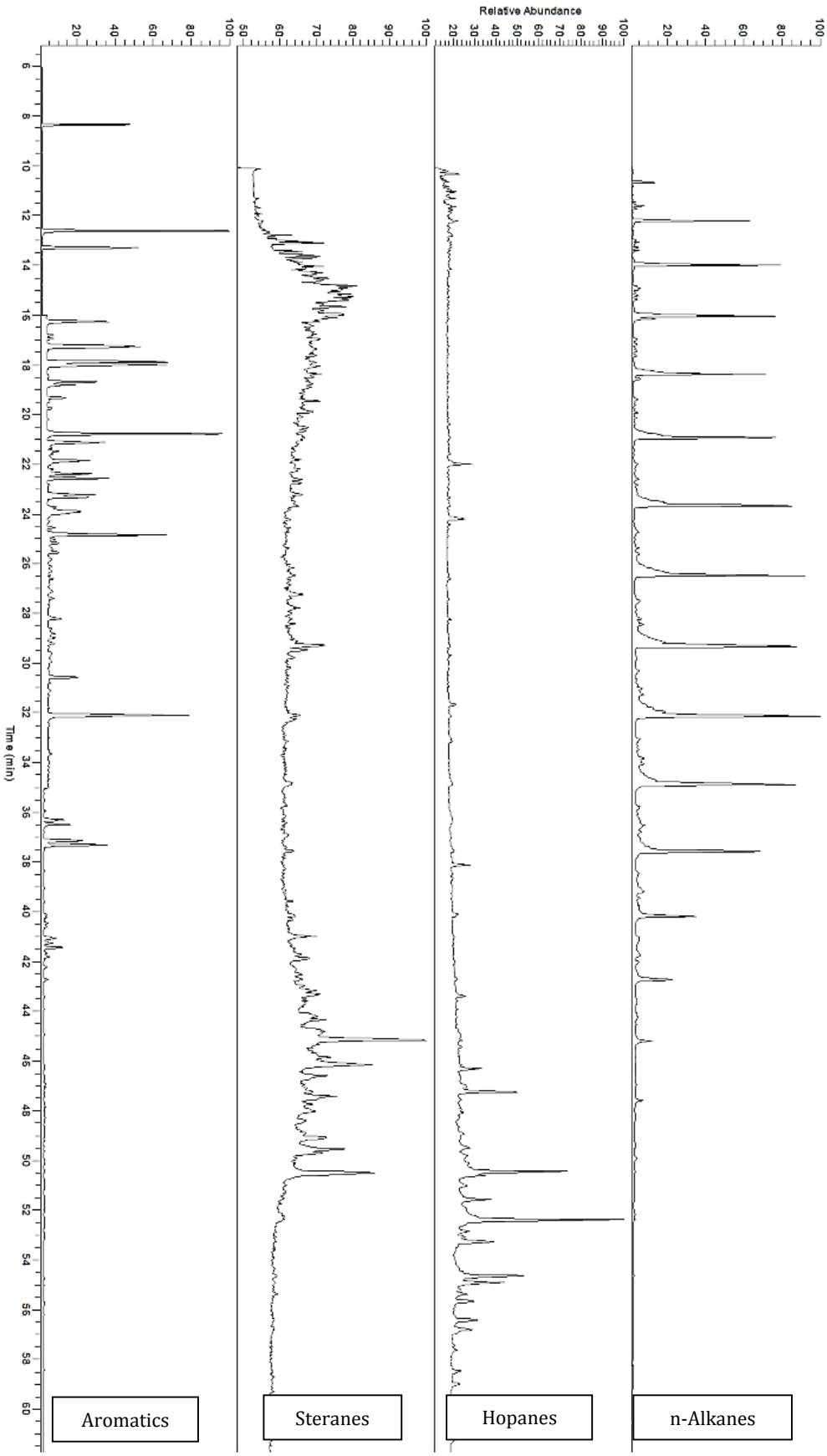

Appendix 2.44: Chromatograms of sample 18/1444.

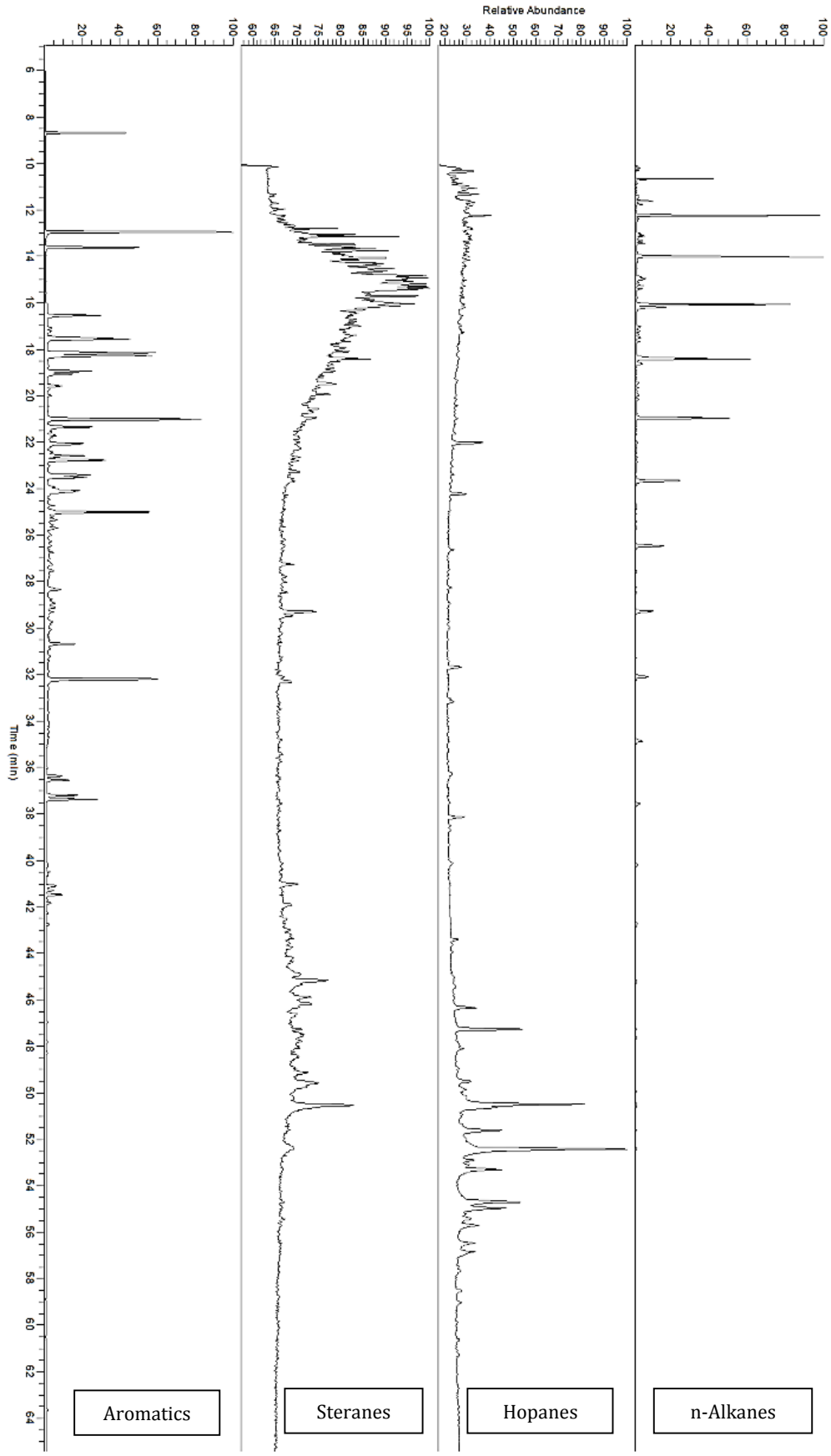

Appendix 2.45: Chromatograms of sample 18/1445.

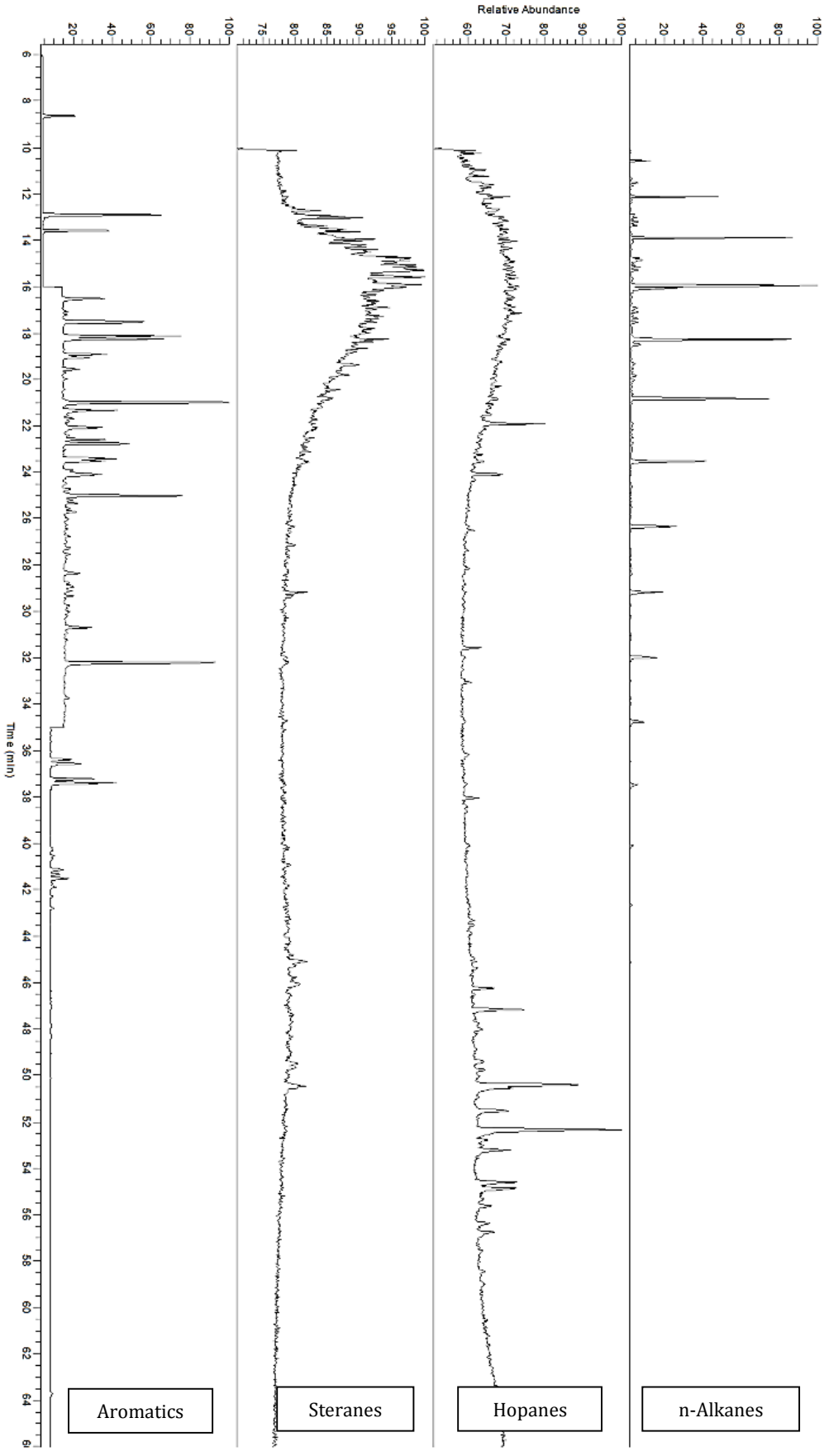

Appendix 2.46: Chromatograms of sample 18/1446.

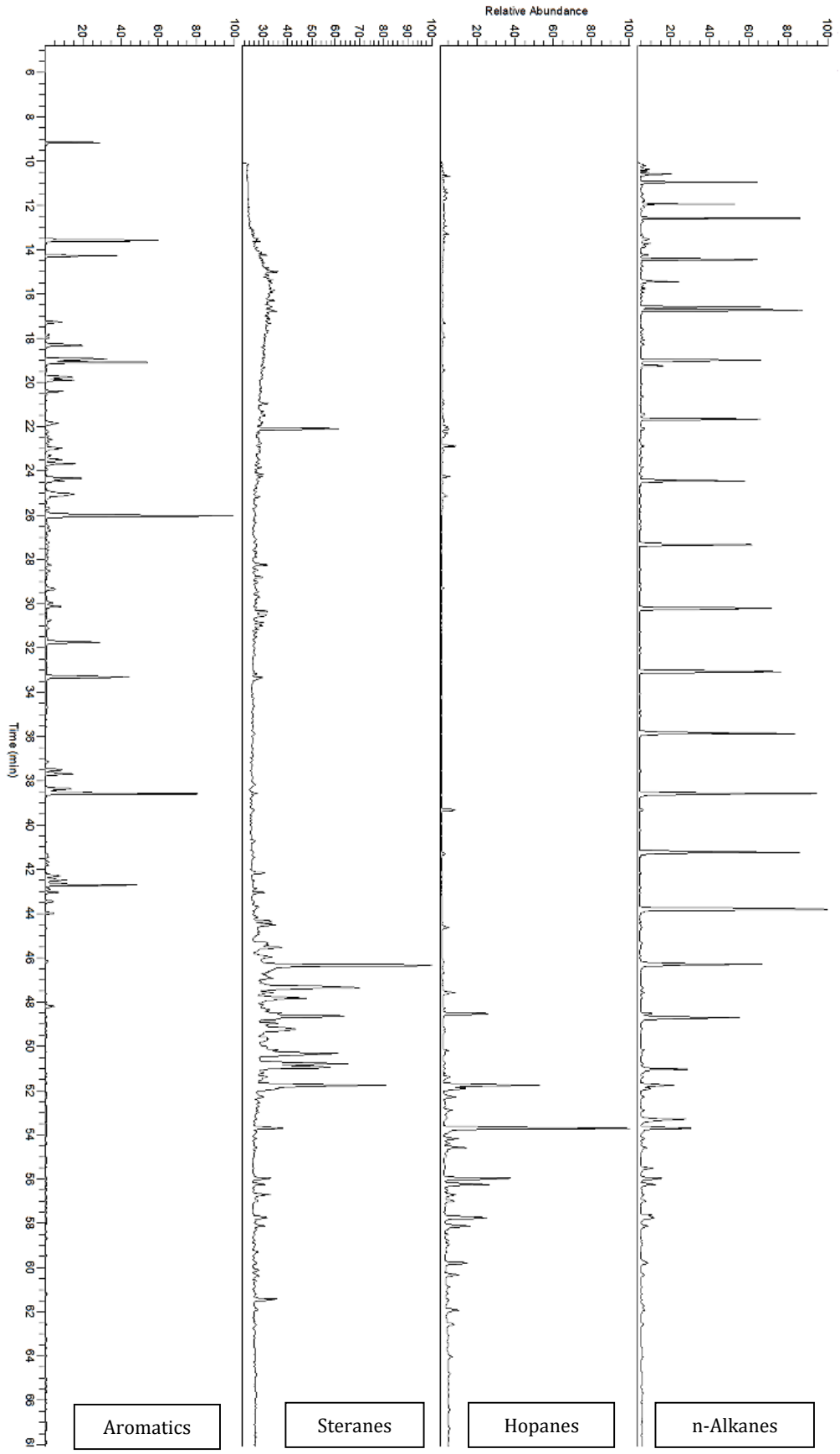

Appendix 2.47: Chromatograms of sample 18/1456.

APPENDIX 3 (CHAPTER 5)

Appendix 3.1: Horner-correction of bottomhole temperatures (BHT) for well calibration.

Well name	MD [m]	Temperature [°C]	Lag time [h]	Circulation time [h]	Corrected temperature [°C]
Alkina-1	2,681	121.11	7.5	1	142.00
Alkina-1	2,681	127.22	10.5		
Alkina-1	2,681	132.78	17.5		
Beanbush-1	3,699	133.33	11	1	155.00
Beanbush-1	3,699	143.33	21.5		
Beanbush-1	3,699	146.11	26.5		
Burley-2	3,706	186.66	4.33	1	251.00
Burley-2	3,706	190.55	4.75		
Burley-2	3,706	197.77	5.33		
Dullingari-1 (2)	2,700	125.55	4	1	143.00
Dullingari-1 (2)	2,700	135.55	10		
Marengo-1	3,008	137.78	7	1	164.00
Marengo-1	3,008	153.33	17.5		
Moothandella-1	2,730	115.56	7.5	1	142.00
Moothandella-1	2,730	127.78	12.5		
Moothandella-1	2,730	130.00	16.5		
Moothandella-1	2,730	132.22	20.5		
Moothandella-1	2,730	132.78	24		
Paning-1	3,181	117.22	6	1	139.00
Paning-1	3,181	125.55	10.5		
Paning-1	3,181	130.55	15		
Paning-1	3,181	132.77	21.5		
Springfield-1	2,789	115.55	5.75	1	140.00
Springfield-1	2,789	127.22	10.25		
Springfield-1	2,789	131.11	16		
Springfield-1	2,789	132.22	19		
Warnie East-1	2,612	125.56	6.25	1	154.00
Warnie East-1	2,612	131.67	8.75		
Warnie East-1	2,612	143.33	17.5		
Jack Lake-1	3,144	117.77	5	1	137.00
Jack Lake-1	3,144	125.00	9		
Jack Lake-1	3,144	130.00	14		
Kirby-1	3,866	174.44	8	1	192.00
Kirby-1	3,866	178.33	10		
Kirby-1	3,866	182.77	16		
Daralingie-1 (3)	2,296	107.22	4.5	1	121.00
Daralingie-1 (3)	2,296	115.00	11		
Daralingie-1 (3)	2,296	116.66	14		

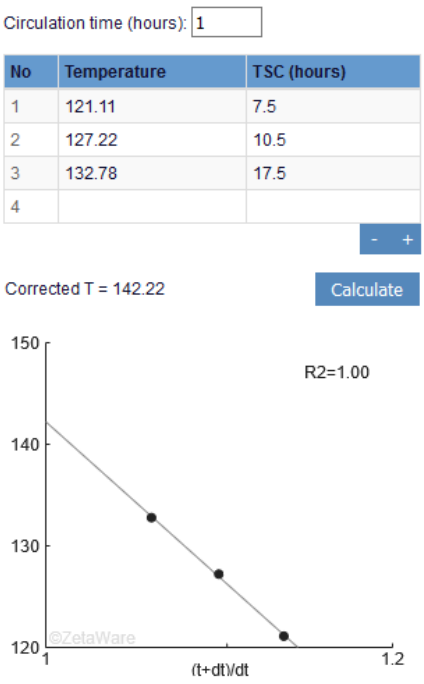

Appendix 3.2: Horner-correction of bottomhole temperatures (BHT) at well Alkina-1 with Zetaware (http://www.zetaware.com/utilities/bht/horner.html).

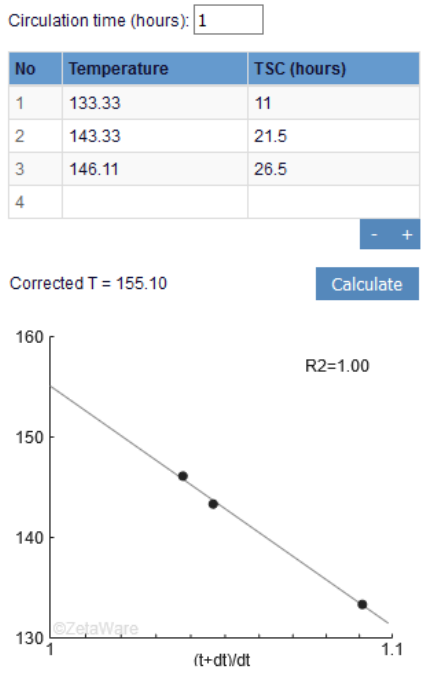

Appendix 3.3: Horner-correction of bottomhole temperatures (BHT) at well Beanbush-1 with Zetaware (http://www.zetaware.com/utilities/bht/horner.html).

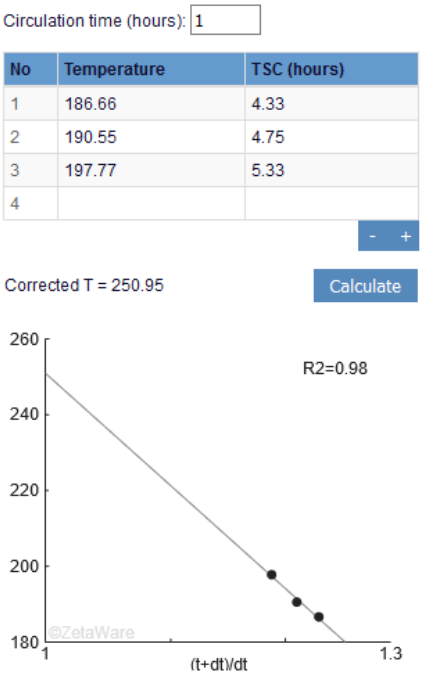

Appendix 3.4: Horner-correction of bottomhole temperatures (BHT) at well Burley-2 with Zetaware (http://www.zetaware.com/utilities/bht/horner.html).

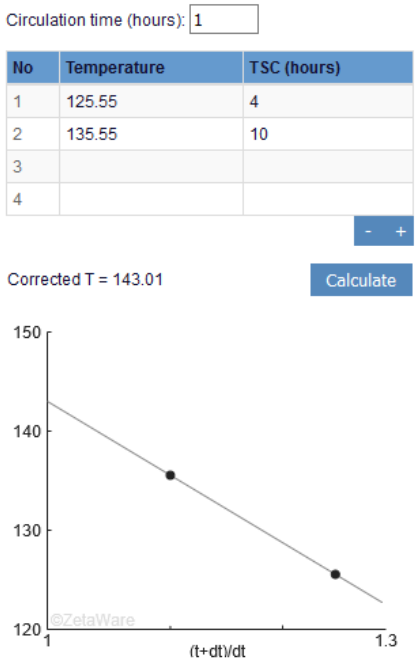

Appendix 3.5: Horner-correction of bottomhole temperatures (BHT) at well Dullingari-1 (values taken from well Dullingari-2) with Zetaware (http://www.zetaware.com/utilities/bht/horner.html).

Circulation time (hours): 1

No	Temperature	TSC (hours)
1	137.78	7
2	153.33	17.5
3		
4		

- +

Corrected T = 164.41 Calculate

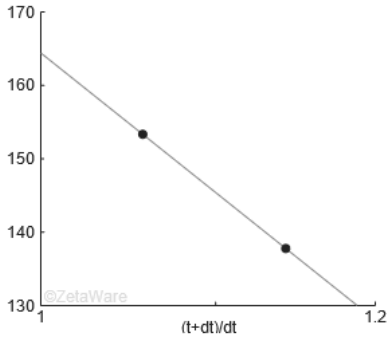

Appendix 3.6: Horner-correction of bottomhole temperatures (BHT) at well Marengo-1 with Zetaware (http://www.zetaware.com/utilities/bht/horner.html).

Circulation time (hours): 1

No	Temperature	TSC (hours)
1	115.56	7.5
2	127.78	12.5
3	130	16.5
4	132.22	20.5
5	132.78	24

- +

Corrected T = 142.11 Calculate

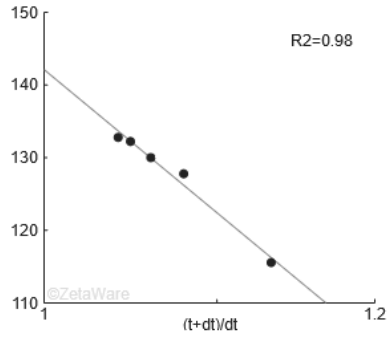

Appendix 3.7: Horner-correction of bottomhole temperatures (BHT) at well Moothandella-1 with Zetaware (http://www.zetaware.com/utilities/bht/horner.html).

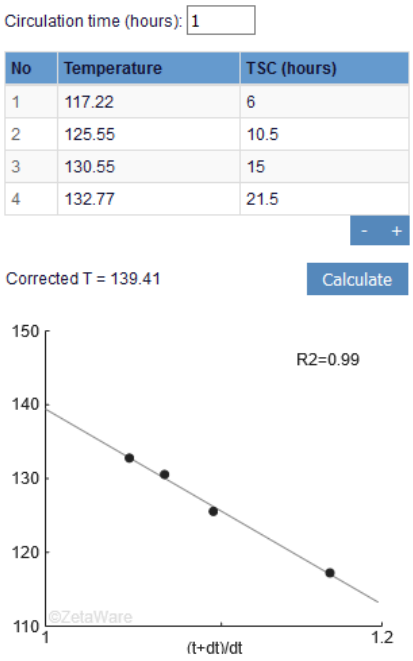

Appendix 3.8: Horner-correction of bottomhole temperatures (BHT) at well Paning-1 with Zetaware (http://www.zetaware.com/utilities/bht/horner.html).

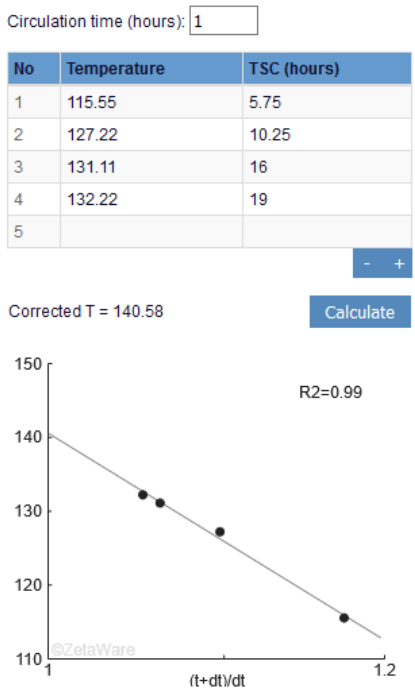

Appendix 3.9: Horner-correction of bottomhole temperatures (BHT) at well Springfield-1 with Zetaware (http://www.zetaware.com/utilities/bht/horner.html).

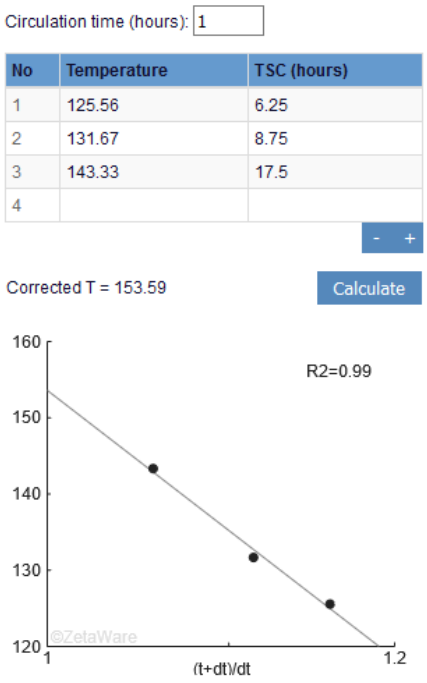

Appendix 3.10: Horner-correction of bottomhole temperatures (BHT) at well Warnie East-1 with Zetaware (http://www.zetaware.com/utilities/bht/horner.html).

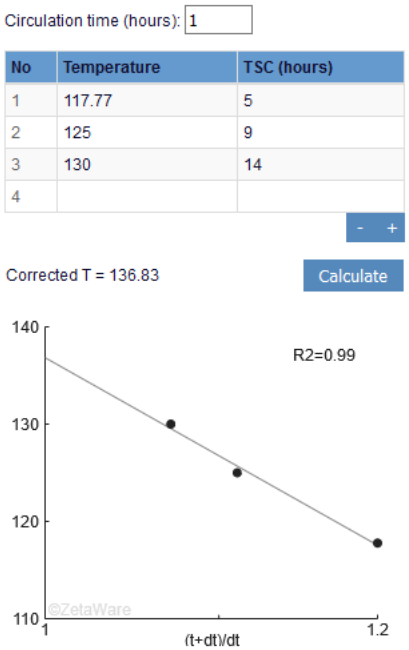

Appendix 3.11: Horner-correction of bottomhole temperatures (BHT) at well Jack Lake-1 with Zetaware (http://www.zetaware.com/utilities/bht/horner.html).

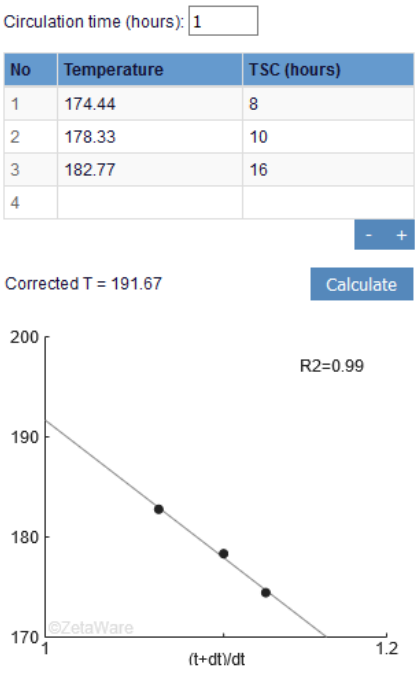

Appendix 3.12: Horner-correction of bottomhole temperatures (BHT) at well Kirby-1 with Zetaware (http://www.zetaware.com/utilities/bht/horner.html).

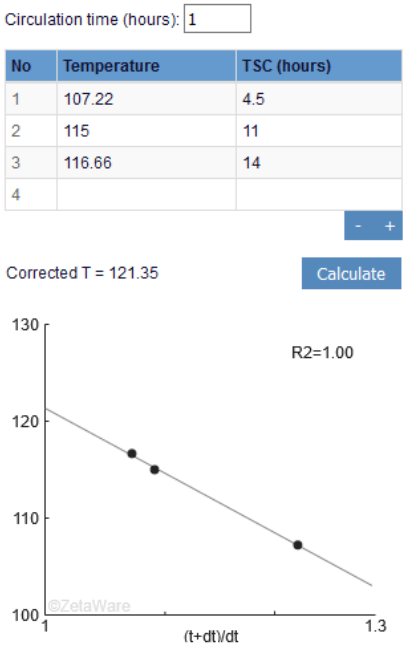

Appendix 3.13: Horner-correction of bottomhole temperatures (BHT) at well Daralingie-1 (values taken from well Daralingie-3) with Zetaware (http://www.zetaware.com/utilities/bht/horner.html).

Appendix 3.14: Applied layer splitting for the Cooper/Eromanga 3D modell. For the first three, the time span was modified and the percentage was calculated (vice versa for the other two).

Layer name	avg thickness	max thickness	Period [Ma]	%
Cenozoic/Quaternary				
Quaternary	10.04	69.6	**12**	19.35
Namba Fm	25.1	174.01	**30**	48.39
Eyre Fm	16.74	116.01	**20**	32.26
total	51.88	359.62	62	100
Toolebuc Fm				
Toolebuc Fm	75.42	136.42	**4**	25
Wallumbilla Fm	226.26	409.25	**12**	75
total	301.68	545.66	16	100
Murta Fm				
Murta Fm	24.01	36.83	**2**	20
Namur Sst	96.05	147.32	**8**	80
total	120.06	184.15	10	100
Nappamerri Gp				
Tinchoo Fm	36.97	255.54	6	**40**
Arrabury Fm	55.46	383.31	9	**60**
total	92.44	638.85	15	100
Glacial sediments				
Tirrawarra Fm	2.38	151.13	1.6	**20**
Merrimelia Fm	9.53	604.52	6.4	**80**
total	11.91	755.65	8	100

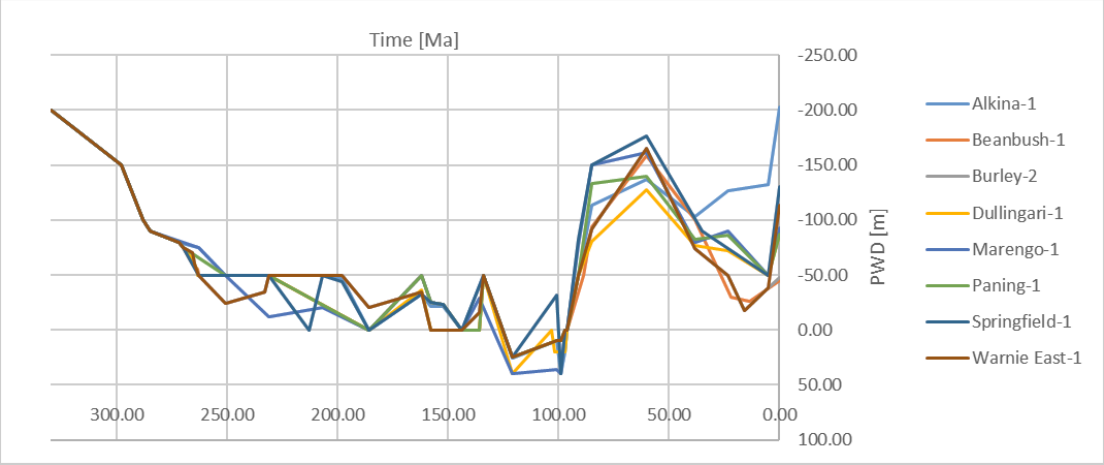

Appendix 3.15: Paleo water depth (PWD) trends of eight calibration wells (modified after Deighton & Hill, 1998, Deighton et al., 2003)

Appendix 3.16: Paleo water depth (PWD) trends of calibration wells.

Alkina-1		Beanbush-1		Burley-2		Dullingari-1	
Age [Ma]	**PWD [m]**	**Age [Ma]**	**PWD [m]**	**Age [Ma]**	**PWD [m]**	**Age [Ma]**	**PWD [m]**
0.00	-202.77	0.00	-45.70	0.00	-48.08	0.00	-86.99
5.00	-132.00	0.05	-45.00	5.00	-38.00	5.00	-50.00
23.50	-127.00	13.61	-26.00	16.00	-18.00	23.50	-72.00
38.00	-103.00	22.00	-30.00	23.50	-50.00	38.00	-77.00
60.00	-137.00	38.00	-100.00	38.00	-74.00	60.00	-128.00
85.00	-113.00	60.00	-159.00	60.00	-165.00	85.00	-81.00
91.00	-50.00	85.00	-94.00	85.00	-92.00	91.00	-50.00
96.00	0.00	88.70	-50.00	91.00	-50.00	96.00	0.00
97.00	20.00	96.00	0.00	96.00	0.00	97.00	20.00
99.00	40.00	97.00	0.00	97.00	0.00	102.00	20.00
101.00	10.00	99.00	10.00	99.00	10.00	103.00	0.00
121.00	25.50	101.00	10.00	101.00	10.00	121.00	40.00
134.00	-50.00	121.00	25.00	121.00	25.00	134.00	-50.00
144.00	0.00	134.00	-50.00	134.00	-50.00	136.00	0.00
152.00	-21.00	136.00	0.00	136.00	-16.00	144.00	0.00
158.00	-21.00	144.00	0.00	144.00	0.00	158.00	0.00
162.00	-33.00	152.00	-23.00	152.00	0.00	162.00	-36.00
186.00	0.00	158.00	-25.00	158.00	0.00	186.00	0.00
198.00	-47.00	162.00	-50.00	162.00	-35.00	231.00	-50.00
207.00	-50.00	186.00	0.00	186.00	-20.12	241.00	-50.00
213.00	-50.00	231.00	-50.00	198.00	-50.00	251.00	-50.00
231.00	-50.00	234.57	-50.00	231.00	-50.00	263.00	-50.00
251.00	-50.00	251.00	-50.00	233.00	-35.00	263.50	-50.00
263.00	-75.00	263.00	-50.00	251.00	-24.00	264.00	-55.00
272.00	-80.00	263.50	-55.00	263.00	-50.00	265.00	-60.00
285.00	-90.00	266.00	-60.00	265.00	-60.00	266.00	-65.00
288.00	-100.00	270.00	-75.00	266.00	-70.00	270.00	-75.00
298.00	-150.00	272.00	-80.00	270.00	-75.00	272.00	-80.00
330.00	-200.00	285.00	-90.00	272.00	-80.00	285.00	-90.00
		288.00	-100.00	285.00	-90.00	288.00	-100
		298.00	-150.00	288.00	-100.00	298.00	-150
		330.00	-200.00	298.00	-150.00	330.00	-200
				330.00	-200.00		

Appendix 3.16 (continued): Paleo water depth (PWD) trends of calibration wells.

Marengo-1		Paning-1		Springfield-1		Warnie East-1	
Age [Ma]	PWD [m]	Age [Ma]	PWD [m]	Age [Ma]	PWD [m]	Age [Ma]	PWD [m]
0.00	-92.40	0.00	-87.08	0.00	-130.73	0.00	-113.26
5.00	-50.00	5.00	-50.00	5.00	-50.00	5.00	-38.00
23.50	-90.00	23.50	-86.00	35.00	-90.00	16.00	-18.00
38.00	-80.00	38.00	-82.86	60.00	-176.00	23.50	-50.00
60.00	-161.00	60.00	-140.00	85.00	-150.00	38.00	-74.00
85.00	-150.00	85.00	-133.00	91.00	-82.00	60.00	-165.00
91.00	-78.00	91.00	-50.00	96.00	0.00	85.00	-92.00
96.00	0.00	96.00	0.00	97.00	0.00	91.00	-50.00
97.00	0.00	97.00	0.00	99.00	40.00	96.00	0.00
99.00	40.00	99.00	10.00	101.00	-32.00	97.00	0.00
101.00	36.00	101.00	10.00	121.00	25.00	99.00	10.00
121.00	40.00	121.00	25.00	134.00	-50.00	101.00	10.00
136.00	-29.00	134.00	-50.00	144.00	0.00	121.00	25.00
144.00	0.00	136.00	0.00	152.00	-23.00	134.00	-50.00
152.00	-23.00	144.00	0.00	158.00	-25.00	136.00	-16.00
158.00	-25.00	152.00	-23.00	162.00	-33.00	144.00	0.00
162.00	-50.00	158.00	-25.00	186.00	0.00	152.00	0.00
186.00	0.00	162.00	-50.00	198.00	-44.00	158.00	0.00
207.00	-20.00	186.00	0.00	207.00	-50.00	162.00	-35.00
231.00	-12.00	231.00	-50.00	213.00	0.00	186.00	-20.00
251.00	-50.00	251.00	-50.00	231.00	-50.00	198.00	-50.00
263.00	-75.00	270.00	-75.00	251.00	-50.00	231.00	-50.00
285.00	-90.00	272.00	-80.00	263.00	-50.00	233.00	-35.00
288.00	-100.00	285.00	-90.00	270.00	-75.00	251.00	-24.00
298.00	-150.00	288.00	-100.00	272.00	-80.00	263.00	-50.00
330.00	-200.00	298.00	-150.00	285.00	-90.00	265.00	-60.00
		330.00	-200.00	288.00	-100.00	266.00	-70.00
				298.00	-150.00	270.00	-75.00
				330.00	-200.00	272.00	-80.00
						285.00	-90.00
						288.00	-100.00
						298.00	-150.00
						330.00	-200.00

Appendix 3.17: Well data sheet for well Alkina-1 with picks / formation tops.

Well data sheet Alkina-1		Picks / formation tops		
Location: Queensland, Australia				
Data Sources: QPED, Geoscience Australia			Well editor	Input table
Well name	**Alkina-1**	**Pick Name**	**MD (m)**	**TVD (m)**
Surface X (km)	654.505	Winton Fm	4.60	-202.77
Surface Y (km)	7100.851	Mackunda Fm	714.45	507.08
Bottom-hole X (km)	654.505	Allaru Mdst	855.57	648.20
Bottom-hole Y (km)	7100.851	Toolebuc Fm	1099.72	892.35
Start Elevation (m) KB	207.37	Wallumbilla Fm	1115.57	908.20
Total Drill Depth (m)	2680.70	WALLUMBILLA FORMATION (UPPER UNIT)	1115.57	908.20
True Vertical Depth (m)	2473.33	WALLUMBILLA FORMATION (LOWER UNIT)	1235.35	1027.98
		Cadna-owie Fm	1433.78	1226.41
Coordinate system	GDA94	CADNA-OWIE FORMATION (UPPER UNIT)	1433.78	1226.41
		CADNA-OWIE FORMATION (LOWER UNIT)	1493.52	1286.15
		Hooray Sst	1535.58	1328.21
		Westbourne Fm	1673.35	1465.98
		Adori Sst	1771.50	1564.13
		Birkhead Fm	1801.37	1594.00
		Hutton Sst	1884.88	1677.51
		Poolowanna Fm	2074.47	1867.10
		POOLOWANNA FORMATION (UPPER UNIT)	2074.47	1867.10
		POOLOWANNA FORMATION (LOWER UNIT)	2123.85	1916.48
		Cuddapan Fm	2193.40	1986.03
		Nappamerri Gp	2214.68	2007.31
		Gilpeppee Member	2214.68	2007.31
		Tinchoo Formation	2214.68	2007.31
		UPPER DOONMULLA MEMBER	2281.43	2074.06
		Doonmulla Member	2281.43	2074.06
		LOWER DOONMULLA MEMBER	2318.31	2110.94
		Arrabury Formation	2367.99	2160.62
		Wimma Sandstone Member	2383.23	2175.86
		Paning Member	2428.65	2221.28
		CALLAMURRA MEMBER	2542.03	2334.66
		Gidgealpa Group	2556.05	2348.68
		Toolachee Fm	2556.05	2348.68
		Patchawarra Fm	2593.24	2385.87
		Adavale Gp equivalent (Basement)	2652.06	2444.69

Appendix 3.18: Calibration data sheet for well Alkina-1 with thermal maturity and BHT.

Calibration data					
Maturity (vitrinite reflectance)				Horner-corrected BHT	
MD (m)	Mean (%Ro)	Min (%Ro)	Max (%Ro)	MD (m)	T (°C)
671.00	0.41	0.53	0.28	2680.00	142.00
694.90	0.42	0.34	0.51		
786.40	0.42	0.35	0.51		
877.80	0.44	0.35	0.53		
892.00	0.43	0.53	0.35		
969.30	0.46	0.36	0.54		
1042.40	0.47	0.39	0.52		
1061.00	0.46	0.59	0.38		
1133.90	0.46	0.41	0.53		
1166.00	0.43	0.53	0.33		
1225.30	0.49	0.39	0.62		
1276.00	0.50	0.63	0.41		
1300.00	0.50				
1316.70	0.50	0.38	0.60		
1356.00	0.51	0.65	0.40		
1400.00	0.70				
1432.60	0.52	0.42	0.69		
1524.00	0.58	0.45	0.75		
1544.10	0.58	0.46	0.69		
1576.40	0.58	0.50	0.65		
1615.00	0.75	0.59	0.88		
1674.00	0.56	0.53	0.61		
1679.00	0.76	0.63	0.86		
1753.00	0.77	0.58	0.93		
1772.70	0.64	0.55	0.71		
1800.50	0.61	0.48	0.73		
1829.00	0.84	0.73	0.93		
1834.90	0.84				
1884.90	0.64	0.60	0.70		
1981.00	0.82	0.74	0.91		
1981.20	0.74	0.70	0.76		
2075.70	0.76	0.62	0.87		
2134.00	0.79	0.67	0.88		
2167.10	0.82	0.66	0.95		
2194.60	0.89	0.81	0.97		
2225.00	0.87	0.67	1.03		
2240.00	0.90				
2243.00	0.93	0.83	1.00		
2250.00	1.10				
2250.00	1.30				
2292.00	0.87	0.79	1.04		
2304.30	1.06	0.94	1.24		
2390.00	0.81	0.74	0.90		
2426.00	0.85	0.80	0.91		
2499.00	0.96	0.79	1.16		
2557.00	1.36	1.19	1.57		
2566.00	1.48	1.36	1.70		
2597.00	1.54	1.37	1.60		
2620.00	1.50				
2627.00	1.50	1.37	1.70		
2658.00	1.48	1.35	1.57		

Appendix 3.19: Boundary conditions for well Alkina-1 (PWD, SWIT, and heat flow).

Boundary conditions					
Modified after Deighton & Hill (1998), Deighton et al. (2003)		Calculated after Wygrala (1989), modified after (Ladant & Donnadieu, 2016; Alley et al., 2019)		Calibration based on Basin%RoDL, Burnham (2016)	
Paleo water depth (PWD)		**SWIT (Australia, 27 °)**		**Heat flow**	
Age (Ma)	**Water depth (m)**	**Age (Ma)**	**T [°C]**	**Age [Ma]**	**mW/m²**
0.00	-202.77	0.00	22.00	0.00	82.00
5.00	-132.00	5.00	19.25	2.00	60.00
23.50	-127.00	23.50	20.28	80.00	60.00
38.00	-103.00	38.00	21.05	85.00	62.00
60.00	-137.00	60.00	18.05	90.00	64.00
85.00	-113.00	85.00	20.65	91.00	67.00
91.00	-50.00	91.00	22.19	93.00	71.00
96.00	0.00	96.00	23.36	97.00	80.00
97.00	20.00	97.00	22.50	98.00	85.00
99.00	40.00	99.00	22.71	98.50	90.00
101.00	10.00	101.00	22.86	99.00	95.00
121.00	25.00	108.00	10.00	99.50	105.00
134.00	-50.00	113.00	5.00	100.50	95.00
144.00	0.00	121.00	5.00	125.00	65.00
152.00	-21.00	125.00	5.00	135.00	60.00
158.00	-21.00	135.00	5.00	200.00	60.00
162.00	-33.00	136.00	20.00	237.00	60.00
186.00	0.00	144.00	22.42	240.00	60.00
198.00	-47.00	152.00	21.47	290.00	60.00
207.00	-50.00	158.00	21.10	310.00	60.00
213.00	-50.00	162.00	20.73	330.00	60.00
231.00	-50.00	186.00	20.47		
251.00	-50.00	198.00	20.91		
263.00	-75.00	207.00	21.52		
272.00	-80.00	213.00	22.53		
285.00	-90.00	231.00	21.44		
288.00	-100.00	251.00	18.51		
298.00	-150.00	263.00	10.00		
330.00	-200.00	272.00	5.00		
		285.00	5.00		
		330.00	18.00		

Appendix 3.20: Well data sheet for well Beanbush-1 with picks / formation tops.

Well data sheet Beanbush-1	
Location: South Australia, Australia	
Data sources: PEPS-SA, Geoscience Australia	
Well name	**Beanbush-1**
Surface X (km)	464.592
Surface Y (km)	6981.804
Bottom-hole X (km)	464.592
Bottom-hole Y (km)	6981.804
Start Elevation (m) KB	50.00
Total Drill Depth (m)	3699.00
True Vertical Depth (m)	3649.00
Coordinate System	GDA94

Picks / formation tops		
	Well editor	Input table
Pick Name	**MD (m)**	**TVD (m)**
Namba Fm	45.70	-4.30
Eyre Fm	164.60	114.60
Winton Fm	242.90	192.90
Mackunda Fm	1155.80	1105.80
Allaru Mdst	1273.50	1223.50
Toolebuc Fm	1472.50	1422.50
Wallumbilla Fm	1493.50	1443.50
T1	1601.40	1551.40
W1	1617.00	1567.00
Cadna-owie Fm	1947.10	1897.10
Murta Fm	2023.90	1973.90
Namur Sst	2087.60	2037.60
Westbourne Fm	2148.80	2098.80
Adori Sst	2300.90	2250.90
Birkhead Fm	2322.30	2272.30
Hutton Sst	2414.00	2364.00
Cuddapan Fm	2645.40	2595.40
Nappamerri Gp	2712.10	2662.10
Wimma Sst Mbr	2810.90	2760.90
Paning Mbr	2925.20	2875.20
Callamurra Mbr	3029.70	2979.70
Toolachee Fm	3201.60	3151.60
Epsilon Fm	3259.20	3209.20
Murteree Sh	3276.60	3226.60
Patchawarra Fm	3296.70	3246.70
Tirrawarra Fm	3542.40	3492.40
Merrimelia Fm	3575.00	3525.00

Appendix 3.21: Calibration data sheet for well Beanbush-1 with thermal maturity and BHT.

Calibration data					
Maturity (vitrinite reflectance)				Horner-corrected BHT	
MD (m)	Mean (%Ro)	Min (%Ro)	Max (%Ro)	MD (m)	T (°C)
457.20	0.24	0.20	0.32	3699.00	155.00
914.40	0.40	0.36	0.49		
1216.20	0.41	0.34	0.52		
1371.60	0.42	0.30	0.55		
1527.00	0.40	0.34	0.46		
1828.80	0.54	0.38	0.60		
1947.70	0.51	0.44	0.57		
2020.80	0.65	0.60	0.72		
2231.10	0.57	0.46	0.67		
2307.30	0.64	0.54	0.71		
2383.50	0.61	0.50	0.73		
2441.40	0.60	0.30	0.58		
2606.00	0.72	0.64	0.79		
2664.70	0.68	0.59	0.76		
2758.40	0.71	0.57	0.75		
2987.00	0.65	0.50	0.74		
3203.40	1.08	1.00	1.18		
3267.50	1.16	1.04	1.24		
3301.00	1.17	1.11	1.30		
3310.80	1.16	1.07	1.36		
3365.00	1.32	1.19	1.44		
3422.90	1.59	1.43	1.78		
3514.30	1.45	1.36	1.47		
3548.60	1.59	1.53	1.67		
3605.80	1.28	1.18	1.40		
3688.10	1.50	1.40	1.58		

Appendix 3.22: Boundary conditions for well Beanbush-1 (PWD, SWIT, and heat flow).

Boundary conditions					
Modified after Deighton & Hill (1998), Deighton et al. (2003)		Calculated after Wygrala (1989), modified after (Ladant & Donnadieu, 2016; Alley et al., 2019)		Calibration based on Basin%RoDL, Burnham (2016)	
Paleo water depth (PWD)		**SWIT (Australia, 27 °)**		**Heat flow**	
Age (Ma)	**Water depth (m)**	**Age (Ma)**	**T [°C]**	**Age [Ma]**	**mW/m²**
0.00	-45.70	0.00	24.00	0.00	62.00
0.05	-45.00	0.05	20.31	2.00	60.00
13.61	-26.00	13.61	20.46	80.00	60.00
22.00	-30.00	22.00	21.13	85.00	61.00
38.00	-100.00	38.00	21.08	90.00	63.00
60.00	-159.00	60.00	17.83	91.00	64.00
85.00	-94.00	85.00	20.85	93.00	66.00
88.70	-50.00	88.70	21.91	97.00	70.00
96.00	0.00	96.00	23.36	98.00	75.00
97.00	0.00	97.00	23.50	98.50	80.00
99.00	10.00	99.00	22.71	99.00	85.00
101.00	10.00	101.00	22.86	99.50	90.00
121.00	25.00	108.00	10.00	100.50	85.00
134.00	-50.00	113.00	5.00	125.00	65.00
136.00	0.00	121.00	5.00	135.00	60.00
144.00	0.00	125.00	5.00	200.00	60.00
152.00	-23.00	135.00	5.00	237.00	60.00
158.00	-25.00	136.00	20.00	240.00	60.00
162.00	-50.00	144.00	22.42	290.00	60.00
186.00	0.00	152.00	21.46	310.00	60.00
231.00	-50.00	158.00	21.05	330.00	60.00
234.57	-50.00	162.00	20.57		
251.00	-50.00	186.00	20.47		
263.00	-50.00	231.00	21.44		
263.50	-55.00	234.57	20.90		
266.00	-60.00	251.00	18.51		
270.00	-75.00	263.00	10.00		
272.00	-80.00	263.50	10.00		
285.00	-90.00	266.00	9.78		
288.00	-100.00	270.00	4.69		
298.00	-150.00	272.00	4.50		
330.00	-200.00	285.00	4.25		
		288.00	4.00		
		298.00	4.70		
		330.00	18.00		

Appendix 3.23: Well data sheet for well Burley-2 with picks / formation tops.

Well data sheet Burley-2			**Picks / formation tops**		
Location: South Australia, Australia					
Data sources: PEPS-SA, Geoscience Australia				Well editor	Input table
Well name	**Burley-2**		**Pick Name**	**MD (m)**	**TVD (m)**
Surface X (km)	464.619		Namba Fm	38.40	-16.16
Surface Y (km)	6925.119		Eyre Fm	57.90	3.34
Bottom-hole X (km)	464.619		Winton Fm	108.50	53.94
Bottom-hole Y (km)	6925.119		Mackunda Fm	883.90	829.34
Start Elevation (m) KB	54.56		Allaru Mdst	976.00	921.44
Total Drill Depth (m)	3705.76		Toolebuc Fm	1250.90	1196.34
True Vertical Depth (m)	3651.20		Wallumbilla Fm	1256.10	1201.54
			Cadna-owie Fm	1649.60	1595.04
Coordinate System	GDA94		Murta Fm	1739.80	1685.24
			McKinlay Mbr	1796.50	1741.94
			Namur Sst	1805.00	1750.44
			Westbourne Fm	1874.50	1819.94
			Adori Sst	2011.40	1956.84
			Birkhead Fm	2052.50	1997.94
			Hutton Sst	2118.40	2063.84
			Poolowanna Fm	2249.10	2194.54
			Nappamerri Gp	2280.50	2225.94
			Toolachee Fm	2672.50	2617.94
			Daralingie Fm	2829.50	2774.94
			Roseneath Shale	2918.80	2864.24
			Epsilon Fm	2978.20	2923.64
			Murteree Shale	3117.80	3063.24
			Patchawarra Fm	3196.40	3141.84
			Tirrawarra Sst	3589.90	3535.34
			Merrimelia Fm	3613.10	3558.54
			Big Lake Suite (Basement)	3661.60	3607.04

Appendix 3.24: Calibration data sheet for Burley-2 with thermal maturity and BHT.

Calibration data					
Maturity (vitrinite reflectance)				Horner-corrected BHT	
MD (m)	Mean (%Ro)	Min (%Ro)	Max (%Ro)	MD (m)	T (°C)
335.30	0.29	0.23	0.32	3705.00	251.00
493.80	0.31	0.27	0.36		
676.70	0.36	0.28	0.47		
768.10	0.39	0.31	0.52		
823.00	0.48	0.41	0.62		
887.00	0.46	0.39	0.61		
969.30	0.51	0.41	0.61		
1033.30	0.51	0.41	0.61		
1097.30	0.53	0.45	0.64		
1243.60	0.58	0.51	0.64		
1371.60	0.57	0.57	0.57		
1670.30	0.68	0.53	0.88		
1758.70	0.69	0.61	0.77		
1874.50	1.15	1.07	1.24		
1947.70	1.15	1.02	1.25		
2002.50	1.33	1.20	1.44		
2081.80	1.52	1.40	1.70		
2103.10	1.53	1.37	1.72		
2249.40	1.43	1.21	1.71		
2267.70	1.67	1.34	2.50		
2566.40	0.29	0.24	0.32		
2670.00	0.42	0.42	0.42		
2685.30	3.22	2.83	3.72		
2697.50	3.25	2.93	3.68		
2734.10	3.25	2.90	3.66		
2758.40	3.21	2.79	3.59		
2798.10	3.32	3.03	3.73		
2819.40	3.53	3.12	3.90		
2865.10	3.63	3.16	4.10		
2916.90	3.59	3.34	3.83		
3026.70	3.95	3.70	4.25		
3090.70	4.05	3.75	4.57		
3267.50	4.75	4.07	5.29		
3334.50	5.12	4.62	5.81		
3355.80	5.72	5.22	6.28		
3441.20	6.27	5.29	6.98		
3470.50	5.69	5.30	6.03		
3470.80	5.51	4.63	6.18		
3490.00	7.00	6.36	7.53		
3541.80	6.58	6.22	7.89		
3636.30	6.81	6.06	7.83		
3657.60	6.70	6.31	7.10		

Appendix 3.25: Boundary conditions for well Burley-2 (PWD, SWIT, and heat flow).

Boundary conditions					
Modified after Deighton & Hill (1998), Deighton et al. (2003)		Calculated after Wygrala (1989), modified after (Ladant & Donnadieu, 2016; Alley et al., 2019)		Calibration based on Basin%RoDL, Burnham (2016)	
Paleo water depth (PWD)		**SWIT (Australia, 27 °)**		**Heat flow**	
Age (Ma)	**Water depth (m)**	**Age (Ma)**	**T [°C]**	**Age [Ma]**	**mW/m²**
0.00	-48.08	0.00	24.00	0.00	110.00
5.00	-38.00	5.00	20.18	2.00	60.00
16.00	-18.00	16.00	20.68	80.00	60.00
23.50	-50.00	23.50	21.05	85.00	61.00
38.00	-74.00	38.00	21.34	90.00	62.00
60.00	-165.00	60.00	17.77	91.00	63.00
85.00	-92.00	85.00	20.87	93.00	70.00
91.00	-50.00	91.00	22.19	97.00	78.00
96.00	0.00	96.00	23.36	98.00	95.00
97.00	0.00	97.00	23.50	98.50	120.00
99.00	10.00	99.00	22.71	99.00	145.00
101.00	10.00	101.00	22.86	99.50	150.00
121.00	25.00	108.00	10.00	100.50	95.00
134.00	-50.00	113.00	5.00	125.00	65.00
136.00	-16.00	121.00	5.00	135.00	60.00
144.00	0.00	125.00	5.00	200.00	60.00
152.00	0.00	135.00	5.00	237.00	60.00
158.00	0.00	136.00	20.00	240.00	60.00
162.00	-35.00	144.00	22.42	290.00	60.00
186.00	-20.12	152.00	21.69	310.00	60.00
198.00	-50.00	158.00	21.31	330.00	60.00
231.00	-50.00	162.00	20.71		
233.00	-35.00	186.00	20.27		
251.00	-24.00	198.00	20.88		
263.00	-50.00	231.00	21.44		
265.00	-60.00	233.00	21.29		
266.00	-70.00	251.00	18.27		
270.00	-75.00	263.00	9.50		
272.00	-80.00	265.00	10.00		
285.00	-90.00	266.00	10.00		
288.00	-100.00	270.00	5.00		
298.00	-150.00	272.00	5.00		
330.00	-200.00	285.00	4.84		
		288.00	5.00		
		298.00	4.38		
		330.00	18.00		

Appendix 3.26: Well data sheet for well Daralingie-1 with picks / formation tops.

Well data sheet Daralingie-1			**Picks / formation tops**		
Location: South Australia, Australia					
Data sources: PEPS-SA, Geoscience Australia				Well editor	Input table
Well name	**Daralingie-1**		**Pick Name**	**MD (m)**	**TVD (m)**
Surface X (km)	399.395		Namba Fm	40.20	8.53
Surface Y (km)	6862.516		Eyre Fm	240.80	209.13
Bottom-hole X (km)	399.395		Winton Fm	296.60	264.93
Bottom-hole Y (km)	6862.516		Mackunda Fm	821.10	789.43
Start Elevation (m) KB	31.67		Oodnadatta Fm	911.40	879.73
Total Drill Depth (m)	2265.88		Coorikiana Sst	1131.40	1099.73
True Vertical Depth (m)	2234.21		Bulldog Sh	1157.60	1125.93
			Cadna-owie Fm	1416.70	1385.03
Coordinate System	GDA94		Murta Fm	1482.90	1451.23
			McKinlay Mbr	1535.00	1503.33
			Namur Sst	1544.40	1512.73
			Westbourne Fm	1593.50	1561.83
			Adori Sst	1643.50	1611.83
			Birkhead Fm	1727.00	1695.33
			Hutton Sst	1776.10	1744.43
			Poolowanna Fm	1860.20	1828.53
			NAPPAMERRI GP	1872.10	1840.43
			Toolachee Fm	1925.40	1893.73
			Daralingie Fm	1962.90	1931.23
			Roseneath Sh	1988.80	1957.13
			Epsilon Fm	2029.40	1997.73
			Murteree Sh	2089.40	2057.73
			Patchawarra Fm	2121.10	2089.43
			Pando Fm	2193.70	2162.03

Appendix 3.27: Calibration data sheet for Daralingie-1 with thermal maturity and BHT.

Calibration data					
Maturity (vitrinite reflectance)				Horner-corrected BHT	
MD (m)	Mean (%Ro)	Min (%Ro)	Max (%Ro)	MD (m)	T (°C)
929.60	0.36	0.24	0.45	2296.00	121.00
1036.30	0.32	0.18	0.42		
1213.10	0.31	0.24	0.38		
1731.30	0.60	0.42	0.70		
1819.70	0.63	0.50	0.84		
1935.50	0.82	0.63	0.84		
1940.10	0.84	0.79	0.92		
1945.50	0.84	0.75	0.92		
1956.80	0.90	0.86	0.96		
1968.70	0.83	0.76	0.91		
1999.50	0.87	0.74	0.98		
2057.40	0.90	0.80	1.05		
2078.70	0.93	0.80	1.02		
2176.30	0.95	0.85	1.15		

Appendix 3.28: Boundary conditions for well Daralingie-1 (PWD, SWIT, and heat flow).

Boundary conditions					
Modified after Deighton & Hill (1998), Deighton et al. (2003)		Calculated after Wygrala (1989), modified after (Ladant & Donnadieu, 2016; Alley et al., 2019)		Calibration based on Basin%RoDL, Burnham (2016)	
Paleo water depth (PWD)		**SWIT (Australia, 27 °)**		**Heat flow**	
Age (Ma)	**Water depth (m)**	**Age (Ma)**	**T [°C]**	**Age [Ma]**	**mW/m²**
0.00	-25.00	0.00	24.00	0.00	73.00
5.00	0.00	5.00	20.56	2.00	60.00
16.00	-50.00	16.00	20.36	80.00	60.00
23.50	-50.00	23.50	21.05	85.00	64.00
38.00	-30.00	38.00	21.78	90.00	68.00
60.00	-100.00	60.00	18.42	91.00	71.00
85.00	-150.00	85.00	20.28	93.00	74.00
91.00	-50.00	91.00	22.19	97.00	85.00
96.00	-25.00	96.00	23.11	98.00	95.00
97.00	20.00	97.00	22.50	98.50	110.00
99.00	20.00	99.00	22.71	99.00	125.00
101.00	0.00	101.00	23.86	99.50	135.00
121.00	25.00	108.00	10.00	100.50	90.00
134.00	-50.00	113.00	5.00	125.00	65.00
136.00	-10.00	121.00	5.00	135.00	60.00
144.00	0.00	125.00	5.00	200.00	60.00
152.00	-15.00	135.00	5.00	237.00	60.00
158.00	0.00	136.00	20.00	240.00	60.00
162.00	-30.00	144.00	22.42	290.00	60.00
186.00	-15.00	152.00	21.54	310.00	60.00
198.00	0.00	158.00	21.31	330.00	60.00
231.00	0.00	162.00	20.77		
233.00	-20.00	186.00	20.32		
251.00	-50.00	198.00	21.38		
263.00	-50.00	231.00	21.94		
265.00	-50.00	233.00	21.44		
266.00	-35.00	251.00	18.01		
270.00	-75.00	263.00	9.50		
272.00	-80.00	265.00	9.50		
285.00	-90.00	266.00	9.65		
288.00	-100.00	270.00	4.25		
298.00	-150.00	272.00	4.20		
330.00	-200.00	285.00	4.10		
		288.00	4.00		
		298.00	4.70		
		330.00	18.00		

Appendix 3.29: Well data sheet for well Dullingari-1 with picks / formation tops.

Well data sheet Dullingari-1			**Picks / formation tops**		
Location: South Australia, Australia					
Data sources: PEPS-SA, Geoscience Australia				Well editor	Input table
Well name	**Dullingari-1**		**Pick Name**	**MD (m)**	**TVD [m]**
Surface X (km)	487.983		Eyre Fm	67.40	-24.16
Surface Y (km)	6888.188		Winton Fm	124.10	32.54
Bottom-hole X (km)	487.983		Mackunda Fm	678.50	586.94
Bottom-hole Y (km)	6888.188		Oodnadatta Fm	776.60	685.04
Start Elevation (m) KB	91.56		Coorikiana Sst	1072.30	980.74
Total Drill Depth (m)	3532.02		Bulldog Sh	1083.00	991.44
True Vertical Depth (m)	3440.46		Cadna-owie Fm	1372.20	1280.64
			Murta Fm	1461.80	1370.24
Coordinate System	GDA94		McKinlay Mbr	1505.10	1413.54
			Namur Sst	1531.60	1440.04
			Westbourne Fm	1580.40	1488.84
			Birkhead Fm	1767.50	1675.94
			Hutton Sst	1799.80	1708.24
			Nappamerri Gp	1884.60	1793.04
			Toolachee Fm	2089.10	1997.54
			Daralingie Fm	2210.10	2118.54
			Roseneath Sh	2224.40	2132.84
			Epsilon Fm	2293.60	2202.04
			Murteree Sh	2354.60	2263.04
			Patchawarra Fm	2411.00	2319.44
			Merrimelia Fm	2731.00	2639.44
			Lycosa Fm (Basement)	2757.80	2666.24
			Narcoonowie Fm	2945.00	2853.44
			Dullingari Gp	2991.30	2899.74

Appendix 3.30: Calibration data sheet for Dullingari-1 with thermal maturity and BHT.

Calibration data					
Maturity (vitrinite reflectance)				Horner-corrected BHT	
MD (m)	Mean (%Ro)	Min (%Ro)	Max (%Ro)	MD (m)	T (°C)
426.70	0.43	0.38	0.48	2700.00	143.00
429.60	0.40				
615.70	0.53	0.48	0.58		
658.40	0.53	0.45	0.62		
716.30	0.42	0.38	0.45		
840.00	0.50				
1067.40	0.57				
1173.50	0.44	0.42	0.45		
1375.30	0.53				
1450.00	0.70				
1511.20	0.58				
1679.40	0.72	0.65	0.75		
1770.90	0.68	0.66	0.70		
1773.90	0.57				
1837.90	0.74	0.66	0.80		
1913.30	0.72				
2087.90	0.75				
2087.90	0.98	0.93	1.05		
2105.90	0.79				
2139.70	1.01	0.94	1.08		
2195.80	0.79				
2197.30	1.28				
2200.70	1.17	1.10	1.26		
2279.90	1.09	1.07	1.14		
2280.50	0.78				
2280.80	1.28	1.18	1.39		
2280.80	1.28	1.18	1.39		
2289.00	1.16	1.07	1.26		
2319.20	1.31	1.26	1.36		
2319.20	1.31	1.26	1.36		
2407.90	1.29	1.13	1.46		
2408.10	1.51				
2414.00	1.24	1.10	1.38		
2462.80	1.41	1.32	1.53		
2468.90	1.05				
2522.60	1.10				
2522.60	1.33				
2535.90	1.43	1.32	1.48		
2599.90	1.66	1.60	1.75		
2629.50	1.77	1.64	1.86		
2679.20	1.83	1.72	1.98		
2706.60	1.89	1.75	2.02		
2708.00	1.72				
2710.00	1.89				
2712.70	1.98	1.85	2.10		
2849.90	1.49				
2990.10	0.95				
3261.40	1.63				
3319.20	1.28				

Appendix 3.31: Boundary conditions for well Dullingari-1 (PWD, SWIT, and heat flow).

Boundary Conditions					
Modified after Deighton & Hill (1998), Deighton et al. (2003)		Calculated after Wygrala (1989), modified after (Ladant & Donnadieu, 2016; Alley et al., 2019)		Calibration based on Basin%RoDL, Burnham (2016)	
Paleo water depth (PWD)		**SWIT (Australia, 27 °)**		**Heat flow**	
Age (Ma)	**Water depth (m)**	**Age (Ma)**	**T [°C]**	**Age [Ma]**	**mW/m²**
0.00	-86.99	0.00	23.00	0.00	75.00
5.00	-50.00	5.00	20.06	2.00	75.00
23.50	-72.00	23.50	20.83	80.00	75.00
38.00	-77.00	38.00	21.30	85.00	78.00
60.00	-128.00	60.00	18.14	90.00	81.00
85.00	-81.00	85.00	20.98	91.00	82.00
91.00	-50.00	91.00	22.19	93.00	83.00
96.00	0.00	96.00	23.36	97.00	85.00
97.00	20.00	97.00	22.50	98.00	86.00
102.00	20.00	102.00	22.93	98.50	87.00
103.00	0.00	108.00	10.00	99.00	88.00
121.00	40.00	113.00	5.00	99.50	90.00
134.00	-50.00	121.00	5.00	100.50	85.00
136.00	0.00	125.00	5.00	125.00	77.00
144.00	0.00	135.00	5.00	135.00	75.00
158.00	0.00	136.00	20.00	200.00	75.00
162.00	-36.00	144.00	22.42	237.00	75.00
186.00	0.00	158.00	21.31	240.00	75.00
231.00	-50.00	162.00	20.71	290.00	75.00
241.00	-50.00	186.00	20.47	310.00	75.00
251.00	-50.00	231.00	21.44	330.00	75.00
263.00	-50.00	241.00	20.02		
263.50	-50.00	251.00	18.01		
264.00	-55.00	263.00	9.50		
265.00	-60.00	263.50	9.50		
266.00	-65.00	264.00	9.50		
270.00	-75.00	265.00	9.72		
272.00	-80.00	266.00	10.00		
285.00	-90.00	270.00	5.00		
288.00	-100	272.00	5.00		
298.00	-150	285.00	4.84		
330.00	-200	298.00	4.38		
		330.00	18.00		

Appendix 3.32: Well data sheet for well Jack Lake-1 with picks / formation tops.

Well data sheet Jack lake-1			**Picks / formation tops**		
Location: South Australia, Australia					
Data sources: PEPS-SA, Geoscience Australia				Well editor	Input table
Well name	**Jack Lake-1**		**Pick Name**	**MD (m)**	**TVD (m)**
Surface X (km)	383.992		Namba Fm	43.90	10.49
Surface Y (km)	6908.671		Eyre Fm	171.90	138.49
Bottom-hole X (km)	383.992		Winton Fm	234.70	201.29
Bottom-hole Y (km)	6908.671		Mackunda Fm	1015.60	982.19
Start Elevation (m) KB	33.41		Allaru Mdst	1085.70	1052.29
Total Drill Depth (m)	3144.01		Toolebuc Fm	1284.70	1251.29
True Vertical Depth (m)	3110.60		Wallumbilla Fm	1291.10	1257.69
			Cadna-owie Fm	1664.20	1630.79
Coordinate System	GDA94		Murta Fm	1723.30	1689.89
			Namur Sst	1776.40	1742.99
			Westbourne Fm	1841.60	1808.19
			Adori Sst	1981.20	1947.79
			Birkhead Fm	2035.20	2001.79
			Hutton Sst	2089.10	2055.69
			Poolowanna Fm	2213.20	2179.79
			NAPPAMERRI GP	2295.40	2261.99
			Toolachee Fm	2444.50	2411.09
			Daralingie Fm	2473.10	2439.69
			Roseneath Sh	2502.70	2469.29
			Epsilon Fm	2517.60	2484.19
			Murteree Sh	2576.80	2543.39
			Patchawarra Fm	2599.00	2565.59
			Tirrawarra Sst	2999.80	2966.39
			Merrimelia Fm	3041.30	3007.89

Appendix 3.33: Calibration data sheet for Jack Lake-1 with thermal maturity and BHT.

Calibration data					
Maturity (vitrinite reflectance)				Horner-corrected BHT	
MD (m)	Mean (%Ro)	Min (%Ro)	Max (%Ro)	MD (m)	T (°C)
879.00	0.30	0.24	0.36	3144.00	137.00
1032.00	0.32	0.24	0.38		
1184.00	0.34	0.30	0.38		
1337.00	0.35	0.32	0.40		
1489.00	0.35	0.31	0.38		
1641.00	0.40	0.38	0.44		
1721.00	0.42	0.40	0.44		
1794.00	0.41	0.37	0.44		
1873.00	0.41	0.41	0.41		
1934.00	0.43	0.00	0.00		
2010.00	0.44	0.38	0.50		
2086.00	0.47	0.40	0.54		
2183.00	0.48	0.48	0.48		
2236.00	0.53	0.46	0.59		
2284.00	0.60	0.53	0.67		
2361.00	0.61	0.58	0.66		
2461.00	0.66	0.55	0.74		
2498.00	0.70	0.60	0.82		
2544.00	0.76	0.67	0.83		
2605.00	0.74	0.64	0.85		
2665.00	0.74	0.65	0.81		
2699.00	0.82	0.74	0.92		
2742.00	0.75	0.68	0.85		
2809.00	0.83	0.72	0.99		
2839.00	0.83	0.69	1.00		
2912.00	0.87	0.73	1.00		
2955.00	0.97	0.87	1.08		
3016.00	0.90	0.66	1.09		
3077.00	0.86	0.70	1.06		

Appendix 3.34: Boundary conditions for well Jack Lake-1 (PWD, SWIT, and heat flow).

Boundary conditions					
Modified after Deighton & Hill (1998), Deighton et al. (2003)		Calculated after Wygrala (1989), modified after (Ladant & Donnadieu, 2016; Alley et al., 2019)		Calibration based on Basin%RoDL, Burnham (2016)	
Paleo water depth (PWD)		**SWIT (Australia, 27 °)**		**Heat flow**	
Age (Ma)	**Water depth (m)**	**Age (Ma)**	**T [°C]**	**Age [Ma]**	**mW/m²**
0.00	-27.31	0.00	24.00	0.00	60.00
2.00	-25.00	2.00	20.38	2.00	55.00
12.00	0.00	12.00	20.66	80.00	55.00
22.00	0.00	22.00	21.44	85.00	57.00
38.00	-20.00	38.00	21.88	90.00	60.00
60.00	-120.00	60.00	18.22	91.00	63.00
85.00	-50.00	85.00	21.28	93.00	68.00
91.00	-50.00	91.00	22.19	97.00	75.00
96.00	0.00	96.00	23.36	98.00	80.00
97.00	0.00	97.00	23.50	98.50	82.00
99.00	10.00	99.00	22.71	99.00	85.00
101.00	10.00	101.00	22.86	99.50	87.00
121.00	25.00	108.00	10.00	100.50	75.00
134.00	-50.00	113.00	5.00	125.00	60.00
136.00	-10.00	121.00	5.00	135.00	55.00
144.00	0.00	125.00	5.00	200.00	55.00
152.00	-10.00	135.00	5.00	237.00	55.00
158.00	0.00	136.00	20.00	240.00	55.00
162.00	-30.00	144.00	22.42	290.00	55.00
186.00	0.00	152.00	21.59	310.00	55.00
231.00	-50.00	158.00	21.31	330.00	55.00
235.00	-50.00	162.00	20.77		
251.00	-50.00	186.00	20.47		
263.00	-50.00	231.00	21.44		
263.50	-55.00	235.00	20.83		
266.00	-60.00	251.00	18.01		
270.00	-75.00	263.00	9.50		
272.00	-80.00	263.50	9.45		
285.00	-90.00	266.00	9.40		
288.00	-100.00	270.00	4.25		
298.00	-150.00	272.00	4.20		
330.00	-200.00	285.00	4.10		
		288.00	4.00		
		298.00	4.70		
		330.00	18.00		

Appendix 3.35: Well data sheet for well Kirby-1 with picks / formation tops.

Well data sheet Kirby-1			**Picks / formation tops**		
Location: South Australia, Australia					
Data sources: PEPS-SA, Geoscience Australia				Well editor	Input table
Well name	**Kirby-1**		**Pick Name**	**MD (m)**	**TVD (m)**
Surface X (km)	482.294		Winton Fm	6.78	-95.30
Surface Y (km)	6940.619		Mackunda Fm	832.10	730.02
Bottom-hole X (km)	482.294		Allaru Mdst	912.90	810.82
Bottom-hole Y (km)	6940.619		Toolebuc Fm	1127.50	1025.42
Start Elevation (m) KB	102.08		Wallumbilla Fm	1134.20	1032.12
Total Drill Depth (m)	3866.39		Cadna-owie Fm	1586.80	1484.72
True Vertical Depth (m)	3764.31		Murta Fm	1681.30	1579.22
			McKinlay Mbr	1739.50	1637.42
Coordinate System	GDA94		Namur Sst	1756.00	1653.92
			Westbourne Fm	1811.70	1709.62
			Adori Sst	1953.80	1851.72
			Birkhead Fm	1976.90	1874.82
			Hutton Sst	2054.40	1952.32
			Nappamerri Gp	2208.60	2106.52
			Toolachee Fm	2652.70	2550.62
			Daralingie Fm	2732.20	2630.12
			Roseneath Shale	2813.30	2711.22
			Epsilon Fm	2868.80	2766.72
			Murteree Shale	3019.30	2917.22
			Patchawarra Fm	3088.80	2986.72
			Tirrawarra Sst	3769.80	3667.72
			Merrimelia Fm	3807.60	3705.52

Appendix 3.36: Calibration data sheet for Kirby-1 with thermal maturity and BHT.

Calibration data					
Maturity (vitrinite reflectance)				Horner-corrected BHT	
MD (m)	Mean (%Ro)	Min (%Ro)	Max (%Ro)	MD (m)	T (°C)
743.70	0.40	0.32	0.47	3866.00	192.00
1880.60	0.89				
1883.00	0.89				
1935.50	0.90	0.85	0.95		
2103.10	1.08				
2186.90	1.19				
2630.40	1.19	1.22	1.31		
2633.40	1.19				
2645.70	1.31	1.25	1.47		
2648.70	1.31				
2654.80	1.31				
2656.00	1.80	1.73	1.88		
2657.00	1.86				
2660.90	1.89	1.82	1.96		
2663.90	1.89				
2682.20	1.97	1.90	2.08		
2691.40	2.02	1.94	2.11		
2712.70	2.03				
2724.30	1.80	1.74	1.90		
2729.80	2.06	1.97	2.12		
2731.00	1.98	1.92	2.08		
2732.50	2.05	1.90	2.16		
2733.10	2.15	2.00	2.30		
2955.90	2.56	2.46	2.63		
2956.50	2.56				
2962.70	2.52	2.42	2.58		
2965.10	2.51	2.46	2.59		
2966.50	2.44	2.40	2.53		
3130.30	2.80	2.58	2.88		
3130.30	2.43	2.15	2.62		
3133.30	2.80				
3173.00	2.91	2.81	3.01		
3240.00	2.98	2.75	3.13		
3312.00	3.36	3.18	3.50		
3313.20	3.41	3.24	3.52		
3313.20	3.04	2.82	3.26		
3337.60	3.41	3.30	3.51		
3352.80	3.50				
3371.10	3.64	3.39	3.81		
3380.20	3.72	3.39	4.02		
3401.60	3.87	3.60	4.11		
3560.10	3.85	3.45	4.11		
3560.10	3.39	3.12	3.64		
3682.00	3.89	3.49	4.14		
3721.60	4.80	4.47	5.04		
3726.00	4.80				
3130.30	2.43	2.15	2.62		
3313.20	3.04	2.82	3.26		
3560.10	3.39	3.12	3.64		

Appendix 3.37: Boundary conditions for well Kirby-1 (PWD, SWIT, and heat flow).

Boundary conditions					
Modified after Deighton & Hill (1998), Deighton et al. (2003)		Calculated after Wygrala (1989), modified after (Ladant & Donnadieu, 2016; Alley et al., 2019)		Calibration based on Basin%RoDL, Burnham (2016)	
Paleo water depth (PWD)		**SWIT (Australia, 27 °)**		**Heat flow**	
Age (Ma)	**Water depth (m)**	**Age (Ma)**	**T [°C]**	**Age [Ma]**	**mW/m²**
0.00	-95.30	0.00	23.00	0.00	76.00
5.00	-50.00	5.00	20.06	2.00	65.00
16.00	-40.00	16.00	20.46	80.00	65.00
23.50	-70.00	23.50	20.85	85.00	70.00
38.00	-60.00	38.00	21.48	90.00	73.00
60.00	-135.00	60.00	18.07	91.00	80.00
85.00	-70.00	85.00	21.08	93.00	82.00
91.00	-50.00	91.00	22.19	97.00	90.00
96.00	0.00	96.00	23.36	98.00	95.00
97.00	0.00	97.00	23.50	98.50	103.00
99.00	10.00	99.00	22.71	99.00	110.00
101.00	10.00	101.00	22.86	99.50	125.00
121.00	25.00	108.00	10.00	100.50	90.00
134.00	-50.00	113.00	5.00	125.00	65.00
136.00	0.00	121.00	5.00	135.00	60.00
144.00	0.00	125.00	5.00	200.00	60.00
152.00	0.00	135.00	5.00	237.00	60.00
158.00	0.00	136.00	20.00	240.00	60.00
162.00	-35.00	144.00	22.42	290.00	60.00
186.00	-20.12	152.00	21.69	310.00	60.00
198.00	-50.00	158.00	21.31	330.00	60.00
231.00	-50.00	162.00	20.72		
233.00	-35.00	186.00	20.27		
251.00	-24.00	198.00	20.88		
263.00	-50.00	231.00	21.44		
265.00	-60.00	233.00	21.29		
266.00	-70.00	251.00	18.27		
270.00	-75.00	263.00	9.50		
272.00	-80.00	265.00	9.40		
285.00	-90.00	266.00	9.30		
288.00	-100.00	270.00	4.25		
298.00	-150.00	272.00	4.20		
330.00	-200.00	285.00	4.10		
		288.00	4.00		
		298.00	4.70		
		330.00	18.00		

Appendix 3.38: Well data sheet for well Marengo-1 with picks / formation tops.

Well data sheet Marengo-1			**Picks / formation tops**		
Location: Queensland, Australia					
Data Sources: QPED, Geoscience Australia				Well editor	Input table
Well name	**Marengo-1**		**Pick name**	**MD (m)**	**TVD (m)**
Surface X (km)	582.473		Winton Fm	6.20	-92.40
Surface Y (km)	7086.464		Mackunda Fm	1002.79	904.19
Bottom-hole X (km)	582.473		Allaru Mdst	1097.28	998.68
Bottom-hole Y (km)	7086.464		Toolebuc Fm	1456.94	1358.34
Start Elevation (m) KB	98.60		Wallumbilla Fm	1464.26	1365.66
Total Drill Depth (m)	3008.40		WALLUMBILLA FM (UPPER UNIT)	1464.26	1365.66
TVD (m)	2909.80		WALLUMBILLA FM (LOWER UNIT)	1578.25	1479.65
			Cadna-owie Fm	1763.60	1665.00
Coordinate System	GDA94		CADNA-OWIE FM (UPPER UNIT)	1763.60	1665.00
			CADNA-OWIE FM(LOWER UNIT)	1814.17	1715.57
			Hooray Sst	1852.88	1754.28
			Murta Member	1852.88	1754.28
			Namur Sst	1928.77	1830.17
			Westbourne Fm	1984.25	1885.65
			Adori Sst	2086.66	1988.06
			Birkhead Fm	2118.97	2020.37
			Hutton Sst	2215.90	2117.30
			HUTTON SST (UPPER UNIT)	2215.90	2117.30
			HUTTON SST (LOWER UNIT)	2317.09	2218.49
			Poolowanna Fm	2420.10	2321.50
			POOLOWANNA FM (UPPER UNIT)	2420.10	2321.50
			POOLOWANNA FM (LOWER UNIT)	2456.69	2358.09
			Cuddapan Fm	2542.64	2444.04
			Nappamerri Gp	2563.37	2464.77
			Tinchoo Formation	2563.40	2464.80
			Gilpeppee Member	2563.40	2464.80
			Doonmulla Member	2638.96	2540.36
			UPPER DOONMULLA MEMBER	2638.96	2540.36
			LOWER DOONMULLA MEMBER	2685.90	2587.30
			Arrabury Formation	2741.68	2643.08
			Wimma Sandstone Member	2741.68	2643.08
			Paning Member	2827.93	2729.33
			CALLAMURRA MEMBER	2886.46	2787.86
			Toolachee Fm	2923.64	2825.04
			Gidgealpa Gp	2923.64	2825.04
			Metasediments (Basement)	2976.68	2878.08

Appendix 3.39: Calibration data sheet for Marengo-1 with thermal maturity and BHT.

Calibration data					
Maturity (vitrinite reflectance)				Horner-corrected BHT	
MD (m)	Mean (%Ro)	Min (%Ro)	Max (%Ro)	MD (m)	T (°C)
718.00	0.39	0.32	0.48	3008.00	164.00
983.00	0.51	0.37	0.63		
1065.00	0.48	0.37	0.65		
1358.00	0.62	0.48	0.73		
1458.00	0.54	0.40	0.70		
1559.00	0.55	0.47	0.67		
1751.00	0.62	0.56	0.66		
1843.00	0.67	0.64	0.69		
1879.00	0.61	0.55	0.68		
1916.00	0.84	0.74	0.94		
2080.00	0.90	0.86	0.93		
2135.00	1.09	0.87	1.20		
2163.00	1.19	1.04	1.26		
2190.00	1.16	1.00	1.26		
2355.00	1.21	1.14	1.29		
2355.00	1.21	1.14	1.29		
2437.00	1.44	1.28	1.57		
2547.00	1.48	1.32	1.74		
2629.00	1.46	1.28	1.70		
2665.00	1.50	1.40	1.58		
2940.00	2.17	1.95	2.41		
2958.00	2.34	2.24	2.49		

Appendix 3.40: Boundary conditions for well Marengo-1 (PWD, SWIT, and heat flow).

Boundary conditions					
Modified after Deighton & Hill (1998), Deighton et al. (2003)		Calculated after Wygrala (1989), modified after (Ladant & Donnadieu, 2016; Alley et al., 2019)		Calibration based on Basin%RoDL, Burnham (2016)	
Paleo water depth (PWD)		**SWIT (Australia, 27 °)**		**Heat flow**	
Age (Ma)	**Water depth (m)**	**Age (Ma)**	**T [°C]**	**Age [Ma]**	**mW/m²**
0.00	-92.40	0.00	23.00	0.00	87.00
5.00	-50.00	5.00	20.06	2.00	65.00
23.50	-90.00	23.50	20.65	80.00	65.00
38.00	-80.00	38.00	21.28	85.00	68.00
60.00	-161.00	60.00	17.81	90.00	72.00
85.00	-150.00	85.00	20.28	91.00	74.00
91.00	-78.00	91.00	21.91	93.00	79.00
96.00	0.00	96.00	23.36	97.00	90.00
97.00	0.00	97.00	23.50	98.00	98.00
99.00	40.00	99.00	22.71	98.50	105.00
101.00	36.00	101.00	22.86	99.00	115.00
121.00	40.00	108.00	10.00	99.50	120.00
136.00	-29.00	113.00	5.00	100.50	85.00
144.00	0.00	121.00	5.00	125.00	70.00
152.00	-23.00	125.00	5.00	135.00	65.00
158.00	-25.00	135.00	5.00	200.00	65.00
162.00	-50.00	136.00	20.00	237.00	65.00
186.00	0.00	144.00	22.42	240.00	65.00
207.00	-20.00	152.00	21.46	290.00	65.00
231.00	-12.00	158.00	21.05	310.00	65.00
251.00	-50.00	162.00	20.57	330.00	65.00
263.00	-75.00	186.00	20.47		
285.00	-90.00	207.00	21.82		
288.00	-100.00	231.00	21.82		
298.00	-150.00	251.00	18.01		
330.00	-200.00	263.00	9.25		
		285.00	4.10		
		288.00	4.00		
		298.00	4.70		
		330.00	18.00		

Appendix 3.41: Well data sheet for well Moothandella-1 with picks / formation tops.

Well data sheet Moothandella-1	
Location: Queensland, Australia	
Data Sources: QPED, Geoscience Australia	
Well name	**Moothandella-1**
Surface X (km)	706.229
Surface Y (km)	7170.257
Bottom-hole X (km)	706.229
Bottom-hole Y (km)	7170.257
Start Elevation (m) KB	147.74
Total Drill Depth (m)	2729.80
True Vertical Depth (m)	2582.06
Coordinate System	GDA94

Picks / formation tops		
	Well editor	Input table
Pick name	**MD (m)**	**TVD (m)**
Winton Fm	5.60	-142.14
Mackunda Fm	827.84	680.10
Allaru Mdst	978.10	830.36
Toolebuc Fm	1297.84	1150.10
Wallumbilla Fm	1325.88	1178.14
WALLUMBILLA FM (UPPER UNIT)	1325.88	1178.14
WALLUMBILLA FM (LOWER UNIT)	1423.42	1275.68
Cadna-owie Fm	1612.39	1464.65
Wyandra Sandstone Member	1612.39	1464.65
CADNA-OWIE FM (UPPER)	1612.39	1464.65
CADNA-OWIE FM (LOWER)	1669.69	1521.95
Hooray Sst	1708.71	1560.97
Westbourne Fm	1851.66	1703.92
Adori Sst	1969.00	1821.26
Birkhead Fm	1994.00	1846.26
Hutton Sst	2090.93	1943.19
HUTTON SST (UPPER UNIT)	2090.93	1943.19
HUTTON SST (LOWER UNIT)	2197.30	2049.56
Poolowanna Fm	2281.12	2133.38
POOLOWANNA FM (UPPER)	2281.12	2133.38
POOLOWANNA FM (LOWER)	2313.43	2165.69
Cuddapan Fm	2375.92	2228.18
Tinchoo Fm	2404.26	2256.52
Nappamerri Gp	2404.26	2256.52
Gilpeppee Member	2404.26	2256.52
Doonmulla Member	2449.98	2302.24
UPPER DOONMULLA MBR	2449.98	2302.24
LOWER DOONMULLA MBR	2486.56	2338.82
Arrabury Formation	2547.21	2399.47
Wimma Sandstone Member	2547.21	2399.47
Paning Member	2592.02	2444.28
Gidgealpa Group	2648.41	2500.67
Toolachee Fm	2648.41	2500.67
Patchawarra Fm	2655.72	2507.98
Adavale Gp equivalent (Basement)	2674.62	2526.88

Appendix 3.42: Calibration data sheet for Moothandella-1 with thermal maturity and BHT.

Calibration data					
Maturity (vitrinite reflectance)				Horner-corrected BHT	
MD (m)	Mean (%Ro)	Min (%Ro)	Max (%Ro)	MD (m)	T (°C)
283.00	0.39			2729.00	142.00
302.00	0.40				
311.00	0.40				
402.00	0.42				
494.00	0.68				
503.00	0.49				
512.00	0.73				
613.00	0.52				
713.00	0.51				
750.00	0.45				
823.00	0.48				
905.00	0.49				
1052.00	0.51				
1180.00	0.50				
1381.00	0.97				
1481.00	0.52				
1576.00	0.47				
1646.00	0.73				
1762.00	0.85				
1817.00	0.75				
1920.00	0.74				
1999.00	0.71				
2063.00	0.86				
2201.00	0.95				
2301.00	0.95				
2387.00	0.98				
2448.00	1.07				
2469.00	0.92				
2649.00	1.33				
2728.00	1.41				
2538.98	0.81				
2061.67	0.85				
2078.13	0.71				
2139.09	0.85				
2286.00	0.75				
2309.71	0.85				
2331.11	1.05				
2362.20	0.81				
2455.16	1.01				
2462.17	0.74				
2501.80	1.22				
2523.13	0.82				
2583.18	0.83				
2589.28	0.44				
2593.24	1.28				
2648.10	1.38				

Appendix 3.43: Boundary conditions for well Moothandella-1 (PWD, SWIT, and heat flow).

Boundary conditions					
Modified after Deighton & Hill (1998), Deighton et al. (2003)		Calculated after Wygrala (1989), modified after (Ladant & Donnadieu, 2016; Alley et al., 2019)		Calibration based on Basin%RoDL, Burnham (2016)	
Paleo water depth (PWD)		**SWIT (Australia, 27 °)**		**Heat flow**	
Age (Ma)	**Water depth (m)**	**Age (Ma)**	**T [°C]**	**Age [Ma]**	**mW/m²**
0.00	-142.14	0.00	22.00	0.00	80.00
5.00	-83.00	5.00	19.73	2.00	60.00
23.50	-90.00	23.50	20.65	80.00	60.00
38.00	-90.00	38.00	21.18	85.00	65.00
60.00	-180.00	60.00	17.62	90.00	70.00
85.00	-135.00	85.00	20.43	91.00	72.00
91.00	-50.00	91.00	22.19	93.00	75.00
96.00	0.00	96.00	23.36	97.00	81.00
97.00	0.00	97.00	23.50	98.00	85.00
99.00	40.00	99.00	22.71	98.50	90.00
101.00	32.00	101.00	22.86	99.00	95.00
121.00	25.00	108.00	10.00	99.50	100.00
136.00	-50.00	113.00	5.00	100.50	80.00
144.00	0.00	121.00	5.00	125.00	65.00
152.00	-23.00	125.00	5.00	135.00	60.00
158.00	-25.00	135.00	5.00	200.00	60.00
162.00	-35.00	136.00	20.00	237.00	60.00
186.00	0.00	144.00	22.42	240.00	60.00
207.00	-20.00	152.00	21.46	290.00	60.00
231.00	-12.00	158.00	21.06	310.00	60.00
251.00	-50.00	162.00	20.72	330.00	60.00
263.00	-75.00	186.00	20.47		
285.00	-90.00	207.00	21.82		
288.00	-100.00	231.00	21.82		
298.00	-150.00	251.00	18.01		
330.00	-200.00	263.00	9.25		
		285.00	4.10		
		288.00	4.00		
		298.00	4.70		
		330.00	18.00		

Appendix 3.44: Well data sheet for well Paning-1 with picks / formation tops.

Well data sheet Paning-1			**Picks / formation tops**		
Location: South Australia, Australia					
Data sources: PEPS-SA, Geoscience Australia				Well editor	Input table
Well name	**Paning-1**		**Pick Name**	**MD (m)**	**TVD (m)**
Surface X (km)	494.682		Eyre Fm	4.90	-87.08
Surface Y (km)	7002.577		Winton Fm	46.94	-45.04
Bottom-hole X (km)	494.682		Mackunda Fm	852.83	760.85
Bottom-hole Y (km)	7002.577		Allaru Mdst	982.98	891.00
Start Elevation (m) KB	91.98		Toolebuc Fm	1192.99	1101.01
Total Drill Depth (m)	3181.50		Wallumbilla Fm	1203.66	1111.68
True Vertical Depth (m)	3089.52		T1	1292.35	1200.37
			W1	1307.90	1215.92
Coordinate System	GDA94		Cadna-owie Fm	1628.85	1536.87
			Murta Fm	1719.68	1627.70
			McKinlay Mbr	1772.11	1680.13
			Namur Sst	1783.08	1691.10
			Westbourne Fm	1834.29	1742.31
			Adori Sst	1963.52	1871.54
			Birkhead Fm	1991.56	1899.58
			Hutton Sst	2088.49	1996.51
			Poolowanna Fm	2321.05	2229.07
			Nappamerri Gp	2371.95	2279.97
			Toolachee Fm	2851.71	2759.73
			Epsilon Fm	2902.92	2810.94
			Murteree Sh	2962.66	2870.68
			Patchawarra Fm	2978.51	2886.53
			Tirrawarra Fm	3037.03	2945.05
			Merrimelia Fm	3059.89	2967.91
			Mooracoochie Volcs (Basement)	3140.66	3048.68

Appendix 3.45: Calibration data sheet for Paning-1 with thermal maturity and BHT.

Calibration data					
Maturity (vitrinite reflectance)				Horner-corrected BHT	
MD (m)	Mean (%Ro)	Min (%Ro)	Max (%Ro)	MD (m)	T (°C)
310.89	0.29	0.22	0.36	3181.00	139.00
749.80	0.36	0.28	0.45		
932.68	0.36	0.30	0.43		
1078.99	0.43	0.36	0.54		
1527.04	0.45	0.42	0.49		
1676.40	0.54	0.43	0.63		
1767.84	0.65	0.50	0.75		
1834.89	0.60	0.53	0.69		
2005.58	0.61	0.54	0.68		
2075.68	0.70	0.58	0.80		
2212.84	0.70	0.62	0.82		
2304.28	0.57	0.53	0.60		
2304.28	0.80	0.75	0.86		
2398.77	0.72	0.63	0.82		
2862.07	1.13	1.02	1.26		
2913.88	1.15	1.00	1.36		
2987.04	1.23	1.04	1.33		
3048.00	1.33	1.16	1.47		
3063.24	1.33	1.18	1.45		

Appendix 3.46: Boundary conditions for well Paning-1 (PWD, SWIT, and heat flow).

Boundary Conditions					
Modified after Deighton & Hill (1998), Deighton et al. (2003)		Calculated after Wygrala (1989), modified after (Ladant & Donnadieu, 2016; Alley et al., 2019)		Calibration based on Basin%RoDL, Burnham (2016)	
Paleo water depth (PWD)		**SWIT (Australia, 27 °)**		**Heat flow**	
Age (Ma)	**Water depth (m)**	**Age (Ma)**	**T [°C]**	**Age [Ma]**	**mW/m²**
0.00	-87.08	0.00	23.00	0.00	66.00
5.00	-50.00	5.00	20.06	2.00	60.00
23.50	-86.00	23.50	20.69	80.00	60.00
38.00	-82.86	38.00	21.25	85.00	62.00
60.00	-140.00	60.00	18.03	90.00	65.00
85.00	-133.00	85.00	20.45	91.00	68.00
91.00	-50.00	91.00	22.19	93.00	71.00
96.00	0.00	96.00	23.36	97.00	78.00
97.00	0.00	97.00	23.50	98.00	80.00
99.00	10.00	99.00	22.71	98.50	82.00
101.00	10.00	101.00	22.86	99.00	85.00
121.00	25.00	108.00	10.00	99.50	90.00
134.00	-50.00	113.00	5.00	100.50	80.00
136.00	0.00	121.00	5.00	125.00	60.00
144.00	0.00	125.00	5.00	135.00	60.00
152.00	-23.00	135.00	5.00	200.00	60.00
158.00	-25.00	136.00	20.00	237.00	60.00
162.00	-50.00	144.00	22.42	240.00	60.00
186.00	0.00	152.00	21.46	290.00	60.00
231.00	-50.00	158.00	21.05	310.00	60.00
251.00	-50.00	162.00	20.57	330.00	60.00
270.00	-75.00	186.00	19.97		
272.00	-80.00	231.00	21.44		
285.00	-90.00	251.00	18.01		
288.00	-100.00	270.00	4.25		
298.00	-150.00	272.00	4.20		
330.00	-200.00	285.00	4.10		
		288.00	4.00		
		298.00	4.70		
		330.00	18.00		

Appendix 3.47: Well data sheet for well Springfield-1 with picks / formation tops.

Well data sheet Springfield-1		Picks / formation tops		
Location: Queensland, Australia				
Data Sources: QPED, Geoscience Australia			Well editor	Input table
Well name	**Springfield-1**	**Pick Name**	**MD (m)**	**TVD (m)**
Surface X (km)	702.633	Winton Fm	4.60	-130.73
Surface Y (km)	7140.688	Mackunda Fm	896.03	760.70
Bottom-hole X (km)	702.633	Allaru Mdst	1012.24	876.91
Bottom-hole Y (km)	7140.688	Toolebuc Fm	1283.82	1148.49
Start Elevation (m) KB	135.33	Wallumbilla Fm	1312.47	1177.14
Total Drill Depth (m)	2788.90	WALLUMBILLA FM (UPPER UNIT)	1312.47	1177.14
TVD (m)	2653.17	WALLUMBILLA FM (LOWER UNIT)	1427.99	1292.66
		Cadna-owie Formation	1603.55	1468.22
Coordinate System	GDA94	Wyandra Sandstone Member	1603.55	1468.22
		CADNA-OWIE FM (UPPER UNIT)	1603.55	1468.22
		CADNA-OWIE FM (LOWER UNIT)	1666.34	1531.01
		Hooray Sst	1704.14	1568.81
		Westbourne Fm	1848.00	1712.67
		Adori Sst	1956.21	1820.88
		Birkhead Fm	1994.00	1858.67
		Hutton Sst	2089.10	1953.77
		HUTTON SST (UPPER UNIT)	2089.10	1953.77
		HUTTON SST (LOWER UNIT)	2185.42	2050.09
		Poolowanna Fm	2268.02	2132.69
		POOLOWANNA FM (UPPER UNIT)	2268.02	2132.69
		POOLOWANNA FM (LOWER UNIT)	2309.47	2174.14
		Cuddapan Fm	2352.14	2216.81
		Gilpeppee Member	2388.72	2253.39
		Tinchoo Formation	2388.72	2253.39
		Nappamerri Gp	2388.72	2253.39
		Doonmulla Member	2449.98	2314.65
		UPPER DOONMULLA MEMBER	2449.98	2314.65
		LOWER DOONMULLA MEMBER	2487.47	2352.14
		Arrabury Formation	2570.68	2435.35
		Wimma Sandstone Member	2570.68	2435.35
		Paning Member	2625.55	2490.22
		Toolachee Fm	2670.96	2535.63
		Gidgealpa Gp	2670.96	2535.63
		Patchawarra Fm	2687.12	2551.79
		Adavale Gp equivalent (Basement)	2741.37	2606.04

Appendix 3.48: Calibration data sheet for Springfield-1 with thermal maturity and BHT.

Calibration data					
Maturity (vitrinite reflectance)				Horner-corrected BHT	
MD (m)	Mean (%Ro)	Min (%Ro)	Max (%Ro)	MD (m)	T (°C)
247.00	0.40			2788.00	140.00
411.00	0.36				
430.00	0.39				
540.00	0.43				
695.00	0.46				
814.00	0.50				
878.00	0.53				
1079.00	0.38				
1125.00	0.54				
1308.00	0.35				
1527.00	0.52				
1588.00	0.48				
1649.00	0.65				
1651.10	0.84				
1762.00	0.80				
1766.62	0.99				
1816.30	0.88				
1817.00	0.79				
1854.70	0.81				
1893.00	0.80				
1910.50	0.68				
1999.49	0.78				
2006.00	0.80				
2019.60	0.90				
2036.07	0.92				
2054.36	0.92				
2055.60	0.94				
2080.26	0.87				
2085.00	0.88				
2147.30	0.83				
2194.30	0.86				
2237.84	0.99				
2268.32	0.98				
2277.00	0.87				
2305.50	0.84				
2333.24	0.95				
2335.00	0.90				
2336.30	0.80				
2371.95	1.32				
2399.70	2.28				
2447.50	2.22				
2497.20	1.08				
2551.00	1.08				
2555.10	1.13				
2674.32	1.28				
2676.75	1.31				
2685.30	1.38				
2688.80	1.14				
2694.44	1.31				
2696.75	1.22				
2758.45	1.27				
2768.20	1.29				

Appendix 3.49: Boundary conditions for well Springfield-1 (PWD, SWIT, and heat flow).

Boundary conditions					
Modified after Deighton & Hill (1998), Deighton et al. (2003)		Calculated after Wygrala (1989), modified after (Ladant & Donnadieu, 2016; Alley et al., 2019)		Calibration based on Basin%RoDL, Burnham (2016)	
Paleo water depth (PWD)		**SWIT (Australia, 27 °)**		**Heat flow**	
Age (Ma)	**Water depth (m)**	**Age (Ma)**	**T [°C]**	**Age [Ma]**	**mW/m²**
0.00	-130.73	0.00	22.00	0.00	78.00
5.00	-50.00	5.00	20.06	2.00	70.00
35.00	-90.00	35.00	21.21	80.00	70.00
60.00	-176.00	60.00	17.66	85.00	72.00
85.00	-150.00	85.00	20.28	90.00	76.00
91.00	-82.00	91.00	21.87	91.00	78.00
96.00	0.00	96.00	23.36	93.00	79.00
97.00	0.00	97.00	23.50	97.00	81.00
99.00	40.00	99.00	22.71	98.00	82.00
101.00	-32.00	101.00	22.86	98.50	83.00
121.00	25.00	108.00	10.00	99.00	84.00
134.00	-50.00	113.00	5.00	99.50	85.00
144.00	0.00	121.00	5.00	100.50	80.00
152.00	-23.00	125.00	5.00	125.00	72.00
158.00	-25.00	135.00	5.00	135.00	70.00
162.00	-33.00	144.00	22.42	200.00	70.00
186.00	0.00	152.00	21.46	237.00	70.00
198.00	-44.00	158.00	21.05	240.00	70.00
207.00	-50.00	162.00	20.74	290.00	70.00
213.00	0.00	186.00	20.47	310.00	70.00
231.00	-50.00	198.00	20.94	330.00	70.00
251.00	-50.00	207.00	21.52		
263.00	-50.00	213.00	22.53		
270.00	-75.00	231.00	21.44		
272.00	-80.00	251.00	18.01		
285.00	-90.00	263.00	9.50		
288.00	-100.00	270.00	4.25		
298.00	-150.00	272.00	4.20		
330.00	-200.00	285.00	4.10		
		288.00	4.00		
		298.00	4.70		
		330.00	18.00		

Appendix 3.50: Well data sheet for well Warnie East-1 with picks / formation tops.

Well data sheet Warnie East-1			**Picks / formation tops**		
Location: Queensland, Australia					
Data Sources: QPED, Geoscience Australia				Well editor	Input table
Well name	**Warnie East-1**		**Pick Name**	**MD (m)**	**TVD (m)**
Surface X (km)	543.093		Winton Formation	6.20	-113.26
Surface Y (km)	6912.236		Mackunda Formation	569.67	450.21
Bottom-hole X (km)	543.093		Allaru Mudstone	662.03	542.57
Bottom-hole Y (km)	6912.236		Wallumbilla Formation	979.63	860.17
Start Elevation (m) KB	119.46		WALLUMBILLA FORMATION (UPPER UNIT)	979.63	860.17
Total Drill Depth (m)	2612.14		WALLUMBILLA FORMATION (LOWER UNIT)	1121.05	1001.59
True Vertical Depth (m)	2492.68		Cadna-owie Formation	1283.82	1164.36
			Wyandra Sandstone Member	1283.82	1164.36
Coordinate System	GDA94		CADNA-OWIE FORMATION (UPPER UNIT)	1283.82	1164.36
			CADNA-OWIE FORMATION (LOWER UNIT)	1313.69	1194.23
			Hooray Sandstone	1370.08	1250.62
			Murta Member	1370.08	1250.62
			Namur Sandstone Member	1442.92	1323.46
			Westbourne Formation	1510.59	1391.13
			Birkhead Formation	1654.15	1534.69
			Hutton Sandstone	1692.25	1572.79
			NAPPAMERRI GROUP	1725.17	1605.71
			Arrabury Formation	1725.17	1605.71
			Paning Member	1725.17	1605.71
			CALLAMURRA MEMBER	1916.58	1797.12
			Toolachee Formation	2002.54	1883.08
			Gidgealpa Group	2002.54	1883.08
			VOLCANICS	2103.12	1983.66
			Daralingie Formation	2228.09	2108.63
			Roseneath Shale	2259.79	2140.33
			Epsilon Formation	2359.15	2239.69
			Murteree Shale	2406.70	2287.24
			Patchawarra Formation	2449.37	2329.91
			BASEMENT	2582.27	2462.81

Appendix 3.51: Calibration data sheet for Warnie East-1 with thermal maturity and BHT.

Calibration data					
Maturity (vitrinite reflectance)				Horner-corrected BHT	
MD (m)	Mean (%Ro)	Min (%Ro)	Max (%Ro)	MD (m)	T (°C)
192.00	0.40	0.27	0.48	2612.00	154.00
493.80	0.45	0.35	0.54		
731.50	0.41	0.31	0.48		
923.50	0.43	0.34	0.51		
1051.60	0.44	0.35	0.55		
1124.70	0.46	0.39	0.54		
1124.80	0.46	0.39	0.54		
1261.90	0.46	0.41	0.51		
1289.30	0.53	0.43	0.63		
1344.20	0.55	0.47	0.69		
1362.50	0.54	0.46	0.64		
1417.30	0.54	0.45	0.67		
1463.00	0.53	0.43	0.65		
1508.80	0.58	0.45	0.71		
1545.30	0.57	0.45	0.69		
1664.20	0.68	0.52	0.87		
1682.50	0.76	0.59	0.85		
1783.10	0.57	0.50	0.76		
1865.40	0.55	0.50	0.72		
1938.50	0.65	0.52	0.78		
2011.70	1.18	1.06	1.27		
2039.10	1.25	1.06	1.30		
2075.70	1.14				
2094.00	4.55	3.92	5.76		
2185.40	4.75	3.27	6.53		
2212.80	1.79	1.09	2.18		
2240.30	1.64	1.41	1.83		
2377.40	1.59				
2487.20	1.96	0.97	2.43		
2569.50	1.20				

Appendix 3.52: Boundary conditions for well Warnie East-1 (PWD, SWIT, and heat flow).

Boundary conditions					
Modified after Deighton & Hill (1998), Deighton et al. (2003)		Calculated after Wygrala (1989), modified after (Ladant & Donnadieu, 2016; Alley et al., 2019)		Calibration based on Basin%RoDL, Burnham (2016)	
Paleo water depth (PWD)		**SWIT (Australia, 27 °)**		**Heat flow**	
Age (Ma)	**Water depth (m)**	**Age (Ma)**	**T [°C]**	**Age [Ma]**	**mW/m²**
0.00	-113.26	0.00	23.00	0.00	85.00
5.00	-38.00	5.00	20.18	2.00	60.00
16.00	-18.00	16.00	20.68	80.00	60.00
23.50	-50.00	23.50	21.05	85.00	62.00
38.00	-74.00	38.00	21.34	90.00	64.00
60.00	-165.00	60.00	17.77	91.00	66.00
85.00	-92.00	85.00	20.87	93.00	68.00
91.00	-50.00	91.00	22.19	97.00	72.00
96.00	0.00	96.00	23.36	98.00	75.00
97.00	0.00	97.00	23.50	98.50	80.00
99.00	10.00	99.00	22.71	99.00	85.00
101.00	10.00	101.00	22.86	99.50	90.00
121.00	25.00	108.00	10.00	100.50	85.00
134.00	-50.00	113.00	5.00	125.00	65.00
136.00	-16.00	121.00	5.00	135.00	60.00
144.00	0.00	125.00	5.00	200.00	60.00
152.00	0.00	135.00	5.00	237.00	60.00
158.00	0.00	136.00	20.00	240.00	60.00
162.00	-35.00	144.00	22.42	290.00	60.00
186.00	-20.00	152.00	21.69	310.00	60.00
198.00	-50.00	158.00	21.31	330.00	60.00
231.00	-50.00	162.00	20.71		
233.00	-35.00	186.00	20.27		
251.00	-24.00	198.00	20.88		
263.00	-50.00	231.00	21.44		
265.00	-60.00	233.00	21.29		
266.00	-70.00	251.00	18.27		
270.00	-75.00	263.00	9.50		
272.00	-80.00	265.00	9.40		
285.00	-90.00	266.00	9.30		
288.00	-100.00	270.00	4.25		
298.00	-150.00	272.00	4.20		
330.00	-200.00	285.00	4.10		
		288.00	4.00		
		298.00	4.70		
		330.00	18.00		

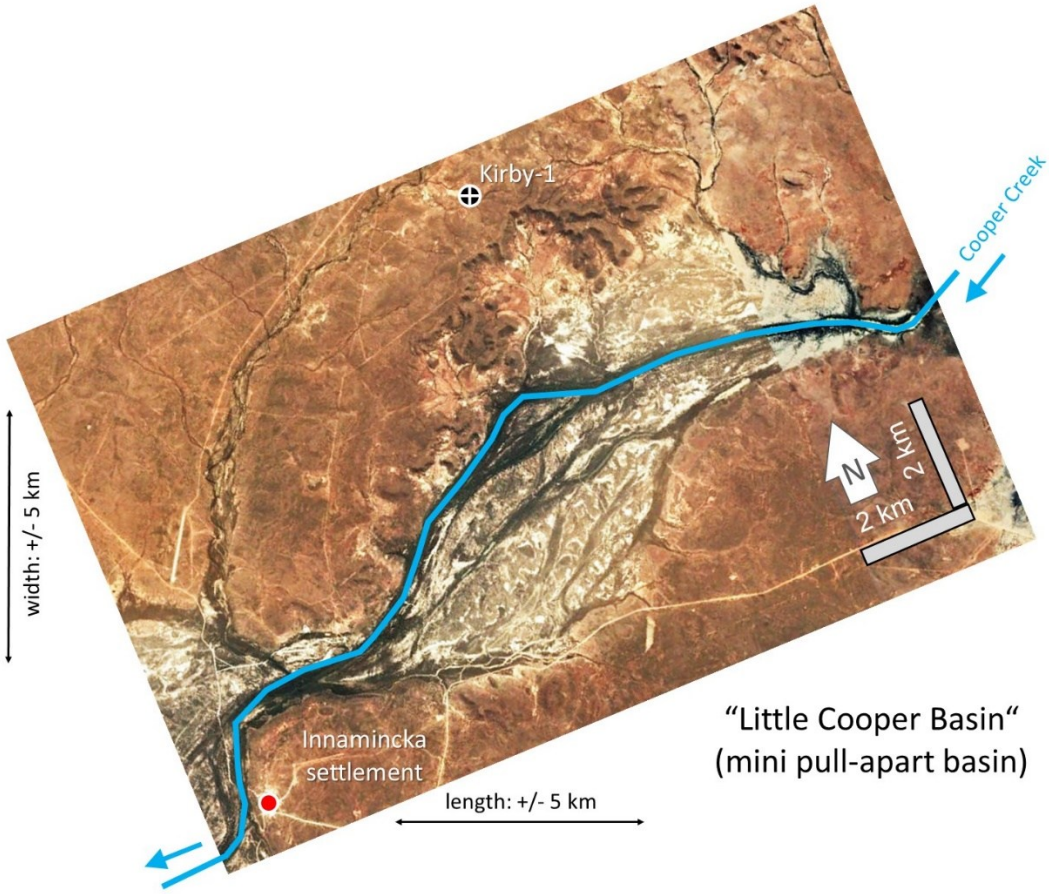

Appendix 3.53: Hey, how are ya? Congratulations, you scrolled down the whole thing! Here is a fractal of the Cooper pull-apart basin for you. This remarkable surficial expression of the tectonic movement in the southwestern domain of the Cooper region is located between the abandoned borehole Kirby-1 and the Innamincka settlement in South Australia. Apparently, a textbook fractal (length: +/- 5 km; width: +/- 5 km) of the underlying rhomboidal Cooper Basin formed exactly in its centre. It is near the location, where the Cooper Creek crosses the GMI Ridge. And even the course of the Cooper Creek is replicating the lazy-s shape of the buried Cooper Basin Master Fault (CBMF, compare **Figure 5.16**). Let’s just call it “Little Cooper Basin” and keep it a secret, OK? No matter how you will go there (by jeep, helicopter, boat, Google Earth, etc), please do me a favour and send me a picture after you found it. Thank you and enjoy the trip! … here are the coordinates: 27°43'1.75"S, 140°48'50.88"E.

CURRICULUM VITAE

Name: **Joschka Röth**
born 26 Jan 1985 in Meckenheim

Address: RWTH Aachen University,
Energy and Mineral Resources Group,
Institute of Geology and Geochemistry of Petroleum and Coal
Lochnerstr. 4-20, 52056 Aachen, Germany

Tel.: +492418095905
Fax: +492418092152
e-mail: joschka.roeth@rwth-aachen.de
joschka.roeth@emr.rwth-aachen.de

Current position

Currently, I am working as project manager at GEO-data GmbH, located in Garbsen, Germany.

https://www.researchgate.net/profile/Joschka_Roeth

Education and academic qualifications

2017 - 2021	PhD candidate (Dr.rer.nat. Geology) – Institute of Geology and Geochemistry of Petroleum and Coal, RWTH Aachen University
04/2014 – 03/2017	M.Sc. in Applied Geosciences – RWTH Aachen University, final mark: 1.4 / 91% / GPA 3.6 / A
10/2010 – 03/2014	B.Sc. in Applied Geosciences – RWTH Aachen University, final mark: 2.1 / 84% / GPA 2.9 / B
02/2008 – 07/2010	University entrance diploma (Abitur) – Oberstufen-Kolleg Bielefeld, major classes: Geology, Chemistry, final mark: 1.9 / 86% / GPA 3.1 / B+
08/2004 – 06/2007	Automotive Management Assistant (dual education / apprenticeship) – Carl-Severing Berufskolleg, Bielefeld, Germany, Mercedes-Benz Neotechnik Göthe & Prior GmbH, Bielefeld, Germany

Professional career

since 03/2021	Project manager – GEO-data GmbH, Garbsen, Germany
06/2017 – 01/2021	Research Associate – Institute of Geology and Geochemistry of Petroleum and Coal, RWTH Aachen University, Aachen, Germany
2019 – 2020	Graduate Research Fellow – Geological Department, Lomonosov Moscow State University, Moscow, Russian Federation
08/2019 – 09/2019	Senior Researcher in the project management team – Innopolis University, Kazan, Republic of Tatarstan, Russian Federation, cooperation with Gazpromneft STC, St. Petersburg, Russian Federation
08/2013 – 05/2017	Geologist/QA Software Tester, Schlumberger GmbH, Aachen, Germany
02/2012 – 07/2016	Research Assistant, several assignments at the Geological Department, RWTH Aachen University, Aachen, Germany

Selected achievements

2021	SPE Giovanni Paccaloni Young Professional Service Award
2020	The Way Ahead Energy Influencer 2020 (SPE International).
2019	SPE Regional Young Member Outstanding Service Award
2017	VAG travel/research grant
2017	Schlumberger Reward of Excellence – Good Job Award 2017
2016	German Section SPE Student Award 2016

Memberships

SPE, Society of Petroleum Engineers,
EAGE, European Association of Geoscientists and Engineers,
AAPG, American Association of Petroleum Geologists,
DGMK e.V., Deutsche Wissenschaftlicher Gesellschaft für Erdöl, Erdgas und Kohle,
VAG e.V., Vereinigung Aachener Geowissenschaftler

Volunteering experience (selection)

since 2021	Regional Liaison Europe, SPE Gaia Sustainability Program
2019 – 2020	Chairperson of the Young Professionals Committee, German Section SPE
2016 – 2019	Volunteer / officer in the Young Professionals Committee, German Section SPE
2015 – 2016	President of the RWTH Aachen University SPE Student Chapter
2001 – 2007	Youth coach and youth spokesperson, Automobilclub Bielefeld e.V.

Aachen, 17.12.2021

Theses, abstracts and publications:

Theses:

Doctoral thesis, summa cum laude (2020): “Thermo-tectonic evolution and source rock maturation in the Gippsland Basin (offshore Victoria) and the central Eromanga Basin (Cooper sub-region), Australia”, supervisor: Univ.-Prof. Dr. Ralf Littke (ralf.littke@emr.rwth-aachen.de, +49 241 80-95748).

Master thesis (2017): „Lithospheric modeling and thermal history of the Gippsland Basin (Victoria, SE Australia)”, supervisor: Univ.-Prof. Dr. Ralf Littke.

Bachelor thesis (2014): “Investigating Roman sediments in Baelo Claudia (southern Spain) with sedimentological and geophysical methods”, supervisor: Univ.-Prof. Dr. Klaus Reicherter (k.reicherter@nug.rwth-aachen.de, +49 241 80-95722).

Articles currently under review:

Röth, J., Littke, R. (202X). Down under and under cover: frequent hydrothermal activity and strike-slip tectonics in the Cooper Basin and central Eromanga Basin confirmed by subsidence history analysis and basin modelling. Submitted to MDPI Geosciences..

Röth, J., Baniasad, A., Froidl, F., Ostlender, J., Boreham, C., Hall, L. Hall, Littke, R. (202X). The Birkhead and Murta formations - organic geochemistry and organic petrography of Mesozoic fluvio-lacustrine source rocks in the Eromanga Basin, central Australia. Submitted to International Journal of Earth Sciences.

Peer-reviewed articles:

Röth, J., Parent, A., Warren, C., Hall, L., Palmowski, D., Koronful, N., Husein, S.S., Sachse, V., Littke, R. (2021). Lithospheric evolution, thermo-tectonic history and source-rock maturation in the Gippsland Basin, Victoria, southeastern Australia. Australian Journal of Earth Sciences. https://doi.org/10.1080/08120099.2021.1938219.

Froidl, F., Littke, R., Baniasad, A., Zheng, T., Röth, J., Böcker, J., Hartkopf-Fröder, C., Strauss, H. (2021). Peculiar Berriasian "Wealden" Shales of Northwest Germany: Organic facies, depositional environment, thermal maturity and kinetics of petroleum generation. Journal of Marine and Petroleum Geology, Vol. 124. https://doi.org/10.1016/j.marpetgeo.2020.104819.

Shekarifard, A., Daryabandeh, M., Rashidi, M., Hajian, M., Röth, J. (2019, corresponding author). Petroleum geochemical properties of the oil shales from the Early Cretaceous Garau Formation, Qalikuh locality, Zagros Mountains, Iran. International Journal of Coal Geology, 206, pp. 1-18, ISSN 0166-5162. https://doi.org/10.1016/j.coal.2019.03.005.

Ghazwani, A., Littke, R., Uffmann, A.K., Baniasad, A., Röth, J. (2018, corresponding author). Petroleum generation and storage in the Pennsylvanian coal-bearing strata of the Münsterland Basin, Western Germany: 3D basin modelling approach. Zeitschrift der Deutschen Gesellschaft für Geowissenschaften, 169(4), pp. 475-494(20).https://doi.org/10.1127/zdgg/2018/0158.

Barroso, P. G. S., Giner-Robles, J. L., Reicherter, K., Pascua, M. Á. R., Grützner, C., Jiménez, I. G., ... & Röth, J. (2016). Los terremotos antiguos del conjunto arqueológico romano de Baelo Claudia (Cádiz, Sur de España): Quince años de investigación arqueosismológica (Ancient earthquakes in the Roman city of Baelo Claudia (Cádiz, South of Spain): Fifteen years of archaeoseismology research). Estudios geológicos, 72(1), 8. DOI: 10.3989/egeol.42284.392

Extended abstracts:

Röth, J., Karpov, Y.A., Kalmykov, A.G., Beseleva, K.V., Littke, R., Kalmykov, G.A. (2020). Thermo-tectonic evolution and numerical petroleum system modeling of one of the oil fields on Krasnoleninsky Arch, SW West Siberian Basin. SPE Russian Petroleum Technology Conference, 26-29 October 2020, Skolkovo, Moscow, Russian Federation. SPE-201959. https://www.spe.org/events/en/2020/conference/20rptc/russian-petroleum-technology-conference.html.

Röth, J., Grützner, C., Mathes-Schmidt, M., Jimenez Garcia, I., Reicherter, K., Silva, P. G., Rojas Pichardo, F. J. (2015). The Baelo Claudia tsunami hypothesis - results from a multi-method sediment analysis of late Roman deposits (Gibraltar Strait, Southern Spain). Miscellanea INGV, 27 Abstracts Volume 6th International INQUA Meeting on Paleoseismology, Active Tectonics and Archaeoseismology. 19 | 24 April 2015, Pescina, Fucino Basin, Italy. https://www.researchgate.net/publication/308476495.

Hürtgen, J., Jomard, H., Baize, S., Thomas, J., Reicherter, K., Röth, J., Cushing, M., Cinti, F. R. (2015). The Southern Upper Rhine Graben - A paleoseismological pre-site survey in the Freiburg area. Miscellanea INGV, 27 Abstracts Volume 6th International INQUA Meeting on Paleoseismology, Active Tectonics and Archaeoseismology. 19 | 24 April 2015, Pescina, Fucino Basin, Italy. https://www.researchgate.net/publication/282903924.

Conference abstracts:

Röth, J., Baniasad, A., Littke, R., Hall, L.S., Boreham, C. (2019). Organic geochemistry and organic petrography of the Birkhead and Murta formations, Eromanga Basin, central Australia. Conference abstract & poster. 29th International Meeting on Organic Geochemistry, Gothenburg, Sweden. DOI: 10.3997/2214-4609.201902812.

Röth, J., Littke, R. (2019). Geochemical and petrographical analysis of the Mesozoic Birkhead and Murta source rock formations, Eromanga Basin, Central Australia. Conference abstract & oral presentation. GeoMünster, 22-25 September 2019, Münster, Germany.

Röth, J., Littke, R., Hall, L.S., Boreham, C. (2018). 3D basin modeling of the Cooper-Eromanga Basin, Australia. Conference abstract & poster. German Section SPE annual Student Technical Conference STC 2018, 8-9 November 2018, Freiberg, Germany.

Frohn, V., Littke, R., Uffmann, A., Röth, J., (2018). Thermal history and petrophysical properties of potential nuclear waste repositories: a numerical modeling study of Mesozoic shales, Lower Saxony Basin. Conference abstract & poster. German Section SPE annual Student Technical Conference STC 2018, 8-9 November 2018, Freiberg, Germany.

Röth, J., Parent, A., Warren, C., Palmowski, D., Littke, R. (2018). Application of crustal thickness inversion for thermal history modeling in the Gippsland Basin, Victoria, Southeastern Australia. Conference abstract & oral presentation. GeoBonn, 2-6 September 2018, Bonn, Germany.

Röth, J., Sachse, V., Parent, A., Warren, C., Palmowski, P., Littke, R. (2017). Crustal evolution and heat flow history of the Gippsland Basin, Victoria, southeastern Australia. Conference abstract & poster. German Section SPE annual Student Technical Conference STC 2017, 8-10 November 2017, Clausthal, Germany.

Röth, J. (2016). Advanced crustal modeling, basement-geometry update and heat flow modeling of the Gippsland Basin (Victoria, SE Australia) by including potential fields (Grav/Mag).

Conference abstract & oral presentation. International Youth Scientific and Practical Congress "Oil & Gas Horizons VIII", Gubkin University, Moscow, Russian Federation.

Röth, J. (2016). Advanced crustal modeling of the Gippsland Basin (Australia). Conference abstract & oral presentation. German Section SPE annual Student Technical Conference STC 2016, 3-4 November 2016, Wietze, Germany.

Baika, K., Psarogiannis, A., Tzigounaki, A., Karamaliki, N., Sarris, A., Vött, A., Fischer, P., Röth, J., Reicherter, K., Dumas, V., Papadopoulus, N.G., Cantoro, G., Manataki, M., Cuenca-Garcia, C., Kalayci, T., Simon, F.X., Donati, J.C., Simirdanis, K., Kalogeropoulos, K., Chrysocheri, E. (2016). Interdisciplinary survey on the maritime installations of ancient Rithymna Archaeological and Geoarchaeological investigations. Conference abstract & poster. 4th Meeting for the Archaeological Work in Crete – 2016.

Sharata, S., Röth, J., Reicherter, K. (2015). Basin evolution in the North African Platform. Conference abstract & poster. Deformation Mechanisms, Rheology and Tectonics (DRT), RWTH Aachen University, 7-11 September 2015, Aachen, Germany.

Hürtgen, J., Röth, J., Jomard, H., Thomas, J., Reicherter, K., Baize, S., Cushing, M., Cinti, F. R. (2015). The Southern Upper Rhine Graben - A paleoseismological challenge - intraplate trench site selection. Conference abstract. Deformation Mechanisms, Rheology and Tectonics (DRT), RWTH Aachen University, 7-11 September 2015, Aachen, Germany.

Kettermann, M., Röth, J., Urai, J. L. (2014). How failure mode transition affects structural complexity in extensional graben settings: insights from excavated scale models. Geometry and Growth of Normal Faults. The Geological Society London, 23rd - 25th June, 2014.

Kettermann, M., Röth, J., Urai, J. L. (2013). Failure mode transition as result of effective stress - insights from analogue modeling using hemihydrate powder and sand. Conference Abstract: Deformation Mechanisms, Rheology and Tectonics (DRT). KU Leuven 16-18 September 2013, Leuven, Belgium.

Additional projects:

Substantial contribution to mapping of active faults for: Hürtgen, J. (2017). The first paleoseismic database of Germany and adjacent Regions PalSeisDB v1. 0 (Doctoral dissertation, Rheinisch-Westfälische Technische Hochschule Aachen). Info: https://www.bgr.bund.de/DE/Themen/Erdbeben-Gefaehrdungsanalysen/Projekte/Ingenieurseismologische_Gefaehrdungsanalysen/laufend/palseisdb.html;jsessionid=B6A0C0331AA0BE5E1D9D9E8B695216FC.1_cid292?nn=5057776.